Deposition of composite coatings by electrochemical means

Ilaria Corni

A thesis submitted in partial fulfilment of the requirements for the degree of

Doctor of Philosophy

of the

University of London

Department of Materials

Imperial College London

Abstract

This thesis describes the development and characterisation of a range of single-phase and composite coatings on stainless steel substrates using electrochemical processing routes.

Electrodeposition and electro co-deposition have been applied to deposit Ni, Ni-Al_2O_3 and Ni-Al films. For electrodeposition of pure Ni the substrate preparation was critical: this was optimised by applying different mechanical and chemical treatments to increase the substrate/coating adhesion through a mechanical interlocking mechanism. The optimal conditions for Ni deposition from a nickel sulphate bath were then determined. Subsequently, Al_2O_3 particles were added to the plating bath and the influence of the process variables (current density, Al_2O_3 particle concentration and size) on the amount of Al_2O_3 co-deposited with Ni was studied. The addition of Al_2O_3 modified both the microstructure and the crystallinity of the Ni matrix and increased the coating micro-hardness compared to pure Ni.

Polyetheretherketone (PEEK) and nano-Al_2O_3 coatings were successfully deposited on to stainless steel substrates by electrophoretic deposition (EPD) from particulate suspensions in ethanol. The same method was also applied to produce PEEK-nano-Al_2O_3 composite coatings for the first time on stainless steel with controlled composition; this composition could be tailored by varying the starting suspension concentration. Using an electric field of 15 $V \cdot cm^{-1}$ and deposition times of 3 min PEEK-nano-Al_2O_3 composite coatings of ~ 40 μm thickness could be produced from suspensions containing 4 wt.% PEEK and 2 wt.% nano-Al_2O_3. The zeta potentials of the PEEK particles, the nano-Al_2O_3 particles and the mixed (diphasic) suspensions in ethanol were determined. TEM observation of particles in suspension was used together with zeta potential data to demonstrate the electrostatic interaction between PEEK and nano-Al_2O_3 particles in ethanol and to explain the EPD mechanism for this system. The deposition yield was found to increase with increasing deposition time and difference of potential applied during EPD. The deposition yield data were employed to produce a neural network model that was able to predict the yield from information about the initial deposition conditions. A heat treatment at 343°C for 30 minutes was needed to densify the coating and to increase the substrate/coating adhesion of pure PEEK and PEEK-nano-Al_2O_3 films. The addition of nano-Al_2O_3 particles decreased the melting temperature and the decomposition temperature compared to pure PEEK. Stainless steel substrates coated with the composite films exhibited better corrosion resistance in chloride environment than uncoated substrates. However composite coatings with high Al_2O_3 content (60-80 wt.%) presented poor mechanical properties; it was demonstrated that by decreasing the Al_2O_3 content to 30 wt.% the mechanical properties, in particular hardness, improved.

The results of the project demonstrated that metal-ceramic and polymer-ceramic composite coatings can be developed on metallic substrate by a smart combination of electrochemical methods.

To my parents, my granny Bruna
and David for their love and support.
To my little Speedy wherever she is.

Acknowledgements

First of all I would like to thank Marie Curie project grant (MEST-CT-2004-514667) for the financial support during these three years and my three advisors Aldo R. Boccaccini, Mary P. Ryan and E. Jane Minay for their guidance and support.

Moreover, I would like to thank all the people who contributed to this research with their help, support, discussion and experience, in no particular order: Eva Garcia Lecina, Ivelin Valkov, Marcello Romagnoli, Paolo Veronesi, Oana Bretcanu, Saša Novak, Katja König, Mahmoud Ardakani, Martin Jackson, Rees Rawlings and Qizhi Chen. In particular, I would like to thank Richard Sweeny for his help and friendship and Richard Chater for his great support, for the long and interesting discussions about science (and not) and would also like to mention that an interesting part of this research would not have been done without his help and interest.

Finally a big THANK YOU goes to everyone that shared with me this path, in good and bad times: David for his love, support and immense patience, my parents and my family who, even partially understanding my life-choices, always supported, comforted and encouraged me to go on in this new life, my "sisters": Oana, Juliana, Xanthippi and Olga for their friendship and for being there, the entire research group, the numerous visitors met during these three years (in particular Nico) and all the other people I shared time with: Luca, Ivan, Valerio, Giulia, Anna, Cristina, Thiana, Fatty, Ursula, Simon and Eila.

Table of Contents

Chapter 1. Introduction 19

Chapter 2. Literature review 21

2.1 Electrochemical deposition of metals 21

2.1.1 Introduction 21

2.1.2 Electrodeposition from a solution with more than one ion 22

2.1.3 Current density and limiting current density 23

2.1.4 Electrochemical deposition of nickel 24

2.2 Electrochemical co-deposition 32

2.2.1 Introduction 32

2.2.2 Experimental parameters 33

2.2.3 Mechanisms for electro co-deposition 39

2.2.4 Deposition of nickel composite coatings 42

2.2.4.1 Electrochemical co-deposition of Ni-Al_2O_3 composite coatings 42

2.2.4.2 Electrochemical co-deposition of Ni-Al composite coatings 53

2.3 Electrophoretic deposition 55

2.3.1 Introduction 55

2.3.2 Properties of charged particles 56

2.3.3 Properties of the suspension 57

2.3.4 EPD parameters 60

2.3.5 Mechanisms for the formation of deposits by EPD 61

2.3.6 Applications of EPD 65

2.3.6.1 Alumina coatings deposited by EPD 66

2.3.6.2 PEEK coatings deposited by EPD 67

2.3.6.3 PEEK composites 69

2.4 Summary 72

Chapter 3. Characterisation techniques 73

3.1 Scanning electron microscopy 73

3.2 Transmission electron microscopy 73

3.3 Focused ion beam-secondary ion mass spectrometry (FIB-SIMS) 74

3.4 X-ray diffraction (XRD) analysis 74

3.5 White light interferometer (Zygo®) 75

3.6 Thermal gravimetric analysis and differential thermal analysis 78

3.7 Differential scanning calorimetry analysis (DSC) 78

3.8 Heating microscopy 78

3.9 Particle size measurements 79

3.10 Zeta potential measurements 79

3.11 Quantitative image analysis 81
3.12 Scratch test analysis 83
3.13 Micro-hardness analysis 83
3.14 Tape test 84
3.15 Corrosion resistance 85
3.16 Compressive strength test 85
3.17 Artificial neural network modelling 86

Chapter 4. Depositions of nickel composite coatings 89
4.1 Materials 89
4.2 Instruments and methods 90
4.3 Surface preparation 92
4.3.1 Mechanical treatments 92
4.3.2 Chemical treatments 106
4.3.3 Tape test 108
4.3.4 Summary 109
4.4 Electrochemical deposition of nickel coatings 109
4.4.1 Composition of the plating solution 110
4.4.2 Potentiostatic experiments using a two-electrode set up 110
4.4.3 Galvanostatic experiments 118
4.4.4 Temperature effect 122
4.4.5 Variables affecting the hydrogen pitting 123
4.4.6 Microstructure and crystallinity of the coatings 124
4.5 Electro co-deposition of nickel-alumina composite coatings 130
4.5.1 Characterization of the alumina powders 132
4.5.2 Galvanostatic experiments 134
4.5.3 Microstructure of Ni-Al_2O_3 composite coatings 135
4.5.4 Three-dimensional-reconstruction of a composite coating using FIB-SIMS 145
4.5.5 Effect of deposition parameters on the amount of Al_2O_3 co-deposited in nickel films 149
4.5.6 Crystallinity of Ni-Al_2O_3 composite coatings 153
4.5.7 Micro-hardness 157
4.5.8 Corrosion resistance 159
4.5.9 Tape test 164
4.6 Electro co-deposition of nickel-aluminium composite coatings 165
4.6.1 Characterizations of the aluminium powder 165
4.6.2 Microstructure of Ni-Al composite coatings 166
4.7 Electro co-deposition mechanism 168
4.8 Summary 170

Chapter 5. Electrophoretic deposition of PEEK-nano-Al_2O_3 composite coatings **172**

5.1 Materials 172

5.2 Instruments and methods 172

5.3 Deposition of PEEK coatings 175

5.3.1 Characterisation of the PEEK powder 175

5.3.2 EPD parameters for PEEK deposition 180

5.3.3 Current intensity 185

5.3.4 Microstructure of PEEK coatings 185

5.3.5 Heat-treatment of PEEK coatings 186

5.4 Deposition of alumina coatings 191

5.4.1 Characterisation of the nano-Al_2O_3 191

5.4.2 EPD of alumina coatings 194

5.4.3 Current intensity 195

5.4.4 Microstructure of alumina coatings 196

5.5 Deposition of PEEK-Al_2O_3 composite coatings 197

5.5.1 Zeta potential measurement of the combined suspensions 197

5.5.2 EPD parameters for deposition 202

5.5.3 Current intensity 202

5.5.4 Weight increase during EPD 204

5.5.5 Application of an Artificial Neural Network for optimising EPD parameters 208

5.5.6 Ratio PEEK-alumina in the coatings 213

5.5.7 Microstructure of the composite coatings 218

5.5.8 Thermal properties 221

5.5.9 Heat-treatment of the composite coatings 224

5.5.10 Mechanical properties 232

5.5.11 Corrosion Resistance 239

5.5.12 Tape test 241

5.6 Summary 244

Chapter 6. Conclusions and Further work **245**

References **251**

Appendix 1. Mechanical treatments on stainless steel substrates employed for nickel deposition. 264

Appendix 2. Chemical treatments on stainless steel substrates employed for Ni deposition 270

Appendix 3. 3D reconstruction of a Ni-Al_2O_3 composite coating 276

Appendix 4. List of conference presentations and publications originated from this work 279

List of Tables

Table 2.1 Composition of nickel sulphate baths [33].

Table 2.2 Composition of the nickel sulphamate bath.

Table 2.3 Composition of the all-nickel chloride bath [33].

Table 2.4 Composition of the mixed sulphate-chloride bath [32].

Table 2.5 Composition of the two main nickel fluoborate baths [32].

Table 2.1 Compositions of alkaline baths employed for nickel deposition [32].

Table 2.7 Results obtained from the electro co-deposition of α-Al_2O_3 and γ-Al_2O_3 from a copper sulphate solution (adapted from table reported by Stojak et al. [16]).

Table 2.8 Some examples of the conditions used to electro co-deposit nickel and other particles from aqueous solutions.

Table 2.9 Conditions used to electro co-deposit nickel-alumina composite coatings.

Table 2.10 Conditions employed in electro co-deposition and sediment co-deposition to produce Ni-Al composite films.

Table 2.11 Principal differences between electroplating and electrophoretic deposition (after ref. [21]).

Table 2.12 Conditions used to deposit alumina coatings by EPD

Table 3.1 Summary of the data employed to measure the zeta potential of different suspensions.

Table 3.2 Classification of the adhesion test result (adapted from the ASTM D 3359-04 method)

Table 4.1 Roughness values for the 0.2 mm thick stainless steel substrate as-received.

Table 4.2 Roughness values for 0.2 mm thick stainless steel substrate ground with 800 grit SiC paper.

Table 4.3 Roughness values for the 0.2 mm thick stainless steel AISI 316L substrate in as-received condition and after grinding with 800 grit SiC paper.

Table 4.4 Roughness values obtained on 2 mm thick AISI 316L samples with different surface treatments and results of the Ni depositions.

Table 4.5 Roughness values of as-received and ground with 800 grit SiC paper samples cut from the same stainless steel sheet.

Table 4.6 Roughness values of as-received and ground with 800 grit SiC paper samples before and after chemical etching with 10% H_2SO_4 for 30 s.

Table 4.7 Roughness values of as-received and ground with 800 grit SiC paper samples before and after chemical etching with 18% HCl for 5 min.

Table 4.8 Roughness values of as-received and ground with 800 grit SiC paper samples before and after chemical etching with 25% HNO_3 for 10 s.

Table 4.9 Ranges in which the parameters were varied for nickel deposition.

Table 4.10 Composition of the bath used for nickel deposition.

Table 4.11 Ratio between the intensity of the XRD peaks and the main peak (111) for nickel films deposited applying different current densities.

Table 4.12 Set of conditions varied to understand how particle size, concentration and current density influence the amount of Al_2O_3 co-deposited in the Ni films.

Table 4.13 Size distribution of the sub-micron-Al_2O_3 particles in water.

Table 4.14 Intensity of Ni crystallographic peaks normalised to the (111) peak for films deposited using different current densities and from baths containing different amounts of Al_2O_3.

Table 4.15 Grain sizes of Ni deposited applying different current densities from baths containing different amounts of nano or sub-micron-Al_2O_3 particles calculated using Sherrer equation.

Table 4.16 Electrochemical parameters obtained from the polarisation curves of stainless steel, pure Ni

films, Ni-sub-micron-Al_2O_3 and Ni-nano-Al_2O_3 films in 0.1 M H_2SO_4 solution.

Table 5.1 Data for the particle size distribution of the PEEK powder in ethanol.

Table 5.2 Summary of the parameters investigated and the ranges in which they have been varied for EPD of PEEK particles.

Table 5.3 Equations that represent the kinetic of EPD from 3P-3A suspensions a) Logarithmic trends fitting the weight increase vs time at constant voltage and b) the same equation also as a function of the voltage.

Table 5.4 Equations representing the kinetic of EPD from 4P-2A suspensions a) Logarithmic trends fitting the weight increase vs time at constant voltage and b) the same equation also as a function of the voltage.

Table 5.5 Training data set for the 3P-3A suspension.

Table 5.6 Training data set for the 4P-2A suspension.

Table 5.7 Validation data set used to test the model for the 3P-3A system.

Table 5.8 Validation data set used to test the model for the 4P-2A system.

Table 5.9 The runs and results for the optimization of the NN independent parameters.

Table 5.10 Theoretical concentration (wt.% and vol.%) of PEEK and nano-Al_2O_3 in the coatings calculated by equation 5.7 if the suspension ratio was maintained during EPD. Considering the PEEK density to be 1.3 $g \cdot cm^{-3}$ [221] and the nano-Al_2O_3 density to be 4 $g \cdot cm^{-3}$ [222].

Table 5.11 Concentrations (wt.% and vol.%) of PEEK and nano-Al_2O_3 in coatings deposited applying 20, 30 and 40 V from the 3A-3P suspension for the indicated deposition times.

Table 5.12 Concentrations (wt.% and vol.%) of PEEK and nano-Al_2O_3 in the coatings deposited applying 20, 30 and 40 V from the 4P-2A suspension for the indicated deposition times.

Table 5.13 Concentrations (wt.% and vol.%) of PEEK and nano-Al_2O_3 in the coatings deposited applying 20 V, 30 V and 40 V from the 5P-1A suspension for the indicated deposition times.

Table 5.14 Values of A_C%, P_C%, A_S% and P_S% obtained experimentally for the two suspensions investigated.

Table 5.15 DSC data of pure PEEK and PEEK-nano-Al_2O_3 composites during the heating cycle.

Table 5.16 Degradation temperatures for PEEK-nano-Al_2O_3 composites with different compositions.

Table 5.17 Micro-hardness results obtained for the PEEK and PEEK-Al_2O_3 (3P-3A, 4P-2A and 5P-1A suspensions) composite coatings.

Table A.1 Roughness values for the 2 mm thick stainless steel AISI 316L in as-received condition.

Table A.2 Roughness values for the 2 mm thick stainless steel substrate polished with 1 μm diamond paste.

Table A.3 Values for the 2 mm thick stainless steel substrate polished with 3 μm diamond paste.

Table A.4 Roughness values for the 2 mm thick stainless steel ground with 800 grit SiC paper.

Table B.1 Roughness values of as-received stainless steel samples before and after chemical etching with 10% H_2SO_4 for 30 s.

Table B.2 Roughness values of stainless steel AISI 316L samples ground with 800 grit SiC paper before and after chemical etching with 10% H_2SO_4 for 30 s.

Table B.3 Roughness values of the as-received stainless steel AISI 316L samples before and after chemical etching with 18% HCl for 5 min.

Table B.4 Roughness values of the stainless steel sample ground with 800 grit SiC paper before and after chemical etching with 18% HCl for 5 min.

Table B.5 Roughness values of the as-received stainless steel AISI 316L samples before and after chemical etching with 25% HNO_3 for 10 s.

Table B.6 Roughness values of the stainless steel sample ground with 800 grit SiC paper before and after

chemical etching with 25% HNO_3 for 10 s.

Table C.1 List of all the FIB-SIMS images used for the 3D reconstruction of a Ni-sub-micron-Al_2O_3 composite coatings.

List of Figures

Figure 2.1 Electrolytic cell for the deposition of the metal M from a solution of the salt MA.

Figure 2.2 Trend of the variation of the limiting current density with the potential applied.

Figure 2.3 SEM images of a) a nickel film grown around a glass particle. The deposition started with the glass particle settled on the cathode (white circle) but the particle moved up by the metal deposition underneath the particle. b) Metal growth profile around a conductive graphite particle as if the particle was part of the electrode (redrawn from ref. [49]).

Figure 2.4 Interactions between a particle and cationic surfactants.

Figure 2.5 Schematic representation of the mechanism of particle co-deposition proposed by Buelens and Celis et al. (redrawn from ref. [58]).

Figure 2.6 SEM micrographs of a) nickel coating and b) Ni-Al_2O_3 composite coatings electro co-deposited from a Watts bath containing 100 g/l of Al_2O_3 particles with size < 1 μm and applying a current density of 20 $mA \cdot cm^{-2}$ (redrawn from ref. [97]).

Figure 2.7 SEM micrographs of a) nickel coating and b) Ni-Al_2O_3 composite coatings electro co-deposited from a Watts bath containing 20 g/l of nano-Al_2O_3 particles and applying a current density of 20 $mA \cdot cm^{-2}$ (redrawn from ref. [100]).

Figure 2.8 Surface morphology of the as-deposited Ni-28Al composite film obtained by Zhou et al. (redrawn from ref. [122]).

Figure 2.9 Schematic representation of the cell used in electrophoretic deposition when the charged particles in suspension are positively charged (redrawn from ref. [23]).

Figure 2.10 Scheme of the double layer surrounding a charged particle and variation of the electric potential from the particle surface to the bulk of the suspension (modified from ref. [17]).

Figure 2.11 Schematic representation of the electrical double layer distortion and thinning mechanism (redrawn from ref. [22]).

Figure 2.12 Basic chemical structure for polyetheretherketone (PEEK) (redrawn from ref. [9]).

Figure 3.1 Schematic representation of Zygo® Interferometer (redrawn from ref. [215]).

Figure 3.2. Schematic representation of the light paths inside the white light interferometer.

Figure 3.3 Schematic representation of rms on a sample (redrawn from ref. [215]).

Figure 3.4 Schematic representation of Ra on a sample (redrawn from ref. [215]).

Figure 3.5 Examples of surface profile and the corresponding bearing ratio plot (redrawn from ref. [215]).

Figure 3.6 Scheme explaining how the bearing ratio plots are obtained (redrawn from ref. [215]).

Figure 3.7 Images of a) the ESA probe and b) the configuration of the outer electrode and the main electrode during the experiments (redrawn from ref. [219]).

Figure 3.8 Images of a) the outer electrode and b) the main electrode of the ESA probe showing the active metal part (redrawn from ref. [219]).

Figure 3.9 Matlab© images of the program and outputs used to determine the vol.% of Al_2O_3 in the films deposited. a) the program, b) cropped image, c) histogram of the scale of grey in the image and d) black and white image from which the percentages are calculated.

Figure 4.1 Schematic representation of the two electrode cell set up.

Figure 4.2 Images of the experimental set up employed for the deposition of nickel and nickel composite coatings.

Figure 4.3 Optical microscopy picture of the surface of 0.2 mm thick stainless steel substrate in as-received condition showing aligned scratches.

Figure 4.4 Comparison between the bearing ratio plots of the stainless steel 0.2 mm thick substrate in as-received state.

Figure 4.5 3D plots of a) point 1, b) point 4 and c) the major area of the surface of the 0.2 mm thick stainless steel substrate in as-received condition. Each point has an area of 1.46 mm x 1.10 mm and the height of the block is 80 μm.

Figure 4.6 Optical microscope picture of the 0.2 mm thick stainless steel surface ground with 800 grit SiC paper showing aligned scratches.

Figure 4.7 Comparison between the bearing ratio plots of the 0.2 mm thick stainless steel surface ground with 800 grit SiC paper. The surface roughness was uniform in the whole sample.

Figure 4.8 3D plot of a representative point of the 0.2 mm thick stainless steel surface ground with 800 grit SiC paper. This area is 1.46 mm x 1.10 mm and the height of the block is 80 μm.

Figure 4.9 Comparison between the bearing ratio plots of the surface of the 0.2 mm thick stainless steel as-received and ground with 800 grit SiC paper showing that the sample ground was rougher than the one as-received.

Figure 4.10 Nickel coating deposited on the 0.2 mm thick as-received stainless steel AISI 316L substrate ultrasonically cleaned in acetone for 5 min. The deposit peeled off from the substrate.

Figure 4.11 SEM image of the interface nickel/stainless steel. The nickel was deposited on stainless steel substrate ground with 800 grit SiC paper and cleaned with acetone and water. The adherence between the two materials was not uniform across the sample.

Figure 4.12 SEM image of the interface nickel/stainless steel on a substrate ground with 800 grit SiC paper and ultrasonically cleaned in acetone for 5 min. The interface is straight and well-defined and the stainless steel/coating adhesion seemed good and uniform.

Figure 4.13 Schematic representations of two different surfaces with the same rms [216]

Figure 4.14 SEM image of the separation between the substrate and the nickel coating deposited from a nickel sulphate bath showing that the deposition started inside the scratches.

Figure 4.15 Comparison between the bearing ratio plots of the 2 mm thick stainless steel surfaces as-received, ground with 800 grit SiC paper, polished with 1μm or 3 μm diamond paste.

Figure 4.16 SEM micrographs of the interface stainless steel/nickel showing a) homogeneous and uniform interface coating/substrate and b) that the substrate surface roughness was maintained in the coating (arrow). The stainless steel as-received was ultrasonically cleaned in acetone for 5 min.

Figure 4.17 Residual depths of three scratch tracks carried out on a nickel coating deposited on the as-received substrate using a Rockwell diamond indenter with radius of 100 μm.

Figure 4.18 Residual depths of three scratch tracks carried out on nickel coating deposited on the substrate ground with 800 grit SiC paper using a Rockwell diamond indenter with 100 μm radius.

Figure 4.19 Residual depths of three scratch tracks carried out on a nickel coating deposited on the as-received substrate using a Rockwell diamond indenter with radius of 10 μm.

Figure 4.20 Residual depths of three scratch tracks carried out on a nickel coating deposited on the substrate ground with 800 grit SiC paper using a Rockwell diamond indenter with radius of 10 μm

Figure 4.21 Optical micrographs of the scratch tracks carried out on nickel coatings deposited on a) and c) the as-received substrate and b) and d) the substrate ground with 800 grit SiC paper using a Rockwell diamond indenter with a) and b) radius of 100 μm or c) and d) radius of 10 μm.

Figure 4.22 Images of nickel coatings deposited on stainless steel ground with 800 grit SiC paper after tape test a) 0% detachment and b) < 5% detachment as shown by the arrow.

Figure 4.23 Potential–pH or Pourbaix diagram for the nickel-water system at 25°C [241].

Figure 4.24 Image of a nickel coating deposited applying $\Delta V = 2.0 \pm 0.1$ V for 60 min showing some holes due to H_2 pitting.

Figure 4.25 Light interferometry images (Zygo®) of a Ni film deposited applying 2.0 ± 0.1 V for 60 min showing a) the deepness of the cavities left by H_2 evolution, b) the same image upside-down and c) the structure of two pinholes with a sharp boundary on one side and smooth on the other side. The area

represented in a) and b) is 1.46 mm x 1.10 mm.

Figure 4.26 SEM images of pinholes due to hydrogen evolution in Ni films deposited applying 2.0 ± 0.1 V for 60 min. a) and b) images from the top, c) cross section of a pinhole in the centre of the film showing a sharp edge on one side and a smooth edge on the opposite.

Figure 4.27 a) Light interferometry image (Zygo®) and b) SEM micrograph of a Ni film deposited applying 2.0 ± 0.1 V for 60 min showing that some coatings were smooth and without cavities.

Figure 4.28 XRD spectra of A) the stainless steel substrate and B) a Ni coating deposited applying 2.0 ± 0.1 V for 30 min showing that the coating is made of crystalline nickel.

Figure 4.29 Three nickel anodes: before deposition (on the left), after deposition at 1.6 ± 0.1 V (centre) and at 2.0 ± 0.1 V (on the right). Their surfaces are considerably different probably due to different processes taking place at the anode surface in different conditions.

Figure 4.30 SEM micrograph of a nickel coating deposited applying -32 $mA \cdot cm^{-2}$ for 30 min.

Figure 4.31 Cyclic voltammetry carried out in a nickel sulphate bath between 0.0 V and -1.5 V with a sweep rate of 5 $mV \cdot s^{-1}$. The black line is the sweep between 0.0 V and -1.5 V (reduction) and the green line the opposite (oxidation) (-1.5 V to 0.0 V).

Figure 4.32 Cyclic voltammetry for a rotating disc (25 rps) graphite electrode in a solution at 293 K containing 5 mM of $NiSO_4$ and 30 mM of $(NH_4)_2SO_4$ with a sweep rate of 1.5 $mV \cdot s^{-1}$ as reported by Njau and Janssen [251].

Figure 4.33 Cyclic voltammetry for a nickel sulphamate solution (dashed line) and a suspension of 2 vol.% of 300 nm Al_2O_3 particles in the nickel sulphamate solution (solid line) with a sweep rate of 10 $mV \cdot s^{-1}$ as reported by Shao and Vereecken [78].

Figure 4.34 Voltage measured vs Ag/AgCl during the deposition of Ni coatings applying a constant current density of a) -10 $mA \cdot cm^{-2}$ for 96 min, b) -20 $mA \cdot cm^{-2}$ for 48 min and c) -32 $mA \cdot cm^{-2}$ for 30 min stirring the solution at 200 rpm.

Figure 4.35 SEM micrograph of a nickel coating deposited at room temperature.

Figure 4.36 SEM micrograph of a nickel coating deposited at 50°C.

Figure 4.37 Coatings deposited from a nickel sulphate bath a) with 0.2 g/l of SDS b) without SDS and keeping the solution still.

Figure 4.38 Coating deposited from a nickel sulphate bath with 0.2 g/l of SDS stirring at 200 rpm.

Figure 4.39 SEM micrographs showing the microstructure of nickel coating deposited applying a current density of -10 $mA \cdot cm^{-2}$ at a) low magnification x1500 and b) high magnification x4500.

Figure 4.40 SEM micrographs showing the microstructure of nickel coating deposited applying a current density of -20 $mA \cdot cm^{-2}$ a) low magnification x1500 and b) high magnification x 4500.

Figure 4.41 SEM micrographs showing the microstructure of nickel coating deposited applying a current density of -32 $mA \cdot cm^{-2}$ a) low magnification x1500 and b) high magnification x 4500.

Figure 4.42 XRD spectra of A) the stainless steel substrate and of coatings deposited from a nickel sulphate bath applying a current density of B) -10 $mA \cdot cm^{-2}$ for 96 min, C) -20 $mA \cdot cm^{-2}$ for 48 min and D) -32 $mA \cdot cm^{-2}$ for 30 min showing that the coatings are made of crystalline nickel.

Figure 4.43 Electrochemical cell containing the nickel solution with 150 g/l of nano-Al_2O_3 particles, a) without stirring and showing the powder deposited on the bottom of the cell and b) stirring and showing the uniformity of the suspension.

Figure 4.44 XRD analysis of the sub-micron powder employed showing that it is α-Al_2O_3.

Figure 4.45 SEM micrograph of sub-micron-Al_2O_3 particles showing their shape and size.

Figure 4.46 Size distribution for the sub-micron-Al_2O_3 particles suspended in water.

Figure 4.47 XRD analysis of the nano-Al_2O_3 powder showing the presence of δ, δ^* and γ-Al_2O_3.

Figure 4.48 TEM micrograph of nano-Al_2O_3 particles showing their shape and size.

Figure 4.49 SEM micrographs of Ni and Ni-Al_2O_3 composite films deposited applying -10 $mA \cdot cm^{-2}$ from a) pure nickel plating bath, and the same bath containing b) 50g/l of sub-micron-Al_2O_3 and c) 50g/l of nano-Al_2O_3. The pure nickel coating presented pyramidal structure that was still partially visible when the nano-Al_2O_3 particles were employed, as indicated by the arrows.

Figure 4.50 SEM micrograph of a Ni-Al_2O_3 composite film deposited applying -10 mA·cm^{-2} from a solution containing 50g/l of sub-micron-Al_2O_3.

Figure 4.51 SEM micrographs of a Ni-Al_2O_3 composite film deposited applying -10 mA·cm^{-2} from a solution containing 50g/l of nano-Al_2O_3.

Figure 4.52 Schematic representation of the electrodes configuration during deposition, and distinction between the two sides of the cathode analysed below.

Figure 4.53 SEM back scattered micrographs of Ni-Al_2O_3 composite films deposited applying -10 mA·cm^{-2} from solution containing 50 g/l (a and b), 100 g/l (c and d), 150 g/l (e and f) of sub-micron-Al_2O_3. The micrographs on the left are of the side facing the anode and those on the right of the opposite side.

Figure 4.54 SEM back scattered micrographs of Ni-Al_2O_3 composite films deposited applying -20 mA·cm^{-2} from solution containing 50 g/l (a and b), 100 g/l (c and d), 150 g/l (e and f) of sub-micron-Al_2O_3. The micrographs on the left are of the side facing the anode and those on the right of the opposite side.

Figure 4.55 SEM back scattered micrographs of Ni-Al_2O_3 composite films deposited applying -32 mA·cm^{-2} from solution containing 50 g/l (a and b), 100 g/l (c and d), 150 g/l (e and f) of sub-micron-Al_2O_3. The micrographs on the left are of the side facing the anode and those on the right of the opposite side.

Figure 4.56 FIB micrographs of Ni-Al_2O_3 composite films deposited applying -10 mA·cm^{-2} from solution containing a) and b) 50 g/l, c) and d) 100 g/l, e) and f) 150 g/l of nano-Al_2O_3. The micrographs on the left are of the side facing the anode and those on the right of the opposite side.

Figure 4.57 FIB micrographs of Ni-Al_2O_3 composite films deposited applying -20 mA·cm^{-2} from solution containing a) and b) 50 g/l, c) and d) 100 g/l, e) and f) 150 g/l of nano-Al_2O_3. The micrographs on the left are of the side facing the anode and those on the right of the opposite side.

Figure 4.58 FIB micrographs of Ni-Al_2O_3 composite films deposited applying -32 mA·cm^{-2} from solution containing a) and b) 50 g/l, c) and d) 100 g/l, e) and f) 150 g/l of nano-Al_2O_3. The micrographs on the left are of the side facing the anode and those on the right of the opposite side.

Figure 4.59 a) FIB micrographs and b) SIMS Al mapping of the same area of a Ni-Al_2O_3 composite films deposited applying -10 mA·cm^{-2} from a solution containing 150 g/l of nano-Al_2O_3 .

Figure 4.60 High resolution FIB micrograph of a Ni-Al_2O_3 composite films deposited applying -20 mA·cm^{-2} from a solution containing 150 g/l of nano-Al_2O_3.

Figure 4.61 FIB-SIMS images showing a) first and b) second ramp milled around the section to be lifted out, c) and d) the two sides of the section when the detachment from the sample was completed a part from the connection bridge.

Figure 4.62 FIB-SIMS images showing a) the needle in contact with the section and a Pt bridge between them, b) the section completely free and detached from the rest of the sample.

Figure 4.63 FIB-SIMS images showing a) the section attached with Pt to the needle and to the Cu stem b) the section attached to the Cu stem.

Figure 4.64 a) Secondary electron and b) secondary ion images of the same surface. In a) few apparent voids are visible and pointed out by arrows; they are not visible in the ion image reported in b). c) Al and d) O SIMS mapping of the same side of the lift out section.

Figure 4.65 3D-reconstruction of a Ni-sub-micron-Al_2O_3 film with the dark areas being the Al_2O_3.

Figure 4.66 Effect of the Al_2O_3 concentration in the electrolyte on the vol.% of a) sub-micron-Al_2O_3 and b) nano-Al_2O_3 embedded into the films for different current densities.

Figure 4.67 Effect of the current density on the vol.% of a) sub-micron-Al_2O_3 and b) nano-Al_2O_3 embedded into the films for different Al_2O_3 concentrations in the electrolyte.

Figure 4.68 Schematic illustration of different particle incorporation in electro co-deposition. a) At slow metal growth rate more particles can reach the surface and be embedded. b) At high metal growth rate less particles can be embedded in the growing film (redrawn from ref. [76]).

Figure 4.69 XRD spectra of coatings deposited applying a current density of -10 mA·cm^{-2} from A) a nickel bath and a nickel bath containing B) 50, C) 100 and D) 150 g/l of sub-micron Al_2O_3 particles.

Figure 4.70 Micro-hardness of pure Ni, a) Ni-sub-micron-Al_2O_3 and b) Ni-nano-Al_2O_3 composite films

for different concentrations of Al_2O_3 in the electrolyte and different current densities.

Figure 4.71 Potentiodynamic curves of a) stainless steel, b) pure Ni films, c) Ni-sub-micron-Al_2O_3 and d) Ni-nano-Al_2O_3 films in 0.1 M NaCl solution.

Figure 4.72 SEM micrographs of pitting corrosion on a) pure Ni films, b) Ni-sub-micron-Al_2O_3 and c) Ni-nano-Al_2O_3 films after the corrosion test carried out in 0.1 M NaCl solution.

Figure 4.73 Polarisation curves of stainless steel, pure Ni films, Ni-sub-micron-Al_2O_3 and Ni-nano-Al_2O_3 films in 0.1 M H_2SO_4 solution.

Figure 4.74 Images of nickel composite coatings deposited on stainless steel ground with 800 grit SiC paper after tape test a) 0% detachment and b) <5% detachment, as indicated by the arrow.

Figure 4.75 XRD analysis of the Al powder

Figure 4.76 SEM image of Al particles used for the co-deposition of Ni-Al composite coatings showing their shape and size.

Figure 4.77 a) low magnification, b) high magnification and c) back scattered (lighter phase is Ni and the darker one is Al) SEM images of a Ni-Al composite coatings deposited applying a current of -32mA·cm^{-2} from a nickel sulphate bath containing 100 g/l of Al particles. The arrows in b) show Al particles partially embedded in the Ni film.

Figure 4.78 SEM back scattered images of a Ni-Al coating deposited applying a current density of -32 mA·cm^{-2} from a nickel sulphate bath containing 100 g/l of Al particles.

Figure 4.79 Surface morphology of a Ni-Al film deposited applying a current density of 450 mA·cm^{-2} from a nickel sulphamate bath containing 120 g/l of Al powder showing white Ni growth on an Al particle (reproduced from ref. [59]).

Figure 4.80 Back scattered SEM micrographs of a) the cross section of a hydrogen pit in a Ni-sub-micron-Al_2O_3 coating deposited from a solution containing 100 g/l of sub-micron-Al_2O_3 applying -20 mA·cm^{-2}, b) the Al_2O_3 distribution around a hydrogen pit in a Ni-sub-micron-Al_2O_3 coating deposited from a solution containing 50 g/l of sub-micron-Al_2O_3 applying -10 mA·cm^{-2}.

Figure 4.81 SEM back scattered micrograph showing the Al distribution around a hydrogen pit in a Ni-Al coating deposited from a solution containing 100 g/l of Al powder applying -32 mA·cm^{-2}.

Figure 5.1 Image of the experimental set up employed to perform electrophoretic deposition in parallel configuration.

Figure 5.2 Images of the cylindrical configuration employed in some of the EPD experiments, a) out of the cell and b) immersed in the suspension.

Figure 5.3 SEM image showing the morphology and size of the PEEK particles.

Figure 5.4 Particle size distribution of the PEEK powder in ethanol.

Figure 5.5 XRD analysis showing the crystallinity of the PEEK powder as received.

Figure 5.6 Change in weight of the PEEK sample with the increase of temperature (TGA) at heating rate of 10°C·min^{-1}.

Figure 5.7 a) Temperature vs time, b) Heat flow vs time and c) Heat flow vs temperature graphs obtained from DTA of PEEK powder with at heating rate of 10°C·min^{-1}.

Figure 5.8 DSC analysis of the pure PEEK powder.

Figure 5.9 Zeta potential vs pH of a 3 wt.% PEEK suspension in ethanol.

Figure 5.10 Zeta potential of a PEEK suspension in ethanol as published by Wang et al. [187].

Figure 5.11 6 wt.% PEEK suspension in ethanol 2 min after the stirring was stopped showing abundant PEEK sedimentation on the bottom of the cell (arrow).

Figure 5.12 PEEK coatings deposited from 6 wt.% suspension in ethanol applying 40 V for 90 s with the two electrodes at 2 cm distance.

Figure 5.13 a) PEEK coatings deposited from a 6 wt.% suspension applying 56.4 V for 30 s with the cylindrical electrode configuration and 1.7 cm distance between the electrodes, as schematically shown in b). The substrate was previously ground with 120 grit SiC paper.

Figure 5.14 PEEK coatings deposited from a 6 wt.% suspension in ethanol applying a) 15.0 V for 5 min and b) 8.0 V for 7 min with the two parallel electrodes at the distance of 2 cm.

Figure 5.15 Coatings deposited from a 1 wt.% PEEK suspension in ethanol with a distance between the electrodes of 0.8 cm and applying a difference of potential of 56.4 V. From left to right the deposition times were 1, 3, 5 and 7 min.

Figure 5.16 Current intensity vs time measured during EPD from a 6 wt.% PEEK suspension in ethanol for different electric fields with the two electrodes separated from 1.5 cm.

Figure 5.17 SEM images of a coating deposited from a 6 wt.% PEEK suspension in ethanol keeping the electrodes at 2 cm distance and applying a difference of potential of 8.0 V for 7 min at a) low, b) medium and c) high magnification, showing coating morphology and microstructure.

Figure 5.18 Images of two PEEK coatings after heat-treatment at 343°C for 30 min with a heating rate of $10°C \cdot min^{-1}$. The circle in b) shows part of the substrate left uncovered after heat-treatment.

Figure 5.19 Images taken with a heating microscope of the same PEEK cubic pellet a) at 25°C and b) 345°C with a heating rate of $10°C \cdot min^{-1}$ and showing the shrinkage of PEEK with temperature.

Figure 5.20 Image of a coating deposited from 1 wt.% PEEK suspension applying 56.4 V for 7 min with 0.8 cm distance between the electrodes. The substrate employed was already coated in the same conditions and heat-treated at 343°C for 30 min with a heating rate of $10°C \cdot min^{-1}$.

Figure 5.21 Representation of the first PEEK coating and of both coatings schematically showing how a uniform coating can be achieved.

Figure 5.22 Images of the specimen coated twice and heat-treated at 343°C for 30 min with a heating rate of $10°C \cdot min^{-1}$; a) flat substrate and b) substrate bent after heat-treatment.

Figure 5.23 SEM images of the second PEEK coating heat-treated at 343°C for 30 min with a heating rate of $10°C \cdot min^{-1}$, a) top view at x 200, b) top view at x 500 and c) cross section.

Figure 5.24 3D plot of the major area of the stainless steel AISI 316L surface obtained by white light interferometry (Zygo®).

Figure 5.25 XRD analysis showing a comparison between the crystallinity of the PEEK powder as received and after heat-treatment at 343°C for 30 min with a heating rate of $10°C \cdot min^{-1}$.

Figure 5.26 Zeta potential vs pH of a 3 wt.% nano-Al_2O_3 suspension in ethanol.

Figure 5.27 Zeta potential of Al_2O_3 (phase not stated) in ethanol as a function of the operational pH, as reported in ref. [137].

Figure 5.28 Zeta potential of Al_2O_3 (phase not stated) in ethanol as a function of pH, as reported by Chen et al. [178].

Figure 5.29 Zeta potential and electrical conductivity of γ-Al_2O_3 suspension in ethanol as a function of pH, as reported in ref. [180].

Figure 5.30 Image of an alumina coating deposited from a 3 wt.% nano-Al_2O_3 suspension applying 40 V for 5 min between two parallel electrodes at the distance of 2 cm and dried in a dessicator for 24 h.

Figure 5.31 Current intensity vs time measured during EPD from a 3 wt.% nano-Al_2O_3 suspension in ethanol for different voltages with the two electrodes at 2 cm distance.

Figure 5.32 a) SEM and b-c) FEG-SEM images of an Al_2O_3 coating deposited from a 3 wt.% nano-Al_2O_3 suspension applying 40 V for 5 min with 2 cm electrode distance and dried in a dessicator for 24 h. a) and b) are low magnification images showing deep cracks, c) is a high magnification image showing the organisation of the nano-Al_2O_3 particles.

Figure 5.33 Zeta potential vs pH of a 3 wt.% PEEK-3 wt.% nano-Al_2O_3 suspension in ethanol.

Figure 5.34 Zeta potential vs pH of a 4 wt.% PEEK-2 wt.% nano-Al_2O_3 suspension in ethanol.

Figure 5.35 Zeta potential vs pH of a 5 wt.% PEEK-1 wt.% nano-Al_2O_3 suspension in ethanol.

Figure 5.36 Graph showing the Zeta potential vs pH for Al_2O_3, PEEK, 3P-3A, 4P-2A and 5P-1A suspensions in ethanol.

Figure 5.37 Model representing the interactions taking place between the oppositely charged PEEK particles and nano-Al_2O_3 particles in suspension.

Figure 5.38 TEM images of the 4P-2A suspension: a) and b) images from the suspension and c) image

from the dried powder embedded in resin, showing a) the nano-Al_2O_3 powder suspended alone, b) and c) the interactions PEEK-nano-Al_2O_3 particles.

Figure 5.39 Images of two coatings deposited from a 3P-3A suspension applying a difference of potential of 30 V for a) 4 min and b) 5 min.

Figure 5.40 Current intensities as function of deposition time when differences of potential of 20, 30 and 40 V were applied during EPD from 3P-3A suspensions.

Figure 5.41 Images of samples deposited from a 4P-2A suspension applying a difference of potential of 40 V for 1 (on the left), 3 (in the centre) and 5 min (on the right).

Figure 5.42 Weight increase of PEEK-nano-Al_2O_3 coatings deposited from a 3P-3A suspension applying 20, 30 and 40 V for different deposition times.

Figure 5.43 Weight increase of PEEK-nano-Al_2O_3 coatings deposited from a 4P-2A suspension applying 20, 30 and 40 V for different deposition times.

Figure 5.44 Weight increase of PEEK-nano-Al_2O_3 coatings deposited by EPD from a 3P-3A suspension as a function of the potential difference and the deposition time.

Figure 5.45 Weight increase of PEEK-nano-Al_2O_3 coatings deposited by EPD from a 4P-2A suspension as a function of the potential difference and the deposition time.

Figure 5.46 The artificial neural network for studying weight versus deposition time and voltage

Figure 5.47 Calculated data versus experimental data obtained for some set of epochs, hidden layers and neurons during the optimization for the 3P-3A and 4P-2A systems.

Figure 5.48 Combined effect of the electric field (voltage) and the deposition time on the deposition yield for the 3P-3A system, calculated using the neural model developed applying the optimized settings (1000 epochs, two hidden layers and 20 artificial neurons for each layer).

Figure 5.49 Combined effects of the electric field (voltage) and the deposition time on deposition yield for the 4P-2A system. These data were calculated using the neural model developed with the best settings: 1000 epochs, two hidden layers with 20 artificial neurons each.

Figure 5.50 Change in weight of a 3P-3A sample with increasing temperature (TGA).

Figure 5.51 SEM images of the top surface of a PEEK-nano-Al_2O_3 coating deposited from a 3P-3A suspension showing the microstructure at a) x180, b) x250, c) x800, d) x6600, e) a PEEK particle covered by nano-Al_2O_3 particles and f) the distribution of the nano-Al_2O_3 particles on a PEEK particle.

Figure 5.52 SEM images of PEEK-nano-Al_2O_3 film deposited from a 4P-2A suspension. a) and b) top surface showing a) the microstructure and b) the high resolution organization of the nano-Al_2O_3 particles on a PEEK particle, c) the cross section.

Figure 5.53 SEM images of PEEK-nano-Al_2O_3 film deposited from 5P-1A suspension showing the microstructure at a) x200, b) x750, c) and d) the distribution of the nano-Al_2O_3 on PEEK particles.

Figure 5.54 DSC analyses of pure PEEK powder and PEEK-nano-Al_2O_3 composite powders.

Figure 5.55 Comparison between the weight variations with the temperature of PEEK-nano-Al_2O_3 composite powders with different amounts of PEEK (TGA analysis).

Figure 5.56 Comparison between the heat flow variations with the temperature of PEEK-nano-Al_2O_3 composite powders with different amounts of PEEK (DTA analysis).

Figure 5.57 Images of a) sample deposited from the 3P-3A, b) the 4P-2A, and c) the 5P-1A suspension and heat-treated at 343°C with a heating rate of 10°C·min^{-1} and 30 min holding time.

Figure 5.58 Image of a sample coated using the 4P-2A suspension and heat-treated at 343°C with a heating rate of 10°C·min^{-1} and 30 min holding time. After the heat-treatment step the coating was manually scratched with a plastic pointy object to qualitatively test the substrate/coating adhesion.

Figure 5.59 SEM images of PEEK-nano-Al_2O_3 films deposited from the 4P-2A suspension and heat-treated at 343°C with a heating rate of 10°C·min^{-1} and 30 min holding. a) at x500, b) at x2500, c) showing a PEEK particle surrounded by nano-Al_2O_3 and d) the microstructure of the nano-Al_2O_3 top layer.

Figure 5.60 SEM images of a film deposited from the 4P-2A suspension and heat-treated at 343°C with a heating rate of 10°C·min^{-1} and 2 h holding time. a) low and b) high magnification.

Figure 5.61 SEM images of a film deposited from the 4P-2A suspension and heat-treated at 343°C with a heating rate of 10°C·min^{-1} and 5 h holding time. a) low and b) high magnification.

Figure 5.62 SEM images of a film deposited from the 4P-2A suspension and heat-treated at 343°C with a heating rate of 10°C·min^{-1} and 20 h holding time. a) low and b) high magnification.

Figure 5.63 Image of pellets containing from left to right: 20 wt.% PEEK-80 wt.% nano-Al_2O_3, 40 wt.% PEEK-60 wt.% nano-Al_2O_3, 70 wt.% PEEK-30 wt.% nano-Al_2O_3 and pure PEEK prepared by manually pressing the powder in a cylindrical die and heat-treated at 343°C for 30 min with a heating rate of 10°C·min^{-1}.

Figure 5.64 PEEK-nano-Al_2O_3 composite film deposited from a 4P-2A suspension and heat-treated at 400°C with a heating rate of 10°C·min^{-1} and 2 hours holding time.

Figure 5.65 SEM images of a film deposited from the 4P-2A suspension and heat-treated at 400°C with a heating rate of 10°C·min^{-1}and 2 h holding time. a) low and b) high magnification.

Figure 5.66 a) Sample deposited from the 4P-2A suspension and heat-treated at 343°C with a heating rate of 10°C·min^{-1} and 20 h holding time, b) The same sample after manually scratching the surface with a plastic pointy object to qualitatively test the substrate/coating adhesion.

Figure 5.67 SEM images of the cross sections of films deposited from the 4P-2A suspension and heat-treated a) at 343°C for 5 h with a heating rate of 10°C·min^{-1} b) at 400°C for 2 h with a heating rate of 10°C·min^{-1}.

Figure 5.68 Image of a PEEK coating heat-treated at 400°C for 2 h with 10°C·min^{-1} heating rate with arrows showing the partially decomposed PEEK.

Figure 5.69 SEM images of a film deposited from a 5P-1A suspension and heat-treated at 343°C with a heating rate of 10°C·min^{-1} and 30 min holding time. a) low and b) high magnification.

Figure 5.70 XRD spectra of A) pure PEEK powder (P indicates the main PEEK peaks), and pellets containing B) 70 wt.% PEEK-30 wt.% nano-Al_2O_3, C) 40 wt.% PEEK-60 wt.% nano-Al_2O_3 all heat-treated at 343°C with a heating rate of 10°C·min^{-1} and 30 min holding, D) pure nano-Al_2O_3. For clarity, scans A, B and C have been displaced upward by 3000, 2000, 1000 cps, respectively.

Figure 5.71 Residual depth profiles of the scratches carried out on PEEK and PEEK-nano-Al_2O_3 coatings deposited from 3P-3A, 4P-2A and 5P-1A suspensions applying a progressive load between 0 and 20 N.

Figure 5.72 Surface maps of the scratch tracks left on a) pure PEEK and b) 3P-3A coatings applying a progressive load between 0 and 20 N. The images were obtained by white light interferometry (Zygo®).

Figure 5.73 a) Image of the two layers PEEK-nano-Al_2O_3 sandwich pellets after heat-treatment. b) SEM images of the contact area between PEEK and nano-Al_2O_3 in the sandwich pellets and b) SEM image of the PEEK side.

Figure 5.74 Micro-hardness values obtained from pure PEEK and PEEK-nano-Al_2O_3 composite pellets with increasing nano-Al_2O_3 content.

Figure 5.75 Compressive stress-strain curves for PEEK-nano-Al_2O_3 composite pellets (20 wt.% PEEK-80 wt.% nano-Al_2O_3, 40 wt.% PEEK-60 wt.% nano-Al_2O_3 and 70 wt.% PEEK-30 wt.% nano-Al_2O_3) tested at room temperature. Note that pure PEEK has compression strength of 130-170 MPa [190].

Figure 5.76 Images of the pellets after the compression strength test: a) 20 wt.% PEEK-80 wt.% nano-Al_2O_3, b) 40 wt.% PEEK-60 wt.% nano-Al_2O_3 and c) 70 wt.% PEEK-30 wt.% nano-Al_2O_3.

Figure 5.77 Potentiodynamic curves in 0.1 M NaCl solution of a) uncoated 316L stainless steel, b) pure PEEK films and composite coatings deposited from c) 5P-1A, d) 4P-2A and e) 3P-3A suspensions.

Figure 5.78 Image of a PEEK film after electrochemical measurement showing severe crevice corrosion and detachment of the coating from the substrate.

Figure 5.79 Images of a) a 3P-3A film after cutting and b) after tape test.

Figure 5.80 Images of a) a 4P-2A film after cutting and b) after tape test, showing both the tape and the film left on the substrate.

Figure 5.81 Images of a) a 5P-1A film and b) the tape used for the tape test, both pictures were taken after the test.

Figure 5.82 Image of a pure PEEK film and the tape used for the tape test, both pictures were taken after the test.

Figure 5.83 SEM images of a part of a 4P-2A film peeled off during the tape test showing a) a low magnification image of the part detached showing holes (arrows) with shape similar to PEEK particles and b) high magnification image showing the high nano-Al_2O_3 content.

Figure 5.84 Image of a pure PEEK film after immersion in 0.1 M NaCl solution for 1 week and following the tape test.

Figure 6.1 Fit to Kikuchi pattern for nickel reflections recorded from a pixel on a FIB milled and polished surface.

Figure 6.2 Grain lattice orientation maps of a Ni coating, with each colour representing a grain obtained with a FIB instrument equipped with electron backscatter diffraction (EBSD). The picture is pixeleted because of the resolution employed (25 nm).

Figure 6.3 a) Image of a PEEK-nano-Al_2O_3 (4P-2A) film deposited on a metallic cylindrical tube and b) SEM image of a NiTi wire coated with PEEK-nano-Al_2O_3 film by EPD using a 4P-2A suspension. Both coatings were sintered at 343°C with a heating rate of 10°C·min-1 and 30 min holding time.

Figure A.1 Optical microscopy picture of the as-received 2 mm thick stainless steel substrate.

Figure A.2 Bearing ratio plots of the as-received surface of the 2 mm thick stainless steel substrate.

Figure A.3 3D plot of the surface of the as-received 2 mm thick stainless steel AISI 316L substrate. This area is 1.46 mm x 1.10 mm and the height of the block is 80 μm.

Figure A.4 Optical microscopy picture of the 2 mm thick stainless steel substrate surface polished with 1 μm diamond paste.

Figure A.5 Bearing ratio plots of the 2 mm thick stainless steel substrate polished with 1 μm diamond paste.

Figure A.6 3D plot of the surface of the 2 mm thick stainless steel substrate polished with 1 μm diamond paste. This area is 1.46 mm x 1.10 mm and the height of the block is 80 μm.

Figure A.7 Optical microscopy picture of the 2 mm thick stainless steel substrate surface polished with 3 μm diamond paste.

Figure A.8 Bearing ratio plots of the 2 mm thick stainless steel substrate polished with 3 μm diamond paste.

Figure A.9 3D plots of the surface a) in point 1, b) in the major area of the 2 mm thick stainless steel AISI 316L substrate polished with 3μm diamond paste. Each point has an area of 1.46 mm x 1.10 mm and the height of the block is 80 μm.

Figure A.10 Optical microscopy picture of the 2 mm thick stainless steel substrate surface ground with 800 grit SiC paper.

Figure A.11 Bearing ratio plots of the surface of the 2 mm thick stainless steel substrate ground with 800 grit SiC paper.

Figure A.12 3D plot of the surface of the 2 mm thick stainless steel AISI 316L substrate ground with 800 grit SiC paper. This area is 1.46 mm x 1.10 mm and the height of the block is 80 μm.

Figure B.1 Bearing ratio plots of the as-received stainless steel substrate surface before and after chemical etching with 10% H_2SO_4 for 30 s.

Figure B.2 Bearing ratio plots of the stainless steel AISI 316L substrate surface ground with 800 grit SiC paper before and after chemical etching with 10% H_2SO_4 for 30 s.

Figure B.3 Bearing ratio plots of the as-received stainless steel substrate surface before and after chemical etching with 18% HCl for 5 min.

Figure B.4 Bearing ratio plots of the surface of the stainless steel substrate ground with 800 grit SiC paper before and after chemical etching with 18% HCl for 5 min.

Figure B.5 Bearing ratio plots of the as-received stainless steel AISI 316L substrate surface before and after chemical etching with 25% HNO_3 for 10 s.

Figure B.6 Bearing ratio plots of the stainless steel substrate surface ground with 800 grit SiC paper before and after chemical etching with 25% HNO_3 for 10 s.

1. Introduction

For many years the deposition of coatings on materials has been employed to improve or change the substrate appearance and/or properties. For example, the characteristics of a low-cost substrate, such as a metal or an alloy, can be enhanced by the deposition of coatings with suitable properties, such as higher hardness, wear, corrosion and oxidation resistance. With the same purpose, the deposition of composite coatings, i.e. formed by the combination of two classes of materials, has recently attracted considerable attention. Composite coatings, e.g. metal-ceramic and polymer-ceramic coatings, have found many applications for their wear resistance, higher hardness and protective function against oxidation and corrosion. Depending on the components other functional properties, e.g. bioactivity, surface reactivity, etc., can be obtained by depositing adequate coatings. The physical and mechanical properties of composites depend also on the amount and distribution of the second phase in the matrix and on the shape and size of the included phase. These four variables can be varied together with the matrix material to produce composites with tailored properties. In particular, the use of particles as reinforcement and the availability of sub-micron and nano powders have led to the production of composites with improved properties due to the highest interface area between reinforcement and matrix compared to conventional micron size powders. The use of sub-micron and nanoparticles has expanded the potential applications of composite films in micro-devices [1-3].

Coating technologies involve processes at high temperatures (e.g. chemical vapour deposition [4] and thermal spraying [5-13]), as well as low-temperature techniques (e.g. electrochemical methods [14-23]). The electrochemical techniques present a number of advantages over the other methods, such as low cost of the equipment, ability to produce thin films on substrates with large sizes and complex geometries, low temperature and ambient pressure processing that avoids problems and costs associated with high temperature and low pressure processes. Moreover electrochemical methods, including electrodeposition, electro co-deposition and electrophoretic deposition, can be employed to produce a great variety of coatings and composite coatings. Some of these methods, however, such as electrophoretic deposition, may need a high temperature stage to aid densification of the coating.

The aim of this project is to investigate in detail the deposition of Ni-Al_2O_3 and polyetheretherketone (PEEK)-Al_2O_3 composite films onto stainless steel by electro co-deposition and electrophoretic deposition, respectively. The evaluation of the effects that each process parameter plays on the microstructure, the composition and the properties of the coatings is fundamental to optimise the experimental conditions to deposit dense coatings free from pores and other microstructural defects. Ni-Al_2O_3 composite coatings were chosen for their relative high hardness, yield strength, tensile strength, corrosion and wear resistance and PEEK-Al_2O_3 composite films because they should provide relatively high thermal stability,

hardness, elastic modulus and tensile strength and should increase the wear resistance compared to pure PEEK coatings. These latter composite coatings have never been produced before, but few studies have been carried out on bulk composite materials with PEEK matrix and Al_2O_3 inclusions [3, 24-29].

This thesis is divided into six chapters presenting the experimental details for the electrochemical deposition of composite films, the results achieved and their evaluation and discussion. Chapter 2 presents an overview of the electrochemical methods employed in this research: electrochemical deposition, electro co-deposition and electrophoretic deposition and reviews the literature with a focus on the deposition of pure nickel, alumina and PEEK films as well as Ni-Al_2O_3, Ni-Al and PEEK-Al_2O_3 composites. Chapter 3 describes the characterization techniques employed in this research, with particular emphasis on the specific instruments and facilities used. Chapters 4 and 5 describe the deposition of Ni-Al_2O_3 and PEEK-Al_2O_3 composite films, respectively. In particular these two chapters cover the materials and methods employed in the separate studies and describe the results obtained which are comprehensively discussed. Chapter 6 concludes the thesis summarising the most important results, drawing key conclusions and presenting detailed suggestions for further research work which would be required to advance the developments in this research field.

2. Literature review

This chapter describes the electrochemical methods employed in this research project: electrochemical deposition, electro co-deposition and electrophoretic deposition. Particular emphasis is given to the parameters influencing the different processes. The findings reported in the literature are also reviewed with a focus on the deposition of pure nickel, alumina and PEEK films as well as Ni-Al_2O_3, Ni-Al and PEEK-Al_2O_3 composites.

2.1 Electrochemical deposition of metals

2.1.1 Introduction

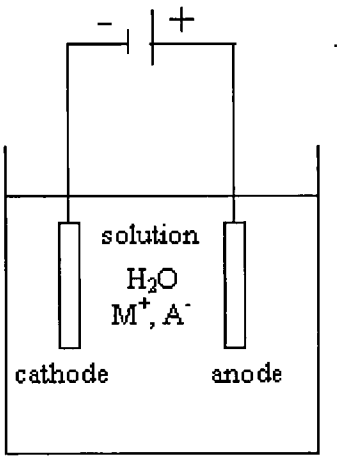


Figure 2.1 Electrolytic cell for the deposition of the metal M from a solution of the salt MA.

Electrodeposition, also known as electroplating and electrochemical deposition, is a common industrial application for the processing of metallic coatings on a surface to enhance or change the appearance and/or the properties of the substrate material. This process occurs in an electrolytic cell that consists of a conductive liquid (the electrolyte or plating bath) and two (anode and cathode) or three (working, auxiliary and reference electrodes) electrodes. The plating bath can be an electrolytic solution (aqueous or organic) or a molten salt where the salt MA dissociates into cations M^+ and anions A^-, which are free to move when an electric field is applied. The main electrodes taking part into the process are the anode/auxiliary electrode (positive electrode) and the cathode/working electrode (negative electrode), as represented in Figure 2.1. When a three electrode cell is employed, the third electrode is the reference electrode that monitors the potential of the working electrode during the process (the electrode at which the interesting process takes place in conventional metal plating is the cathode). The electrolytic cell is connected to an external power supply that forces an electric current into the cell providing the required energy to drive the reaction in the opposite of its spontaneous direction. When a potential difference is applied between the two electrodes the cations migrate

towards the cathode and the anions toward the anode generating a current.

To deposit a metallic film the object to be coated must be negatively charged (cathode) so that the positive metallic ions M^{n+} will be attracted to it and when they reach it, they will be reduced to the metallic state M^0 taking up n electrons (e^-) provided by the cathode:

$$M^{n+} + n\,e^- \rightarrow M^0_{(s)} \qquad [2.1]$$

If the current density applied ensures that the metallic ions M^{n+} in the solution continue to reach the cathode and the electrons needed for the reduction are available at the cathode there will be deposition. The anode employed in an electrolytic cell can be a soluble anode or an insoluble (inert) anode. If the anode is soluble during the electroplating the metal M^0 is oxidized to ion M^{n+} and the anode dissolves away:

$$M^0_{(s)} \rightarrow M^{n+} + n\,e^- \qquad [2.2]$$

The ions M^{n+} go into the solution and start to migrate toward the cathode, while the electrons left on the anode move toward the cathode through the external electric circuit. In this case the anode must be made of the same metal M that is deposited on the cathode; otherwise the solution will be contaminated by cations different from those that should be deposited, resulting in an impure deposit. Moreover, in this situation, the concentration of the deposited metal in the solution will be constant during the deposition because the dissolving anode will replace the amount of metal deposited at the cathode. The net outcome of this process is the transfer of metal from the anode to the cathode.

If the anode is an inert electrode during the electroplating process it remains unchanged and the electrons are produced by the oxidation of water (with oxygen evolution) or anions, which of them depends on the concentration of the solution and the potential of the anode. During the deposition the concentration of M^{n+} in the solution slowly decreases and therefore it is fundamental to supply ions in order to maintain a constant concentration.

2.1.2 Electrodeposition from a solution with more than one ion

If the solution contains more than one ion, it is possible to predict which one will be deposited knowing the respective reduction potentials. The standard reduction potentials E° vs SHE (standard hydrogen electrode) of redox couples (reduced and oxidized form of the same substance $A^{(x+n)+}/A^{x+}$) in the standard state (temperature of 298 K, pressure of 1 atm and molar concentration) are listed in the electrochemical series. When the conditions applied are not standard the potential E of a redox couple can be calculated using Nernst equation:

$$E = E^0 + \frac{RT}{nF}\ln\frac{a_{Ox}}{a_{Red}} \qquad [2.3]$$

where E° is the standard electrode potential of the redox couple, T is the temperature in K, R the gas constant (8.5145 $J \cdot K^{-1} \cdot mol^{-1}$), n the number of electrons transferred during the reaction, F the Faraday's constant (= 96485 $C \cdot mol^{-1}$) and a_{Ox} and a_{Red} are respectively the activities of the oxidized and reduced species. The activity of a substance in the solution is defined as its

effective concentration (as long as the solution can be considered "dilute"). In an ideal solution there are not interactions between the particles and therefore their concentration and their activity are the same. Instead in a real solution there are electrostatic and covalent interactions between the particles and generally the activity is lower than the concentration. The activity of a particle X can be expressed by:

$$a_X = \gamma_X \cdot C_X \qquad [2.4]$$

where C_X is the concentration of the particle X in the solution and γ_X is the activity coefficient, which is a value between 0 and 1. The activity coefficient is characteristic for each substance and takes into account the interactions between the particles in the solution. In a very dilute solution (10^{-3} mol·l^{-1}) the interactions between the particles can be ignored and γ_X is 1, therefore the activity and the concentration are considered to be the same and Nernst equation becomes:

$$E = E^0 + \frac{RT}{nF}\ln\frac{[Ox]}{[\mathrm{Re}d]} = E^0 + \frac{0.025679}{n}\ln\frac{[Ox]}{[\mathrm{Re}d]} = E^0 + \frac{0.0591}{n}\log\frac{[Ox]}{[\mathrm{Re}d]} \qquad [2.5]$$

where [Ox] and [Red] are the concentrations of the oxidized and reduced species, respectively. In the last two members of eq. 2.5 T is 298 K and only a concentration change is taken into account. If the reduced form is a pure metal its concentration is considered 1 [30].

When there are two or more substances in solution that can be reduced, it is fundamental to consider the processes occurring at the cathode to select the appropriate potential for the reduction of only the desired component. For example, if in the solution there are two metals A and B and A has a more negative standard potential (less noble) than B. If the standard potentials of A and B are at least 0.1 V different, it is possible to reduce only B at some potential, while both can be reduced applying more negative potentials. Moreover it must be taken into account that during the deposition of a metal from an aqueous solution there is often hydrogen evolution that can be due to the reduction of hydrogen ions or to water electrolysis depending on the difference of potential applied and on the substances in solution. If hydrogen is deposited together with the metal, the process efficiency will be low and the deposit may be spongy and porous [14, 31] or the incorporation of atomic hydrogen may introduce brittleness into the film.

2.1.3 Current density and limiting current density

The current density j [A·dm^{-2}] is defined as the current applied i [A] divided by the area of the electrode A [dm^2]:

$$j = \frac{i}{A} \qquad [2.6]$$

The current density is a fundamental parameter in electrodeposition and should be maintained constant and at the right value during the deposition. When a difference of potential (E) is applied in an electrolytic cell the positive ions migrate towards the cathode and, if the cathode is at the right potential, they are reduced. If the applied voltage is further increased the number

of reduced ions in a given time rises and so does the current (see part A in Fig. 2.2). At the same time, the difference in concentration between the interface cathode/solution and the bulk of the solution increases as does the rate of diffusion of the ions. Continuing to increase the applied voltage a situation can be reached in which all the ions that arrive at the cathode by diffusion are instantaneously reduced. At this point even a further increase in voltage will not affect the current density (j) (see Fig. 2.2). Under these conditions the number of reduced ions completely depends on the diffusion and the corresponding current density is the limiting current density. This value of current is the maximum that can be reached and it will not be exceeded unless, increasing the voltage, other reactions will take place at the cathode (see part B in Fig. 2.2). For example if the voltage reaches the potential for the discharge of hydrogen ions the limiting current density will increase and the excess will be used to liberate hydrogen [14].

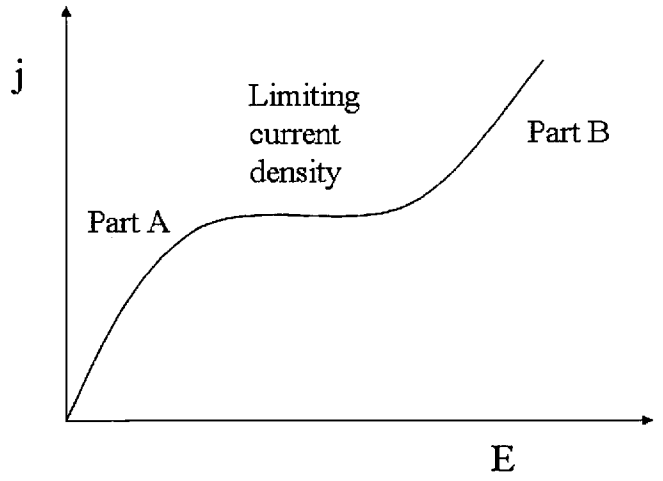


Figure 2.2 Trend of the variation of the current density with the potential applied.

2.1.4 Electrochemical deposition of nickel

A well-known method used to deposit metallic coatings is the electrochemical deposition described in section 2.1.1. This technique largely depends on the plating conditions, such as electrode potential or current density, substrate material, composition and purity of the electrolyte, additives, pH, bath temperature, agitation and mode of deposition (direct current *vs* pulse plating or galvanostatic *vs* potentiostatic), which are characteristic for each metal and difficult to control and standardize. In order to obtain reproducible and consistent results it is fundamental to operate with extreme care during the experimental procedure.

The deposition of nickel from aqueous solutions has been extensively studied in the past centuries [14, 32, 33] and in this section just the bath composition and the types of electrodes employed will be considered. The effects of different parameters on the preferred orientation [34-42], the grain size [35-41, 43-45] and the surface morphology [35, 45, 46] of electroplated nickel films are extensively reported in the literature.

A) Composition of nickel baths

In 1837 nickel was electrochemically deposited for the first time starting from an aqueous solution containing nickel salts. In this procedure a nickel ion (Ni^{2+}) is reduced to metallic nickel (Ni^0) gaining 2 electrons (e^-):

$$Ni^{2+}_{(aq)} + 2e^- \rightarrow Ni^0_{(s)} \qquad [2.7]$$

The baths used to deposit nickel over the centuries have been mainly based on acid solutions even though it is also possible to achieve deposition using alkaline baths. The first bath industrially used was the Watts solution. Later, other baths were employed and developed for special purposes; among them the only one largely employed was the nickel sulphamate bath [32, 33].

i) Nickel sulphate bath

Table 2.1 Composition of nickel sulphate baths [33].

Solution	150-400 g/l of nickel sulphate $NiSO_4 \cdot 6H_2O$
	20-80 g/l of nickel chloride $NiCl_2 \cdot 6H_2O$ or 10-40 g/l of sodium chloride NaCl
	15-50 g/l of boric acid H_3BO_3
pH	3.0-4.0
T	40-70°C
Current density	32-110 $mA \cdot cm^{-2}$

The nickel sulphate bath was formulated by Watts in 1916. Its composition covers the range listed in Table 2.1. Watts did not mention agitation, but recommended using the bath hot. In fact, it has been suggested that in nickel deposition the temperature affects the cathode efficiency, the structure of the nickel coating (smaller grain size at lower temperatures) and the mechanical properties of the coating [32]. However, until 1931 the majority of nickel plating baths in Europe and in the USA were operated at room temperature [33] and, even more recently, numerous groups [2, 34, 47-55] have employed this bath at room temperature. The main advantages of the nickel sulphate bath are:

1. Nickel sulphate is available in a high purity grade and is less expensive than the chemicals used in other baths. For the same reason sometimes nickel chloride is substituted by sodium chloride.
2. The nickel sulphate solution is less corrosive to plant and equipment than the nickel chloride solution (chloride ions are corrosive) and therefore it can be used in industrial processes.
3. This bath is easy to use and to maintain.
4. Nickel sulphate is highly soluble in water (570 g/l at 50°C) and is a source of uncomplexed nickel ions. The latter property is fundamental because in a concentrated

solution the attraction of opposite charged ions by Columbic forces takes place and when this attraction is high the effective concentration (activity) of free ions in the solution is reduced. When the concentration of Ni^{2+} is low the result is a rough deposit and for this reason the concentration should be high.

5. The coatings deposited from this bath present lower internal stress values compared with those obtained from a nickel chloride bath and therefore in almost all the baths the concentration of nickel chloride is limited (low concentration do not influence the deposit properties). High Cl^- concentration produces deposits with worst properties than those obtained from sulphate baths, but low Cl^- concentration is normally used to assist the dissolution of the nickel anode [32, 33].

ii) Nickel sulphamate bath

Table 2.2 Composition of the nickel sulphamate bath.

Solution	300-450 g/l of nickel sulphamate $Ni(NH_2SO_3)_2$
	0-30 g/l of nickel chloride $NiCl_2 \cdot 6H_2O$
	30-40 g/l of boric acid H_3BO_3
pH	3.0-5.0
T	30-50°C
Current density	54-215 $mA \cdot cm^{-2}$

Nickel sulphamate is a salt of the strong monobasic sulphamic acid. The structure of this acid is similar to the sulphuric acid but with one hydroxyl group replaced by an amino group. The nickel sulphamate bath, as a solution for the nickel deposition, was introduced by Piontelli and Cambi in 1938 and in 1950 it was introduced into the electroplating industry by Barrett. The composition of this bath can vary slightly and it is reported in Table 2.2. The main advantages of this bath compared with the sulphate bath are:

1. A higher rate of deposition. In fact it is possible to employ high current density with a lower nickel concentration (180-200g/l) without worsening the deposit properties.
2. A lower internal stress value in the deposit. This can be explained considering that the deposition can be conducted without or at low chloride contents. Many solutions contain just 5 g/l of $NiCl_2$ to achieve good anodic efficiency.

The two main drawbacks of this bath are the high sensitivity to impurities and the higher cost of chemicals. In addition, it has to be noticed that this bath cannot be employed at temperatures higher than 55°C, since at this temperature the sulphamate decomposes [32, 33, 56].

iii) Nickel chloride bath

There are two main types of nickel chloride baths: the first one contains mainly nickel chloride, the other one is similar to a sulphate bath but with a higher $NiCl_2$ content. The

composition of the all-nickel chloride bath proposed by Wesley and Carey in 1939 is reported in Table 2.3. The main disadvantages of this bath compared with the nickel sulphate bath are its high corrosion, higher costs and lower purity of the chemicals used, brittleness and higher internal stress values of the deposit obtained. The advantages of this bath are the higher concentration of nickel ions ($[Ni^{2+}]$ = 1.05-1.26 mol/l instead of $[Ni^{2+}]$ = 0.57-1.52 mol/l in a nickel sulphate bath) and the higher electrical conductivity of the bath compared with the nickel sulphate bath. These two properties lead to a better current distribution and therefore to a better metal distribution on the substrate. The presence of Cl^- has two main effects: it assists the anode corrosion and increases the diffusion coefficient of the Ni^{2+} permitting the use of higher current densities [32, 33]. The composition of the mixed sulphate-chloride electrolytes bath is given in Table 2.4. The main advantage of this bath compared with other baths is a higher electrical conductivity, which permits the use of lower voltages resulting in a better metal distribution on the cathode.

Table 2.3 Composition of the all-nickel chloride bath [33].

Solution	250-300 g/l of nickel chloride $NiCl_2 \cdot 6H_2O$
	30 g/l of boric acid H_3BO_3
	0.4 ml/l of 30% hydrogen peroxide H_2O_2 (as anti-pitting agent)
pH	3.8
T	55°C
Current density	10-140 $mA \cdot cm^{-2}$

Table 2.4 Composition of the mixed sulphate-chloride bath [32].

Solution	200 g/l of nickel chloride $NiCl_2$
	Up to 100 g/l of nickel sulphate $NiSO_4$
	30-50 g/l of boric acid H_3BO_3
pH	2.5-4.0
T	40-70°C

iv) Nickel fluoborate bath

The nickel fluoborate bath (main compositions listed in Table 2.5) did not achieve a great popularity for Ni deposition. The properties of the coatings are similar to those obtained from Watts bath, but a disadvantage of this solution is the higher cost of the chemicals [32, 33].

v) Alkaline solutions for nickel deposition

Alternatively nickel can be deposited from baths containing alkaline electrolytes, but these baths have been rarely used and therefore they are of little industrial importance. The compositions of some of these baths are reported in Table 2.6 [32].

Table 2.5 Composition of the two main nickel fluoborate baths [32].

	Kern bath	Lajner and Pantschenko bath
Solution	300-450 g/l of nickel fluoborate $Ni(BF_4)_2$	80-100 g/l of nickel fluoborate $Ni(BF_4)_2$
	5-40 g/l of fluoboric acid HBF_4 to adjust the pH	15 g/l of nickel chloride
	30-40 g/l of boric acid H_3BO_3	10 g/l of boric acid H_3BO_3
pH	2.0-3.5	3.0
T	40-80°C	50°C
Current density	10-140 $mA \cdot cm^{-2}$	Up to 215 $mA \cdot cm^{-2}$

B) Buffering agents

Usually during nickel electroplating there is co-deposition (reduction) of hydrogen ions and therefore the pH of the solution at the cathode tends to increase steadily. In order to have consistent results, it is fundamental to work with a constant pH value and therefore a buffer is added to the solution. A buffer is a chemical that can accept or give up hydrogen ions keeping their concentration more-or-less constant. In nickel plating, the buffering agent normally employed is boric acid. This chemical is used in all the four acid baths described above (see Tables 2.1-2.5). The boric acid owes its buffering action to this dissociation:

$$H_3BO_3 + H_2O \leftrightarrow H_2BO_3^- + H_3O^+ \qquad [2.8]$$

that renders it able to give up H^+ replacing those reduced during the deposition. This chemical is effective between pH 3 and 5 and therefore it is convenient considering that all these solutions (see Tables 2.1-2.5) operate near this range.

When a nickel salt solution is electrolysed, the pH in the cathode layer increases (higher pH) quickly forming basic salts or hydroxides. The hydroxides normally precipitate when the pH is a little over 6, but they may precipitate even when the pH is lower. When high current densities are applied the pH rises more quickly near the cathode and the formation of these precipitates is more likely. Therefore baths operating at particularly high current densities must have a higher concentration of boric acid to control the pH. A minimum concentration of 40 g/l should be employed, but in some cases it should be raised to above 50 g/l to avoid burning nickel deposits (a burn deposit is rough and is produced when an excessive current density is applied, this deposit contains oxides and other inclusions) [32, 33].

C) Levelling and anti-pit agents

In order to improve the properties of the coating and to solve or minimize some problems occurring during the deposition levelling and anti-pit agents are added to the nickel bath. *Levelling agents* should reduce surface irregularities in the deposit. *Anti-pit or wetting agents* are added to avoid pitting, which causes the formation of small cavities (pin-holes) in the film.

Table 2.2 Compositions of alkaline baths employed for nickel deposition [32].

	Bath 1	Bath 2	Bath 3	Bath 4	Bath 5	Bath 6	Bath 7	Bath 8	Bath 9	Bath 10
$NiSO_4 \cdot 7H_2O$	210 g/l	400 g/l	-	-	120 g/l	-	-	100 g/l	-	250 g/l
$NiCl_2 \cdot 6H_2O$	60 g/l	-	-	30 g/l	-	-	20-40 g/l	-	85 g/l	50 g/l
$(NH_4)_2SO_4$	50 g/l	20 g/l	-	-	-	-	-	-	-	-
KCl	-	10 g/l	-	-	-	10 g/l	-	-	-	-
NH_4OH	-	(25%) 250 ml/l	(sp.gr.0.91) 200 g/l	(30%) 175 ml/l	(28%) 30-60 g/l	-	-	-	-	-
$Ni(NH_4)_2(SO_4)_2$	-	-	100 g/l	-	-	-	-	-	-	-
Sodium sulphite	-	-	180 g/l	-	-	-	-	-	-	-
Sodium citrate	-	-	10 g/l	-	60 g/l	-	-	66 g/l	66 g/l	-
NH_4Cl	-	-	-	50 g/l	-	-	-	-	-	-
Ammonium citrate	-	-	-	65 g/l	-	20 g/l	-	-	-	-
$Na_4P_2O_7 \cdot 10H_2O$	-	-	-	-	65 g/l	73 g/l	-	-	-	-
$NaHSO_3$	-	-	-	-	2 g/l	-	-	5 g/l	5 g/l	-
Citric acid	-	-	-	-	30 g/l	-	-	-	-	-
NaCl	-	-	-	-	30 g/l	-	-	35 g/l	-	-
Potassium pyrophosphate	-	-	-	-	-	200 g/l	-	-	-	-
Tartaric acid	-	-	-	-	-	-	30-60 g/l	-	-	-
Sodium sulphate	-	-	-	-	-	-	-	-	75 g/l	-
EDTA	-	-	-	-	-	-	-	60 g/l	40 g/l	153 g/l
Triethanolamine	-	-	-	-	-	-	-	40 ml/l	40 ml/l	4.5 g/l
Hexamine	-	-	-	-	-	-	-	-	-	1 g/l
Saccharin	-	-	-	-	-	-	-	-	-	4.5 g/l
$Ni(NO_3)_2$	-	-	-	-	-	-	-	20 g/l	20 g/l	-
T[°C]	25-80	20-35	50-60	25	20-35	50-60	40	60	60	55
pH	8.5	Over 8	7.5	9.0-9.2	7.5-9.0	9	5.3-6.2	7	7.5	4.5
Current [A/ft^2]	20-100	5-15	15-20	30	2-20	50	10-100	40	40	Up to 60

Pitting is one of the main problems occurring during Ni deposition and it is mainly caused by:

1. residual grease left on the surface;
2. inclusions of very fine particles which are too small to cause roughness in the deposit;
3. gas bubbles adhering to the cathode (hydrogen pitting).

The first and the second causes can be solved cleaning carefully the cathode surface to remove particles (e.g. particles produced during the polishing treatment), oil and grease (using organic solvents). The third cause can be explained considering that hydrogen bubbles adhere to the cathode surface during the deposition and the deposit grows around them leaving pits. These bubbles are due to the reduction of hydrogen ions H^+ that are adsorbed on the metal surface M and reduced to hydrogen (M-H):

$$H^+ + e^- + M \rightarrow M\text{-}H \qquad [2.9]$$

and then converted into a gas molecule of H_2:

$$2\ M\text{-}H \rightarrow 2M + H_2 \qquad [2.10]$$

The nickel reduction and the hydrogen reduction take place at similar electrode potentials and therefore the side reaction (hydrogen evolution) cannot be avoided. Another problem caused by hydrogen, besides pitting, is that a certain quantity of it may enter into the metal coating (M-H) making it brittle and producing pores in its structure (spongy and porous deposits).

The adherence of bubbles on the cathode surface can be considerably reduced increasing the movement around the cathode and reducing the interfacial tension (or surface tension), so that the gas bubbles are more easily detached from the cathode surface. The movement is generally increased by agitating the solution or moving the cathode. The agitation can be achieved by magnetic stirring, mechanical stirring or air agitation (this is not suitable if there are foaming surfactants in the solution). The disadvantage of agitation is that it is a difficult variable to control quantitatively and to reproduce on a bigger scale; therefore sometimes instead of stirring the solution, it is preferred to move the cathode itself (rotating electrodes).

The surface tension is reduced by adding wetting or anti-pit agents to the solution. It is critical that these chemicals do not react in the solution generating products that can influence the phenomena taking place at the cathode. Moreover it has to be mentioned that sometimes these additives are not enough to avoid pitting. The first wetting agent used by Waite and Martin in 1941 in nickel deposition was sodium dodecyl sulphate (also known as sodium lauryl sulphate) (SDS) $CH_3(CH_2)_{11}SO_4Na$, which is a negatively charged surfactant satisfying the characteristics listed above [32, 33].

D) Electrodes used in nickel deposition

The cathode and anode efficiency during the deposition should be as close to 100% as possible in order to avoid wastage of power and time, ensuring an economically efficient process. The nickel deposition normally presents cathode efficiency between 95 and 97%, but

if during the deposition there is a considerable hydrogen evolution this value drops. Therefore it is essential to operate in conditions in which the hydrogen reduction is limited [33].

i) Anode

As described in section 2.1.1, in nickel plating the anode can be soluble or inert and in the case it is soluble it should be made of nickel. When a nickel anode is employed, the main process taking place at the anode surface is the nickel oxidation that leads to the dissolution of the anode itself:

$$Ni^0_{(s)} \rightarrow Ni^{2+}_{(aq)} + 2\,e^- \qquad E^\circ\,(Ni^0/Ni^{2+}) = +0.25\ V\ vs\ SHE \qquad [2.11]$$

The use of a nickel anode ensures that the concentration of nickel in the bath will be constant during the whole process. Moreover, the anode should dissolve smoothly and without the undercutting of grains, so that there is no production of small nickel particles, which are a waste of material and can be incorporated in the deposit resulting in a rough coating (to remove these particles from the bath the anode can be enclosed in a bag [57] or the solution can be filtered regularly). Under normal conditions the dissolution of a highly pure (99.9%) nickel anode is not satisfactory; in order to improve it, the pH should be less than 4.5 and the bath should contain at least 6 g/l of chloride ions which assist the anode corrosion. These two conditions are followed in the four acid baths previously described (see Tables 2.1-2.5).

Another reaction taking place at the anode is the gas evolution. Normally this gas is oxygen due to water electrolysis, but if chloride ions are in the solution they can be oxidised to produce gaseous chlorine. During these experiments the evolution of chlorine is unlikely to happen because the small amount produced will dissolve in water giving hypochlorous acid (HClO) [33].

ii) Adhesion between cathode and coating

The adhesion between the deposit and the substrate is a fundamental parameter in electrodeposition. The substrates can be:

1. *Made of the same material as the coating.* In this case perfect bond strength should be achieved between them and the crystal lattice of the cathode should continue in the coating.
2. *Made of a different material.* This is the most common situation considering that generally a material is coated with a different material to achieve new properties. In this case the adhesion depends on the strength of the interatomic forces between the two materials. The film structure is strongly influenced by the substrate structure because the deposited ions take positions immediately adjacent to those in the metal lattice. In addition the structure of the metallic substrate is more likely to be continued in the coating if the deposition is carried out at low current density resulting in a good adhesion between the coating and the substrate.

Generally before the deposition, the surface is chemically or mechanically treated. If these treatments are inadequate or incorrect the adhesion between the two materials can be poor. A poor adhesion can be explained as a total or partial loss of contact between the two phases during the deposition and can lead to the separation between the two materials and, in the extreme case, to the coating peeling off from the substrate. A lack of adhesion can be explained and improved considering:

1. *Presence of surface contaminants.* This problem can be partially solved by cleaning the substrate surface to remove the most common contaminants, e.g. greases and oils can be removed using organic solvents.
2. *Presence of oxide films.* This problem can be solved treating the surface with acid to remove the oxide or grinding the substrate to take away the oxide layer on top of it. During these treatments it must be taken into account that different metals present different rates with which they re-form the oxide on their surface; this has to be taken into consideration to determine the transfer rate of the substrate from the cleaning solution to the plating bath [33].

Moreover it has to be taken into account that electroplating will not cover surface imperfections such as scratches, dents or pits but will render them even more pronounced. Therefore it is important to remove any undesirable surface marks on the substrate before the deposition.

2.2 Electrochemical co-deposition

2.2.1 Introduction

From the 1960s, electrochemical or electro co-deposition has been used as a method to deposit particles or fibres in a metallic matrix to produce composite films. The particles/ fibres are held in suspension in an electroplating bath and are co-deposited with the metal (Cu, Cr, Ni, Co and alloys) during its electrochemical deposition (for further details see section 2.1). The main difference between electro co-deposition and electro deposition is the presence in the pure plating bath of these insoluble particles/fibres which can be pure metals, ceramics or organic materials and can have size ranging from nm to over 100 μm. The metal matrix keeps the second phase together and improves the substrate/coating adhesion [15, 16, 58].

In electro co-deposition the electrodes are vertically positioned in the plating bath, whereas when the cathode is horizontally positioned the process is called sediment co-deposition. This technique was firstly developed by Viswanathan and Ghouse [51]. During sediment co-deposition, the solution is periodically stirred to suspend the particles that subsequently sediment on the cathode surface due to a combination of electrophoresis and gravity factors. If the substrate is not flat its position must be constantly changed in order to achieve a uniform particle distribution on every side of it. However, the distinction between these two techniques is not well-defined [47, 48, 59].

The application of these techniques to different types of particles and different plating baths enables the production of a large range of composite films with many potential applications and excellent mechanical properties such as wear resistance, corrosion resistance and lubrication, depending on the properties, the amount and the distribution of the co-deposited particles [15, 16, 58]. Furthermore, the rising availability of smaller particle sizes has increased the potential applications of these composite coatings [58]. For example, sub-micron powders promote the homogeneity of the composite through the increase of the contact area between metal and particle and also permit the application of composite materials in microdevices and thin films [2]. For example, oxide particles like Al_2O_3 and TiO_2 [60] or fibres and whiskers [61] have been deposited with metals to produce composite coatings with a significantly higher yield strength and hardness compared with the pure metal (e.g. Qu et al. [61] found that the micro-hardness of a pure nickel deposit is 192 HV while that of a nickel-alumina whiskers film is 346 HV). Metallic films containing hard materials, like diamond, WC and SiC, protect the substrate from abrasion. Sub-micron powders, like Al_2O_3, $BaSO_4$, Si_3N_4, V_2O_5 and Cr_2O_3 are deposited to decrease the corrosion rate of the metal. Graphite, MoS_2 and PTFE are electro co-deposited to produce composite coating that can be employed in moving contact because they reduce the friction between the surfaces [15, 16].

2.2.2 Experimental parameters

From the studies of Hovestad and Janssen [15], Stojak et al. [16] and Low et al. [58], it was shown that the electro co-deposition is influenced by many interdependent experimental parameters including particle characteristics (surface charge, particle concentration, type, shape, size), electrolyte composition (bath constituents and additives, surfactant, bath temperature, pH), current density, hydrodynamics and cell configuration. In the literature different or even contradicting results are often reported for different particle-electrolyte combinations and cell configurations (parallel plate electrode, rotating disk electrode RDE and rotating cylinder electrode RCE). Some of the disagreements encountered are a direct consequence of incomparable hydrodynamics due to the method employed to suspend particles in the solution. Therefore it is hard to achieve a clear picture of the exact effect that each parameter plays in the process. However, the major part of the recent investigations carried out on the electro co-deposition have suggested that the three main factors influencing the co-deposition processes are the current density, the particle type and concentration and the agitation of the bath or the electrode movement [15, 16, 58].

i) Surface charge

Some variables such as pH, bath constituents and their concentration, additives and particle type influence the surface charge of the particles, which can be obtained by measuring the zeta-potential (discussed in section 2.3.2). This parameter is fundamental for a better

understanding of the process because a positive surface charge enhances the attraction of the particles to the cathode (electrophoresis) and therefore their co-deposition.

A completely different theory was proposed by Bund and Thiemig [62, 63] who observed that negatively charged particles were better incorporated into the film than those positively charged. In the authors' opinion [62, 63] the negatively charged Al_2O_3 particles in nickel or copper plating baths were attracted by the positively charged double layer around the cathode and when they entered the double layer their negatively charged shell was stripped off and the particles were incorporated in the growing metal film.

ii) Particle concentration and type

The concentration of the particles in the bath is an important factor. In fact, for a wide range of particle-electrolyte systems, it was observed that at low particle concentration the co-deposition process was limited by the supply of particles to the electrode and that by increasing the particle concentration in the bath the amount of particles embedded in the metal matrix rose until reaching a saturation state. But the correlation between the concentration of particles suspended and the amount of particles co-deposited was not proportional and depended on the particle-electrolyte system. The concentration of particles suspended in the solution has been varied between 2 and more than 200 g/l producing composite coatings containing an average of 1-10 vol.% of particles. Furthermore, it must be noticed that the amount of incorporated particles in the coating could increase up to 50 vol.% by applying sediment co-deposition [16].

Table 2.7 Results obtained from the electro co-deposition of α-Al_2O_3 and γ-Al_2O_3 from a copper sulphate solution (adapted from table reported by Stojak et al. [16])

Bath composition	Particle size and crystal phase	Particle loading (g/l)	Current density ($mA \cdot cm^{-2}$)	Analytical method	Co-deposition results
250 g/l $CuSO_4$ pH 1.0-3.0	0.02 μm α-Al_2O_3	30	40	Gravimetric	3.3 vol%
250 g/l $CuSO_4$ pH 1.0-3.0	0.02 μm γ-Al_2O_3	30	40	Gravimetric	No incorporation

The type of particles affects their incorporation in the coating. For example, Hovestad et al. [15] reported that Greco and Baldauf found that the amount of TiO_2 co-deposited with Ni under the same conditions employed for co-depositing Al_2O_3, was three times more than the amount obtained in Ni-Al_2O_3 coatings. It was also observed that even the particle crystallographic phase played a significant role on the quantity of particles incorporated in the coating: no γ-Al_2O_3 was co-deposited with copper under the same conditions in which α-Al_2O_3 was co-deposited, see results obtained by Chen et al. [15] reported in Table 2.7. This behaviour was explained considering that in those conditions α-Al_2O_3 presented a positive zeta potential whereas γ-Al_2O_3 was negatively charged and therefore it could not be deposited on the cathode; this explanation was in disagreement with the findings reported by Bund and Thiemig [62, 63].

Stappers and Fransaer [49] investigated how the surface properties (hydrophilicity and hydrophobicity) and the electrical conductivity of the particles influenced their incorporation into the composite by studying the metal growth around them by atomic force microscopy (AFM) and SEM. They electrodeposited nickel-iron multi-layers around the particles and etched the iron layers from the cross section to expose the structure of the individual layers and obtain information about the metal growth. They [49] observed that the metal deposition took place underneath hydrophilic glass particles, which were consequently pushed up by the process before being incorporated (see Figure 2.3 a)) and a hole was formed at the metal-particle interface, but not underneath hydrophobic poly-methyl-meth-acrylate (PMMA) particles and graphite particles. The incorporation of the glass particle and of the PMMA particles took place by the metal simply growing around them. Whereas when conductive graphite particles were incorporated the deposition took place on their surface as if the particles were part of the electrode [49] (see Figure 2.3 b)), similar observations were also reported for Al particles by Susan et al. [64].

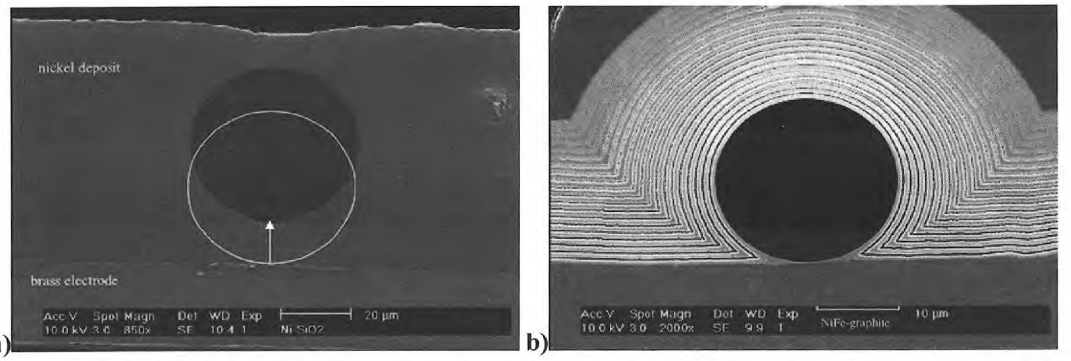


Figure 2.3 SEM images of a) a nickel film grown around a glass particle. The deposition started with the glass particle settled on the cathode (white circle) but the particle moved up by the metal deposition underneath the particle. b) Metal growth profile around a conductive graphite particle as if the particle was part of the electrode (redrawn from ref. [49]).

iii) Particle shape

The influence of the particle shape in co-deposition has not been studied hitherto. However, the particle shape should indirectly influence the co-deposition process affecting other factors playing a role in co-deposition, such as the adsorption of different quantity of ions on the particle surface and the suspension stability [15, 58]. The ratio between the volume and the surface area of a particle depends on its shape and therefore it may be reasonable to suppose that different shapes behave differently, probably because they adsorb different quantity of ions.

iv) Particle size

The influence of particle size on the amount of second phase co-deposited strongly depends on the system studied. In fact:

1. In some systems, such as Ni-Cr (Bazzard and Boden [65] found that increasing the particle size from 5 to 30 μm the quantity of Cr co-deposited with Ni rose.), Cu-P (In their experiments Graydon and Kirk [66] increased the particle size from 3 to 20 μm obtaining a higher concentration of P co-deposited with Cu.) and Cu-Al_2O_3 (Chen et al. [66] carried out experiments from suspensions with the same concentration of α-Al_2O_3 with particle size 0.3 and 1.0 μm obtaining a higher quantity of α-Al_2O_3 co-deposited when the bigger particles were employed.) the percentage of co-deposited particles increased with the use of bigger particles.
2. In other systems the influence of particle size was negligible (Verelst et al. [67] deposited Ni-Al_2O_3 composite films using Al_2O_3 with particle size between 0.3 and 2.2 μm and they did not observe any influence of the particle size on the amount of co-deposited particles).
3. In other systems the percentage of co-deposited particles decreased using larger particles, such as Ag-Al_2O_3 (Suzuki and Asai [68] noticed that increasing the particle size from 0.5 to 2 μm the quantity of α-Al_2O_3 co-deposited with Ag decreased.) and Ni-Al_2O_3 (Brandes and Goldthorpe [69] observed that the dispersion of finer particles in the deposit was more uniform and that increasing the particle size from 5 to 30-40 μm the amount of α-Al_2O_3 co-deposited decreased.).

No explanations have been given in the literature to clarify these different effects.

v) Bath constituents and additives

It was observed that plating baths made of different metals or different salts of the same metal produce different incorporation rates of the same particle. Kuo et al. [70] observed that in the system Ni-Al_2O_3 also a different concentration of the same salts in the bath influenced the quantity of the co-deposited second phase. Moreover additives, which are often added to plating bath, such as bath brighteners, wetting agents and surfactants, affect the co-deposition. Different brighteners produce different effects, but they generally increase the particle co-deposition. Instead wetting agents normally produce a decrease of the amount of embedded particles. Their different behaviours mainly depend on their chemical structure. In fact cationic additives promote co-deposition and anionic additives reduce it because they confer a negative charge to the particles. The surfactants (normally adsorbed on the particle surface) improve the stability of the suspension increasing the wettability of the suspended particles. In particular cationic surfactants (Figure 2.4) represent a great advantage because they confer to the particles a positive charge, which stops the particles from agglomerating and electrostatically attracts them to the cathode. The main drawback in the use of surfactants is that they are embedded in the deposit together with the particles on which they are adsorbed; however, normally the amount of surfactant adsorbed is insignificant and hence does not affect the composite properties [15].

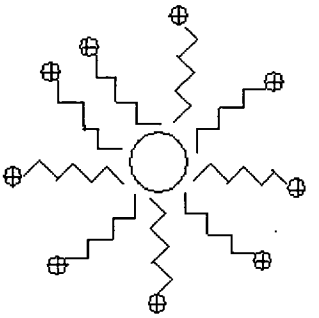


Figure 2.4 Interactions between a particle and cationic surfactants.

Furthermore the addition of small quantities of monovalent cations, like Tl^+, Ce^+, Rb^+ and NH_4^+, or amines, like TEPA (tetra-ethylene-pent-amine), alanine and EDTA (ethylene-diamine-tetra-acetic-acid) increase the co-deposition. This effect can be explained considering that the adsorption of metallic cations confers to the particles a positive surface charge. A rise in the ion adsorption on the particle surface was observed increasing the concentration of the metallic ions and adding additives, such as TEPA and EDTA, to the solution. Consequently, it was assumed that TEPA and EDTA promote co-deposition enhancing the adsorption of metal ions on the particle surface [15, 16].

vi) Bath temperature

The effect of the temperature seems to vary for different particle-electrolyte systems. In some systems no effect of temperature on the vol.% of embedded particles was observed. In other systems the vol.% of co-deposited particles increased with the bath temperature whereas in other systems the opposite behaviour was observed [15].

vii) pH

The effect of the pH resulted similar for different systems. Martin and Williams [71] observed that the pH of the bath plays an important role in ensuring the particle co-deposition on the cathode. This was explained considering that the pH can influence the particle surface charge (zeta potential) rendering them positive or negative (see section 2.3.2). In general it was observed that when the pH is above 2 there is a little influence on the quantity of particles embedded in the deposit, while when it is below 2 there is a sharp decrease in the amount of incorporated particles (e.g. SiC and Al_2O_3)[15, 16, 72].

viii) Current density

Numerous galvanostatic techniques (direct current, pulsed direct current [61, 73-75] and pulsed reverse current [1]) can be employed to deposit composite coatings but direct current is the most commonly used [58]. The effect of the current density on the amount of particles co-deposited was extensively investigated and different behaviours were described by Stojak et al. [16]. It was observed that increasing the current density:

1. In some systems the amount of co-deposited particles decreased (e.g. Takeuchi et al.[16] found that the quantity of diamond particles co-deposited with Ni diminished rising the current density and Bazzard and Boden [65] found the same trend for the quantity of Cr particles co-deposited with Ni).
2. In other systems there was little or no influence on the amount of occluded particles (e.g. Sautter [72] reported that the current density did not influence the co-deposition of Al_2O_3 with Ni.).
3. In other systems this amount increased (e.g. Kariapper and Foster [16] observed an increase of the amount of TiO_2 co-deposited with Ni increasing the current density).

Moreover, it has also to be noted that for the Ni-Al system it has been reported by Susan et al. [64] that increasing the current density the vol.% of Al co-deposited in the coating increased until reaching a maximum and then decreased. All these behaviours can be explained considering that applying higher current densities all the particles at the cathode interface would be incorporated, but at the same time it can also happen that these conditions enhance just the deposition of the metal decreasing the amount of second phase co-deposited.

ix) Hydrodynamics

The mixing of the bath is fundamental to keep the particles suspended and to transport them to the cathode. The hydrodynamics of the system has control over the rate, the direction and the force with which the suspended particles hit the cathode surface. The contact between the particles and the cathode is fundamental to achieve electro co-deposition even if this contact does not guarantee that the particles will be incorporated in the film.

In electro co-deposition the parallel plate electrode configuration has been largely employed for its simple design and for the relatively uniform current density that can be achieved, but a major disadvantage of this system is the incomparable hydrodynamics due to the different ways employed to mix the suspension, such as stirring, vibrating a perforated plate at the bottom of the cell, bubbling gas or pumping the suspension through the cell. In parallel plate electrode configuration the agitation has two main functions: to transport the particles from the bulk to the cathode surface and to keep the particles suspended. Stojak et al. [16] reported that an increase in bath agitation was found by Greco and Baldauf to increase the amount of deposited particles in Ni-Al_2O_3 and Ni-TiO_2 systems. In the same review [16] it was also reported that Snaith and Groves observed a decrease in the quantity of incorporated particles increasing the bath agitation in systems like Cu-SiC and Cu-$CrBr_2$. Therefore, it may be thought that increasing the agitation a larger number of particles reach the electrode enhancing the amount of particles incorporated in the deposit, but if the bath agitation is too powerful the time that the particles spend at the electrode surface is not enough and they are swept away before being embedded in the coating [15, 16, 58].

A better control of the hydrodynamics and of the mass transport during the deposition

can be achieved using rotating electrodes [16] employed by few researchers [1, 2, 52, 76-79]. Vidrine and Podlaha [1] deposited Ni-Al_2O_3 composite films stirring the solution to keep the particles suspended and rotating the electrode at 1600 rpm. Under the same hydrodynamics, they [1] observed that the particle concentration in the deposit increased with increasing current density in a citrate bath and decreased using a chloride bath. They [1] also reported that lower rotation rates (225 rpm instead of 1600 rpm) favoured the particle incorporation independently from the current density employed. Opposite results were reported by Shao et al. [76-78], who observed that the Al_2O_3 incorporation from sulphamate baths increased with increasing rotation rate and decreasing current density. From these results it is clear that even controlling the hydrodynamics other factors, such as the current density, the composition of the bath and the rotation rate, strongly influence the particle incorporation.

2.2.3 Mechanisms for electro co-deposition

The mechanisms of electro co-deposition are still not well understood but some models have been proposed in the last decades. A comprehensive overview of all of them was conducted by Hovestad and Janssen [15], Stojak et al. [16] and Low et al. [58] and they are reported below. In 1962 Whithers [15] explained the mechanism of electro co-deposition suggesting that particles with a positive surface charge were attracted to the cathode by electrophoresis. Two years later Martin and Williams [71] proposed that the particles were transported to the cathode by electrophoresis or by bath agitation and that they were subsequently mechanically entrapped in the growing metal film. In 1967 Brandes and Goldthorpe [69] refused the mechanical entrapment of the particles in the coating and suggested the presence of an attractive electrostatic force that held the particles at the cathode surface for a sufficient time to be incorporated in the growing metal layer. In their [69] opinion this attractive force may be due to a small charge on the particle surface. This suggestion may partially explain, considering the effect of the gravitational force, why the incorporation in the deposit of small particles is easier than that of larger particles. In 1968 Saifullin and Khalilova [15] presented a model to calculate the weight percent of co-deposited particles, that was based only on the mechanical entrapment and for this reason it was subsequently rejected by the scientific community. In 1971 Bazzard and Boden [65] suggested that, due to the bath agitation, the particles collide with the cathode surface and if they stay there for a certain time they are incorporated in the film. They [65] developed the following equation to calculate the wt.% of embedded particles in the film:

$$x = \frac{\frac{4}{3}\pi \cdot r^3 d}{\frac{4}{3}\pi \cdot r^3 d + 4\pi \cdot r^2 e_M \cdot j \cdot t} \times 100 \qquad [2.12]$$

where $4\pi \cdot r^3 d/3$ is the mass of each particle deposited (with radius r and density d) and

$4\pi \cdot r^2 \cdot e_M \cdot j \cdot t$ is the quantity of metal deposited in a time t applying a current density j (e_M is the electrochemical equivalent of the metal) supposing a current of $4\pi \cdot r^2 \cdot j$ on the spherical particles. This equation was rejected by the scientific community because it did not take into account the effects of pH, temperature and bath composition [15].

i) Model of Guglielmi

In 1972 Guglielmi proposed a two-step mechanism based on electrophoresis and adsorption of particles on the cathode. In the first step, the *loose adsorption*, the particles are weakly adsorbed on the cathode surface while the electrode is still surrounded by a layer of ions and solvent molecules. There is not a real contact between the cathode and the particles and this adsorption is mainly physical. This step results in a high degree of coverage of the cathode by the particles that are surrounded by a cloud of adsorbed ions. In the second step, the *strong adsorption*, the particles lose the ionic cloud and become strongly adsorbed on the electrode. This step depends on the electric field at the cathode and therefore it is thought to have an electrochemical character. Finally, the strongly absorbed particles are entrapped in the growing metal layer. Furthermore, Guglielmi developed an equation to explain the effect of the current density on the volume fraction of embedded particles:

$$\frac{\alpha}{1+\alpha} = \frac{zF\rho v_0}{M \cdot j} \exp[(B-A)\eta] \frac{kc_p}{1+kc_p} \qquad [2.13]$$

where α is the volume fraction of embedded particles, z is the valence of the metal ion, F is Faraday's constant, ρ and M are the density and the atomic mass of the deposited metal, v_0 and B are undefined kinetic constants of the metal-particle system considered, j is the current density, A is the Tafel constant of the reduction of the metal, η is the electrode overpotential, k is a constant depending on the particle electrode interaction and c_p is the particle concentration in the bath. This was the first model that could be experimentally verified. Several researchers validated this model with their experiments, but at the same time the model was criticised by the scientific community because it did not take into account fundamental parameters such as: size and type of particles, bath composition, temperature, pH and hydrodynamics [15, 16, 58].

ii) Model of Buelens and Celis et al.

Celis et al. [15, 16, 64, 80] noticed that Guglielmi's model could not explain the behaviour of some systems and therefore they supposed that two processes play a fundamental role in the co-deposition mechanism: the adsorption of ions onto the particle surface and the ions reduction at the cathode creating a physical bond between the particle and the cathode. Based on these postulates and on agitation, Celis et al. [15, 16, 58, 80] proposed a five step mechanism for co-deposition, that is depicted in Figure 2.5. In the first step the particles in the bulk of the solution adsorb ions on their surface gaining an ionic cloud. In the second step the particles are transported by bath agitation to the hydrodynamic boundary layer, then (third step)

they diffuse through the diffusion layer and reach the cathode surface. Finally the particles are incorporated in the film in two steps, similar to those described by Guglielmi: the particles surrounded by an ionic cloud are adsorbed on the cathode surface and become incorporated in the deposit by the reduction of some of the adsorbed ions. Moreover, Celis et al. [15, 16, 58, 80] suggested that the particles are embedded only if a certain amount of the adsorbed ions is reduced. This assumption supports the field-assisted adsorption described by Guglielmi that underline the differences between the loose adsorption and the strong adsorption step.

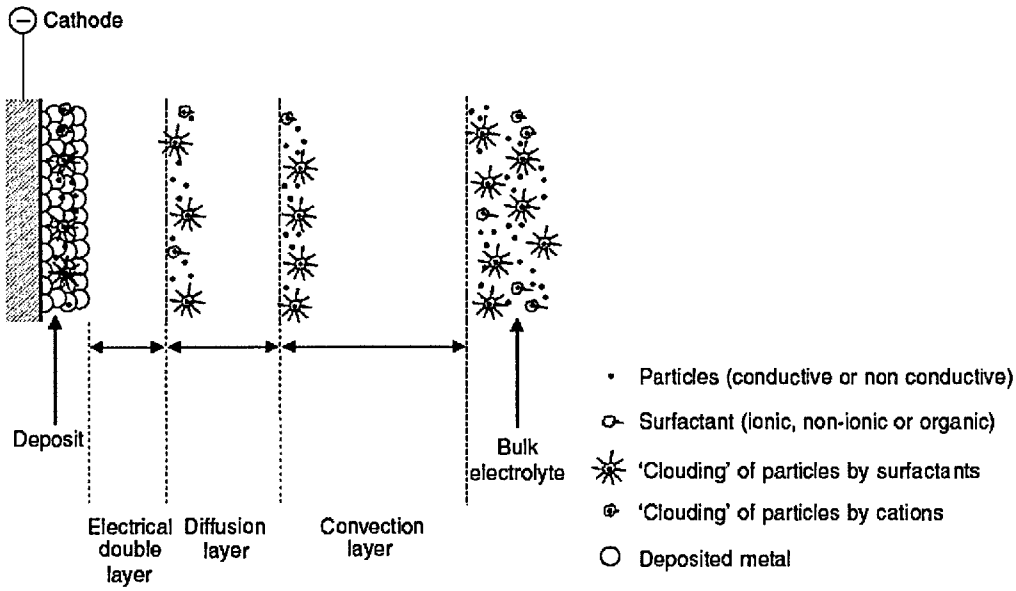


Figure 2.5 Schematic representation of the mechanism of particle co-deposition proposed by Buelens and Celis et al. (redrawn from ref. [58]).

Subsequently Buelens and Celis [15, 16, 58, 64, 80] developed a probability equation to calculate the weight percent of particles embedded in the deposit ($w\%$) at a given current density:

$$w(\%) = \frac{W_p N_p P}{\frac{M_m i}{nF} + W_p N_p P} \cdot 100 \qquad [2.14]$$

where W_p is the weight of one particle, N_p the number of particles that reach the electrode per unit time and surface area, P the probability of the particle to be co-deposited and $M_m i/nF$ is the weight of metal deposited obtained using Faraday`s law. The central assumption of this equation is that a certain quantity of the ions adsorbed on the particle should be reduced to achieve particle incorporation. This model takes into account that the particles need to stay close to the electrode surface for a certain time (as it was hypothesised before by Brandes and Goldthorpe [69] and by Bazzard and Boden [65]) to be incorporated and therefore not all the particles will be embedded.

iii) Recent models

Recently, more elaborate models that predict the particle probability to be incorporated in a film using a statistical approach have been developed. These models consist of many, often interrelated, equations containing a wide set of parameters and render difficult to understand the effect that each individual experimental parameter has on the process and therefore the use of extensive computer calculations is needed [15, 16].

The flexibility and reliability of the models proposed to describe the behaviour of a wide range of metal-particle combinations still needs validation and it is important that future models will consider the effect of particle characteristics (type, dimensions and concentration), operating parameters (temperature, current density, pH and hydrodynamics) and bath composition (concentrations, presence of surfactants and additives) on the amount of second phase co-deposited in the composite. Moreover, another important factor that has not been taken into account in all the models proposed so far is the effect of particle inclusion in the metallic film, i.e. the particles might reduce the cathode surface area if they are non conductive or enlarge it if they are conductive [58].

2.2.4 Deposition of nickel composite coatings

Extensive research has been reported in the literature on the wide range of composite coatings that can be produced by electro co-deposition [15, 16, 58], some examples of the conditions employed to deposit Ni composite coatings are listed in Table 2.8. This section will mainly focus on the application of electro co-deposition for the production of Ni-Al_2O_3 and Ni-Al composite films, which are the systems studied in this project. Tables 2.8-2.10 show the conditions employed to electro co-deposit Ni composite coatings. An important point to be considered is that the plating solution should not contain undesirable particles, which otherwise would be co-deposited during the process. Therefore cleaning procedures, such as filtration, must be applied to the bath to eliminate the undesirable particles and the anode can be enclosed in a bag to prevent that the materials dissolved from the anode contaminate the plating bath [57, 74, 75].

2.2.4.1 Electrochemical co-deposition of Ni-Al_2O_3 composite coatings

The production of Ni-Al_2O_3 composite coatings has attracted considerable attention for their properties, such as higher hardness [12, 52, 57, 61, 62, 75, 78, 79, 81-94], yield strength [72, 95], ultimate tensile strength [95], tensile strength [57, 89], wear [12, 54, 75, 81, 87, 90, 91, 93, 94, 96] and corrosion resistance [83, 97-101]. These coatings have been deposited using thermal spraying [12, 13], magnetron sputtering [102], electroless deposition [83, 86, 87, 99, 103], pulse laser deposition [88], electrophoretic deposition [104-106], electrochemical co-deposition [1, 2, 52-55, 57, 61, 62 70, 72-79, 81, 82, 84, 85, 89-95, 97, 98, 100, 101, 107-112] and a two step mechanism consisting of electrophoretic deposition of alumina coating and

subsequent electrochemical deposition of nickel [96]. The electro co-deposition technique has been also employed to produce Ni-Al_2O_3 functionally graded materials by changing the bath or the deposition conditions during the deposition process [84, 110, 112]. The characteristics of the nickel plating baths and of the Al_2O_3 particles employed to produce composite coatings by electro co-deposition are listed in Table 2.9. A summary of all the findings reported in the literature is reported below.

i) Effects of the deposition parameters

It is well known that the concentration of particles in the bath, the current density and the particle size are the main parameters influencing the amount of second phase embedded in the composite coatings. The influence of these parameters on the Ni-Al_2O_3 deposition has been studied and also other parameters have been recognized to influence the process.

An increase of the Al_2O_3 volume fraction in the coating was observed when the Al_2O_3 concentration in the plating bath increased [57, 72, 78, 82, 84, 98, 101, 110, 112]. Ferkel et al. [82] observed a 2 vol.% of Al_2O_3 co-deposited in the film with 8.3 g/l of Al_2O_3 suspended in the bath. Sautter [72] obtained 2 vol.% of Al_2O_3 in coatings deposited from solution with 25 g/l of Al_2O_3 and 5 vol.% of Al_2O_3 from baths containing 150 g/l of Al_2O_3. The upper limit observed by this researcher [72] was due to the suspension viscosity which made impossible to obtain good stirring. Banovic et al. [84, 110] reported a 40 vol.% of Al_2O_3 in samples deposited from a solution containing 225 g/l of Al_2O_3. Nwoko and Shreir [57] observed that for particle concentration in the Watts bath < 60 g/l the amount of Al_2O_3 co-deposited increased but decreased for higher concentrations, probably for the incapacity to keep all the particles suspended and due to the increase of agglomeration. Shao et al. [78] reported that the amount of Al_2O_3 co-deposited increased with the concentration in the bath until reaching a plateau when the particle size was 300 nm, whereas when smaller particles (50 nm) were employed the concentration increased linearly over the whole range analysed. Conversely Xiong et al. [74] and Bund and Thiemig [62] observed that the particle content in the coatings was just slightly influenced by the particle concentration in the bath.

The current density presented controversial effects. Nwoko and Shreir [57], Xiong et al. [74], Webb et al. [2], Thiemig et al. [92] and Vidrine et al. [1] observed that increasing the current density the amount of Al_2O_3 co-deposited increased and then decreased. Sautter [72] reported a small effect of the current density on the amount of Al_2O_3 co-deposited from a Watts solution containing 50 g/l of Al_2O_3. Erler et al. [98], Banovic et al. [84, 110], Shao et al. [76, 78] and Aruna et al. [85] observed that the amount of Al_2O_3 increased with decreasing current density. Thiemig et al. [92] also stated that the influence of the current density on the deposition results was extremely connected to the hydrodynamics and the cell configuration.

Different influences of the particle size on the amount of particle co-deposited have been reported. Brandes and Goldthorpe [69] and Aruna et al. [85] observed a decrease of the amount

Table 2.8 Some examples of the conditions used to electro co-deposit nickel and other particles from aqueous solutions.

Ref	$Ni(NH_2SO_3)_2$	$NiSO_4$	$Ni(BF_4)_2$	$NiCl_2$	H_3BO_3	SDS	Other chemicals	Suspended particles	pH	Means to keep the particles suspended
[51]	-	240 g/l	-	45 g/l	30 g/l	0.5 g/l	-	1-100 g/l graphite	4.5 - 5.5	Continuous mechanical stirring during deposition
[113]	-	-	280 g/l	-	40 g/l	0.1 g/l	5 g/l free fluoboric acid	50 g/l Zirconia (8.1 μm)	3.0	Mechanically controlled stirring
[114]	-	260 g/l	-	30 g/l	30 g/l	-	-	Zirconia	3.0	-
[115]	-	300 g/l	-	45 g/l	45 g/l	-	1 g/l saccharin	10-50 g/l ZrO_2 (4-10 nm)	2.5	Mechanical stirring
[116]	350 g/l	-	-	-	35 g/l	0.1 g/l	15 g/l NH_4Cl	30 g/l CeO_2 (30 nm)	-	Stirring for 2h before deposition
[50]	-	250 g/l	-	-	15 g/l	0.1 g/l	15 g/l NH_4Cl	30 g/l La_2O_3 (1-2 μm)	6.0	Mechanical agitation
[60]	400 g/l	-	-	5 g/l	30 g/l	-	0.5g/l anti pit agent	Variable amounts of TiO_2 powder (1 μm)	4.0 ± 0.2	-
[117]	-	250 g/l	-	-	20 g/l	-	Surface active agent	10-120 g/l TiO_2 (20 nm)	3.0	-
[65]	600 g/l	-	-	10 g/l	40 g/l	-	-	200 g/l Cr (< 75 μm and 5 μm -30 μm)	4.0	Rotating paddle
[118]	-	260 g/l	-	13 g/l	12.5 g/l	0.3 g/l	-	50wt.% SiC (20 nm)	4.0	Stirred for 24hrs before the deposition.
[119]	-	300 g/l	-	40 g/l	35 g/l	-	-	SiC (0.7 μm)	4.0	-

Table 2.9 Conditions used to electro co-deposit nickel-alumina composite coatings.

Ref	$Ni(NH_2SO_3)_2$	$NiSO_4$	$NiCl_2$	H_3BO_3	SDS	Other chemicals	Suspended particles	pH	T [°C]	Current density (-i)	Means to keep the particles suspended
[73]	485 g/l	-	8 g/l	22 g/l	-	0.5 g/l surfactant	10-150 g/l γ-Al_2O_3 (25nm)	3.5 - 4.0	25	150-770 $A \cdot m^{-2}$	-
[57]	-	300 g/l	45 g/l	30 g/l	-	-	Al_2O_3 (5-50nm)	3.5-4.0	50±1	10-40 $mA \cdot cm^{-2}$	N_2 was bubbled through the solution
[107]	500 g/l	-	8.5 g/l	26 g/l	-	-	1 to 15 g/l of δ- and γ-Al_2O_3 (25 nm)	3.1	-	25$mA \cdot cm^{-2}$	-
[98]	-	250 g/l	30 g/l	30 g/l	0.3 g/l	-	0.5 – 50 g/l of γ-Al_2O_3(13 nm)	4.2±0.2	55±2	0.5-8.0 $A \cdot dm^{-2}$	Stirring
[1]	-	Variable	-	-	-	88 g/l $Na_3C_6H_5O_7 \cdot 2H_2O$	25 g/l γ-Al_2O_3 (32 nm)	4.0	-	13.3-92.8 $mA \cdot cm^{-2}$	Stirring the solution and RDE.
[1]	230 g/l	-	8 g/l	30 g/l	-	-	25 g/l γ-Al_2O_3 (32 nm)	4.0	-	1-140 $mA \cdot cm^{-2}$	Stirring the solution and RDE
[1]	-	-	48 g/l	25 g/l	-	25 g/l	10 g/l γ-Al_2O_3 (32 nm)	3.0-4.5	-	39.8-92.8 $mA \cdot cm^{-2}$	Stirring the solution and RDE
[61]	350 g/l	-	15 g/l	30 g/l	-	-	50 g/l Al_2O_3 (80 nm)	4.2	40±1	Pulse co-deposition	Stirring the solution at 600rpm
[70]	38-308 g/l	-	10 g/l	40 g/l	-	-	5 g/l Al_2O_3 (80 nm)	4.0	50	3 $A \cdot dm^{-2}$	Stirring at 200rpm
[76]	400 g/l	-	10 g/l	30 g/l	0.5 g/l	0.1 g/l coumarin $C_9H_6O_2$	80 g/l Al_2O_3 (300 nm)	About 3.0	-	5-40 $mA \cdot cm^{-2}$	Stirring for 1h for suspension stability. RDEat 500-2000rpm
[77]	310 g/l	-	10 g/l	30 g/l	0.5 g/l	0.1 g/l coumarin $C_9H_6O_2$	4-80 g/l Al_2O_3 (50 or 300 nm)	About 3.0	-	20$mA \cdot cm^{-2}$	Stirring for 1 h for suspension stability. RDEat 500-2000rpm
[108]	-	250 g/l	160g/l	-	-	-	10 g/l of Al_2O_3 (50-315 µm)	3.0	50	1-300 $mA \cdot cm^{-2}$	Mechanical stirring at 1200-1700rpm
[97, 101]	-	300 g/l	60 g/l	30 g/l	0.2 g/l	-	20-100 g/l of α-Al_2O_3(< 1µm)	3.80-3.85	20	2 $A \cdot dm^{-2}$	Stirring at 800rpm
[81]	-	300 g/l	50 g/l	40 g/l	0.1 g/l	0-0.3 g/l Hexadecyl pyridinium bromide(HPB)	20 g/l of α-Al_2O_3 (< 0.8µm)	4.0	40-45	3 $A \cdot dm^{-2}$	Stirring at 300rpm

[62]	270 g/l	-	5 g/l	40 g/l	-	-	1-10g/l of γ-Al_2O_3 (13 nm)	4.3	40	1-10 $A \cdot dm^{-2}$	Stirring at 250rpm
[62]	-	50 g/l	-	-	-	250 g/l $K_4P_2O_7$ 25 g/l $C_6H_8O_7 \cdot H_2O$	1-10g/l of γ-Al_2O_3 (13 nm)	9.5	40	1-10$A \cdot dm^{-2}$	Stirring at 250rpm
[74]	430 g/l	-	-	35 g/l	0.2 g/l	2.3 g/l nickel bromide	50 g/l of γ-Al_2O_3 (50 nm)	4.0 ± 0.1	48±3	3.4-50 $mA \cdot cm^{-2}$	Magnetic stirring
[79]	-	-	-	-	-	-	150 g/l of γ-Al_2O_3 (14 nm)	3.5-4.5	50	2000 $A \cdot m^{-2}$	RDE
[82]	-	-	-	-	-	-	1.7-8.3 g/l of γ-Al_2O_3 (14 nm)	2.5-4.5	45	115 $A \cdot m^{-2}$	-
[72]	-	300 g/l	45 g/l	30 g/l	-	0.2 v/o N13-wetting agent	0-150 g/l of γ-Al_2O_3 (10-40 nm)	1-5	20-80	1-5 $A \cdot dm^{-2}$	Stirring
[95]	-	Sulfate	-	-	-	-	2.2 µm and 0.3 µm Al_2O_3	-		-	-
[52]	-	315 g/l	-	25 g/l	-	-	30 g/l of α-Al_2O_3 (300 nm) or γ -Al_2O_3 (50 nm)	3.2	Room T	12.5 $mA \cdot cm^{-2}$	RDE
[78]	310 g/l	-	3 g/l	31 g/l	0.5 g/l	0.1 g/l coumarin	4-80 g/l of Al_2O_3 (50 or 300 nm)	3.0	-	5-40 $mA \cdot cm^{-2}$	RDE
[2]	-	-	26 g/l	25 g/l	-	25 g/l NaCl, 1.5g/l sodium saccharin, 0.01g/l FC95 surfactant	2-20 g/l of γ-Al_2O_3 (10 nm)	3.0	Room T	2-50 $mA \cdot cm^{-2}$	RDE
[110]	400 g/l	-	5 g/l	30 g/l	0.5 g/l	0.1 g/l coumarin	A-Al_2O_3 (0.6-0.8 µm)	4.0±0.2	50±2	5-250 $mA \cdot cm^{-2}$	-
[84]	400 g/l	-	5 g/l	30 g/l	0.5 g/l	0.1 g/l coumarin	75, 150, 225 g/l of α-Al_2O_3 (0.6-0.8 µm)	4.0±0.3	50±2	5-250 $mA \cdot cm^{-2}$	Stirring at 400rpm
[85]	215 g/l	-	10 g/l	30 g/l	0.2 g/l	-	100 g/l of α-Al_2O_3 (5.5 µm) or α- and γ-Al_2O_3 (0.54µm)	4	-	0.23-5.4 $A \cdot dm^{-2}$	-
[90]	275 g/l	-	6 g/l	30 g/l	0.2 g/l	-	150 g/l of Al_2O_3 (1µm)	4	50	0.8-1 $A \cdot dm^{-2}$	Stirring at 200rpm

[112]	-	300 g/l	35 g/l	40 g/l	0.05-0.15 g/l	0.8-1.2 g/l saccharin	20-120g/l of α-Al_2O_3(0.5 μm)	3.6-4	50±3	10 A·dm^{-2}	Stirring at 350rpm
[91]	90 g/l	-	3 g/l	40 g/l	-	-	39 g/l of δ-Al_2O_3 (30 nm)	4-5	50±2	4 A·dm^{-2}	Gentle stirring
[92]	270 g/l		10 g/l	40 g/l	-	-	0-120g/l of γ-Al_2O_3 (13 or 50 nm)	4.3	40	1-10 A·dm^{-2}	-
[100]	-	264 g/l	24 g/l	12 g/l	0.3 g/l	-	20g/l of Al_2O_3 (13 nm)	4	40	2 A·dm^{-2}	Stirring at 300rpm
[53-55]	-	264 g/l	-	-	-	56 g/l ammonium citrate, 23 g/l ammonium acetate, 105 g/l ammonia	20 g/l of Al_2O_3 (30-50 nm)	7-7.4	20	-	-
[93]	-	300 g/l	45 g/l	30 g/l	-	-	10 g/l /l of α-Al_2O_3 (100 nm)	4	50	3 A·dm^{-2}	Magnetic field (0.5-10 T)

Table 2.10 Conditions employed in electro co-deposition and sediment co-deposition to produce Ni-Al composite films.

Ref	$Ni(NH_2SO_3)_2$	$NiSO_4$	$NiCl_2$	H_3BO_3	SDS	Other chemicals	Suspended particles	Current density	pH	T	Means to keep the particles suspended
[64, 110]	400 g/l	-	5 g/l	30 g/l	0.5 g/l	0.1 g/l Coumarin	150 to 225 g/l Al powder (1-4 μm)	10-250 mA·cm^{-2}	4.0 ± 0.1	50°C	Magnetic stirring at 400 rpm
[121, 122]	-	150 g/l	-	15 g/l	0.1 g/l	15 g/l NH_4Cl	Al powder (75 nm and 1-5 μm) (quantity not mentioned)	20 mA·cm^{-2}	5.5-6.0	35°C	A reciprocating perforated plate
[47, 48]	-	270 g/l	45 g/l	40 g/l	0.2 g/l	-	5-150 g/l Al particles (3 μm)	20-90 mA·cm^{-2}	4.0	Room T	Magnetic stirring (400 rpm) following on/off time 1200/10 s
[59, 124]	56 g/l	-	-	9 g/l	-	15 g/l $(NH_4)_2SO_4$ 15 g/l CH_3COOH	20-140 g/l Al particles (75 μm)	200-450 mA·cm^{-2}	3.5 -4.5	20°C and 50°C	Magnetic stirring at 150 rpm

of α-Al_2O_3 co-deposited increasing the particle size from 5 to 30-40 μm or from 0.54 to 5.5 μm, respectively. Whereas, Shao et al. [78] reported that bigger particles (300 nm vs 50 nm) were incorporated in the film in higher volume fraction but lower particle number density. Verelst et al. [95] reported that the particle size (0.3 and 2.2 μm) did not influence the amount of particle co-deposited.

The concentration of electrolyte in the bath and the bath composition affect also the amount of Al_2O_3 co-deposited. Vidrine et al. [1] reported that the amount of Al_2O_3 co-deposited was between 0.14 and 1.03 wt.% (0.31 and 2.28 vol.%) from a citrate bath and between 2 and 7 wt.% (4.39 and 14.48 vol.%) from a chloride bath starting from a suspension containing 25 g/l of Al_2O_3 with size 32 nm. Kuo et al. [70] observed that decreasing the concentration of electrolyte in the bath from 1.2 M to 0.3 M produced an increase from 8.37 to 26.78 vol.% of the amount of nano-Al_2O_3 co-deposited. This increase was explained considering that the smaller agglomerates at lower Ni^{2+} concentration presented more opportunities to be adsorbed onto the electrode. However, it was also observed that a further decrease of the Ni^{2+} concentration to 0.1 M produced a slightly decrease of the amount of Al_2O_3 particles co-deposited (24.65 vol.%) because of the lower current efficiency and the obstruction of the adsorption of Al_2O_3 particles on the cathode by the hydrogen evolution. They [70] also observed that employing lower Ni^{2+} concentrations a more uniform Al_2O_3 distribution in the film was achieved.

Moreover, Sautter [72] also reported that the bath temperature and the bath pH between 2 and 5 did not influence the amount of Al_2O_3 co-deposited, but bath pH lower than 2 produced a considerable decrease in the amount of Al_2O_3 co-deposited, in agreement with findings obtained with copper electrolytes containing SiC or Al_2O_3 particles [15]. Similar results were also reported by Nwoko and Shreir [57], who observed a decrease in Al_2O_3 co-deposition with decreasing pH and explained it considering the decrease of nickel deposition efficiency that lowers the deposition rate diminishing the rate of entrapment of the particles and at the same time increases the hydrogen evolution thus not allowing the particles to be deposited.

Webb et al. [2] and Shao et al. [78] observed in correspondence of the higher amount of Al_2O_3 co-deposited a decrease of the metal current efficiency, that was attributed to the competition between the nickel deposition, which is charge-transfer controlled, and the Al_2O_3 co-deposition, which is limited by the mass transfer when higher current densities are employed. Whereas Barmak et al. [110] observed that the deposition rate was not affected by the particles in the bath for current densities between 0 and 25 $A \cdot dm^{-2}$. They [110] also observed that at higher current densities the Al_2O_3 presence interferes with Ni deposition.

All the depositions considered here are obtained from conventional direct current plating. In the literature it has been reported that pulse reverse plating (if the pulse length is long enough) can be employed to increase the concentration of particles embedded in the film by dissolving a fraction of plated metal during the reverse pulse therefore increasing the amount of

co-deposited particles [1, 74]. This process however has not been taken into consideration for the present project.

ii) Agglomeration

Following the increasing interest in the production of nano-materials, many researchers have reported the production of composite coatings containing Al_2O_3 particles smaller than 100 nm [1, 2, 52-54, 61, 62, 70, 72-74, 78, 79, 82, 91, 92, 94, 98, 100, 107, 109]. Although the production of nano-composite coatings advanced rapidly, some problems such as the uniform distribution of nanoparticles in the matrix, the control of the amount of reinforcement co-deposited and the nanoparticle agglomeration are still unsolved [70]. In fact, nanoparticles present a strong tendency to agglomerate in the bath because of their high surface energy [54, 57, 62, 70, 72, 79, 85] and, during co-deposition, the agglomerates are embedded in the coating reducing the potential mechanical properties of the composites. Consequently numerous studies have been carried out to reduce particle agglomeration in solution employing chemical or physical methods. The chemical methods consisted of adding surfactants, macro-molecules or metal cations in the electrolytic bath; when these chemicals are adsorbed on the particle surfaces they produce electrostatic or steric interactions that improve effectively the repulsions between particles improving their distribution in the film. The physical method consists of applying ultrasonic energy that destroys the binding energy between the agglomerated particles [70].

Kuo et al. [70] observed a considerable decrease of the agglomerate sizes applying both chemical and physical methods and they also reported that a decrease of agglomeration considerably enhanced the amount of particles co-deposited. They [70] also observed that decreasing the ionic strength of a nickel sulphamate bath the average agglomerate size decreased. The same behaviour was also reported by Vidrich et al. [107] and by Erler et al. [98]. Vidrich et al. [107] observed that increasing the ion concentration in solution the zeta potential decreased and the Al_2O_3 agglomeration size rose. This result was explained considering that at higher ion concentrations the electrolytic double layer is compressed and the electrostatic repulsions between particles decrease while Van der Waals attractions dominate. Therefore the strongest agglomerations take place close to the isoelectric point. Bund and Thiemig [62] observed that the agglomeration behaviour of nano-Al_2O_3 particles depended also on the type of bath, in fact 200 nm size agglomerates were observed in sulphamate bath and 100 nm in pyrophosphate bath. Erler et al. [98] treated the suspension with ultrasonic vibration and by measuring the particle size they confirmed that this method successfully broke the Al_2O_3 agglomerates, which remained of the same size for a week. Shao et al. [78] reported that the nano-Al_2O_3 was well dispersed when the concentration in the film was < 16 vol.%, but that for concentrations higher than 20 vol.% the aggregation became significant.

The same agglomeration problem was also observed when bigger Al_2O_3 particles (0.8

μm) were employed, as described by Chen et al. [81] and Banovic et al. [84]. Chen et al. [81] observed that the vol.% of Al_2O_3 co-deposited increased with the surfactant (hexadecyl-pyridinium-bromide (HPB)) concentration, as also observed by Ger [120] for the Ni-SiC system. This behaviour was explained considering that the particle zeta potential increased gradually with the increase of the surfactant concentration. Chen et al. [81] also observed that adding HPB decreased the agglomeration of the Al_2O_3 particles in suspension and in the film and improved their distribution in the Ni matrix. The mechanical properties of the composite coatings were strongly related to the amount of HPB in the bath: micro-hardness and wear resistance increased for HPB concentration below the optimum and then decreased because of the increase in brittleness of the metal matrix caused by the HPB inclusions.

iii) Microstructure

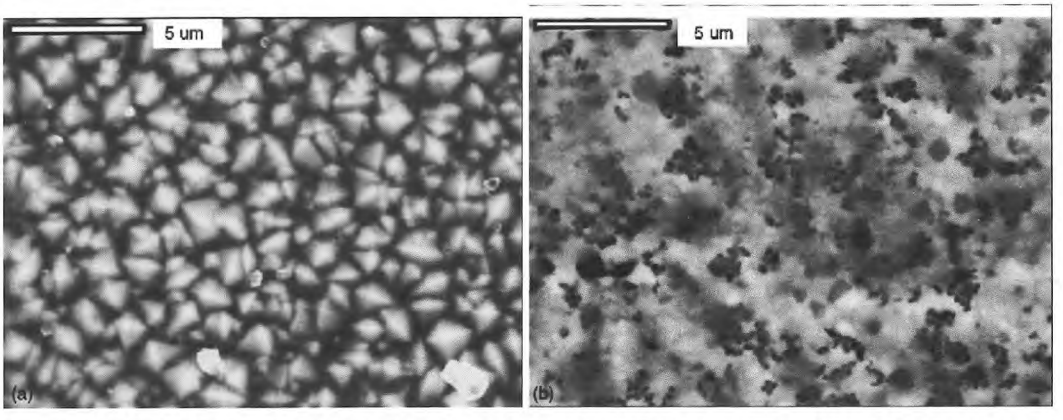


Figure 2.6 SEM micrographs of a) nickel coating and b) Ni-Al_2O_3 composite coatings electro co-deposited from a Watts bath containing 100 g/l of Al_2O_3 particles with size < 1 μm and applying a current density of 20 mA·cm^{-2} (redrawn from ref. [97]).

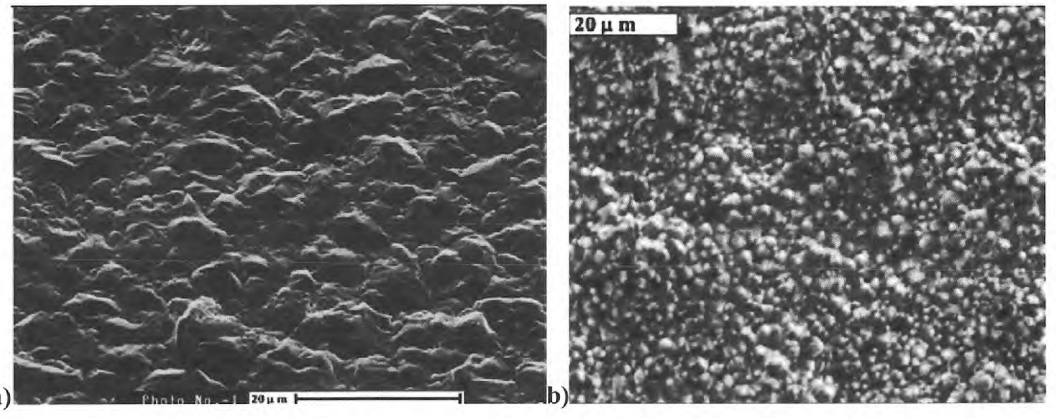


Figure 2.7 SEM micrographs of a) nickel coating and b) Ni-Al_2O_3 composite coatings electro co-deposited from a Watts bath containing 20 g/l of nano-Al_2O_3 particles and applying a current density of 20 mA·cm^{-2} (redrawn from ref. [100]).

It has been extensively reported in the literature that the introduction of a second phase in an electro co-deposited film modifies the crystallographic structure of the metal and that the

kind of particles, their size and their concentration influence the properties of the metal matrix. Bund and Thiemig [62] reported that the nickel films deposited from the sulphamate bath have a well-defined columnar structure and that this structure changes to the unoriented dispersion type when Al_2O_3 particles were added; whereas the films deposited from the pyrophosphate bath with and without Al_2O_3 presented a granular structure with fine grains. Szczygiel et al. [97] and Ciubotariu et al. [100] observed that the co-deposition of Al_2O_3 with particle size < 1 μm [97] or 13 nm [100] changed the nickel structure from a regular pyramidal crystal structure to a disordered structure (see Fig. 2.6 and 2.7). The Al_2O_3 particles were uniformly distributed in the film; some of them emerged from the nickel surface and others, even if completely embedded in it, were not fully covered by the Ni because non conductive [97, 100].

Aruna et al. [85] noticed that the current density influenced the crystalline orientations of nickel and Ni-Al_2O_3 films and that the nickel grain size did not increase with increasing current density, but decreased with the incorporation of Al_2O_3 powder; an opposite behaviour (size increased with increasing current density but did not vary with the presence of Al_2O_3 particles) was reported by Banovic et al. [84]. Banovic et al. [84] also observed that the composite films deposited applying a current density below 1 $A \cdot dm^{-2}$ were relatively smooth whereas when higher current densities were applied some structures, attributed to the Ni growth around Al_2O_3 particles, were observed. When higher current densities were applied the Ni was reduced faster than it could diffuse across the surface producing a rough growth and the formation of a ridge; whereas under lower current densities the nickel was deposited slowly allowing its diffusion and the production of a smoother surface [84].

Different distributions of Al_2O_3 in the films were reported. Nwoko and Shreir [57] observed that the Al_2O_3 particles were randomly distributed in the films and that the Al_2O_3 inclusions increased the number of dislocations compared to pure Ni films. Erler et al. [98] noted that the nanoparticles were incorporated as clusters and that they were not uniformly distributed. In fact in the first 2-3 μm of the layer there were zero or very few particles. This effect was explained considering that at the beginning the deposition can occur only on electrode areas without particles and a particle free layer is deposited and then the particles can stick to the rough nickel surface being consequently embedded by the growing metal layer.

Verelst et al. [95] observed that the Ni-Al_2O_3 interface was not continuous and contained large voids in the as deposited composite film, this weak interface changed after treatments at 1200°C when a solid state reaction took place between Al_2O_3 and Ni probably producing a strong interface and improving the mechanical properties of the composite. Contrary, Shao et al. [78] reported that the Al_2O_3 particles were well-adherent to the Ni matrix with no voids along the boundary. Erler et al. [98] measured the residual stresses in pure nickel coatings and in composite coatings containing nano-Al_2O_3 or nano-TiO_2 particles and observed completely different behaviours due to the different particle influences on the crystallisation mechanism of Ni and the development of different crystalline structures. Tu et al. [53, 55] observed by X-Ray

Photoelectron Spectrometry (XPS) that there is a chemical bond between the nanoparticles and the nickel matrix, in particular the bond takes place between the unsaturated chemical bonds of oxygen atoms and the Ni atoms. These chemical bonds produce compact bindings between the nanoparticles and the Ni matrix and can advantageously improve the film properties. They [53, 55] also reported that the nanoparticles increased the current efficiency and decreased the overpotential of the process catalysing the Ni deposition through nucleation centres.

iv) Mechanical properties

The addition of Al_2O_3 to Ni films influences the coating mechanical properties; a brief summary of the results reported in the literature is presented here.

Numerous researchers reported that the inclusion of Al_2O_3 in Ni coatings increased their hardness [52, 54, 61, 75, 78, 81, 82, 84, 85, 89-94] thanks to the reinforcement hard nature and its influence on the metal microstructure and grain size [62, 84]. Few researchers [52, 78, 84, 89, 93] observed that the hardness increased linearly with the amount of Al_2O_3 embedded in the coatings. Moreover, considering the same particle concentration in the films (0.5 vol.% [78] and 8 vol.% [89]) it seemed that the smallest particles increased more effectively the hardness than the bigger one. Bund and Thiemig [62] employed two different baths to carry out the co-deposition of Ni-Al_2O_3 coatings and observed that the micro-hardness considerably increased with the amount of Al_2O_3 in the coatings deposited from a sulphamate bath, whereas only a slightly variation was observed when a pyrophosphate bath was employed.

The yield strength [72, 95] and the ultimate tensile strength [95] were observed to increase with the incorporation of Al_2O_3 in the coatings; the tensile strength increased as much as four times with the incorporation of Al_2O_3 [57, 89]. These increases were at the expense of the ductility (elongation at rupture) that decreased drastically with the amount of Al_2O_3 co-deposited in the film [89, 95]. Composites containing 2.2 μm Al_2O_3 particles seemed slightly stronger than those with smallest particles (0.3 μm), but the latter were able to maintain the matrix ductility [95]. The opposite behaviour was reported by Ding et al. [89], who observed that composites with smaller particles were more brittle than those with bigger particles.

Wang et al. [91], Feng et al. [93] and Xu et al. [54, 94] observed that the wear resistance of Ni-Al_2O_3 films was higher than that of pure nickel. Chen et al. [81] explained this behaviour considering the reinforcement hard nature. In another study the same group [75] observed a decrease of the wear resistance of Ni-Al_2O_3 films under dry sliding conditions with increasing Al_2O_3 content; this unexpected behaviour was due to the roughness of the Ni matrix. In fact they [75] also reported that the wear resistance of the same coatings under oil-lubricated conditions increased with increasing amounts of Al_2O_3 because the oil prevented adhesive wear and in these conditions the anti-wear performances of the coatings depended on the Al_2O_3 content and not on the coating roughness.

vi) Corrosion resistance

The results reported in the literature for the corrosion properties of Ni-Al_2O_3 composite coatings are inconsistent, possibly due to the fact that the inclusion of the second phase affects the surface morphology of the films in different ways modifying the protective properties. For example, Erler et al. [98] observed that the corrosion resistance of Ni-Al_2O_3 composite coatings under salt spray test deteriorated compared to pure Ni coatings and considerably different behaviours were observed between specimens produced under the same plating conditions. The corrosion difference between pure Ni and Ni-Al_2O_3 films was explained considering a higher diffusion of the chloride ions at the interface Ni-Al_2O_3 [98]. Szczygieł and Kołodziej [97, 101] observed that the anticorrosion properties of Ni-Al_2O_3 composite coatings in Na_2SO_4 and in NaCl solutions were higher than that of pure Ni due to the change in the metal texture and microstructure following the co-deposition of the second phase, as shown in Figure 2.6. Ciubotariu et al. [100] reported that the corrosion resistance of the nanostructured Ni-Al_2O_3 films was higher than that of pure Ni in both 0.5 M K_2SO_4 and 0.5M NaCl solutions for the finer surface structures of the composites compared to pure Ni (see Figure 2.7) and the insulator action of the Al_2O_3 particles [100].

2.2.4.2 Electrochemical co-deposition of Ni-Al composite coatings

Composite films containing Al particles have recently attracted considerable attention for their resistance to oxidation at high temperatures [121-123] and their relative high hardness [64]. The high temperature oxidation resistance is due to the presence of enough Al content (6-7 wt.% [123]) in the film to develop a slow-growing, thermodynamically stable and continuous layer of α-Al_2O_3. Conversely, lower Al content would deteriorate the oxidation resistance of the coatings compared to pure nickel [121-123]. It has to be mentioned that often conventional commercial alloys cannot form this α-Al_2O_3 scale because their Al content is not high enough and higher Al content would increase the material brittleness [121, 122]. Therefore the deposition of composite films containing Al is a solution to protect substrates with poor oxidation resistance at high temperature. The hardness increase of coatings containing a low amount of Al was explained by Susan et al. [64] considering the refinement of the matrix microstructure. They [64] also underlined that higher amounts of Al would produce an opposite effect due to the softness of this material compared to nickel. Ni-Al composite coatings have been deposited using electrochemical methods, such as electro co-deposition [64, 121-123] and sediment co-deposition [47, 48, 59, 124], the conditions employed are listed in Table 2.10. The electro co-deposition of Ni-Al composite films was studied by Susan et al. [64, 123] and Zhou et al. [121, 122].

Susan et al. [64] observed that the films were without voids, cracks or other defects and that the distribution of Al particles in the Ni matrix was uniform. Moreover, some of the Al particles on the coating surface were completely surrounded by nickel and other were not. This

phenomenon was explained considering that the electrically conductive particles embedded into the coating become part of the cathode and the nucleation and growth of the metal took place also on their surfaces. While Zhou et al. [121, 122] found that the as deposited film contained a high density of pores and pinholes. Moreover they observed that in the major area of the deposit (see letter A in Fig. 2.8) the Al particles were surrounded by nickel, while in other parts (see letter B in Fig. 2.8) there were fresh deposits enriched with Al and in some parts there were pores and holes (see letter C in Fig. 2.8) due to the breakage of fresh deposits during rinsing.

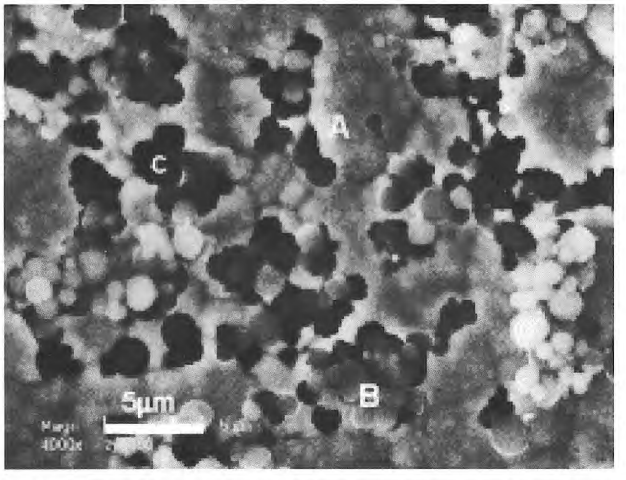


Figure 2.8 Surface morphology of the as-deposited Ni-28Al composite film obtained by Zhou *et al.* (redrawn from ref. [122]).

Susan et al. [64] calculated the volume per cent (vol.%) of Al embedded in the Ni matrix when different current densities were applied obtaining that the Al content in the film was maximum (20 vol.%) when the Al concentration in the bath was 225 g/l and the current density 50 $mA \cdot cm^{-2}$. While a further increase in the current density caused a decrease of Al content to about 12 vol.%. The same trend was also observed when the Al concentration in the bath was 150 g/l, but in this case the Al content in the coating was lower. Zhou et al. [121, 122] deposited composite films containing 28.0 wt.% of Al, this value cannot be compared with the results obtained by Susan et al. [64] because the authors [121, 122] did not mention the concentration of Al particles in the suspension. Zhou et al. [121] noticed an increased of the Al content in the coating increasing the concentration of Al particles in the bath (as it was also observed by Susan et al. [64]), but they did not study the dependence of these two variables. Moreover, they [121] compared films containing micron and nano-Al particles concluding that the distribution of nanoparticles was more homogeneous than that of micron-particles, even if in some parts of the deposit the nanoparticles were agglomerated into clusters.

2.3 Electrophoretic deposition

2.3.1 Introduction

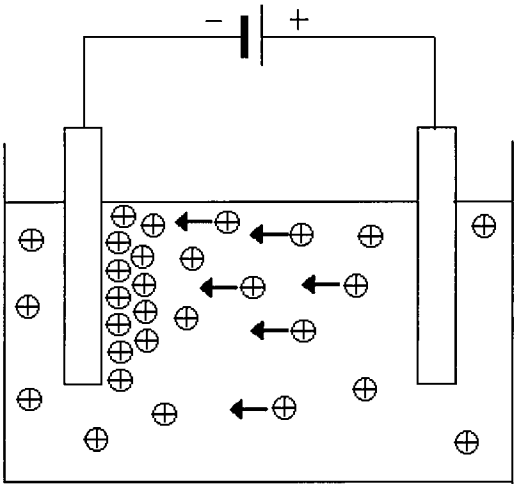


Figure 2.9 Schematic representation of the cell used in electrophoretic deposition when the charged particles in suspension are positively charged (redrawn from ref. [23]).

Electrophoretic deposition (EPD) is an electrochemical method used to produce coatings [17-20, 23, 125, 126] and free standing objects [17, 127, 128]. The interest in EPD has recently increased both in academia and in the industrial sector because of its cost-effectiveness (short time and simple apparatus required), its ability to produce coatings onto substrates with complicated shapes [129] and its high versatility making EPD a method applicable to deposit any solid material (metal, polymer and ceramic) that is available as a fine powder (< 30 μm) or as a colloidal suspension [17-23, 125]. During the past decades EPD has been largely employed for the deposition of coatings. However, this technique has also shown potential to produce composite materials by infiltrating porous substrates (e.g. fibre fabrics) with a second phase [17-19, 23, 126] and it enables the deposition of layered materials using two suspensions with different compositions (e.g. by moving the substrate from one suspension to another, when the desired thickness is reached it is possible to develop coatings having layers of different compositions [17, 23, 125, 126, 130, 131]). In addition to layered composites, EPD facilitates the deposition of functionally graded materials by *gradually* changing the composition of the suspension [17-19, 23, 125, 126, 132]. This kind of materials presents a gradual change in the composition from one face to the other allowing a similar gradual change in the properties. An example of application for functionally graded materials is the joining of a metal layer and a ceramic one, considering that they present very different thermal expansion coefficients leading to very high residual stresses during cooling, the production of functionally graded metal-ceramic coating could possibly solve this problem [105]. EPD has also been used to deposit nanoparticles or carbon nanotubes [18, 19, 23, 133] to produce advanced nano-structured

functional coatings. The increasing interest in the field of EPD has led to the establishment of the international EPD: Fundamentals and Applications conference series [134, 135].

EPD occurs in two steps. In the first step, an electric field is applied between two electrodes and the charged particles in suspension move toward the opposite charged electrode (electrophoresis) while in the second step, the particles accumulate at the electrode and create a relatively compact and homogeneous film (deposition) (see Figure 2.9). Therefore in order to apply this technique it is fundamental to produce a stable suspension containing charged particles free to move in the suspension [17, 18, 20-23]. The main differences between EPD and electrochemical deposition of a metal, which was discussed in section 2.1, are listed in Table 2.11 [21]. It follows that EPD is a non-faradic process governed by laws different from those governing electroplating [125]. After electrophoretic deposition, a heat-treatment step is normally required to further densify the deposit and to eliminate porosity [17, 18, 20-23, 125]; this is another difference compared to electrodeposition.

Table 2.11 Principal differences between electroplating and electrophoretic deposition (after ref. [21]).

	Electroplating	**EPD**
Moving species	Ions	Solid particles
Charge transfer on deposition	Electrons for ions reduction	None
Required conductance of the liquid medium	High	Low
Preferred liquid	Water	Organic
Deposition rate	~ 0.1 $\mu m \cdot min^{-1}$	~ 1 $mm \cdot min^{-1}$

2.3.2 Properties of charged particles

When two phases come into contact, there is a redistribution of positive and negative charges on their interface producing a so-called electric double layer that is of the order of few nanometers. The charge redistribution process can be due to different mechanisms:

1. the adsorption of ions onto the particle surface from the liquid [136];
2. the dissociation of ions from the solid phase to the liquid;
3. the adsorption or the orientation of dipolar molecules on the particle surface;
4. direct electron transfer between the two phases [17, 21, 22].

Considering ceramic or glass particles in water or organic liquids, the last mechanism does not apply, but the other three invariably occur. A charged particle in suspension is surrounded by a shell of counter ions (ions with an opposite charge), as shown in Figure 2.10. The concentration of these counter ions is higher close to the particle (double-layer or Stern layer) than in the bulk of the suspension. When an electric field is applied, the counter ions and the particles should move in opposite directions because they have opposite charges. However, as a result of the attraction between them, part of the ions surrounding the particle will move in the same direction of the particle, and therefore the direction of the particle depends on the net charge of

the double-layer and not just on its individual charge [17, 22].

A measure of the surface charge of a particle is given by the zeta-potential ζ, which is defined as the potential of a particle at the surface of shear, which is the limit between the liquid moving with the particle (double-layer) and the liquid that does not move with it (see Figure 2.10). The value and the sign of zeta-potential are influenced by many factors, such as the presence of electrolytes, the suspension concentration and the pH. Moreover, it has to be noticed that zeta-potential can be positive for a negative particle if the charge of the specifically adsorbed ions is higher than the particle charge. Therefore this is a fundamental parameter to determine the particle behaviour under an applied electric field and to predict if there will be anodic, cathodic or no net deposition [17, 21, 22].

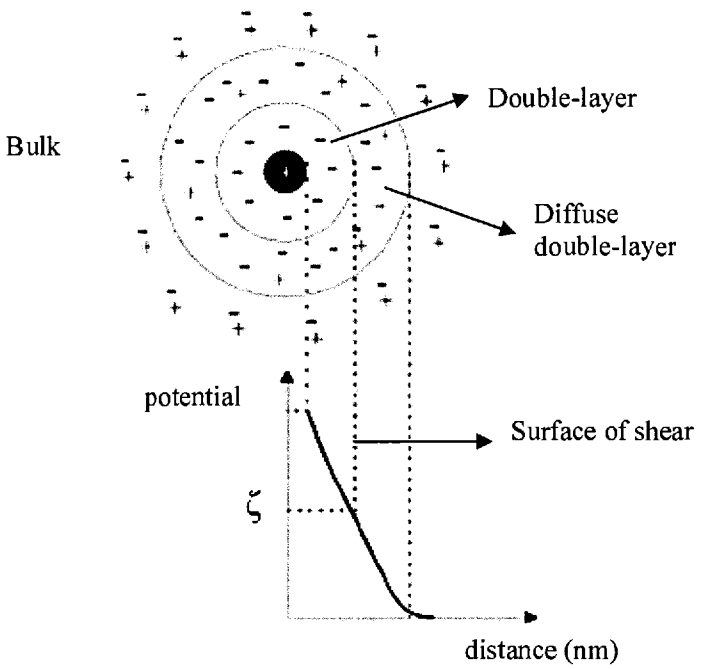


Figure 2.10 Scheme of the double layer surrounding a charged particle and variation of the electric potential from the particle surface to the bulk of the suspension (modified from ref. [17]).

2.3.3 Properties of the suspension

Successful EPD relies on the preparation of a stable suspension containing charged particles (high zeta-potential) and with low ionic conductivity (the stability of suspensions is usually reduced with increasing ionic concentration [17]) and low viscosity. Suspensions are usually characterised by numerous parameters that will be discussed below [17, 20].

i) Particle sizes

There is not a general rule to specify the suitable particle size for EPD, in fact good deposition results for a variety of materials with particle size from a few nm to 30 μm have been reported. The fundamental characteristic for successful EPD is the complete dispersion

and stability of the particles in the suspension. The main problem connected to the deposition of large particles is their tendency to sediment due to gravity, making the deposition of uniform films difficult. In order to deposit large particles a very strong surface charge or a large electrical double layer region must be achieved [20], so that the coulombic force compensates the gravitational force.

ii) Suspension media

The liquids used in EPD should be inert to the powder and they may be either distilled water or organic solvents. The main drawback of using aqueous suspensions for EPD is the electrolysis of water that occurs at low voltages (about 5 V) and produces gas evolution at the electrodes. The gas evolution is unavoidable if the applied electric field is strong enough to have relatively short deposition times and the consequence is the production of a deposit with inclusion of gas bubbles. Another drawback related to the use of water is the adsorption of water in the deposit that causes major shrinkage and cracking during drying [17]. Organic media generally have a lower dielectric constant (the dissociating power of the liquid) than water. This is a disadvantage because the particle charge is reduced, but at the same time higher field strengths (about 100–1000 $V \cdot cm^{-1}$) can be applied because in these liquids the problems due to the electrolytic gas evolution are reduced. Therefore in EPD the use of organic liquids has been usually preferred over water, even if it is possible to obtain successful deposits from both media and the use of water is still of current interest because it is less expensive and less harmful for the environment compared to organic solvents [17].

The organic media typically used can be distinguished in two main groups: alcohols and aprotic solvents. Alcohols are similar to water and therefore the acid/base chemistry involved between the particles and the liquid does not change significantly when the medium is an alcohol instead of water [17]. In fact Wang et al. [137] analysed the electrophoretic mobility of alumina in ethanol (dielectric constant $\varepsilon = 25$) observing a variation from positive at low pH to negative at high pH, entirely analogous to the behaviour observed in water. They [137] also showed that electrostatic stabilization in ethanol is possible. Examples of aprotic solvents are ketones, ethers and hydrocarbons. Their dielectric constants (ε) are around 15 for ketones and lower than 10 for ethers and hydrocarbons (the dielectric constant of water is 78.5). Powers [138] carried out EPD of β-Al_2O_3 from different organic solvents and demonstrated that in order to achieve deposition the solvent dielectric constant was required to be between 12 and 25. Solvents with a lower dielectric constant did not dissociate enough to produce a reasonable charge on the particles, while solvents with dielectric constants higher than 25 reduced the size of the double layer and the electrophoretic mobility. An explanation of this behaviour was not provided; it must be taken into consideration that it was possible to deposit coatings from aqueous solution, with a dielectric constant considerably higher than 25 [17, 20, 21].

iii) Conductivity of suspensions

The conductivity of the suspension is an important factor in EPD experiments and therefore it needs to be considered. It has been reported [20] that if the suspension conductivity is too high the particle motion is low because the large amount of free ions in suspension is the main current carrier. If the suspension conductivity is too low the particles charge electronically and the suspension loses stability. There is therefore a range of conductivity suitable for EPD that differs for different particle-media systems and it is influenced by the suspension concentration, the pH and the temperature. For example, it has been reported in the literature [139] that it was possible to deposit alumina film from ethanolic suspensions at 30°C with concentration of 5 wt.% or 10 wt.% and conductivity of 140-170 $\mu S \cdot cm^{-1}$ or 270-320 $\mu S \cdot cm^{-1}$.

iv) pH

In section 2.3.2, the ways that particles in suspension obtain a surface charge was described. Most oxides in aqueous suspension will obtain a charge by adsorption or de-sorption of protons due to a chemical reaction of the surface groups, which can be acidic, alkaline, or amphoteric. This reaction depends on the pH of the suspension. At this point it is worthwhile introducing two properties strongly related to the pH: the point of zero charge (pzc) and the isoelectric point (iep). The *point of zero charge* (pzc) is the value of pH at which H^+ and OH^- are adsorbed in equal amounts whilst the pH that leads to no net charge on the surface is termed *isoelectric point* (iep) or the *point of zero zeta potential* (pzzp). These two points, pzc and iep, can be different when, for example, multivalent metal ions are added to the suspension. Therefore in order to achieve a stable suspension containing charged particles it is fundamental to change its pH (by adding acid or base) and to set it far from either pzc or iep [17].

v) Zeta potential and suspension stability

As already mentioned in section 2.3.2, the particle zeta potential is an important factor in EPD since it plays a role in the suspension stability: suspensions containing highly and uniformly charged particles are stable. The suspension stability depends on electrostatic interactions and van der Waals forces between the suspended particles. In order to avoid particle agglomeration high electrostatic repulsion, achieved with high particle charge, is required. In general, the higher the zeta potential absolute value the better the particle dispersion in suspension. The zeta potential can be controlled and varied by adding to the suspension charging agents, such as acids, bases and specifically adsorbed ions.

The suspension stability depends on the settling rate and on the ability of the particles to avoid flocculation. Stable suspensions do not flocculate and do not form deposits on the bottom of the container (which flocculating suspensions generally do). It is therefore important to produce a stable suspension but it has also to be considered that if a suspension is too stable, the repulsive forces between the suspended particles will not be overcome by the applied

electric field and therefore there will not be deposition [20].

2.3.4 EPD parameters

The most influencing parameters in EPD are the process parameters, such as the applied voltage (or current), the deposition time and the suspension concentration.

i) Effect of the deposition time

The relationship between deposition yield and time for a fixed applied field is linear at the beginning of the process and then it reaches a plateau. When EPD is carried out under constant voltage, this trend is explained considering that the potential difference between the electrodes is kept constant but the electric field decreases with deposition time because an insulating layer of material is deposited on the electrode surface [20, 22].

ii) Effect of the applied voltage

Normally, the deposition yield increases with increasing difference of potential applied. It has to be considered that the quality of the deposit depends also on the magnitude of the applied field and if moderate fields (10-100 $V \cdot cm^{-1}$) are employed uniform coatings are deposited. This phenomenon is explained considering that the packing of the particles in the film is influenced by their accumulation rate. Therefore if high electric fields are applied the particles move fast towards the electrode and they might not be able to find their best position to form a close-packed structure [20].

iii) Effect of the suspension concentration

In contrast to other colloidal processes, such as slip casting and tape casting, in EPD it is possible to use suspensions with low concentration of solid particles. These suspensions present relatively low viscosity and permit to deposit relatively high density coatings (green density of about 40-60 vol.%) from suspensions with low solid loadings (1-2 vol.%) [17].

iv) Hamaker`s equation

The quantity of material deposited during EPD is directly proportional to the three parameters discussed above: deposition time, applied voltage and suspension concentration. This value can be theoretically calculated using Hamaker`s equation [20, 21, 125]:

$$M = \int_0^t aAC\mu E \cdot dt \qquad [2.15]$$

where M is the mass deposited in the time t, a is a coefficient representing the fraction of particles near the electrode that are deposited, A the electrode area [m^2], C the particle concentration in the suspension [kg/m^3], μ the electrophoretic mobility [m^2/Vs] and E the electric field applied [$V \cdot m^{-1}$] [20, 21, 125]. A, C and E are externally controlled parameters, while μ depends on the properties of the suspension. In the simplified double layer theory the

interface is treated as a pure capacitor and the electrophoretic mobility μ is given by Smoluchowski`s equation [21]:

$$\mu = \frac{\varepsilon \cdot \zeta}{4\pi\eta} \qquad [2.16]$$

where ε is the dielectric constant of the liquid, ζ the zeta potential and η is the viscosity of the liquid. This equation is valid if the double layer region is relatively small compared to the particle radius, in other words for systems of large particles in aqueous suspensions. Whereas when the system consists of small particles in a non-ionizing solvent it is more appropriate to use Hückel`s equation:

$$\mu = \frac{\varepsilon \cdot \zeta}{6\pi\eta} \qquad [2.17]$$

which is valid just for spherical particles [21]. In addition, it has to be considered that the speed of a particle in the suspension is due to four different forces acting on the particle. The first force accelerates the particle and is due to the interaction of the surface charge with the electric field. All the other forces slow the particle and are due to the viscosity of the suspension, the electric forces exerted on the counter ions in the double layer and the distortion of the double layer when the particle moves, due to a dislocation between the centre of negative and positive charges [17].

2.3.5 Mechanisms for the formation of deposits by EPD

The mechanisms of electrophoretic deposition have been largely studied in the past decades but it is still not completely clear. A better understanding of the mechanisms is needed to avoid time-consuming trial-and-error experiments to determine the best parameters for the deposition [17, 18, 20, 23]. It is possible to distinguish four basic mechanisms for the formation of deposits by EPD: particle accumulation, charge neutralization, zeta-potential lowering or electrochemical coagulation, and electrical double layer distortion and thinning. Additional theoretical and modelling studies have being also carried out to clarify the mechanisms of deposition and the role of the electrochemical parameters on the complex interactions between solvent, particles and electric field.

i) EPD due to particle accumulation

Hamaker and Verwey [140, 141] observed similarities between the formation of deposits by electrophoresis and gravitation. In fact, in both processes, the pressure exerted by the arriving particles enables the particles close to the deposit to prevail over the inter-particle repulsion. Therefore the primary function of the applied electric field in EPD is to move the particles towards the electrode to accumulate. This mechanism can also explain depositions of coatings onto membranes that are not serving as electrodes.

ii) EPD due to charge neutralization

Grillon et al. [142] suggested that the charged particles are neutralized when they touch the electrode or the deposit and become static. This mechanism explains the deposition of single particles and monolayers and the deposition of powders charged by the addition of salts to the suspension (e.g. the experiments described by Brown and Salt [143]). However, this mechanism cannot clarify depositions carried out for longer time and EPD processes in which the particle-electrode contact is not permitted, e.g. when the deposition occurs on a semi-permeable membrane between the electrodes (this phenomenon is explained by the particle accumulation mechanism proposed by Hamaker-Verwey, as above) [17, 20, 22, 23, 126].

iii) EPD due to zeta-potential lowering or electrochemical coagulation

This mechanism requires the reduction of the repulsive forces between the suspended particles. Koelmans [144] calculated the rise of the ionic strength close to the electrode when a difference of potential is applied and discovered that the value of ionic strength was similar to that required to flocculate a suspension. This behaviour was due to an increase of the electrolyte concentration around the particles. Therefore, Koelmans [144] proposed a mechanism based on the fact that an increase of the electrolyte concentration produces a decrease of the repulsion between the particles close to the electrode (lower zeta-potential) and consequently the particles coagulate. Considering that a finite time is needed for the increase of the electrolyte concentration next to the electrode, it can be concluded that a certain time has to pass in order to have deposition. This critical time is inversely proportional to the square of the applied voltage, i.e. the higher the applied potential the shorter the time required for deposition, and therefore this time can be very short and it is often not observed [17, 20, 22, 23, 126].

iv) EPD due to electrical double layer distortion and thinning mechanism

Sarkar and Nicholson [22] proposed a model mainly based on the distortion of the particle double layer to explain the invalidation of the electrochemical coagulation mechanism when there is no increase of electrolyte concentration near the electrode. They noted that when a positive particle and its shell are moving towards the cathode, the electrical double layer (EDL) is distorted (thinner ahead and wider behind), as shown in Figure 2.11, due to fluid dynamics and to the effect of the applied electric field. As a result, the counter ions (negative) in the extended tail experience a smaller coulombic attraction to the positively charged particle and can more easily react with other cations moving towards the cathode. This process reduces the thickness of the double-layer and therefore, when another particle with a thin double-layer is approaching, the two particles come close enough to interact through van der Waals attractive forces and coagulate. This mechanism is plausible considering a high concentration of particles close to the electrode (or high collision frequency) and for incoming particles with thin double layer heads, coagulating with particles already in the deposit.

Subsequently Nicholson et al. [126] showed that the EDL-based model previously proposed by Sarkar and Nicholson [22] was not complete and suggested a new theory based on a decrease of the concentration of H^+ at the cathode due to hydrogen H_2 discharge or other chemical reactions. Therefore the local pH increased towards the isoelectric point (iep), zeta-potential decreased and the particles coagulated. This mechanism can be generally applied for all the suspensions containing hydrogen ions.

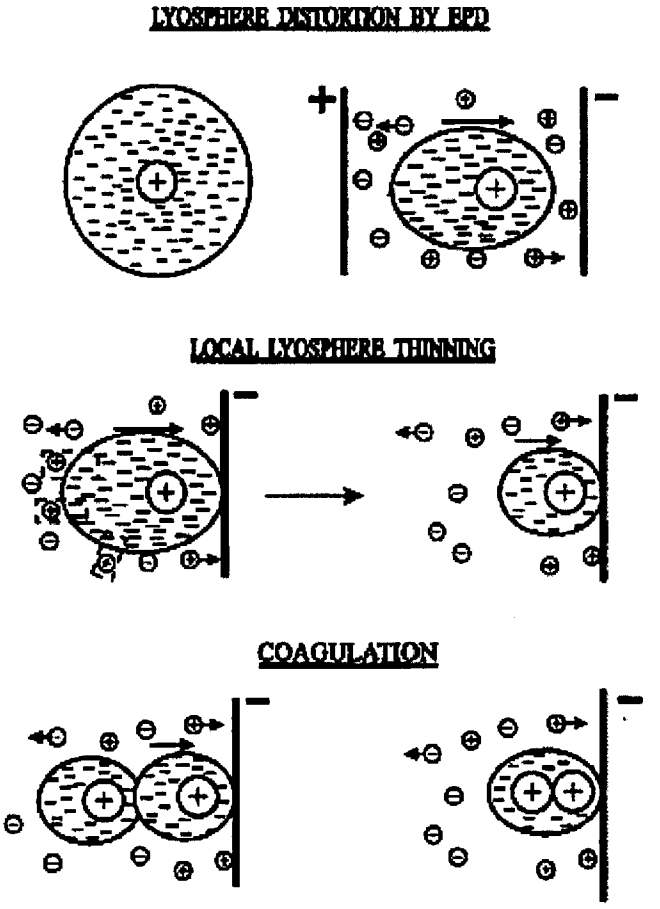


Figure 2.11 Schematic representation of the electrical double layer distortion and thinning mechanism (redrawn from ref. [22]).

v) Novel theories and models

Studies of electrodynamic particle aggregation during EPD have been carried out under steady [145] and alternating electric fields [146]. These models produced equations for the time evolution of the probability of separation between deposited particles in different conditions. These equations are able to explain the experimentally observed clustering of colloidal particles deposited near an electrode in a direct current electric field by considering convection by electro-osmotic flow about the particles [147]. Numerical simulations have been also employed to a limited extent to model the accumulation of charged particles on an electrode during EPD [148, 149]. These studies are of fundamental and practical interest to describe the local

variations of particle interaction during deposition, which can be used to optimize the EPD technique.

Regarding the growth of colloidal films during EPD, Sarkar et al. [150] provided another fundamental study observing the deposition of silica particles on silicon wafers as a function of deposition time. They compared the nucleation and growth of the silica particle layer with that of atomic film growth via molecular-beam epitaxy and noticed a prominent similarity between the two processes. From this observation a new direction for further research could follow in order to optimize the microstructure of EPD films. Theoretical work was also carried out by Van der Biest et al. [151-154] who produced a model to predict the yield of the electrophoretic deposition process taking into account the changes of the electric field over the suspension due to the potential drop over the growing deposit. This model was validated for Al_2O_3 suspensions in ethanol with different concentrations and with addition of HNO_3.

Another relevant study was published by Van Tassel and Randall [155] that electrophoretically deposited Al_2O_3 powder from an acidic suspension obtaining a very uniform, dense layer and observed an anomalous voltage rise across the deposited particulate layer. They showed that these two effects can be explained by the formation of an ion depleted conduction layer in the solvent at the deposition electrode, which presents an extremely high voltage gradient. Therefore the electrophoretic force on the particles in this layer is considerably higher than the force on particles in the rest of the system and this high voltage gradient layer also produces a large self-levelling effect for deposition thickness.

More recently Ristenpart et al. [156, 157] have studied, both theoretically and experimentally, the flow around a charged spherical colloid next to an electrode in order to understand the nature of long-range particle-particle attraction near the electrodes. From their studies it was clear that the direction of flow of a particle depends on the sign of the dipole coefficient and that the flow consists of two components: the electro-osmotic flow (EOF) and the electrohydrodynamic (EHD) flow. The electro-osmotic flow (EOF) is proportional to the current density and the particle zeta potential, while the electrohydrodynamic (EHD) flow derives from the product of the current density and the applied potential. Comparing these two components, Ristenpart et al. [156, 157] found that the attractive EHD flow predominated far from the particle, whereas the attractive EOF predominated over the repulsive EHD flow close to the particle. Moreover, they also observed that under certain conditions, the two flows are both directed toward the particle producing aggregation. Another relevant study was published by Mohanty et al. [158] on the optimisation of the electrophoretic deposition of alumina from iso-propanol suspensions using statistical design of the experiments. Finally, Ciou et al. [159] employed an artificial neural network model to predict the kinetic behaviour of EPD. This new model produced improved numerical accuracy and presented outstanding capability for the prediction of kinetic behaviour compared to a modified Hamaker`s law.

The novel theoretical and modelling approaches summarised in this section represent

examples of the few efforts available in the literature to investigate basic phenomena occurring during EPD. It is important to highlight here the necessity for further theoretical and modelling work in the field of EPD and the need for establishing reliable correlations between model variables and the experimental processing EPD conditions.

2.3.6 Applications of EPD

Several reviews have been published giving complete overviews about the great range of applications of EPD, including coatings, composites, layered materials and functionally graded materials [17-23, 125, 126, 132, 133]. This section will be mainly focused on the application of EPD to produce alumina (Al_2O_3) coatings, polyetheretherketone (PEEK) coatings and Al_2O_3-PEEK composite coatings, which are the systems relevant for the present project.

A difference from EPD from a single component, the deposition of two or more components contemporarily from the same suspension is a complex and difficult process. Two different situations can be distinguished depending on the charge (zeta potential) of the materials in the suspension. If the suspended species have the same charge, they will move toward the same electrode under the influence of the electric field and they will be deposited at different rates depending on their respective concentration in the suspension [17, 20]. For example, Wang et al. [160] described the co-deposition of diamond and borosilicate glass particles from an ethanolic suspension and they reported that it is possible to modify the composition of the coatings by varying the concentration of the two materials in suspension. Theoretically, if the two components have opposite charges the positively charged particles would deposit on the negative electrode while the negatively charged particles on the positive electrode. If this is the case, it is possible to employ appropriate additives, such as surfactants, that will make the sign and the magnitude of the zeta potential of the components comparable. However, it has also been reported in the literature that materials having opposite charges can be co-deposited on the same electrode in the absence of any modifiers. This is because the two species may associate with one another *in the suspension*, e.g. by forming composite particles due to electrostatic interactions between opposite surface charges [161-165] or by adsorption of one particle onto the surface of the other [22]. Sarkar and Nicholson [22] mentioned that if a suspension contains two components with opposite charges the coarser component would absorb the finer and behave as the fine material. For example, in ethanol at pH 4 Al_2O_3 particles are positively charged and SiC particles are negatively charged; hence SiC-Al_2O_3 composite particles behave like if they would be 100% positively charged due to the adsorption of the small (positive) Al_2O_3 particles on the negatively charged SiC particles. Moreover, Boccaccini et al. [161] investigated the production of mullite ceramic from biphasic suspension of similar size SiO_2 and Al_2O_3 particles. They [161] observed that the two species presented opposite charges at pH 4 (aqueous suspension) and that a strong electrostatic attraction took place between them producing composite particles that migrated towards the negative electrode in the

EPD cell. Singh et al. [164] reported the deposition of TiO_2-CNTs (carbon nanotubes) composite coatings thanks to the formation of TiO_2-coated CNTs, which formed because of the electrostatic interactions between positively charged TiO_2 nanoparticles and negatively charged CNTs in suspension. Yousefpour et al. [162] deposited hydroxyapatite (HA)-polytetrafluoro-ethylene (PTFE) coatings by EPD and they observed the formation of composite particles in suspension due to the electrostatic interactions between the positively charged HA and the negatively charged PTFE. Castro et al. [163] observed that in ethanol there are electrostatic interactions between negative ZrO_2 particles and positive MgO particles. They [163] also reported that the ZrO_2 particles can be covered by the positive MgO particles and therefore the MgO particles can compensate the negative surface charge of ZrO_2. Pang and Zhitomirsky [165] deposited HA-chitosan composite coatings on 316L stainless steel and observed that the addition of chitosan to the HA suspension increased the HA deposition rate for the adsorption of the chitosan on the HA nanoparticles, that stabilized the suspension and increased the nanoparticle charge.

2.3.6.1 Alumina coatings deposited by EPD

In the last few decades alumina coatings have been widely developed using EPD. The interest in Al_2O_3 coatings is based on its oxidation resistance and on its high hardness, which can be useful for tribological applications [166, 167], for the production of Al_2O_3 matrix composite reinforced with 2D or 3D metallic phase [168] and Al_2O_3 coated fibres employed as reinforcing elements in ceramic composites [169].

The conditions applied by different groups to perform electrophoretic deposition of Al_2O_3 are listed in Table 2.12. Analysing the conditions applied it is noted that both nano and micron Al_2O_3 particles were successfully deposited from both aqueous [128, 139, 166, 170-175] and organic suspensions [127, 137, 169, 176-184]. The organic solvent mainly employed was ethanol [127, 137, 169, 177-182, 184], although Wang et al. [176] demonstrated that it was possible to deposit Al_2O_3 from acetone and Besra et al. [183] from butane-1-olo.

Moreover, Kaya et al. [185] and Boccaccini et al. [186] demonstrated that Al_2O_3 coatings may be deposited from a boehmite (γ-AlOOH) sol, which is a colloidal dispersion of very fine solid particles (10 nm-2 μm) in a liquid medium. The coatings deposited with this technique needed to be densified via a sintering process carried out at very high temperatures (> 1600°C), due to the dehydration process and to the large and extensive pore network that develops during the transformation to α-Al_2O_3 phase:

$$\gamma\text{-}AlOOH \xrightarrow{400^{\circ}C} \gamma\text{-}Al_2O_3 \xrightarrow{800^{\circ}C} \delta\text{-}Al_2O_3 \xrightarrow{1000^{\circ}C} \theta\text{-}Al_2O_3 \xrightarrow{1100\text{–}1200^{\circ}C} \alpha\text{-}Al_2O_3$$

The final sintered microstructure of Al_2O_3 derived from pure boehmite was seen to be relatively porous even thought the deposit was sintered at 1600°C for many hours. To avoid this problem the sol can be seeded with crystallographically suitable modifiers (α-Al_2O_3, γ-Al_2O_3 and δ-

Al_2O_3) which permits to produce high-density Al_2O_3 coatings with controlled microstructure, after sintering at temperatures of 1100°C-1300°C [185, 186].

2.3.6.2 PEEK coatings deposited by EPD

Polyetheretherketone (PEEK) (or also poly(aryletheretherketone)) has the basic structure shown in Figure 2.12 and a basic formula of $(-O-C_6H_4-O-C_6H_4-CO-C_6H_4-)_n$. It is a polyaromatic, semi-crystalline (30-35% crystallinity) thermoplastic polymer exhibiting excellent mechanical properties (e.g. high strength, excellent stiffness and toughness, excellent tribological properties) and chemical resistance. It is thermally stable with a melting temperature of 330-385°C and a glass transition temperature of 143°C. Therefore this material can be employed in numerous fields, such us aerospace, automotive and electronics. In addition, PEEK is biocompatible and has found a wide range of biomedical applications (e.g. dental, orthopaedic and cardiovascular devices) [6-11, 187-191]. Thus, even though PEEK is mechanically weak it represents a very attractive material for coatings.

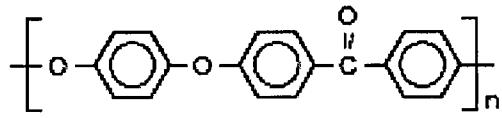


Figure 2.12 Basic chemical structure for polyetheretherketone (PEEK) (redrawn from ref. [9]).

Numerous studies have been reported for the production of PEEK coatings on metallic substrates using thermal spraying [6-11] and printing technique [192, 193]. Thermal spraying consists of injecting the PEEK powder into a flame or a plasma jet where the powder is melted and propelled towards the substrate in order to produce the coating. Printing consists of mixing powders in water to produce a slurry that is then homogeneously applied on the substrate surface and then dried and sintered. Another method to deposit PEEK coatings onto conductive substrates is EPD from ethanolic suspensions, as it has been explored by Wang et al. [187, 189] and Boccaccini et al. [188].

Wang et al. [187] prepared PEEK suspensions in ethanol with a concentration of 20 g/l and they added small amounts of dilute acid (acetic acid) or alkaline to adjust the pH at 5.5. In these conditions the PEEK particles resulted negatively charged (-20 mV) and therefore they were deposited on the anode. The suspension was ultrasonically mixed for 30 min and magnetically stirred for 3 hours to produce stable suspensions even if some difficulties were observed due to the easy sedimentation of the PEEK powders. The depositions were carried out on a conductive carbon rod (3 cm^2), using a stainless steel cylinder as counter electrode (they were kept at 2 cm distance), applying a constant-current density of ~0.167 $mA \cdot cm^{-2}$ and stirring the suspension during the whole deposition process. During EPD, the voltage was observed to increase with the increase of film thickness and it was noted that the voltage should not increase over 150V to not damage the quality of the coating. High deposition rate (high electric

Table 2.12 Conditions used to deposit alumina coatings by EPD

	Al_2O_3 concentration	Al_2O_3 size	Solvent	Additives	pH	ΔV/ Current density	Means to keep the particles suspended
[176]	20 g of Al_2O_3 in 220 ml	0.4 μm	Acetone	n-butylamine to increase particle charging	-	50 V (3 cm)	10 min ultrasonic mixing
[183]	20 wt.% of Al_2O_3	0.8-1 μm	Butane-1-ol	-	-	150-300 V (1.5 cm)	5 min stirring and 20 min ultrasonic mixing
[179]	100 g/l of α-Al_2O_3	0.6 μm	Ethanol	HCl / HNO_3 / CH_3COOH / PEI	-	175 V (3.5 cm)	15 min ultrasonic mixing + 1 hour magnetic stirring
[178]	9 g of Al_2O_3 in 100 ml	0.2 μm	Ethanol	HCl / NH_4OH to change the Ph	2.2-11	100 V (3 cm)	-
[127]	2 g of α-Al_2O_3 in 200 ml	0.2 μm	Ethanol	4 ml of 0.01 M HCl	-	100 V (3 cm)	15 min ultrasonic mixing
[169]	3 g of δ-Al_2O_3 in 25 g	13 nm	Ethanol	-	4.5-5.5	60 V (3 cm)	1 hour ultrasonic mixing
[177]	25 wt.% of α-Al_2O_3	100-300 nm	Ethanol	4wt.% of 4-hydroxybenzoic acid as dispersant	-	100 V (2 cm)	Ultrasonic mixing
[180]	5 wt.% of γ-Al_2O_3	5 μm	Ethanol	Polyscylic acid and aluminium isopropoxide	8	10 V	20 min stirring and ultrasonic mixing
[181]	1g of γ-Al_2O_3 in 100 ml	40 nm	Ethanol	-	3	10-20 V	-
[181]	2.5g of α-Al_2O_3 in 100ml	200 nm	Ethanol	-	3	10-20 V	-
[139]	5, 10, 20wt.% of α-Al_2O_3	-	Distilled water	0-5wt% of polyelectrolyte to stabilise the slurry.	-	2.8-6.4mA/cm^2	Stirring during the deposition
[174]	0-20 wt.% of Al_2O_3	0.5 μm	Distilled water	Ammonium salt of poly(acrylic acid) as a dispersant	-	1.4 mA·cm^{-2} , 2.8 mA·cm^{-2}, 4.2 mA·cm^{-2} (2 cm)	magnetic agitation during the deposition
[170, 171]	10 vol.% of α-Al_2O_3	0.2 μm	Distilled water	-	4.0	Magnetic field 10 T (2 cm)	ultrasonic mixing
[172]	3-5 vol.% of γ-Al_2O_3	33 nm	Distilled water	HCl / NH_4OH to change the pH	2-12	3 mA·cm^{-2} (2 cm)	10 min ultrasonic mixing
[128]	5 wt.% of α-Al_2O_3	0.5 μm	Distilled water	Dolapix, carbonic acid based polyelectrolyte	-	1.6, 6.4, 12.8 mA·cm^{-2} (2 cm)	-
[173]	3.2 wt.% of α-Al_2O_3	-	Distilled water	Acrysol A-5 as dispersant, triethilamine to change the pH	7.8-8.2	30 V	-
[166]	20 wt.% of α-Al_2O_3	150 nm	Distilled water	0.5wt.% celacol as binder	4	10 V (1.7 cm)	Ball mixed for 24 hours

field and concentration) can easily cause the coating to peel off from the substrate or the production of a non-uniform coating. In another paper, Wang et al. [189] employed a suspension containing 3 g of PEEK that was ultrasonically dispersed for 20 min in 100 ml of ethanol (99.86%). The pH was adjusted to pH 8 using HNO_3 and NH_4OH. The depositions were carried out applying a constant field of 50 $V \cdot cm^{-1}$ for 5 min between a stainless steel cathode and a graphite anode.

Boccaccini et al. [188] prepared suspensions with concentrations between 1 and 6 wt.% of PEEK in ethanol and they adjusted the suspension pH to 5.5 by adding 0.5 wt.% of HCl (0.1 M) and NaOH following the zeta potential findings (-20 mV) reported by Wang et al. [187]. The suspension was ultrasonically mixed for 30 min to disperse the particles and magnetically stirred for 5 min before each deposition. The depositions were carried out applying a constant field of 10 $V \cdot cm^{-1}$ for 5 min between a Nitinol wire with a diameter of 0.27 mm (substrate) and a tube-like stainless steel counter electrode.

Both groups carried out a sintering step to densify the film and to improve its adhesion to the substrate. A heat-treatment at 350°C for 20 min with a heating rate of $5°C \cdot min^{-1}$ was carried out by Wang et al. [187]. They observed that the film firmly adhered to the carbon rod probably thanks to the coating permeating to the porous carbon structure. Boccaccini et al. [188] heat-treated the samples in argon atmosphere (to reduce the possible oxidation of the Nitinol substrate) at 340°C for 20 min with a heating rate of $5°C \cdot min^{-1}$. Under these conditions a homogeneous and well-adherent coating was also produced.

2.3.6.3 PEEK composites

As underlined in section 2.3.6.2, PEEK presents good wear resistance and high thermal stability and for this reason it can be seen as a unique polymer for the production of high temperature and high wear resistant polymer-ceramic composites. Numerous studies have been carried out to determine the friction, wear, thermal and mechanical properties of PEEK and PEEK composites filled with fibres [194-200], inorganic particles [3, 24-29, 192, 193, 201-214] and organic compounds [194, 197, 200] and prepared using different techniques, such as compression moulding [24, 26, 194, 201-205, 207, 211, 212], injection moulding [194-197, 199, 200, 213], hot pressing [3, 25, 27-29, 209, 210] and thermolamination [208] for the production of bulk materials, and printing [192, 193] for the production of coatings. The composite properties depend on the filler concentration, shape, dimension and characteristics and on the interfacial bonding strength between the filler and the polymer. These composites present unique properties that can be tailored to meet specific requirements (e.g. low density and coefficient of thermal expansion, high strength and stiffness, chemical and thermal shock resistance, low thermal conductivity and electrical insulation properties) and render them valuable in many fields, such as aerospace, electronics, automotive, marine structures and biomedical applications [27]. Up to date, only few studies have been carried out for the

production of PEEK-Al_2O_3 bulk composite materials [3, 24-29, 205, 206] and a literature search has indicated that no previous attempts to fabricate *composite coatings* combining PEEK and Al_2O_3 have been reported.

Nandar et al. [25] prepared PEEK-Al_2O_3 composites by physical blending at 350°C the two materials in different weight ratios: 30-70, 50-50 and 70-30. The Al_2O_3 particles employed had size of around 100 μm. From the thermal analysis of the blend two observations were made: the melting point of the mixture was lower than the melting point of pure PEEK, probably due to the more homogeneous heat transfer produced by the Al_2O_3 and the thermal stability of the composite increased with increasing Al_2O_3 content. The flexural strength of pure PEEK was the highest and decreased with increasing amount of Al_2O_3. While the flexural modulus was minimum for pure PEEK and maximum for the 70 wt.% PEEK-30 wt.% Al_2O_3 composite, this value further decreased increasing the Al_2O_3 concentration. According to these results, the authors [25] concluded that 30 wt.% was the highest Al_2O_3 content that should be incorporated in the composites to keep mechanical properties at a reasonable level [25].

Kuo et al. [26] observed that the hardness, elastic modulus and tensile strength of PEEK-nano-Al_2O_3 (~30 nm) composites increased with increasing concentration of Al_2O_3 between 2.5 and 10 wt.%. They also expected that increasing the amount of reinforcement over 10 wt.% would further increase the hardness and the elastic modulus of the composite at the expense of the tensile strength. At higher concentrations, the particles would start to agglomerate but for wear applications a higher nanoparticle content is desired [26]. In another study on the same composite, Kuo et al. [205] observed that some nanoparticles were arranged in clusters in the composite whereas the majority of them were homogeneously dispersed in the PEEK matrix.

Kuo et al. [26] observed using XRD that with the addition of nanoparticles no new crystalline phases had formed concluding that there were no chemical interactions between PEEK and Al_2O_3. It was also indicated that low Al_2O_3 concentration would increase the crystallinity of the PEEK matrix due to heterogeneous nucleation but that higher amounts of Al_2O_3 would decrease the crystallinity due to a decrease in the mobility of the polymer chains. DSC analysis [26, 205] showed that the crystallization temperature decreased with increasing cooling rate and that a slower cooling rate produced a slightly higher crystallinity for both PEEK and PEEK composites. The crystallization temperature of the composites decreased for low Al_2O_3 contents (2.5 wt.%) and increased with increasing Al_2O_3 due to the heterogeneous nucleation effect that would gradually provide more sites for nucleation. Another factor affecting the crystallization temperature of the composites was the higher thermal conductivity of the Al_2O_3 compared to PEEK, which are 30 and 0.2 WmK^{-1}, respectively. However, it has been found that different nucleation agents (different morphology and content) could produce opposite effects on the heat of crystallization [205]. Kuo et al. [26] reported no significant changes in the melting points of the composites, whereas in another work [205] they observed a slightly decrease of the melting temperatures, as also reported by Nandar et al. [25]. The TGA

analysis determined that increasing the nanoparticle content, the degradation temperature of the PEEK composite continuously increased [26], as also observed by Nandar et al. [25].

Goyal et al. [3, 27, 28] prepared PEEK-Al_2O_3 composites by mixing 25 μm PEEK powder with 8 μm [27, 28] or 39 nm [3] Al_2O_3 powder in ethanol and subsequently hot pressing at 15 MPa and 350°C. The Al_2O_3 concentration was varied between 0 and 50 wt.% [27], 60 wt.% [28] or 30 wt.% [3], as determined by thermogravimetric analysis. The micron-Al_2O_3 particles were uniformly distributed in all composites and there were no aggregates present [27, 28], whereas in the PEEK-nano-Al_2O_3 composites [3] some aggregates were observed when the Al_2O_3 concentration was 10 wt.% or higher. The interfacial adhesion between the micron-Al_2O_3 particles and the PEEK was strong in composite containing less then 30 wt.% Al_2O_3 and low for composites with higher Al_2O_3 contents [28]. It was also determined that the thermal stability of the composites in air (determined considering as degradation temperature the temperature at which the material lost 10 wt.%) increased with the incorporation of both micron and nano-Al_2O_3 particles [3, 27, 28], as also observed by Kuo et al. [26] and Nandar et al. [25]. However, a decrease in the thermal stability of the composites was also observed (although still higher than that of pure PEEK) when the content of nano-Al_2O_3 particles raised over 30 wt.%, due to the agglomeration tendency of the nanoparticles. Differential scanning calorimetry (DSC) analysis showed an increase of 2-4°C of the melting temperature with increasing amount of micron-Al_2O_3 [27] and of 1-6°C with 0-10 wt.% of nano-Al_2O_3 [3], probably due to the homogeneous dispersion of the particles in the composite that increased the crystallinity of the PEEK matrix [3, 27]. This result is however in contrast with the findings reported by Nandar et al. [25] and by Kuo et al. [205]. Goyal et al. [3, 27] observed that the presence of micron and nano-Al_2O_3 in the composite increased the crystallization temperature by 12°C in comparison to pure PEEK, indicating that the addition of Al_2O_3 enhanced the rate of PEEK crystallization; opposite results were reported by Kuo et al. [26,205]. The increase of crystallization was further confirmed by the XRD analysis showing a slight decrease of *d*-spacing with increasing Al_2O_3 content in the composites probably due to the higher perfection of the crystals [27].

Qiao et al. [24] produced bulk composites adding to 250 μm size PEEK powder 5 wt.% of nano (15 and 90 nm) or sub-micron (0.5 μm) Al_2O_3 particles and observed that the introduction of alumina particles, both sub-micron and nano, into the bulk material reduced the wear coefficient, but not the friction coefficient of PEEK.

Xiong et al. [29] used hot pressing to prepare PEEK composites containing 1 wt.% to 9 wt.% of nano-Al_2O_3 particles and reported that the wear rate and the friction coefficient of PEEK were greatly reduced by the presence of 1 to 9 wt.% of nano-Al_2O_3.

The production of PEEK-Al_2O_3 composite bulk materials was also registered in a patent [206]. In this patent a composite made of PEEK, 15-20 wt.% Al_2O_3 particles (< 5 μm), 3-8 wt.% of graphite particles (< 5 μm) and 6-9 wt.% of carbon powder (< 30 μm) was employed to produce a sealing ring for a shaft in order to prevent leakage of oil and to reduce abrasion.

2.4 Summary

From the studies reported in the literature and reviewed in this chapter it emerged that further research is needed to better understand a few key questions still unresolved in the field of deposition of composite coatings by electrochemical means. These key questions are summarised below and provide the basis for setting the specific aims and objectives of the present research project.

1. Contradictory results were reported in the literature about the influence of the electro co-deposition parameters on the amount of particles co-deposited with the metal for different metal-particle systems, including the Ni-Al_2O_3 system of interest in this study. A lack of previous investigations focusing on the combined effect of relevant processing parameters (applied current density, particle concentration in the bath and particle size) affecting co-deposition of Ni-Al_2O_3 composite films was also observed. Thus the first objective of the project was to comprehensively investigate the deposition of composite coatings in the Ni-Al_2O_3 system.
2. Numerous mechanisms have been proposed in the literature to explain the particle co-deposition process in combination with metal electrolytic deposition, but full understanding of the mechanisms involved has not been achieved to date. Moreover, different behaviours have been observed for conductive and insulating particles. Thus a second objective of the present project was to design experiments with the specific aim of gaining more fundamental knowledge about the mechanisms of co-deposition. The results should enable to draw conclusions about the link between process parameters and co-deposition behaviour.
3. Considering that no studies on the deposition of PEEK-Al_2O_3 composite coatings by either EPD or other techniques have been so far reported in the literature and that research on PEEK-Al_2O_3 bulk composites demonstrates their improved properties compared to pure PEEK (e.g. lower wear coefficient, higher hardness and thermal stability), a third aim of this project was to develop a fabrication method based on EPD to deposit these composite coatings for the first time on metallic substrates, and to characterise the key properties of the coatings produced.
4. Given that EPD mechanisms, in particular for diphasic polymer-ceramic suspensions, are not completely understood and that further predictive modelling and theoretical approaches are needed to investigate EPD, the fourth aim of the project was to use the wealth of results gained on EPD of PEEK, Al_2O_3 and PEEK-Al_2O_3 to derive analytical tools aiming at predicting deposit yield and composition.

3. Characterisation techniques

3.1 Scanning electron microscopy

Two scanning electron microscopes (SEM): JEOL JSM 5610 LV and JEOL JSM 840 were used for high quality secondary images of the deposited coatings and to analyse the starting powders with a standard voltage of 5-20 kV. The JEOL JSM 5610 LV is equipped with a backscattered electron detector that distinguishes alumina and aluminium (Al=26.98 amu) from nickel (Ni=58.69 amu) considering their different atomic weight. In the backscattered images Al and Al_2O_3 are seen as the dark phases and Ni is the light grey phase. Before imaging, the non conductive samples were gold coated for 2 min at 20 mA employing the sputter coater Emitech K550 (Quorum Technologies Ltd, East Sussex, United Kingdom) resulting in a thickness of ~14 nm.

A Gemini LEO 1525 Field Emission Gun Scanning Electron Microscope (FEG-SEM) was employed for high resolution images of the alumina coatings, PEEK-Al_2O_3 and Ni-Al_2O_3 composite coatings.[1] Before the analysis the non conductive samples were chromium-coated for 1 min applying a current intensity of 75 mA using Emitech K575X (Quorum Technologies Ltd, East Sussex, United Kingdom) obtaining a thickness of ~15 nm.

The samples for the powder analysis were prepared placing some powder on carbon tape. To analyse the cross section of the stainless steel coated samples the specimens were embedded in epoxy resin. Struers Epofix resin and hardener were used in a weight ratio of 25:3, respectively. It took about 12 hours to cure before grinding with Struers SiC paper (grit size of 600, 800, 1200 and 4000) and polishing with Struers diamond paste sprays (3 μm and 1 μm). Before microstructural analysis these samples were gold coated as described above.

3.2 Transmission electron microscopy

In order to determine the shape and size of the nano-Al_2O_3 particles, a sample was prepared by suspending some powder in ethanol and sonicating it for 30 min. Then a drop of the suspension was placed on the TEM copper grid and after drying the deposit was analysed using a JEOL JEM-2010 Transmission Electron Microscope (TEM) (high resolution) with LaB_6 filament.[2] The dispersion of the PEEK-Al_2O_3 suspension and the interactions between these two types of particles in suspension were analysed with a JEOL 2000 FX Electron Microscope (TEM) equipped with LaB_6 filament. Two samples were prepared in epoxy resin (Struers Epofix resin and hardener in a weight ratio of 25:3): the first sample contained the powder dried from few ml of a 4 wt.% PEEK-2 wt.% Al_2O_3 suspension in ethanol, the second

[1] The experiments were carried out with extensive assistance of Dr. M. Ardakani (Imperial College London).
[2] The experiment was carried out with extensive assistance of Dr. D. Daniel (Imperial College London).

sample contained few ml of the same suspension. The resin was then cut into 1 mm^2 stripes and sectioned using a diamond knife on a Power Tome XL microtome (RMC, Boeckeler Instruments)[3] to obtain 1 mm^2 samples with a thickness of ~90 nm. The samples were carbon coated with Emitech K450 (Quorum Technologies Ltd, East Sussex, United Kingdom) before the TEM analysis.[4]

3.3 Focused ion beam-secondary ion mass spectrometry (FIB-SIMS)

The FIB-SIMS analysis was carried out using the FEI-FIB 200 TEM workstation equipped with a SIMS detector.[5] A gallium ion source was the primary ion beam employed with energy of 30 keV. All the specimens were tilted to align their top surface perpendicular to the ion beam. To analyse the cross sections of the Ni-nano-Al_2O_3 composite films the samples were prepared as for SEM analysis (see section 3.1). The gold coated resin specimens were then mounted on the instrument holder and covered with Al tape with silver particles to enhance the electric contact. Once the area of interest was found the analysis was carried out using a beam current of 5 nA for sputtering away the gold layer and the top part of the specimen. A much lower beam current of 50 pA was employed to record images of the samples to minimize material removal during imaging. The SIMS mappings of the Al atoms (26.9) were carried out using a current beam of 50 pA and a beam dwell time of 4 ms.

To accomplish the three-dimensional reconstruction of the composite coating a specimen without any further preparation and half covered in Al tape was inserted into the FIB instrument. The volume to be lifted out was chosen and a 1-2 μm thick platinum layer was deposited in-situ on the top part of it. The 10 μm x 20 μm x 25-30 μm (depth) volume was then cut-out from the rest of the sample by milling with a beam current of 3-7 nA. This volume was then lifted out from the original sample and attached to a Cu stem. The surface of the specimen was then cleaned with a beam current of 1 nA and it was ready for the analysis. Fifteen slices ~100 nm thick were milled away with a beam current of 1 nA to determine the 3D microstructure of the composite and for each one of them few analyses were carried out:

- an image of the top part of the specimen (platinum layer) to determine the thickness of the layer sputtered away taken with a beam current of 30-50 pA;
- an image of the side of the sample tilted of 45° taken with a beam current of 30-50 pA;
- the corresponding SIMS mapping of the Al (26.9) and O (15.9) atoms (just for one slice) carried out with a current beam of 300 pA and a beam dwell time of 0.5 ms.

3.4 X-ray diffraction (XRD) analysis

A Philips X-ray diffractometer with PW 1710 X-ray generator using a Cu Kα radiation

[3] The experiment was carried out by R. D. Brooker (Imperial College London).
[4] The experiment was carried out with extensive assistance of Dr. Q. Chen (Imperial College London).
[5] The experiments were carried out with extensive assistance of R. J. Chater (Imperial College London).

was used to determine the crystallinity of the coatings and of the starting materials. For the analysis of the Ni coatings, the Ni-Al_2O_3 composite coatings and the Al powder 2θ was scanned from 5° to 100° with a step size of 0.04° and 1 s per step. The XRD analysis of the Al_2O_3 powder was carried out between 2θ 10° and 80° with a step size of 0.04° and 2 s per step for the sub-micron-Al_2O_3 powder and 30 s per step for the nano-Al_2O_3 powder. The PEEK powder before and after heat treatment and the PEEK-Al_2O_3 pellets after heat treatment were scanned between 2θ 10° and 40° and 10° and 60°, respectively with step size of 0.04° and a scan time of 4 s per step. X-Pert High Score and X-Pert data viewer programs (PANalytical ©) were employed to strip the $K\alpha_2$ signal from the XRD data and to measure the properties (position, net height and FWHM (full-width-half-max)) of the peaks.

3.5 White light interferometer (Zygo®)

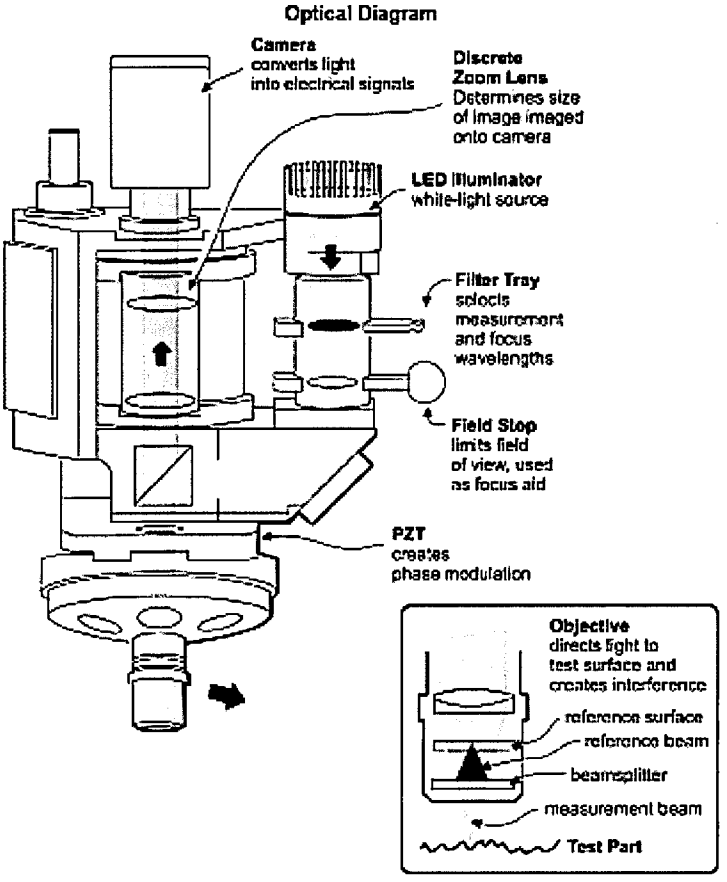


Figure 3.1 Schematic representation of Zygo® Interferometer (redrawn from ref. [215]).

Zygo® Interferometer uses white light to obtain images of the sample surface and to provide surface structure analysis through a software that converts the data obtained. All the measurements of Zygo® Interferometer are carried out in a piece of equipment similar to the one schematically shown in Figure 3.1. This instrument uses a light beam that is divided into two portions by a beam splitter within the interferometric objective. One of these portions is

directed to and is reflected from the test surface whereas the other portion is directed and reflected from an internal high quality reference surface in the objective (Figure 3.2). Both portions are then directed onto a solid-state camera and they interfere producing an image of light and dark bands (fringes) that indicate the surface structure of the point tested [215]. When the information in one point is collected the objective is vertically moved with a piezoelectric transducer in another point that has to be scanned. As the objective scans the surface a video system captures the intensities at each camera pixel and the software converts these intensities into height obtaining a height map of the area scanned. These results are displayed as solid images (e.g. 3D plots), plots (e.g. bearing ratio plots), and numeric representations of the surface (e.g. rms and Ra values).

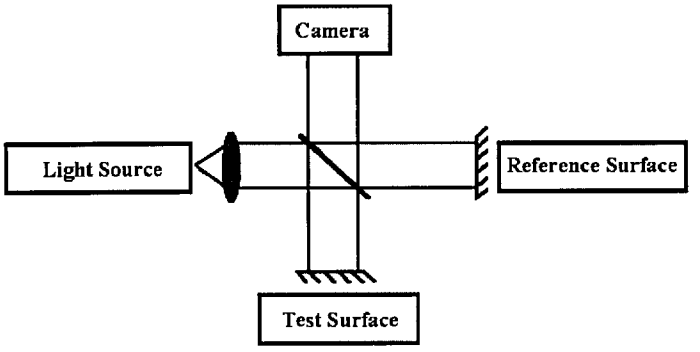


Figure 3.2. Schematic representation of the light paths inside the white light interferometer.

Rms (see Figure 3.3) is a roughness parameter of an area weighted statistically given by the root mean square deviation from the central line and expressed by:

$$rms = \sqrt{\frac{y_1^{\,2} + y_2^{\,2} + \ldots + y_n^{\,2}}{n}} \qquad [3.1]$$

where $y_1, y_2 \ldots y_n$ are the deviations of n discrete elements from a central line defined as the best fit surface selected with the Remove control [215, 216]. The Remove control is an option of the software that permits to remove from the data a surface figure and it is fundamental for this and for the following data to be meaningful. Rms is an average of the roughness of the surface analysed and therefore it can be considered representative of that particular surface [215].

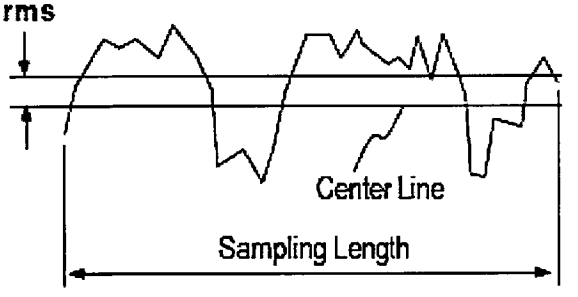


Figure 3.3 Schematic representation of rms on a sample [redrawn from ref. 215].

Ra (see Figure 3.4) is a roughness parameter of a chosen area expressed by:

$$Ra = \frac{y_1 + y_2 + ... + y_n}{n} \qquad [3.2]$$

where $y_1, y_2..y_n$ are the deviations from the central line selected with the Remove control and n is the number of discrete elements [215].

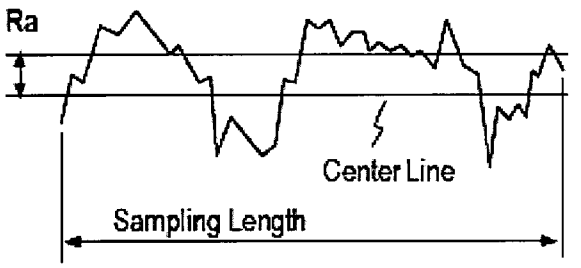


Figure 3.4 Schematic representation of Ra on a sample (redrawn from ref. [215]).

Description	*Profile*	*Bearing Ratio Plot*
Ground surface with random heights		
Honed surface with peaks removed		
Turned surface with dominating peaks		

Figure 3.5 Examples of surface profile and the corresponding bearing ratio plot (redrawn from ref. [215]).

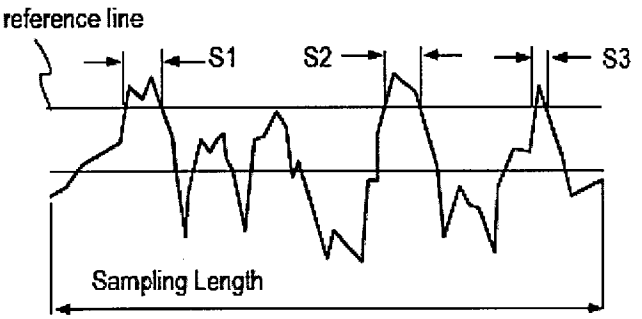


Figure 3.6 Scheme explaining how the bearing ratio plots are obtained (redrawn from ref. [215]).

The *Bearing Ratio Plot* displays on the horizontal axis the percentage of points at a specified depth below the highest point (tp%) and on the vertical axis the depths of the data. Examples of surface profiles and the correspondent bearing ratio plot are shown in Figure 3.5. To explain how these data are obtained the description can be simplified and limited to a slice of data, even if the bearing ratio plot represents the whole surface. A reference line is drawn parallel to the substrate to intersect the data at the same deepness (Figure 3.6) and the bearing ratio is calculated with the following equation:

$$Bearing \cdot Ratio = \frac{S_1 + S_2 + S_3}{L} x100\% \quad [3.3]$$

where L is the length of the sample and S_x is the subtended length [215].

In this research Zygo® Interferometer with MetroPro software was employed to analyse the surface roughness of the stainless steel samples before and after mechanical and chemical treatments and the shape of the scratch tracks left on pure PEEK and PEEK composite coatings. In all experiments a magnification of x 5 (0.5 zoom x 10 lens) was employed; in these condition an area of 1.46 mm x 1.10 mm was analysed with around $3.07 \cdot 10^5$ pixels (1 point every 2 μm). In order to determine the stainless steel surface roughness 3D plots, rms and Ra values and bearing ratio plots were examined. In all these experiments and for all the data obtained the removed figure was a cylinder because the stainless steel surfaces were not flat but slightly bended due to the guillotine used to cut the larger foils into smaller pieces. Rms and Ra values were measured in different parts of the samples and to obtain a representative value of the entire surface the average of them and the corresponding standard deviation were calculated.

3.6 Thermal gravimetric analysis and differential thermal analysis

For the thermal gravimetric analysis (TGA) and the differential thermal analysis (DTA) of PEEK and PEEK-Al_2O_3 mix powders a Stanton Redcroft STA 780 instrument was employed. Approximately 10 mg of material was placed in a platinum crucible and heated from room temperature to 750°C at a heating rate of 10°C·min^{-1} in flowing air.

3.7 Differential scanning calorimetry analysis (DSC)

For the DSC analysis of pure PEEK and PEEK-Al_2O_3 powders with different compositions a differential scanning calorimeter Q2000 from TA Instruments (New Castle, Delaware, USA) was employed. Approximately 5 mg of material was placed in an aluminium pan with lid and the sample was encapsulated before running the experiment; pan and lid were also supplied by TA Instruments (New Castle, Delaware, USA). An empty pan and lid were used s a reference. The samples were heated from room temperature to 450°C at a heating rate of 10°C·min^{-1} in flowing helium at a rate of 50 ml·min^{-1}.

3.8 Heating microscopy

The experiments were performed on PEEK samples using a standard heating microscope (Leitz Wetzlar, GmbH) equipped with a digital camera. The samples were 3 mm x 3 mm x 3 mm and prepared by uniaxial pressing the PEEK powder. They were introduced in the furnace of the microscope at room temperature (25°C) and then the temperature was increased until the PEEK powder was completely decomposed with a heating rate of 10°C·min^{-1} in air. The

dimensional changes of the PEEK samples were measured from the images using the Image Tool © and the shrinkage was calculated using the following equation:

$$shrinkage\ (\%) = \frac{A_0 - A_t}{A_0} \cdot 100 \qquad [3.4]$$

where A_0 is the initial area and A_t is the area at 343°C, as also described by Adell et al. [217].[6]

3.9 Particle size measurements

A Malvern Mastersizer particle size analyser (Malvern Instruments Ltd. Malvern, UK) was employed to analyse the particle size distribution of PEEK and sub-micron-Al_2O_3 powders. Suspensions containing 3 wt.% of PEEK powder in ethanol and 1 g of sub-micron-Al_2O_3 powder in 50 ml of water were prepared and ultrasonically mixed for 30 min before the measurements were carried out.

3.10 Zeta potential measurements

Zeta potential provides important information on the powder surface charge in suspension avoiding time-consuming trial and error attempts to prepare stable suspensions for EPD; it is well known that a suspension is stable at pH at least two pH values away from the isoelectric point (iep) (see section 2.3.3). In this project some zeta potential measurements have been carried out using ZetaProbe by Colloidal Dynamics (Warwick, USA)[7], that can analyse samples with concentration from 0.5 up to 60 vol.%, whereas traditional characterization techniques (for example, Zeta PALS-zeta potential analyzer by Brookhaven Instrument Corporation) require much more diluted samples. The difference in sample concentration depends on the different methods employed by the two instruments to measure the zeta potential. Zeta PALS by Brookhaven Instrument Corporation uses a laser to measure Zeta potential and therefore the suspension must be transparent. While ZetaProbe measures the zeta potential using an ultrasonic and electroacoustic sensor (Electricsonic amplitude ESA) as the one shown in the Figure 3.7 [218, 219] permitting the application to more concentrated suspensions. This instrument is also equipped with a mechanical stirring to ensure the homogeneity of the suspension and a standard probe to measure pH (pH range: 1-13), conductivity (conductivity range: 0-5 S/m) and temperature (temperature range: 10-50°C).

The ESA probe consists of two electrodes (as shown in Figure 3.8). In the outer electrode the exposed metal is the active part whereas in the other electrode the active part is the niobium (Nb) foil. The active metal part of the outer electrode must face the niobium foil electrode during the experiments and in order to obtain consistent results a homogeneous sample must be present between them. An AC electric field is applied between the two electrodes and the

[6] Experiment carried out by Dr. O. Bretcanu (Politecnico di Torino, Italy).
[7] Experiments carried out in collaboration with Dr. Saša Novak (Jožef Stefan Institute, Slovenia).

charged particles in suspension move back and forward generating sound waves. The sound waves are proportional to the electric field strength and are an indication of the particle velocity. The particle velocity divided by the AC field strength gives the dynamic mobility from which the zeta potential can be calculated using an appropriate formula. The ESA signal also includes a contribution from the electrolyte in which the particles are suspended, but usually the electrolyte signal is smaller than that from the colloidal particles and can be neglected, as it happened in the experiments here described [218, 219].

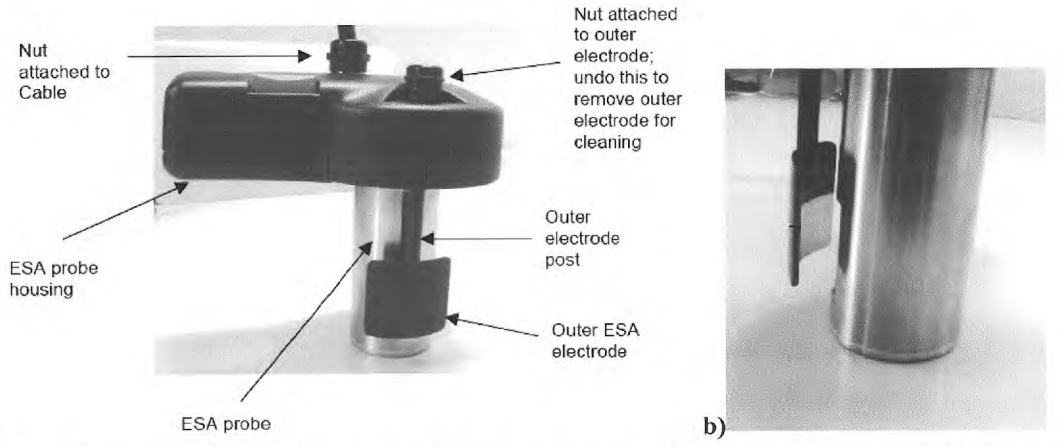


Figure 3.7 Images of a) the ESA probe and b) the configuration of the outer electrode and the main electrode during the experiments (redrawn from ref. [219]).

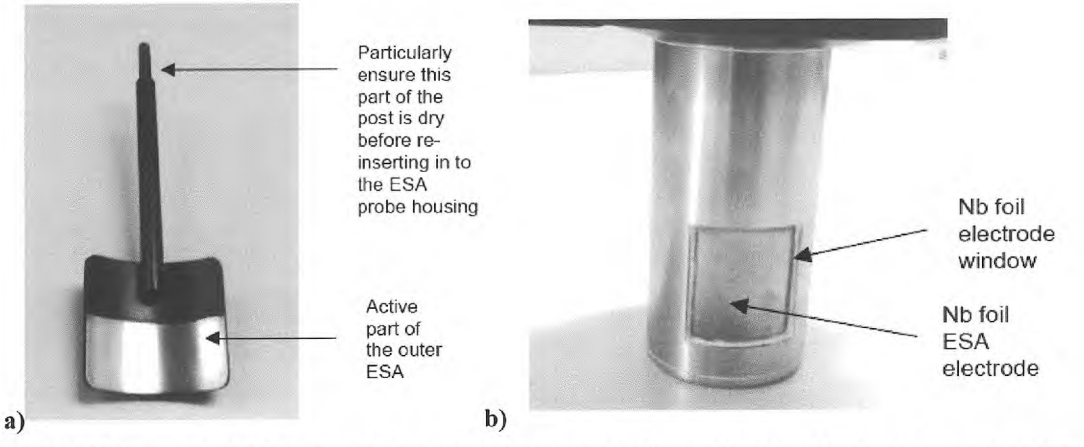


Figure 3.8 Images of a) the outer electrode and b) the main electrode of the ESA probe showing the active metal part (redrawn from ref. [219]).

All the zeta potential measurements were carried out in a beaker containing 280 ml of a suspension that was previously sonicated for 30 min. The ZetaProbe, an electrode to measure the pH and two pipettes connected to the instrument in order to change the pH by the addition of a certain amount of acid (1 M HCl) or alkaline (1 M NaOH) solution were also inserted in the container. In all experiments the equilibration time, which is the time between reaching the next pH point and the next measurement, was chosen to be 480 s, considering the slow

response of pH electrodes in ethanol and the long time needed to acquire stable pH readings [137]. The pH is a measure of the acidity in aqueous solutions and therefore in non aqueous solvents it loses its validity ("operational" pH) [20, 137, 184, 220].

In order to measure the suspension zeta potential the potentiometric series (measurements carried out after the suspension pH has changed to the desired value) has been employed varying the pH between 2 and 13 and supplying the information required to the Zeta Probe (see Table 3.1). All the data listed in Table 3.1 without giving a reference were obtained from the instrument database apart from the data marked with the symbol:*. These data: density and dielectric constant of 3 wt.% PEEK-3 wt.% Al_2O_3, 4 wt.% PEEK-2 wt.% Al_2O_3 and 5 wt.% PEEK-1 wt.% Al_2O_3 suspensions were calculated using the rule of mixtures:

$$Xc = Xa \cdot Va + Xp \cdot Vp \qquad [3.5]$$

where Xc is the property calculated (density or dielectric constant) for the composite and Xa, Xp, Va and Vp are the property (density or dielectric constant) and the volume fraction of Al_2O_3 and PEEK, respectively.

Table 3.1 Summary of the data employed to measure the zeta potential of different suspensions.

Properties	3 wt.% PEEK	3 wt.% Al_2O_3	3wt.% PEEK - 3wt.% Al_2O_3	4wt.% PEEK- 2wt.% Al_2O_3	5wt.% PEEK- 1wt.% Al_2O_3
Particle density	1.3 $g \cdot cm^{-3}$ [221]	4 $g \cdot cm^{-3}$ [222]	1.96 $g \cdot cm^{-3}$ *	1.68 $g \cdot cm^{-3}$ *	1.46 $g \cdot cm^{-3}$ *
Particle concentration	3 wt.%	3 wt.%	6 wt.%	6 wt.%	6 wt.%
Particle dielectric constant	3.2	10	5.2*	4.4*	3.6*
Solvent density	0.79 $g \cdot cm^{-3}$	0.79 $g \cdot cm^{-3}$	0.79 $g \cdot cm^{-3}$	0.79 $g \cdot cm^{-3}$	0.79 $g \cdot cm^{-3}$
Solvent viscosity	1.08 mPa·s	1.08 mPa·s	1.08 mPa·s	1.08 mPa·s	1.08 mPa·s
Solvent dielectric constant	24.6	24.6	24.6	24.6	24.6
Acid used/ concentration	HCl 1 mol/l	HCl 1 mol/l	HCl 1 mol/l	HCl 1 mol/l	HCl 1 mol/l
Base used / concentration	NaOH 1 mol/l	NaOH 1 mol/l	NaOH 1 mol/l	NaOH 1 mol/l	NaOH 1 mol/l
Sample volume	280 ml	280 ml	280 ml	280 ml	280 ml

3.11 Quantitative image analysis

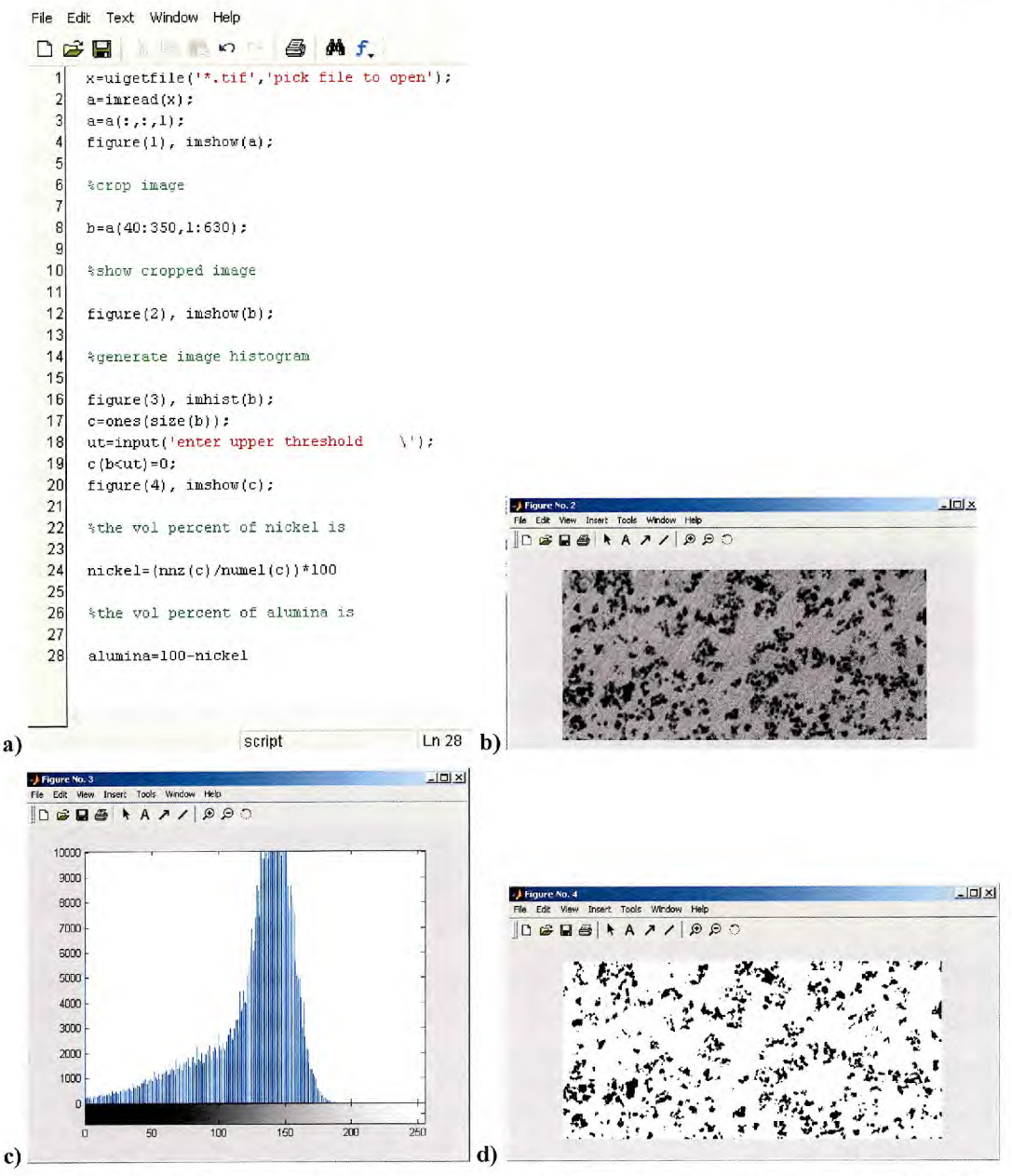


Figure 3.9 Matlab© images of the program and outputs used to determine the vol.% of Al_2O_3 in the films deposited. a) the program, b) cropped image, c) histogram of the scale of grey in the image and d) black and white image from which the percentages are calculated.

In order to determine the vol.% of Al_2O_3 in the Ni composite films a quantitative image analysis was carried out using Matlab© and the program shown in Figure 3.9 a).[8] This program is divided in few steps:

1. It shows the image to be analysed.
2. It crops the image to discard the resin (used to embed the specimen) and the substrate from the area to be analysed following the instruction of the operator and shows the result (Figure 3.9 b)).

[8] Program written by Paul Shearing (Imperial College London)

3. It generates a histogram (Figure 3.9 c)) with a scale of grey to help the operator to choose the threshold between nickel and alumina phases in the image.
4. It produces a new black and white image (Figure 3.9 d)) in which the white area is the nickel and the black area is the alumina to check if the threshold given was correct.
5. The percentages of the two colours/materials in the image are given as a result.

For the Ni-sub-micron-Al_2O_3 films back scattered SEM images (for better contrast between Al_2O_3 and Ni, due to their different atomic weights) at magnification x 2500 were taken in eight different areas of the cross section (four for each side). For the Ni-nano Al_2O_3 films four images (two for each side) were taken using a FIB-SIMS at magnification x 6500.

3.12 Scratch test analysis

The adhesion between the stainless steel substrate and the nickel, PEEK and PEEK-Al_2O_3 films were measured by a CSM Instrument Scratch Tester (CSM Instruments, Peseux, Switzerland) connected to a computer equipped with the CSM Instruments Scratch 3.87.01 software. The instrument was also equipped with an acoustic detector. Rockwell diamond indenters with different diameters were used for all the experiments: for PEEK and PEEK-Al_2O_3 films the indenter had a radius of 200 μm, while for the Ni films indenters with 10 μm or 100 μm radius were employed. The different indenters were chosen depending on the coating properties to penetrate as deep as possible into the coating and almost reach the substrate. Three scratches were made on each sample applying a progressive normal load from 0.1 N to 20 N with a loading rate of 19.9 $N \cdot min^{-1}$ and a scratch speed of 1 $mm \cdot min^{-1}$ obtaining a total scratch length of 1 mm. [9]

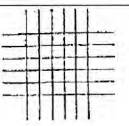
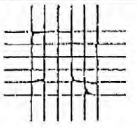
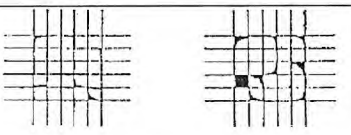
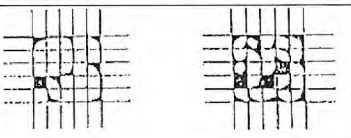
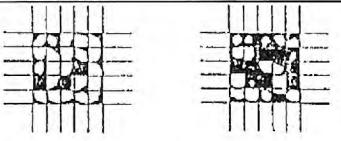
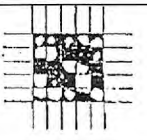
3.13 Micro-hardness analysis

The micro-hardness of PEEK, PEEK-Al_2O_3, Ni and Ni-Al_2O_3 composite coatings and of pure PEEK and PEEK-Al_2O_3 pellets with different compositions was measured using a Micro-hardness Indentec Zwick/Roell ZHV instrument (Zwick GmbH e Co, Ulm, Germany) equipped with a Vickers diamond indenter. The measurements were carried out under a load of 0.245 N (25 g) for 15 s on the top surface of the coatings/pellets. The pure Ni and Ni-Al_2O_3 composite coatings were analysed as deposited, whereas the PEEK and PEEK-Al_2O_3 coatings/pellets were analysed after heat treatment. Ten measurements were taken for each sample and three samples analysed for each condition, the measured values were averaged. For these measurements the advantages of the PEEK and PEEK-Al_2O_3 pellets compared to the coatings were the elimination of the substrate effect and that they could be polished to obtain flat and smooth surfaces leading to more reproducible data.

[9] Experiments carried out in collaboration with Dr. P. Veronesi (University of Modena, Italy).

3.14 Tape test

Table 3.2 Classification of the adhesion test result (adapted from the ASTM D 3359-04 method)

Classification	% area removed	Surface of coating after tape test and adhesion range
5B	0% None	
4B	Less than 5%	
3B	5-15%	
2B	15-35%	
1B	35-65%	
0B	Greater than 65%	

In this study the ASTM D 3359-04 method B was used to determine the adhesion of PEEK, Ni, PEEK-Al_2O_3 and Ni-Al_2O_3 composite coatings on stainless steel substrates. This method is suitable for coatings with thickness between 0 and 125 μm. This standard test method measures the adhesion by tape test and consists of few steps:

1. Design on the coating a lattice pattern with a sharp razor blade (Agar Scientific, Stansted, UK) and check by light reflection that the cutting edge reached the substrate. The pattern should have between 6 and 11 straight cuts on each direction at 90° between each other. The cutting is carried out to provide a free edge from which the peeling can start without overcoming the cohesion of the film.
2. Brush the coating surface lightly to make sure that any detached flakes or parts are removed.
3. Cut a piece 7.5 cm long of 2.5 cm wide semitransparent pressure-sensitive Permacel P-99 tape (Robert McKeown Company, Branchburg, New Jersey, USA.). Apply the centre of this piece over the area of the coating to be analysed and to ensure good contact rub it

firmly with the eraser on the top of a pencil; the colour under the tape can be used as an indication. The same batch of tape should be used for all the experiments for accurate comparison.

4. Within 90 ± 30 s of application, remove the tape by grabbing a free end and taking it rapidly back on itself with an angle as close as possible to 180°.

The adhesion between the substrate and the coating is then qualitatively evaluated by comparing the grid area with the illustrations reported in Table 3.2. This method only determines if the adhesion is at a generally adequate level but cannot distinguish between higher levels of adhesion.

This test was applied to pure Ni films deposited on stainless steel substrates treated with different abrasive and different acids, to Ni-Al_2O_3 composite films deposited in different conditions, to pure PEEK films and to composite films deposited from the 3P-3A, 4P-2A and 5P-1A suspensions after heat treatment before and after immersing the samples in 0.1M NaCl solution (BDH Laboratory supplies, Poole, UK) for 1 week. After immersion and before the test the samples were cleaned with distilled water and let dry. Four samples for each composition were tested.

3.15 Corrosion resistance

An Auto AC DSP device from ACM Instruments (Cumbria, UK) was employed to determine the corrosion resistance of stainless steel and deposited coatings in chloride or sulphuric acid environments. Sodium chloride (NaCl) by BDH Laboratory supplies (Poole, UK) or sulphuric acid (H_2SO_4) by Sigma Aldrich (Gillingham, UK) were employed to prepare 0.1 M solution in distilled water. Standard pitting potential measurements were made in NaCl solution increasing the potential with a sweep rate of 1 $mV \cdot s^{-1}$ from the rest potential to more positive potentials until a current of 5 $mA \cdot cm^{-2}$ was reached (potentiodynamic anodic polarization). In order to determine the corrosion current density and the corrosion potential in sulphuric acid the potential was varied linearly using a sweep rate of 1 $mV \cdot s^{-1}$ from cathodic to anodic in a range of ± 500 mV vs the rest potential. The corrosion current density and the corrosion potential were obtained by the intersection of the extrapolated anodic and cathodic currents in the Tafel plot. All these experiments were carried out in a three electrode set-up: with the sample as working electrode, a platinum wire as counter electrode and a saturated calomel electrode (SCE) (Thermo Electron Corporation, Fife, Scotland) as a reference electrode. The sample area was kept constant and controlled using a micro super XP-2000 lacquer (Hi-Tex Products Ltd., Poole, UK).

3.16 Compressive strength test

Compressive strength tests have been carried out using a Zwick/Roell Z010 instrument (Zwick GmbH e Co, Ulm, Germany) on PEEK-Al_2O_3 pellets with different compositions after

heat treatment. The samples were cylinders with diameter between 7.80 and 9.50 mm and height between 9 and 12 mm; the ratio of height to diameter was always higher than 1:1 (dimensions employed by Rae et al. [190]). Five specimens for each composition were analysed applying a crosshead speed of 0.5 $mm \cdot min^{-1}$ and the test was stopped when a strain of 50% was reached.

3.17 Artificial neural network modelling

In the last few years the interest in artificial neural networks has largely increased thanks to their ability to be applied in many areas, from finance to medicine and engineering (e.g. detection of medical phenomena, applications in material science and prediction of the stock market fluctuations) [223]. In fact, this method can theoretically be applied to every situation in which a relationship between independent (inputs) and dependent (outputs) variables exists, even if the relationship between them is complex. Artificial neural networks have become a powerful technique in all areas of science and especially in chemistry [224]. The broad success achieved by the artificial neural networks can be explained considering that they are easier to use compared to other statistical models and that they represent sophisticated modelling techniques able to model very complex functions [225].

An artificial neural network (ANN), also called a "neural network" (NN), is a form of mathematical regression or classification model. It is an interconnected assembly of simple processing units or nodes whose functionality is loosely based on the animal neuron [223, 225]. In other words, neural networks are non-linear data modelling or decision making tools that can be used to represent complex relationships between inputs and outputs or to find patterns in sets of data. In general terms, a neural network has an input layer, an output layer and any number of hidden layers. The layers are formed by neurons that are simple processors capable of very simple mathematical tasks and, from the connections of the neurons, it is possible to obtain more complex results. The input neurons are in the input layer and they have the role to introduce the data in the network. They send the data to the neurons contained in the hidden layers through a connection and, during the passage from a layer to the next forward, the data are multiplied for a number, also called "weight". The weight can be a real number, negative, positive or null and it is characteristic of each connection [225]. The neurons in the hidden layer receive modified data from all the input neurons with which are connected; all the data are summed and the result obtained becomes the argument of the function contained in the neuron. This function is the activation function and it is generally one of the following [226]:

Linear function: $y = \beta \cdot x$ where β=constant [3.6]

Sigmoid function: $y = \frac{1}{1+e^{-x}}$ [3.7]

Tanh function: $y = \frac{e^{x} - e^{-x}}{e^{x} + e^{-x}}$ [3.8]

Logarithmic function: $y = \log(1+x)$ if $x \geq 0$ [3.9]

$y = \log(1-x)$ if $x < 0$ [3.10]

Sine function: $y = \sin(x)$ [3.11]

Then, the elaborated data are sent to the output element. During the transfer they can be multiplied again by other weights. In the output neuron, the values from all connected hidden units are again summed and the result (y_i) is compared with the experimental data (x_i) using an error function as, for example, the total quadratic error:

$$E = \frac{1}{2}\sum(x_i - y_i)^2 \quad [3.12]$$

If the calculated and experimental values differ for more than a prefixed value, the process is repeated changing the weights of the connections, which initially are randomly chosen, until the differences between calculated and expected values are below the limit set by the operator. According to ref. [225], the decrease of the prediction error during each epoch is carried out using a gradient descent method like the back propagation algorithm:

$$w(t+1) = w(t) + \alpha\frac{\partial E}{\partial w_{w(t)}} + \beta(w(t) - w(t-1)) \quad [3.13]$$

where $w(t+1)$ is the updated and $w(t)$ is the old weight, E is the difference between theoretical and experimental data, α is a learning parameter (generally between 0 and 1), β is a momentum (generally between 0 and 1). After a variable number of epochs, which can vary from few tens to thousands, the calculation comes to a convergence.

Normally a set of experimental data is employed to train the neural network model and another set of experimental data to check the accuracy of the model in predicting the experimental results. This last set is the validation data set and it can be used also to avoid over-fitting (e.g. the model predicts extremely well the behaviour of the training data but not that of other data). To avoid overfitting, the training of the neural network is stopped when the error with respect to the validation data set is minimum. Once the neural network is trained it can be applied to predict behaviours or to optimise processes in the area in which it has been trained.

In this research, the neural network approach was applied to develop a quantitative understanding of the effect of different parameters on the yield of EPD of PEEK-Al_2O_3 composite systems on stainless steel substrates. As described in section 2.3, in EPD there are two kinds of parameters: those related to the suspension and the substrate (type of solvent, solvent dielectric constant, type of particle and particle size, suspension concentration and conductivity, viscosity of the suspension, zeta potential, pH and conductivity of the substrate) and those strictly related to the process (distance between the electrodes, difference of potential applied, deposition time). The data used for the Artificial Neural Network modeling were obtained from depositions carried out from the same suspensions (3P-3A or 4P-2A) and on the

same type of substrate and therefore the first group of variables did not influence the results; whereas the variation of few process parameters, such as the difference of potential applied (ΔV) and the deposition time, influenced the deposition yield. These two parameters were chosen to investigate the possibility of effectively optimizing and understanding EPD of these composite materials using a neural network approach.[10] This is the first time that such an analysis has been carried out in EPD.

In the neural network terminology the inputs chosen were the difference of potential applied and the deposition time and the output was the deposition yield per area ($g \cdot cm^{-2}$). In order to produce a matrix of data to train the model the deposition time was increased minute by minute (1 min, 2 min, 3 min, etc.) keeping the difference of potential applied constant and stopping when the coatings started to peel off upon drying. Each sample was weighed before and after the deposition and the coating area was measured to determine the deposition yield. The same experiment was repeated 4 times for each condition and the average of the 4 data was used for the statistical modelling; a standard deviation of 7% was considered for each measurement. The differences of potential employed were 20 V, 30 V and 40 V and the two electrodes were always kept at 2 cm distance. In order to optimize the fitting of the experimental data, the neural network independent parameters, such as the number of interactions (epochs), hidden layers and artificial neurons in each hidden layer, were varied. Subsequently, to verify the reliability of the two models, 4 data (input-output) for each suspension were experimentally produced choosing the inputs within the range of those used to produce the model (validation data set) and these data were compared with the values predicted by the two models.

[10] The modeling was carried out by Dr. M. Romagnoli (Univerista` di Modena e Reggio Emilia, Italy)

4. Depositions of nickel composite coatings

Pure nickel films have been widely employed for their corrosion resistance [14, 31-33], this property can be combined with the good properties of alumina producing Ni-Al_2O_3 composite films presenting enhanced hardness [12, 52, 57, 61, 62, 75, 78, 79, 81-94] and wear resistance [12, 54, 75, 81, 87, 90, 91, 93, 94, 96] and maintaining the corrosion resistance of nickel [83, 97-100]. In this research the deposition of these composite coatings by electrochemical co-deposition has been studied starting from the optimization of the surface preparation before deposition and the determination of the best conditions to deposit pure nickel films. Particular interest has been dedicated to the influence of the concentration of the particles in the bath, the current density and the particle sizes on the amount of Al_2O_3 co-deposited. Few experiments have been also carried out on the co-deposition of Ni-Al composite coatings to observe differences between the incorporation of conductive and non-conductive particles. The results achieved using the characterization techniques presented in chapter 3 are presented and discussed here after the materials and methods sections.

4.1 Materials

It is well known that nickel can be electrodeposited from different baths (see section 2.1.4), as reported in the literature [14, 32, 33]. Among the different baths investigated, the nickel sulphate bath or Watts bath was chosen for this research. The chemicals used to prepare the Watts bath were: nickel sulphate hexahydrate $NiSO_4 \cdot 6H_2O$ (>99.0%) (Fluka, Gillingham, UK), nickel chloride hexahydrate $NiCl_2 \cdot 6H_2O$ (98.0%) (Riedel-deHaën, Gillingham, UK), boric acid H_3BO_3 and sodium dodecyl sulphate (SDS) $CH_3(CH_2)_{11}SO_4Na$ (99%) (Sigma Aldrich, Gillingham, UK). In order to produce Ni-Al_2O_3 composite coatings by electrochemical co-deposition two kinds of powders were suspended in the electrolyte: sub-micron-α-Al_2O_3 powder (A-16 SG) supplied by Bassermann Minerals GmbH (Mannheim, Germany) (henceforth referred to as "sub-micron-Al_2O_3") and nano-γ-Al_2O_3 powder (544833) with a surface area between 35 and 43 $m^2 \cdot g^{-1}$ purchased from Sigma Aldrich (Gillingham, UK) (henceforth referred to as "nano-Al_2O_3"). To electro co-deposit Ni-Al composite coatings an Al powder with particle size < 25 μm (99%) supplied by Goodfellow (Huntingdon, UK) was added to the nickel sulphate bath.

The electrodes used for the deposition were a nickel anode, a stainless steel cathode and, when the three electrode cell was utilized, a silver/silver chloride (Ag/AgCl) reference electrode (Thermo Electron Corporation, Fife, Scotland). The anodes were cut from a nickel sheet (thickness 0.15 mm) with purity 99.9% supplied by BDH Laboratory supplies (Poole, UK). The cathodes were cut in pieces of 1 cm x 1 cm x 0.2 mm or in pieces of 1 cm x 1 cm x 2 mm with a guillotine from an austenitic stainless steel AISI 316L (Fe/Cr18/Ni10/Mo3) foil,

both supplied by Advent Research Materials Ltd. (Oxford, UK). The acetone employed to clean the substrates before the deposition was purchased from BHD Laboratory Supplies (Poole, UK). Moreover 800 grit SiC paper, 1 μm and 3 μm diamond paste spray, supplied by Struers (Solihull, UK) were employed to mechanical treat the substrates and nitric acid (HNO_3) 65%, hydrochloric acid (HCl) 37% and sulphuric acid (H_2SO_4) 30% obtained from Sigma Aldrich (Gillingham, UK) were employed to chemically treat the substrates before the depositions.

4.2 Instruments and methods

An electronic balance HR-120-EC from A&D Instruments Ltd. (Abingdon, UK) with a readability of 0.0001 g was used to prepare the nickel solutions and to add Al_2O_3 and Al powders to the plating bath. A Fisher Scientific (Loughborough, UK) magnetic stirrer (60-1200 rpm)/hot plate (30-550°C) was employed. The magnetic stirrer kept the particles suspended during the electro co-deposition and increased the movement of the bath around the cathode to reduce the adhesion of hydrogen bubbles on the cathode surface. The heating slab was used to maintain the temperature (monitored by a thermometer) of the plating bath constant during some depositions by surrounding the cell with another recipient containing distilled water. The pH of the solutions/suspensions were measured using a Jenway 3510 pH meter (Jenway, Essex UK) and an ultrasonic bath USC300D VWR International (Leuven, Belgium) was used for preparing the plating solutions and the suspensions and for cleaning the substrate surfaces.

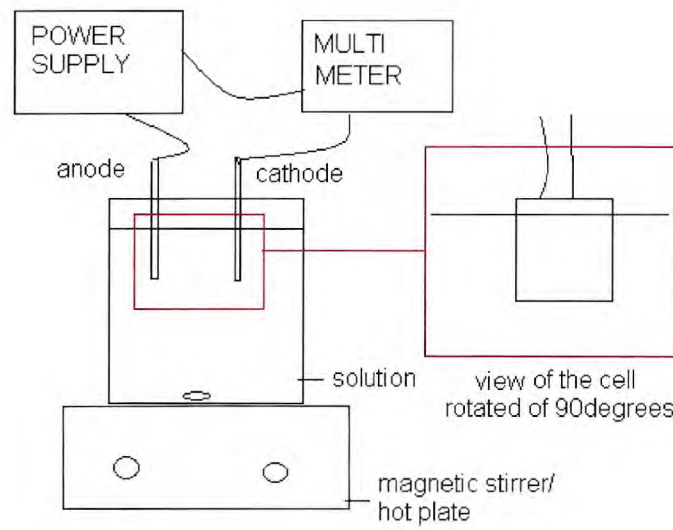


Figure 4.1 Schematic representation of the two electrode cell set up.

In this part of the study the films were deposited applying electrochemical methods: electrochemical deposition or electroplating and electrochemical co-deposition using a two electrode cell connected to a power supply (experimental set up schematically represented in Figure 4.1) or a three electrode cell connected to a potentiostat/galvanostat. In the two electrode

cell system the electrochemical cell consisted of a 100 ml beaker containing 50 ml of plating solution and two square shaped (1.0 cm x 1.0 cm) electrodes (anode and cathode). While in the three electrode cell system the electrochemical cell was a 250 ml beaker containing 175 ml of plating solution and three electrodes: two square shaped (1.0 cm x 1.0 cm) electrodes (working electrode and counter electrode (also called secondary or auxiliary electrode)) and a reference electrode: Ag/AgCl, with a standard potential of +0.2224V vs SHE.

In the two electrode cell set-up (Figure 4.1) the instrument was a TT*i* EL561 power supply (Thurlby Thandar Instrument, Huntingdon, UK) connected to a TT*i* 1906 computing multimeter (Thurlby Thandar Instrument, Huntingdon, UK). The TT*i* EL561 power supply works at constant voltage and constant current with automatic crossover, which permits a continuous transition from constant current to constant voltage in response to the solution processes. It is possible to work in constant current mode if the current applied is less then the limiting current. Whereas, if the current applied is higher than the limiting current, the instrument automatically switch to the constant potential mode. Moreover, it must be noted that the potential transmitted to each electrode by the power supply is not defined and the only controlled parameters are the difference of potential between the two electrodes and the current density when the electrode area is known.

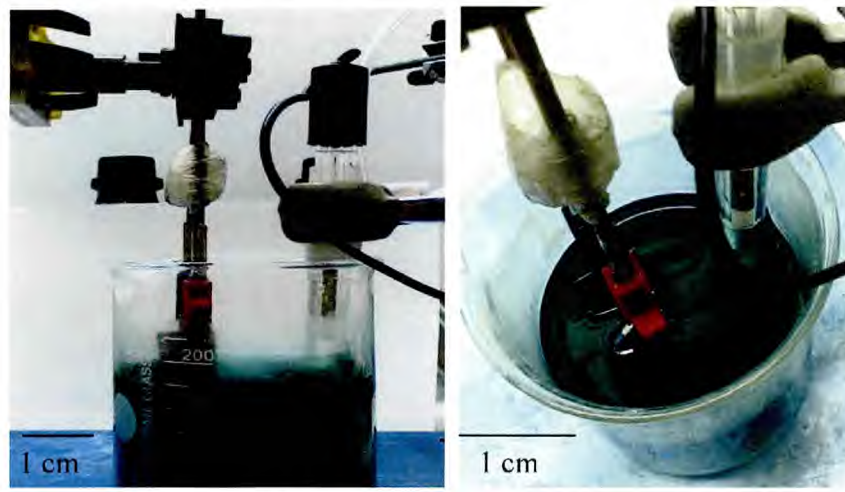


Figure 4.2 Images of the experimental set up employed for the deposition of nickel and nickel composite coatings.

In the three electrode cell set-up (see Figure 4.2) the instrument was an Auto AC DSP device from ACM Instruments (Cumbria, UK) working in constant current (galvanostatic) or constant voltage (potentiostatic) mode. This instrument is connected to a computer equipped with the DC analysis V 3.53.02 (© ACM Instruments 1997) software. When the device works in potentiostatic mode, it controls and keeps the potential of the working electrode at a constant value vs the reference electrode and monitors the variation of current during the experiment. The device can achieve it thanks to an electric circuit that maintains constant the potential across the cell by changing the resistance of the electric circuit and altering correspondingly the

current provided to the system, following Ohm's law. When the galvanostatic mode is applied the current flowing through the electrolytic cell is maintained constant and the corresponding voltage is measured vs the reference electrode.

Before the depositions the electrode surfaces were carefully treated using mechanical and/or chemical treatments (see section 4.3). The electrodes were inserted in the cell by holding them with two conductive crocodile clips fixed to two copper bars. The two copper bars were kept still and in a precise position by a holder in order to maintain the electrodes at a constant distance during the experiments and one aligned with the other. Before the experiments the electrodes were thoroughly immersed in the solution avoiding the contact between the clips and the bath to prevent contamination. Their alignment and their distance were accurately checked and measured.

4.3 Surface preparation

It is well known that in order to obtain a good adhesion between the substrate and the film the surface preparation is essential prior to coating. Sautter [72] reported that the surface preparation is particularly important when nickel is deposited on stainless steel as the adhesion of these two materials is very poor if special surface treatments are not carried out. There is no unique method for surface treatment as the method is influenced by the type of substrate, the contaminants present on its surface and sometimes by the type of film to be applied. The main surface contaminants for stainless steel are grease and the oxide protective layer [227].

In this part of the project various cleaning methods, mechanical and chemical treatments were applied to two stainless steel AISI 316L substrates with different thickness (0.2 and 2 mm) to understand how these treatments influenced the substrate/coating adhesion. In all these experiments nickel was deposited from a nickel sulphate bath (the bath characteristics will be described in section 4.4) at room temperature applying a constant current density of -32 $mA \cdot cm^{-2}$ for 30 min using the two electrode cell with 1.5 cm distance between the electrodes.

4.3.1 Mechanical treatments

The first set of experiments was carried out on both stainless steel AISI 316L substrates in as-received condition or treated with different abrasives. Three treatments were carried out on 0.2 mm thick stainless steel foils:

1. The as-received substrate was ultrasonically cleaned in acetone for 5 min.
2. The surface of the substrate was manually ground with 800 grit SiC paper for 30 s on each side and then it was cleaned with acetone and distilled water.
3. The surface was manually ground with 800 grit SiC paper for 30 s on each side then the substrate was cleaned as in treatment 1. This treatment was similar to that carried out by Zhou et al. [121, 122].

Four mechanical treatments were performed on the 2 mm thick stainless steel substrate since its thickness permitted easier handling:

1. The as-received substrate was ultrasonically cleaned in acetone for 5 min.
2. The surface was mechanically polished with 1 μm diamond paste spray and then cleaned as in treatment 1.
3. The surface was mechanically polished with 3 μm diamond paste spray and then cleaned as in treatment 1.
4. The surface of the substrate was manually ground with 800 grit SiC paper for 30 s on each side to obtain even and aligned scratches and then cleaned as in treatment 1.

Ultrasonically cleaning in acetone for 5 min was mainly used to remove fats, oils and other organic materials from the stainless steel surface [227] and also to eventually remove from the substrate surface dust and particles originated only from the grounding or polishing treatments.

The aspect of all these surfaces was analysed by optical microscopy and using 3D plots obtained by Zygo® analysis (see section 3.5). In addition, the surface roughness of each sample was measured by Zygo® instrument in at least six points obtaining bearing ratio plots, rms (root-mean-square) and Ra (roughness average) values (see section 3.5).

A) Stainless Steel AISI 316L substrate 0.2 mm thick

The stainless steel foils produced by cold rolling and annealing were analysed in as-received condition and after grinding with 800 grit SiC paper, the results are described below.

i) Surface as-received

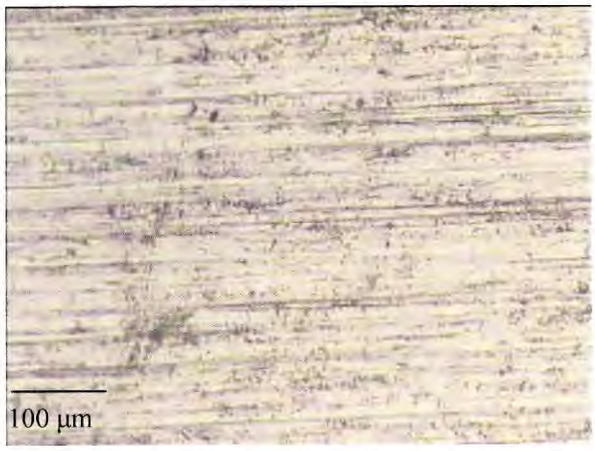


Figure 4.3 Optical microscopy picture of the surface of 0.2 mm thick stainless steel substrate in as-received condition showing aligned scratches.

Table 4.1 Roughness values for the 0.2 mm thick stainless steel substrate as-received.

Point	1	2	3	4	5	6	Average
Rms (μm)	0.112	0.172	0.175	0.214	0.181	0.197	0.18 ± 0.04
Ra (μm)	0.073	0.099	0.109	0.139	0.100	0.108	0.10 ± 0.02

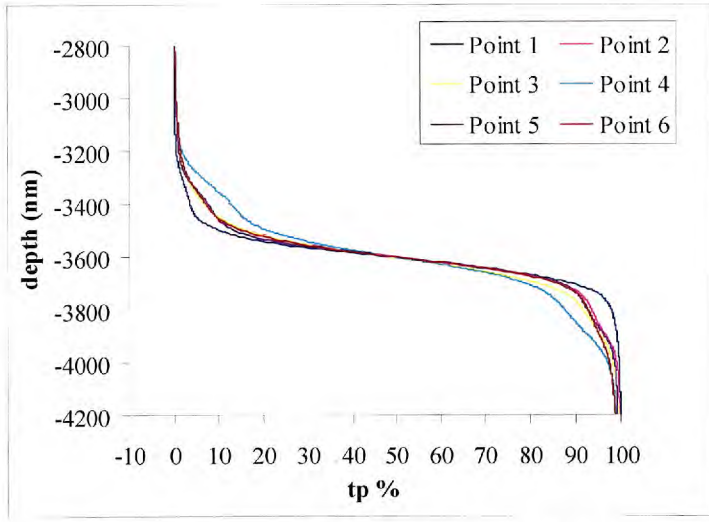


Figure 4.4 Comparison between the bearing ratio plots of the stainless steel 0.2 mm thick substrate in as-received state.

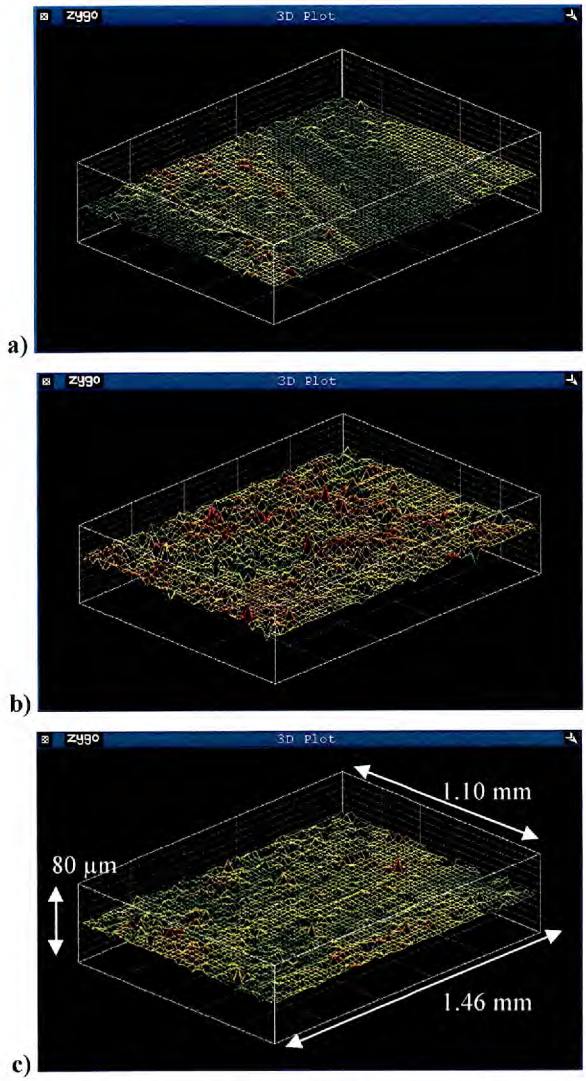


Figure 4.5 3D plots of a) point 1, b) point 4 and c) the rest of the surface of the 0.2 mm thick stainless steel substrate in as-received condition. Each point has an area of 1.46 mm x 1.10 mm and the height of the block is 80 µm.

The surface of the as-received material presented aligned scratches, as shown in Figure 4.3, due to the process employed for its production. It was analyzed in 6 points by Zygo® technique obtaining the data listed in Table 4.1 and the bearing ratio plots shown in Figure 4.4. The surface roughness in four of the analysed points (2, 3, 5 and 6) was similar, as shown by the bearing ratio plots in Figure 4.4 and the rms and Ra values in Table 4.1, and its aspect can be represented by the 3D plot in Figure 4.5 c). Moreover, analysing the bearing ratio plots (Figure 4.4) it can be seen that in point 1 the surface was smoother (see 3D plot in Figure 4.5 a)) and in point 4 (see 3D plot in Figure 4.5 b)) the surface presented more peaks (0-20 %) and more pits (80-100 %) than in the major part of the sample (see 3D plot in Figure 4.5 c)). Therefore the roughness of the surface in as-received condition seemed not to be uniform.

ii) Surface ground with 800 grit SiC paper

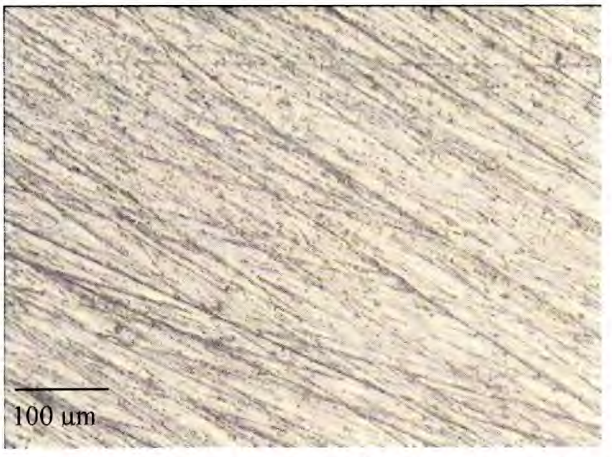


Figure 4.6 Optical microscope picture of the 0.2 mm thick stainless steel surface ground with 800 grit SiC paper showing aligned scratches.

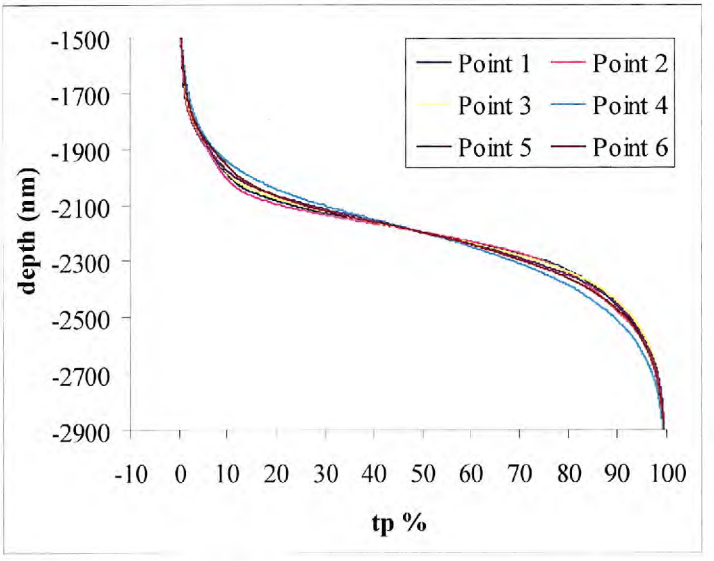


Figure 4.7 Comparison between the bearing ratio plots of the 0.2 mm thick stainless steel surface ground with 800 grit SiC paper. The surface roughness was uniform in the whole sample.

Table 4.2 Roughness values for 0.2 mm thick stainless steel substrate ground with 800 grit SiC paper.

Point	1	2	3	4	5	6	Average
Rms (μm)	0.211	0.213	0.210	0.242	0.218	0.222	0.22 ± 0.01
Ra (μm)	0.146	0.146	0.148	0.179	0.156	0.160	0.16 ± 0.01

The surface ground with 800 grit SiC paper still presented aligned scratches, as shown in Figure 4.6. Six measurements were carried out on this surface by Zygo® technique obtaining the data reported in Table 4.2 and the bearing ratio plots in Figure 4.7. These results (Table 4.2 and Figure 4.7) shows that the surface roughness was similar in the whole sample and it can be represented by the 3D plot in Figure 4.8.

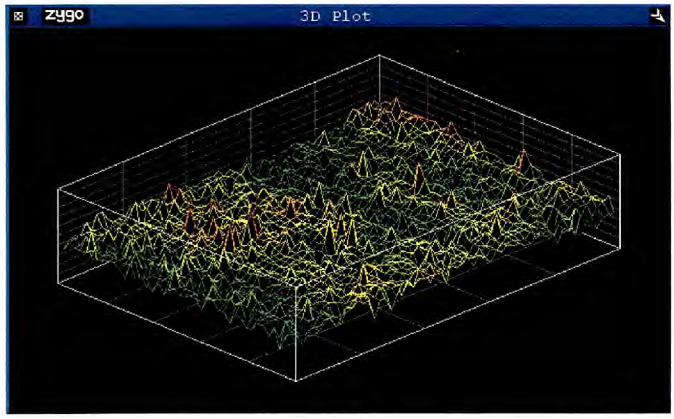


Figure 4.8 3D plot of a representative point of the 0.2 mm thick stainless steel surface ground with 800 grit SiC paper. This area is 1.46 mm x 1.10 mm and the height of the block is 80 μm.

iii) Comparison between as-received and ground surfaces

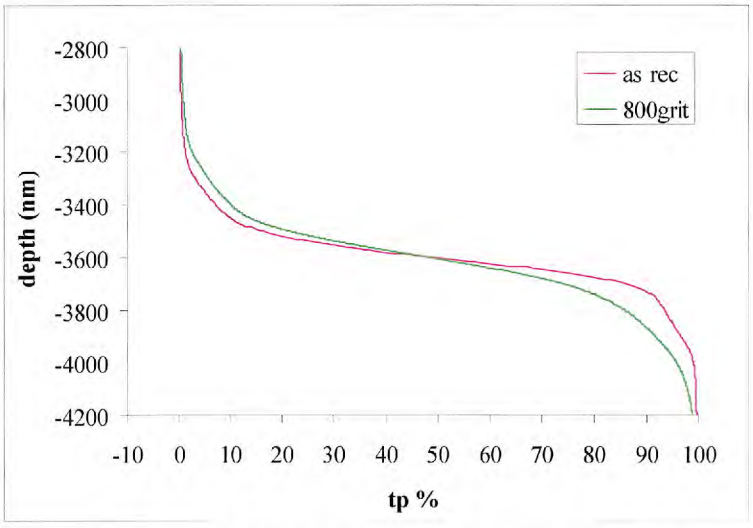


Figure 4.9 Comparison between the bearing ratio plots of the surface of the 0.2 mm thick stainless steel as-received and ground with 800 grit SiC paper showing that the sample ground was rougher than the one as-received.

Table 4.3 Roughness values for the 0.2 mm thick stainless steel AISI 316L substrate in as-received condition and after grinding with 800 grit SiC paper.

Sample	as-received	800 grit SiC
rms (μm)	0.18 ± 0.04	0.22 ± 0.01
Ra (μm)	0.10 ± 0.02	0.16 ± 0.01

Comparing the rms and the Ra values of these two samples (listed in Table 4.3) it was clear that the sample ground with 800 grit SiC paper was rougher than the as-received sample (these values have been proven to be significantly different from each other using the t-test [228]). The same evaluation can be achieved comparing a bearing ratio plot chosen as representative of the major part of the surface as-received (points 2, 3, 5 and 6) with one plot of the surface ground with 800 grit SiC paper, chosen as representative of the entire surface (Figure 4.9). From this comparison, it was clear that the surface as-received was smoother than the surface ground and in particular the main difference was noted for tp% > 60 meaning that the scratches in the ground surface were deeper than in the as-received surface.

iv) Nickel deposition on stainless steel 0.2 mm thick

Nickel depositions were carried out on the stainless steel substrates treated in the three different ways described above in order to understand how the cleaning methods and the mechanical treatments influenced the substrate/coating adhesion. In the first method the substrate as-received was ultrasonically cleaned in acetone for 5 min. The nickel coating peeled off from the substrate as shown in Figure 4.10.

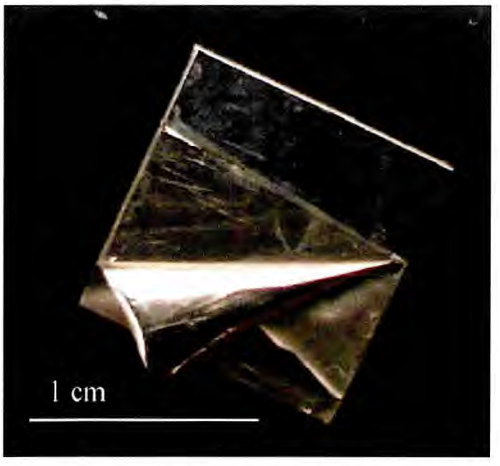


Figure 4.10 Nickel coating deposited on the 0.2 mm thick as-received stainless steel AISI 316L substrate ultrasonically cleaned in acetone for 5 min. The deposit peeled off from the substrate.

In the second method the substrate was manually ground with 800 grit SiC paper and cleaned with acetone and distilled water. The cross section of the interface substrate/coating is shown in Figure 4.11 and shows that the adherence between the two materials was not uniform

across the sample, in fact in some areas there was delamination and in other areas the interface was coherent, straight and well-defined.

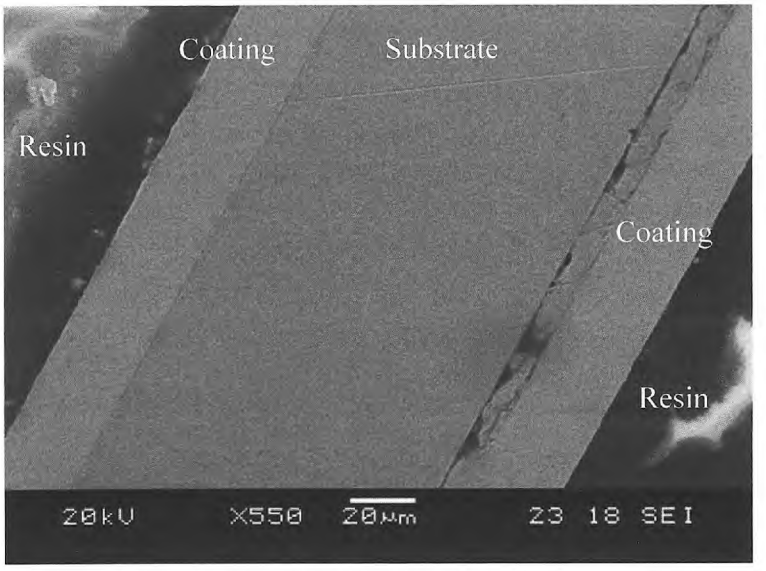


Figure 4.11 SEM image of the interface nickel/stainless steel. The nickel was deposited on stainless steel substrate ground with 800 grit SiC paper and cleaned with acetone and water. The adherence between the two materials was not uniform across the sample.

In the third method the sample was manually ground with 800 grit SiC paper and then it was ultrasonically cleaned in acetone for 5 min. The cross sections of the interface substrate/coating, shown in Figure 4.12, illustrate that the interface was straight and well-defined and that the adhesion was good and uniform in the whole sample.

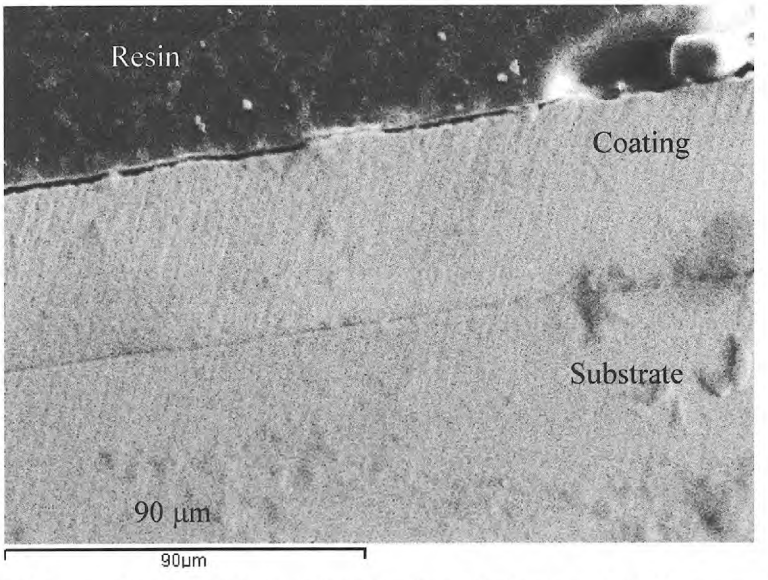


Figure 4.12 SEM image of the interface nickel/stainless steel on a substrate ground with 800 grit SiC paper and ultrasonically cleaned in acetone for 5 min. The interface is straight and well-defined and the stainless steel/coating adhesion seemed good and uniform.

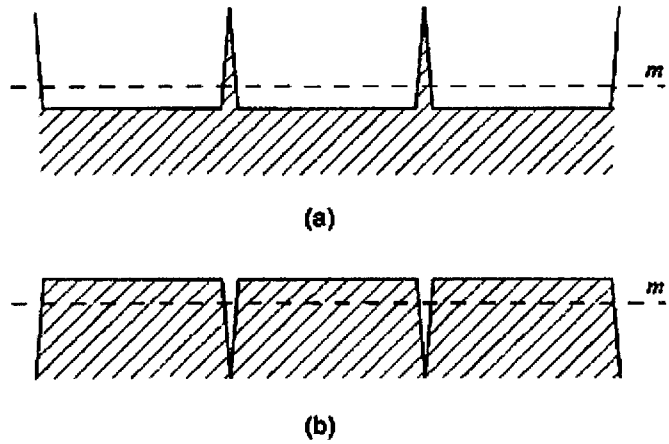


Figure 4.13 Schematic representations of two different surfaces with the same rms [216]

Considering the surface roughness of the two substrates (Table 4.3) and the deposition results, it seemed that the roughness was responsible for the adhesion between the coating and the substrate. In fact the nickel coating peeled off from the as-received substrate with a rms of 0.18 ± 0.04 μm and a Ra of 0.10 ± 0.02 μm but it did not peel off from the rougher substrate (ground with 800 grit SiC paper), with a rms of 0.22 ± 0.01 μm and a Ra of 0.16 ± 0.01 μm. From these results it can be thought that the substrate/coating adhesion increases with the substrate roughness and that the increase of adhesion is due to a mechanical interlocking effect between the two materials, as also proposed in the literature [229-235]. In particular Liu and Gao [233] deposited Ni coatings by electroless plating on Mg and Mg alloys and evaluated the substrate/coating adhesion by scratch test. From these experiments, they concluded that the adhesion strength of the coatings deposited on the rougher substrate (Ra = 0.37 ± 0.06 μm) resulted to be higher than that deposited on the smoother substrate (Ra = 0.15 ± 0.03 μm) thanks to a mechanical interlocking effect between the two materials. Ye et al. [234] electrochemically deposited Zn coatings on steel substrates with surface roughness (Ra) between 0.177 and 0.997 μm and they determined the adhesion strength between the coating and the substrate by four-point bending test. They [234] concluded that the main phenomenon determining the adhesion between the substrate and the coating was a mechanical interlocking effect influenced by the surface roughness. The highest adhesion strength was measured for a surface roughness around 0.3 μm; a further increase of Ra did not modify the adhesion strength between the two materials. The roughness values reported in the literature [233, 234] as necessary to achieve a good substrate/coating adhesion were slightly higher than those listed in Table 4.3. The difference observed can be due to different behaviours of the systems considered but also to the different methods and parameters employed to analyse the surfaces. In particular it has to be underlined that rms values produce a closer approximation of the surface compared to Ra values, from the way they are calculated (see section 3.5). However, at the same time in some occasion rms values do not give sufficient information about the surface morphology and they are not able to distinguish between two different surfaces, as those shown

in Figure 4.13, while this can be achieved using the bearing ratio plots [216], extensively employed in this study.

The interlocking mechanism between the stainless steel and the nickel is also supported by the start of the deposition inside the scratches left on the substrate surface by the grounding treatment, as shown in Figure 4.14. The surface of the as-received substrate (Figure 4.3) also presented aligned scratches, but they were probably not deep enough to hold the coating through a mechanical interlocking effect and this can probably explain the peeling off of the coating.

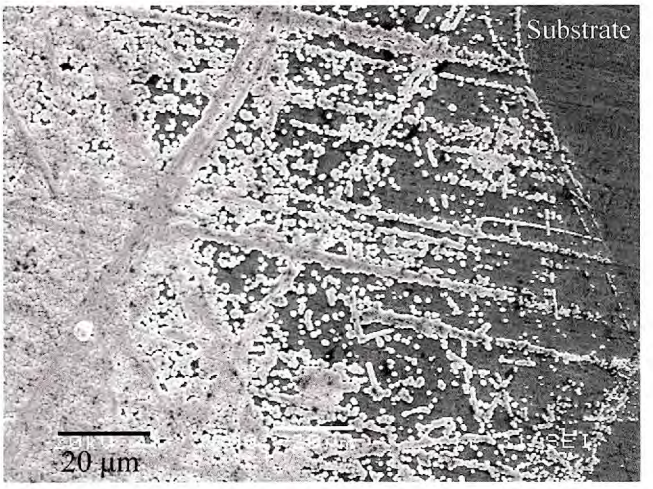


Figure 4.14 SEM image of the separation between the substrate and the nickel coating deposited from a nickel sulphate bath showing that the deposition started inside the scratches.

In addition, it can be also observed that the adhesion between stainless steel and nickel was significantly influenced by the cleaning procedure. In fact ultrasonically cleaning the substrate in acetone (see Figure 4.12), instead of simply cleaning it with acetone and distilled water (see Figure 4.11), produced a more uniform, sharp and well-defined interface on the whole sample. This was probably due to the higher effectiveness of the ultrasonic method for removing grease and oil from the substrate and even to remove particles (e.g. dust and residues from the grinding process) attached to the surface.

B) Stainless Steel AISI 316L substrate 2 mm thick

The same analysis carried out above on the 0.2 mm thick stainless steel substrates was repeated also on 2 mm thick stainless steel specimens. This stainless steel was produced by cold rolling followed by annealing and descaling. In this part of the study three different mechanical treatments were carried out: polishing with 1 µm diamond paste, polishing with 3 µm diamond paste and grinding with 800 grit SiC paper. In addition, the as-received substrate was also investigated. This investigation is reported in Appendix 1.

i) Comparison between the different mechanical treatments

Table 4.4 Roughness values obtained on 2 mm thick AISI 316L samples with different surface treatments and results of the Ni depositions.

Surface treatments	Measures		
	rms (μm)	Ra (μm)	Ni deposition
As-received	0.32 ± 0.01	0.18 ± 0.01	Good
1 μm diamond paste	0.07 ± 0.02	0.05 ± 0.01	Peeled off
3 μm diamond paste	0.07 ± 0.02	0.04 ± 0.02	Peeled off
800 SiC paper	0.25 ± 0.01	0.17 ± 0.01	Good

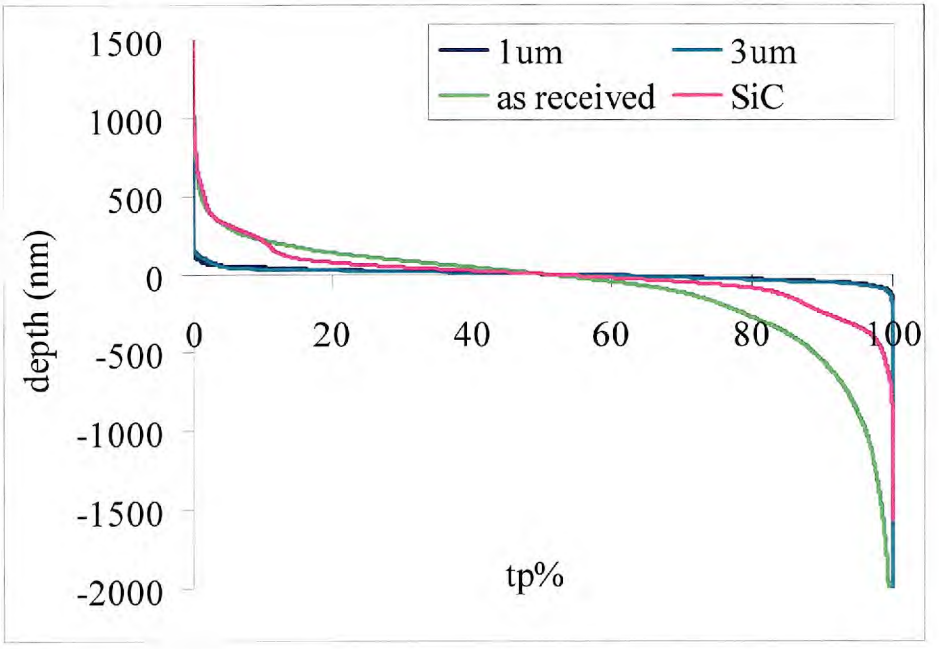


Figure 4.15 Comparison between the bearing ratio plots of the 2 mm thick stainless steel surfaces as-received, ground with 800 grit SiC paper, polished with 1μm or 3 μm diamond paste.

From the rms and Ra values of the surfaces treated with the three mechanical methods (polished with 1 μm diamond paste, polished with 3 μm diamond paste and ground with 800 grit SiC paper) and of the as-received sample (see Table 4.4) it resulted that the as-received sample was rougher than the others, followed by the sample ground with 800 grit SiC paper and the samples polished with 3 μm and 1 μm diamond paste. The values measured on the surface as-received and ground have been proven to be significantly different from each other using the t-test [228], while those of the surfaces treated with diamond pastes resulted considerably similar using the t-test. The same conclusion can be also drawn comparing the bearing ratio plots shown in Figure 4.15 that shows that the samples polished with 1 and 3 μm diamond paste were extremely similar and smoother than the samples ground and as-received. The surfaces of these last two samples were comparable in the peaks (0-30 tp%) but considerably different in the deepness (60-100 tp%), with the as-received sample presenting

deeper valleys. These results were in perfect agreement with what was expected considering the roughness of the abrasives employed. However, it has to be noted that the as-received surface showed an opposite behaviour to that shown by the 0.2 mm thick stainless steel, being the rougher surface (see section 4.3.1 A).

ii) Nickel deposition on stainless steel 2 mm thick

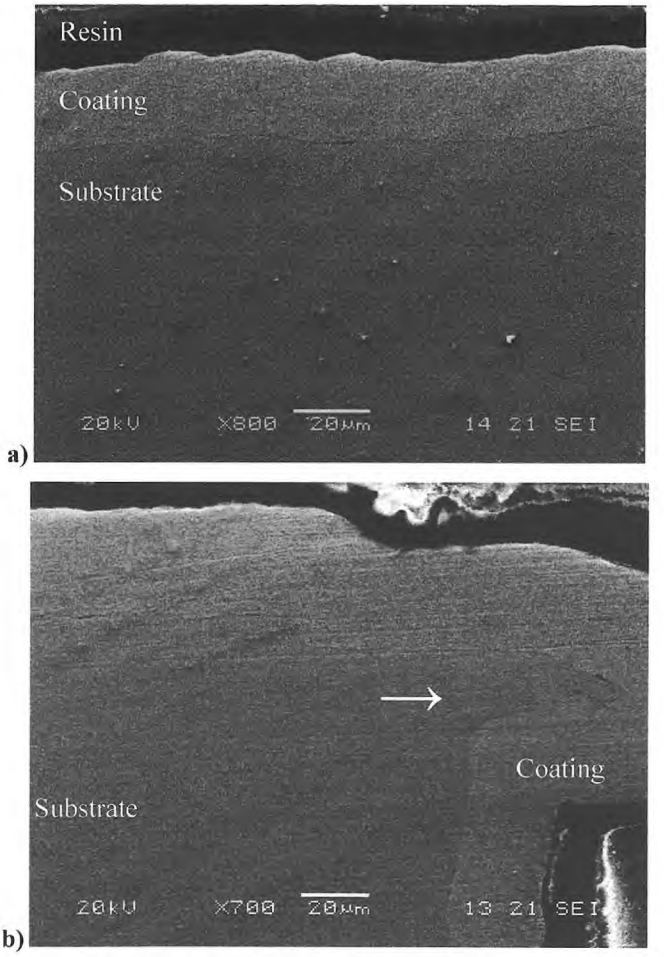


Figure 4.16 SEM micrographs of the interface stainless steel/nickel showing a) homogeneous and uniform interface coating/substrate and b) that the substrate surface roughness was maintained in the coating (arrow). The stainless steel as-received was ultrasonically cleaned in acetone for 5 min.

Nickel was deposited on the four different treated stainless steel substrates immediately after ultrasonically cleaning in acetone for 5 min, since this seemed to be the best cleaning treatment following the results described in section 4.3.1 A. From these results, it was observed that the coatings peeled off from the stainless steel substrates polished with 1 µm and 3 µm diamond paste (see Table 4.4), respectively, and therefore these two mechanical treatments were not further investigated. The interface stainless steel/nickel of the coatings deposited on the substrates in as-received condition was homogeneous, uniform and without defects and gaps in the whole sample (Figure 4.16 a)). Moreover it was observed that the surface roughness was maintained in the coating that consequently resulted quite irregular, as shown by the arrow

in Figure 4.16 b). The same behaviours were also observed when the substrate surface was ground with 800 grit SiC paper before the deposition.

The surface roughness and the deposition results in Table 4.4 indicated that the surface roughness was responsible for the substrate/coating adhesion thanks to an interlocking mechanism, as frequently reported in the literature [229-235] and as also observed for the thinner stainless steel substrate and discussed in section 4.3.1 A. Considering all the data obtained on the two substrates (Tables 4.3 and 4.4), it seemed that the surface roughness (rms) for the nickel-stainless steel AISI 316L system should be larger than 0.18 μm in order to avoid the coatings peeling off from the substrate.

iii) Scratch test

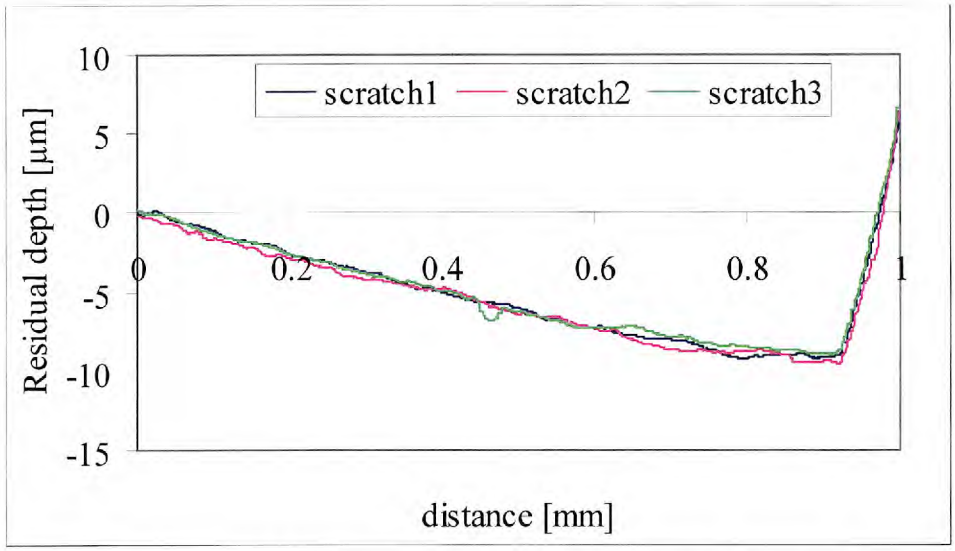


Figure 4.17 Residual depths of three scratch tracks carried out on a nickel coating deposited on the as-received substrate using a Rockwell diamond indenter with radius of 100 μm.

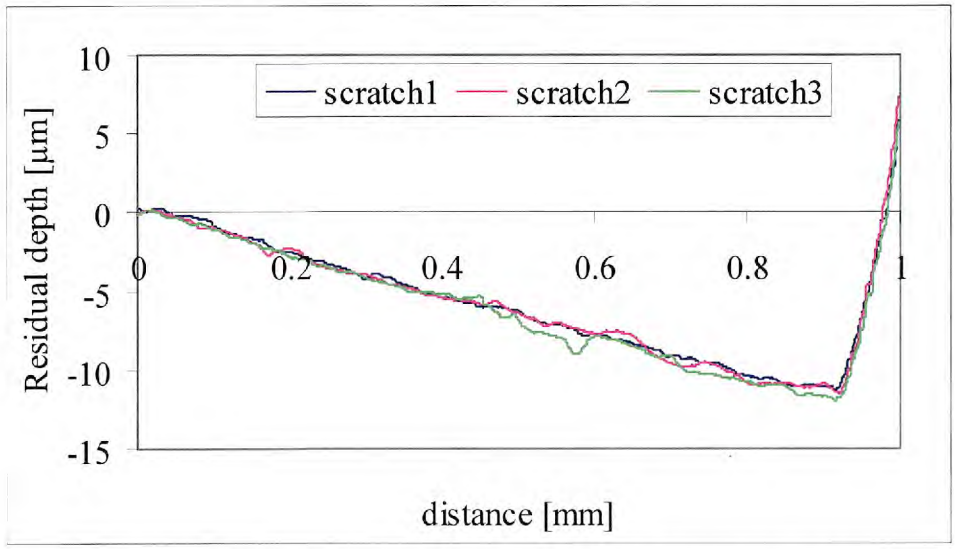


Figure 4.18 Residual depths of three scratch tracks carried out on nickel coating deposited on the substrate ground with 800 grit SiC paper using a Rockwell diamond indenter with 100 μm radius.

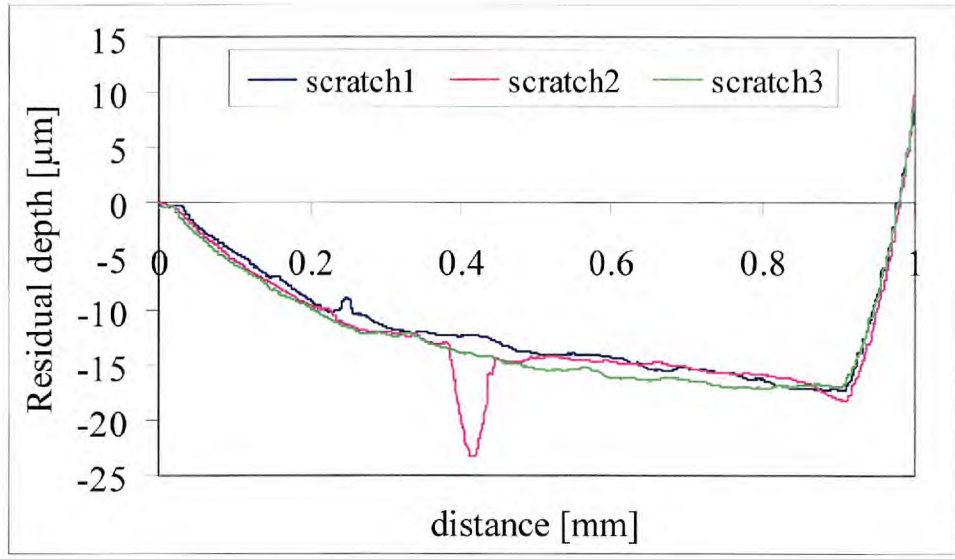


Figure 4.19 Residual depths of three scratch tracks carried out on a nickel coating deposited on the as-received substrate using a Rockwell diamond indenter with radius of 10 µm.

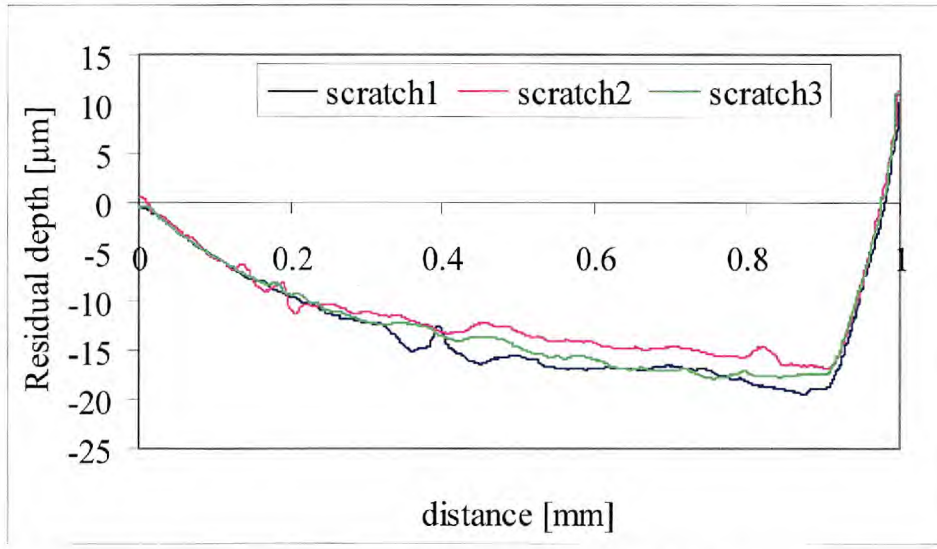


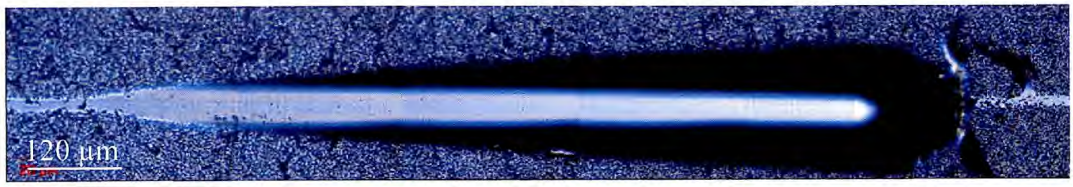
Figure 4.20 Residual depths of three scratch tracks carried out on a nickel coating deposited on the substrate ground with 800 grit SiC paper using a Rockwell diamond indenter with radius of 10 µm

In order to evaluate the substrate/coating adhesion, a scratch test was carried out on nickel coatings deposited in the same conditions (nickel sulphate bath, room temperature, -32 $mA \cdot cm^{-2}$, 30 min, 1.5 cm) on 2 mm thick stainless steel substrates in as-received state and ground with 800 grit SiC paper. Both substrates were ultrasonically cleaned in acetone for 5 min before the deposition. These two samples were chosen among the seven samples analysed because they were the two that gave better results in term of adhesion from the cross section analysis and also because the 2 mm thick stainless steel substrate was easier to handle compared to the thinner stainless steel.

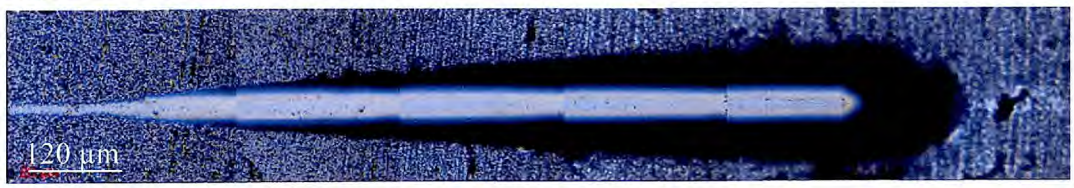
The first set of scratches were carried out using a Rockwell indenter with 100 µm radius and applying a progressive normal load from 0.1 to 20 N with a loading rate of 19.9 $N \cdot min^{-1}$

and a scratch speed of 1 mm·min^{-1} obtaining a total scratch length of 1 mm. The residual depths (depth after the scratch has been carried out) of the scratches are shown in Figures 4.17 and 4.18 for the surface as-received and ground, respectively. Comparing the residual depths of the three scratches obtained on the same sample it was clear that the coatings presented homogeneous properties. The same conclusion could be also attained when the smaller indenter (radius of 10 µm) was employed to produce scratches on nickel films deposited on both surfaces applying the same conditions (results shown in Figures 4.19 and 4.20); even if in this second case a slightly higher variability could be observed. From the comparison of the residual depths of the scratches obtained using indenters with different sizes, 10 µm or 100 µm radius (see Figures 4.17-4.20), it was clear that the smaller indenter penetrated more into the film than the bigger indenter due to the higher load per area applied. However, even when the 10 µm indenter was employed, the substrate was not reached during the test and no acoustic signal variation was detected demonstrating that the coating did not cracked or debond [236].

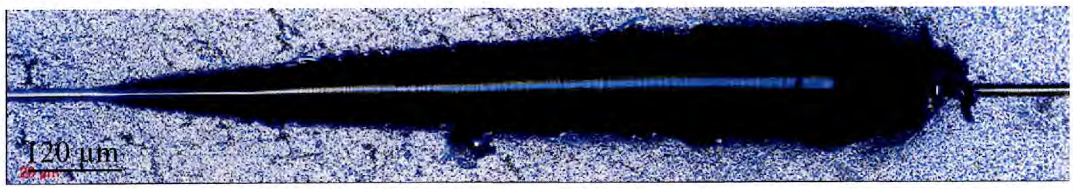
a) as-received - 100 µm



b) ground - 100 µm



c) as-received - 10 µm



d) ground - 10 µm

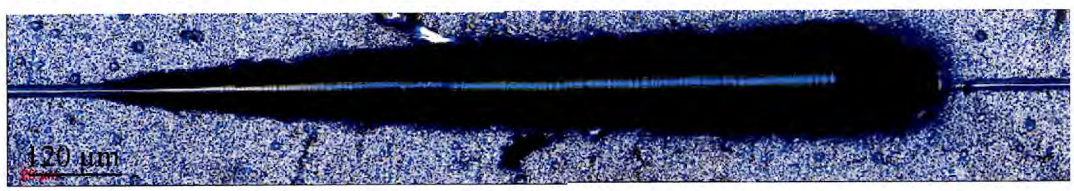


Figure 4.21 Optical micrographs of the scratch tracks carried out on nickel coatings deposited on a) and c) the as-received substrate and b) and d) the substrate ground with 800 grit SiC paper using a Rockwell diamond indenter with a) and b) radius of 100 µm or c) and d) radius of 10 µm.

From the analysis of all the tracks of the scratches produced with the two indenters (Fig. 4.21), it is possible to evaluate the adhesion between the substrate and the coating [233, 236].

The scratch tracks left in all conditions applied were smooth and no noticeable cracks were observed inside or outside the tracks, similar to the findings of Mu et al. [236] for nickel films deposited by electroless plating on steel substrates. This behaviour is probably due to the deformability of the nickel or to the low load applied. It could be concluded that the coatings remained fully adherent to the substrate and fully coherent to themselves independent from the substrate surface preparation before the deposition.

4.3.2 Chemical treatments

It has been mentioned in the literature [59, 98, 124, 227, 237] that stainless steel substrates can be chemically etched before the deposition to improve the substrate/coating adhesion by removing oxides from their surface (through their conversion into soluble compounds). The oxide protective layer formed on the stainless steel surface is between 1 and 4 nm thick and it has been the object of numerous researches [238-240] from which it emerged that it is greatly modified by the environment [238], e.g. in acid environment the oxide passive film tends to be enriched in Cr compared to the base alloy due to the dissolution of Fe in this environment [239, 240].

Table 4.5 Roughness values of as-received and ground with 800 grit SiC paper samples cut from the same stainless steel sheet.

rms (μm)	
Samples as-received	Samples ground with 800 grit SiC paper
0.32 ± 0.01	0.25 ± 0.01
0.31± 0.01	0.292 ± 0.009
0.33 ± 0.01	0.31± 0.02
0.38 ± 0.02	0.32 ± 0.01

The influence of chemical treatments on the surface roughness and on the nickel/stainless steel interface has been studied to determine the best surface treatment needed to achieve uniform and sharp interfaces. Three solutions have been employed in this study: 10% H_2SO_4 for 30 s [98], 18% HCl for 5 min [59, 124] and 25% HNO_3 for 10 s [237]. These treatments were carried out only on the 2 mm thick stainless steel samples because on this substrate it was possible to achieve better uniformity of the grounding treatment thanks to its thickness. Moreover, following the results achieved and described in section 4.3.1, just the substrate in as-received condition and the substrate manually ground with 800 grit SiC paper were chosen to carry out the chemical etching study among the four conditions initially investigated (as-received, ground with 800 grit SiC paper, polished with 1 μm and 3 μm diamond paste). Straight before the deposition, each substrate was chemically etched, rinsed with distilled water and ultrasonically cleaned in acetone for 5 min, as described in section 4.3.1. These treatments

have been carried out carefully immediately before the deposition in order to minimise surface aging after etching. The only difference between the sample described here and those described in section 4.3.1 is the chemical etching treatment.

Table 4.6 Roughness values of as-received and ground with 800 grit SiC paper samples before and after chemical etching with 10% H_2SO_4 for 30 s.

Surface treatment	Before etching		After etching with a solution 10% of H_2SO_4 for 30 s	
	rms (μm)	Ra (μm)	rms (μm)	Ra (μm)
As-received	0.31 ± 0.01	0.17 ± 0.01	0.31 ± 0.01	0.171 ± 0.009
ground	0.31 ± 0.02	0.23 ± 0.02	0.31 ± 0.02	0.23 ± 0.01

Table 4.7 Roughness values of as-received and ground with 800 grit SiC paper samples before and after chemical etching with 18% HCl for 5 min.

Surface treatment	Before etching		After etching with a solution 18% of HCl for 5 min	
	rms (μm)	Ra (μm)	rms (μm)	Ra (μm)
as-received	0.33 ± 0.01	0.19 ± 0.01	0.33 ± 0.01	0.195 ± 0.008
ground	0.292 ± 0.009	0.22 ± 0.01	0.288 ± 0.008	0.214 ± 0.007

Table 4.8 Roughness values of as-received and ground with 800 grit SiC paper samples before and after chemical etching with 25% HNO_3 for 10 s.

Surface treatment	Before etching		After etching with a solution 25% of HNO_3 for 10 s	
	rms (μm)	Ra (μm)	rms (μm)	Ra (μm)
As-received	0.38 ± 0.02	0.199 ± 0.007	0.39 ± 0.01	0.207 ± 0.009
ground	0.32 ± 0.01	0.243 ± 0.008	0.32 ± 0.02	0.24 ± 0.01

The surface roughness parameters (Ra, rms and bearing ratio plots) of each sample were measured by means of Zygo® in 9 points of the substrate surface and the average of these values was considered representative for that particular surface, but not for all the surfaces treated in the same way. In fact, it was noticed that the roughness of the samples as-received and ground with 800 grit SiC paper might slightly vary from one sample to another even if they were cut from the same stainless steel sheet (Table 4.5). In order to understand how chemical etching influences the surface roughness, the average roughness of the six samples (as-received and ground with 800 grit SiC paper treated with the three different acids) was measured before and after each chemical treatment on the same sample, so that any variation in roughness could be attributed exclusively to the chemical treatment. The 9 bearing ratio plots acquired for the same sample were plotted in the same graph to assess the uniformity of the sample surface and a bearing ratio plot, chosen as representative of the entire surface, was used for comparison of the surface roughness before and after the chemical treatment. The values for rms and Ra and

the bearing ratio plots obtained for the six samples are listed and discussed in Appendix 2. From the study reported in Appendix 2 and the brief summary of the surface roughness of the stainless steel surfaces before and after chemical etching with H_2SO_4 (Table 4.6), HNO_3 (Table 4.7) and HCl (Table 4.8) it seemed that etching did not modify the stainless steel surface roughness (rms and Ra) with the resolution used in this analysis (x 5, 1 point every 2 μm).

A parallel study of the interface stainless steel/nickel was carried out on all the six samples to understand how the chemical etching (with H_2SO_4, HNO_3 and HCl) combined with the mechanical treatment (as-received and ground with 800 grit SiC paper) influenced the adhesion between the two materials. From this analysis it resulted that all the stainless steel/nickel interfaces were sharp, well defined and without defects. They were also uniform and the roughness of the substrate surface was maintained in the coating, as described in section 4.3.1.

4.3.3 Tape test

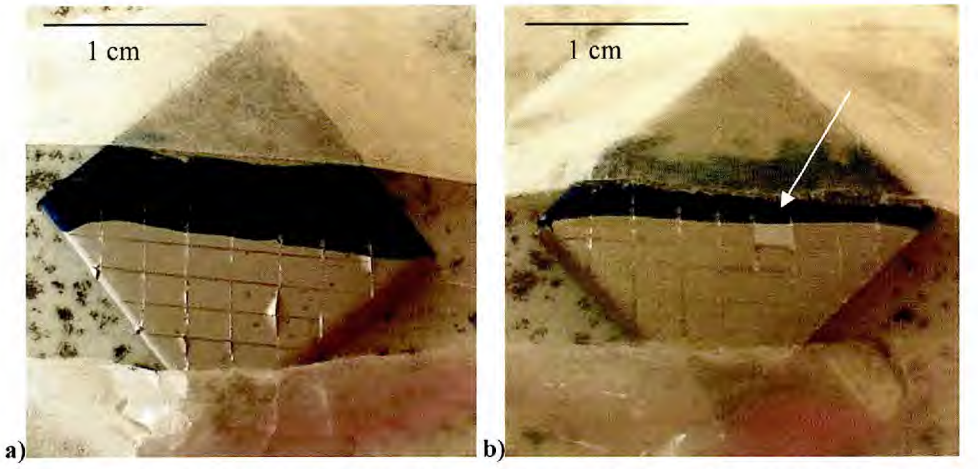


Figure 4.22 Images of nickel coatings deposited on stainless steel ground with 800 grit SiC paper after tape test a) 0% detachment and b) < 5% detachment as shown by the arrow.

The purpose of a film is generally to protect or decorate the substrate and therefore a good substrate/coating adhesion is essential. Considering that the substrate material and its surface preparation strongly affect the substrate/coating adhesion, a method to evaluate the adhesion of films on surfaces treated with different methods is fundamental. In sections 4.3.1 and 4.3.2 a complete analysis of the substrate roughness after different mechanical and chemical treatments and a microscopic analysis of the nickel/stainless steel interfaces were carried out to determine the best surface treatment. In this section the adhesion of nickel coatings to 2 mm thick stainless steel substrates as-received or ground with 800 grit SiC paper 2 mm thick stainless steel substrates with and without chemical etching (10% H_2SO_4 for 30 s, 25% HNO_3 for 10 s, 18% HCl for 5 min) was qualitatively assessed using the tape test standard method described in section 3.14. Three samples for each condition were tested and compared with the illustrations reported in Table 3.2 and the results are described below.

All the adhesion tests carried out produced similar results, as those shown in Figure 4.22. Most of the coatings demonstrated a good adhesion with 0% of coating detached (Figure 4.22 a)) whereas few coatings slightly peeled off (< 5% detachment) in the area of the sample close to the nail varnish (Figure 4.22 b)). From this study it resulted that the nickel adhesion to the substrate as-received or ground with 800 grit SiC paper was reasonably good with and without chemical etching.

4.3.4 Summary

From the surface roughness values (rms and Ra) and the deposition results described in section 4.3.1 and 4.3.2, it was concluded that the substrate surface roughness was responsible for the substrate/coating adhesion thanks to an interlocking mechanism between the two materials, as also invoked in the literature for similar coatings [233, 234]. It was also found that ultrasonically cleaning the substrate in acetone for 5 min before the deposition was a key step to obtain uniform and sharp interfaces, again in agreement with the literature [227]. Chemically etching the substrates with 10% H_2SO_4 for 30 s or 25% HNO_3 for 10 s or 18% HCl for 5 min seemed not to modify the stainless steel surface roughness and produced homogeneous and well defined substrate/coating interfaces. Considering that there were no differences between these results and those achieved without chemical etching and no influences on the adhesion determined by tape test; the chemical etching was no longer applied.

Summarising, it seemed that the best surface preparation consisted of grinding the substrate with 800 grit SiC paper and ultrasonically cleaning it in acetone for 5 min right before the electrochemical deposition. Therefore, in all the experiments described in this chapter this was the surface preparation method employed. The ground substrate was chosen over the as-received substrate, which also produced good coating adhesion, to ensure that all the starting surfaces presented similar and controlled characteristics.

4.4 Electrochemical deposition of nickel coatings

Table 4.9 Ranges in which the parameters were varied for nickel deposition using both the 2 and 3 electrode cell set-up.

Composition of the plating solution	Nickel sulphate bath	Nickel sulphate bath + 0.2 g/l of SDS
pH	4.0 ± 0.5	
Difference of potential applied	1.0 ± 0.1 V ÷ 3.0 ± 0.1 V	
Distance between the two electrodes	1.5 cm	
Current density applied	-10, -20 and -32 $mA \cdot cm^{-2}$	
Deposition time	Between 1 and 96 min	
Stirring rate	0 rpm	200 rpm
Temperature	Room temperature	50°C

Electrochemical deposition is generally a complicated process depending on many variables strictly correlated one to the other and therefore it is difficult to understand the individual influence of each variable on the process itself. The ranges in which these variables have been varied to deposit Ni in this study are listed in Table 4.9. The first aim of this research was to determine the conditions to deposit a good-quality nickel coating, considering the preparation of the substrate surface described in section 4.3, the bath composition and the other parameters influencing the process (temperature, difference of potential or current density applied, deposition time and stirring rate).

4.4.1 Composition of the plating solution

The solution employed to deposit nickel coatings was for all the experiments a Watts bath with the composition reported in Table 4.10. This composition is within the range given for the nickel sulphate bath in Table 2.1 (section 2.1.4 A)) [32, 33]. Before use the solution was ultrasonically mixed for 60 min to completely dissolve all the chemicals. Some of the experiments were carried out by adding 0.2 g/l of sodium dodecyl sulphate (SDS) to the bath achieving the composition described by Liu and Chen [47, 48], as it will be discussed in section 4.4.5. The pH of the plating solution was measured before and after the depositions and it was 4.0 ± 0.5. It was observed that the pH did not change during the process due to the buffering action of the boric acid (see section 2.1.4 B)) [32, 33].

Table 4.10 Composition of the bath used for nickel deposition.

Bath composition	
270 g/l of $NiSO_4 \cdot 6\ H_2O$	0.973 M
45 g/l of $NiCl_2 \cdot 6\ H_2O$	0.189 M
40 g/l of H_3BO_3	0.65 M

4.4.2 Potentiostatic experiments using a two-electrode set up

In order to electrochemically deposit a coating it is necessary to apply a potential difference between two electrodes in an electrochemical cell, so that the ions in the solution can migrate toward the opposite charged electrode and, if the electrode potential is appropriate, they can be reduced or oxidized.

From the Pourbaix or E/pH Diagram [241] reported in Figure 4.23 it is possible to evaluate the stability of nickel in aqueous solution as a function of pH and potential [242]. Knowing that the pH of the bath employed was 4.0 ± 0.5, it is clear from the E/pH diagram that the two species stable at potentials < +1.0 V vs SHE (< +0.78 V vs Ag/AgCl) are Ni and Ni^{2+}. The conversion between Ni^{2+} and Ni is expressed by the following reaction:

$$Ni^{2+}_{(aq)} + 2e^- \rightarrow Ni_{(s)} \qquad E^o = -0.250 \text{ V vs SHE} \qquad [4.1]$$

that correspond to line 9 in Figure 4.23 and the reduction potential from a solution with $[Ni^{2+}]$ = 1.16 M (as reported in Table 4.10) can be calculated using Nernst equation (as described in section 2.1.2), considering the concentration of the metal [Ni] = 1:

$$E = E^0 + \frac{0.0591}{n}\log\frac{[Ox]}{[Red]} = -0.250 + \frac{0.0591}{2}\log\frac{[Ni^{2+}]}{[Ni]} = -0.248 \text{ V vs SHE} \qquad [4.2]$$

The potential E is -0.248 V vs SHE (-0.470 V vs Ag/AgCl), but during these potentiostatic experiments it was not possible to measure the working electrode potential since a two electrode cell was employed.

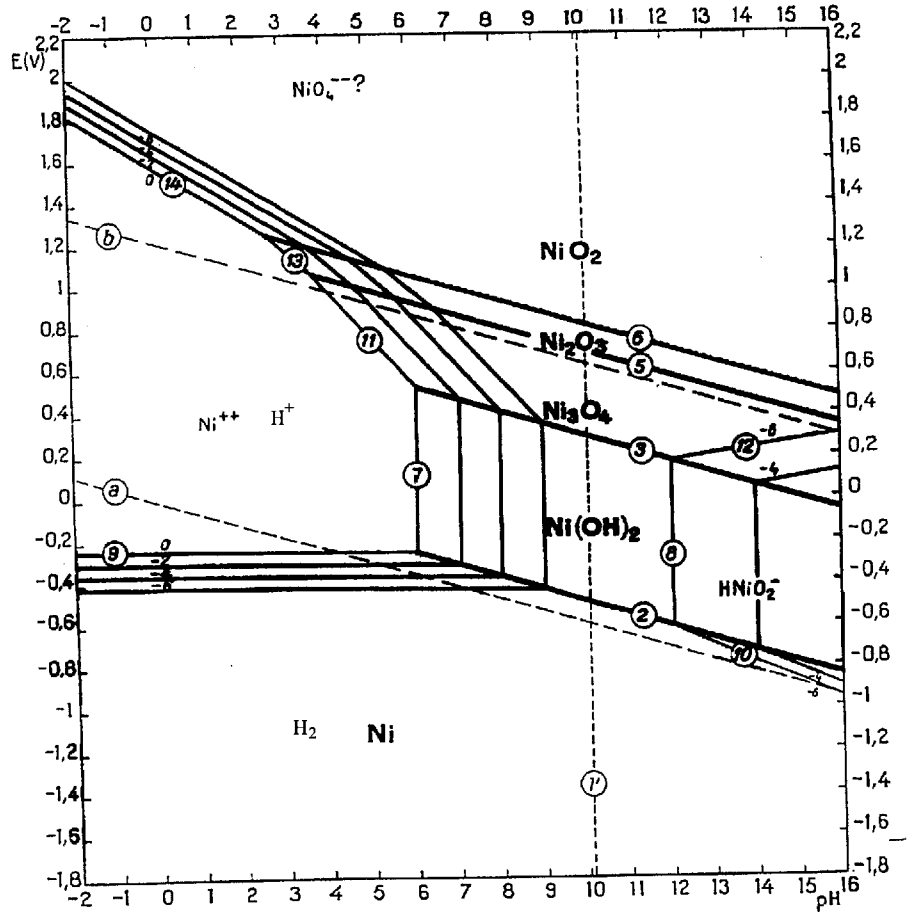


Figure 4.23 Potential (vs SHE)–pH or Pourbaix diagram for the nickel-water system at 25°C [241].

The other process taking place at the cathode is the hydrogen reduction:

$$2H^+ + 2e^- \rightarrow H_2 \qquad E^o = 0 \text{ V vs SHE} \qquad [4.3]$$

and represented by line "a" in Figure 4.23 [241]. Below line "a" hydrogen gas H_2 is stable and above this line the hydrogen ion H^+ is stable. The hydrogen reduction is strictly related to its concentration in the solution (pH) and the reduction potential can be calculated using Nernst equation (as described in section 2.1.2) considering the bath pH ~ 4 and the $[H^+] = 10^{-4}$ M:

$$E = E^0 + \frac{0.0591}{n}\log\frac{[H^+]}{[H]} = 0.000 + \frac{0.0591}{1}\log[10^{-4}] = -0.236V \text{ vs SHE} \qquad [4.4]$$

In these conditions the theoretical reduction potentials of nickel (E = -0.248 V vs SHE) and hydrogen (E = -0.236 V vs SHE) are very close and therefore the reductions of these two species have similar probability to happen. However, the existence of a considerable overpotential needed to produce hydrogen allows Ni to be deposited from a nickel sulphate solution at higher efficiency than hydrogen [33]. The hydrogen reduction produces hydrogen bubbles that adhere to the cathode surface, grow and then move towards the top of the bath (hydrogen evolution) leaving pinholes in the coating, as shown in Fig. 4.24-4.26. In addition the hydrogen reduction might render the nickel coating weaker (see section 2.1.4 C)) and it also affects the efficiency of the deposition process, as part of the energy applied is lost to produce hydrogen. In order to decrease the hydrogen ion reduction at the cathode surface the difference of potential can be modified, or to decrease the hydrogen adhesion to the substrate surface sodium dodecyl sulphate (SDS) can be added to the plating solution, or the movement around the cathode can be increased by stirring (as described in section 2.1.4 C)). The effect of SDS and the movement of the liquid around the cathode on the hydrogen pitting will be examined in section 4.4.5.

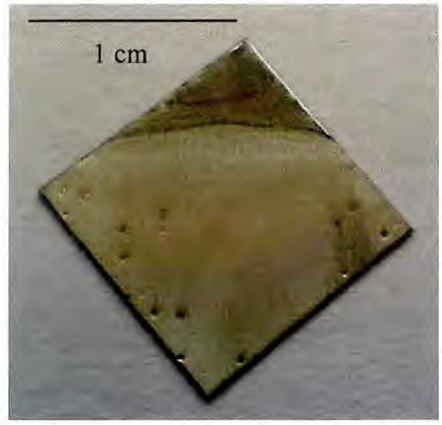


Figure 4.24 Image of a nickel coating deposited applying ΔV= 2.0 ± 0.1 V for 60 min showing some holes due to H_2 pitting.

In the literature nickel deposition has been mainly performed galvanostatically (i.e. constant current) (see section 2.1.4) and therefore a trial-and-error process was applied here to identify the difference of potential to be employed. In order to do it, the influence of the applied difference of potential (ΔV) on Ni deposition was studied varying ΔV between 1.0 ± 0.1 V and 3.0 ± 0.1 V using the two electrode cell described in section 4.2. For these experiments the distance between the two electrodes (nickel anode and stainless steel cathode) was kept constant at 1.5 cm and all the other parameters (room temperature, nickel solution) were unvaried. A difference of potential of 1.0 ± 0.1 V did not produce any deposition, whereas ΔV = 3.0 ± 0.1 V liberated numerous bubbles on both electrodes and the deposited Ni film was broken. Therefore it was thought that the ΔV needed to achieve nickel deposition from this solution was between 1.0 ± 0.1 and 3.0 ± 0.1 V.

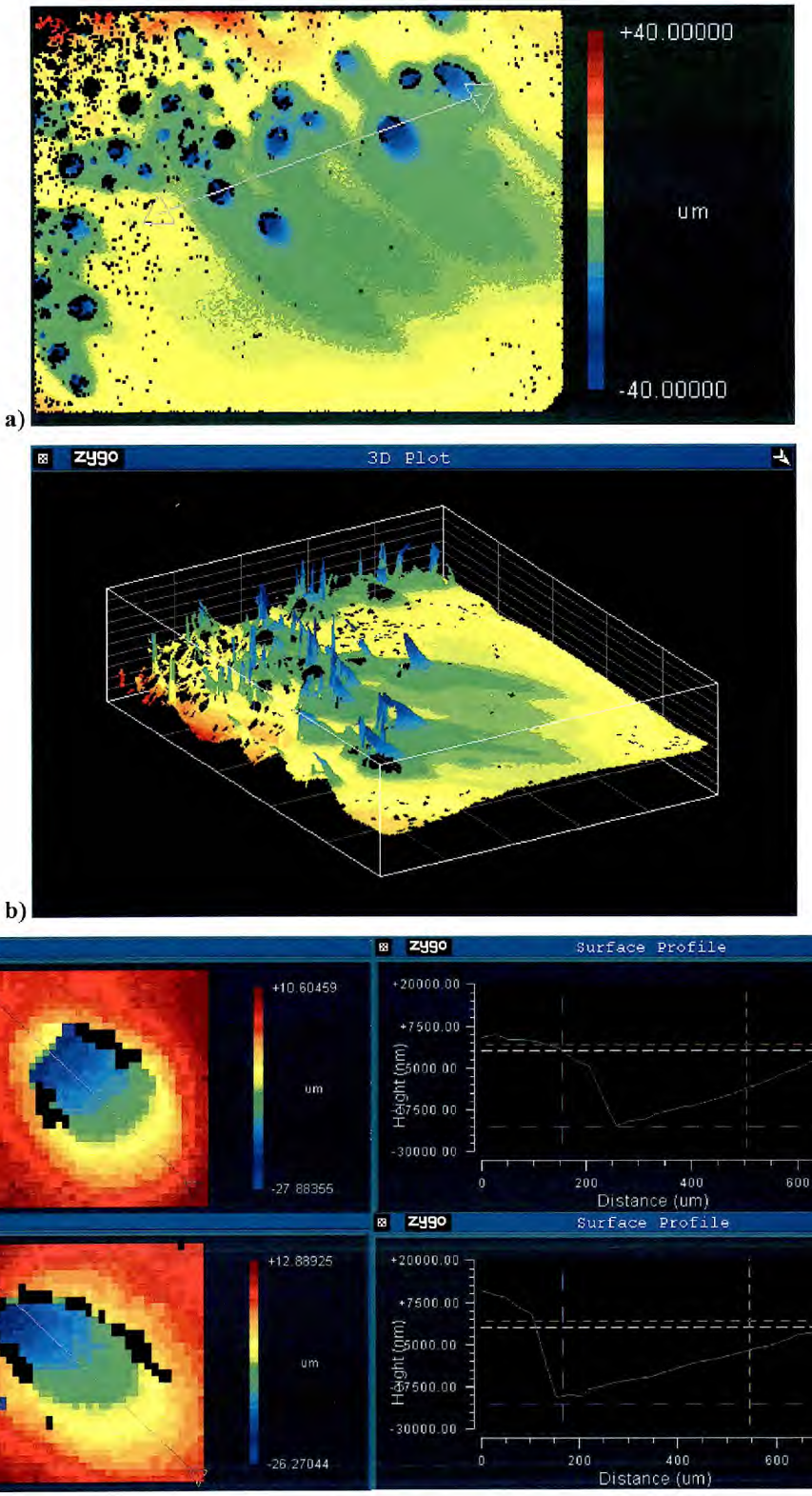
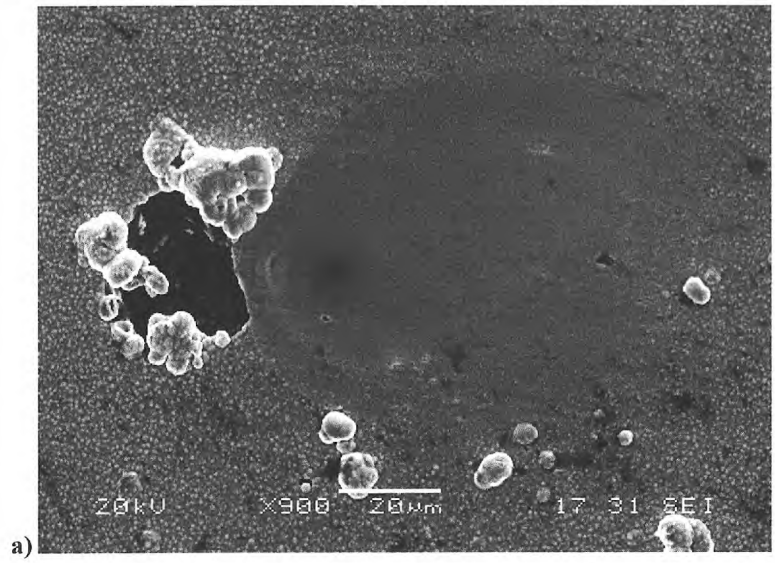
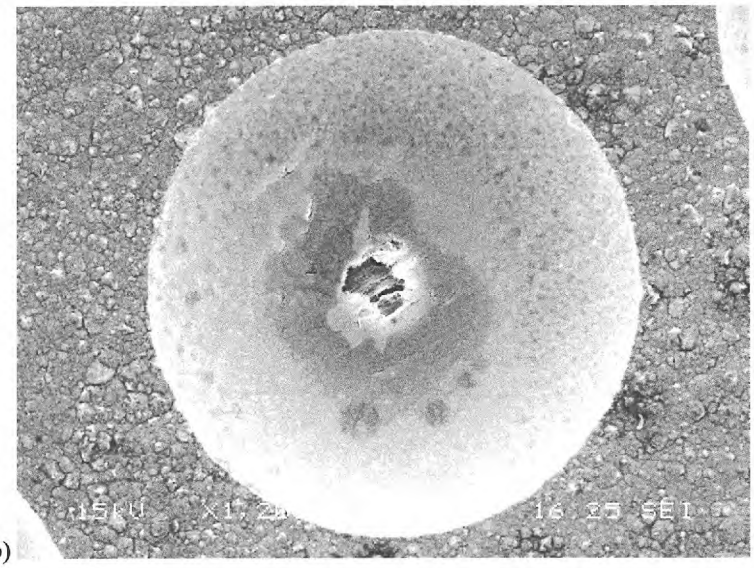


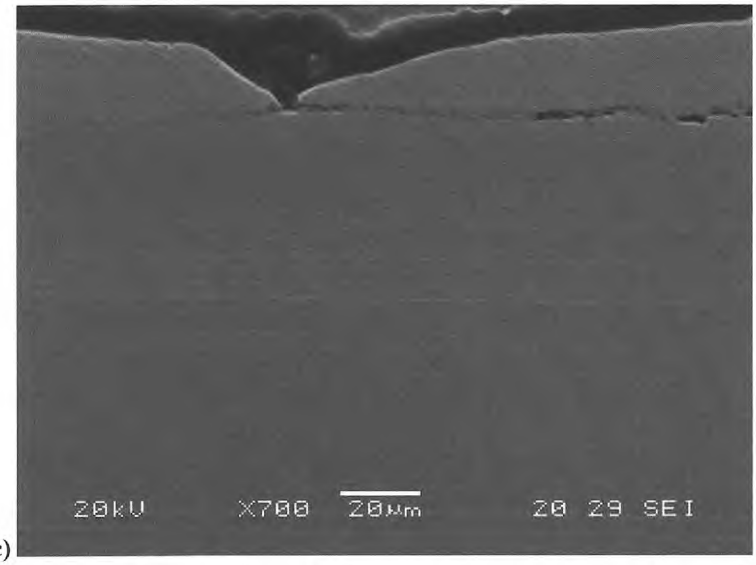
Figure 4.25 Light interferometry images (Zygo®) of a Ni film deposited applying 2.0 ± 0.1 V for 60 min showing a) the deepness of the cavities left by H_2 evolution, b) the same image upside-down and c) the structure of two pinholes with a sharp boundary on one side and a smooth on the other side. The area represented in a) and b) is 1.46 mm x 1.10 mm.



a)



b)



c)

Figure 4.26 SEM images of pinholes due to hydrogen evolution in Ni films deposited applying 2.0 ± 0.1 V for 60 min. a) and b) images from the top, c) cross section of a pinhole in the centre of the film showing a sharp edge on one side and a smooth edge on the opposite.

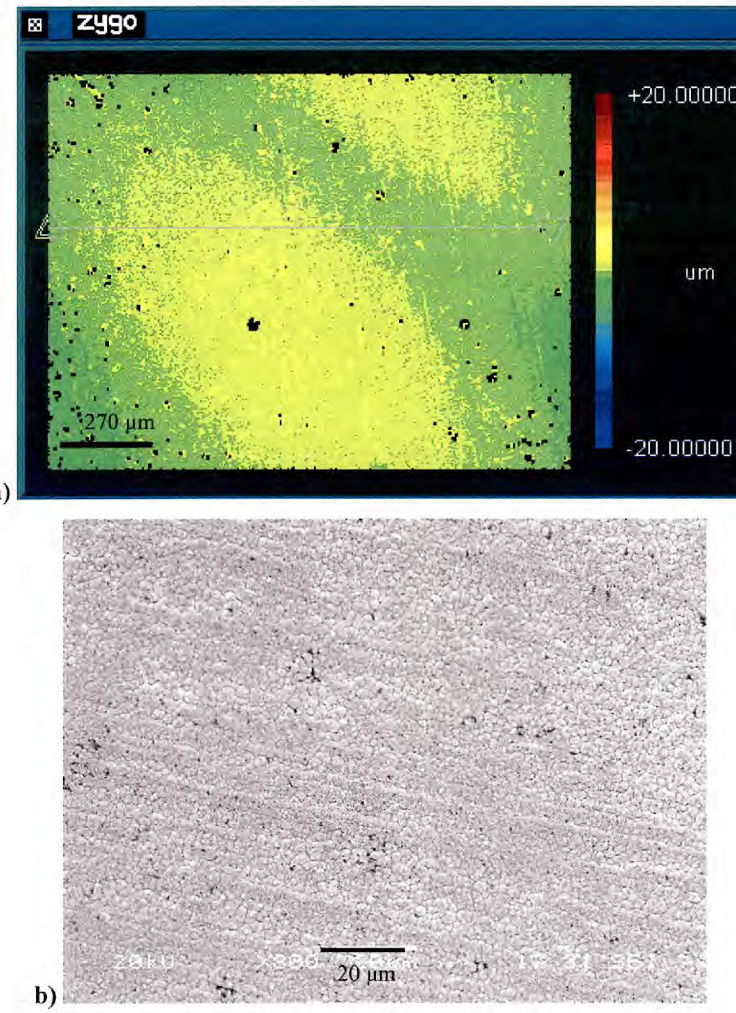


Figure 4.27 a) Light interferometry image (Zygo®) and b) SEM micrograph of a Ni film deposited applying 2.0 ± 0.1 V for 60 min showing that some coatings were smooth and without cavities.

Some of the coatings deposited applying a difference of potential of 2.0 ± 0.1 V presented cavities as a result of H_2 evolution, as shown in Figures 4.24-4.26, whereas other coatings were smooth and without cavities (Fig. 4.27). Figure 4.25 b) represents the coating surface (Fig. 4.25 a)) upside down (looking at it from the stainless steel surface). This image clearly exhibits the numerous pinholes in the coating, their deepness and their structure. The structure of the pinholes was expected to be symmetrical and cylindrical (as the one shown in Fig. 4.26 b)) because the bubbles have a round shape and they adhere to the surface not permitting the deposition. The pinhole pictured in Figure 4.26 b) was round and with very sharp edges and in its centre it was possible to observe the stainless steel substrate. These perfectly round shape pinholes were observed just in the part of the film close to the interface air/solution; whereas in the rest of the coating it seemed that the boundary of the pinholes was sharp on one side and smooth in the opposite one (see Fig. 4.25 a) and b), and in more detail Fig. 4.25 c)). This structure of the pinholes may be explained by the fact that hydrogen bubbles were produced on the substrate surface and slowly grew during the deposition. Then, when they reached a certain volume, they started to move towards the top of the bath leaving a pinhole in

the coating with a sharp side (towards the lower part of the cell) and a smooth side (towards the top of the solution). The same structure was also confirmed by the SEM micrographs in Figures 4.26 a) and c). In particular the pinhole cross-section observed in Figure 4.26 c) was remarkably similar to the surface profile shown in Figure 4.25 c).

Applying a difference of potential of 2.0 ± 0.1 V for 30 min the coating deposited from the Watts bath was nickel, as shown by the XRD analysis reported in Figure 4.28. The XRD spectrum presented five main reflection lines characteristic of the nickel crystalline structure (see spectrum B in Figure 4.28), in agreement with those reported in the literature [36, 42, 43, 75, 90, 113, 116, 117, 236, 243-249], and two extra signals attributed to the stainless steel substrate (see spectrum A in Figure 4.28) [248]. The highest reflection intensity for the nickel coating deposited in these condition is the (111) crystallographic orientation.

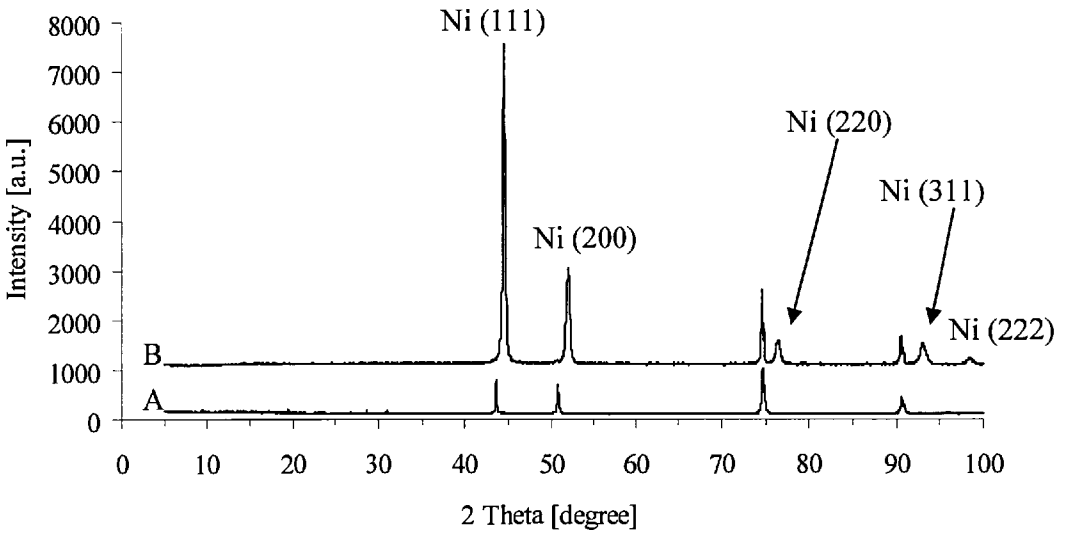


Figure 4.28 XRD spectra of A) the stainless steel substrate and B) a Ni coating deposited applying 2.0 ± 0.1 V for 30 min showing that the coating is made of crystalline nickel.

In order to study the effect of the potential difference on the reduction of hydrogen ions, ΔV was lowered by 0.1 V for a set of experiments until reaching a potential of 1.5 ± 0.1 V. Applying ΔV = 1.9 ± 0.1 V some of the coatings still presented pinholes similar to those described above and others were smooth and uniform. The coatings deposited with ΔV = 1.8 ± 0.1 V were similar to those obtained before but they seemed to present fewer holes. Hence it appeared that lowering the difference of potential was a solution to decrease the hydrogen evolution. For this reason the potential difference was lowered again to 1.7 ± 0.1 V, some of the films deposited were uniform but others still presented pinholes. When 1.6 ± 0.1 V was employed, it seemed that better coatings were deposited: some of them were quite uniform while other presented few pores and they were rough. Since some of the films deposited at ΔV = 1.6 ± 0.1 V still presented pinholes, ΔV was further decreased to 1.5 ± 0.1 V, some coatings deposited were uniform and smooth whereas others were rough and with cavities.

From these results, it seemed that lowering the potential difference between the electrodes the hydrogen reduction decreased. This deduction was further based on the analysis of the anodes after depositions carried out at different voltages. The surfaces of three nickel anodes are shown in Figure 4.29: the anode on the left is a nickel anode before the deposition; the central one after depositions carried out at 1.6 ± 0.1 V and the one on the right after depositions at 2.0 ± 0.1 V. The surfaces of the anodes before and after the depositions were considerably different and this may be due to the anode dissolution during the process (as described in section 2.1.4 D)). In addition, the surface of the anode after depositions carried out at $\Delta V = 1.6 \pm 0.1$ V resulted smoother than that obtained applying $\Delta V = 2.0 \pm 0.1$ V. This result may be explained considering that applying a lower difference of potential the nickel anode dissolved uniformly producing a thinner and smoother anode; whereas when a higher difference of potential 2.0 ± 0.1 V was applied the overpotential facilitated the nucleation of O_2 bubbles (water electrolysis) that excavated the surface in a heterogeneous manner producing a rough surface.



Figure 4.29 Three nickel anodes: before deposition (on the left), after deposition at 1.6 ± 0.1 V (centre) and at 2.0 ± 0.1 V (on the right). Their surfaces are considerably different probably due to different processes taking place at the anode surface in different conditions.

Comparing coatings deposited under the same conditions, it became apparent that the potentiostatic deposition of Ni using a two electrode cell was not reproducible, as shown in Figures 4.24-4.27. This observation may probably be explained considering that the sensitivity of the power supply (two electrode cell) was not enough to carry out the electrochemical deposition of nickel (see section 2.1.2), because of the strong dependence of the process on the cathode potential. A consequence of the low reproducibility of this technique was the difficulty encountered to understand the effects that each parameter (e.g. potential applied and surface preparation) had on the deposition process. For this reason further experiments were carried out applying a constant current density (see section 4.4.3), as suggested in the literature [32, 33]. Advantages of the galvanostatic deposition against the potentiostatic are that the galvanostatic procedure can be easily scaled-up for industrial applications, since it is possible to achieve reproducible conditions with a simple power supply (two electrode set-up), and that uniform

depositions can be obtained independently from the electrode geometry/cell configuration, that instead has a fundamental importance when potentiostatic conditions are applied.

4.4.3 Galvanostatic experiments

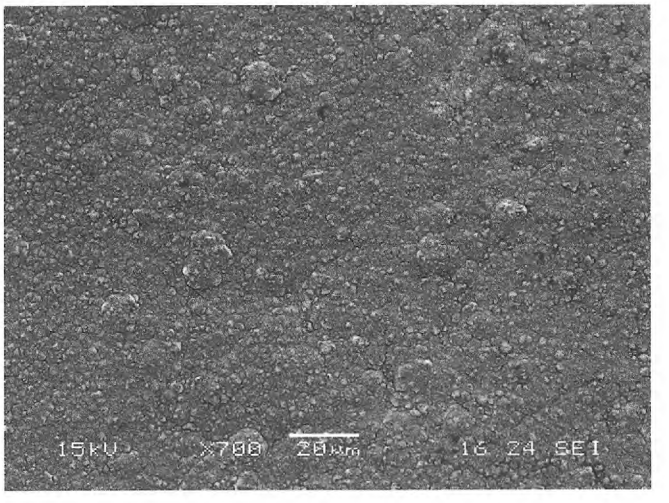


Figure 4.30 SEM micrograph of a nickel coating deposited applying -32 mA·cm^{-2} for 30 min.

The constant current density experiments were carried out using both instruments (2 and 3 electrode cells) and keeping the electrodes (stainless steel and nickel) at 1.5 cm distance. In order to calculate the current needed to produce the appropriate current density the area of the cathode immersed in the solution was measured. This area has to be constant during the experiment and therefore, after the accurate preparation of the cathode surface (as described in section 4.3) and before the deposition, a layer of nail varnish was carefully applied all around the part of the substrate that was at the interface air/solution, leaving a part of the stainless steel free to ensure the contact between the clip and the substrate. When the nail varnish was dried the area of the electrode enclosed by the nail varnish was measured and the current i to be applied calculated using eq. 2.6 in section 2.1.3 where j is the current density and A the area of the cathode.

For the experiments carried out with the two electrode set-up a current density of -32 mA·cm^{-2} was selected because, according to the literature [33], it seemed that with slower deposition the substrate/coating adhesion was better and considering that, from Table 2.1 in section 2.1.4, this current seemed to be the lowest current density utilizable for the deposition of nickel from the bath employed. In these conditions the deposition rate was ~11 nm·s^{-1}. A micrograph of a coating deposited applying a constant current density of -32 mA·cm^{-2} is shown in Figure 4.30. It seemed that the films deposited in these conditions presented relatively less pinholes and were more reproducible than those deposited potentiostatically (see Figures 4.24-4.27) further confirming the superiority of this method compared to the potentiostatic from a reproducibility and quality point of view. For these reasons and for the possibility of easily scale-up galvanostatic processes this method will be carried forward in this project.

When the three electrode cell was employed, it was possible to study the electrochemical properties (i.e. redox potential of the species in solution) of the solution by cyclic voltammetry [250]. The cyclic voltammetry is a potentiodynamic electrochemical measurement in which a potential is applied to a working electrode and the correspondent current is measured. The potential is measured between the working electrode and the reference electrode while the current is measured between the working electrode and the counter electrode. The potential applied is varied with a constant rate in a range of potential, e.g. Va to Vb, and when Vb is reached the scan direction is reversed and the range Vb to Va is scanned. After the scan is completed a current-potential plot is produced obtaining the cyclic voltammogram, which gives an estimation of the processes taking place in the range studied. In the forward scan current peaks are shown in correspondence of the potential at which species can be reduced. In fact the current increases until the reduction potential is reached (current maximum) and then the current decreases due to the diminution of the specie concentration at the electrode surface. When the potential scan is reversed, there will be potentials at which the species that have been reduced in the first part can be re-oxidised producing current of reverse polarity. The oxidation peaks normally present shapes similar to the reduction peaks.

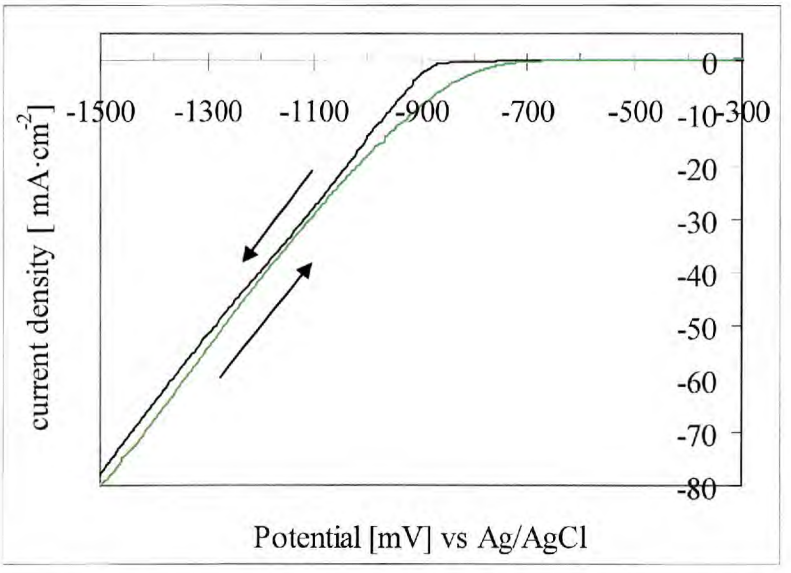


Figure 4.31 Cyclic voltammetry carried out in a nickel sulphate bath between 0.0 V and -1.5 V with a sweep rate of 5 mV·s^{-1} and electrode area of 1.19 cm^2. The black line is the sweep between 0.0 V and -1.5 V (reduction) and the green line the opposite (oxidation) (-1.5 V to 0.0 V).

The cyclic voltammetry of the nickel sulphate bath was carried out between 0.0 V and -1.5 V with a sweep rate of 5 mV·s^{-1} (= 300 mV·min^{-1}) using the stainless steel ground with 800 grit SiC paper as a working electrode, a nickel counter electrode and an Ag/AgCl reference electrode; the cyclic voltammetry is shown in Figure 4.31. During the reduction sweep (0.0 V to -1.5 V, black line in Figure 4.31) the Ni counter electrode dissolved and the stainless steel was nickel covered and during the oxidation sweep (-1.5 V to 0.0 V, green line in Figure 4.31)

the Ni film deposited on the stainless steel dissolved away and a nickel film was deposited on the Ni counter electrode. Increasing the electrode potential (0.0 V to -1.5 V), it seemed that the nickel deposition started at about -0.850 V vs Ag/AgCl (=-0.62 V vs SHE) (Figure 4.31) and that the reaction rates became faster and the current density ($i < 0$) increased, without reaching the limiting current density of the process (see section 2.1.3). This result is in agreement with those reported in the literature and shown in Figures 4.32 [251] and 4.33 [78].

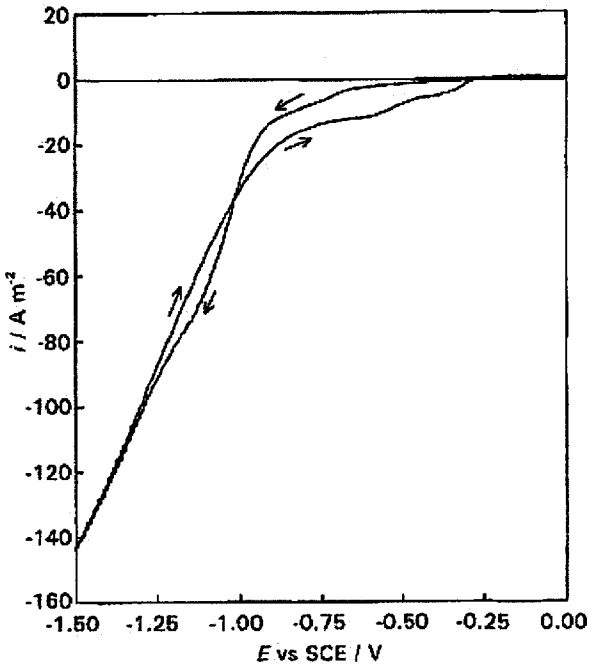


Figure 4.32 Cyclic voltammetry for a rotating disc (25 rps) graphite electrode in a solution at 293 K containing 5 mM of $NiSO_4$ and 30 mM of $(NH_4)_2SO_4$ with a sweep rate of 1.5 $mV \cdot s^{-1}$ as reported by Njau and Janssen [251].

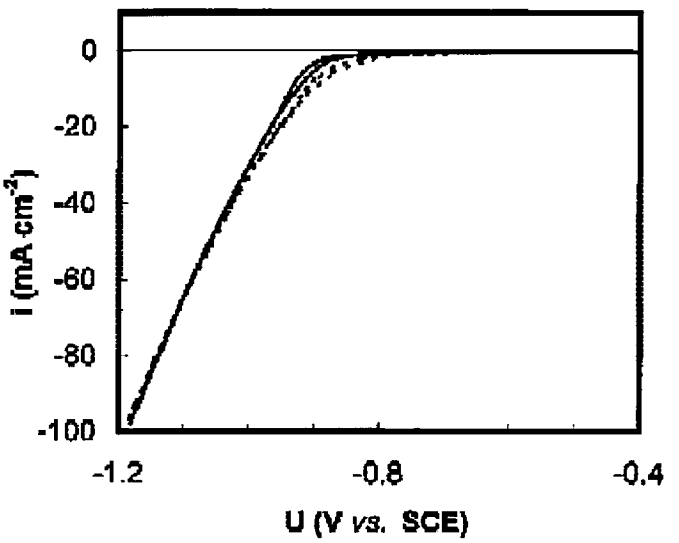


Figure 4.33 Cyclic voltammetry for a nickel sulphamate solution (dashed line) and a suspension of 2 vol.% of 300 nm Al_2O_3 particles in the nickel sulphamate solution (solid line) with a sweep rate of 10 $mV \cdot s^{-1}$ as reported by Shao and Vereecken [78].

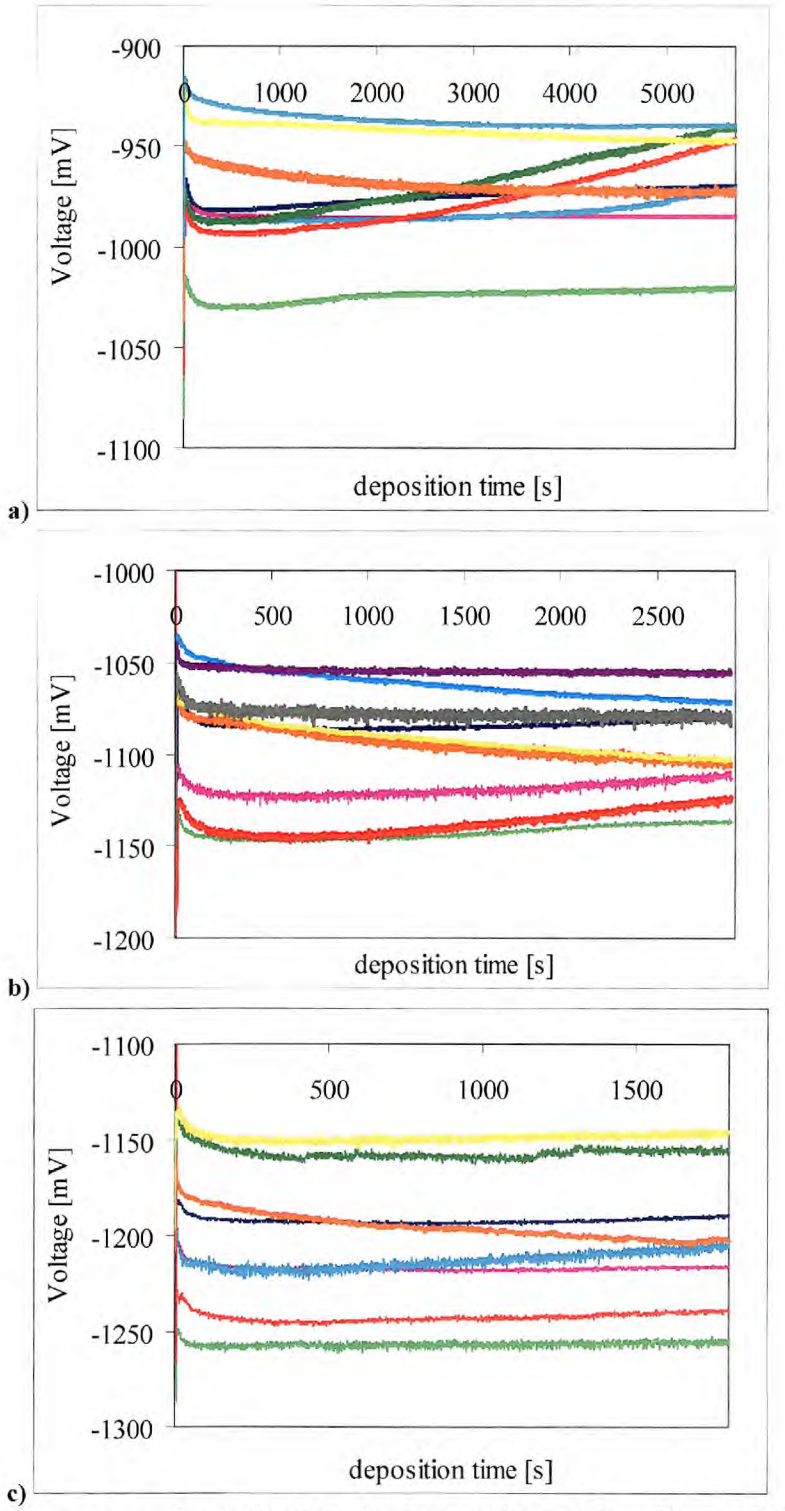


Figure 4.34 Voltage measured vs Ag/AgCl during the deposition of Ni coatings applying a constant current density of a) -10 mA·cm^{-2} for 96 min, b) -20 mA·cm^{-2} for 48 min and c) -32 mA·cm^{-2} for 30 min stirring the solution at 200 rpm.

In this research nickel was deposited using the 3 electrode set-up applying current densities of -10, -20 and -32 mA·cm^{-2}. From the cyclic voltammetry reported in Figure 4.31 it resulted that the depositions were not diffusion controlled since the current densities employed were lower than the diffusion-limited current density (section 2.1.3). The current density was

varied to observe its influence on the deposited nickel films (as it will be described in section 4.4.6) and also as a comparison with the Ni-Al_2O_3 composite coatings described in section 4.5. With the variation of the current density applied (-10, -20 and -32 $mA \cdot cm^{-2}$) the deposition time was varied from 30 to 96 min to maintain a constant total charge transfer equal to 57.6 $C \cdot cm^{-2}$. In these conditions it was expected that all the films had thicknesses of around 20 μm assuming that the current efficiency of the process was not a function of the current density [38, 78].

The variation of the potential during the galvanostatic deposition was monitored and the results are shown in Figure 4.34. When the same current density was applied slightly different voltage responses were measured (see Fig. 4.34) probably because of experimental errors in measuring the electrode area. The average voltage was -980 mV for a current density of -10 $mA \cdot cm^{-2}$ (Figure 4.34 a)), -1100 mV for -20 $mA \cdot cm^{-2}$ (Figure 4.34 b)) and -1200 mV for -32 $mA \cdot cm^{-2}$ (Figure 4.34 c)). These potential values were slightly higher than those expected from the cyclic voltammetry in Figure 4.31; the small differences can be due to experimental errors on measuring the electrode areas of the samples analysed, as also demonstrated by the variations in voltages reported in Figure 4.34. Similar trends and voltage values to those shown in Figure 4.34 c) were also obtained when the depositions were carried out applying -32 $mA \cdot cm^{-2}$ on stainless steel substrates as-received, 0.2 g/l of SDS were added to the plating bath or the bath was not stirred during the deposition process. The decrease in voltage observed in the first part of the deposition (see all the curves reported in Figure 4.34) is due to the higher overpotential needed to deposit Ni on stainless steel compared to that needed to deposit Ni on Ni.

4.4.4 Temperature effect

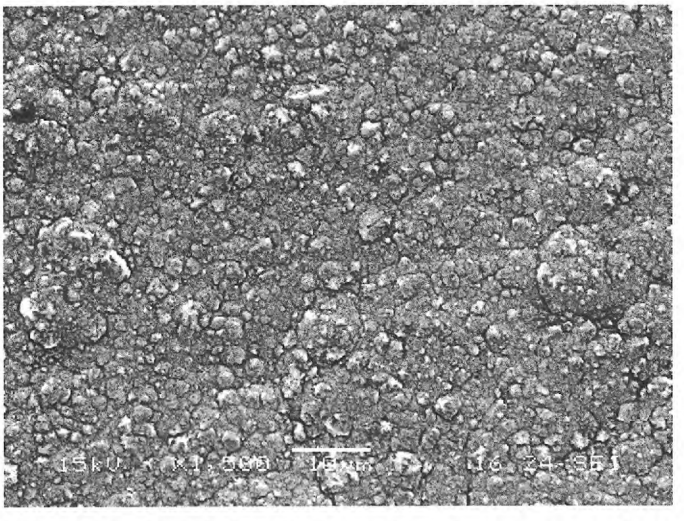


Figure 4.35 SEM micrograph of a nickel coating deposited at room temperature.

In section 2.1.4 A) it has been suggested that the bath temperature influences the structure of nickel coatings, the cathode efficiency and the mechanical properties of the Ni films [32]. In order to understand the temperature effect, coatings deposited at room

temperature (see Fig. 4.35) were compared with those deposited from the bath kept at 50°C (see Fig. 4.36), but no remarkable differences were observed. Moreover, when a bath temperature of 50°C was employed, the solution evaporated during the deposition process and the results were not reproducible after few experiments. Consequently frequent changes of the solution were needed involving higher costs for the pure chemicals and for the disposal of the toxic solution. For this reason all the following experiments were carried out at room temperature for easier handling of the system, as also proposed by other authors [2, 33, 34, 47-55].

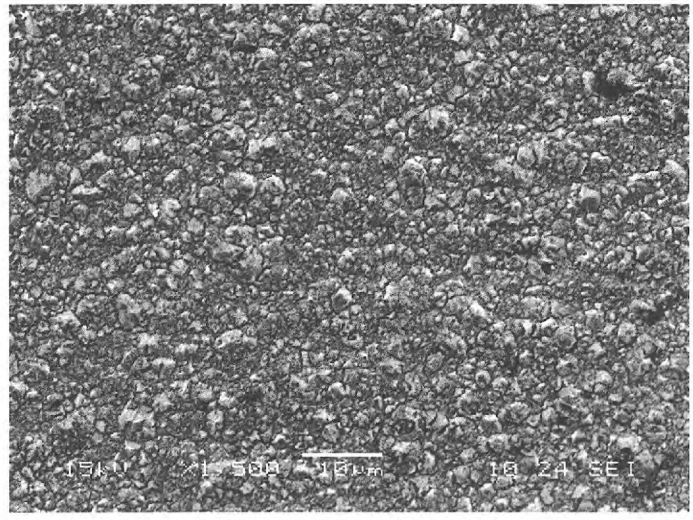


Figure 4.36 SEM micrograph of a nickel coating deposited at 50°C.

4.4.5 Variables affecting the hydrogen pitting

Most of the coatings deposited from the nickel sulphate bath potentiostatically and some of the coatings deposited galvanostatically presented hydrogen pitting, as described and shown in section 4.4.2. Two methods have been suggested in the literature [32, 33] to decrease the hydrogen pitting during nickel deposition: the addition of a wetting agent to the solution or the agitation of the bath to decrease the adhesion of the hydrogen bubbles to the substrate surface.

In the literature (Tables 2.8-2.10 in section 2.2), it has been largely employed a concentration less than 0.5 g/l of SDS in the plating bath to reduce the hydrogen pitting. In this research, some depositions have been carried out from a plating bath containing 0.2 g/l of SDS (bath composition used by Liu and Chen [47, 48]) under a current density of -32 $mA \cdot cm^{-2}$ obtaining the result shown in Figure 4.37 a); this film was considerably rougher than the corresponding coating deposited in the same conditions but without SDS (Figure 4.37 b)). It was therefore concluded that the addition of SDS to the plating bath would not improve the coating quality.

The second method described in the literature to decrease hydrogen pitting is stirring; therefore the solution was stirred at 200 rpm during the deposition (the same stirring rate employed to co-deposit composite coatings). It was observed that coatings deposited from a solution containing 0.2 g/l of SDS while stirring presented numerous deep holes, as shown in

Figure 4.38 and that the coating roughness increased compared to that of coatings deposited from the same bath without stirring (Figure 4.37 a)). When SDS was not added to the bath and the depositions were carried out at a constant current density of -32 $mA \cdot cm^{-2}$ stirring or keeping the solution still, the Ni coatings were smooth (Figure 4.37 b)), even if sometimes pitting was observed. Considering these results and that the stirring is necessary to deposit composite coatings, SDS was not used anymore.

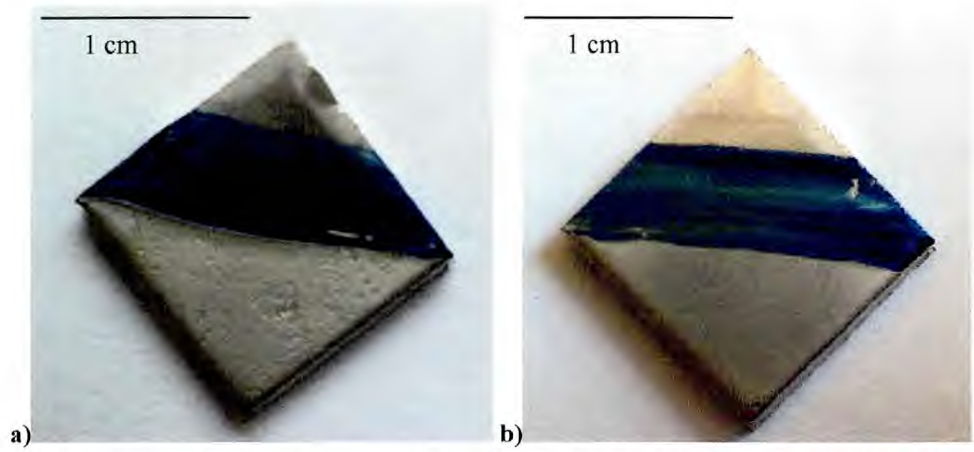


Figure 4.37 Coatings deposited from a nickel sulphate bath a) with 0.2 g/l of SDS b) without SDS and keeping the solution still.

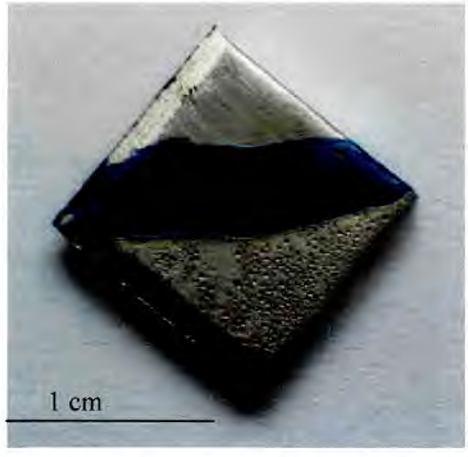


Figure 4.38 Coating deposited from a nickel sulphate bath with 0.2 g/l of SDS stirring at 200 rpm.

4.4.6 Microstructure and crystallinity of the coatings

From all studies carried out and reported in this section, it seemed that the best Ni coatings were deposited from a Watts bath at room temperature stirring at 200 rpm using the three electrode cell with stainless steel substrates prepared as described in section 4.3 and applying current densities of -10 $mA \cdot cm^{-2}$ for 96 min, -20 $mA \cdot cm^{-2}$ for 48 min or -32 $mA \cdot cm^{-2}$ for 30 min. The surface morphology of the nickel coatings deposited in these conditions was analysed by SEM (see Figures 4.39-4.41) and described below. The typical pyramidal structure reported in the literature for the nickel coating morphology [33, 44, 46, 62, 92, 97, 100] is more

evident and regular in films deposited applying -10 mA·cm^{-2} (Figure 4.39) than in those deposited applying -20 mA·cm^{-2} (Figure 4.40) and -32 mA·cm^{-2} (Figure 4.41), that seemed to have smoother structures. In all the three nickel films it seemed that the relatively large pyramidal surface structures were surrounded by smaller structures, as also observed by Thiemig et al. [62, 92]. The different morphologies of these coatings can be explained considering the variation of the current densities that can modify the presence of inhibitors at the cathode/solution interface.

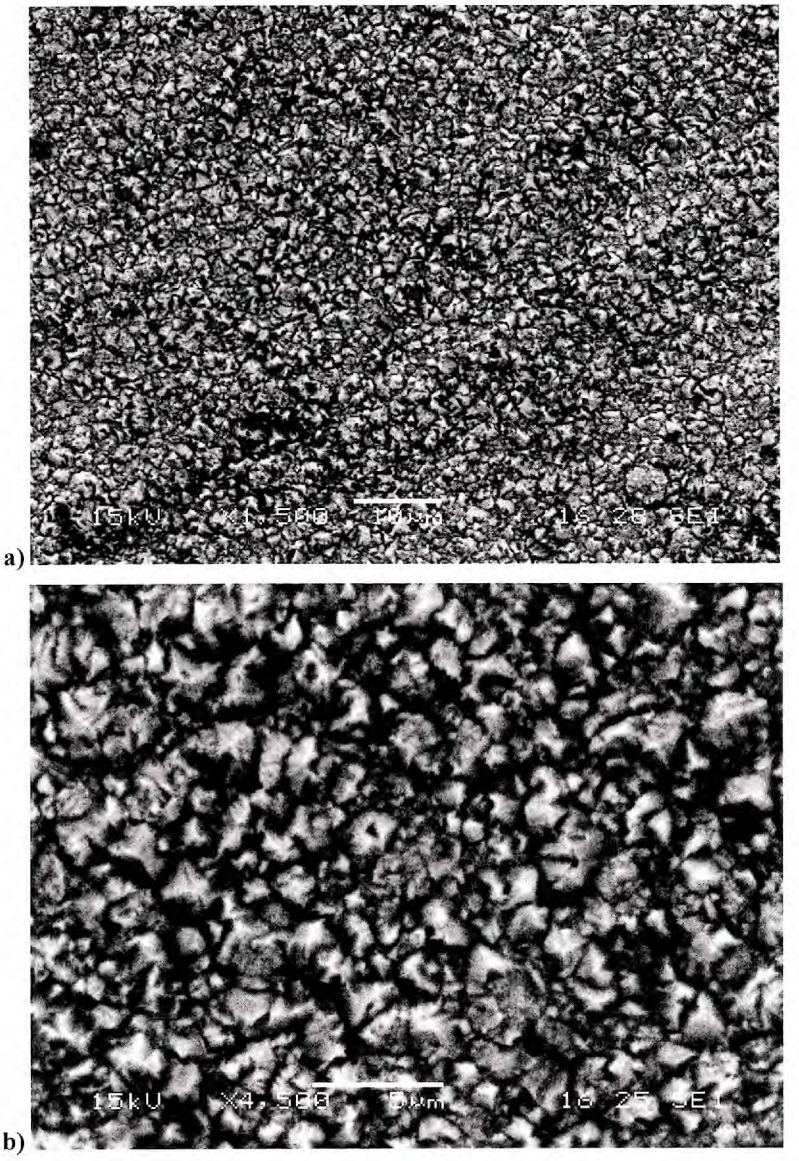
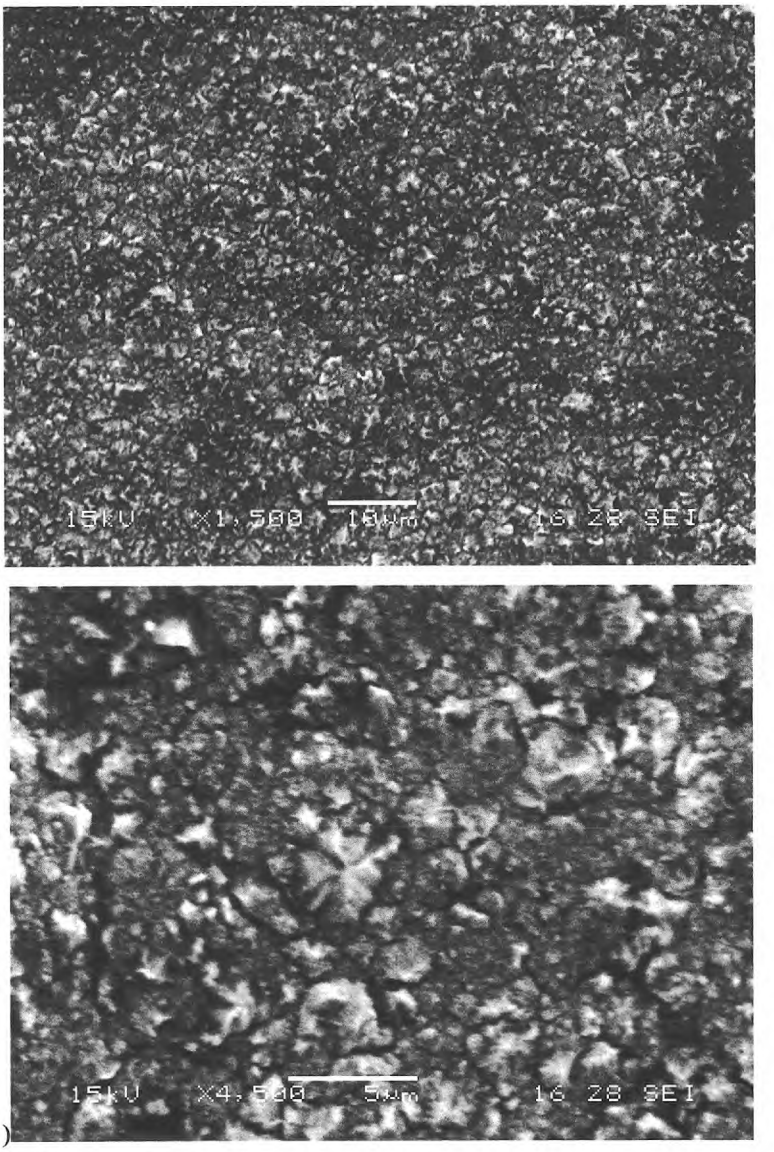


Figure 4.39 SEM micrographs showing the microstructure of nickel coating deposited applying a current density of -10 mA·cm^{-2} at a) low magnification x1500 and b) high magnification x4500.

A variation of the nickel preferred orientation with the current density was expected considering the studies reported by Amblard et al. [41, 252], who observed that the texture of thick (~10 μm) nickel deposits did not depend on the substrate orientation but just on the electrolyte composition, the cathodic potential or current density, the temperature and the pH.

They [41] explained this observation in terms of inhibition. The presence of selective inhibitors, which change under different conditions, promotes the growth of particular crystal structures and inhibits the growth of others. In a bath free from inhibiting species the (200) would be the preferred crystal texture, but in the nickel plating baths there are other species, such as hydrogen and nickel hydroxide, that play a main role in the crystal growth modifying the crystal structure, in favour of the (220) and the (111) crystalline phases. In this study, the influence of the current density on the nickel preferred crystalline orientation was investigated using XRD analysis. The diffraction patterns of the three nickel coatings are shown in Figure 4.42; they all show four main reflection lines attributed to the nickel coating, in agreement with those reported in the literature [36, 42, 43, 75, 90, 113, 116, 117, 236, 243-249], and four signals due to the stainless steel substrate (spectrum A in Figure 4.42), in agreement with the spectrum reported by Lira-Cantu et al. [248].



a)

b)

Figure 4.40 SEM micrographs showing the microstructure of nickel coating deposited applying a current density of -20 mA·cm^{-2} a) low magnification x1500 and b) high magnification x 4500.

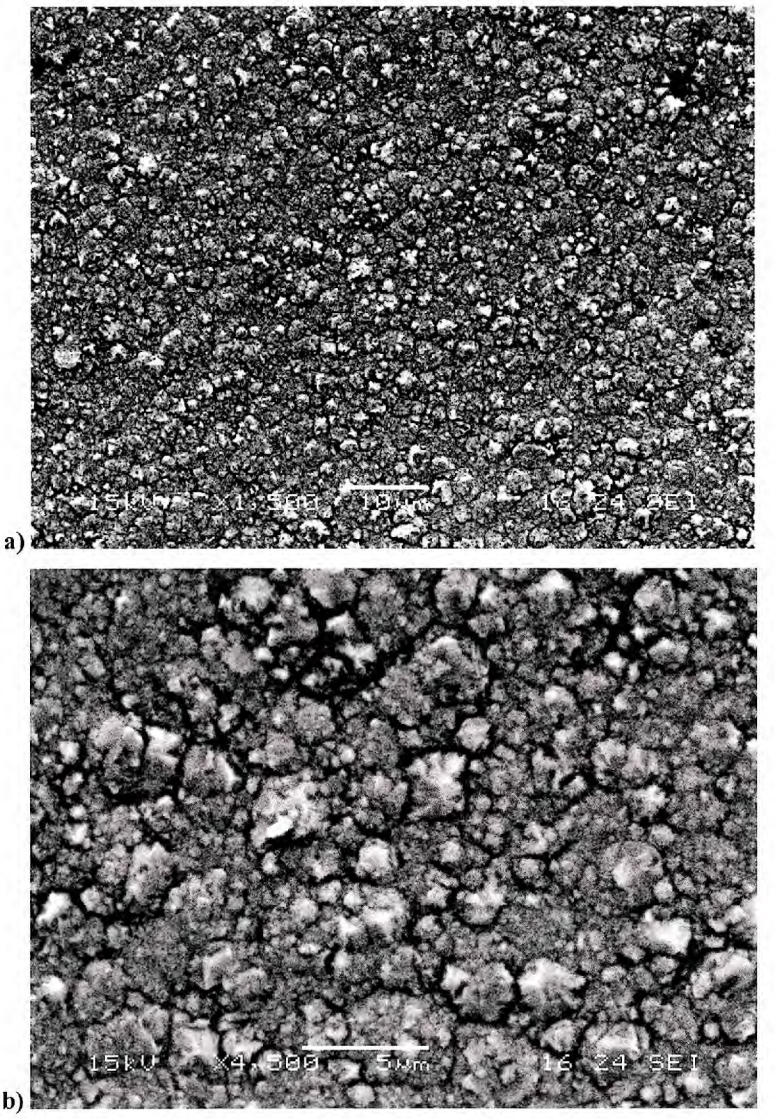


Figure 4.41 SEM micrographs showing the microstructure of nickel coating deposited applying a current density of -32 mA·cm^{-2} a) low magnification x1500 and b) high magnification x 4500.

All the three nickel films presented (111) preferred orientation, as also reported by numerous other researchers [36, 37, 40, 42-44, 85, 117, 244, 245, 247, 248, 253], whereas other groups [36, 92, 246] observed that the main peak was the (200), probably for the higher current density applied during the deposition [85, 92, 246], the higher bath temperature [92, 246], or for the presence of other chemicals in the plating bath [36]. It is also interesting to note that the coatings deposited potentiostatically from the same plating bath and at room temperature (Figure 4.28) showed the same crystalline structure and the predominance of the (111) crystallographic peak. In order to determine how the current density influenced the preferred crystalline orientation of the deposited nickel films, the intensities of the (111), (200), (220) and (311) reflections have been normalised to the (111) reflection, that was the preferred orientation of the three nickel coatings, obtaining the data reported in Table 4.11. Increasing the current density from -10 to -20 mA·cm^{-2} strongly increased the (200) peak and slightly

increased the (220) and (311) orientation signals. A further increase of the current density to -32 mA·cm^{-2} did not significantly modify the (200) and (311) crystallographic orientation peaks but considerably increased the (220) peak (see Figure 4.42 and Table 4.11).

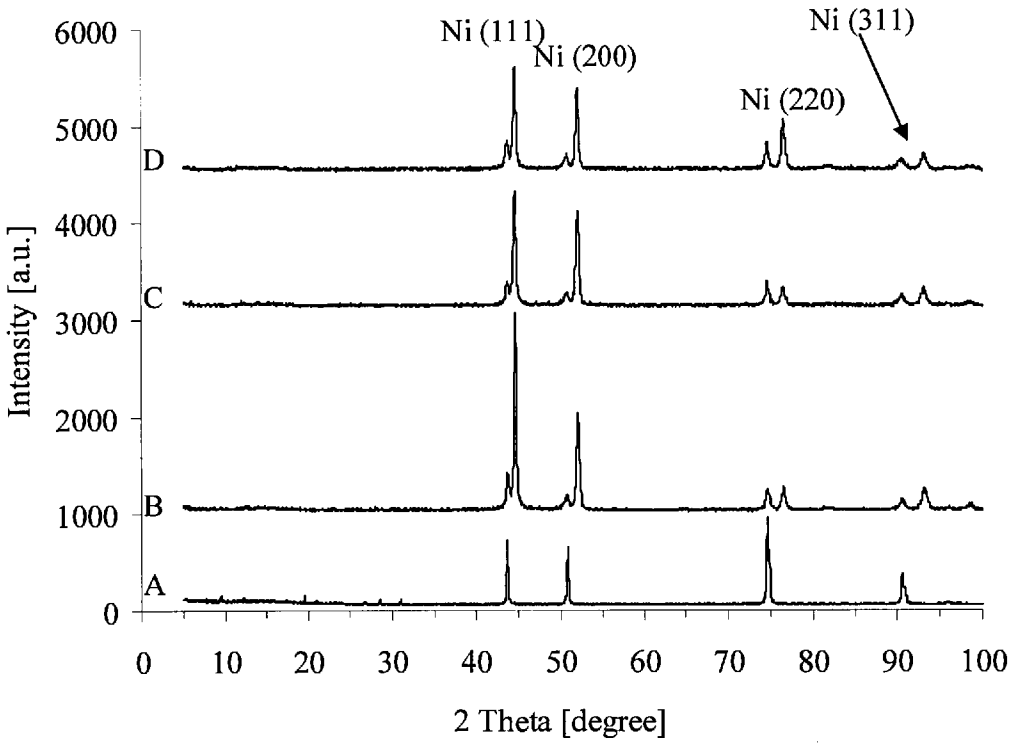


Figure 4.42 XRD spectra of A) the stainless steel substrate and of coatings deposited from a nickel sulphate bath applying a current density of B) -10 mA·cm^{-2} for 96 min, C) -20 mA·cm^{-2} for 48 min and D) -32 mA·cm^{-2} for 30 min showing that the coatings are made of crystalline nickel.

Table 4.11 Ratio between the intensity of the XRD peaks and the main peak (111) for nickel films deposited applying different current densities.

Current density	I(reflection)/I(111)			
	(111)	(200)	(220)	(311)
-10 mA·cm^{-2}	1	0.50	0.14	0.13
-20 mA·cm^{-2}	1	0.83	0.19	0.19
-32 mA·cm^{-2}	1	0.80	0.51	0.20

The structure of the deposited films depends on the rate of formation of new nuclei and the growth of the old ones, e.g. if the conditions employed favoured the formation of new nuclei a fine-grain deposit is formed, whereas if the growth of the existing nuclei is preferred a large grain deposit is produced. The presence of inhibitors in the plating bath strongly influences the grain growth [45]. Nanocrystalline materials with grain size smaller than 100 nm typically present improved hardness, wear and corrosion resistance compared to materials with bigger grains. The grain size can be determined from the XRD peaks by using the Sherrer

equation [254], that is based on the line broadening produced by crystals with size < 100 nm and can be written as follow:

$$crystallite\ size = \frac{0.9 \cdot \lambda}{\beta \cdot \cos\theta} \qquad [4.5]$$

where λ is the wavelength of the x-ray beam (1.54 Å), β is the line broadening (full-width-half-max in radians) and θ is the Bragg angle. All the diffraction lines have a measurable broadening due to instrumental broadening, even when the crystallites are >100 nm, therefore to calculate β produced just by the crystallites with size <100 nm the following equation is employed:

$$\beta^2 = Bm^2 - Bs^2 \qquad [4.6]$$

where Bm is the line broadening of the material with unknown crystallite size and Bs is that of a standard with crystallites > 100 nm (instrument broadening) and with a reflection line close to the one of the unknown [36, 39, 245, 254, 255]. In order to apply the Sherrer equation it is fundamental to assume that there are no residual strains between the crystallites, since strains can also contribute to line broadening [254]. The negligible contribution of internal stresses to the XRD line-broadening in electrodeposited nickel coatings was reported by Cziraki et al. [39], who measured the Ni grain size by TEM analysis and applying Sherrer equation obtaining results in good agreement. Good agreement between the grain size measured by TEM and XRD was also reported by Li et al. [117] and Moti et al. [36] and the use of the Sherrer equation to measure the grain size has been widely employed by numerous researchers working on Ni plating [36, 37, 39, 44, 85, 90, 92, 115, 117, 243, 245, 256].

In this study a silica standard with particle size ~1 mm was employed and the reflection lines at 2θ 28.46° and 56.15° were used to calculate Bs after stripping the $K\alpha_2$ signal, as also described by Park et al. [255]. The FWHM of the two lines of the standard was 0.12°. The line broadening Bm of the (111) Ni reflection line [36, 37, 90] was determined after stripping the $K\alpha_2$ signal and these data were used to calculate β and the crystallite sizes of Ni films deposited at different current densities using eq. 4.6 and 4.5. The error (standard deviation) affecting the line broadening was calculated by repeating five times the XRD analysis of a Ni sample and measuring the FWHM of the (111) Ni reflection line after stripping the $K\alpha_2$ signal and assuming that the strains in the film were negligible and that the grain size was homogeneous. The error resulted to be ± 0.01° (corresponding to ±1 nm) and it was applied to all the measurements carried out. From the data obtained it was clear that the Ni grain size decreased with increasing current density: 40 ± 1 nm (-10 $mA \cdot cm^{-2}$) to 33 ± 1 nm (-20 $mA \cdot cm^{-2}$) and 31 ± 1 nm (-32 $mA \cdot cm^{-2}$). The fact that all the nickel films deposited in this research are nanocrystalline demonstrates that the deposition parameters employed (plating bath, pH, temperature, stirring) induce a considerable nucleation and reduce the grain growth. The grain size obtained are slightly higher than those reported by Aruna et al. [85] (25-26 nm), who did not use the line broadening correction (eq. 4.6); similar results would have been obtained in this research without applying the correction.

The decrease of grain size with increasing current density was also reported by other groups [40, 44] for nickel coatings deposited from nickel sulphate baths applying current densities less than -75 $mA \cdot cm^{-2}$ and it was explained considering that higher current densities reduce the concentration of metal ions near the cathode with a consequent increase of the overpotential that produces higher nucleation rates generating more and smaller grains [33, 257]. The opposite tendency (increase of grain size increasing the current density) has been observed for films deposited from other baths [38, 39, 118] and explained considering a decrease in the Ni-ion concentration [39] or the co-deposition of hydrogen at the cathode interface [38]. These differences can be also attributed to different kinetics in different plating bath [41].

It has also to be underlined that the large pyramidal surface structures observed in Fig. 4.39-4.41 are much larger (order of 1 μm) than the actual crystallites, which have been measured to be around 31-40 nm from the XRD-line broadening. It can be therefore thought that each surface pyramidal structure is a colony, which is a group of fine grains surrounded by relatively deep crevice, as explained by Weil et al. [45] and Banovic et al. [46]. Differences between the surface structure and the crystallites were also reported by Ebrahimi and Ahmed [38] and Thiemig et al. [92]. Ebrahimi and Ahmed [38] observed that the surface roughness of the deposited films was related to the grain size but much larger than that; in particular they observed that the surface structure of a film deposited applying -50 $mA \cdot cm^{-2}$ was micrometer size and the grain size was 60 nm. Thiemig et al. [92] reported that the deposited films presented pyramids with size of few microns whereas the grain size measured from the XRD-line broadening was just 200 nm, an order of magnitude smaller.

4.5 Electro co-deposition of nickel-alumina composite coatings

This section of the project is meant to demonstrate that it is possible to deposit Ni-Al_2O_3 composite coatings by electro co-deposition, as also reported in the literature [1, 2, 52-55, 57, 61, 62, 70, 72-79, 81, 82, 84, 85, 89-95, 97, 98, 100, 101, 107-112], and to achieve a better understanding of the effects that the process variables (concentration of Al_2O_3 particles in the plating bath, applied current density and particle size) have on the amount of Al_2O_3 co-deposited in the composite films. The effect of just the concentration [62, 82], just the current density [1, 2, 57, 76-78, 92] and the combined effects of concentration and current density [57, 72, 74, 84, 98, 110], current density and particle size [85] and concentration and particle size [77, 78] have been studied in the literature (see section 2.2.4.1). A lack of the study of the combined effects of all these three parameters in the same range (concentration, current density and particle size) is evident and it was carried out here using a matrix of experiments as the one shown in Table 4.12. The Al_2O_3 powder used in this part of the investigation has been described in section 4.1.

Table 4.12 Set of conditions varied to understand how particle size, concentration and current density influence the amount of Al_2O_3 co-deposited in the Ni films.

Al_2O_3 concentration in the suspension	Current density		
	-10 mA·cm^{-2}	-20 mA·cm^{-2}	-32 mA·cm^{-2}
0 g/l			
50 g/l			
100 g/l			
150 g/l			

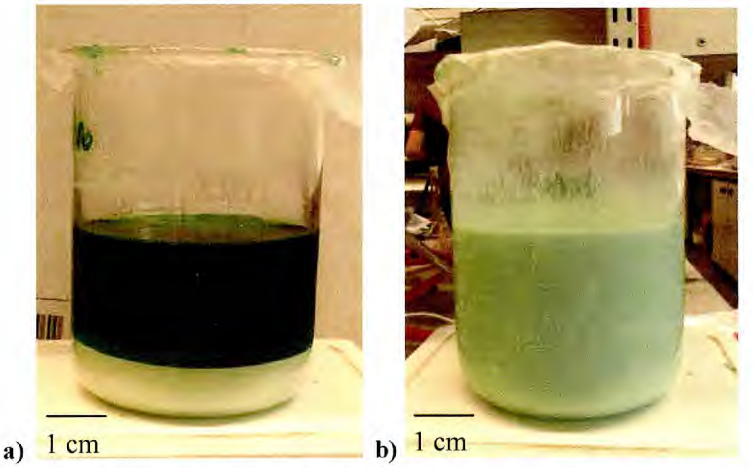


Figure 4.43 Electrochemical cell containing the nickel solution with 150 g/l of nano-Al_2O_3 particles, a) without stirring and showing the powder deposited on the bottom of the cell and b) stirring and showing the uniformity of the suspension.

The deposition of Ni-Al_2O_3 films was carried out applying the same conditions used to deposit pure nickel coatings using the three-electrode cell set up, as described in section 4.4. The same plating bath was employed for all the experiments since it was known from the literature [1, 62] that also the plating bath influences the co-deposition behaviour. The electrolyte had the composition reported in Table 4.10. The pH of the suspensions with different amounts of sub-micron or nano-Al_2O_3 powders was 4.0 ± 0.5; the pH was not influenced by the deposition process and by the amounts of Al_2O_3 probably due to the buffering effect of the boric acid, as also observed in section 4.4.1. The stainless steel substrates were ground with 800 grit SiC paper and ultrasonically cleaned in acetone for 5 min prior to the deposition (as described in section 4.3). To produce coatings with similar thickness (~20 μm) applying different current densities, the total charge was fixed at 57.6 C·cm^{-2} during the deposition by modifying the deposition time (-10 mA·cm^{-2} for 5760 s, -20 mA·cm^{-2} for 2880 s and -32 mA·cm^{-2} for 1800 s) and assuming that the current efficiency of the process was not a function of the current density [78].

Different amounts of Al_2O_3 were added to the nickel bath (see Figure 4.43 a)) and the suspension obtained was sonicated for 30 min to disperse the particles and to break up possible

solid agglomerates. The suspension was stirred for 15 min before starting the deposition to enhance uniformity and it was also constantly stirred at 200 rpm during the deposition in order to homogeneously suspend the Al_2O_3 particles, as shown in Figure 4.43 b). The same stirring bar (3.7 cm long and 0.8 cm wide) was employed for all the experiments in order to assure consistency of the hydrodynamics. The working and counter electrodes were always kept at 1.5 cm distance and they were always suspended in the same part of the bath (just outside the vortex produced by stirring) since the hydrodynamics is a fundamental variable of the process and strongly influences the results obtained [16].

4.5.1 Characterization of the alumina powders

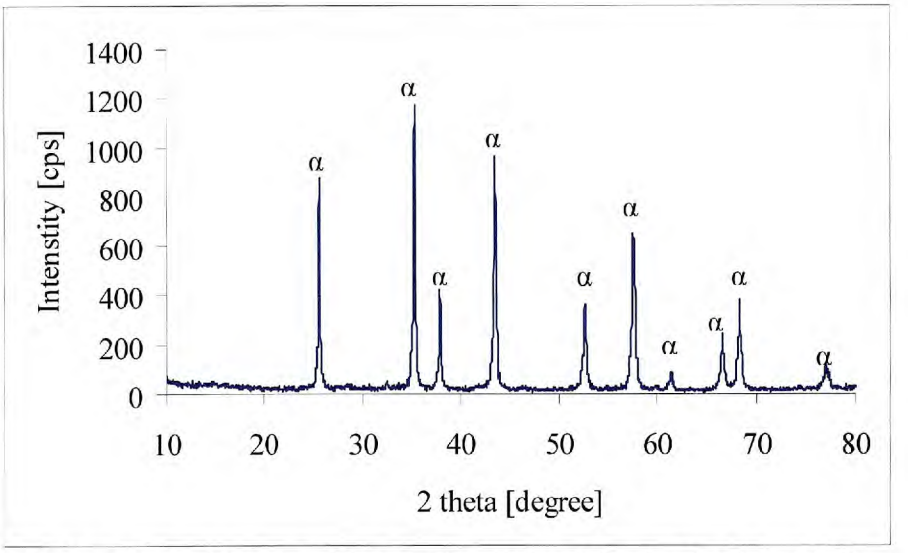


Figure 4.44 XRD analysis of the sub-micron powder employed showing that it is α-Al_2O_3.

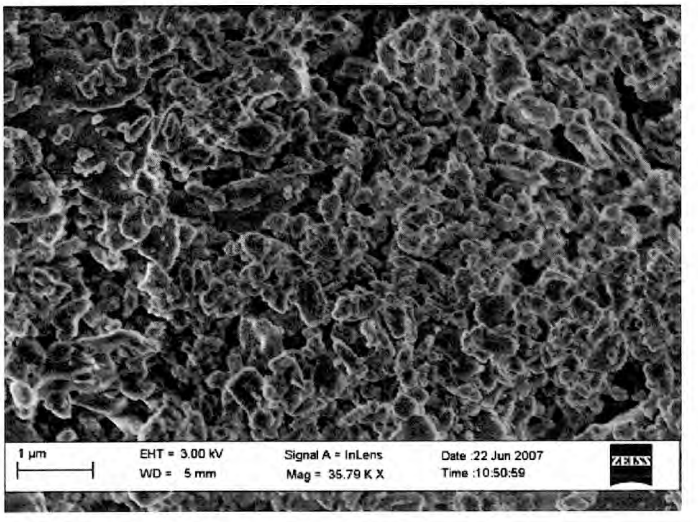


Figure 4.45 SEM micrograph of sub-micron-Al_2O_3 particles showing their shape and size.

For the deposition of nickel-alumina composite coatings two different Al_2O_3 powders were employed: sub-micron and nano-Al_2O_3 powder. These two powders were chosen in order

to understand how the particle size influenced the amount of second phase co-deposited with the nickel coating. The XRD analysis of the sub-micron-Al_2O_3 powder shows that it is α-Al_2O_3 (Figure 4.44) [258] and the SEM micrograph in Figure 4.45 shows that the particles are not round but slightly flat and oblong and with particle size less than 1 μm. The SEM sample was prepared as described in section 3.1. The particle size distribution was measured in water using a Low Angle Laser Light Scattering technique (as described in section 3.9), where the diffraction angle is inversely proportional to the particle size [259]. The results obtained are shown in Figure 4.46 and Table 4.13. The majority of the Al_2O_3 particles were between 0.2 and 2.2 μm with a D_{50} (average of the particle size) of 0.5 μm. The particle size obtained from this analysis is in agreement with the values revealed by the SEM analysis (Figure 4.46).

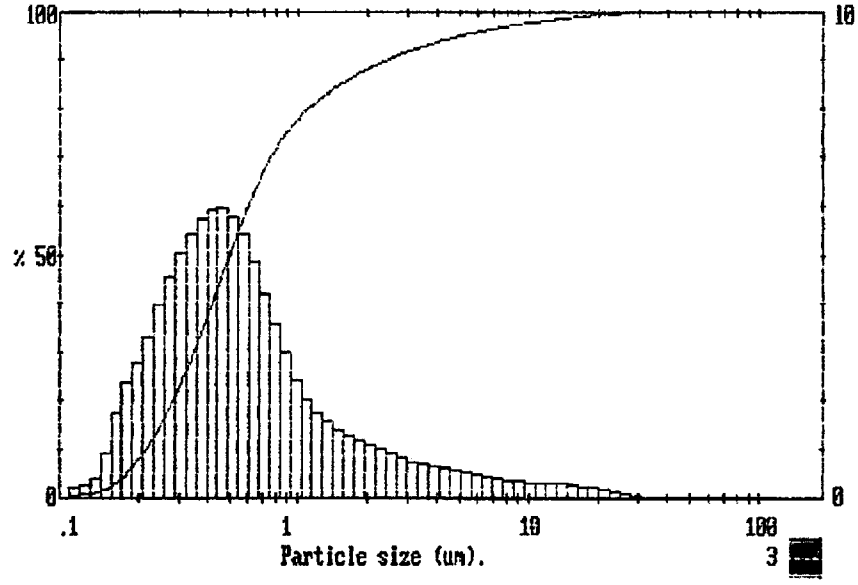


Figure 4.46 Size distribution for the sub-micron-Al_2O_3 particles suspended in water.

Table 4.13 Size distribution of the sub-micron-Al_2O_3 particles in water.

High Size	Under %	High Size	Under %	High Size	Under %	High Size	Under %	High Size	Under %	High Size	Under %	
80.0	100	24.9	99.9	7.75	97.0	2.41	90.1	0.75	69.6	0.23	12.5	D[4,3]
71.9	100	22.4	99.8	6.97	96.6	2.17	89.1	0.68	65.4	0.21	9.2	1.24 μm
64.7	100	20.1	99.6	6.27	96.1	1.95	87.9	0.61	60.5	0.19	6.4	D[3,2]
58.2	100	18.1	99.4	5.64	95.7	1.75	86.8	0.55	55.1	0.17	4.0	0.42 μm
52.3	100	16.3	99.2	5.07	95.2	1.58	85.5	0.49	49.3	0.15	2.3	D[v,0.9]
47.1	100	14.6	98.9	4.56	94.6	1.42	84.0	0.44	43.3	0.14	1.3	2.39μm
42.3	100	13.2	98.6	4.10	94.0	1.28	82.5	0.40	37.4	0.12	0.9	D[v,0.1]
38.1	100	11.8	98.3	3.69	93.3	1.15	80.7	0.36	31.6	0.11	0.7	0.22μm
34.2	100	10.7	98.0	3.32	92.6	1.03	78.7	0.32	26.2	0.10	0.5	D[v,0.5]
30.8	100	9.58	97.7	2.98	91.9	0.93	76.2	0.29	21.1			0.5 μm
27.7	100	8.62	97.3	2.68	91.0	0.83	73.2	0.26	16.5			

The XRD analysis of the nano-Al_2O_3 particles revealed that this powder was a mixture between δ*-Al_2O_3, δ-Al_2O_3 and γ-Al_2O_3 (Figure 4.47). The TEM micrograph of the particles showed that they were perfectly round and with sizes varying between 10 and 100 nm; the majority of the nanoparticles seemed to be between 10 and 50 nm (Figure 4.48).

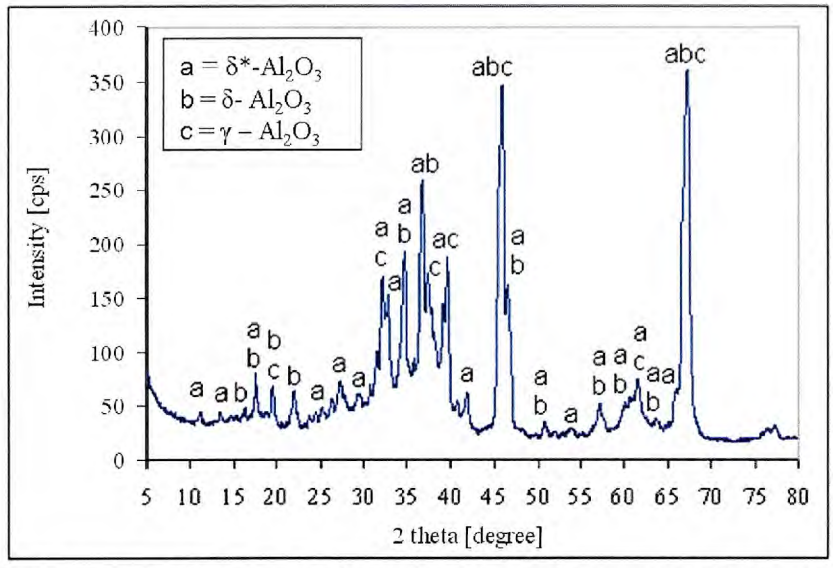


Figure 4.47 XRD analysis of the nano-Al_2O_3 powder showing the presence of δ, δ* and γ-Al_2O_3.

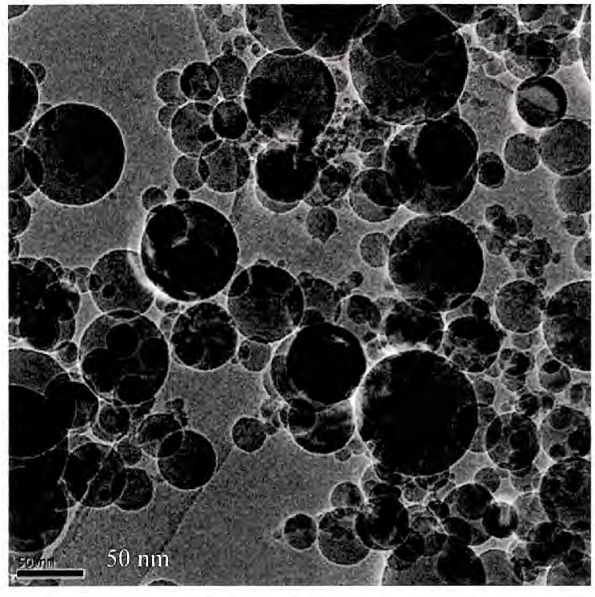


Figure 4.48 TEM micrograph of nano-Al_2O_3 particles showing their shape and size.

4.5.2 Galvanostatic experiments

Ni-Al_2O_3 composite films were deposited under the same conditions used to deposit pure Ni films (see section 4.4) in order to have a direct comparison and to identify the effect of the Al_2O_3 particles on the Ni deposition process and on the film properties. The composite films were deposited applying three different current densities: -10, -20 and -32 $mA \cdot cm^{-2}$. The variation of the potential during the deposition of both composites was monitored and the trends potential *vs* deposition time obtained were similar and in the same ranges of those reported for deposition of pure Ni and shown in Figure 4.34. It has to be underlined that for the deposition of pure nickel and nickel composite films the variation of the voltage under the same deposition conditions was considerably large (Figure 4.34) and therefore it was difficult to identify any effect of the suspended Al_2O_3 particles on the Ni electrochemistry.

4.5.3 Microstructure of Ni-Al_2O_3 composite coatings

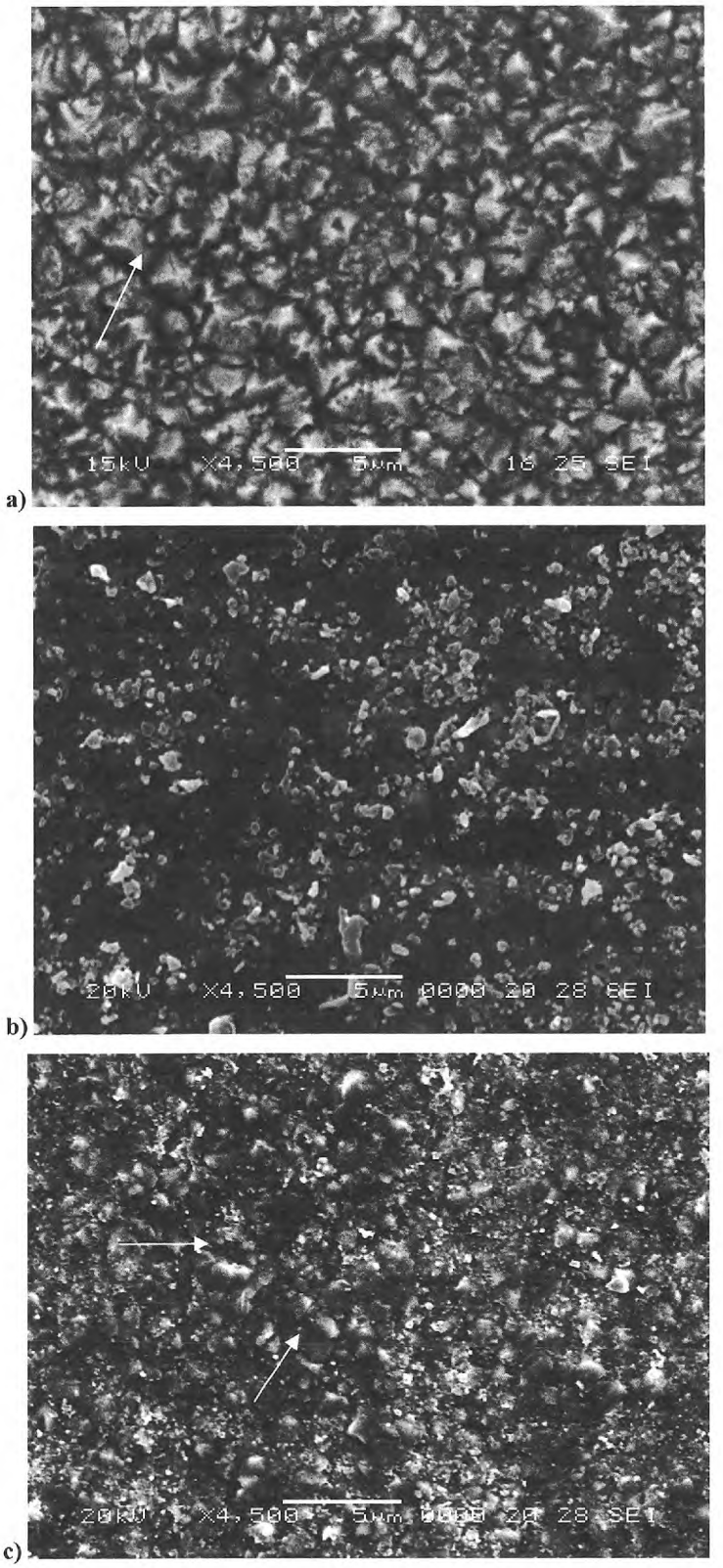


Figure 4.49 SEM micrographs of Ni and Ni-Al_2O_3 composite films deposited applying -10 mA·cm^{-2} from a) pure nickel plating bath, and the same bath containing b) 50g/l of sub-micron-Al_2O_3 and c) 50g/l of nano-Al_2O_3. The pure nickel coating presented pyramidal structure that was still partially visible when the nano-Al_2O_3 particles were employed, as indicated by the arrows.

It has been widely reported in the literature that the microstructure of electrodeposited Ni changes by introducing a second phase [62, 84, 85, 90-92, 97, 100, 116, 117, 246, 247] and by modifying the deposition current density, as also observed in Figures 4.39-4.41 and discussed in section 4.4.6.

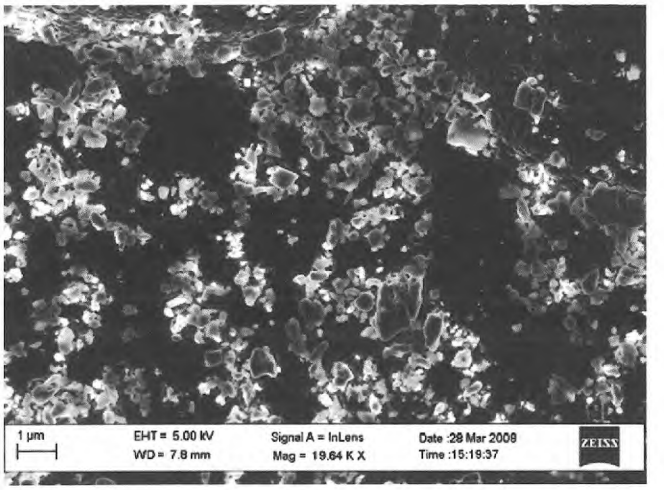


Figure 4.50 SEM micrograph of a Ni-Al_2O_3 composite film deposited applying -10 mA·cm^{-2} from a solution containing 50 g/l of sub-micron-Al_2O_3.

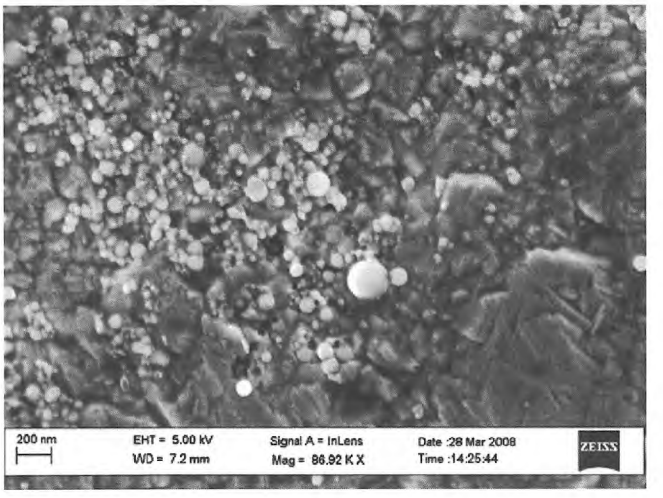


Figure 4.51 SEM micrographs of a Ni-Al_2O_3 composite film deposited applying -10 mA·cm^{-2} from a solution containing 50 g/l of nano-Al_2O_3.

In order to establish the effect of sub-micron and nano-Al_2O_3 particles on the microstructure of Ni composite films, samples deposited applying -10 mA·cm^{-2} from solutions containing 50 g/l of sub-micron or nano-Al_2O_3 powder were examined and compared with pure nickel films deposited in the same conditions (see Figure 4.49). This current density was chosen since the nickel coatings deposited in these conditions presented a pyramidal structure, as shown in Figure 4.49 a), more evident than that presented by coatings deposited at higher current densities (see section 4.4.6). It is clear from the micrographs in Figure 4.49 that the inclusion of both nano and sub-micron-Al_2O_3 particles, lighter parts in the darker nickel matrix,

modifies the Ni microstructure. In particular, it seemed that the sub-micron-Al_2O_3 particles had a stronger influence on the Ni microstructure suppressing the pyramidal structure (Figure 4.49 b)), that conversely was still partially visible in Ni-nano-Al_2O_3 composites (Figure 4.49 c)). Similar results were also reported by Szczygiel et al. [97] and Banovic et al. [84] for Ni-sub-micron-Al_2O_3 composites and by Ciubotariu et al. [100] for Ni-nano-Al_2O_3 composites and also for different types of particle inclusions [116, 118]. Moreover, since the Al_2O_3 particles are not conductive the Ni could not directly grow on them but just around them and therefore some particles were still clearly visible on the coating surface (Fig. 4.49 b) and c) and Fig. 4.50 and 4.51). This is in agreement with observations reported by other researchers [84, 97, 100].

In order to examine the particle distribution in the composite films, cross sectional analysis was performed for each of the 18 different conditions employed. From this study it emerged that in each film the particle distribution was similar along the same side of the substrate and therefore a single micrograph could be considered representative of the whole side. In order to provide a general idea of the particle distribution in the composite films two micrographs, one for each side of each sample (cathode) (as schematize in Fig. 4.52), are reported in Fig. 4.53-4.55 for the 9 different Ni-sub-micron-Al_2O_3 composites and in Fig. 4.56-4.58 for the Ni-nano-Al_2O_3 composites. The effects of the different deposition conditions on the amount of Al_2O_3 co-deposited in the composites will be discussed in section 4.5.5.

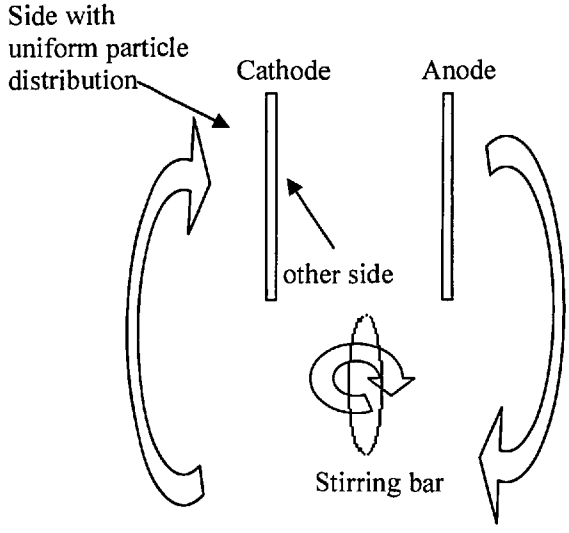


Figure 4.52 Schematic representation of the electrodes configuration during deposition, and distinction between the two sides of the cathode analysed below.

Comparing the two sides of each sample, both with sub-micron and nano-Al_2O_3 particles (see Figures 4.53-4.58), it emerged that the concentration and the distribution of Al_2O_3 were remarkably different. On the side of the coating facing the nickel anode during the deposition (see Figures 4.53-4.58 on the left) the Al_2O_3 particles seemed less homogeneously distributed compared with the opposite side of the substrate (see Figures 4.53-4.58 on the right) where higher concentrations and more uniform Al_2O_3 distributions were obtained.

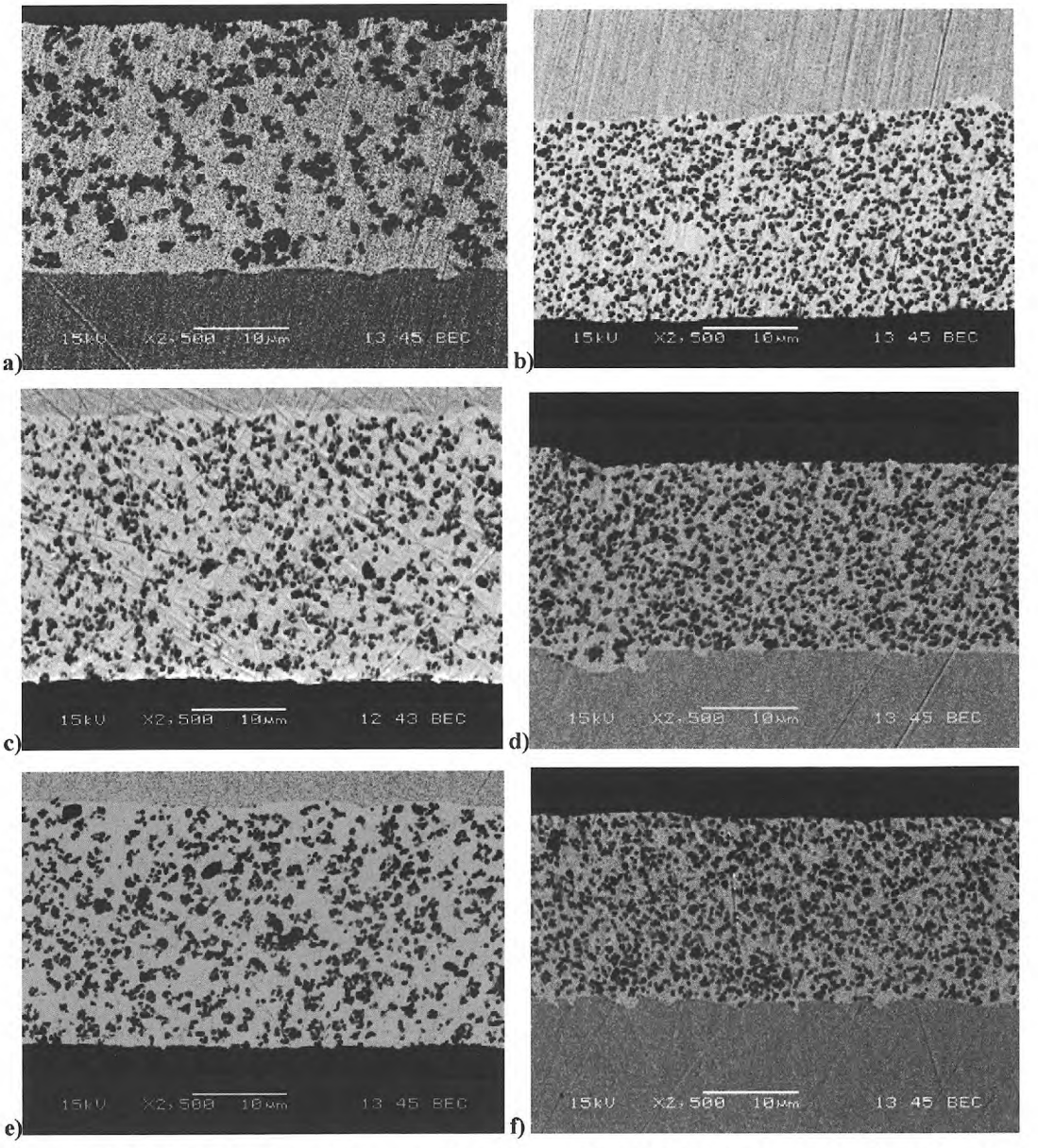
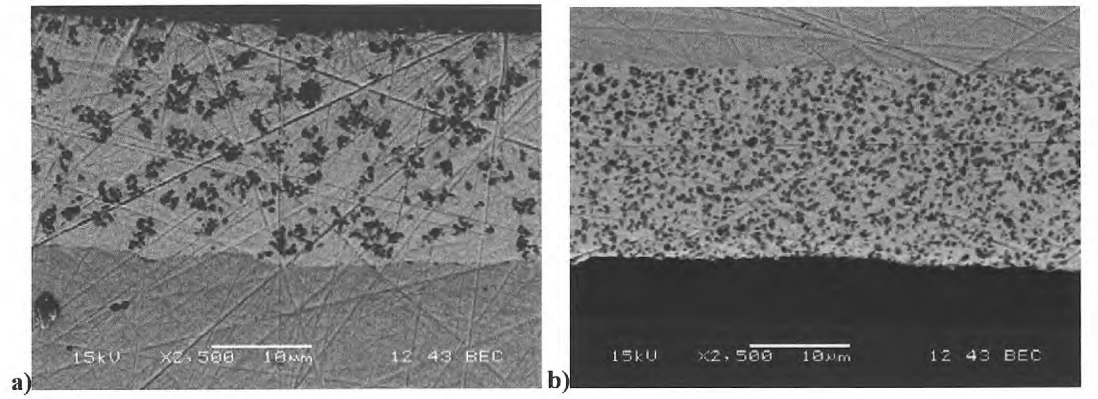


Figure 4.53 SEM back scattered cross section micrographs of Ni-Al_2O_3 composite films deposited applying -10 mA·cm^{-2} from solution containing 50 g/l (a and b), 100 g/l (c and d), 150 g/l (e and f) of sub-micron-Al_2O_3. The micrographs on the left are of the side facing the anode and those on the right of the opposite side.



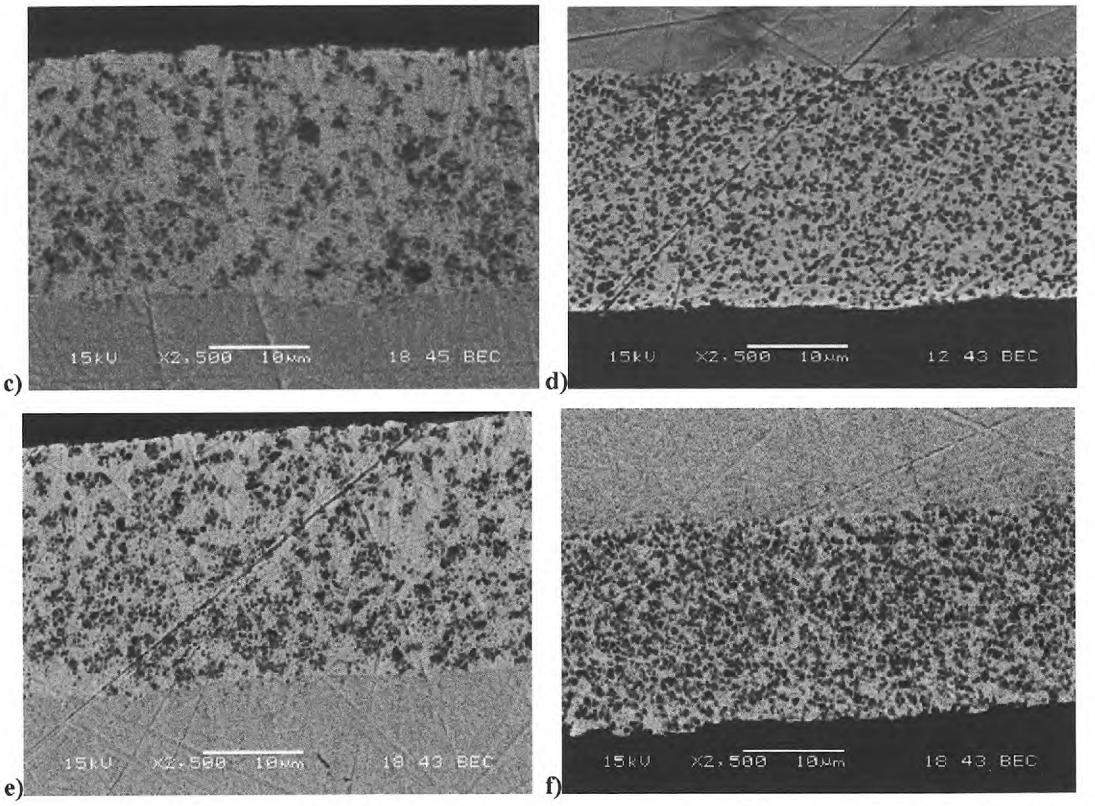
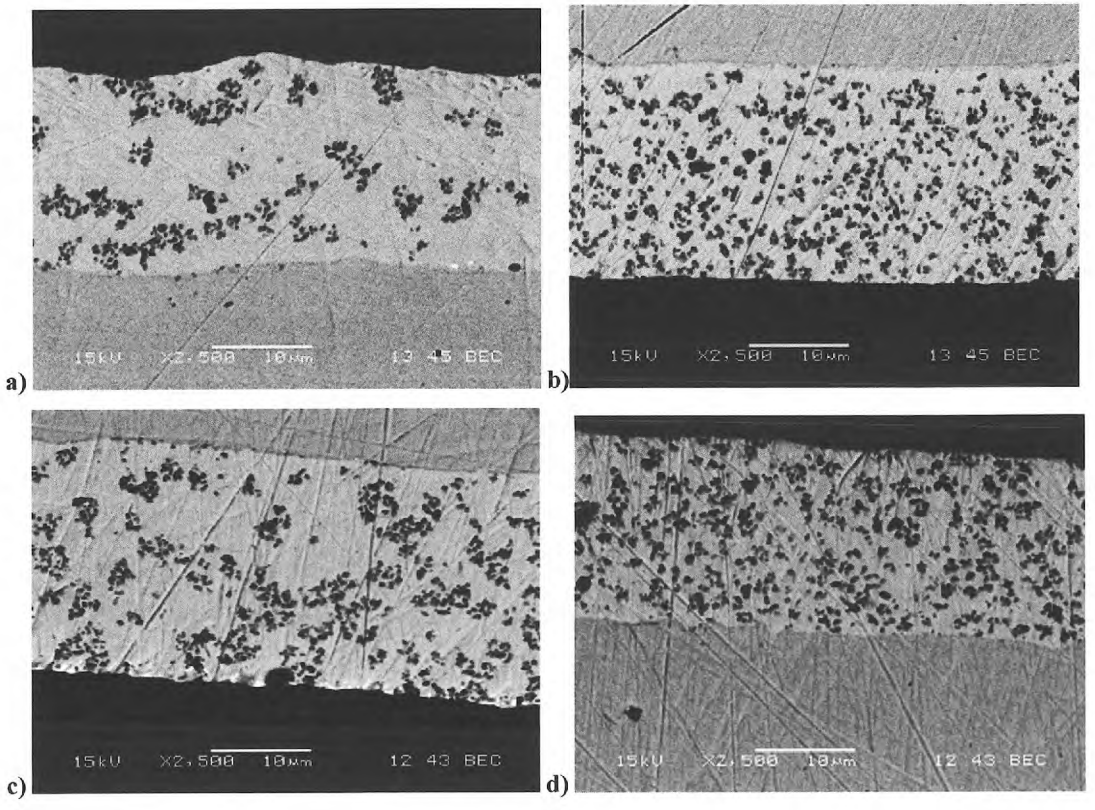
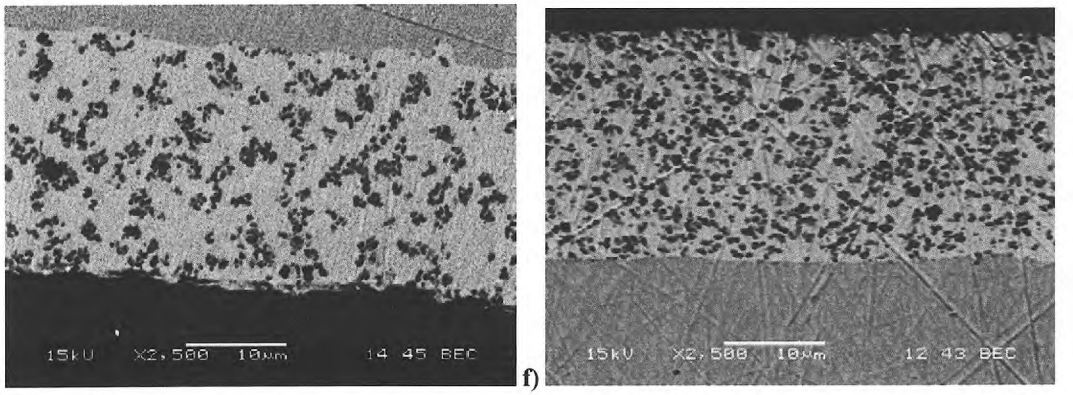


Figure 4.54 SEM back scattered cross section micrographs of Ni-Al_2O_3 composite films deposited applying -20 mA·cm^{-2} from solution containing 50 g/l (a and b), 100 g/l (c and d), 150 g/l (e and f) of sub-micron-Al_2O_3. The micrographs on the left are of the side facing the anode and those on the right of the opposite side.





e) f)

Figure 4.55 SEM back scattered cross section micrographs of Ni-Al_2O_3 composite films deposited applying -32 mA·cm^{-2} from solution containing 50 g/l (a and b), 100 g/l (c and d), 150 g/l (e and f) of sub-micron-Al_2O_3. The micrographs on the left are of the side facing the anode and those on the right of the opposite side.

The different amounts of embedded Al_2O_3 between the two sides of the cathode can be attributed to different suspension hydrodynamics. In the conditions employed for electro co-deposition the electric field is considerably small and therefore the electrophoretic effect on the suspended particles is not balancing the hydrodynamics, which strongly influences the co-deposition process and renders not comparable results obtained using systems with different hydrodynamics (e.g. rotating electrodes and parallel electrodes) [16]. It has been demonstrated by Dong et al. [112] studying Ni-Al_2O_3 co-deposition on a regular octagonal prism cathode that the Al_2O_3 concentration between the eight sides of the cathode varied between 2-3 vol.% due to the different probability of collision particle-cathode on each face of the prism. For all the depositions carried out in this research the position of the electrodes in the bath, the stirring bar and the stirring rate were left unvaried in order to have equivalent hydrodynamics. The stirring bar rotated clockwise during the deposition and therefore also the fluid was moving in the same direction hitting mainly the side of the cathode not facing the anode, as represented in Fig. 4.52. Consequently, it is likely that this side of the sample was hit by more particles approaching constantly the electrode that were therefore uniformly embedded in the growing metal film. This is a main explanation of the fact that different particle concentrations and distributions were observed on the two sides of the cathode. Dong et al. [112] reported that the side of the cathode not facing the anode was the one with lower Al_2O_3 concentration; this contradictory result can be due to the different cathode-stirring bar positions in the two set-ups and on the different sizes of the cathodes (2 mm thick in this research and a regular octagonal prism in [112]) producing different relative distances/positions.

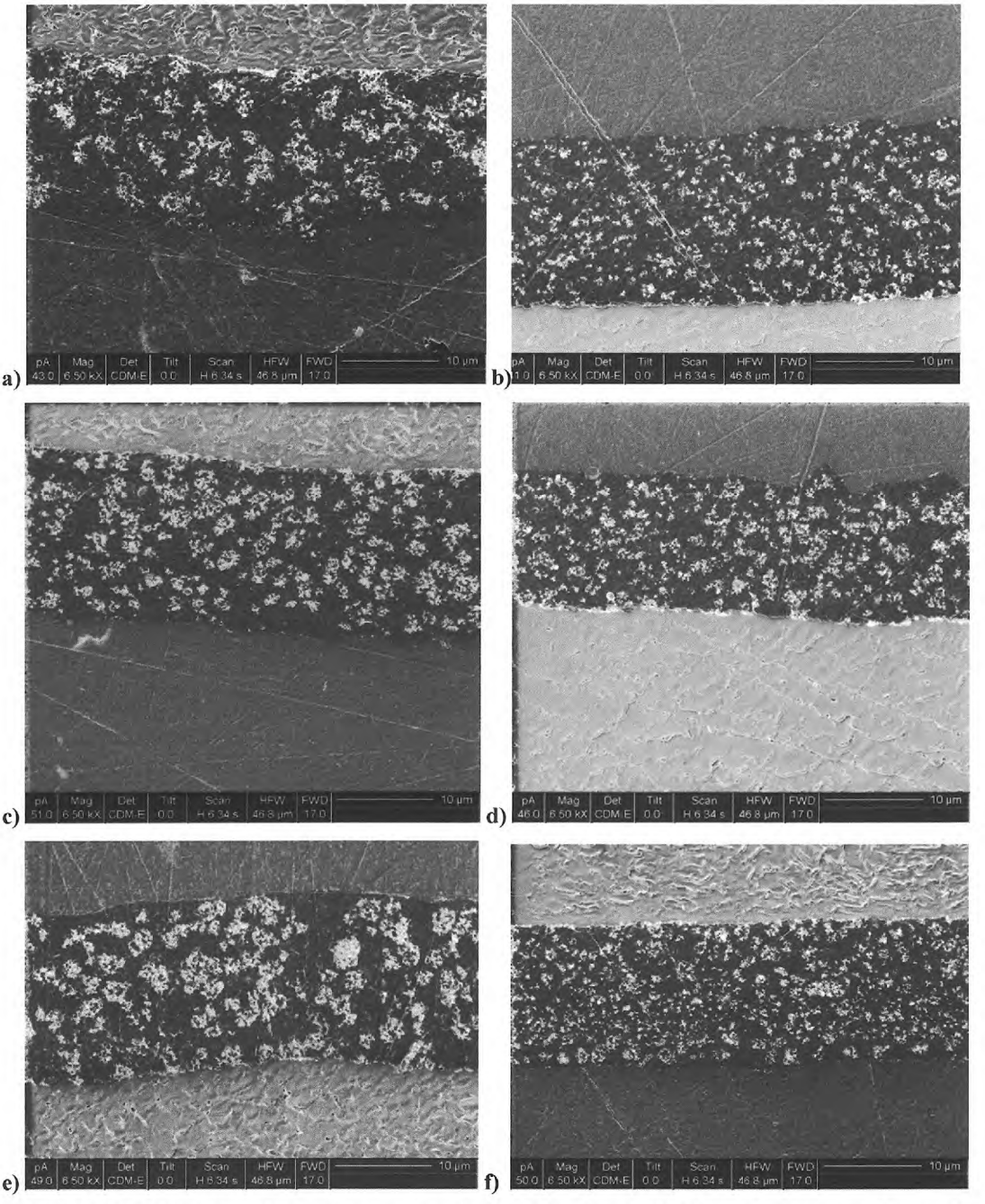


Figure 4.56 FIB cross section micrographs of Ni-Al_2O_3 composite films deposited applying -10 mA·cm^{-2} from solution containing a) and b) 50 g/l, c) and d) 100 g/l, e) and f) 150 g/l of nano-Al_2O_3. The micrographs on the left are of the side facing the anode and those on the right of the opposite side.

The fact that the sub-micron-Al_2O_3 particles were deposited in groups in one side of the film (see Fig. 4.53-4.55 on the left) cannot be due to the particle agglomeration in the suspension, since they were uniformly dispersed on the other side of the film (see Fig. 4.53-4.55 on the right), but it was probably due to the deposition mechanism. It can be thought that once few particles were embedded in a part of the film the film roughness increased producing a higher possibility for new particles to be "trapped" and consequently embedded in that portion of the film so that the particles were embedded in groups. A similar hypothesis was

formulated by Erler et al. [98], to explain the fact that the Al_2O_3 particles were not incorporated in the first 2-3 μm of the film. It has to be underlined that the embedment in groups was mainly observed in the side of the cathode facing the anode that, in agreement with the stirring conditions, was the side of the cathode approached by less particles due to the position in the bath.

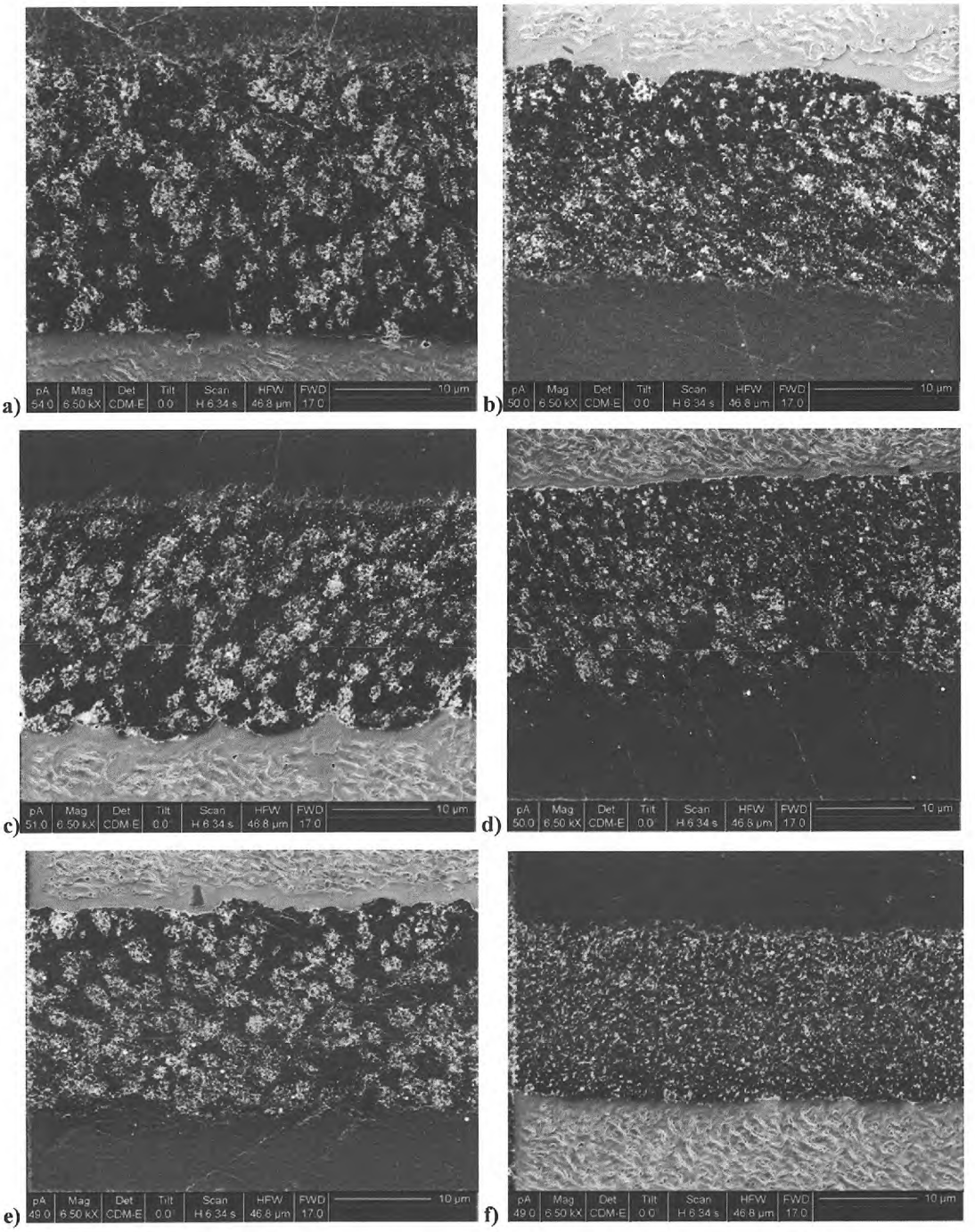


Figure 4.57 FIB cross section micrographs of Ni-Al_2O_3 composite films deposited applying -20 mA·cm^{-2} from solution containing a) and b) 50 g/l, c) and d) 100 g/l, e) and f) 150 g/l of nano-Al_2O_3. The micrographs on the left are of the side facing the anode and those on the right of the opposite side.

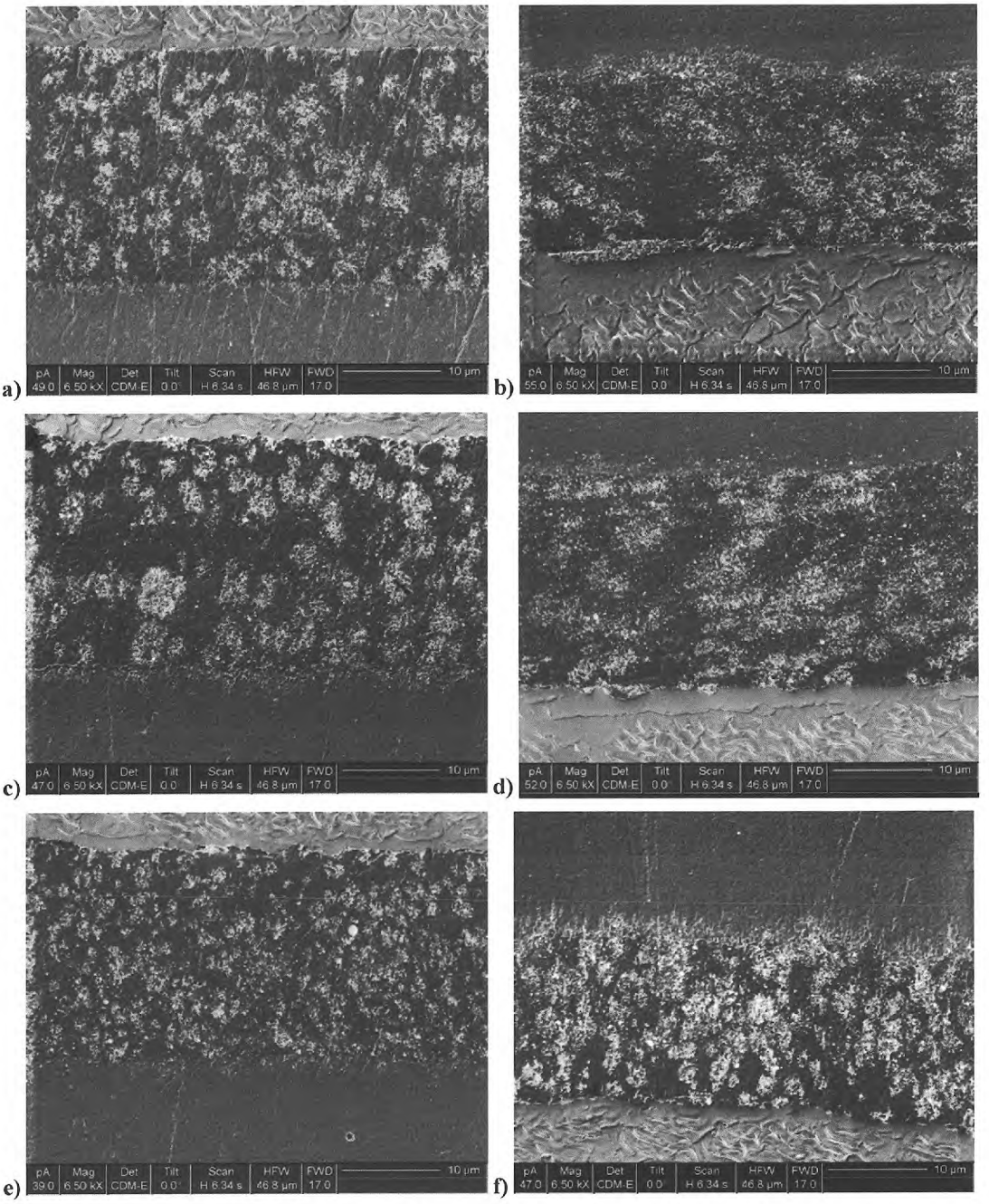


Figure 4.58 FIB cross section micrographs of Ni-Al_2O_3 composite films deposited applying -32 mA·cm^{-2} from solution containing a) and b) 50 g/l, c) and d) 100 g/l, e) and f) 150 g/l of nano-Al_2O_3. The micrographs on the left are of the side facing the anode and those on the right of the opposite side.

The distribution of the nano-Al_2O_3 particles was more difficult to asses due to their smaller sizes and the difficulties encountered in analysing these films. From the FIB-SIMS analyses reported in Figures 4.56-4.58 it seemed that the nano-Al_2O_3 particles were slightly agglomerated in *both* sides of the coating; the agglomeration size seemed to change with the conditions employed and with the side of the cathode. However, at higher magnifications (see Figure 4.59) it seemed that the particles were not agglomerated but deposited in groups as also

observed for the Ni-sub-micron-Al_2O_3 composites. Figure 4.60 shows a high resolution FIB image of a Ni-nano-Al_2O_3 composite in which the Al_2O_3 particles seemed well-dispersed and not agglomerated.

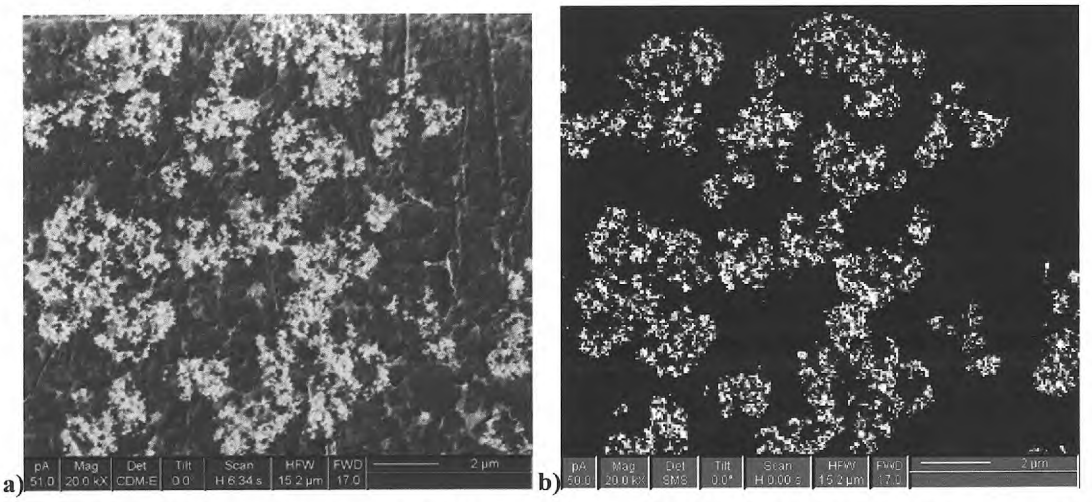


Figure 4.59 a) FIB micrographs and b) SIMS Al mapping of the same area of a Ni-Al_2O_3 composite films deposited applying -10 mA·cm^{-2} from a solution containing 150 g/l of nano-Al_2O_3 .

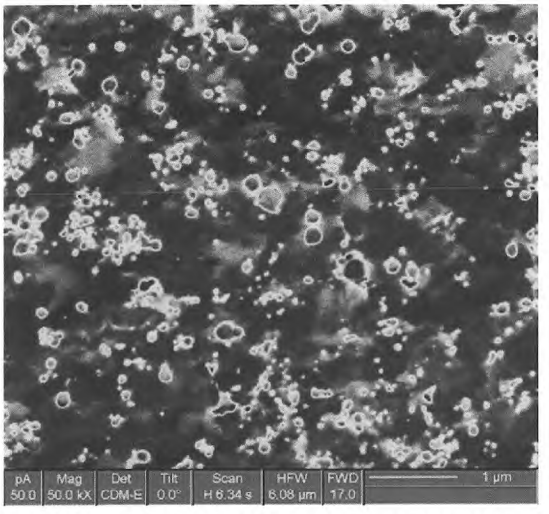


Figure 4.60 High resolution FIB micrograph of a Ni-Al_2O_3 composite films deposited applying -20 mA·cm^{-2} from a solution containing 150 g/l of nano-Al_2O_3.

From the comparison of the coating thickness deposited on the two sides of the stainless steel (Figures 4.53-4.58) it can be observed that generally the coating on the side of the substrate facing the anode was slightly thicker than the one deposited on the opposite side probably for different deposition rates, similar results were also reported by Dong et al. [112] and by Wakabayashi et al. [43]. Dong et al. [112] observed a difference in thickness between the two opposite sides up to 50% with and without the alumina particles. They explained this difference considering the variation of the cathode-anode distance between the different faces of the prism and the consequent different current density. In this research the distance between the two sides of the cathode was just 2 mm (substrate thickness) and therefore the differences in

thickness was always much lower (maximum of 20%).

The variation of the coating thickness on flat substrates has to be taken into consideration when the process is scaled-up and when complex shape electrodes are employed. It is known that the metal deposition takes preferentially place on external corners and protrusions compared to depressions and internal edges. Therefore, to scale up the deposition of Ni and Ni-Al_2O_3 composite films achieving uniform coating thickness it is necessary to design an electrochemical cell with appropriate electrode geometry, e.g. multiple spaced anodes or anodes with special shapes mimicking the substrate geometry [260].

4.5.4 Three-dimensional-reconstruction of a composite coating using FIB-SIMS

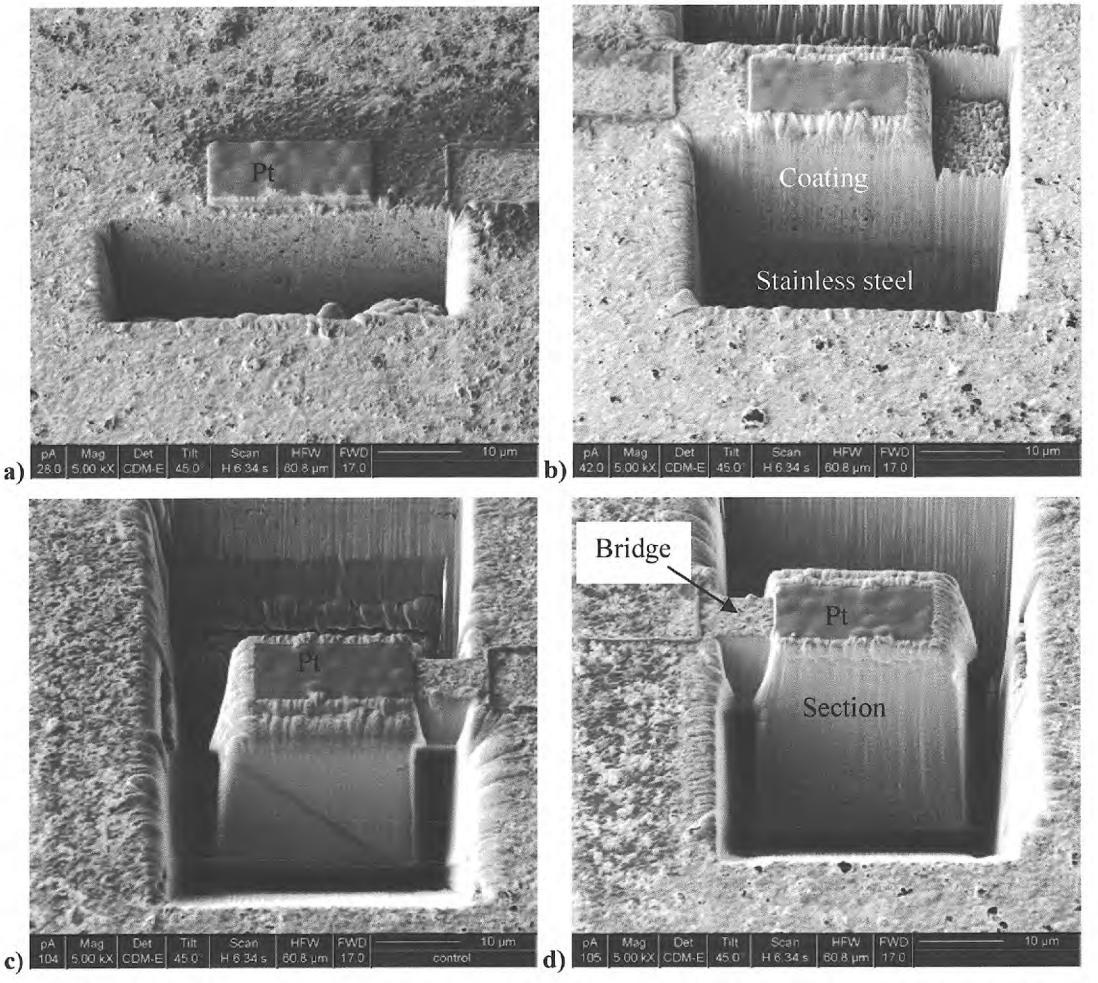


Figure 4.61 FIB-SIMS images showing a) first and b) second ramp milled around the section to be lifted out, c) and d) the two sides of the section when the detachment from the sample was completed a part from the connection bridge.

A 3D-reconstruction of a composite coating deposited applying -32 $mA \cdot cm^{-2}$ from a bath containing 50 g/l of sub-micron-Al_2O_3 particles was carried out using the FIB-SIMS as described below. A sample without any further preparation was subjected to a four step

process similar to the one described by Lekström and Shollock [261] to prepare TEM sections. The first step consisted of depositing *in-situ* on the region of interest a 1-2 μm thick 10 x 20 μm platinum layer (Figure 4.61 a)) needed to protect the material surface and also to identify the section to be lifted out from the sample. The section was chosen to be a volume of 10 μm x 20 μm x 25-30 μm (depth). In the second step (sample cut-out), the two long sides and one of the short sides of the volume to be lifted out were milled with a beam current of 3-7 nA keeping the gallium ion beam perpendicular to the sample surface and rotating the stage of 180° angle (Figure 4.61 b)). Subsequently, the stage was tilted at 45° angle to mill the material underneath the volume to be lifted-out and to completely separate the volume and the specimen (Figure 4.61 c) and d)). At this point, the section was attached to the rest of the sample only on one side that was thinned leaving just a connection bridge (Figure 4.61 c) and d)). It is interesting to point out that in Figure 4.61 b) the interface between the stainless steel and nickel coating is clearly visible as the two materials presented slightly different colours.

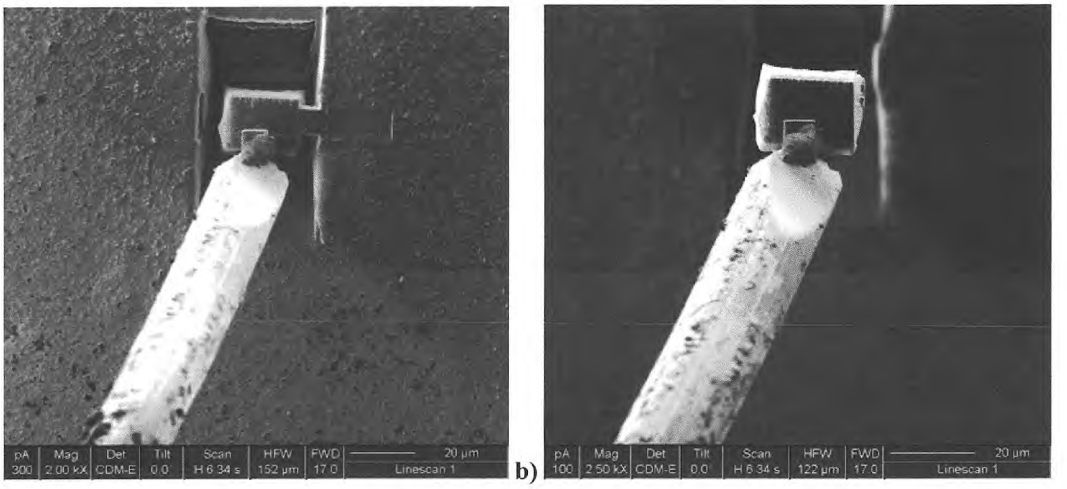


Figure 4.62 FIB-SIMS images showing a) the needle in contact with the section and a Pt bridge between them, b) the section completely free and detached from the rest of the sample.

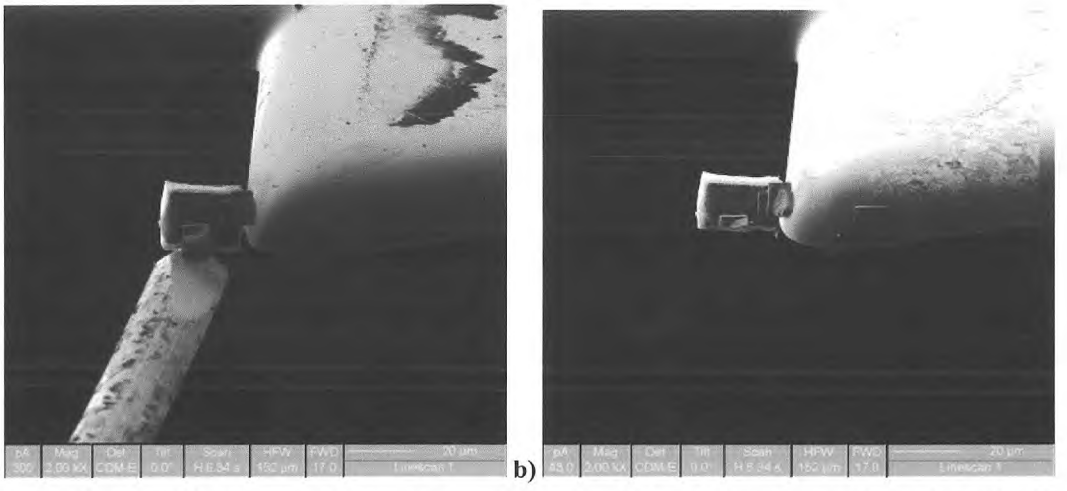


Figure 4.63 FIB-SIMS images showing a) the section attached with Pt to the needle and to the Cu stem b) the section attached to the Cu stem.

In the third step (sample lift-out) of the process, a needle was brought into contact with the section to be lifted-out and the two objects were welded together *via* a Pt bridge, as shown in Figure 4.62 a). At this point, the section was attached to the needle by the Pt bridge and to the sample by the bridge connection (Figure 4.62 a)), that was then sputtered away to completely free the section (Figure 4.62 b)). Figure 4.62 a) shows clearly the triangular prism hole produced on the surface of the specimen by the process carried out. In the last step of the process the free section was brought into contact with a Cu stem and welded to it through two Pt bridges (Figure 4.63 a)) (the second bridge was deposited to add additional strength to the connection) and finally the Pt bridge between the needle and the section was removed to obtain the section connected just to the Cu stem (Figure 4.63 b)).

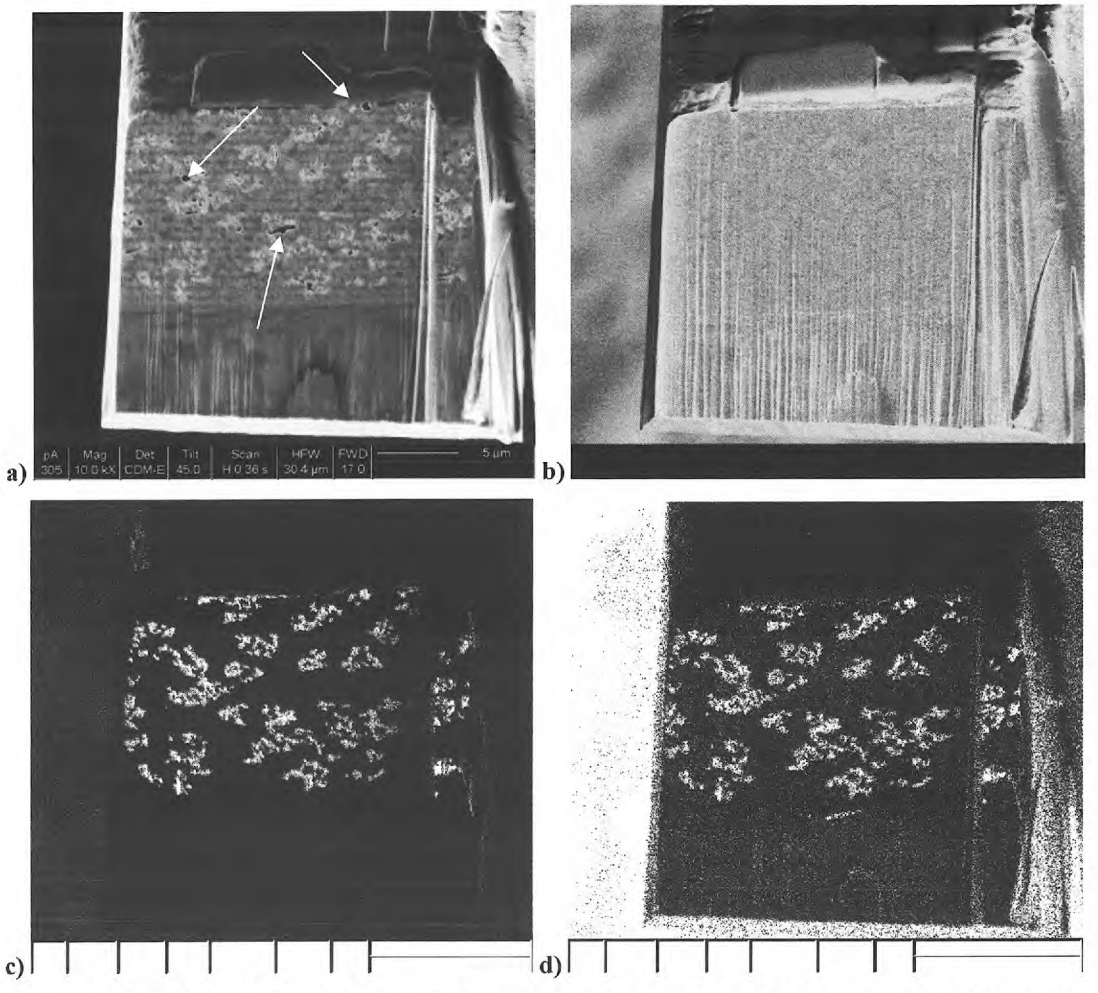


Figure 4.64 a) Secondary electron and b) secondary ion images of the same surface. In a) few apparent voids are visible and pointed out by arrows; they are not visible in the ion image reported in b). c) Al and d) O SIMS mapping of the same side of the lift out section.

The surface of the section was then cleaned by sputtering away the top surface and some of the Pt bridges left, as shown in Figure 4.64. Figure 4.64 a) is a secondary electron image of the section with few black parts looking like holes in the material (see arrows). However the ion image (Figure 4.64 b)) of the same surface demonstrated that these areas were not voids.

On the same surface the SIMS mapping of the Al atoms (Figure 4.64 c)) and of the O atoms (Figure 4.64 d)) were also performed to confirm that the signals of these two materials were in the same positions, as expected. Comparing the SIMS mapping (Figures 4.64 c) and d)) with the secondary electron image (Figure 4.64 a)) it is evident that the Al_2O_3 sometimes appeared white and sometimes black in secondary electron images taken on the sample tilted of 45°. Therefore the SIMS mapping of the Al atoms seemed better than the electron images to identify the alumina when the sample was tilted at 45° angle.

Fifteen slices were then milled away from the lift-out section with a current beam of 1 nA and from each one three images were taken: the top part of the specimen (platinum layer) to determine the thickness of the slice spattered away by difference with the initial one, a secondary electron image and a SIMS Al mapping of the surface tilted of 45°, all these images are reported in Appendix 3.

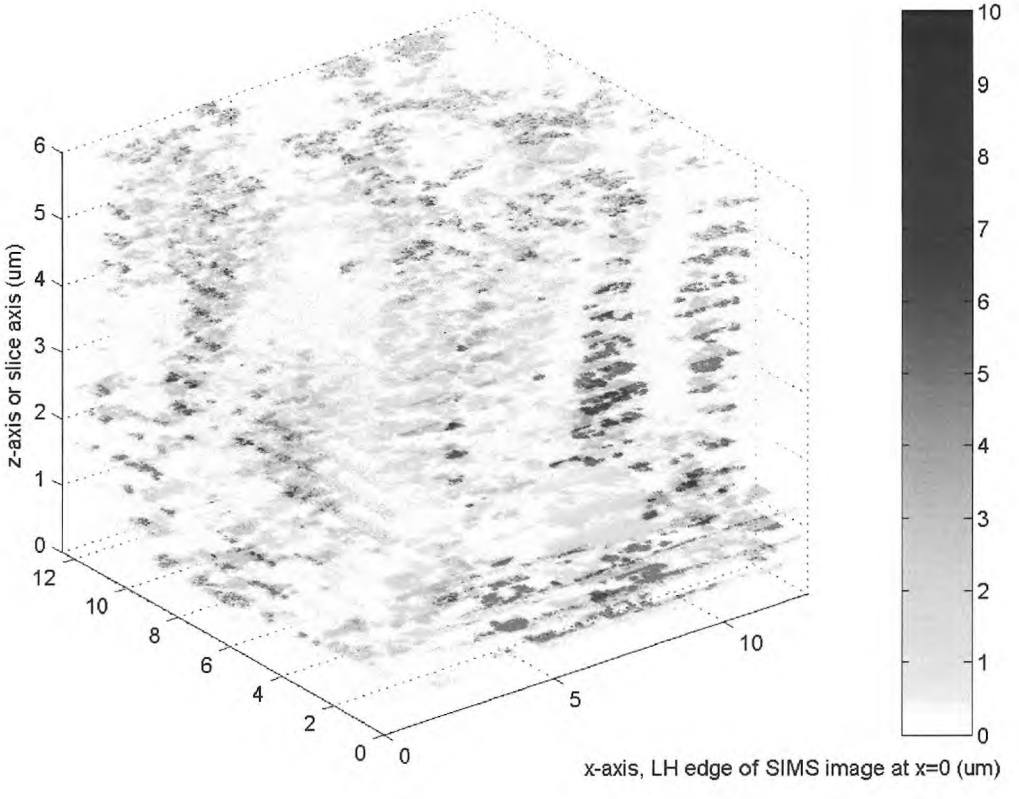


Figure 4.65 3D-reconstruction of a Ni-sub-micron-Al_2O_3 film with the dark areas being the Al_2O_3.

The SIMS mapping of the Al atoms were then employed to produce a 3D-reconstruction of the film using Matlab. A similar study was reported by Wilson et al. [262] to produce a 3D-reconstruction of a solid-oxide fuel-cell anode. The data employed for the 3D-reconstruction were taken just from the top left area of each slice since it has been observed that the SIMS signals of the right hand side areas of the deeper slices were weak due to the screening effect of the part of sample not sputtered away (see Appendix 3). The 3D-reconstruction shown in

Figure 4.65 demonstrates that in the volume of the composite film analysed the Al_2O_3 was homogeneously distributed. In section 4.5.3 it was stated that the Al_2O_3 distribution in the coating cross section was similar along the same side of the substrate; therefore it could be concluded that the electro co-deposition method is able to produce composite coatings with uniform particle distribution in the same side of the cathode.

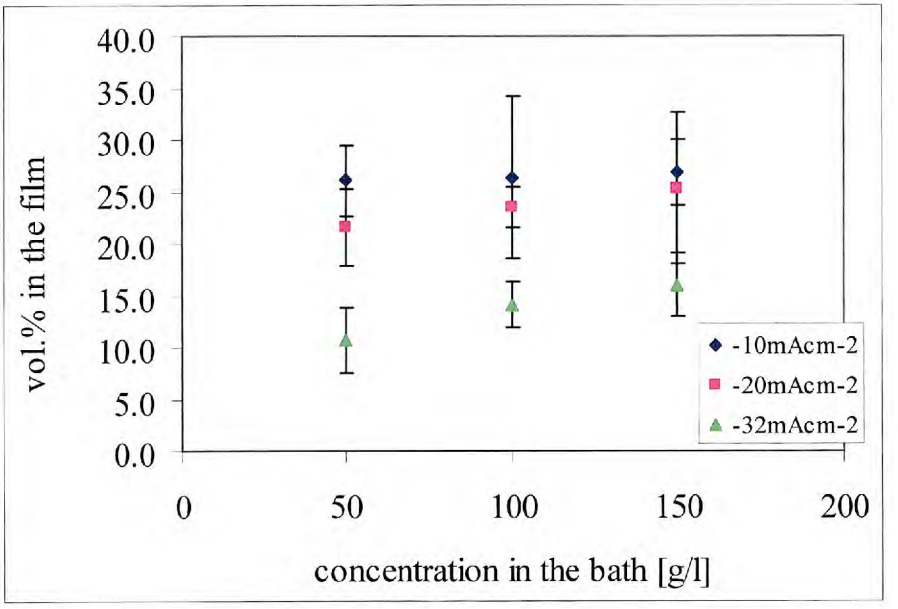
4.5.5 Effect of deposition parameters on the amount of Al_2O_3 co-deposited in nickel films

It has been extensively reported in the literature [1, 2, 57, 62, 69, 70, 72, 74, 78, 82, 84, 85, 92, 95, 98, 110, 112] that the amount of Al_2O_3 co-deposited in the composite films can be influenced by the particle concentration in the electrolyte, the current density, the particle size, the stirring rate and the cell configuration. The influence of the particle size (<1 μm and ~50 nm), their concentration in the bath (0, 50, 100 and 150 g/l of Al_2O_3) and the applied current density (-10, -20 and -32 $mA \cdot cm^{-2}$) on the amount of Al_2O_3 co-deposited was evaluated by quantitative image analysis (described in Figure 3.9 and section 3.11), that calculates the area % of Al_2O_3 in the film. Assuming that the material is isotropic (demonstrated in section 4.5.4) the area and the volume can be considered the same; the same approximation (area = volume) and quantitative analysis were also employed by other researchers [70, 84, 91, 112]. The cross section images of all the samples are shown in Figures 4.53-4.58 and the results are discussed below. The analysis of the cross sections of Ni-Al_2O_3 composite films described in section 4.5.3 revealed a difference in Al_2O_3 concentration between the two sides of the cathode. Therefore, in order to obtain representative values four images for each side were taken for the Ni-sub-micron-Al_2O_3 films and two images for each side for the Ni-nano-Al_2O_3 films; the images were taken as described in section 3.11. The values for all the images were then averaged and the errors calculated with the standard deviation. The difference between the two sides was calculated to be an average of 5% for the Ni-sub-micron-Al_2O_3 composites, while for the nickel-nano-Al_2O_3 films the difference was around 1.5%. In the data analysed here both sides of the samples have been considered.

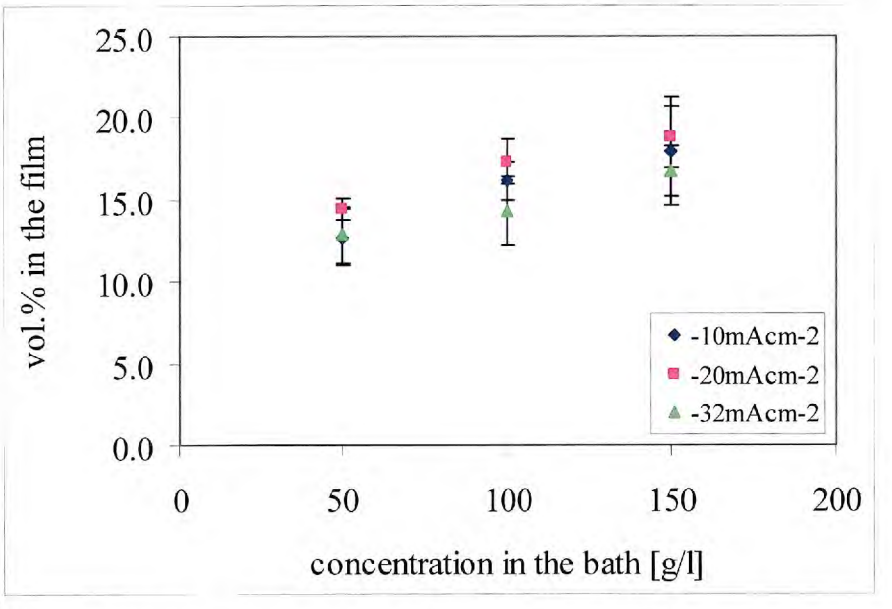
i) Effect of the alumina concentration in the bath

From the data shown in Figure 4.66 a) and b), it emerged that the amount of Al_2O_3 co-deposited increased with increasing Al_2O_3 concentration in the bath for all the current densities applied and both kinds of Al_2O_3 particles; this increase was not proportional to the amount of alumina suspended in the bath. This behaviour was expected considering that higher bath concentrations increased the particle availability at the interface cathode/suspension that could therefore be embedded in the growing nickel layer. Similar behaviours were also reported in the literature for the Ni-Al_2O_3 system [72, 78, 82, 84, 98, 110, 112]. The amount of sub-micron-Al_2O_3 embedded in the coatings from solution containing 150 g/l of Al_2O_3 and applying a

current density of -10 mA·cm^{-2} (27 ± 3 vol.%) was similar to the results reported by Banovic et al. [84] applying similar condition from a sulphamate bath (32 vol.%). The vol.% of nano-Al_2O_3 deposited from a solution containing 150 g/l of Al_2O_3 and applying a current density of -20 mA·cm^{-2} (19 ± 2 vol.%) was much higher than that reported by Sautter [72] applying the same conditions from a sulphate bath (5 vol.%), probably for the different stirring rate employed in the two research.



a)



b)

Figure 4.66 Effect of the Al_2O_3 concentration in the electrolyte on the vol.% of a) sub-micron-Al_2O_3 and b) nano-Al_2O_3 embedded into the films for different current densities.

ii) Effect of the current density

The data in Figure 4.67 a) for the sub-micron-Al_2O_3 particles show that the amount of second phase co-deposited decreased increasing the current density from -10 to -32 mA·cm^{-2}

when the suspension concentration was unvaried, as also observed in the literature [76, 78, 84, 98, 110]. This trend can be explained considering that when lower current densities are applied the nickel deposition is slower and therefore more Al_2O_3 particles have time to reach the interface coating-solution and be embedded in the film [84].

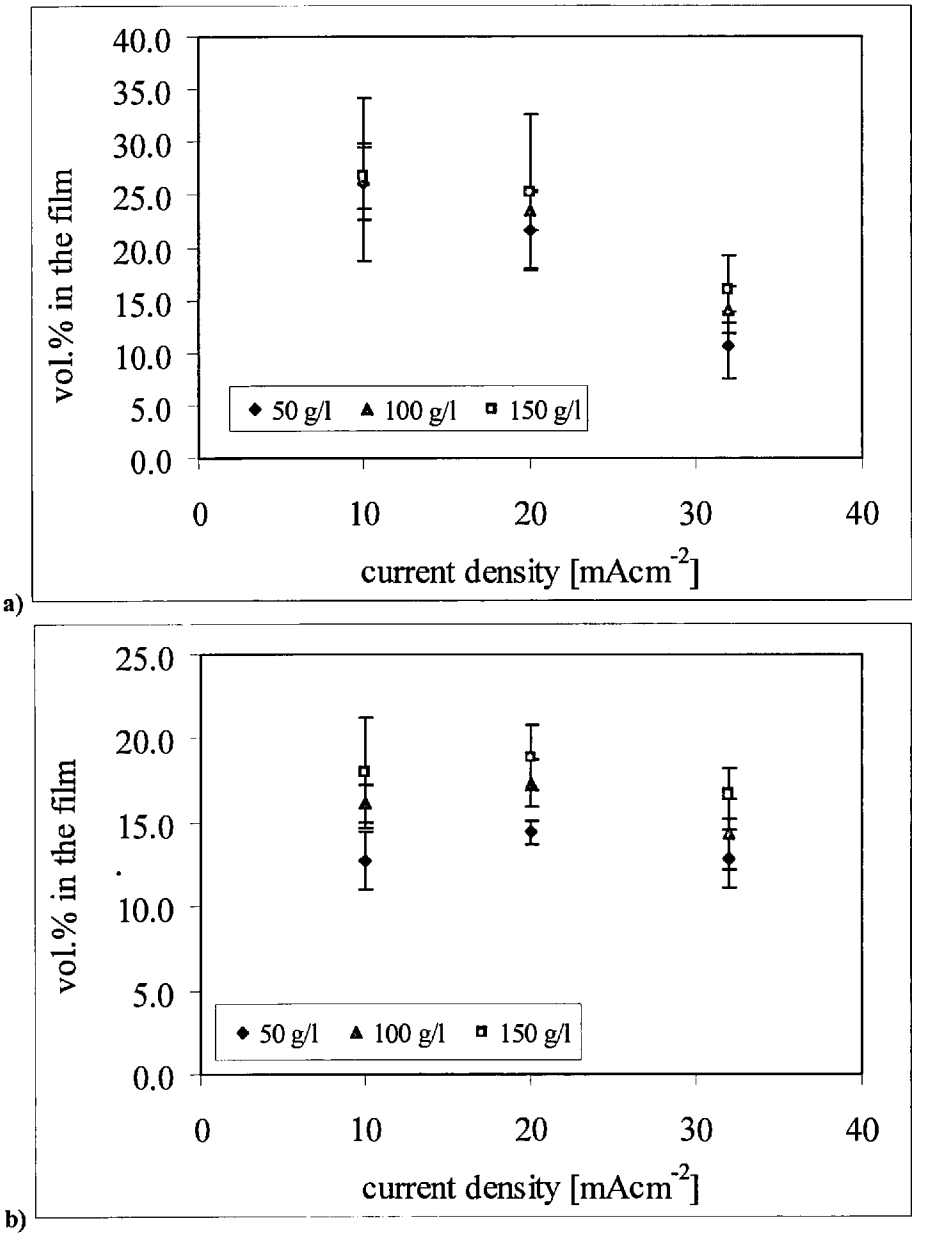


Figure 4.67 Effect of the current density on the vol.% of a) sub-micron-Al_2O_3 and b) nano-Al_2O_3 embedded into the films for different Al_2O_3 concentrations in the electrolyte.

While, for the nano-Al_2O_3 particles (Figure 4.67 b)) it seemed that the amount of Al_2O_3 co-deposited increased by increasing the current density from -10 to -20 $mA \cdot cm^{-2}$ and decreased by further increasing the current density to -32 $mA \cdot cm^{-2}$ for all the concentrations of Al_2O_3 examined. Similar trends were reported in the literature for the Ni-Al_2O_3 system [1, 2, 57, 74, 92]. The maximum incorporation of nano-Al_2O_3 particles applying a current density of -

20 $mA \cdot cm^{-2}$ (Figure 4.67 b)) was also reported by Nwoko and Shreir [57], that used a nickel sulphate bath containing Al_2O_3 particles with size between 5 and 50 nm.

These two different behaviours are explained below considering that the co-deposition of the second phase in the metallic film depends on the growing rate of the metal (deposition current density), the flux of particles and their residence time at the metal/solution interface (stirring rate, particle size and concentration in suspension) [76, 77], assuming that the particle transport to the interface is controlled by convective diffusion. If the metal growth rate is slow in comparison to the residence time, the particles approaching the cathode have sufficient time to diffuse away before being incorporated into the film; while, if the metal deposition rate is fast compared to the particle residence time, all the particles reaching the surface will be embedded in the composite film. Therefore, in order to have maximum incorporation the metal deposition rate has to be sufficiently high to entrap in the film all the approaching particles, as shown schematically in Figure 4.68 a), but not too high so that the particles would not have enough time to reach the electrode surface (Figure 4.68 b)) [76].

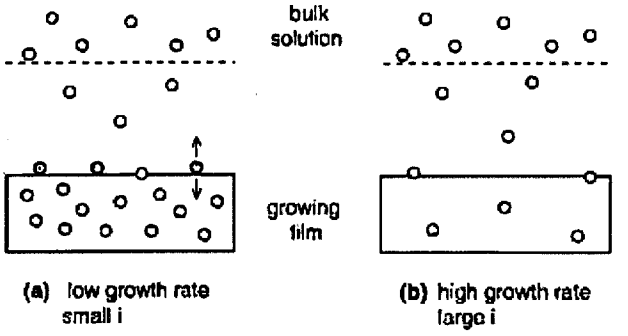


Figure 4.68 Schematic illustration of different particle incorporation in electro co-deposition. a) At slow metal growth rate more particles can reach the surface and be embedded. b) At high metal growth rate less particles can be embedded in the growing film (redrawn from ref. [76]).

When the same suspension is employed the particle flux to the electrode surface and the residence time at the cathode are constant since the concentration, the stirring rate and the particle size are maintained the same. The higher concentration of sub-micron-Al_2O_3 co-deposited applying a current density of -10 $mA \cdot cm^{-2}$ (Figure 4.67 a)) can be explained considering the slow growth of the metal that gave sufficient time to more Al_2O_3 particles to reach the interface and be embedded in the film. Under these conditions, more particles reaching the electrode were embedded in the film and their amount depended on the flux of particles at the electrode and therefore on the solution concentration and on the stirring rate. It is interesting to underline that when the current density applied was -10 $mA \cdot cm^{-2}$ the amount of Al_2O_3 co-deposited was not greatly influenced by the particle concentration in suspension, probably because even when lower concentrations (50 and 100 g/l) were employed a high flux of particles was constantly approaching the electrode and the residence time was long enough

to be embedded. When higher current densities (-20 and -32 $mA \cdot cm^{-2}$) were applied the amount of particles co-deposited decreased because even if the flux of particles at the cathode was unvaried the metal film grew faster; the concentration of Al_2O_3 in the bath was a determining factor in the amount of Al_2O_3 co-deposited since it strongly influenced the flux of particles at the cathode. These two differences are schematically represented in Figure 4.68.

A different behaviour was observed for the co-deposition of the nano-Al_2O_3 particles (Figure 4.67 b)) that showed a maximum Al_2O_3 incorporation when a current density of -20 $mA \cdot cm^{-2}$ was applied. This trend was explained considering that applying a current density of -32 $mA \cdot cm^{-2}$ the metal growth rate was too fast and less particles had enough time to reach the interface coating-solution and be co-deposited, as shown in Figure 4.68 b). While, when a current density of -10 $mA \cdot cm^{-2}$ was applied the metal film was growing too slowly and the nano-Al_2O_3 particles had therefore time to be moved away before being incorporated.

iii) Effect of the particle size

The amount of Al_2O_3 co-deposited in the films (see Figures 4.66-4.67) was strongly influenced by the particle size for all the suspension concentrations and current densities applied. The amount of sub-micron-Al_2O_3 co-deposited varied between 11 and 27 vol.% while in the same conditions the quantity of nano-Al_2O_3 varied just between 12 and 19 vol.%. The higher vol.% of co-deposited sub-micron-Al_2O_3 particles compared to nanoparticles is probably due to their greatly different volumes (assuming radiuses of 25 nm and 400 nm the differences in volume would be 16^3). Consequently, in coatings with the same Al_2O_3 concentration the particle number density was considerably higher when nano-Al_2O_3 particles were employed instead of sub-micron-Al_2O_3 particles. Similar results were also reported by Shao et al. [77, 78] for 300 and 50 nm size particles. The fact that the range in which the concentration of co-deposited nano-Al_2O_3 varied was less influenced by the conditions employed compared to that of sub-micron-Al_2O_3 (see Figures 4.66-4.67) can be explained considering that there were more nano-Al_2O_3 particles available at the interface ready to be embedded in the growing film and therefore both the particle concentration in the bath and the metal deposition rate only slightly influenced the co-deposition process.

4.5.6 Crystallinity of Ni-Al_2O_3 composite coatings

In the literature it has been extensively described that the crystallinity of the electrodeposited nickel changes by introducing a second phase, such as CeO_2, WC, TiO_2, SiC, Si_3N_4 or Al_2O_3 particles [62, 84, 85, 90-92, 97, 100, 116, 117, 244, 246, 247] and by modifying the deposition current density, as also observed in Figure 4.42 and discussed in section 4.4.6. A variation of the nickel preferred orientation with the addition of Al_2O_3 was expected considering that the nickel crystallization strongly depends on the bath composition, as discussed in section 4.4.6, and that the variation of inhibiting species can influence the Ni

crystal growth, e.g. the addition of particles can produce a random orientation of the Ni crystallites [90, 116, 244]. In order to determine the influence of sub-micron and nano-Al_2O_3 particles on the preferred crystalline orientation and the grain size of the composite films, XRD analysis has been carried out on samples deposited at different current densities from the three baths containing different amounts of Al_2O_3 particles. These spectra have been compared to those of pure nickel obtaining the results listed in Table 4.14; just the XRD spectra of Ni-sub-micron-Al_2O_3 composite coatings deposited at -10 $mA \cdot cm^{-2}$ are reported, as an example, in Figure 4.69 (the spectra have been carried out between 2θ 5° and 100° but just the 40-100° portion is shown since the main Ni crystallographic peaks are in this area).

Table 4.14 Intensity of Ni crystallographic peaks normalised to the (111) peak for films deposited using different current densities and from baths containing different amounts of Al_2O_3.

Current density $mA \cdot cm^{-2}$	Concentration of Al_2O_3 g/l		I(reflection)/I(111)			
			(111)	(200)	(220)	(311)
-10	0		1	0.5	0.14	0.13
	Sub-micron	50	1	0.65	0.09	0.11
		100	1	0.61	0.11	0.12
		150	1	0.63	0.08	0.10
	Nano	50	1	1.14	0.06	0.08
		100	1	0.57	0.04	0.09
		150	1	0.09	0.04	0.25
-20	0		1	0.83	0.19	0.19
	Sub-micron	50	1	0.41	0.16	0.13
		100	1	0.45	0.20	0.14
		150	1	0.43	0.16	0.13
	Nano	50	1	0.56	0.15	0.12
		100	1	0.49	0.17	0.15
		150	1	0.47	0.18	0.14
-32	0		1	0.80	0.51	0.20
	Sub-micron	50	1	0.43	0.44	0.14
		100	1	0.48	0.49	0.16
		150	1	0.42	0.44	0.13
	Nano	50	1	0.43	0.34	0.15
		100	1	0.39	0.34	0.14
		150	1	0.33	0.36	0.13

The preferred crystallographic orientation for all the pure nickel and composite films, except from the one deposited applying -10 $mA \cdot cm^{-2}$ from a bath containing 50 g/l of nano-

Al_2O_3 particles, was the (111). In order to determine how the amount of co-deposited Al_2O_3, the kind of Al_2O_3 (sub-micron or nano size) and the applied current density influenced the preferred orientation of the nickel films, the intensities (height of the peaks) of the (111), (200), (220) and (311) nickel reflections have been normalised to the (111) reflection obtaining the data reported in Table 4.14.

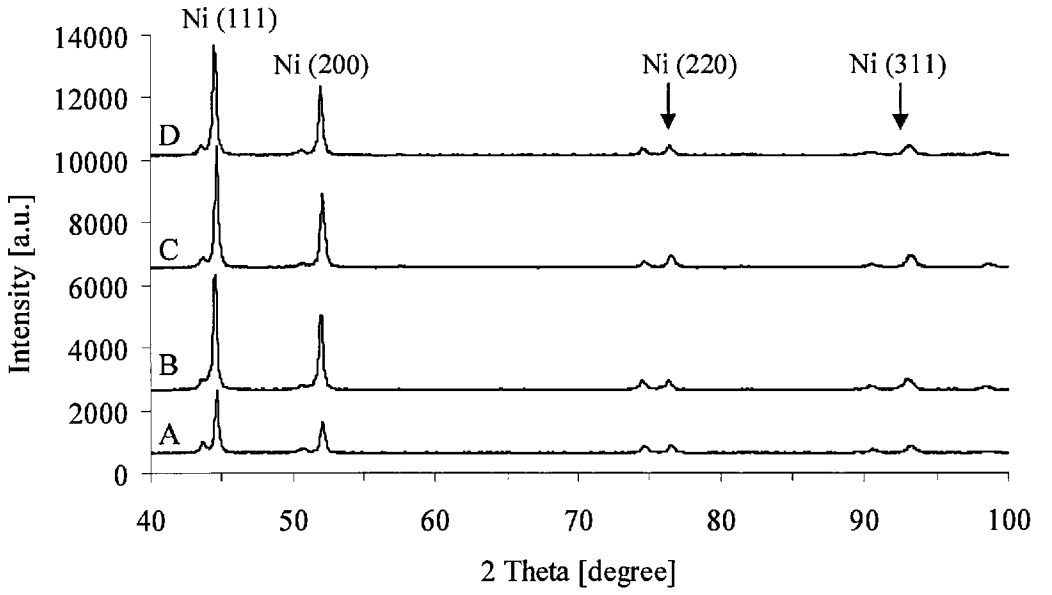


Figure 4.69 XRD spectra of coatings deposited applying a current density of -10 mA·cm^{-2} from A) a nickel bath and a nickel bath containing B) 50, C) 100 and D) 150 g/l of sub-micron-Al_2O_3 particles.

The addition of sub-micron-Al_2O_3 particles to the nickel bath when a current density of -10 mA·cm^{-2} was applied (see Figure 4.69 and Table 4.14) enhanced the (200) crystallographic orientation compared to pure Ni and slightly decreased the (220) and (311) intensities. The composite texture did not change with the concentration of Al_2O_3 in the bath since it seemed that the amounts co-deposited were very similar in all the conditions employed, as shown in Fig. 4.67 a). The addition of 50 g/l of nano-Al_2O_3 particles in the bath at the same current density (Table 4.14) increases the degree of texture in the (200) Ni crystallographic direction, and this was the preferred orientation for coatings deposited in these conditions. However, further additions of nano-Al_2O_3 particles in the electrolyte increased the concentration of Al_2O_3 co-deposited (Fig. 4.67 b)) and weakened the (200) peak that was almost indistinguishable when the solution contained 150 g/l of nano-Al_2O_3. In this latter coating there was an increase of the (311) Ni orientation signal. The variation of the Ni crystalline orientation with the amount of nano-Al_2O_3 in the electrolyte was also reported by Erler et al. [98] for Ni-nano-Al_2O_3 films deposited on stainless steel from a nickel sulphate bath with 0.3 g/l of SDS and a temperature of 55 ± 2°C. They [98] observed that applying a current density of -10 mA·cm^{-2} pure nickel presented (220) preferred orientation and that by adding 0.5 g/l of nano-Al_2O_3

particles the texture did not change, whereas when 5 g/l of nano-Al_2O_3 particles were added into the bath the Ni texture varied to (200), (220) and (311) and when higher content (50 g/l) were employed the (220) orientation peak disappeared leaving just the (200) and (311). Erler et al. [98] did not explain the intensity variation and reported that when higher current densities were applied (-20 and -40 $mA \cdot cm^{-2}$) the (200) was the Ni preferred orientation independent from the particle content in the bath. The variation of the Ni crystalline orientation with the amount of nano-Al_2O_3 in the electrolyte is probably due to an underlying mechanism that controls the texture; this mechanism has not yet been resolved and further work is needed to understand this behaviour.

When current density of -20 or -32 $mA \cdot cm^{-2}$ were applied the addition of sub-micron or nano-Al_2O_3 particles (Table 4.14) halved the intensity of the (200) peak and slightly decreased the intensity of the (311) orientation peak compared to pure nickel. It was also observed for both current densities that increasing nanoparticle content seemed to slightly decrease the intensity of the (200) peak (see Fig. 4.67 b) and Table 4.14). The intensity of the (220) peak was left almost unvaried by the addition of nano and sub-micron-Al_2O_3 particles applying a current density of -20 $mA \cdot cm^{-2}$, while when a current density of -32 $mA \cdot cm^{-2}$ was applied the peak intensity decreased compared to pure Ni, but did not vary much with the addition of different amounts of Al_2O_3 particles.

Table 4.15 Grain sizes of Ni deposited applying different current densities from baths containing different amounts of nano or sub-micron-Al_2O_3 particles calculated using Sherrer equation.

Current density ($mA \cdot cm^{-2}$)	Amount of Al_2O_3 (g/l)	Grain size (nm)	
		Sub-micron-Al_2O_3	Nano-Al_2O_3
-10	0	40 ± 1	
	50	40 ± 1	45 ± 1
	100	40 ± 1	42 ± 1
	150	36 ± 1	45 ± 1
-20	0	33 ± 1	
	50	35 ± 1	36 ± 1
	100	32 ± 1	33 ± 1
	150	33 ± 1	33 ± 1
-32	0	31 ± 1	
	50	29 ± 1	29 ± 1
	100	35 ± 1	30 ± 1
	150	30 ± 1	29± 1

The variation of the nickel grain size with the inclusions of sub-micron and nano-Al_2O_3 particles in the films was calculated applying Sherrer equation (eq. 4.5 in section 4.4.6) to the

(111) Ni XRD-line broadening [36, 37, 90] of the Ni-Al_2O_3 composite XRD spectra. The XRD-line broadening was calculated after stripping the $K\alpha_2$ signal and after correcting the instrument broadening using equation 4.6 and the silica standard, as described in section 4.4.6. The calculated grain sizes are listed in Table 4.15 with the respective errors, calculated as described in section 4.4.6; they varied from 29 ± 1 to 45 ± 1 nm. These values are slightly higher than those reported by Aruna et al. [85] (16-26 nm) and Srivastava et al. [90] (23 nm), who did not use the line line-broadening correction (equation 4.6); similar results would have been obtained in this research without applying the line broadening correction.

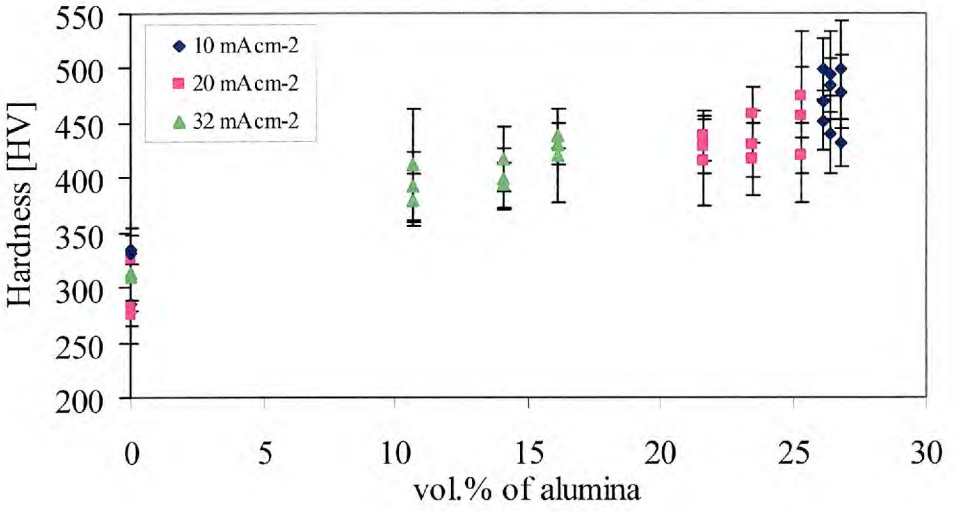
It seems that the Ni grain size decreased slightly increasing the current density from -10 to -32 $mA \cdot cm^{-2}$ when both sub-micron and nano-Al_2O_3 particles were added to the electrolyte, as also observed for pure Ni films and described in section 4.4.6. The co-deposition of Al_2O_3 particles seemed to play a marginal effect on the crystallite sizes, as also reported by Moller and Hahn [115] for Ni-ZrO_2 and Li et al. [117] for Ni-TiO_2 composite coatings deposited from sulphate baths. Other researchers reported a slight decrease of the Ni grain size with inclusion of Al_2O_3 [53, 55, 85, 90, 92], SiC [90, 118, 243], Si_3N_4 [90] and ZrO_2 [249] particles in the films and explained it considering that the particle inclusions increase the nucleation sites and perturb the metal growth producing smaller grains [53, 55, 118, 249].

4.5.7 Micro-hardness

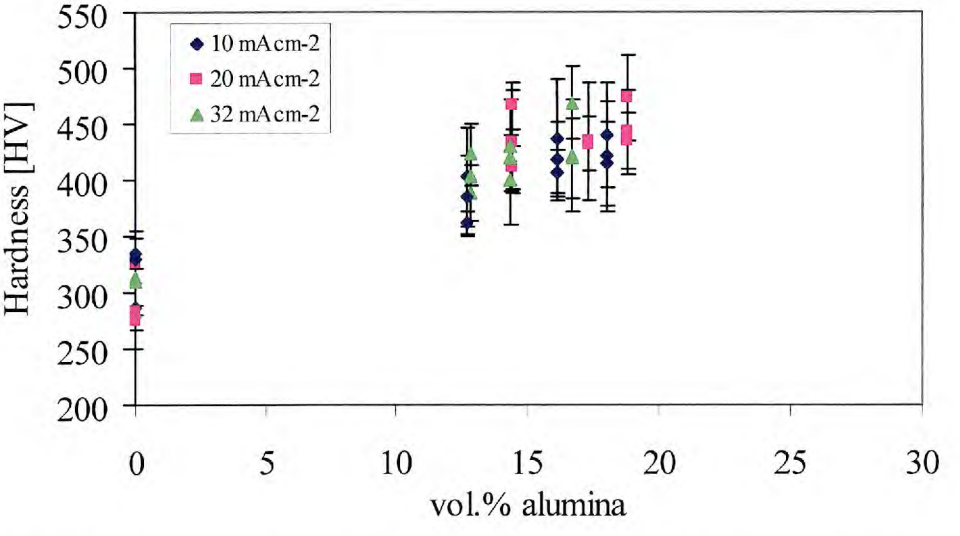
The micro-hardness of the Ni and Ni-Al_2O_3 composite films with sub-micron and nano-Al_2O_3 particles is shown in Figure 4.70. These data have been measured applying the lowest possible load available in the instrument (0.245 N) (section 3.13) to obtain indentation depths (1/7 of the indentation diagonal) less than 1/10 of the coating thickness in order to measure just the coating properties and not any substrate contribution [263-265].

The deposited Ni films presented a micro-hardness between 275 and 335 HV (Figure 4.70) independent of the current density applied. The data in Figure 4.70 clearly show that the hardness of the composite increased compared to that of pure nickel with the addition of Al_2O_3 particles, in agreement with literature findings [52, 54, 61, 62, 75, 78, 81, 82, 84, 85, 89-94]. The hardness values measured in this research are in the same range of the values reported by Chen et al. [81] (320 HV for pure nickel and 470 HV for composites containing 8.5 vol.% of 0.8 μm Al_2O_3 particles co-deposited from a Watt bath), and Srivastava et al. [90] (370 HV for Ni-Al_2O_3 composites containing 1 μm Al_2O_3 particles deposited from a sulphamate bath). The higher hardness of the Ni-Al_2O_3 composite films compared to pure Ni films has been explained in the literature considering a combination of the metal hardness (influenced by the metal microstructure) and the concentration of hard particles in the composite [62, 75, 81, 91, 92]. In particular, it has been reported that the reinforcements influence the composite hardness through their hard nature, a strengthening effect (the particles obstruct the motion of the dislocations) [91, 243] and by modifying the metal microstructure (crystalline orientation and

size) (as reported in section 4.5.6); the latter is also influenced by the current density employed during the deposition (section 4.4.6).



a)



b)

Figure 4.70 Micro-hardness of pure Ni, a) Ni-sub-micron-Al_2O_3 and b) Ni-nano-Al_2O_3 composite films for different concentrations of Al_2O_3 in the electrolyte and different current densities.

Considering that the two sides of the composite samples contained slightly different Al_2O_3 concentrations (~5% for Ni-sub-micron-Al_2O_3 and ~1.5% for Ni-nano-Al_2O_3 films) (see section 4.5.3 and 4.5.5), the hardness of few composites was measured on both sides of the same sample to determine eventual differences. All the differences resulted within the experimental error and no influence of different particle concentration was detected probably for the large variation observed in samples deposited in the same conditions (Figure 4.70).

The hardness of composites containing sub-micron (see Figure 4.70 a)) and nano-Al_2O_3 particles (Figure 4.70 b)) increased with increasing Al_2O_3 concentration, a part from few exceptions. For example, Figure 4.70 a) shows that the composite hardness did not vary

significantly when the sub-micron-Al_2O_3 particle content varied from 16.1 to 21.6 vol.% changing the current density from -32 $mA \cdot cm^{-2}$ (150 g/l) to -20 $mA \cdot cm^{-2}$ (50 g/l) and Figure 4.70 b) shows that coatings with similar nano-Al_2O_3 content (14.3-14.4 vol.%) presented different hardness, with the one deposited applying -20 $mA \cdot cm^{-2}$ (50 g/l) being harder than the film deposited at -32 $mA \cdot cm^{-2}$ (100 g/l). These behaviours may be explained considering the different contribution of the metal to the overall hardness, due to different grain size and crystalline orientation (see Table 4.14 and 4.15). Overall, it is difficult to understand the reasons behind the hardness variation under different conditions, since the Ni microstructure (crystalline orientation and grain size) and the Al_2O_3 content in the films are both contributing to the final value and also for the hardness variation observed when films were deposited in the same conditions (see Figure 4.70). Comparing the hardness of the two composite films (see Figure 4.70), it seems that the same amount of nanoparticles would increase slightly more the hardness of the composite compared to the sub-micron particles, as also observed by Shao et al. [78] and explained considering the higher particle number density that stops more effectively the movement of the dislocations.

4.5.8 Corrosion resistance

Nickel coatings have been widely employed for their high corrosion resistance in different environments (atmosphere, alkalis, melted hydroxides, diluted mineral acids) thanks to their ability to grow an oxide protective layer on their surface. However, Ni coatings are not resistant to corrosion in presence of chloride ions, because these ions delay the formation of the oxide protective layer making the local corrosion possible on the Ni surface [266]. In this study the corrosion resistance of Ni-Al_2O_3 composite films in chloride solution has been tested to determine how the Al_2O_3 addition modifies the Ni corrosion properties; inconsistent results have been reported in the literature [97, 98, 100, 101]. It is also known from the literature [267, 268] that stainless steel is subject to pitting corrosion in chloride environment. In this research the effect of the Al_2O_3 particles on both the general dissolution and tendency to localised corrosion was studied by assessing the corrosion behaviour of Ni, Ni-Al_2O_3 and stainless steel in 0.1 M H_2SO_4 and 0.1 M NaCl solutions using potentiodynamic polarisation curves (see section 3.15), as also described by other authors [35, 101, 266, 269-272]. The results are shown in Figures 4.71 and 4.73.

The corrosion experiments, as it will be for the tape test experiments described in section 4.5.9, have been carried out only on few samples, chosen as representative of all the conditions studied in this chapter. The samples chosen are pure Ni deposited at a current density of -20 $mA \cdot cm^{-2}$ and Ni-Al_2O_3 deposited applying the same current density from solution containing 150 g/l of nano or sub-micron-Al_2O_3 particles. The nickel sample was chosen for comparison with the two composites that presented analogous Al_2O_3 content (20-25 vol.%), the same grain size (33 ± 1 nm) (see Table 4.15) and considerably similar crystalline structures (see Table

4.14). The similar Al_2O_3 concentration is important to determine the effect of different particle size on the composite properties.

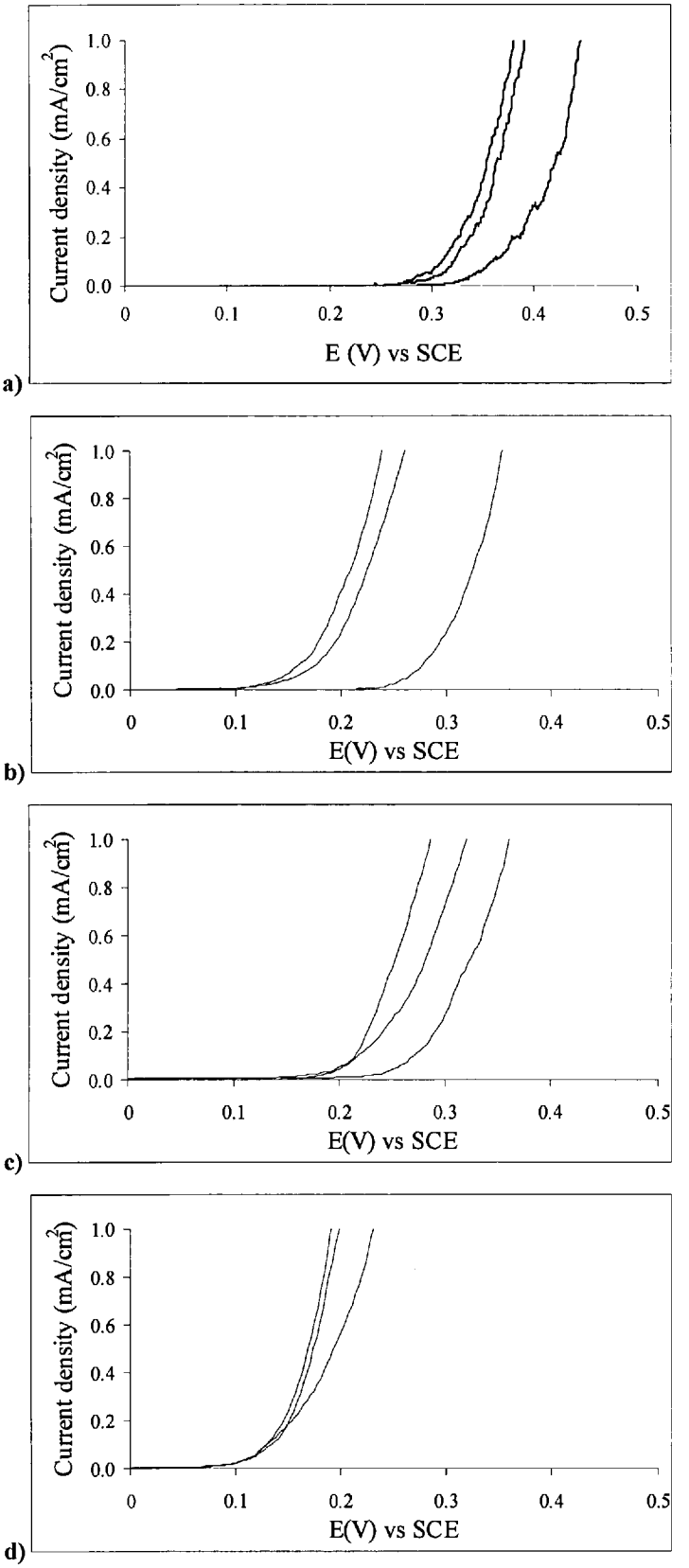


Figure 4.71 Potentiodynamic curves of a) stainless steel, b) pure Ni films, c) Ni-sub-micron-Al_2O_3 and d) Ni-nano-Al_2O_3 films in 0.1 M NaCl solution.

In the linear potentiodynamic polarisation curves [242] carried out in 0.1 M NaCl, the corrosion resistance is related to the sharp increase in current corresponding to the pitting corrosion. The potential at which this occurs is termed the "pitting potential" and its value can be used to compare the corrosion resistance of different materials. In this study the "pitting potential" has been chosen as the potential required to produce a current density of 1 $mA \cdot cm^{-2}$. It is important to underline that the results obtained by this kind of experiment are partly related to the surface properties of the sample analysed and therefore a variation between the data is expected and it is important to run a series of tests; three samples were therefore tested for each type of coating and the averaged values considered.

The average pitting potential of the as received stainless steel AISI 316 L substrate was + 405 mV (SCE) (see Figure 4.71 a)), for pure Ni films was + 287 mV (SCE) (see Figure 4.71 b)), for Ni-sub-micron-Al_2O_3 composite coatings was + 323 mV (SCE) (see Figure 4.71 c)) and for Ni-nano-Al_2O_3 composite coatings + 208 mV (SCE) (see Figure 4.71 d)). From these results it was clear that the stainless steel substrate was more corrosion resistant in chloride environment compared to the three different deposited films. Between the deposited coatings, the Ni-sub-micron-Al_2O_3 composite films presented better corrosion resistance in 0.1 M NaCl solution than pure Ni films and it was observed that the corrosion resistance decreased further if the sub-micron-Al_2O_3 was substituted with nano-Al_2O_3, as also observed by Lampke et al. [267] for Ni-TiO_2 composite films.

The corrosion resistance is strongly influenced by the microstructure of the films, e.g. grain size, surface morphology and texture [101, 266, 270, 271]; the three samples analysed presented the same grain size (see Table 4.15), but slightly different textures (see Table 4.14) and different surface morphology (strongly affected by the introduction of Al_2O_3 as described in section 4.5.3). The higher corrosion resistance of Ni-sub-micron-Al_2O_3 coatings compared to pure Ni coatings can be explained considering the lower metallic area exposed to the chloride solution in the composite [266, 271], and that the sub-micron-Al_2O_3 particles hinder the Ni dissolution and therefore the pit growth. This second explanation is further supported by the comparison between the pitting morphology of pure nickel (Figure 4.72 a)), which showed smooth rounded pits, and Ni-sub-micron-Al_2O_3 composites (Figure 4.72 b)), which were rough-edged indicating that the sub-micron-Al_2O_3 particles disrupted the dissolution pathway. When nano-Al_2O_3 particles were embedded in the Ni coating the corrosion resistance decreased compared to pure Ni probably because the contact area between the metal matrix and the chloride environment was not sufficiently reduced and the corrosion current was not uniformly distributed on the sample surface producing local corrosion, as proposed by Lampke et al. [266]. The edges of the pits in Ni-nano-Al_2O_3 composites (Figure 4.72 c)) were less smooth than those of pure Ni and less ragged than those in Ni-sub-micron-Al_2O_3 composites probably because the nano-Al_2O_3 particles were not big enough to prevent the pit expansion.

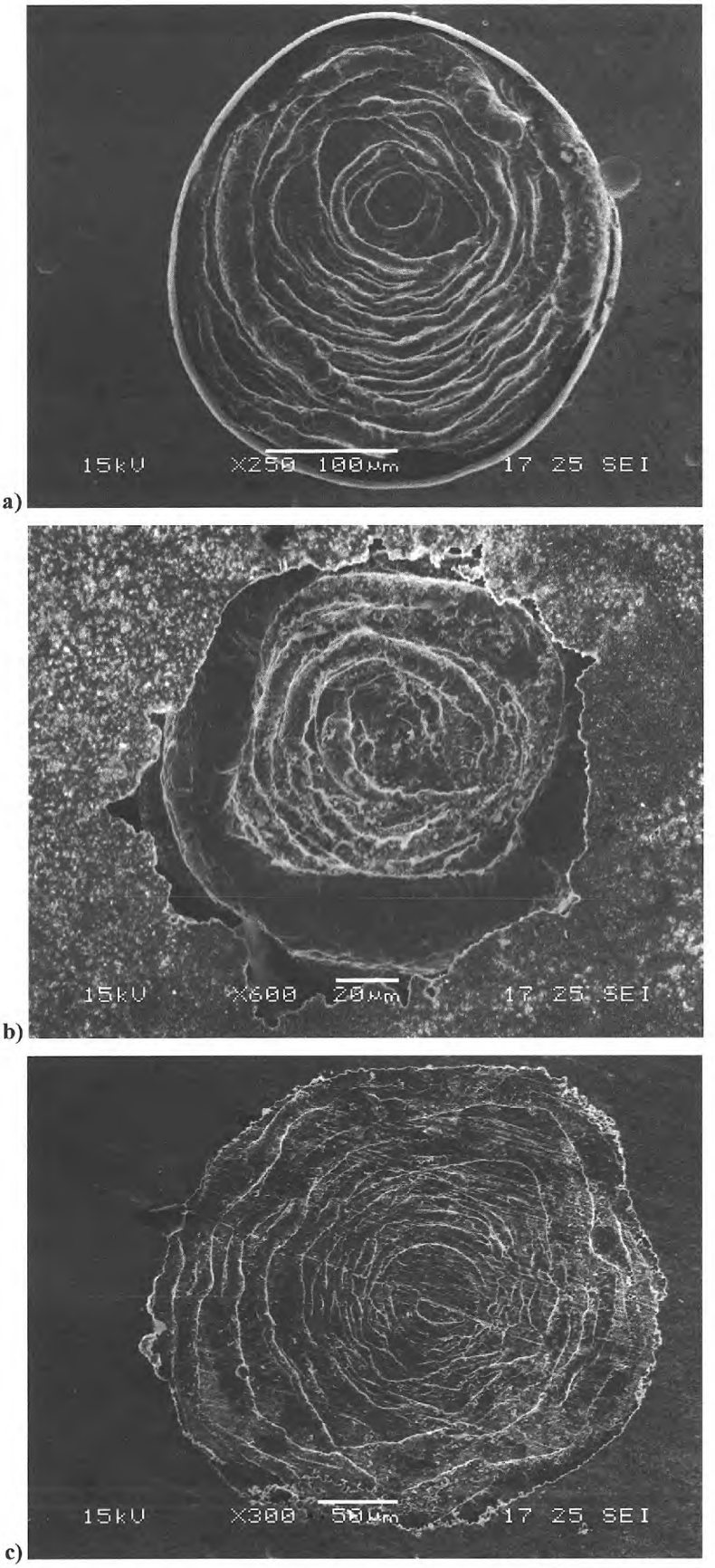


Figure 4.72 SEM micrographs of pitting corrosion on a) pure Ni films, b) Ni-sub-micron-Al_2O_3 and c) Ni-nano-Al_2O_3 films after the corrosion test carried out in 0.1 M NaCl solution.

The potentiodynamic polarisation curves carried out on stainless steel, pure nickel coatings and Ni-Al_2O_3 composite films in 0.1 M H_2SO_4 have been plotted as E vs Log (i) in Figure 4.73, commonly known as Tafel plot [242]. The advantage of this plot is that the potential at which the current density changes from negative to positive is clearly visible. Moreover, the corrosion current density (Icorr) and the corrosion potential (Ecorr) can be calculated from the intercept of the Tafel slopes to compare the corrosion rate and the corrosion potential of different materials. In this case the two lines have been drawn following the linear part of the curve. The part of the Tafel plot for potential E more positive than Ecorr describes the corrosion processes taking place at the working electrode (positive current density). In particular, the current increase is due to the metal dissolution (active region) and the following current decrease (passive region) is due to the formation of a passive layer on the metal that protects it from further corrosion.

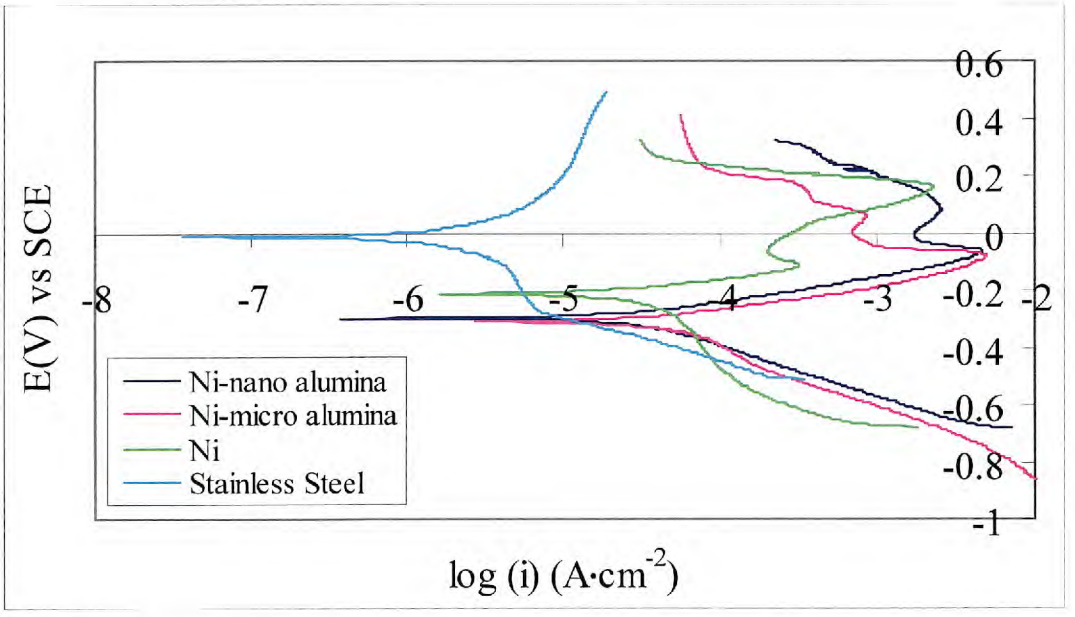


Figure 4.73 Polarisation curves of stainless steel, pure Ni films, Ni-sub-micron-Al_2O_3 and Ni-nano-Al_2O_3 films in 0.1 M H_2SO_4 solution.

Table 4.16 Electrochemical parameters obtained from the polarisation curves of stainless steel, pure Ni films, Ni-sub-micron-Al_2O_3 and Ni-nano-Al_2O_3 films in 0.1 M H_2SO_4 solution.

Sample	Icorr ($\mu A \cdot cm^{-2}$)	Ecorr (V)
Stainless steel	3.373	-0.150
Ni	34.32	-0.213
Ni-sub-micron-Al_2O_3	33.10	-0.311
Ni-nano-Al_2O_3	26.84	-0.298

Comparing the polarisation data (Figure 4.73) of the four materials in acid environment, it was clear that the corrosion rate of pure Ni and Ni-Al_2O_3 composite films containing both

sub-micron or nano-Al_2O_3 particles was higher than that of the stainless steel, and therefore the deposited coatings were less corrosion resistant than stainless steel in 0.1 M H_2SO_4 solution. The same conclusion could be also reached comparing the corrosion current densities (Icorr) and the corrosion potentials (Ecorr) (Table 4.16) of the four different materials (the deposited coatings presented more negative Ecorr and higher Icorr compared to the stainless steel). Icorr of the deposited films were all very similar, indicating similar corrosion rates in acid environment. Between the three films, pure Ni seemed to be the more corrosion resistant with higher Ecorr and lower energy needed to produce the oxide protective layer (this implies that if the coating breaks the construction of a passive film would be more difficult to obtain for the composites than for pure nickel). The two bumps observed in the Tafel plots of pure Ni and Ni-Al_2O_3 composites in the passive region are characteristic of the construction of a Ni passive film in two steps. The decrease of the corrosion resistance with the addition of particles can be explained considering that the solution can easily infiltrate at the interface metal/particle, as proposed in the literature [98, 271].

4.5.9 Tape test

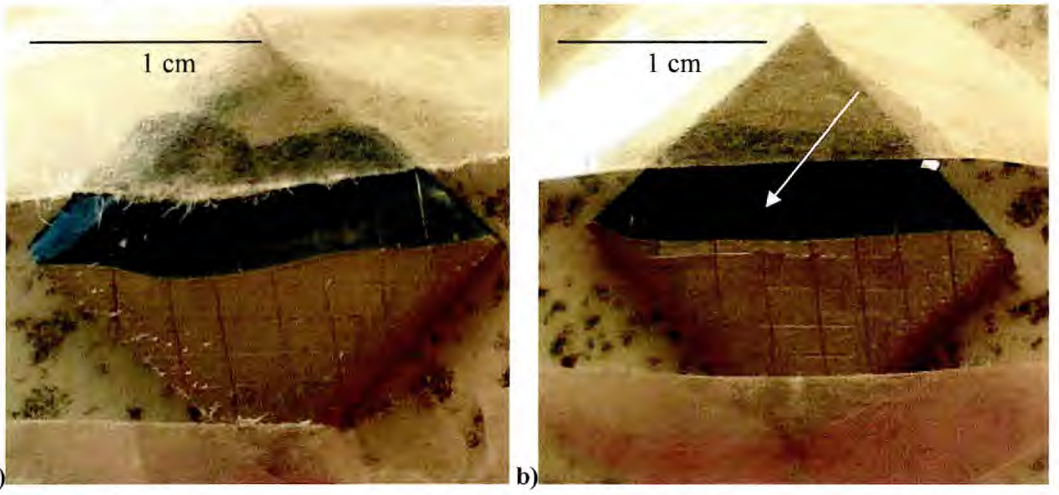


Figure 4.74 Images of nickel composite coatings deposited on stainless steel ground with 800 grit SiC paper after tape test a) 0% detachment and b) <5% detachment, as indicated by the arrow.

Coatings are normally deposited to protect or decorate the substrate and consequently a good adhesion between the substrate and the film is fundamental. The preparation of the substrate surface before Ni deposition was studied and optimized in section 4.3 and the same conditions were employed for all the following depositions. The substrate/coating adhesion has been qualitatively evaluated using the tape test standard method described in section 3.14 and already applied on pure Ni films in section 4.3.3. This method was carried out on three different samples: pure nickel deposited applying -20 $mA \cdot cm^{-2}$ and Ni-Al_2O_3 composite films deposited applying the same current density from solution containing 150 g/l of nano or sub-micron-Al_2O_3 particles, for the reasons already explained in section 4.5.8. These three coatings

were chosen to evaluate the influence of the different alumina powder on the adhesion of the coating to the substrate. Three samples for each composition were tested and compared with the illustrations reported in Table 3.2. The results are described below.

Most of the coatings analysed presented good adhesion with 0% of coating detachment (Figure 4.74 a)) apart from one film that slightly peeled off (< 5% detachment) in the area of the film close to the nail varnish (Figure 4.74 b)); similar behaviour was also observed when pure Ni films were analysed (see section 4.3.3). From this study it was concluded that the presence of alumina in the composites did not influence the substrate/coating adhesion and that good adhesion was achievable with this method.

4.6 Electro co-deposition of nickel-aluminium composite coatings

The deposition of Ni-Al composite coatings has been also carried out in this research, mainly to establish the differences in the incorporation behaviour of conductive (Al) and non-conductive (Al_2O_3) particles into nickel films.

4.6.1 Characterizations of the aluminium powder

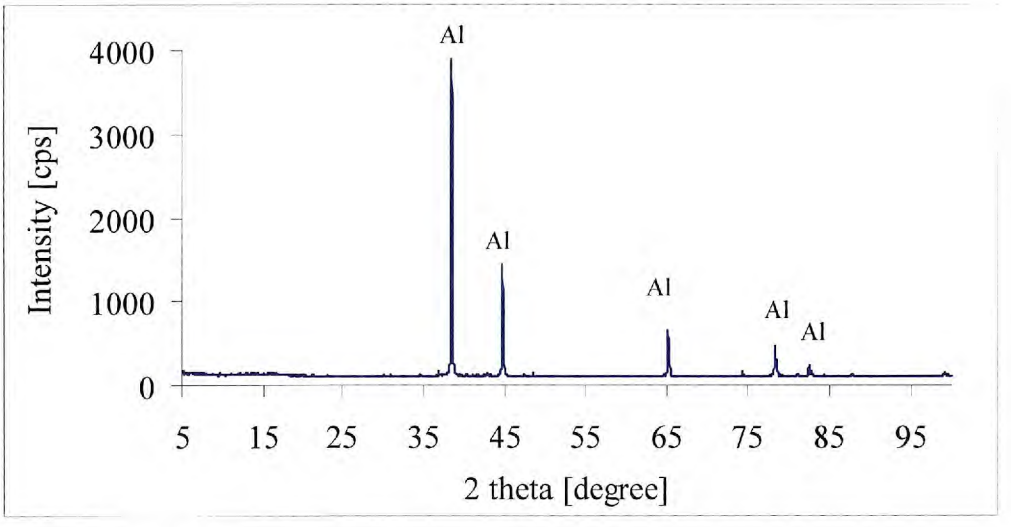


Figure 4.75 XRD analysis of the Al powder.

The Al powder employed to deposit Ni-Al composite coatings consisted of particles that were < 25 μm (according to the manufacturer). The XRD analysis (Figure 4.75) of this powder proved that it was Al (PDF 4-0787) and the SEM analysis reported in Figure 4.76 showed that the particles were slightly oblong with different shapes and sizes varying between 2 and 30 μm.

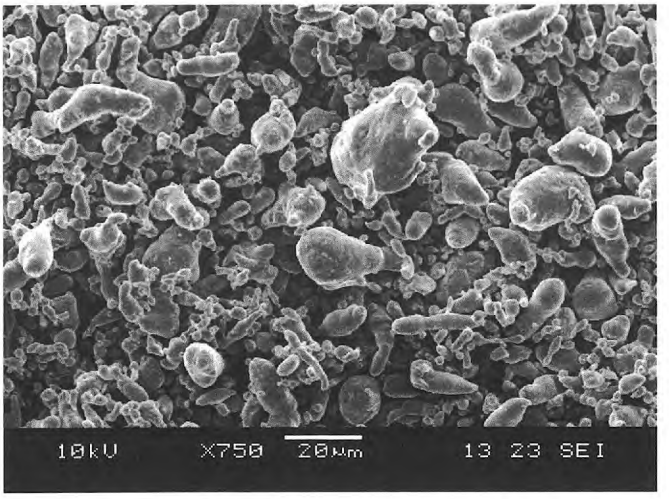
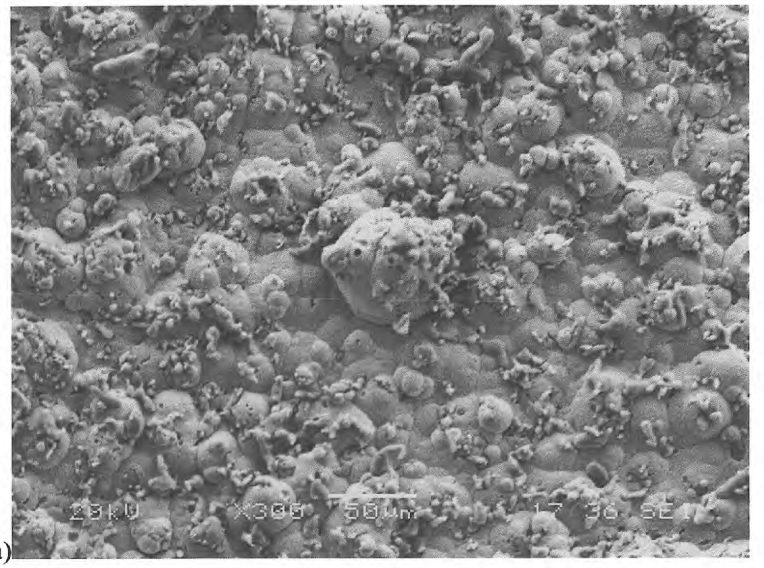


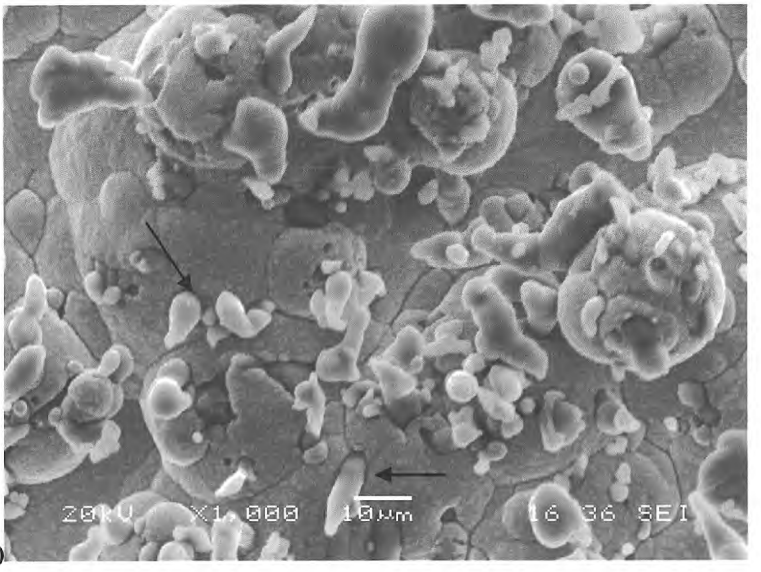
Figure 4.76 SEM image of Al particles used for the co-deposition of Ni-Al composite coatings showing their shape and size.

4.6.2 Microstructure of Ni-Al composite coatings

a)



b)



c)

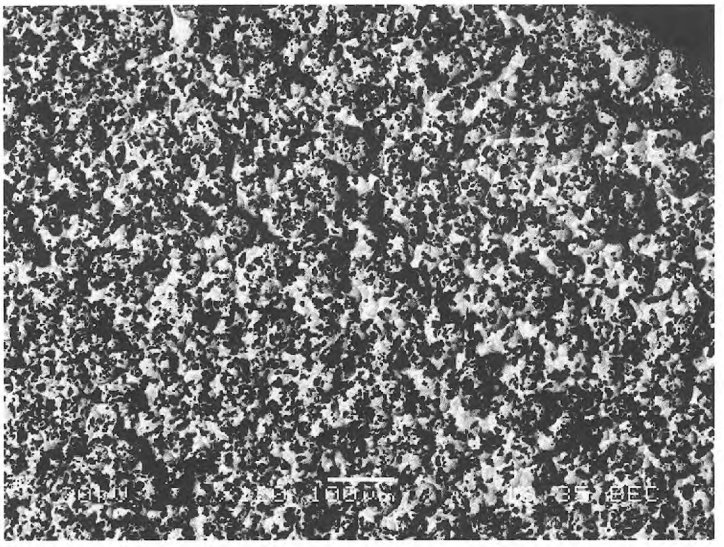


Figure 4.77 a) low magnification, b) high magnification and c) back scattered (lighter phase is Ni and the darker one is Al) SEM images of a Ni-Al composite coatings deposited applying a current of -32 mA·cm^{-2} from a nickel sulphate bath containing 100 g/l of Al particles. The arrows in b) show Al particles partially embedded in the Ni film.

Ni-Al composite coatings were successfully deposited applying a current density of -32 mA·cm^{-2} for 30 min from a nickel plating bath containing 100 g/l of Al particles. The top morphology of a Ni-Al composite is shown in Figure 4.77. The slightly oblong Al particles are clearly visible on the surface of the film (Fig. 4.77 a) and b)) and some of them are partially embedded in the Ni layer (see arrows in Fig. 4.77 b)). The back scattered low magnification image in Figure 4.77 c) demonstrates that the Al particles were uniformly distributed into the composite film.

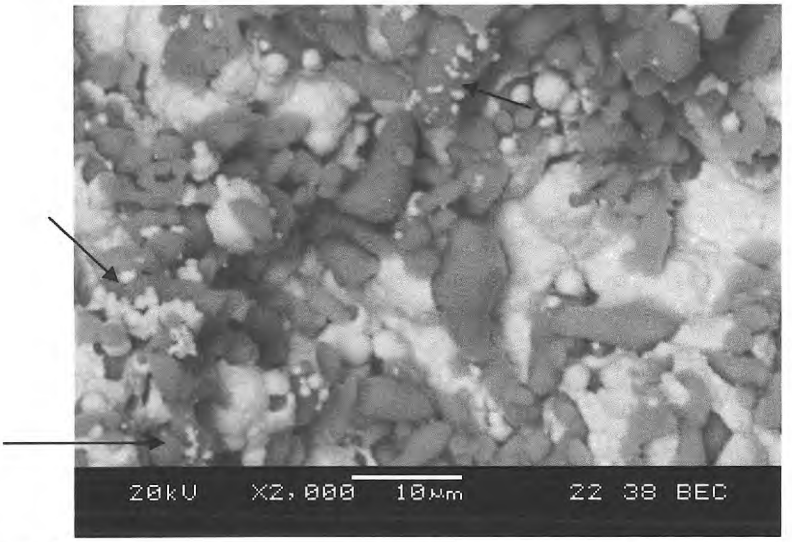


Figure 4.78 SEM back scattered images of a Ni-Al coating deposited applying a current density of -32 mA·cm^{-2} from a nickel sulphate bath containing 100 g/l of Al particles.

The main difference between the incorporation of conductive (Al) or non conductive (Al_2O_3) particles into the Ni matrix by electro co-deposition is the different growth of the metal around the particles. In fact, it has been mentioned in section 4.5.3 that the Al_2O_3 particles were still clearly visible on the top of the coating (Figures 4.49 b) and c), 4.50 and 4.51) since the Ni could not directly grow on them but just around them. Conversely, when Al particles were embedded in the composite the Ni deposition could take place also on them as if the particles were part of the electrode [49, 64] (white dots indicated by the arrows in Figure 4.78). Similar results were also reported by Naploszek-Bilnik et al. [59] and reproduced for comparison in Figure 4.79.

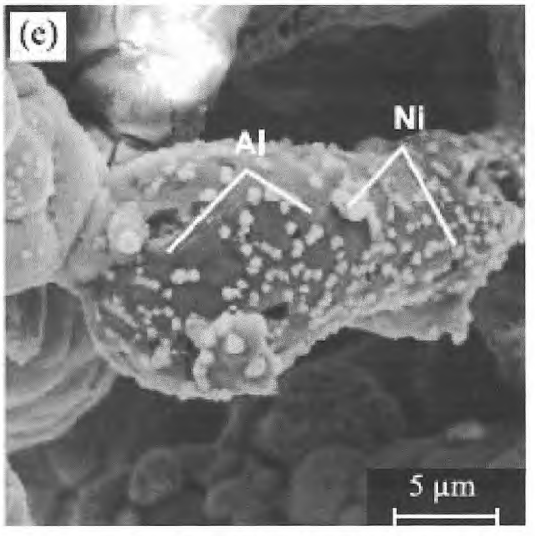


Figure 4.79 Surface morphology of a Ni-Al film deposited applying a current density of 450 $mA \cdot cm^{-2}$ from a nickel sulphamate bath containing 120 g/l of Al powder showing white Ni growth on an Al particle (reproduced from ref. [59]).

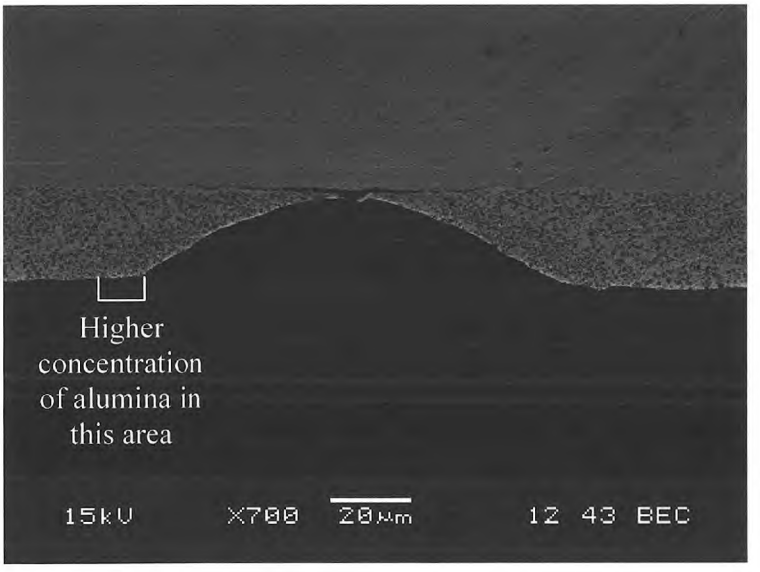
4.7 Electro co-deposition mechanism

The electro co-deposition mechanism is still not completely understood but some models have been suggested in the last few decades and were summarised in section 2.2.3 [15, 16, 58]. The common base of all the proposed models is that the particles reach the cathode by electrophoresis or by bath agitation and then they are mechanically entrapped or incorporated into the growing metal film. It has also been proposed in the literature that, in order to have incorporation of the particles into the film, the particle adsorption on the cathode surface and the reduction of the metal ions adsorbed on the particle surface are fundamental [15, 16, 58, 65, 69, 71]; these latter mechanisms are difficult to prove and support experimentally.

The experiments described in sections 4.5 and 4.6 demonstrated that both Al and Al_2O_3 particles were successfully incorporated into the Ni film. Considering that the electric field involved during the electro co-deposition (< 1 $V \cdot cm^{-1}$) is much smaller than that employed in EPD (10-100 $V \cdot cm^{-1}$) (see section 2.3) it can be suggested that bath agitation is the main factor

to keep the particles suspended and to transport the particles from the bulk of the solution to the cathode surface, as also proposed by Bazzard and Boden [65]. This hypothesis is supported by the different particle distributions observed between the two sides of the cathode, largely discussed in section 4.5.3, and also by the higher particle distribution observed around the pits left by the hydrogen bubbles and shown in Figure 4.80 for Ni-sub-micron-Al_2O_3 and in Figure 4.81 for Ni-Al composites. The cross section image in Figure 4.80 a) and the top surface in Figure 4.80 b) clearly show that in the part of the film around the hole left by the hydrogen bubble the concentration of co-deposited Al_2O_3 was higher than in the rest of the film. This behaviour can be explained considering that the Al_2O_3 particles brought to the cathode surface by bath agitation were stopped by the growing hydrogen bubble and trapped between the substrate and the bubble. In this portion of interface there was accumulation of Al_2O_3 particles resulting in a higher concentration of Al_2O_3 than in other parts of the interface. Similar behaviour was also observed for Ni-Al composite systems, as reported in Figure 4.81. From these findings it is clear that the bath agitation plays a fundamental role in electro co-deposition.

Figure 4.77 b) clearly shows that some Al particles were partially embedded in the Ni layer (see arrows) and not completely covered by Ni (see Figure 4.77). The same behaviour was also observed for Al_2O_3 particles (Figures 4.49-4.51), but since these particles were much smaller than the Al particles (< 1 μm vs < 25 μm) this structure was less evident. Furthermore, it is shown in Figure 4.78 that the nickel deposition could start on the Al particles already embedded in the film (white dots indicated by the arrows), in agreement with the model proposed by Buelens and Celis [15, 16, 64] and described in section 2.3.3, even though more studies are needed to prove the reliability of this model. Since the reduction of the adsorbed ions is only possible on the conductive Al particles and not on Al_2O_3 particles this phenomenon cannot describe the main mechanism of the co-deposition process.



a)

b)

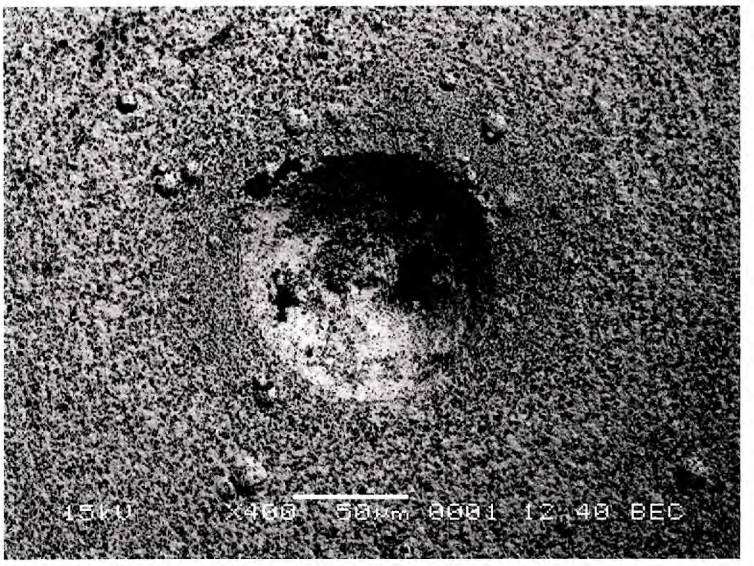


Figure 4.80 Back scattered SEM micrographs of a) the cross section of a hydrogen pit in a Ni-sub-micron-Al_2O_3 coating deposited from a solution containing 100 g/l of sub-micron-Al_2O_3 applying -20 mA·cm^{-2}, b) the Al_2O_3 distribution around a hydrogen pit in a Ni-sub-micron-Al_2O_3 coating deposited from a solution containing 50 g/l of sub-micron-Al_2O_3 applying -10 mA·cm^{-2}

Summarising, in order to have electro co-deposition the second phase needs to reach the electrode surface and then the amount of particles embedded depends on the metal deposition rate (current density) and on the number of collisions between the particles and the cathode surface. This second parameter is mainly influenced by the particle concentration in suspension and by bath agitation, as already discussed in section 4.5.5.

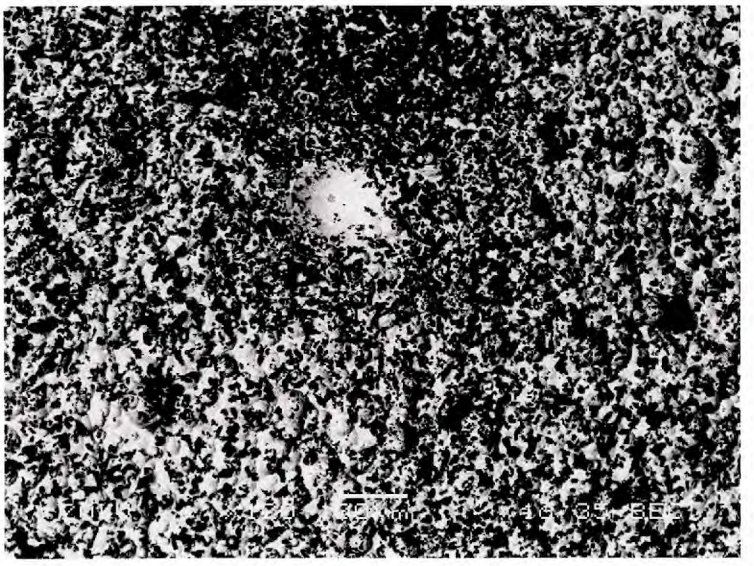


Figure 4.81 SEM back scattered micrograph showing the Al distribution around a hydrogen pit in a Ni-Al coating deposited from a solution containing 100 g/l of Al powder applying -32 mA·cm^{-2}.

4.8 Summary

This chapter presented the work carried out for the deposition of nickel composite coatings on stainless steel substrate. The preparation of the substrate surface before deposition was fundamental to achieve good substrate/coating adhesion. The mechanical treatment increased the substrate surface roughness, which was considered to be the reason for an improved substrate/coating adhesion due to an interlocking mechanism between the two materials. Ultrasonically cleaning in acetone effectively removed grease, oil and eventual particles from the surface assuring the production of sharp, uniform and well defined interfaces.

Nano-crystalline Ni coatings were successfully deposited galvanostatically from a nickel sulphate plating bath at room temperature. The optimised conditions employed for the nickel deposition were successfully applied to co-deposit both Al and Al_2O_3 particles in the films. The distribution and concentration of Al_2O_3 particles in the coatings depended on the solution hydrodynamics and on the conditions employed (particle concentration in the bath, particle size and current density). The amount of Al_2O_3 co-deposited in the films increased with the particle concentration in the bath and strongly depended on the metal growing rate, the flux of particles at the cathode, their residence time at the metal/solution interface and their size. The addition of Al_2O_3 influenced both the microstructure and the crystallinity of the nickel matrix and resulted in an increase in micro-hardness. The pure nickel and Ni-Al_2O_3 composite films resulted less corrosion resistance than stainless steel in both chloride and acid environment. In chloride environment the Ni-sub-micron-Al_2O_3 composite films presented better corrosion resistance than pure Ni and Ni-nano-Al_2O_3 films.

5. Electrophoretic deposition of PEEK-nano-Al_2O_3 composite coatings

The aim of this part of the project is to investigate the deposition of polyetheretherketone (PEEK)-Al_2O_3 composite coatings on stainless steel AISI 316L substrates by electrophoretic deposition (EPD). Up to date the production of PEEK-Al_2O_3 composite coatings has not been investigated by either EPD or other techniques, but from studies on PEEK-Al_2O_3 composite bulk materials it is known that the composite has lower wear coefficient [24, 29], higher hardness, elastic modulus and tensile strength [26] than pure PEEK and that the addition of Al_2O_3 increases the thermal stability of PEEK rendering the composite a promising material for high-temperature applications [3, 25-28]. The results obtained applying the characterization techniques presented in chapter 3 are presented and discussed after the materials and methods sections.

5.1 Materials

The materials employed for this part of the work were nano-γ-Al_2O_3 powder (544833) with particle size of ~50 nm and surface area between 35 and 43 $m^2 \cdot g^{-1}$ purchased from Sigma Aldrich (Gillingham, UK) (henceforth referred to as "nano-Al_2O_3") and PEEK powder (Victrex® PEEK 150XF) purchased from Victrex® Manufacturing Ltd. (South Yorkshire, UK) with particle size <25 μm. The suspension media employed to prepare all the suspensions was ethanol with purity of 99.7-100% (VWR International Ltd., Lutterworth, UK). EPD was carried out on stainless steel AISI 316L (Fe/Cr18/Ni10/Mo3) foils with thickness of 0.2 or 2.0 mm obtained from Advent Research Materials Ltd. (Oxford, UK). These substrates were cut by a guillotine into 1.0 cm x 1.0 cm pieces. These pieces were used as electrodes, both cathode and anode, in the EPD cell. The electrodes were thoroughly ultrasonically cleaned in acetone (BHD Laboratory supplies, Poole, UK) for 5 min before EPD.

5.2 Instruments and methods

An electronic balance HR-120-EC from A&D Instruments Ltd. (Abingdon, UK) with a readability of 0.0001 g was used to weigh the components of the suspensions and the substrates before and after deposition. An ultrasonic bath USC300D VWR International (Leuven, Belgium) was employed to clean the substrate surfaces before EPD and to sonicate all the suspensions for 30 min in order to disperse the particles and break up any possible solid agglomerates. A Fisher Scientific (Loughborough, UK) magnetic stirrer (60-1200 rpm) was used to mix the suspension before each deposition and a Jenway 3510 pH meter (Jenway, Essex UK) to measure the suspension pH.

All the experiments for the electrophoretic deposition of PEEK, nano-Al_2O_3 and PEEK-nano-Al_2O_3 coatings were carried out using the experimental set up shown in Figure 5.1. The EPD cell consisted of a 100 ml plastic jar containing 50 ml of suspension and two electrodes. The substrate was always a flat and square (1.0 cm x 1.0 cm) stainless steel piece, whereas the counter-electrode was flat and square shaped in the parallel configuration or a 2.0 cm radius cylinder made of stainless steel in the circular configuration (as shown in Figure 5.2). Before deposition the electrodes were ultrasonically cleaned in acetone for 5 min in order to eliminate grease from the surface. The electrodes were inserted in the cell by holding them with two conductive clips fixed to two copper bars. The two copper bars were kept still and in a precise position by a holder in order to maintain the electrodes at a constant distance and parallel to each other during the experiments. Before EPD, the electrodes were thoroughly immersed in the suspension avoiding any clip-suspension contact to prevent contamination. The electrode alignment and the distance between them were accurately checked and measured before each experiment.

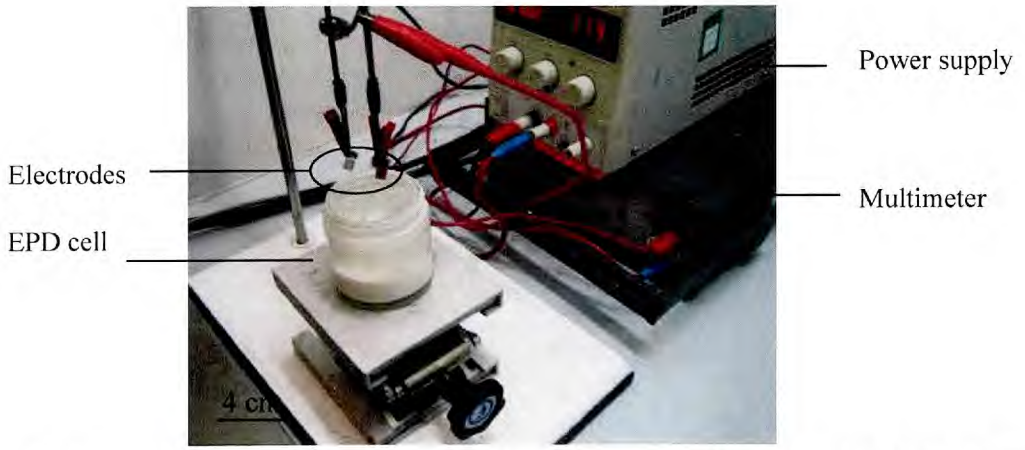
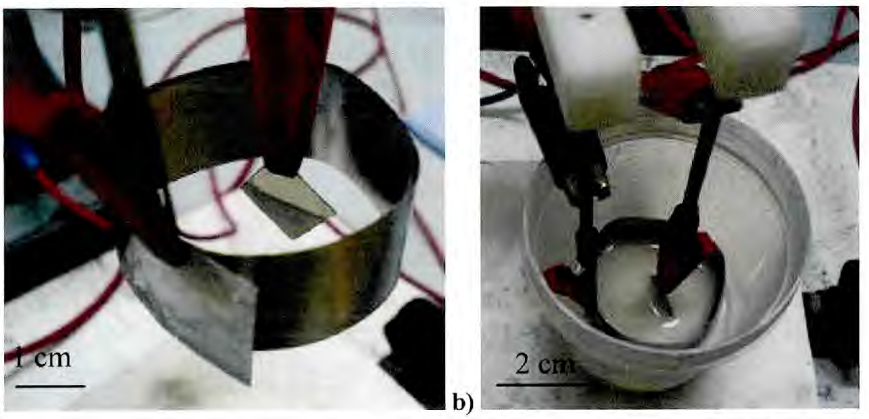


Figure 5.1 Image of the experimental set up employed to perform electrophoretic deposition in parallel configuration.



a) **b)**

Figure 5.2 Images of the cylindrical configuration employed in some of the EPD experiments, a) out of the cell and b) immersed in the suspension.

The experiments were carried out employing a TT*i* EL561 power supply (Thurlby Thandar Instrument, Huntingdon, UK) connected to a TT*i* 1906 computing multimeter (Thurlby Thandar Instrument, Huntingdon, UK). The power supply was connected to one of the copper bars of the cell directly through a cable and to the other one through the multimeter originating a series arrangement. The system was so connected in order to transmit a constant potential to the two electrodes and to know their respective charges to distinguish the cathode (negative electrode) from the anode (positive electrode). In addition the multimeter was connected to a computer to record the variation of current intensity during EPD. The accuracy of the multimeter is 0.08 % + 12d (where d is digits). For example, the error on a current of 0.061 μA was (0.061 x 0.08% + 0.012) μA (=0.016 μA).

All EPD experiments were conducted applying a constant difference of potential between the two electrodes, which were kept at a constant known fixed distance during the process, in order to produce a constant and known electric field. The distance between the electrodes is not a fundamental variable in EPD, but it is strictly correlated to the potential difference applied. In fact ΔV between the two electrodes is given by:

$$\Delta V = \Delta V_{anode} + \Delta V_{cathode} + \Delta V_{suspension} \quad [5.1]$$

where ΔV_{anode} and $\Delta V_{cathode}$ are the potential differences of the two interfaces metal/suspension and $\Delta V_{suspension}$ is the potential difference of the bulk of the suspension. The contributions of ΔV_{anode} and $\Delta V_{cathode}$ can be considered constant because the interfaces do not change during the experiments. While $\Delta V_{suspension}$ strongly depends on the resistance R of the suspension, which is expressed by:

$$R = \rho \cdot l / A \quad [5.2]$$

where ρ [Ω·cm] is the resistivity, l [cm] the length of the path (distance between the two electrodes) and A [cm^2] the cross section of the suspension (cross section of the two electrodes in the suspension). In this system, ρ and A are constant and therefore ΔV depends just on the distance l between anode and cathode.

In the present study 50 ml suspension were employed at room temperature for a total deposition time of 150 min, independently of the duration of each individual deposition, because the composition could have considerably changed due to the evaporation of the ethanol and to the loss of the deposited powder. After the deposition the samples were dried at room temperature in the laboratory or in a desiccator (just the nano-Al_2O_3 samples) for 24 h.

As described in section 2.3.1, the coatings deposited by EPD usually require a suitable heat-treatment after the deposition to further densify the deposit and to increase its adhesion to the substrate. This treatment on PEEK and PEEK-nano-Al_2O_3 coatings was carried out using a heating rate of $10°C \cdot min^{-1}$ in an electric ashing furnace from Carbolite (Chelmsford, England). The same furnace was also employed to determine the weight ratio of PEEK and nano-Al_2O_3 in coatings deposited applying different conditions. This study was carried out weighing around 20 mg of powder obtained from four coatings deposited in the same conditions before and after

a heat-treatment at 700°C with a heating rate of $10°C \cdot min^{-1}$, that completely burn out the PEEK powder and leaves just nano-Al_2O_3 in the platinum container.

5.3 Deposition of PEEK coatings

5.3.1 Characterisation of the PEEK powder

i) SEM analysis

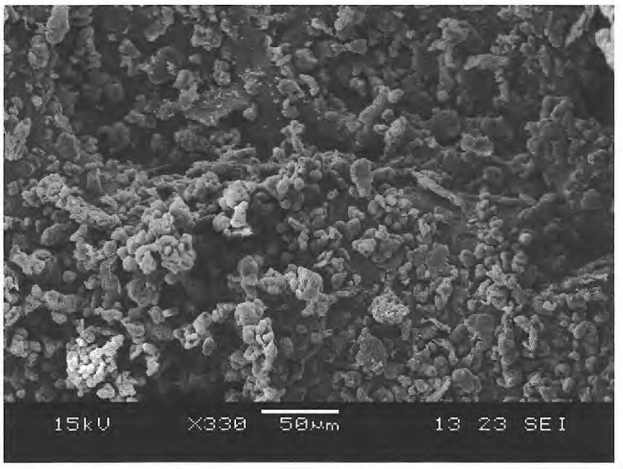


Figure 5.3 SEM image showing the morphology and size of the PEEK particles.

The morphology and size of the PEEK particles employed are shown in Figure 5.3. The particles present a size range between 5 and 45 µm and different shapes, some are flatter and some more oblong than others. The powder was used in the as-received condition for this investigation.

ii) Particle size distribution

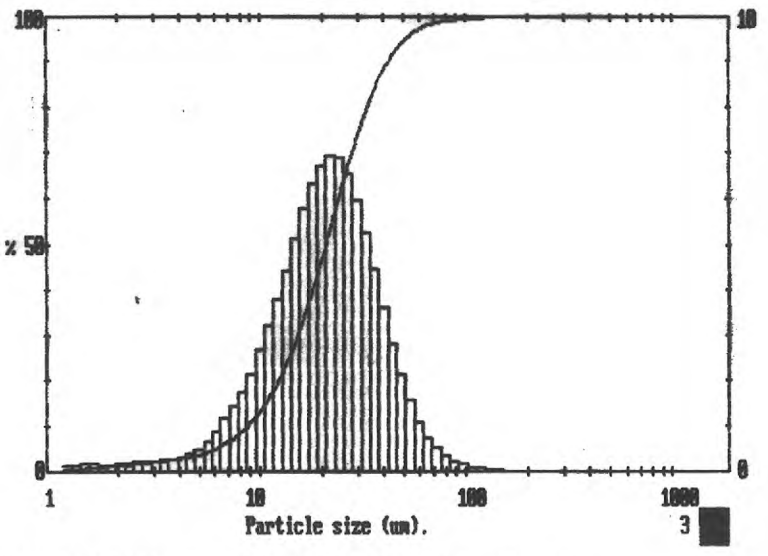


Figure 5.4 Particle size distribution of the PEEK powder in ethanol.

Table 5.1 Data for the particle size distribution of the PEEK powder in ethanol.

High Size	Under %	High Size	Under %	High Size	Under %	High Size	Under %	High Size	Under %	High Size	Under %	
600	100	203	100	68.5	98.4	23.1	57.1	7.82	8.1	2.64	1.8	D[4,3]
544	100	184	100	62.1	97.7	21.0	50.2	7.08	6.6	2.39	1.6	23.88 μm
493	100	166	100	56.2	96.5	19.0	43.5	6.42	5.5	2.17	1.4	D[3,2]
446	100	151	100	50.9	94.9	17.2	37.1	5.82	4.6	1.97	1.2	13.88 μm
404	100	137	99.9	46.2	92.8	15.6	31.3	5.27	3.9	1.78	1.1	D[v,0.9]
366	100	124	99.9	41.8	89.9	14.1	26.2	4.77	3.4	1.61	0.9	41.92 μm
332	100	112	99.8	37.9	86.3	12.8	21.7	4.33	3.0	1.46	0.8	D[v,0.1]
301	100	102	99.7	34.3	81.8	11.6	17.9	3.92	2.7	1.32	0.6	8.70 μm
273	100	92.1	99.6	31.1	76.5	10.5	14.7	3.55	2.5	1.20	0.4	D[v,0.5]
247	100	83.4	99.3	28.2	70.6	9.52	12.0	3.22	2.2			20.92 μm
224	100	75.6	99.0	25.5	64.0	8.63	9.8	2.92	2.0			

The PEEK particle size in ethanol suspension containing 3 wt.% of powder was determined using a Low Angle Laser Light Scattering technique (see section 3.9) based on the fact that the diffraction angle is inversely proportional to the particle size [259]. The results obtained are shown in Figure 5.4 and listed in Table 5.1. The majority of the PEEK particles were between 10 and 40 μm with a D_{50} (average particle size) of 20.92 μm; this range is in agreement with the SEM analysis reported in Fig. 5.3. Moreover, the particle size measurement in Figure 5.4 showed that some PEEK particles were < 150 μm; this result is in contrast with the SEM analysis and can be explained considering particle agglomerations in suspension.

iii) XRD analysis

The PEEK powder as received was semi crystalline, as shown in the XRD analysis reported in Figure 5.5; this result is in agreement with the XRD spectra shown for PEEK Victrex in previous investigations [26, 192, 201, 208].

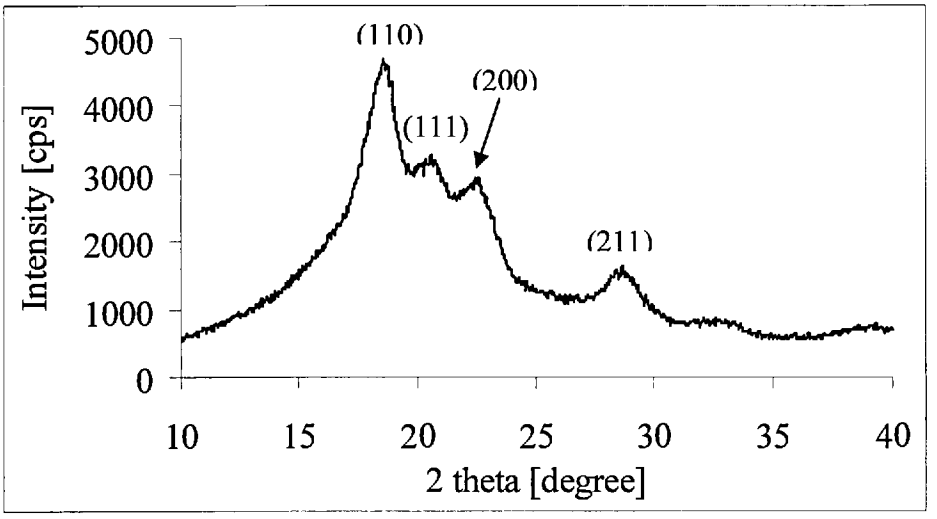


Figure 5.5 XRD analysis showing the crystallinity of the PEEK powder as received.

iv) TGA and DTA analysis

The thermal gravimetric analysis of the PEEK powder shown in Figure 5.6 provides information on the PEEK thermal stability as a function of the temperature. The TGA graph (Figure 5.6) obtained applying a heating rate of 10°C·min^{-1} shows that the PEEK powder is considerably stable at temperatures below 550°C. At this temperature the PEEK powder started to burn out and consequently the weight started to decrease. At 650°C the material was completely decomposed.

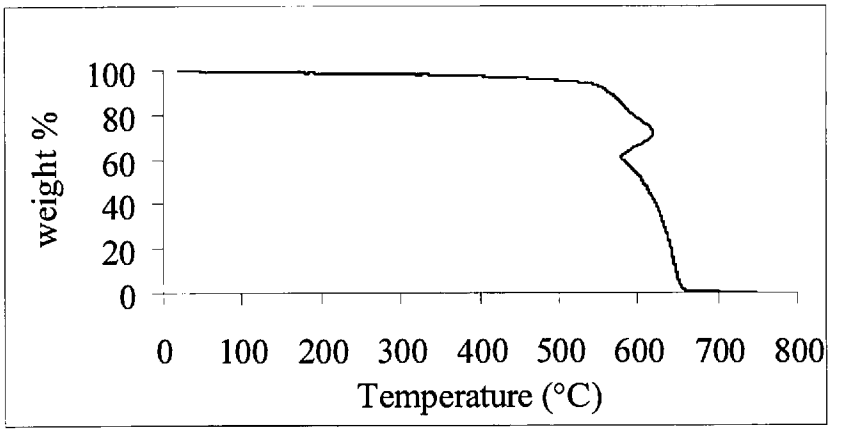
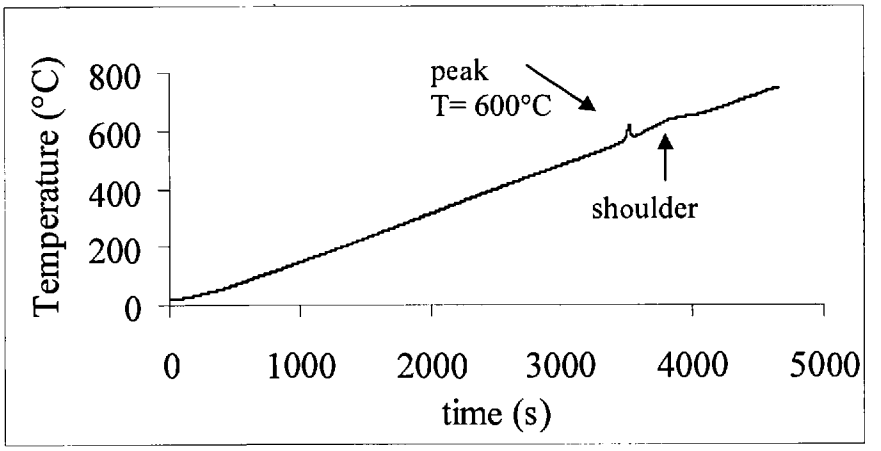


Figure 5.6 Change in weight of the PEEK sample with the increase of temperature (TGA) at heating rate of 10°C·min^{-1}.

It could be observed that even if constant heating rate of 10°C·min^{-1} was applied the increase in temperature during the experiment was not linear (10°C·min^{-1}), in fact an exothermic peak and a shoulder are visible in Figure 5.7 a) at around 600°C and they are probably due to two considerably exothermic reactions of decomposition of the polymer. The effect of these two exothermic reactions is also shown by the two exothermic peaks in Figure 5.7 b). Moreover, in the DTA graph shown in Figure 5.7 c) it can be seen an endothermic peak between 320°C and 360°C that correspond to the melting of the PEEK powder. This temperature is in agreement with the value of 343°C reported in the literature [6-9, 187-190] and by the manufacturer [221].

a)



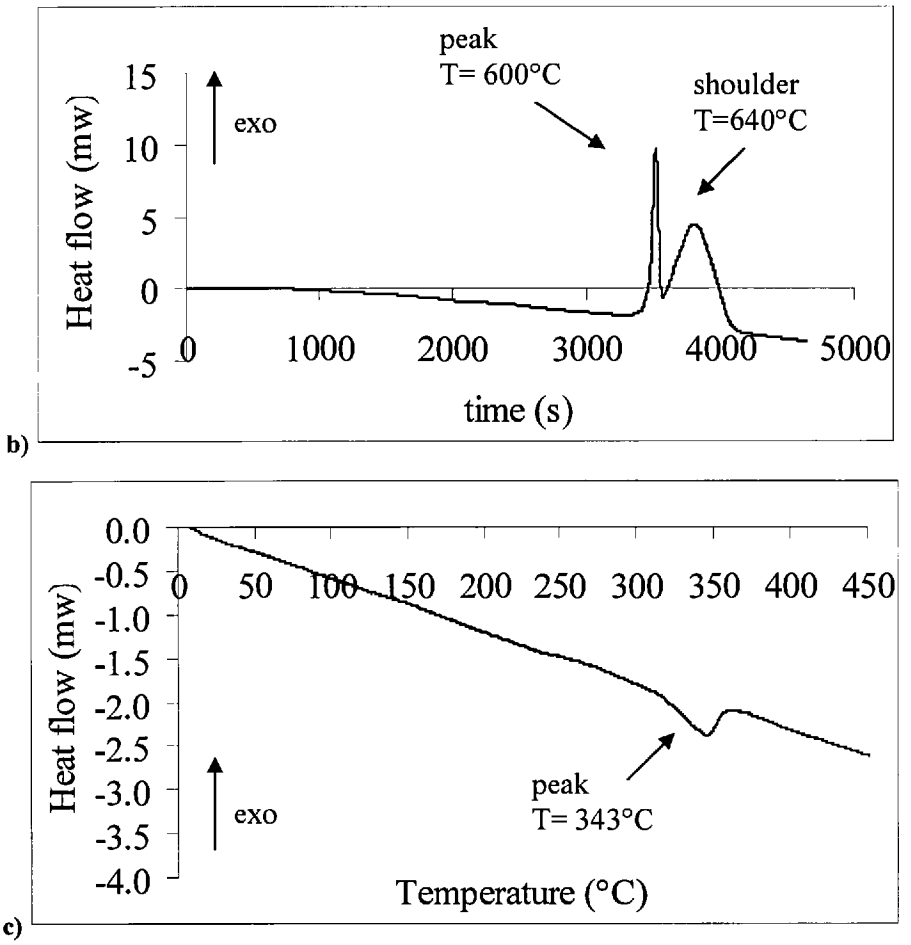


Figure 5.7 a) Temperature vs time, b) Heat flow vs time and c) Heat flow vs temperature graphs obtained from DTA of PEEK powder with at heating rate of 10°C·min^{-1}.

v) DSC analysis

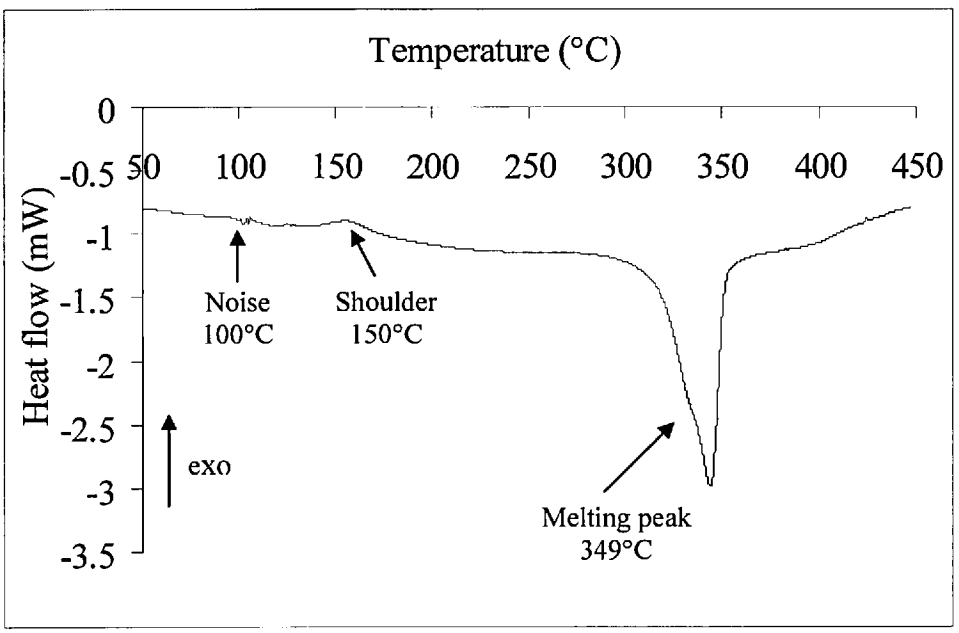


Figure 5.8 DSC analysis of the pure PEEK powder.

Figure 5.8 shows the DSC analysis of pure PEEK powder. At around 100°C there was some noise that was not observed in samples with different amounts of PEEK (see section 5.5.8) and at around 150°C there was a shoulder that could probably be the PEEK glass transition temperature, as also reported by Simonin and Liao [10] on Victrex® PEEK powder and by Bas et al. [273] on PEEK powder produced by a different manufacturer. The main peak shown by this analysis was the distinct melting endothermic peak at 349°C in the same range of temperature of the one obtained from the DTA analysis (Figure 5.7 c)). The starting material was semi-crystalline, as shown in Figure 5.5, and no crystallization exothermic peaks were observed during heating, as also reported by Simonin and Liao [10].

The heat of fusion of PEEK powder, calculated from the area of the melting peak, was 58.88 $J \cdot g^{-1}$. It is known from the literature [274, 275], that the % of crystallinity of a polymer can be estimated from the DSC analysis knowing the enthalpy of melting of the sample and that of the 100% pure crystalline polymer and assuming a crystalline/amorphous behaviour of the polymer. Knowing that the heat of fusion of 100% pure crystalline PEEK is 130 $J \cdot g^{-1}$ [10, 26, 205] it was possible to estimate the degree of crystallinity of the as received powder to be 45% [274, 275].

vi) Zeta potential analysis

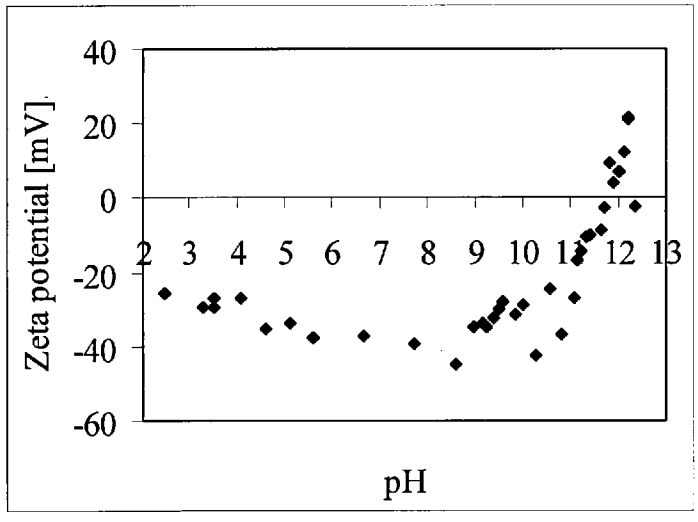


Figure 5.9 Zeta potential vs pH of a 3 wt.% PEEK suspension in ethanol.

The variation of the zeta potential with the "operational" pH for a 3 wt.% PEEK suspension in ethanol was measured as described in section 3.10 and it is shown in Figure 5.9. Figure 5.9 shows that the PEEK particles in ethanol present a negative zeta potential between pH 2 and 12 with the higher zeta potential of -40 mV at around pH 8, which is the pH of the suspension in as prepared conditions. The isoelectric point was around pH 12 and the conductivity of the as prepared suspension was 9 $\mu S \cdot cm^{-1}$.

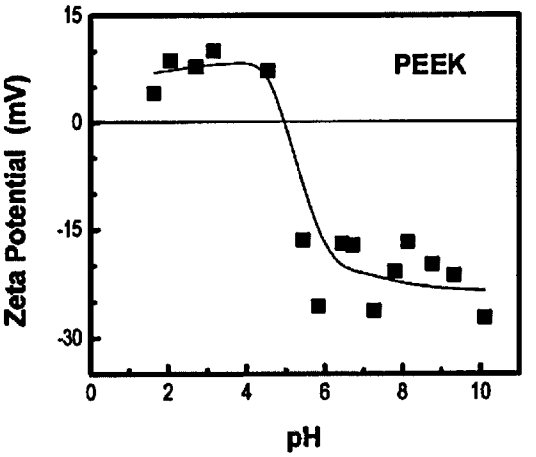


Figure 5.10 Zeta potential of a PEEK suspension in ethanol as published by Wang et al. [187].

It has to be underlined that the zeta potential values obtained in this study were remarkably different from those reported in the literature by Wang et al. [187, 189] and shown in Figure 5.10. In fact for Wang et al. [187, 189] the isoelectric point is at pH 5 instead of pH 12 and the zeta potential is positive at pH < 5 instead of being negative as emerged from this study (Figure 5.9). This difference can be probably due to the different instruments employed; in fact the Zeta Plus (Brookhaven Instrument Corporation) employed by Wang et al. [187, 189] utilizes a laser to measure the zeta potential and therefore the suspension analysed must be at least 20 times more dilute that the one analysed in this research (see section 3.10).

However, even if the zeta potential trends in Figure 5.9 and Figure 5.10 are remarkably different, both sets of data present the higher negative zeta potential occurring at an operational pH of 8, which is the pH employed for the deposition of PEEK in this research and by Wang et al. [189]. Considering the difficulties in measuring the pH in ethanol (e.g. pH is a measure of the acidity in aqueous media and therefore it loses its validity for non aqueous media [20, 184]), the possibility of using the suspension in as prepared condition is also an advantage not needing to change the pH adding hydrochloric acid, as described by Wang et al. [187] and Boccaccini et al. [188].

5.3.2 EPD parameters for PEEK deposition

Initially ethanol was chosen as a suspension media to electrophoretically deposit PEEK coatings following the results reported in the literature by Wang et al. [187, 189] and Boccaccini et al. [188] and described in section 2.3.6.2. It seemed from the literature that the main effect contributing to the stability of polymeric suspensions in ethanol was the steric effect between the loose polymer chains extending out of the polymer particles. To achieve a well dispersed suspension the polymer chains should be in an extended configuration to produce steric repulsions when the chains interact [189].

Subsequently, from the measurements reported in Figure 5.9, it was clear that ethanol would have been a good suspension media considering that at pH around 8 the suspension

presented low conductivity and high zeta potential, both essential prerequisites for stable suspensions. The suspension at pH 8 was also employed for EPD by Ma et al. [189], whereas Wang et al. [187] and Boccaccini et al. [188] used the suspension at pH 5.5.

Considering that the particles presented a high negative charge at pH 8 (Figure 5.9) the deposition was expected to occur on the positive electrode. In order to optimize the EPD of PEEK particles a test matrix for a range of variables (deposition time, suspension concentration, difference of potential, distance between the electrodes and electrode configuration) was designed (Table 5.2). The parameters in Table 5.2 were systematically varied in wide ranges and their influence on the deposit quality was comprehensively studied to optimize the EPD conditions, as discussed below.

Table 5.2 Summary of the parameters investigated and the ranges in which they have been varied for EPD of PEEK particles.

Parameters	Range
Suspension concentration	1, 3, 4, 5, 6 wt.%
Deposition time	30 s to 10 min
Difference of potential applied	6 to 56 V
Distance between the electrodes	0.8 to 2.0 cm
Electrode configurations	Parallel electrodes and circular configuration

i) Deposition time

The first experiments were carried out for less than 3 min because it was observed that very shortly after the stirring was stopped (< 2 min) most PEEK particles in suspension started to settle (Figure 5.11). In order to counteract the sedimentation, some experiments were carried out while magnetic stirring the suspension but no deposition was observed even when a very slow stirring rate was employed. This behaviour was explained considering that stirring generates a flow in the liquid that can interact with the movement of the particles under the electric field influence.

Therefore, in order to obtain relatively thick films in a short deposition time, it was necessary to apply high electric fields or to use highly concentrated suspensions. Some experiments were carried out using a 6 wt.% suspension and applying 40 V between two parallel electrodes at 2 cm distance, but in this case the films were deposited mainly on the edges of the substrate, as shown in Figure 5.12. These results demonstrated that the particles were highly charged in the suspension, in agreement with the zeta potential measurements shown in Figure 5.9, but it was also apparent that the electric field was higher on the substrate edges than in the centre, as also demonstrated by the studies reported by Kurnosov et al. [276].

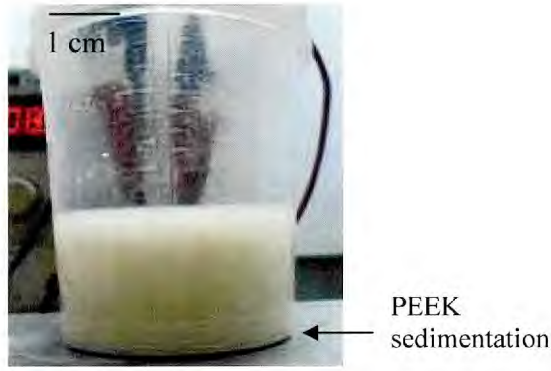


Figure 5.11 6 wt.% PEEK suspension in ethanol 2 min after the stirring was stopped showing abundant PEEK sedimentation on the bottom of the cell (arrow).

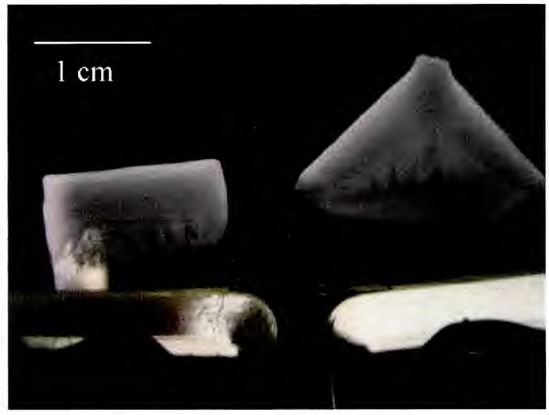


Figure 5.12 PEEK coatings deposited from 6 wt.% suspension in ethanol applying 40 V for 90 s with the two electrodes at 2 cm distance.

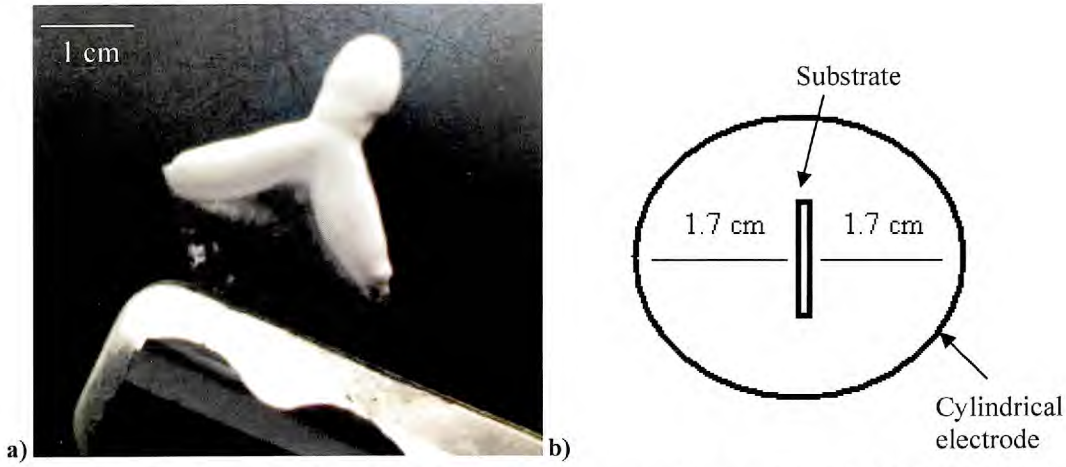


Figure 5.13 a) PEEK coatings deposited from a 6 wt.% suspension applying 56.4 V for 30 s with the cylindrical electrode configuration and 1.7 cm distance between the electrodes, as schematically shown in b). The substrate was previously ground with 120 grit SiC paper.

In order to homogenise the electric field, the cylindrical configuration of the EPD cell (see Figure 5.2 and Figure 5.13 b)) was employed, but even in these conditions a considerable edge effect was still observed. Moreover, when the sample was taken out from the suspension,

it was observed that a large agglomerate slid down and fell from the substrate; therefore it seemed that the coating was too heavy to be supported by the electrode. This was a further confirmation that the particles in the suspension were highly charged and that they were deposited by EPD. In order to increase the keying effect adhesion between the two materials, as described in section 4.3, the substrate surface was roughened with 120 grit SiC paper before deposition and the deposition time was reduced to 30 s. Also in these conditions the coating slid off the substrate as shown in Figure 5.13 a). All these coatings were fragile and parts of them easily flaked off.

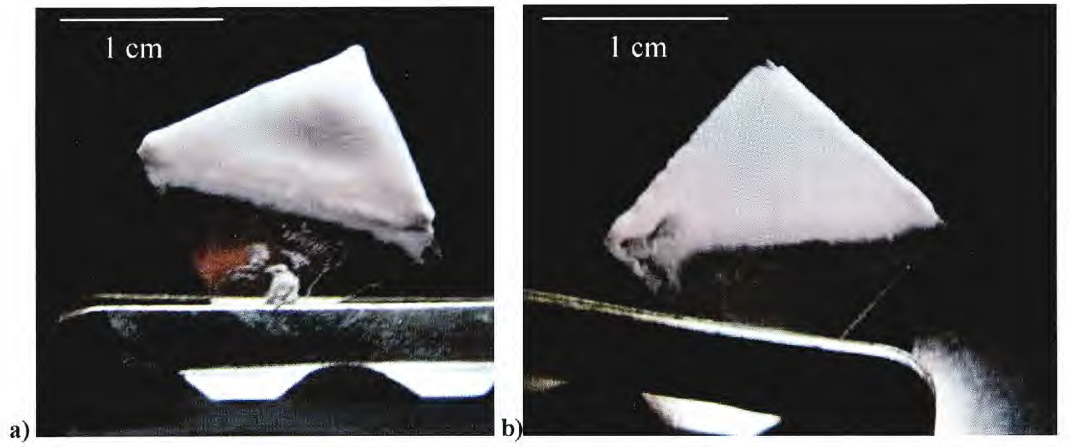


Figure 5.14 PEEK coatings deposited from a 6 wt.% suspension in ethanol applying a) 15.0 V for 5 min and b) 8.0 V for 7 min with the two parallel electrodes at the distance of 2 cm.



Figure 5.15 Coatings deposited from a 1 wt.% PEEK suspension in ethanol with a distance between the electrodes of 0.8 cm and applying a difference of potential of 56.4 V. From left to right the deposition times were 1, 3, 5 and 7 min.

Considering that uniform coatings are needed and that the edge effect has to be eliminated or at least decreased, the deposition rate was lowered by decreasing the electric field (variation of difference of potential, distance between the electrodes or both) and allowing longer deposition time. The deposited films seemed to be more uniform and the edge effect smaller, as shown in Figure 5.14 a) and b).

Similar results were also obtained using a more dilute suspension (1 wt.%); in this case a

higher electric field (56.4 V, electrode distance of 0.8 cm) was needed to achieve deposition and it was observed that the longer the deposition time the thicker the films deposited, as expected from Hamaker's equation (equation 2.15 in section 2.3.4) and shown in Figure 5.15. In the two middle samples in Figure 5.15 it is observed that an area of the coating has not been covered; this phenomenon has been observed in few samples and can be explained by the surface tension allowing the liquid to travel up into the crocodile clip during the deposition and, when the sample is removed from the cell the liquid is released washing away part of the coating. This defect can be easily eliminated avoiding contact between the suspension and the clip during the deposition.

ii) Suspension concentration

The effect of suspension concentration was investigated varying this parameter from 1 to 6 wt.%, as described by Wang et al. [187] and Boccaccini et al. [188]. It was observed visually that with increasing PEEK concentration, the rate of deposition and the thickness of the deposit increased keeping all the other parameters constant. This behaviour was explained by Hamaker's law (equation 2.15 in section 2.3.4), that states that the yield of the deposition is directly proportional to the concentration of the particles in suspension. In a more concentrate suspension the number of charged particles deposited per unit of time is higher.

iii) Difference of potential and distance between the electrodes

The difference of potential applied in combination with the distance between the electrodes (d) defines the magnitude of the electric field which plays a fundamental role in the EPD process. It was observed that increasing the electric field strength the thickness of the deposited coatings from the same suspension increased (compare Figures 5.12 (20 $V \cdot cm^{-1}$) and 5.14 b) (4 $V \cdot cm^{-1}$)); this behaviour is explained considering the higher deposition rate due to higher electrophoretic mobility of the suspended particles [22]. This observation was in perfect agreement with Hamaker's law (equation 2.15 in section 2.3.4) that states that the deposit weight is directly proportional to the electric field applied. However, it was also observed that when higher electric fields were applied the coatings presented edge effects if more concentrated suspensions were employed, as discussed above (see the edge effect in Fig. 5.12).

iv) Summary of deposition results

From all the results achieved and discussed above it was determined that both suspension concentration and electric field have similar effects on the PEEK deposition kinetics and that different suitable combinations of these two parameters permit the deposition of uniform and reproducible PEEK coatings. Uniform coatings were obtained at 7 min deposition time from a 1 wt.% PEEK suspension applying 56.4 V (d = 0.8 cm), a 4 wt.% PEEK suspension applying 20 V (d = 1.5 cm) and a 6 wt.% PEEK suspension applying 8 V (d = 1.5 cm). These three

combinations of the parameters affecting the EPD were thus recognised as the best conditions to achieve uniform PEEK deposits.

Moreover it can be stated that in order to avoid the edge effect a slow deposition rate is needed; this can be achieved varying the suspension concentration and the electric field, e.g. by keeping a low suspension concentration and increasing the electric field and vice versa. Applying slow deposition rates, the deposition time should be obviously longer in order to obtain relatively thick films. It was also observed that magnetically stirring the suspension before deposition did not significantly affect the uniformity of the coating when longer deposition times were employed because the PEEK particles were quite heavy and started to sediment not long after the stirring was stopped. All the coatings were deposited on the positive electrode (anode) meaning that the PEEK particles were negatively charged, confirming the zeta potential results (see Figure 5.9 in section 5.3.1).

5.3.3 Current intensity

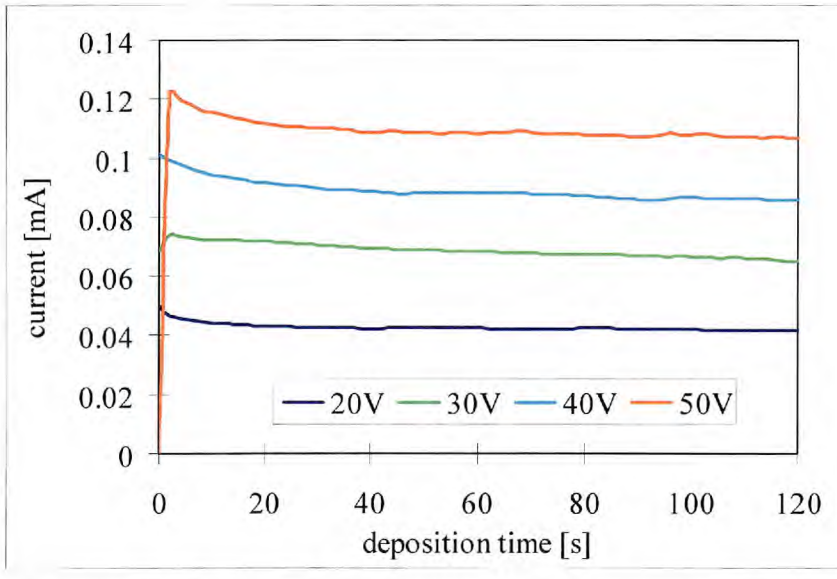


Figure 5.16 Current intensity vs time measured during EPD from a 6 wt.% PEEK suspension in ethanol for different electric fields with the two electrodes separated from 1.5 cm.

The current intensity measured during all the experiments increased with increasing applied voltage, in agreement with Ohm's first law considering that the resistance of the solution remains constant during the process. Moreover, the current intensity slightly decreased during EPD at constant voltage because of the increase of the coating thickness, which produces an ohmic resistance causing the drop of the potential applied. These behaviours are represented in Figure 5.16 where the current intensity was measured during EPD from a 6 wt.% PEEK suspension.

5.3.4 Microstructure of PEEK coatings

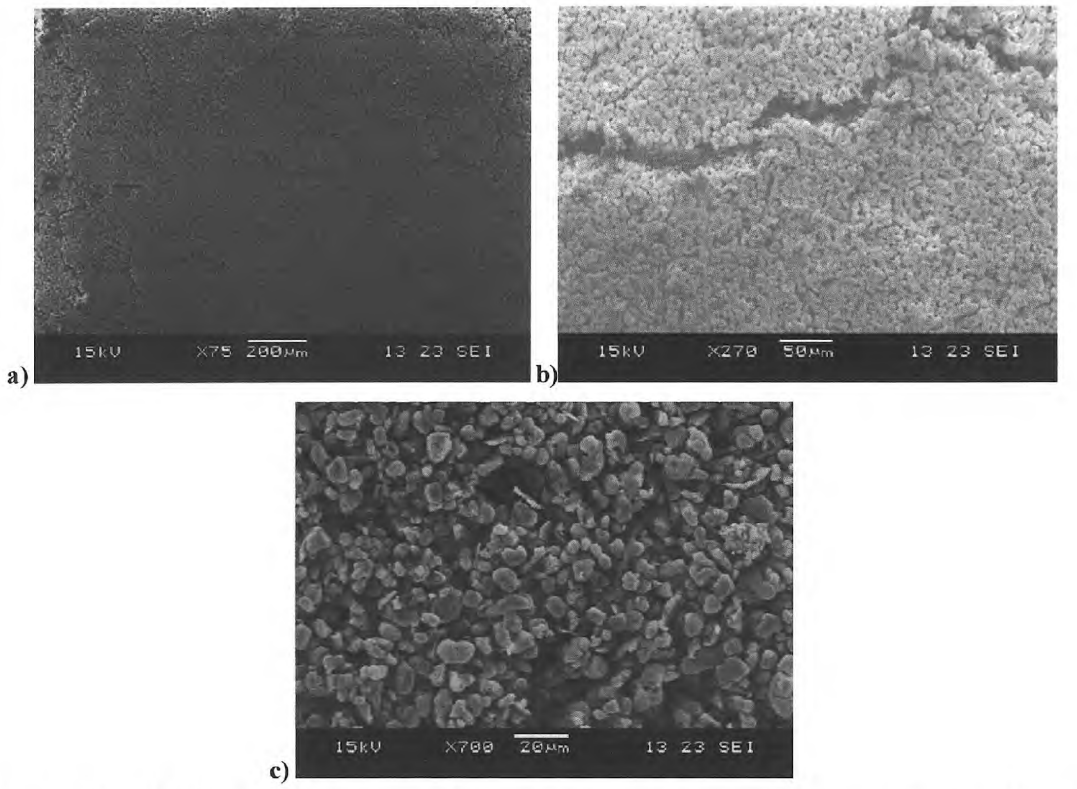


Figure 5.17 SEM images of a coating deposited from a 6 wt.% PEEK suspension in ethanol keeping the electrodes at 2 cm distance and applying a difference of potential of 8.0 V for 7 min at a) low, b) medium and c) high magnification, showing coating morphology and microstructure.

Figure 5.17 shows SEM images at different magnifications of a PEEK coating obtained by EPD from a 6 wt.% PEEK suspension applying a difference of potential of 8.0 V for 7 min and keeping the electrodes ad 2 cm distance. It was observed that the coatings were uniform all over the substrate surface, but they exhibited numerous micro-cracks (Figure 5.17 b)). It is worth noting that the mean size of the deposited particles (see Figure 5.17 c)) was smaller than that of the starting material (Figure 5.3), probably because the bigger (heavier) particles precipitated during the deposition.

5.3.5 Heat-treatment of PEEK coatings

The as deposited PEEK coatings were fragile and easily flaked off the substrates, therefore a heat-treatment was needed to densify the coatings and to increase their adhesion to the substrate increasing also the film mechanical properties. Knowing that the melting temperature of PEEK is ~343°C, as stated by the manufacturer [221] and confirmed by the DTA analysis reported in Figure 5.7 c); the heat-treatment step was carried out at this temperature (343°C) with a heating rate of $10°C \cdot min^{-1}$ and 30 min holding time, similar conditions to those reported by Wang et al. [187] and Boccaccini et al. [188].

The colour of the PEEK coating is a rapid indication of the heating process undertaken by the material; in fact the PEEK is white before heat-treatment (see Figure 5.14) and brown

(light or dark) after melting (Figure 5.18). After the heat-treatment in these conditions, the coatings seemed quite uniform (see Figure 5.18 a)), even if in some coatings it was possible to observe part of the substrate left uncovered (see Figure 5.18 b)). This behaviour is easily explained considering that PEEK shrinks 42% during melting, as shown in Figure 5.19. The PEEK shrinkage was calculated using heating microscopy (see section 3.8) and applying equation 3.4 in section 3.8 to the area of the pellet at 25°C (Figure 5.19 a)) and at 343°C (Figure 5.19 b)). It could be therefore concluded that the conditions employed: 343°C for 30 min with a heating rate of 10°C·min^{-1} were optimal to heat-treat the PEEK coatings even though the substrate coverage was not satisfactory.

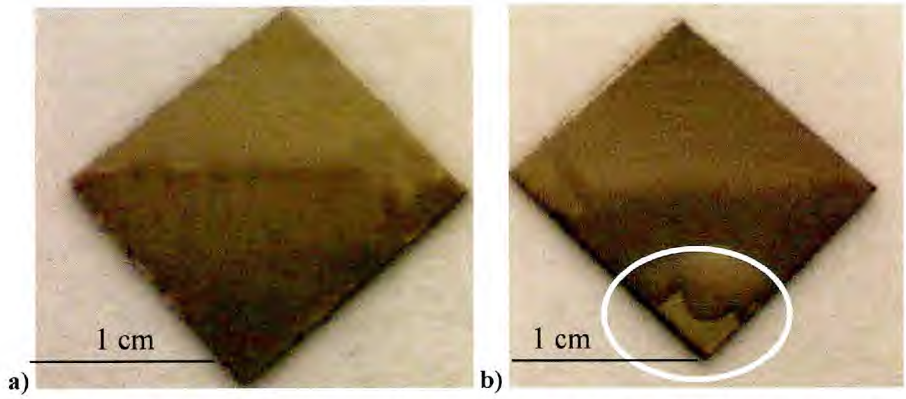


Figure 5.18 Images of two PEEK coatings after heat-treatment at 343°C for 30 min with a heating rate of 10°C·min^{-1}. The circle in b) shows part of the substrate left uncovered after heat-treatment.

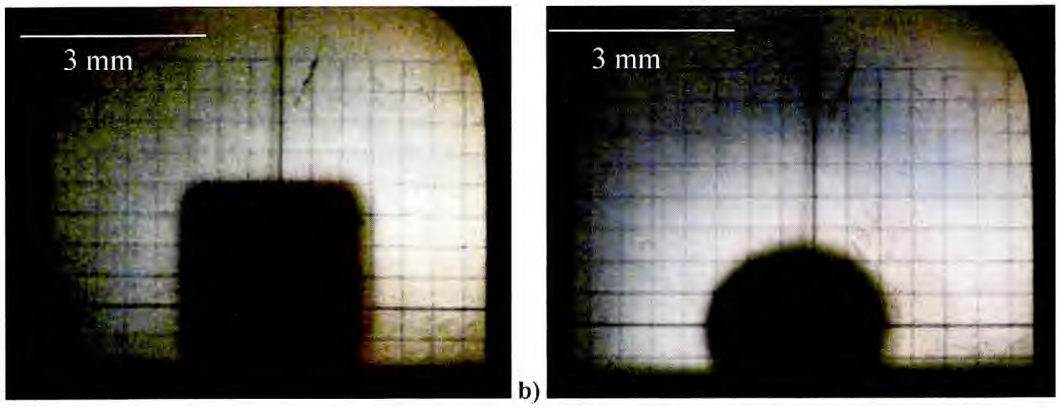


Figure 5.19 Images taken with a heating microscope of the same PEEK cubic pellet a) at 25°C and b) 345°C with a heating rate of 10°C·min^{-1} and showing the shrinkage of PEEK with temperature.

Therefore, in order to increase coverage, thickness and uniformity of the deposited coatings, both the electrophoretic deposition and the heat-treatment were repeated on the same substrate twice. Figure 5.20 shows a PEEK coating deposited on a substrate that was previously coated and heat-treated. It can be seen that there was deposition of PEEK over the previous coating and that the second coating was not uniform. This result can be explained considering that where the previous coating was thinner or absent the electric field was higher producing a

thicker deposit, whereas where the previous coating was thick there was no deposition, as schematically represented in Figure 5.21. The second coating was also heat-treated under the same conditions producing a quite uniform film without cracks that covered the whole area of the substrate, as shown in Figures 5.22 and 5.23.

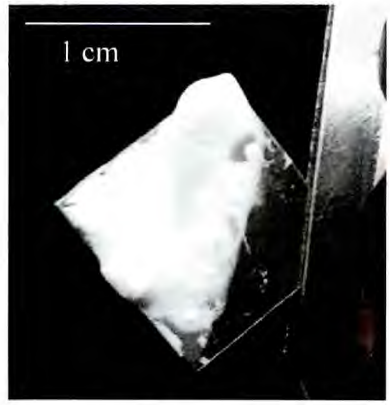
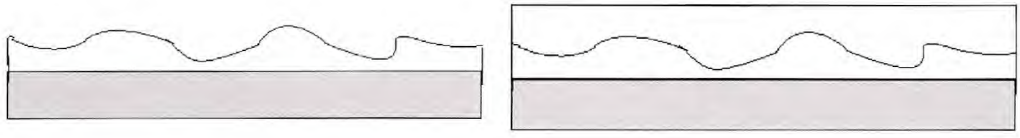


Figure 5.20 Image of a coating deposited from 1 wt.% PEEK suspension applying 56.4 V for 7 min with 0.8 cm distance between the electrodes. The substrate employed was already coated in the same conditions and heat-treated at 343°C for 30 min with a heating rate of 10°C·min^{-1}.



First coating First and second coating

Figure 5.21 Representation of the first PEEK coating and of both coatings schematically showing how a uniform coating can be achieved.

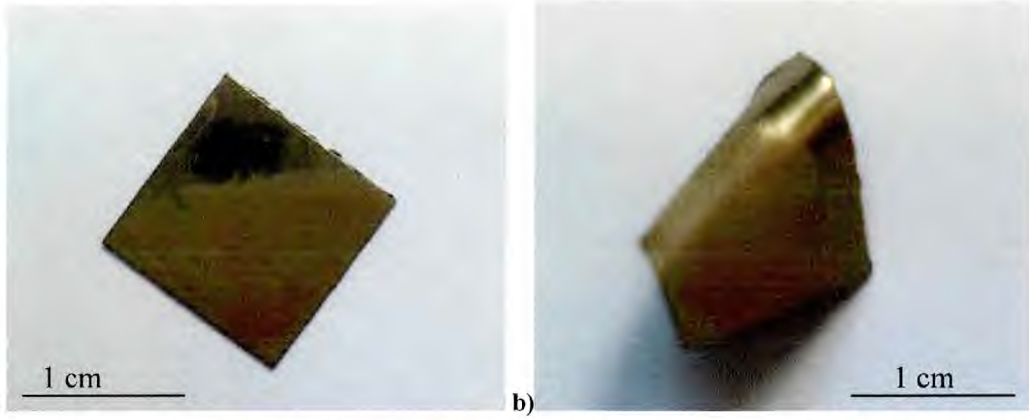


Figure 5.22 Images of the specimen coated twice and heat-treated at 343°C for 30 min with a heating rate of 10°C·min^{-1}; a) flat substrate and b) substrate bent after heat-treatment.

The microstructure analysis of the PEEK coating after the second heat-treatment step showed that the deposited PEEK powder was completely melted and that there were no cracks with the substrate being completely covered by the deposited film (Figure 5.23 a) and b)).

Figure 5.23 c), which is a cross section of the PEEK coated substrate, shows that the coating thickness was uniform and of around 25 μm and that the film was well adherent to the substrate in the whole sample. From the cross section analysis it seemed that the coating was fully dense and without residual porosity. Moreover from the observation of the bent sample (Figure 5.22 b)) it seemed that there was a qualitatively good stainless steel/PEEK coating adhesion. Therefore the heat-treatment conditions employed (343°C for 30 min with a heating rate of 10°C·min^{-1}) could be considered optimal.

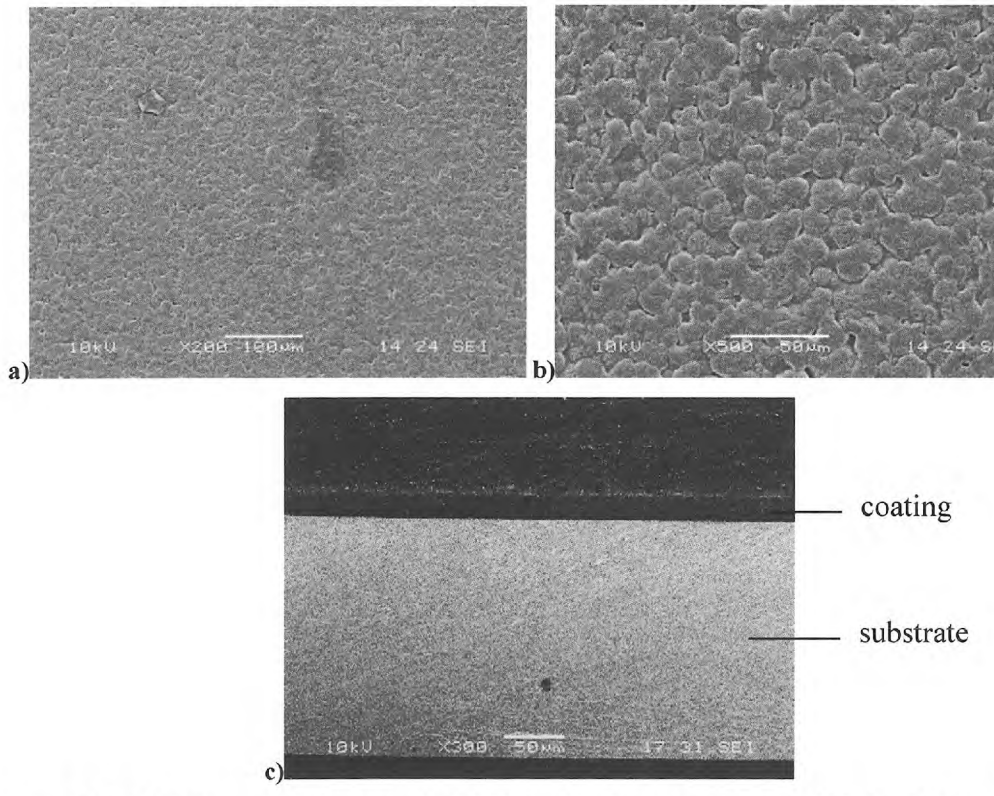


Figure 5.23 SEM images of the second PEEK coating heat-treated at 343°C for 30 min with a heating rate of 10°C·min^{-1}, a) top view at x 200, b) top view at x 500 and c) cross section.

The adhesion between the stainless steel substrate and the PEEK film considerably increases after the heat-treatment. This phenomenon was explained considering that during the heat-treatment the polymer melts and permeates in the substrate surface and during cooling solidifies within the substrate surface cavities providing a mechanical interlocking effect between the two materials, as also observed by Wang et al. [187] for PEEK films deposited by EPD and by Palathai et al. [7] for the deposition of PEEK coatings by thermal spraying. A good adhesion between stainless steel and PEEK was also observed when PEEK pellets were melted in the same conditions employed for the PEEK coatings on a stainless steel stand. The surface of the stainless steel substrate employed can be represented by the 3D plot shown in Figure 5.24 and presented an average rms of 0.18 ± 0.04 μm and Ra of 0.10 ± 0.02 μm (for more details see section 4.3) as measured by Zygo®.

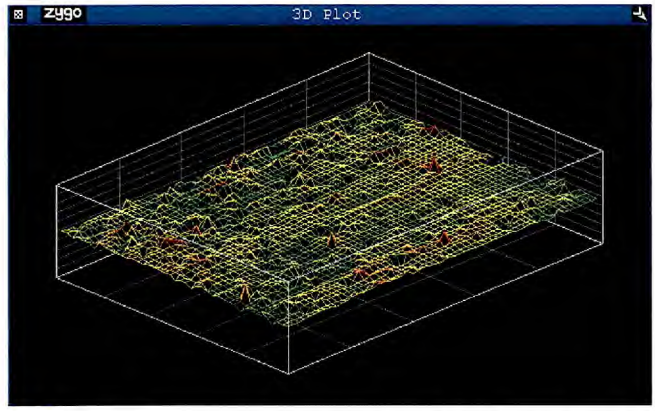


Figure 5.24 3D plot of the major area of the stainless steel AISI 316L surface obtained by white light interferometry (Zygo®).

During the heat-treatment also the PEEK crystallinity changed, as shown by the comparison between the XRD spectra of the starting material and of the PEEK powder-treated at 343°C for 30 min with a heating rate of 10°C·min^{-1} reported in Figure 5.25. Similar XRD spectra were also reported in previous investigations [3, 27, 201, 208, 209, 277, 278]. The position of the peaks did not change during the heat-treatment, but their intensity become higher due to the increase of crystallinity of the material. In particular, it could be observed a thinning of all the peaks and a greater increase of the (200) peak compared to the others, as also reported by Arous et al. [277].

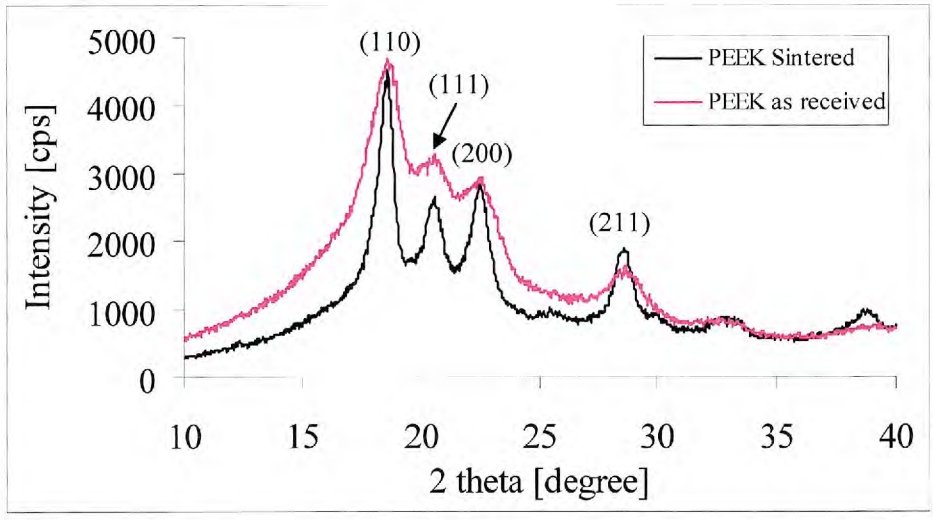


Figure 5.25 XRD analysis showing a comparison between the crystallinity of the PEEK powder as received and after heat-treatment at 343°C for 30 min with a heating rate of 10°C·min^{-1}.

Studies about the influence of the heat-treatment temperature on the PEEK crystallinity have been reported in the literature using both annealing and melting. From the annealing studies [6, 11, 277, 278], it emerged that the crystallinity of amorphous PEEK increased with increasing temperature between 160°C and 320°C and increasing holding time. From DSC

studies on molten PEEK, it has been reported that the crystallization temperature shifts to lower temperatures as the cooling rate increases (indicatively in the range of 5-30°C·min^{-1}) [26, 205] and is between 311°C and 260°C depending on the cooling conditions [3, 26, 27, 201, 205, 209, 273]. In all the experiments carried out in this research (coatings and pellets), PEEK was heated up to the melting temperature (343°C), kept at this temperature for 30 min and cooled down at a constant and reproducible cooling rate of around 1°C·min^{-1} (loss of heat of the closed ashing furnace). Being the crystallization temperature (160-320°C) lower than the melting temperature (343°C), during cooling the molten samples reached the crystallization temperature and this explains the increase of crystallinity of the PEEK powder after the heat-treatment (Figure 5.25). In addition, the slow cooling through the crystallization temperature further enhances the PEEK crystallinity; it has been reported by Kuo et al. [205] that the lower the cooling rate used the higher the crystalline fraction of the material due to the longer available crystallization time; whereas PEEK samples cooled extremely rapidly, e.g. quenched in ice/water, have been reported to remain amorphous [10, 278].

5.4 Deposition of alumina coatings

5.4.1 Characterisation of the nano-Al_2O_3

i) TEM analysis

The distribution of the nano-Al_2O_3 particles in the suspension employed for EPD and their shape and size range are shown in Figure 4.48. From the TEM observations it was clear that the nano-Al_2O_3 particles were well-dispersed in the suspension, they were spherical and with size between 10 and 100 nm, whereas the size range given by the manufacturer was 40-47 nm.

ii) XRD analysis

The XRD analysis of the nano-Al_2O_3 powder (Figure 4.47) shows that this powder is a mixture of δ*-Al_2O_3 (46-1215, orthorhombic), δ-Al_2O_3 (16-0394, tetragonal) and γ-Al_2O_3 (48-0367).

iii) Zeta potential analysis

The variation of the zeta potential with the "operational" pH of a 3 wt.% nano-Al_2O_3 suspension in ethanol was measured as described in section 3.10 and it is shown in Figure 5.26. Figure 5.26 shows that the zeta potential of nano-Al_2O_3 particles in ethanol is positive in all the pH range analysed (2-13). The higher zeta potential is + 60 mV at around pH 5.5 which is the pH of the suspension without any addition of acid or base. This suspension was remarkably stable against sedimentation for few days and its excellent dispersion can further confirm that

the nano-Al_2O_3 particles were highly charged in these conditions and had little tendency to coagulate. The considerable stability of the suspension can be also due to the nano-size of the particles employed. As already mentioned for the PEEK suspension (section 5.3.1), the opportunity to use the suspension in as-prepared condition is a great advantage since there is no need to adjust the pH avoiding possible experimental errors, due to the difficulties in measuring the pH in ethanol. The conductivity of the suspension as prepared was 11 $\mu S \cdot cm^{-1}$.

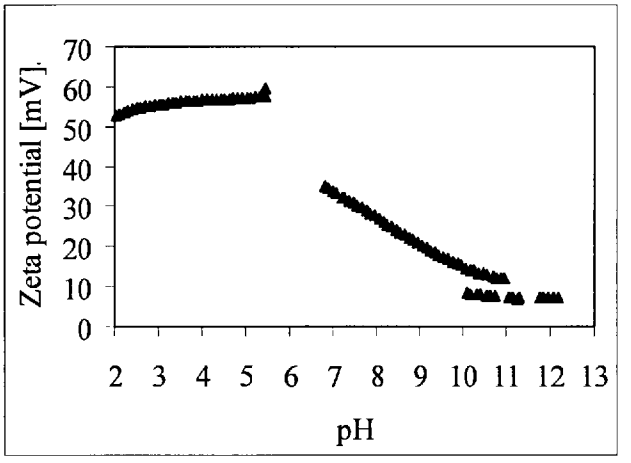


Figure 5.26 Zeta potential vs pH of a 3 wt.% nano-Al_2O_3 suspension in ethanol.

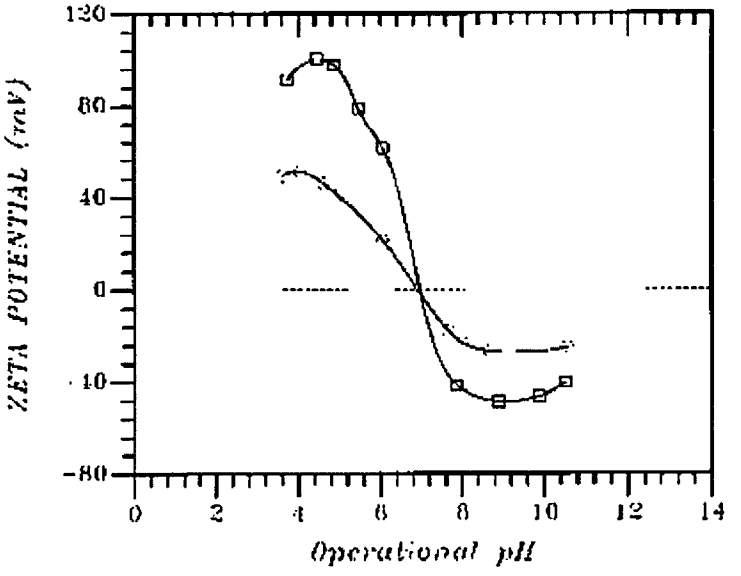


Figure 5.27 Zeta potential of Al_2O_3 (phase not stated) in ethanol as a function of the operational pH, as reported in ref. [137].

It has to be mentioned that the zeta potential variation shown in Figure 5.26 was remarkably different from that reported in the literature [137, 178, 180, 182, 183] and shown in Figures 5.27-5.29. All these data show an isoelectric point that varies from pH 7.1 (Figure 5.27) [137], to pH 9 (Figure 5.28) [178] and 9.5 (Figure 5.29) [180], while, as shown in Figure 5.26, the isoelectric point of the suspension used in this study is probably at pH higher then 12. It is

important to note that the zeta potential measurements reported in Figures 5.27 and 5.28 were carried out on the same kind of alumina powder (AKP-50, Japan) and they are quite different probably for the use of different instruments, methods and different suspension concentration. In fact Wang et al. [184] reported that the isoeletric point can shift to higher operational pH values with increasing particle concentration in suspension. This second explanation is not certain since in the literature [137, 178] the suspension concentration was not reported.

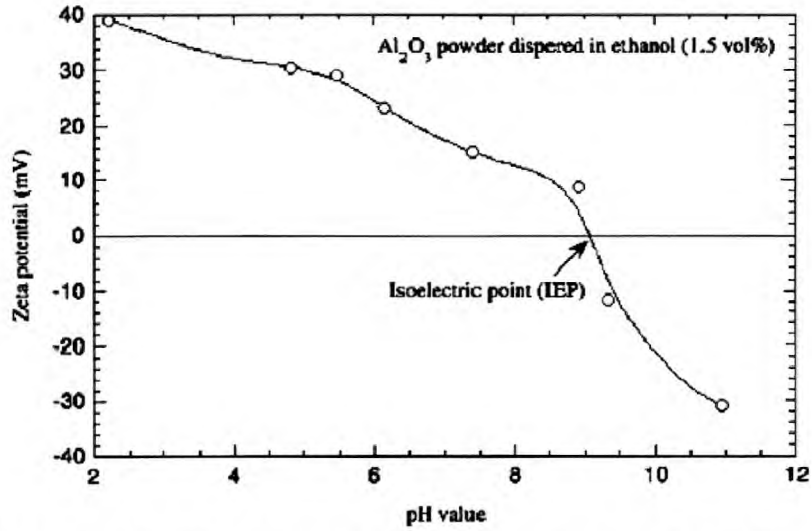


Figure 5.28 Zeta potential of Al_2O_3 (phase not stated) in ethanol as a function of pH, as reported by Chen et al. [178].

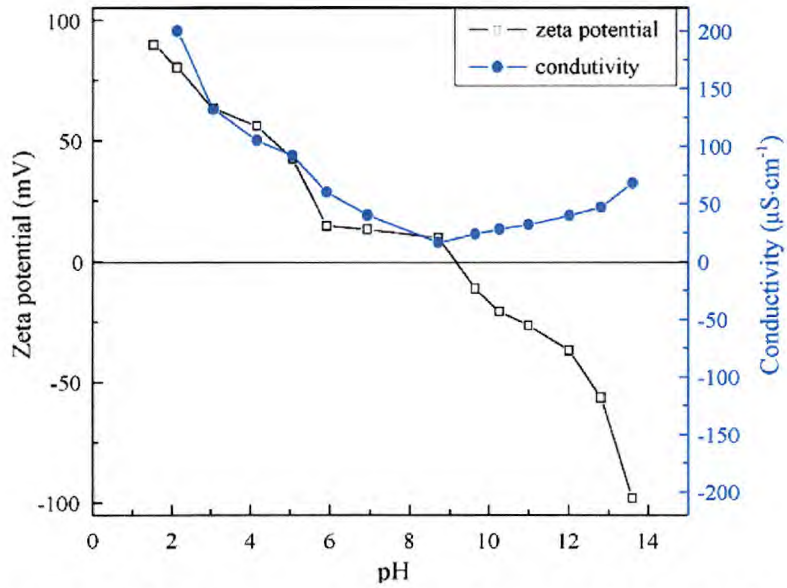


Figure 5.29 Zeta potential and electrical conductivity of γ-Al_2O_3 suspension in ethanol as a function of pH, as reported in ref. [180].

The existence of the isoelectric point for Al_2O_3 suspensions has been explained considering an acidity-dependent surface charge of the alumina particles in ethanol. In fact all

the oxides present high surface charge in suspension due to the surface hydroxyl groups (-OH) available on their surfaces, which:

- lose a proton in presence of OH^- (basic pH) and become negatively charged, for example: $AlOH + OH^- \rightarrow AlO^- + H_2O$
- or gain a proton in presence of H^+ (acidic pH) and become positively charged, for example: $AlOH + H^+ \rightarrow AlOH_2^+$

Considering the point of zero charge as the pH value at which the surface concentration of (AlO^-) and ($AlOH_2^+$) are equal, the surface charge would be negative at pH > pH (pzc) and positive at pH < pH (pzc) [22, 137, 178, 182, 183, 220].

Moreover, it is fundamental to state that, even if the zeta potential trends in Figure 5.26 and those reported in the literature (Figures 5.27-5.29) are fairly different, all of them present high positive values of zeta potential in the acidic region, which is the region of pH employed for the deposition of alumina in this research, as discussed next.

5.4.2 EPD of alumina coatings

The deposition of pure Al_2O_3 coatings on stainless steel by EPD was not the major aim of this project considering the numerous researches carried out on this topic in the last 20 years (see section 2.3.6.1) from both aqueous and organic suspensions. However, some nano-Al_2O_3 depositions were carried out here for comparison with PEEK coatings and PEEK-nano-Al_2O_3 composite coatings.

For the nano-Al_2O_3 deposition, it was decided to use ethanol as a suspension media to maintain the conditions as similar as possible to those applied to deposit PEEK in section 5.3. This decision was based on the fact that the main goal of this part of the project was the deposition of PEEK-nano-Al_2O_3 composite coatings in one step; therefore the use of similar conditions to deposit PEEK and nano-Al_2O_3 separately should have provided information on the behaviour of these two materials in ethanol to better understand the production of the composite. The nano-Al_2O_3 powder was suspended in ethanol as described by Boccaccini et al. [169] with a concentration of 3 wt.% instead of 12 wt.% and it was sonicated for 30 min. There was no need to change the suspension pH because from the zeta potential measurements reported in Figure 5.26, it resulted that these particles presented the highest positive charge in ethanol in as-prepared conditions (pH around 5.5). Moreover, considering the high stability of the suspension, magnetic stirring before the deposition was not needed.

The deposition of nano-Al_2O_3 coatings was carried out varying the difference of potential between 10 and 40 V between two stainless steel electrodes at 2.0 cm distance and modifying the deposition time to achieve relatively thick coatings. All depositions took place on the negative electrode (cathode) as expected considering the positive zeta potential of the particles (Figure 5.26). From all the conditions employed it seemed that those producing the more homogeneous coating were the following: a difference of potential of 40 V for 5 min with the

two parallel electrodes at the distance of 2 cm. The coatings were uniform immediately after the deposition, but they cracked upon drying as shown in Figure 5.30. The cracks were visible to the naked eye even when a slower drying process, achieved keeping the samples in a dessicator for 24 hours, was employed. It was also observed that the thicker the coating the more it flaked off.

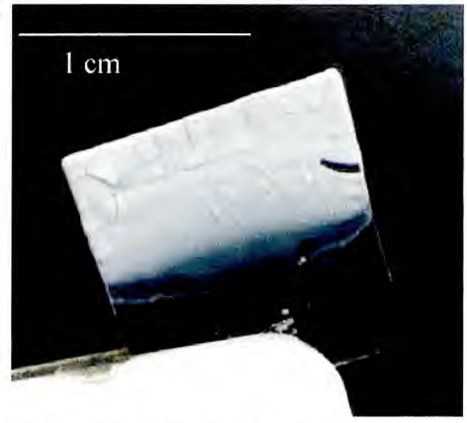


Figure 5.30 Image of an alumina coating deposited from a 3 wt.% nano-Al_2O_3 suspension applying 40 V for 5 min between two parallel electrodes at the distance of 2 cm and dried in a dessicator for 24 h.

The cracking of Al_2O_3 films on steel plates upon drying was also reported in previous research [125, 169, 181] and explained considering the stress produced by the capillary pressure of the solvent (ethanol) diffusing towards the surface of the film to evaporate [125, 181] or considering the different shrinkage between the coating and the substrate during the drying process [125, 169]. This difference in shrinkage produces tensile stresses that lead to the formation and propagation of cracks [125, 169]. It has been reported in the literature that to avoid cracking upon drying, the capillary pressure of the solvent has to be reduced; this can be achieved using a low surface tension solvent (e.g. ethanol) or slowing down the drying process by increasing the vapour pressure of the solvent in the drying chamber, or using freeze drying that removes all the capillary stresses subliming the solvent phase. Belaroui et al. [181] reported that even using almost saturated vapour pressures the microcracks in nano-Al_2O_3 coatings were still visible and in order to decrease the amount of microcracks the film thickness should have been less than 1 μm.

5.4.3 Current intensity

The current intensity was monitored during the experiments and some data are shown in Figure 5.31. Two main behaviours can be observed: the current intensity increased applying a stronger electric field, as expected by Ohm's first law, and the current intensity slightly decreased with the deposition time due to the increased ohmic resistance of the film that produces the drop of the potential applied. These behaviours were also observed during PEEK deposition, as shown in Figure 5.16 in section 5.3.3.

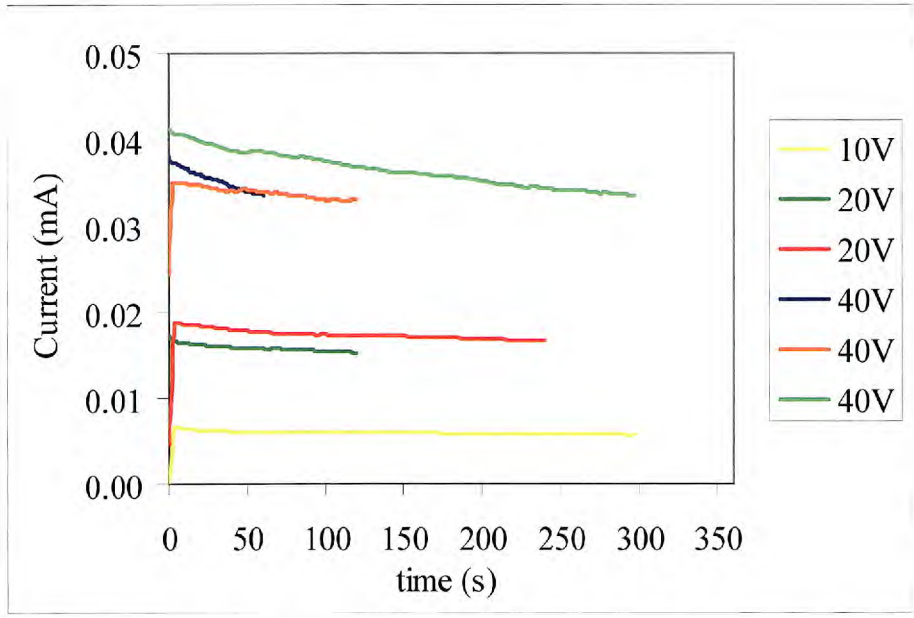


Figure 5.31 Current intensity vs time measured during EPD from a 3 wt.% nano-Al_2O_3 suspension in ethanol for different voltages with the two electrodes at 2 cm distance.

5.4.4 Microstructure of alumina coatings

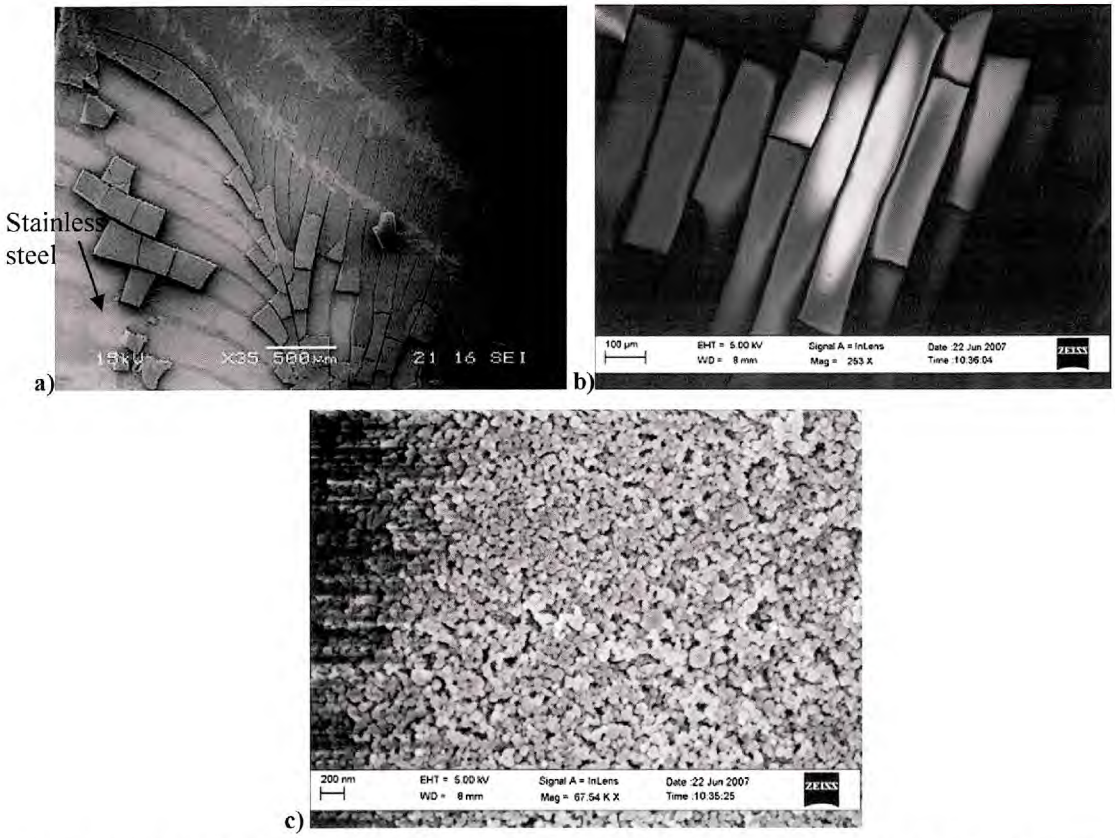


Figure 5.32 a) SEM and b-c) FEG-SEM images of an Al_2O_3 coating deposited from a 3 wt.% nano-Al_2O_3 suspension applying 40 V for 5 min with 2 cm electrode distance and dried in a dessicator for 24 h. a) and b) are low magnification images showing deep cracks, c) is a high magnification image showing the organisation of the nano-Al_2O_3 particles.

Figure 5.32 shows the microstructure of a nano-Al_2O_3 coating deposited using the optimized conditions (difference of potential of 40 V for 5 min and 2 cm distance between the two parallel electrodes) described in section 5.4.2. Figure 5.32 a) and b) clearly demonstrate that the coatings presented numerous, quite regular and deep cracks and that the coating adhesion to the substrate was quite poor, in particular in Figure 5.32 a) the stainless steel substrate was clearly visible in parts of the sample were the alumina film peeled off. Figure 5.32 c) shows that the nano-Al_2O_3 particles were densely packed in the coating.

5.5 Deposition of PEEK-Al_2O_3 composite coatings

In general there are two different ways to deposit composite coatings using EPD: a two step process or a single step process. On the one hand, if the two materials do not suspend together in the same suspension or if they have opposite charges and consequently migrate towards opposite electrodes when an electric field is applied, the deposition has to be carried out in two steps. In this particular case a nano-Al_2O_3 coating would be deposited first and let dry and then a PEEK coating would be deposited on the same substrate. The subsequent heat-treatment step should melt the PEEK layer and let it infiltrate into the nano-Al_2O_3 coating cracks producing a composite coating. Knowing the amount of nano-Al_2O_3 and the amount of PEEK deposited in a certain deposition time it should be possible to control the ratio of the two materials in the composite.

On the other hand, if it is possible to suspend the two materials in the same suspension media and if applying an electric field the two materials will migrate towards the same substrate, a composite coating can be produced in a single step. Theoretically, in order to have deposition on the same electrode the two materials should have the same charge, as described by Wang et al. [160] for the co-deposition of diamond and borosilicate glass from an ethanolic suspension. In this case, it is possible to modify the composition of the coatings by varying the concentration of the two materials in suspension [17, 20, 160]. However, materials having opposite charges can be co-deposited by being one adsorbed on the surface of the other [22] or by forming composite particles in the suspension following electrostatic interactions between opposite surface charges, as described in section 2.3.6 [161-165]. From the zeta potential results of nano-Al_2O_3 and PEEK reported in sections 5.3.1 vi) and 5.4.1 iii), it is known that nano-Al_2O_3 particles are positively charged and that PEEK particles are negatively charged in ethanol. Therefore, when a difference of potential is applied, the PEEK and the nano-Al_2O_3 particles should migrate in opposite directions unless electrostatic interactions take place between them in the suspension leading to PEEK-nano-Al_2O_3 composite particles.

5.5.1 Zeta potential measurement of the combined suspensions

The deposition of PEEK-nano-Al_2O_3 composite coating has been carried out from ethanolic suspensions containing 6 wt.% of powder with different ratios PEEK-nano-Al_2O_3.

Ethanol was chosen as the suspension medium because it was demonstrated in sections 5.3 and 5.4 that both PEEK and nano-Al_2O_3 particles can be deposited from this organic medium. A concentration of 6 wt.% seemed to be the highest possible concentration usable for the EPD of PEEK [187-189] and for this reason it was chosen as the total concentration for the mixtures employed in this part of the study.

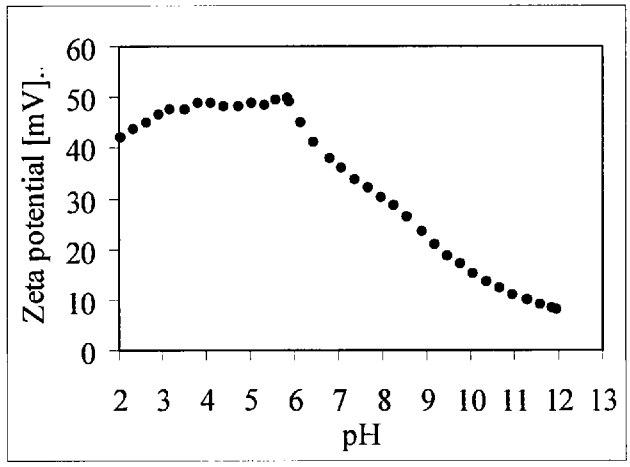


Figure 5.33 Zeta potential vs pH of a 3 wt.% PEEK-3 wt.% nano-Al_2O_3 suspension in ethanol.

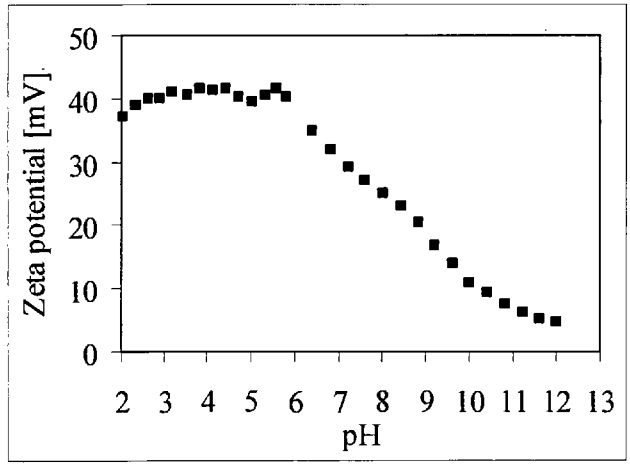


Figure 5.34 Zeta potential vs pH of a 4 wt.% PEEK-2 wt.% nano-Al_2O_3 suspension in ethanol.

The suspensions analysed contained 3 wt.% of PEEK and 3 wt.% of nano-Al_2O_3 (from now on referred to as 3P-3A), 4 wt.% of PEEK and 2 wt.% of nano-Al_2O_3 (from now on referred to as 4P-2A) and 5 wt.% of PEEK and 1 wt.% of nano-Al_2O_3 (from now on referred to as 5P-1A). The zeta potential of these three suspensions for operational pH values between 2 and 13 were measured as described in section 3.10 and shown in Figures 5.33-5.35. The zeta potential data of the three suspensions (Figures 5.33-5.35) were positive between pH 2 and 11. The highest zeta potential resulted to be + 50 mV at around pH 6 for the 3P-3A suspension (Figure 5.33), + 40 mV at pH around 5.5 for the 4P-2A suspension (Figure 5.34) and + 27 mV at pH 5.5 for the 5P-1A suspension (Figure 5.35). The highest zeta potential values of these

three suspensions were achieved without any addition of acid or base, as also observed for the PEEK and the nano-Al_2O_3 suspensions and described in sections 5.3.1 and 5.4.1. This result represents a significant advantage avoiding the possibility of incurring in experimental errors which could possibly arise adding acid or base to the suspension due to the problem of accurately measuring the pH in ethanol, as also discussed above. The conductivity of the as prepared 3P-3A, 4P-2A and 5P-1A suspensions were all relatively low with values of 49, 62 and 23 $\mu S \cdot cm^{-1}$, respectively.

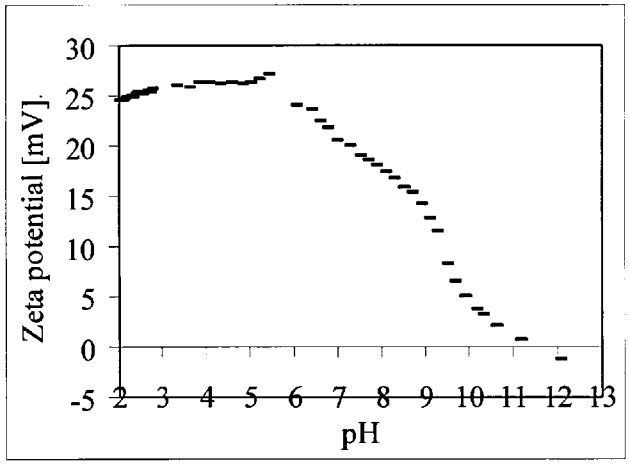


Figure 5.35 Zeta potential vs pH of a 5 wt.% PEEK-1 wt.% nano-Al_2O_3 suspension in ethanol.

Comparing the zeta potential values of the five suspensions (see Figure 5.36), it is possible to observe that the behaviours of 3P-3A, 4P-2A and 5P-1A suspensions were quite similar to that of the nano-Al_2O_3 suspension and completely different from that of the PEEK suspension. The zeta potential values for the nano-Al_2O_3, 3P-3A and 4P-2A suspensions were almost overlapped for pH higher than 7, whereas for pH lower than 7 it was possible to observe that the higher the PEEK amount in the mixture the lower the zeta potential values. This behaviour can be explained by considering that for the same concentration of the two materials the number of nano-Al_2O_3 particles was much higher than that of PEEK particles (due to their respective sizes) and therefore the nano-Al_2O_3 contribution to the total zeta potential was overall higher. Another possible explanation is the occurrence of electrostatic interactions between the small positively charged nano-Al_2O_3 particles and the large negatively charged PEEK particles, whereby the nano-Al_2O_3 particles cover the surface of the PEEK particles mediating and shielding their charge, as also proposed in the literature for other biphasic suspensions, such as hydroxyapatite and polytetrafluoroethylene [162], ZrO_2 and MgO [163], TiO_2 and CNTs (carbon nanotubes) [164], Al_2O_3 and SiO_2 [161] and hydroxyapatite and chitosan [165]. This explanation agrees with Sarkar and Nicholson [22], who have indicated that if a suspension contains two components with opposite charges the coarser component would adsorb the finer and the "composite" particle could behave as the fine material under the influence of an applied electric field.

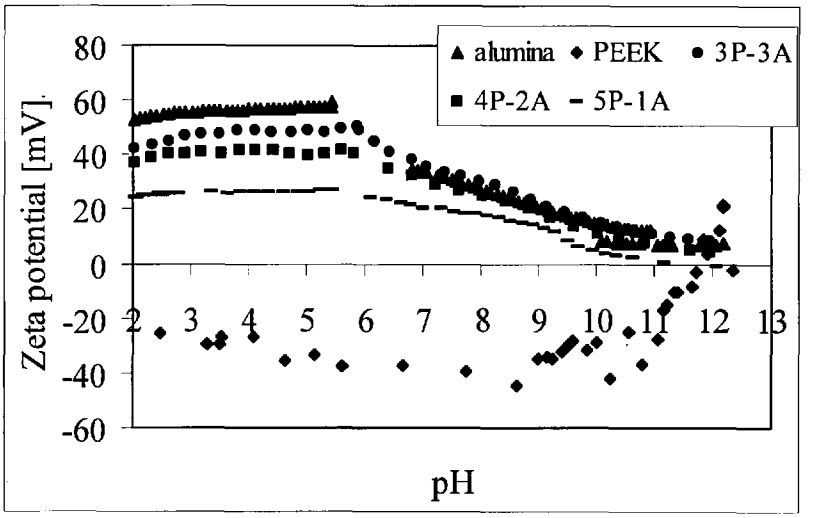


Figure 5.36 Graph showing the Zeta potential vs pH for nano-Al_2O_3, PEEK, 3P-3A, 4P-2A and 5P-1A suspensions in ethanol.

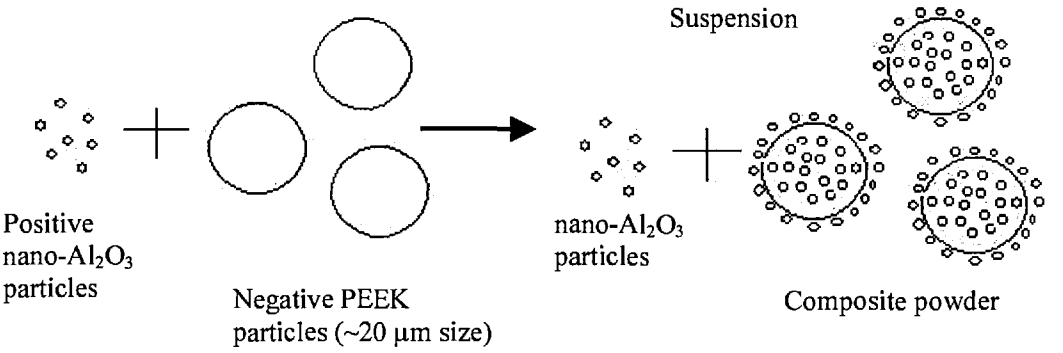


Figure 5.37 Model representing the interactions taking place between the oppositely charged PEEK particles and nano-Al_2O_3 particles in suspension.

Considering the models reported in the literature [22, 161-165] and the relative dimensions of the PEEK and the nano-Al_2O_3 particles employed here, it can be assumed that the nano-Al_2O_3 particles would cover the surface of the large PEEK particles and the overall electrophoretic behaviour of the composite (PEEK-nano-Al_2O_3) particles would be similar to that of a large Al_2O_3 particle, as schematically shown in Figure 5.37. This model has been further confirmed by TEM observations (for the preparation of the samples see section 3.2) on the mixed suspension, as reported in Figures 5.38 b) and c), which show a PEEK particle surrounded by nano-Al_2O_3 particles. The dark grey PEEK particles have been shrivelled and shifted by microtome cutting producing voids (white area). However, nano-Al_2O_3 particles were still visible around PEEK particles and this is a further indication of the strong electrostatic interaction between them (Figures 5.38 b) and c)). Moreover, Figure 5.38 a) shows that in the suspension some nano-Al_2O_3 particles were well-dispersed and suspended without interacting with the PEEK particles. Therefore it is expected that during EPD two types of components will be deposited on the cathode: nano-Al_2O_3 and PEEK-nano-Al_2O_3 composite particles, both positively charged.

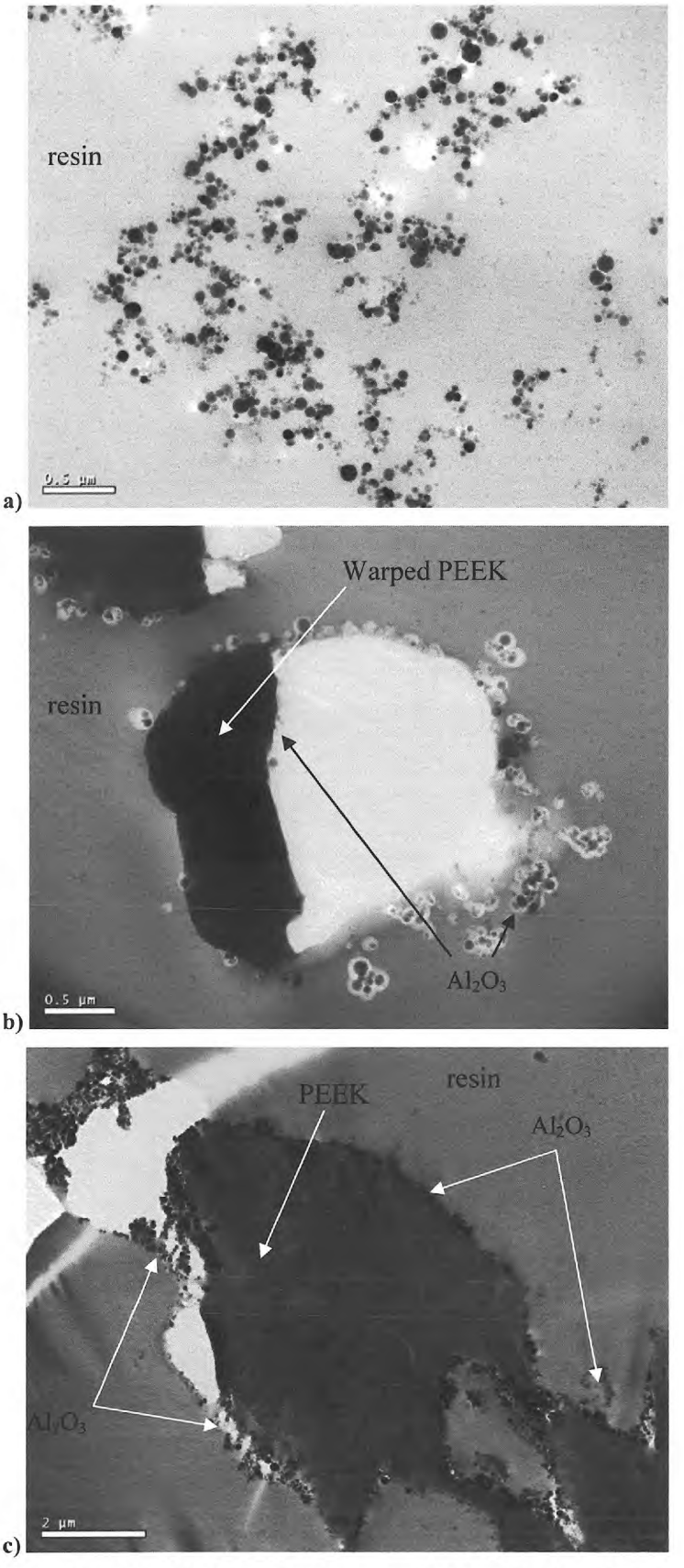


Figure 5.38 TEM images of the 4P-2A suspension: a) and b) images from the suspension and c) image from the dried powder embedded in resin, showing a) the nano-Al_2O_3 powder suspended alone, b) and c) the interactions PEEK-nano-Al_2O_3 particles.

For the other suspensions employed to electrophoretically deposit PEEK-nano-Al_2O_3 composite coatings the zeta potential was not measured but similar behaviour to those observed for 3P-3A, 4P-2A and 5P-1A suspensions were anticipated.

5.5.2 EPD parameters for deposition

The depositions were carried out from 2P-4A (2 wt.% PEEK and 4 wt.% nano-Al_2O_3), 3P-3A (3 wt.% PEEK and 3 wt.% nano-Al_2O_3), 3.5P-2.5A (3.5 wt.% PEEK and 2.5 wt.% nano-Al_2O_3), 4P-2A (4 wt.% PEEK and 2 wt.% nano-Al_2O_3), 5P-1A (5 wt.% PEEK and 1 wt.% nano-Al_2O_3) and 5.5P-0.5A (5.5 wt.% PEEK and 0.5 wt.% nano-Al_2O_3) ethanolic suspensions sonicated for 30 min. Differences of potential of 20, 30 and 40 V were applied for different deposition times between two parallel stainless steel electrodes kept at 2.0 cm distance. It was observed that the suspensions started to sediment after 3-4 min, as also observed for pure PEEK suspensions (see Figure 5.11 in section 5.3.2), and therefore, in order to increase the amount of material suspended, they were all magnetically stirred for 7 min before carrying out EPD. The only exception were 5P-1A and 5.5P-0.5A suspensions that were stirred for at least 15 min before deposition to increase the homogeneity of the coatings due to the facility of sinking of the composite powder, due to the high content in PEEK of these two suspensions. Homogeneous deposits were produced using all these conditions from 3P-3A, 3.5P-2.5A, 4P-2A and 5P-1A suspensions.

Few experiments were carried out from the 2P-4A, 3.5P-2.5A and 5.5P-0.5A suspensions. The 2P-4A suspension was not deeply investigated because it was observed that the deposited coatings easily flaked off and were remarkably similar to the nano-Al_2O_3 coatings described in section 5.4 probably for the high amount of nano-Al_2O_3 in suspension. The 3.5P-2.5A suspension, with composition intermediate between the 3P-3A and 4P-2A suspensions, was employed only for few experiments in order to observe if the coating composition was intermediate between those deposited from 3P-3A and 4P-2A suspensions, as it will be discussed later on in this section. The 5.5P-0.5A suspension was employed to deposit coatings with theoretically lower nano-Al_2O_3 content, but no deposition was achieved even applying higher electric fields and this behaviour was explained considering that the low amount of nano-Al_2O_3 in the suspension was probably not enough to positively charge the PEEK particles.

5.5.3 Current intensity

The current intensity was monitored during each deposition carried out applying difference of potential of 20, 30 and 40 V with a distance between the electrodes of 2 cm. The deposition time was increased in one minute for each experiment and EPD was stopped when the deposited film flaked off upon drying. The flaking off of the coatings was probably due to the achieved thickness since the coating composition did not vary with the deposition time, as it will be described in section 5.5.6. Figure 5.39 shows that the number of visible cracks on the

coating surface increased considerably with increasing deposition time, e.g. from 4 to 5 min.

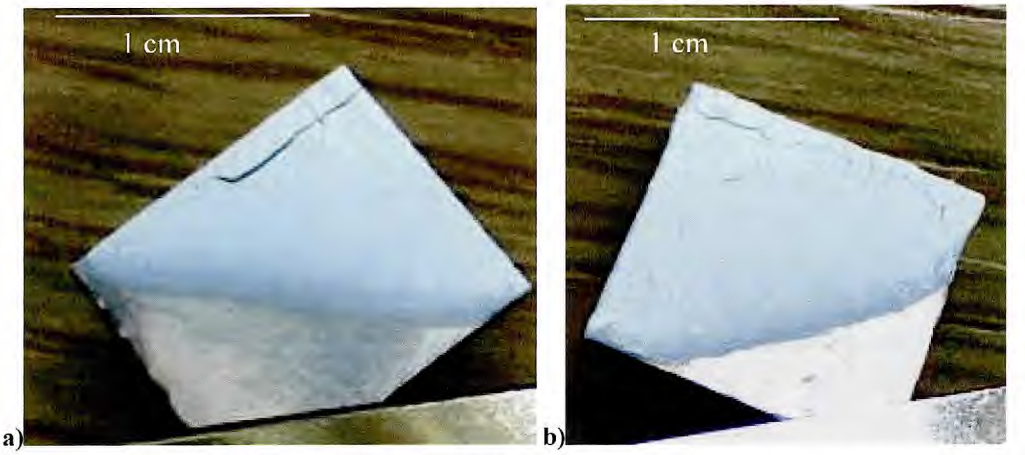


Figure 5.39 Images of two coatings deposited from a 3P-3A suspension applying a difference of potential of 30 V for a) 4 min and b) 5 min.

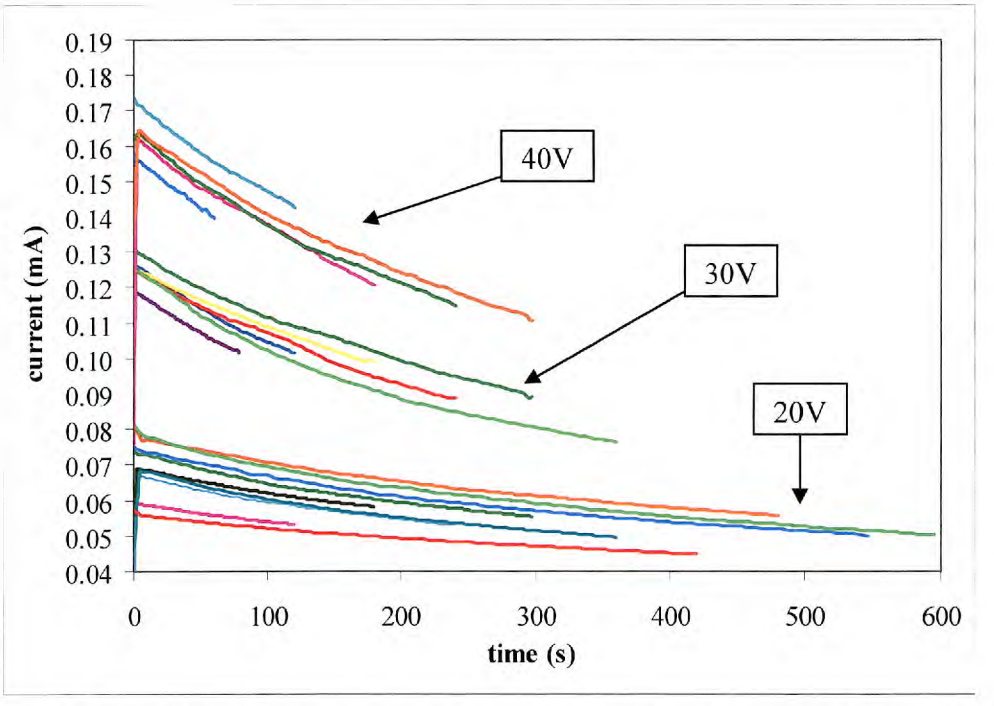


Figure 5.40 Current intensities as function of deposition time when differences of potential of 20, 30 and 40 V were applied during EPD from 3P-3A suspensions.

The current intensities obtained applying different potential differences from different suspensions were analysed and a representative behaviour is reported in Figures 5.40. It was clear that the higher the difference of potential applied the higher the current intensity. At the initial stage of EPD, this behaviour is in perfect agreement with Ohm`s first law:

$$\Delta V = I \cdot R \qquad [5.3]$$

where the resistance R, in this case, is a constant because the suspension is the same during the experiments. Therefore if the difference of potential applied (ΔV) increases the current

intensity (I) also increases. The same behaviour was also observed during the depositions of PEEK (see section 5.3.3) and nano-Al_2O_3 (see section 5.4.3) coatings. The differences in current intensity observed in Figure 5.40 when the same potential difference was applied for different deposition times were within the experimental error of the instrument (see section 5.2) and they were also partially due to the slightly different electrode areas (~1 cm^2) in the different experiments. Equation 5.3 is valid only at the initial stage of the deposition because once the deposition starts further factors influence ΔV, as discussed below.

A steady decrease of current intensity during deposition was observed for all the conditions applied (Figure 5.40) and it can be explained considering that the applied potential is given by equation 5.1 [179]. During EPD a non conductive coating forms on the substrate (in this case, negative electrode) producing an increase in resistance and therefore a drop of the potential applied, which increases with the coating thickness and therefore with the deposition time. This drop of potential is responsible for the decreasing of the current intensity during EPD carried out at constant voltage, as also discussed in the literature [125, 179]. Similar but less marked behaviours were also observed during the deposition of PEEK (see section 5.3.3) and nano-Al_2O_3 (see section 5.4.3) coatings.

5.5.4 Weight increase during EPD

It is well known from the literature and confirmed by the previous results (described in section 5.3.2) that the coating weight increases with increasing deposition time and difference of potential applied. Figure 5.41 shows that the coatings became thicker the longer the deposition time. In order to determine the weight increase as function of deposition time and electric field, the samples were weighed before and after EPD and the coating areas were measured. The same experiment was repeated four times for each condition and the average of the four measurements with the associated error (standard deviation) (7%) are reported in Figures 5.42 and 5.43 for the 3P-3A and the 4P-2A suspensions, respectively.

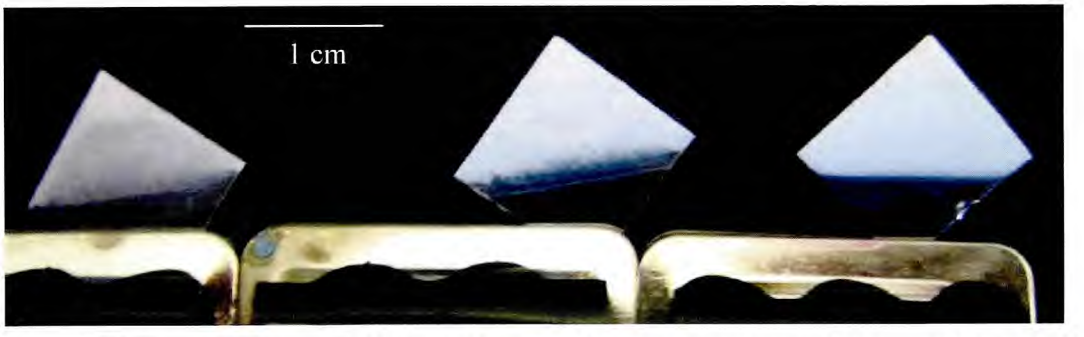


Figure 5.41 Images of samples deposited from a 4P-2A suspension applying a difference of potential of 40 V for 1 (on the left), 3 (in the centre) and 5 min (on the right).

As expected, the coating weight increased with *deposition time* for all differences of potentials investigated (see Fig. 5.42 and 5.43); this increase was not linear but logarithmic.

The weight increase was higher at the beginning of EPD (faster deposition rate) and then gradually decreased (slower deposition rate) theoretically reaching zero after a certain period of time. The decrease of deposition rate is directly related to the decrease of current intensity observed in Figure 5.40, which is due to a drop of the difference of potential and therefore of the electric field [179].

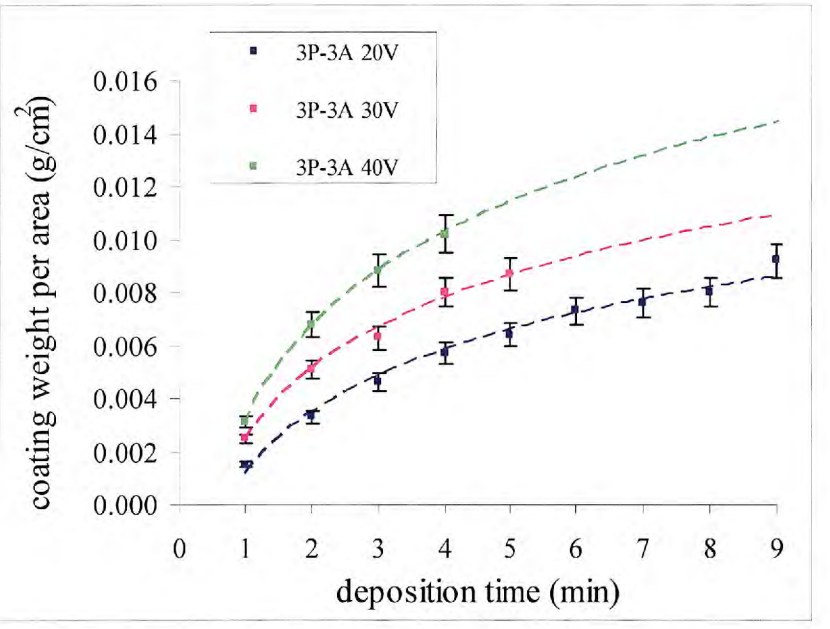


Figure 5.42 Weight increase of PEEK-nano-Al_2O_3 coatings deposited from a 3P-3A suspension applying 20, 30 and 40 V for different deposition times.

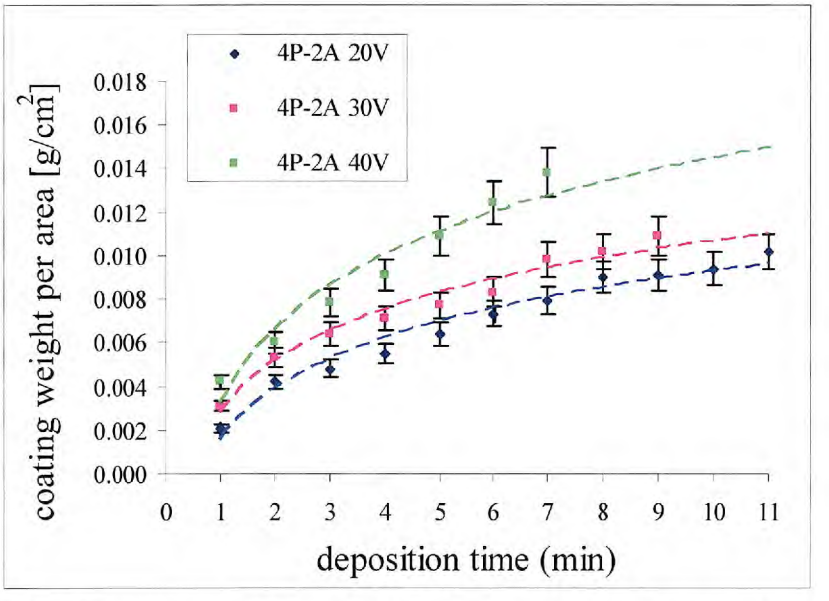


Figure 5.43 Weight increase of PEEK-nano-Al_2O_3 coatings deposited from a 4P-2A suspension applying 20, 30 and 40 V for different deposition times.

Moreover, it was also observed for both suspensions (Figures 5.44 and 5.45) that the deposited weight increased almost linearly with the *potential difference* applied for the same

deposition time, in agreement with the Hamaker's law (equation 2.15 in section 2.3.4), which states that the amount of material deposited during EPD is proportional to the applied electric field, i.e. higher electric fields generate higher particle velocity and faster deposition rates.

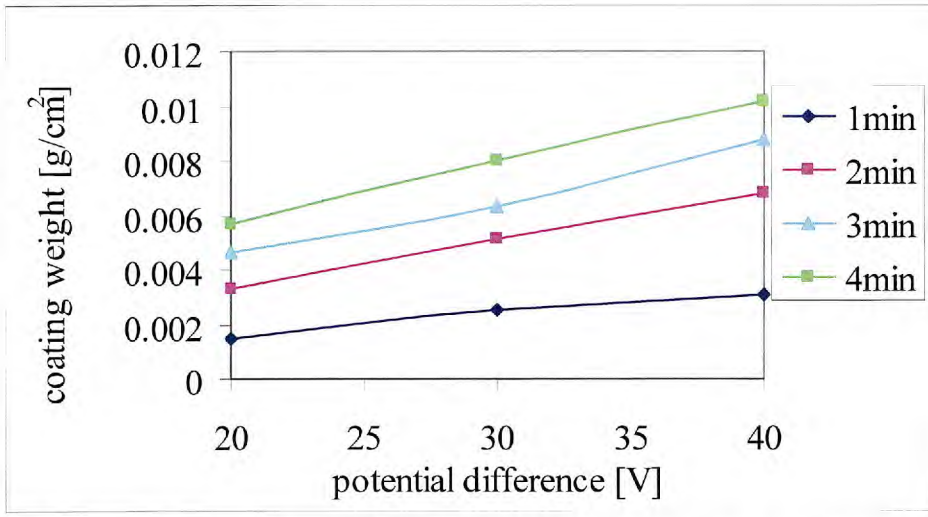


Figure 5.44 Weight increase of PEEK-nano-Al_2O_3 coatings deposited by EPD from a 3P-3A suspension as a function of the potential difference and the deposition time.

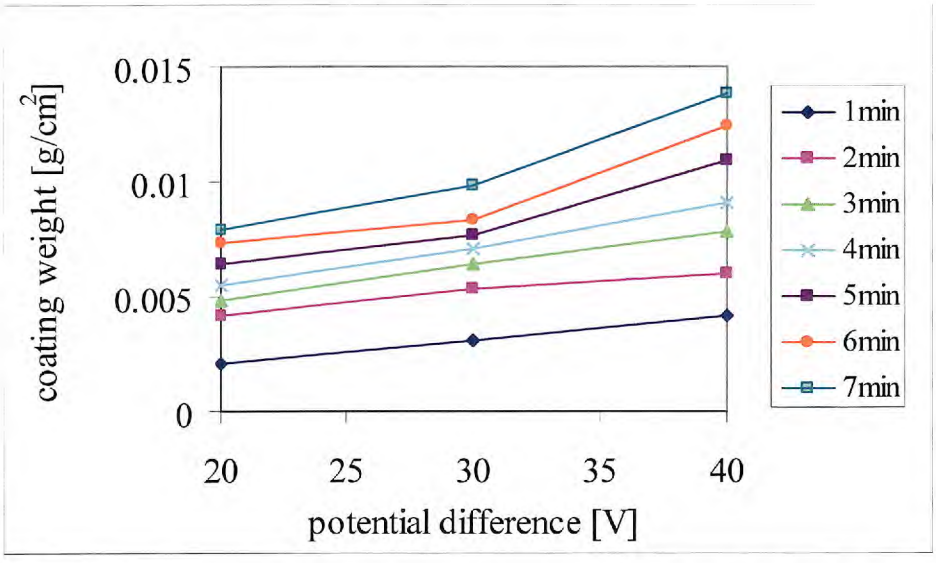


Figure 5.45 Weight increase of PEEK-nano-Al_2O_3 coatings deposited by EPD from a 4P-2A suspension as a function of the potential difference and the deposition time.

The increase in weight with the potential applied and the deposition time was also in agreement with the behaviour observed when the deposition was carried out increasing the deposition time minute by minute keeping the voltage difference and the distance between the electrodes constant (see Figures 5.42 and 5.43). In fact, it was observed that applying a difference of potential of 20 V from a 3P-3A suspension the deposition could be carried out for 9 min before the coating started to crack and flake off, whereas when the differences of

potential were 30 and 40 V the longest deposition times were 5 and 4 min, respectively. Instead when the depositions were carried out from the 4P-2A suspension applying differences of potential of 20, 30 and 40 V the longer deposition times were 11, 9 and 7 min, respectively. Similar behaviours (logarithmic increase of the film weight with the time and the difference of potential applied) were also expected for the other suspension concentrations employed.

Comparing these results it is clear that when the suspension contained higher concentrations of PEEK (4P-2A compared to 3P-3A) longer deposition times could be employed before the coatings started to crack and flake off demonstrating that the PEEK had a "gluing" effect in these coatings. It has been observed so far that:

1. Pure nano-Al_2O_3 coatings presented extremely poor adhesion to the substrate and cracks were visible to the naked eye (see Figure 5.30).
2. Pure PEEK coatings were difficult to deposit because of the low suspension stability and often presented edge effects (see section 5.3.2).

Whereas PEEK-nano-Al_2O_3 composite coatings did not crack as much as the pure nano-Al_2O_3 coatings, probably thanks to the presence of PEEK that may accommodate strains associated with drying, and they were uniform and without edge effects; these two advantages render this new composite material a very convenient combination for the production of coatings by EPD.

Prediction of the coating weight

Table 5.3 Equations that represent the kinetic of EPD from 3P-3A suspensions a) Logarithmic trends fitting the weight increase vs time at constant voltage and b) the same equation also as a function of the voltage.

V	Weight increase vs time and V	R^2
20V	a) $W = 0.003 \ln(t) + 0.0014$ b) $W = (0.00015 \ln(t) + 0.00007)*V$	0.9927
30V	a) $W = 0.0038 \ln(t) + 0.0024$ b) $W = (0.00013 \ln(t) + 0.00008)*V$	0.9883
40V	a) $W = 0.0051 \ln(t) + 0.0032$ b) $W = (0.00013 \ln(t) + 0.00008)*V$	0.9995

By fitting the first four points (time 1 to 4 min) of each one of the six logarithmic curves in Figures 5.42 and 5.43 it was possible to obtain the weight increase (W) as a function of deposition time (t) (see equations a) in Tables 5.3 and 5.4) and as a function of deposition time (t) and potential applied (V) (see equations b) in Tables 5.3 and 5.4). Equations b) were obtained by dividing equations a) by the potential applied in order to obtain an equation of general validity. All six equations presented high correlation coefficient R^2 (Tables 5.3 and 5.4). The coefficients appearing in equations b) for the 3P-3A (Table 5.3) and for the 4P-2A (Table 5.4) systems were considerably similar (the small differences observed can be due to the

experimental errors affecting the weight measurements) and therefore two general equations can be proposed as representative for each suspension (W in gram, t in min and V in volt):

3P-3A system: $W = (0.00013 \ln(t) + 0.00008)*V$ [5.4]

4P-2A system: $W = (0.00010 \ln(t) + 0.00011)*V$ [5.5]

The coefficients in eq. 5.4 and 5.5 depend on the system properties and therefore on the different PEEK-nano-Al_2O_3 ratios in the two suspensions. This dependence of the deposition yield from the applied voltage and the deposition time can be employed to predict the amount of material deposited under different conditions from a known suspension.

Table 5.4 Equations representing the kinetic of EPD from 4P-2A suspensions a) Logarithmic trends fitting the weight increase vs time at constant voltage and b) the same equation also as a function of the voltage.

V	Weight increase vs time and V	R^2
20V	a) $W = 0.0024 \ln(t) + 0.0022$ b) $W = (0.00012 \ln(t) + 0.00011)*V$	0.9818
30V	a) $W = 0.0029 \ln(t) + 0.0032$ b) $W = (0.00010 \ln(t) + 0.00011)*V$	0.9968
40V	a) $W = 0.0035 \ln(t) + 0.004$ b) $W = (0.00009 \ln(t) + 0.00010)*V$	0.9425

5.5.5 Application of an Artificial Neural Network for optimising EPD parameters

As reported in section 2.3.5, despite the numerous improvements of EPD and the large range of applications of the technique, the basic understanding of the mechanisms controlling the process, in particular the deposition step, is still poor and there is an insistent need for further theoretical and modelling work to gain full and quantitative understanding of the EPD mechanism and of the effect that EPD parameters (e.g. suspension concentration, deposition time, electric field) have on the deposition yield. The majority of the experimental studies are currently carried out employing inadequate and time-consuming trial-and-error approaches, as reviewed recently [23]. For this reason, the EPD data obtained from the 4P-2A and 3P-3A suspensions and reported in section 5.4.5 have been employed here to investigate if a neural network approach can be applied to study the EPD of PEEK-nano-Al_2O_3 composite systems to explore potential applications of the neural network to EPD.

As mention in section 3.17, to produce a neural network there must be inputs (values of the relevant variables) and outputs (predictions or control signals). The neural network learns and develops the relationship between inputs and outputs through a training that can be supervised or unsupervised. The supervised training was chosen for this research and it consists of a set of data containing examples of inputs and corresponding outputs of the system studied

through which the network understands the relationship between them. The neural network is trained using these data and the weights of the connections are adjusted to minimize the prediction errors. Once the network is properly trained, the function that relates the inputs to the outputs are known and the network could consequently predict unknown outputs [225]. For a more detailed description of the neural networks approach, see section 3.17.

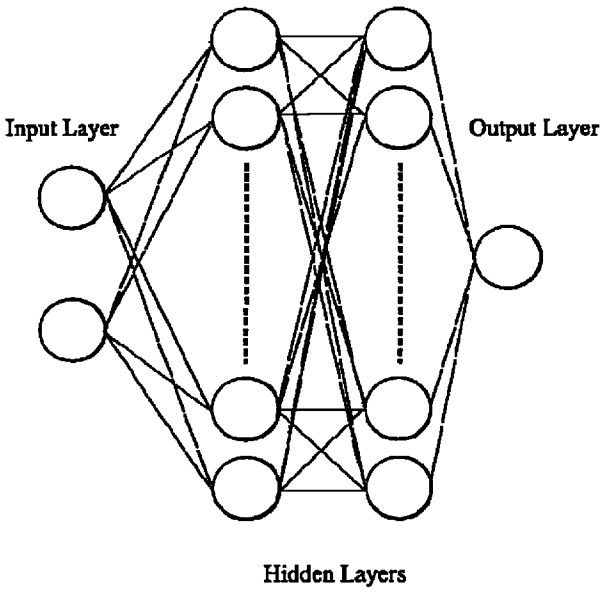


Figure 5.46 The artificial neural network for studying weight versus deposition time and voltage

A feed-forward back propagation neural network was designed to model the input and the output data produced experimentally. Its structure is represented in Figure 5.46. This network consisted of an input layer with two neurons (one for the deposition time and the other for the applied voltage), one or two hidden layers with 10 or 20 neurons each and an output layer with only one neuron for the deposition yield. The activation function employed was a sigmoid activation function:

$$y = \frac{1}{1+e^{-x}} \qquad [5.6]$$

and the training data sets were those shown in Figures 5.42 and 5.43 and listed in Tables 5.5 and 5.6 for the 3P-3A and 4P-2A suspensions, respectively. Furthermore, in order to avoid overfitting and to test the prediction capabilities of the model, two validation data sets (reported in Tables 5.7 and 5.8 for the 3P-3A and 4P-2A systems, respectively) were also employed. The neural network consists also of some independent parameters of its architecture, such as the number of epochs, hidden layers and artificial neurons in each hidden layer, which can be set and varied to improve the fitting of the data. In order to optimize the independent parameters of the NN model just described these parameters were varied (the number of epochs 500 or 1000, hidden layers 1 or 2, neurons per hidden layer 10 or 20) and the correlation coefficients R^2 between the experimental and theoretical data were calculated for each set of independent parameters (see Table 5.9). During this analysis, the other parameters of the back propagation

algorithm shown in equation 3.13 in section 3.17 were kept constant (the learning parameter was 0.5 and the momentum was zero), the inputs (Tables 5.5 and 5.6) were presented in random order during the training and the initial weights were chosen randomly at the start of each training.

Table 5.5 Training data set for the 3P-3A suspension.

	ΔV = 20 V	ΔV = 30 V	ΔV = 40 V
Deposition time	Weight ($g \cdot cm^{-2}$)	Weight ($g \cdot cm^{-2}$)	Weight ($g \cdot cm^{-2}$)
1 min	0.0015	0.0025	0.0031
2 min	0.0033	0.0051	0.0068
3 min	0.0046	0.0063	0.0088
4 min	0.0057	0.0080	0.0102
5 min	0.0064	0.0087	-
6 min	0.0073	-	-
7 min	0.0076	-	-
8 min	0.0080	-	-
9 min	0.0092	-	-

Table 5.6 Training data set for the 4P-2A suspension.

	ΔV = 20 V	ΔV = 30 V	ΔV = 40 V
Deposition time	Weight ($g \cdot cm^{-2}$)	Weight ($g \cdot cm^{-2}$)	Weight ($g \cdot cm^{-2}$)
1 min	0.0021	0.0031	0.0042
2 min	0.0042	0.0053	0.0060
3 min	0.0048	0.0064	0.0078
4 min	0.0055	0.0071	0.0091
5 min	0.0064	0.0077	0.0109
6 min	0.0073	0.0083	0.0124
7 min	0.0079	0.0098	0.0138
8 min	0.0090	0.0102	-
9 min	0.0091	0.0109	-
10 min	0.0094	-	-
11 min	0.0102	-	-

Table 5.7 Validation data set used to test the model for the 3P-3A system.

Voltage	Dep.time	Experimental Weight ($g \cdot cm^{-2}$)	Theoretical weight ($g \cdot cm^{-2}$)	Difference
40 V	3.5 min	0.0088	0.00895	-0.00015 (-1.6%)
30 V	4.5 min	0.0085	0.00835	0.00015 (1.7%)
25 V	4.5 min	0.0076	0.00723	0.00037 (4.9%)
35 V	4.5 min	0.0106	0.00924	0.00100 (9.0%)

Figure 5.47 shows the calculated data versus the experimental data for some sets of epochs, hidden layers and neurons, for the two systems studied. The correlation coefficient R^2 was very close to 1 for all the tests carried out and listed in Table 5.9 demonstrating that there was a high agreement between the calculated and experimental data, also considering the relatively small number of points used. Statistically, there is only a probability of less than

0.05% that an equal number of non correlated points have the same R^2 when different independent parameters are used [279].

Table 5.8 Validation data set used to test the model for the 4P-2A system.

Voltage	Dep.time	Experimental weight ($g \cdot cm^{-2}$)	Theoretical weight ($g \cdot cm^{-2}$)	Difference
25 V	5.5 min	0.0074	0.00706	0.00034 (4.6%)
35 V	4.5 min	0.0078	0.00846	-0.00066 (-8.5%)
20V	4.5 min	0.0058	0.00561	0.00019 (3.3%)
40V	3.5 min	0.0087	0.00864	0.000061 (0.7%)

Table 5.9 The runs and results for the optimization of the NN independent parameters.

Run	Epoch (nr)	Hidden layer (nr)	Neuron per hidden layer (nr)	R^2 for 4P-2A	R^2 for 3P-3A
1	500	1	10	0.9485	0.9512
2	1000	1	10	0.9485	0.9679
3	500	2	10	0.9428	0.9571
4	1000	2	10	0.9552	0.9804
5	500	1	20	0.9502	0.9522
6	1000	1	20	0.9498	0.9596
7	500	2	20	0.9498	0.9545
8	1000	2	20	0.9594	0.9830

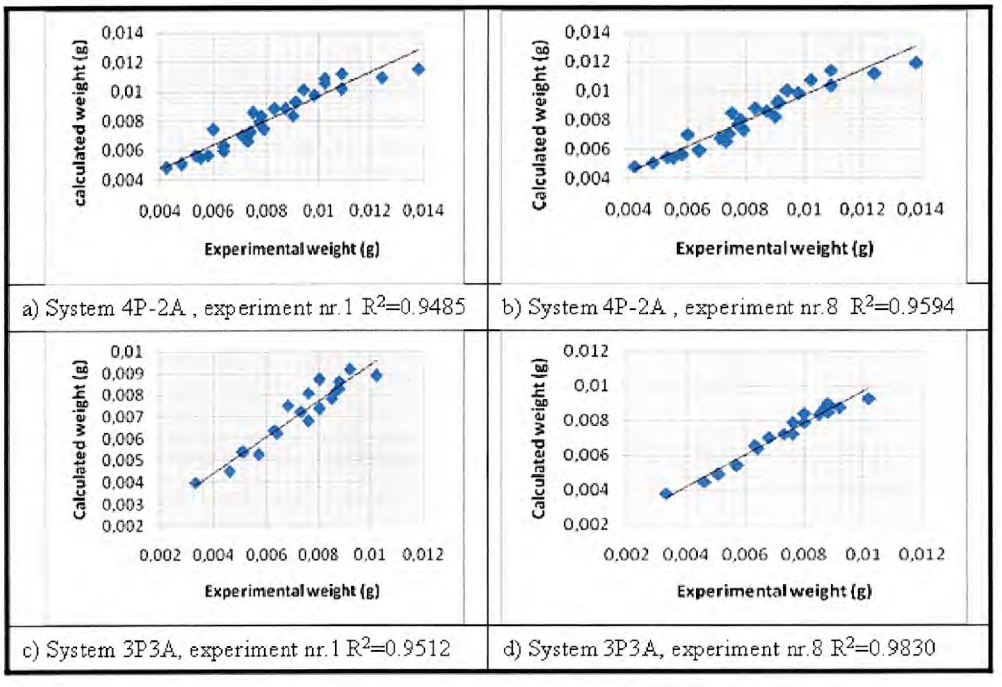


Figure 5.47 Calculated data versus experimental data obtained for some set of epochs, hidden layers and neurons during the optimization for the 3P-3A and 4P-2A systems.

Table 5.9 shows that the correlation coefficient R^2 for the 3P-3A system improved with the number of hidden layers and the number of epochs; in particular, the number of epochs

seemed to be the most effective parameter, but the different ranges in which the two parameters have been varied do not permit a fair comparison. The neural model for the 4P-2A system seemed to be less sensible to the variation of the identified independent variables. In this case, models with lower number of epochs, hidden layers and neurons for hidden layers should still permit to obtain results as valid as those produced by more complex models, with the advantage of shortened the computing time, which would be much more evident when wider set of training data are employed. Since in this study the number of training and validation data was relatively small, the computing time was not a problem and from now on in this work, neural network models with two hidden layer, 20 artificial neurons for hidden layer and 1000 epochs were employed.

Figure 5.48 shows the data for the 3P-3A system calculated using the neural network model developed applying the best settings (1000 epochs, two hidden layers with 20 artificial neurons each). A direct relationship between the deposition yield and both the voltage and the deposition time appeared evident. In particular, the deposition time seemed to be more effective than the voltage in affecting the weight deposited. The concave shape of the surface indicated that there was an interaction between the two independent variables. It has to be underlined that the part of the 3D plot in Figure 5.48 for high voltages (30-40V) and long deposition time (> 4-5 min) could not be accurate since it was extrapolated by the NN model in a range of variables in which the model was not trained. The model suggested that the weight increase was not linear with deposition time but logarithmic, as also observed and discussed in section 5.5.4.

Figure 5.49 presents a 3D plot for the 4P-2A system showing the interactions between the deposition yield, the difference of potential applied and the deposition time calculated using the neural model developed (1000 epochs, two hidden layers with 20 artificial neurons each). A direct relationship between the deposition yield and the deposition time is evident, as also observed for the 3P-3A system (Figure 5.48), while the voltage influence seemed to be smaller than that observed for the 3P-3A system. The shape of the 3D plot (Figure 5.49) does not show concavity meaning that there were no interactions between the deposition time and the voltage in the range investigated. The model suggested a slight decrease of the slope at the higher values of voltage and deposition time which, also in this case, is confirmed experimentally as explained in section 5.5.4.

Comparing the experimental data of the validation data set and the theoretical data produced by the optimised neural network models for the 3P-3A and 4P-2A systems, it is clear that the maximum difference obtained is of about 9% (see Tables 5.7 and 5.8). This difference is probably mainly due to the experimental errors affecting the measurements, that were recorded to be 7% (standard deviation) (see section 5.5.4). Therefore it could be deduced that the two neural network models were considerably precise in predicting the deposition yield in the range of variables in which the two models were trained and it can be asserted that the neural network approach can be relevant in the general field of processing materials by EPD

contributing to tackle the current gap of quantitative predictive tools.

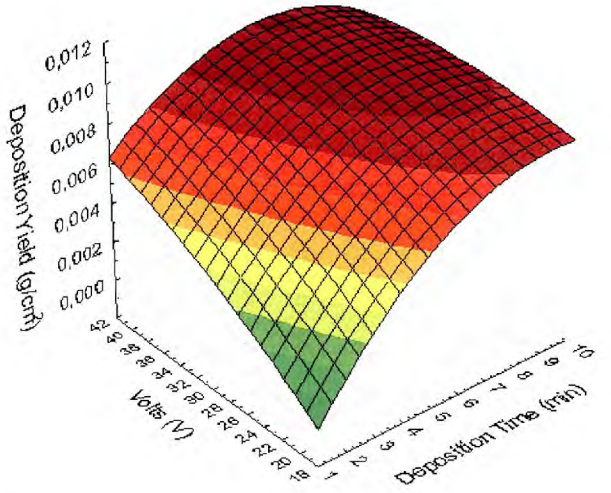


Figure 5.48 Combined effect of the electric field (voltage) and the deposition time on the deposition yield for the 3P-3A system, calculated using the neural model developed applying the optimized settings (1000 epochs, two hidden layers and 20 artificial neurons for each layer).

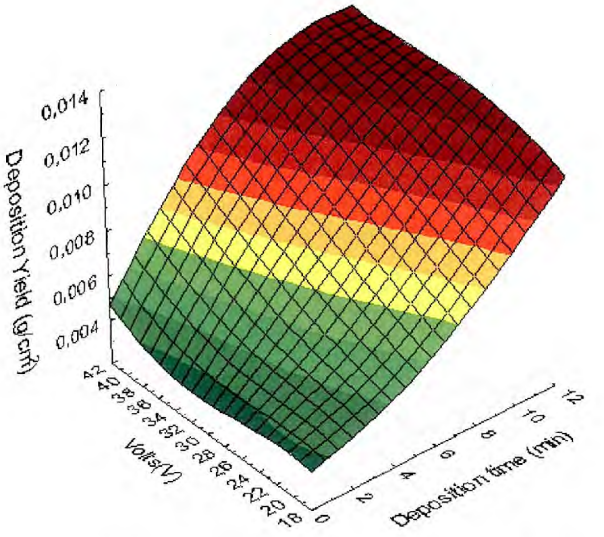


Figure 5.49 Combined effects of the electric field (voltage) and the deposition time on deposition yield for the 4P-2A system. These data were calculated using the neural model developed with the best settings: 1000 epochs, two hidden layers with 20 artificial neurons each.

5.5.6 Ratio PEEK-alumina in the coatings

Assuming that PEEK and nano-Al_2O_3 particles were deposited in the film in the same ratio they were in the suspension, the predicted compositions of the coatings deposited from 3P-3A, 4P-2A and 5P-1A suspensions are listed in Table 5.10. In order to calculate the vol.% of one component knowing its weight fraction in the composite, the following equation was

employed [28]:

$$V_f = \frac{W_f}{W_f + \frac{(1-W_f)p_f}{p_m}} \quad [5.7]$$

where V_f, W_f and p_f are the volume, the weight and the density of the component, respectively and p_m is the density of the other material. The density of PEEK is 1.3 $g \cdot cm^{-3}$ [221] and the density of nano-Al_2O_3 is 4.0 $g \cdot cm^{-3}$ [222].

Table 5.10 Theoretical concentration (wt.% and vol.%) of PEEK and nano-Al_2O_3 in the coatings calculated by equation 5.7 if the suspension ratio was maintained during EPD. Considering the PEEK density to be 1.3 $g \cdot cm^{-3}$ [221] and the nano-Al_2O_3 density to be 4 $g \cdot cm^{-3}$ [222].

	wt.% Al_2O_3	wt.% PEEK	vol.% Al_2O_3	vol.% PEEK
3P-3A	50	50	25	75
4P-2A	33	67	14	86
5P-1A	17	83	6	94

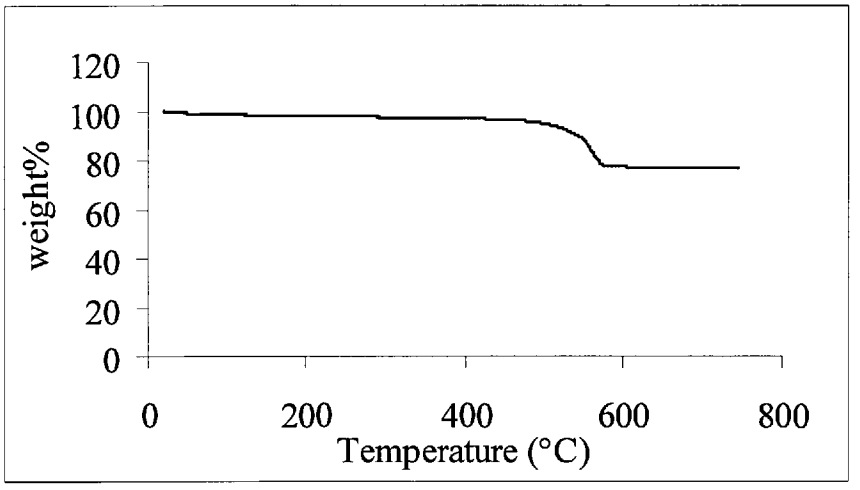


Figure 5.50 Change in weight of a 3P-3A sample with increasing temperature (TGA).

In order to determine the actual PEEK-nano-Al_2O_3 ratio, four coatings were deposited for each deposition time and difference of potential applied (20, 30 and 40 V) and the powder was scratched off the substrates and subsequently heat-treated, as also described by Pang et al. [165, 280]. Thermal gravimetry analysis (see section 3.6) of the powder deposited from the 3P-3A suspension applying a difference of potential of 30 V for 4 min using a linear heating rate of 10°C·min^{-1} from room temperature to 770°C is shown in Figure 5.50 and demonstrates that the PEEK-nano-Al_2O_3 mixture was considerably stable at temperatures below 500°C, when the PEEK started to decompose and that at 570°C the PEEK was completely decomposed leaving just nano-Al_2O_3 in the container; while it was observed for pure PEEK that the decomposition started at 550°C and that it was completely decomposed by 660°C (see PEEK TGA analysis in

Figure 5.6). The decomposition of PEEK was consequently used to determine the weight ratio of the two materials in the coatings using a heat-treatment at 700°C with a heating rate of 10°C·min^{-1} and no holding, as described in section 5.2. The volume ratio of the two materials in the coating was also calculated using eq. 5.7. Several measurements on powder deposited under the same conditions were repeated and a 3% maximum difference was found; it was therefore assumed that all measurements were affected by a maximum 3% error (this error is reported in Tables 5.11-5.13).

Table 5.11 Concentrations (wt.% and vol.%) of PEEK and nano-Al_2O_3 in coatings deposited applying 20, 30 and 40 V from the 3A-3P suspension for the indicated deposition times.

ΔV = 20 V				
Deposition time	**wt.% Al_2O_3**	**wt.% PEEK**	**vol.% Al_2O_3**	**vol.% PEEK**
2 min	79 ± 2	21 ± 2	55 ± 2	45 ± 2
3 min	79 ± 2	21 ± 2	55 ± 2	45 ± 2
4 min	78 ± 2	22 ± 2	54 ± 2	46 ± 2
5 min	75 ± 2	25 ± 2	50 ± 2	50 ± 2
6 min	80 ± 2	20 ± 2	56 ± 2	44 ± 2
7 min	79 ± 2	21 ± 2	55 ± 2	45 ± 2
8 min	84 ± 2	16 ± 2	62 ± 2	38 ± 2
9 min	77 ± 2	23 ± 2	52 ± 2	48 ± 2
ΔV = 30 V				
Deposition time	**wt.% Al_2O_3**	**wt.% PEEK**	**vol.% Al_2O_3**	**vol.% PEEK**
2 min	82 ± 2	18 ± 2	60 ± 2	40 ± 2
3 min	83 ± 2	17 ± 2	60 ± 2	40 ± 2
4 min	80 ± 2	20 ± 2	56 ± 2	44 ± 2
5 min	76 ± 2	24 ± 2	50 ± 2	50 ± 2
ΔV = 40 V				
Deposition time	**wt.% Al_2O_3**	**wt.% PEEK**	**vol.% Al_2O_3**	**vol.% PEEK**
2 min	80 ± 2	20 ± 2	56 ± 2	44 ± 2
3 min	80 ± 2	20 ± 2	57 ± 2	43 ± 2
4 min	79 ± 2	21 ± 2	55 ± 2	45 ± 2

For the 3P-3A and the 4P-2A suspensions, the deposition time was varied minute by minute to observe if the PEEK-nano-Al_2O_3 ratio in the composites was constant during the process or changed with the deposition time; the results are listed in Tables 5.11 and 5.12 for the 3P-3A and 4P-2A suspensions, respectively. This study was carried out following the sedimentation observed at the bottom of the container few minutes after the stirring was stopped. Considering that the nano-Al_2O_3 suspensions were more stable than the PEEK suspensions, it was assumed that the sedimenting powder would have been PEEK with consequent possible decrease of the PEEK concentration in the coating with the deposition time. From the results reported in Tables 5.11 and 5.12 and taking into account the experimental errors, the relative concentrations of PEEK and nano-Al_2O_3 in the films deposited under different conditions can be considered reproducible and independent from the deposition time. Consequently, only fewer conditions were analysed to determine the PEEK-alumina weight ratio in coatings deposited from 5P-1A suspensions (Table 5.13) and it was assumed that the data obtained were representative of the system.

Table 5.12 Concentrations (wt.% and vol.%) of PEEK and nano-Al_2O_3 in the coatings deposited applying 20, 30 and 40 V from the 4P-2A suspension for the indicated deposition times.

ΔV = 20 V				
Deposition time	**Wt.% Al_2O_3**	**wt.% PEEK**	**vol.% Al_2O_3**	**vol.% PEEK**
2 min	56 ± 2	44 ± 2	29 ± 2	71 ± 2
3 min	60 ± 2	40 ± 2	33 ± 2	67 ± 2
4 min	65 ± 2	35 ± 2	37 ± 2	63 ± 2
5 min	59 ± 2	41 ± 2	32 ± 2	68 ± 2
6 min	61 ± 2	39 ± 2	34 ± 2	66 ± 2
7 min	65 ± 2	35 ± 2	38 ± 2	62 ± 2
8 min	66 ± 2	34 ± 2	39 ± 2	61 ± 2
9 min	65 ± 2	35 ± 2	38 ± 2	62 ± 2
10 min	62 ± 2	38 ± 2	34 ± 2	66 ± 2
11 min	61 ± 2	39 ± 2	34 ± 2	66 ± 2
ΔV = 30 V				
Deposition time	**Wt.% Al_2O_3**	**wt.% PEEK**	**vol.% Al_2O_3**	**vol.% PEEK**
2 min	58 ± 2	42 ± 2	31 ± 2	69 ± 2
3 min	63 ± 2	37 ± 2	35 ± 2	65 ± 2
4 min	64 ± 2	36 ± 2	36 ± 2	64 ± 2
5 min	63 ± 2	37 ± 2	35 ± 2	65 ± 2
6 min	61 ± 2	39 ± 2	33 ± 2	67 ± 2
7 min	62 ± 2	38 ± 2	35 ± 2	65 ± 2
8 min	64 ± 2	36 ± 2	36 ± 2	64 ± 2
9 min	65 ± 2	35 ± 2	38 ± 2	62 ± 2
ΔV = 40 V				
Deposition time	**Wt.% Al_2O_3**	**wt.% PEEK**	**vol.% Al_2O_3**	**vol.% PEEK**
2 min	55 ± 2	45 ± 2	29 ± 2	71 ± 2
3 min	55 ± 2	45 ± 2	28 ± 2	72 ± 2
4 min	62 ± 2	38 ± 2	34 ± 2	66 ± 2
5 min	62 ± 2	38 ± 2	34 ± 2	66 ± 2
6 min	60 ± 2	40 ± 2	33 ± 2	67 ± 2
7 min	61 ± 2	39 ± 2	34 ± 2	66 ± 2

Table 5.13 Concentrations (wt.% and vol.%) of PEEK and nano-Al_2O_3 in the coatings deposited applying 20 V, 30 V and 40 V from the 5P-1A suspension for the indicated deposition times.

ΔV = 20 V				
Deposition time	**Wt.% Al_2O_3**	**wt.% PEEK**	**vol.% Al_2O_3**	**vol.% PEEK**
3 min	30 ± 2	70 ± 2	12 ± 2	87 ± 2
5 min	30 ± 2	70 ± 2	12 ± 2	88 ± 2
ΔV = 30 V				
Deposition time	**Wt.% Al_2O_3**	**wt.% PEEK**	**vol.% Al_2O_3**	**vol.% PEEK**
3 min	32 ± 2	68 ± 2	13 ± 2	87 ± 2
5 min	27 ± 2	73 ± 2	11 ± 2	89 ± 2
ΔV = 40 V				
Deposition time	**Wt.% Al_2O_3**	**wt.% PEEK**	**vol.% Al_2O_3**	**vol.% PEEK**
3 min	31 ± 2	69 ± 2	13 ± 2	87 ± 2
5 min	33 ± 2	67 ± 2	14 ± 2	86 ± 2

From these analyses, it was found that coatings deposited from a 3P-3A suspensions contained 16-25 wt.% (or 38-50 vol.%) of PEEK and 75-84 wt.% (or 50-62 vol.%) of nano-Al_2O_3, those deposited from a 4P-2A suspension contained 34-45 wt.% (or 61-72 vol.%) of PEEK and 55-66 wt.% (or 28-39 vol.%) of nano-Al_2O_3 and those deposited from a 5P-1A suspension contained 67-73 wt.% (or 86-89 vol.%) of PEEK and 27-33 wt.% (or 11-14 vol.%) of nano-Al_2O_3 when the same difference of potential was applied for different deposition times

and also when the difference of potential was varied from 20 to 40 V. The amount of nano-Al_2O_3 in the coatings assessed experimentally was much higher than that expected if the PEEK and the nano-Al_2O_3 particles were deposited stoichiometrically, as shown from the data reported in Tables 5.10-5.13. This behaviour could be explained considering the faster sedimentation of the large PEEK particles compared to the nano-Al_2O_3 particles.

The fact that the concentration ratio between PEEK and nano-Al_2O_3 in the films did not depend on the difference of potential applied and on the deposition time but just on the suspension composition confirmed the formation in the suspension of PEEK-nano-Al_2O_3 composite particles (see Fig. 5.37 and 5.38) with composition depending on the suspension content. It can be therefore suggested that PEEK-nano-Al_2O_3 composite particles are formed in the suspension and behave as single component particles with fixed properties. The TEM analysis of the suspension showed the presence of PEEK-nano-Al_2O_3 composite particles (Fig. 5.38 b) and c)) and nano-Al_2O_3 particles (Fig. 5.38 a)). These two kinds of particles exhibited similar positive charges (see zeta potentials in Fig. 5.36) but different sizes (few nm and few μm); therefore an increase of the electric field would favour the deposition on the negative electrode of the smaller particles (alumina) because they would have higher velocity. However, considering the relatively small weight of the nano-Al_2O_3 particles compared to the PEEK-nano-Al_2O_3 composite particles and their low concentration in suspension (TEM analysis), it can be concluded that the contribution of these particles to the Al_2O_3 weight would not greatly influence the final results.

Prediction of coating composition

In order to investigate the link between the relative amount of PEEK and nano-Al_2O_3 in suspension and their respective amounts in the deposited coatings, the following numerical analysis was carried out. The relationship between the amounts of PEEK and nano-Al_2O_3 in the coating (P_C and A_C, respectively) can be written as a function of the respective amounts in the suspension (P_S and A_S), as follows:

$$\frac{A_C\%}{P_C\%} = k\frac{A_S\%}{P_S\%} \qquad [5.8]$$

where A_C% and P_C% are the amounts (wt.%) of nano-Al_2O_3 and PEEK in the coating and A_S% and P_S% are their amount (wt.%) in the suspension and k is a constant. This relationship gives the value of the weight or volume ratio between PEEK and nano-Al_2O_3 in coatings deposited from a suspension of known composition. Similarly, the relationship:

$$\frac{P_S\%}{A_S\%} = k\frac{P_C\%}{A_C\%} \qquad [5.9]$$

provides information about the suspension composition needed to deposit a film with a particular weight or volume ratio between PEEK and nano-Al_2O_3. The constant that connect these two relationships is:

$$k = \frac{A_C\%/P_C\%}{A_S\%/P_S\%} = \frac{A_C\% \cdot P_S\%}{A_S\% \cdot P_C\%} \qquad [5.10]$$

From the experiments carried out for the 3P-3A and 4P-2A suspensions, the values for $A_C\%$, $P_C\%$, $A_S\%$ and $P_S\%$ are known and listed in Table 5.14. $A_C\%$ and $P_C\%$ were calculated from the average of all the data obtained applying different ΔV for different deposition times and listed in Tables 5.11 and 5.12.

For the 3P-3A suspension: $$k = \frac{79.4\%/20.6\%}{50\%/50\%} = 3.8 \qquad [5.11]$$

For the 4P-2A suspension: $$k = \frac{61.5\%/38.5\%}{33.3\%/66.6\%} = 3.2 \qquad [5.12]$$

Table 5.14 Values of $A_C\%$, $P_C\%$, $A_S\%$ and $P_S\%$ obtained experimentally for the two suspensions investigated.

	3P-3A	4P-2A
$A_C\%$	79.4 wt.%	61.5 wt.%
$P_C\%$	20.6 wt.%	38.5 wt.%
$A_S\%$	50.0 wt.%	33.3 wt.%
$P_S\%$	50.0 wt.%	66.7 wt.%

These two values: k=3.8 and k=3.2 are remarkably similar and the difference between them is probably due to experimental errors; consequently, it can be considered that k=3.5, using an average value obtained from the two suspensions. Therefore, using this value of k and equation 5.8, it should be possible to predict the coating ratio of any other suspension. For example, for a suspension with an intermediate composition, e.g. 3.5P-2.5A, equation 5.8 can be written as:

$$\frac{A_C\%}{P_C\%} = 3.5\frac{2.5\%}{3.5\%} = 2.5 \qquad \text{or} \qquad A_C\% = 2.5P_C\% \qquad [5.13]$$

and the PEEK-nano-Al_2O_3 composite coating deposited from this suspension should contain 28.6 wt.% of PEEK and 71.4 wt.% of nano-Al_2O_3; experimentally a composition of 28 wt.% of PEEK and 72 wt.% of nano-Al_2O_3 was found, in perfect agreement with the theoretical expectations. When a 5P-1A suspension was employed for the coating deposition, equation 5.8 predicts that films containing 58.8 wt.% of PEEK and 41.2 wt.% of nano-Al_2O_3 would be deposited whereas from the experimental data reported in Table 5.13 the films were found to contain 69.5 wt.% of PEEK and 30.5 wt.% of nano-Al_2O_3. In this case the ability of the equation proposed to predict the coating compositions was poor. Therefore it can be concluded that equation 5.8 with k=3.5 is suitable for predicting coating composition in a range of suspension compositions between the 3P-3A and the 4P-2A suspensions, where the value of k seemed constant, but the equation is not applicable outside this suspension composition range.

5.5.7 Microstructure of the composite coatings

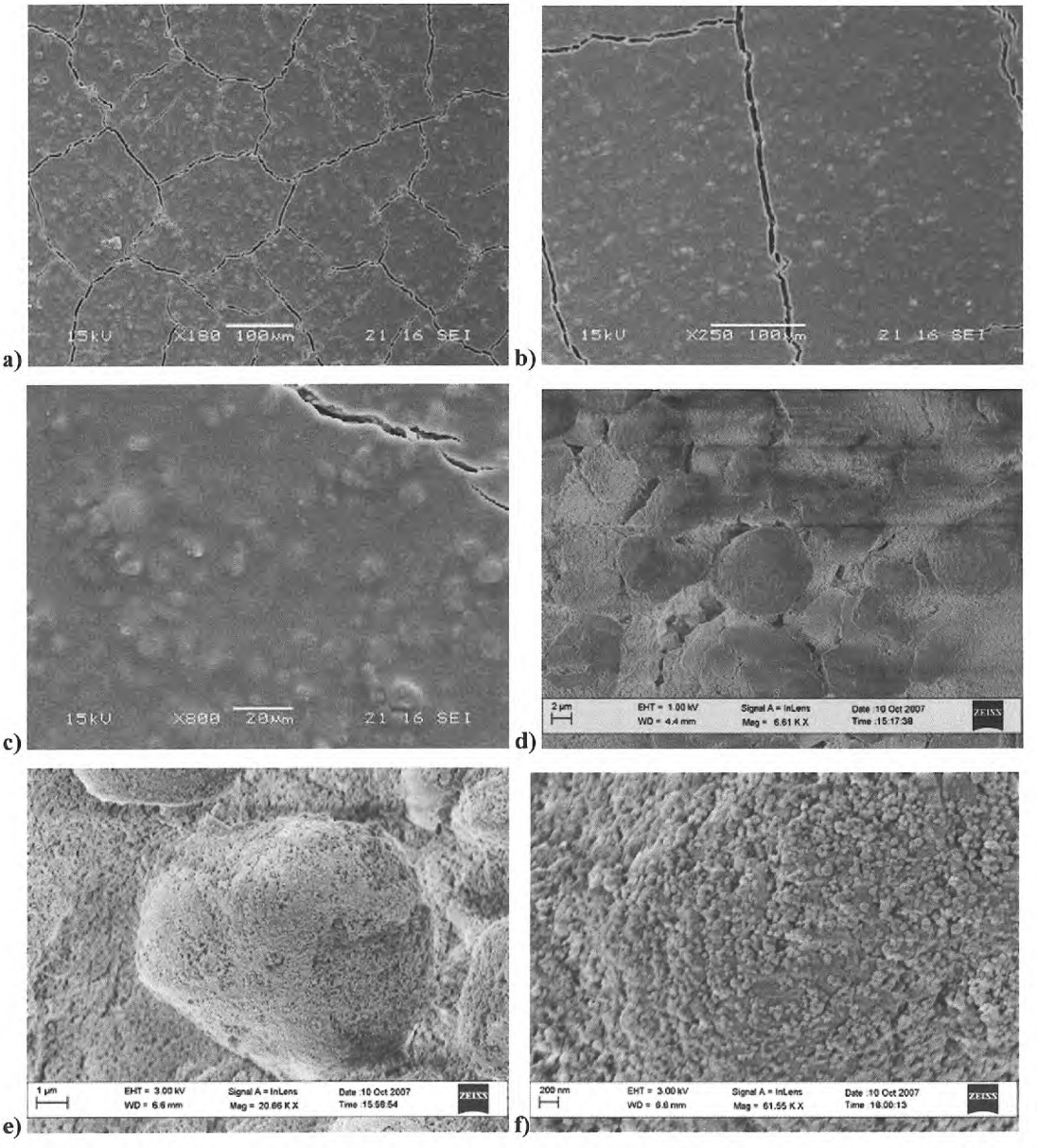


Figure 5.51 SEM images of the top surface of a PEEK-nano-Al_2O_3 coating deposited from a 3P-3A suspension showing the microstructure at a) x180, b) x250, c) x800, d) x6600, e) a PEEK particle covered by nano-Al_2O_3 particles and f) the distribution of the nano-Al_2O_3 particles on a PEEK particle.

Figures 5.51-5.53 show the microstructure of the top surface of coatings deposited applying a difference of potential of 30 V for 3 min from 3P-3A, 4P-2A and 5P-1A suspensions, respectively. The top surface of the coatings deposited from the 3P-3A and 4P-2A suspensions presented some cracks, less remarkable than those of the pure nano-Al_2O_3 coatings shown in Figures 5.30 and 5.32, and some PEEK particles, as lumps, emerging from the coating (see Fig. 5.51 a), b), c), d) and e) and 5.52 a)); not many PEEK particles were visible due to the high amount of nano-Al_2O_3 in these two films (80 wt.% and 60 wt.%, respectively). The top surface of these coatings (see Fig. 5.51 f) and 5.52 b)) was completely covered by nano-Al_2O_3 particles of morphology, at high magnification, considerably similar to that of the

nano-Al_2O_3 coatings shown in Figure 5.32 c).

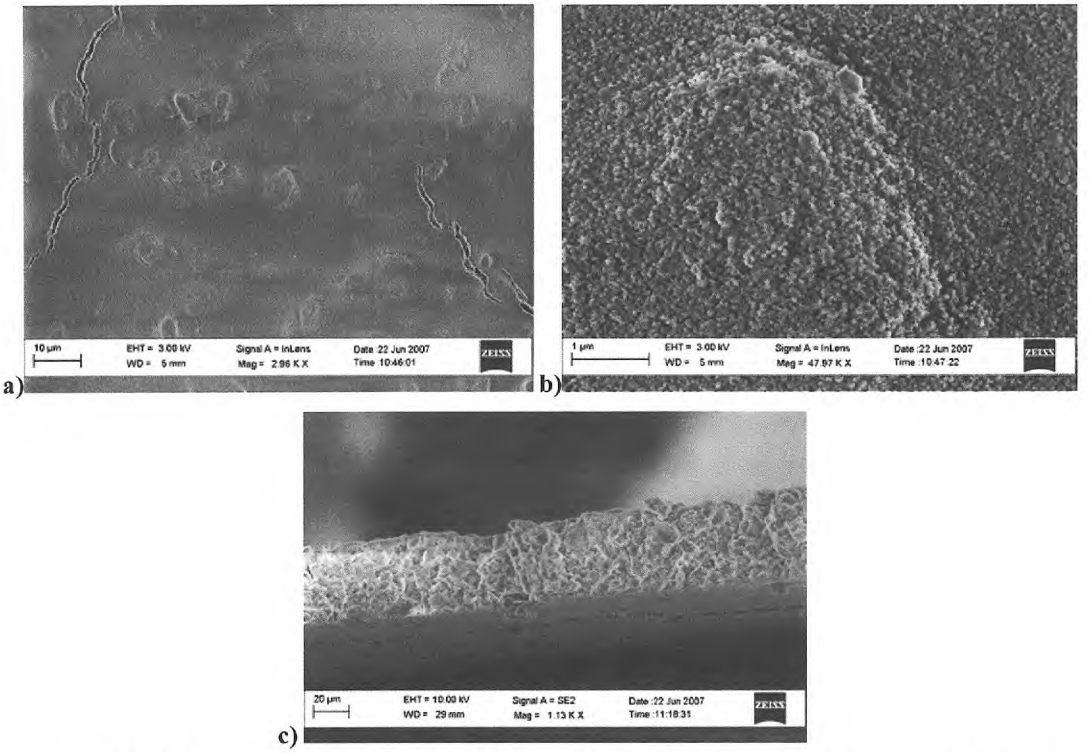


Figure 5.52 SEM images of PEEK-nano-Al_2O_3 film deposited from a 4P-2A suspension. a) and b) top surface showing a) the microstructure and b) the high resolution organization of the nano-Al_2O_3 particles on a PEEK particle, c) the cross section.

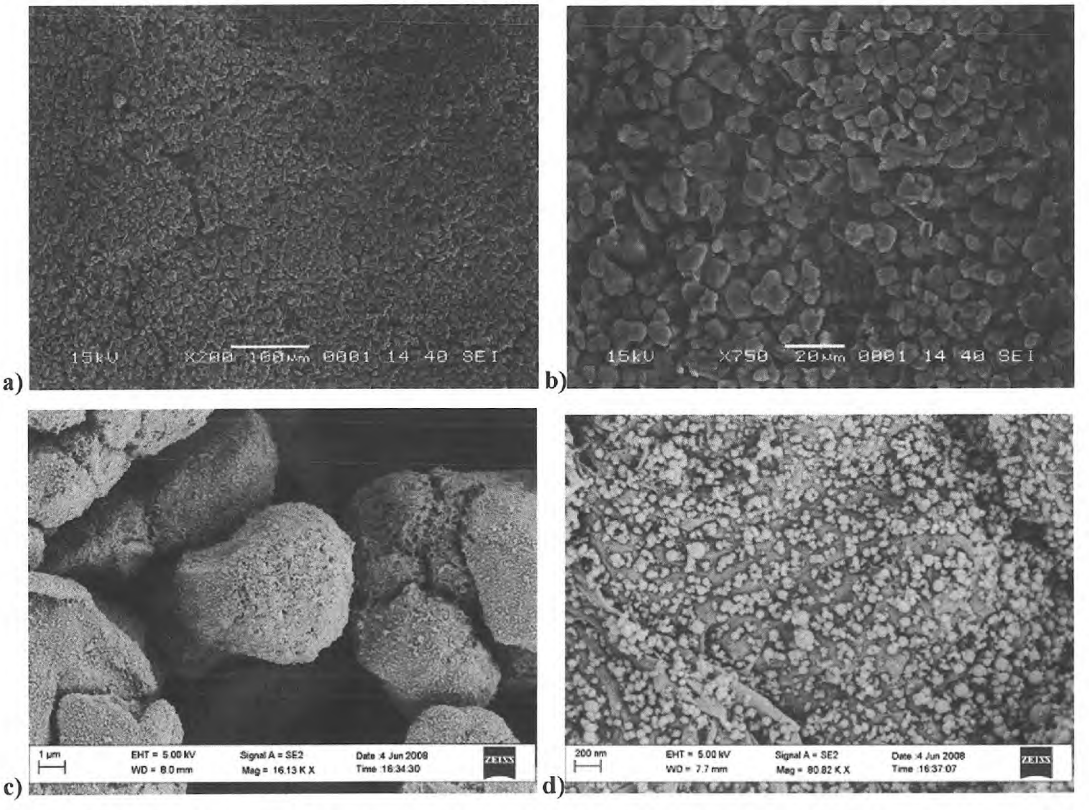


Figure 5.53 SEM images of PEEK-nano-Al_2O_3 film deposited from 5P-1A suspension showing the microstructure at a) x200, b) x750, c) and d) the distribution of the nano-Al_2O_3 on PEEK particles.

The films deposited from the 5P-1A suspension were highly rich in PEEK (70 wt.%) and their top surface showed clearly the PEEK particles (Fig. 5.53) with a distribution similar to pure PEEK coatings (see Fig. 5.17). Higher magnification analysis (see Fig. 5.53 c) and d)) of these coatings demonstrated that all the PEEK particles were covered by a layer of nano-Al_2O_3, which was necessary to render the PEEK particles positively charged. The nano-Al_2O_3 layer on the PEEK particles deposited from 5P-1A suspension (Fig. 5.53 d)) was not as continuous as the one observed for films deposited from 3P-3A and 4P-2A suspensions (Fig. 5.51 f) and 5.52 b)) due to the smaller amount of nano-Al_2O_3 in suspension. Fig. 5.52 c) shows the cross section of a coating deposited from a 4P-2A suspension applying 30 V for 3 min demonstrating the formation by EPD of homogeneous PEEK-nano-Al_2O_3 ~ 40 μm thick coatings.

5.5.8 Thermal properties

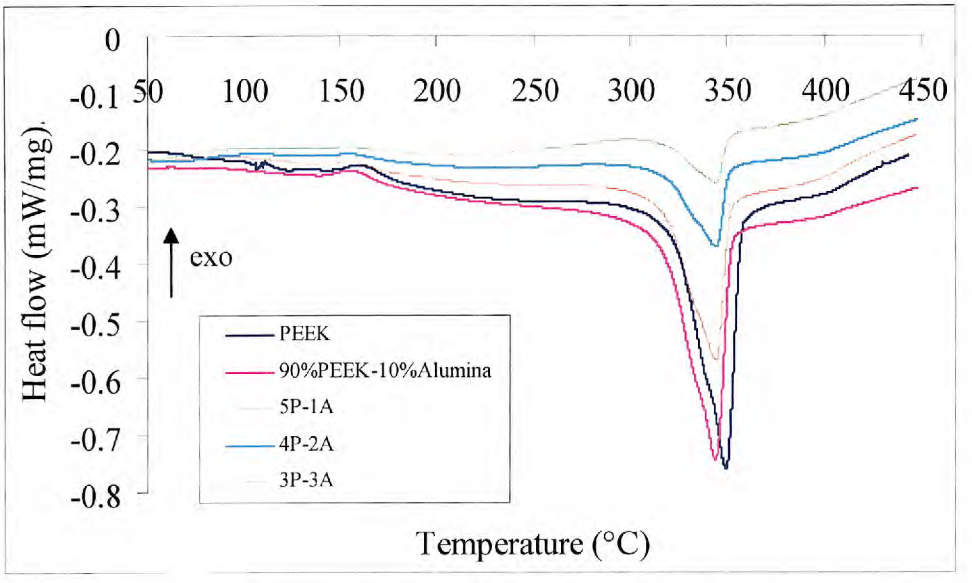


Figure 5.54 DSC analyses of pure PEEK powder and PEEK-nano-Al_2O_3 composite powders.

Since the PEEK melts and decomposes at much lower temperatures than the Al_2O_3, it was fundamental to study how the presence of nano-Al_2O_3 in the PEEK composites influenced the polymer thermal behaviour (i.e. melting temperature and degradation temperature). These studies have been carried out using DSC between room temperature and 450°C (as described in section 3.7) and DTA and TGA between room temperature and 750°C (as described in section 3.6) applying in all cases a heating rate of 10°C·min^{-1}. The powders analysed were pure PEEK, a mixture containing 90 wt.% PEEK and 10 wt.% nano-Al_2O_3 and the powders deposited from 5P-1A, 4P-2A and 3P-3A suspensions containing around 70 wt.% PEEK and 30 wt.% nano-Al_2O_3, 40 wt.% PEEK and 60 wt.% nano-Al_2O_3 and 20 wt.% PEEK and 80 wt.% nano-Al_2O_3, respectively.

The aim of the DSC study was to determine if the melting temperature (Tm) of PEEK was influenced by the amount of nano-Al_2O_3 in the composite. A comparison between the DSC

heating curves of all these composite powders is shown in Figure 5.54 and the corresponding melting temperatures (Tm) (the tip of the melting peak), onset melting temperatures (Ton) (the start of the peak) and heat of fusion (the area of the melting peaks) are listed in Table 5.15. From the melting temperatures and the onset melting temperatures listed in Table 5.15, it was observed that the melting temperature of pure PEEK was slightly higher (~5°C) than that of the composites containing from 10 to 80 wt.% of nano-Al_2O_3, which all had similar melting behaviours. The decrease of the melting temperature with the addition of nano-Al_2O_3 in the composite was also reported by Nandar et al. [25] and Kuo et al. [205] and it was explained considering the higher thermal conductivity of Al_2O_3 compared to PEEK (30 and 0.2$W \cdot m^{-1} \cdot K^{-1}$) that produces a more homogeneous heat transfer in the composites.

Table 5.15 DSC data of pure PEEK and PEEK-nano-Al_2O_3 composites during the heating cycle.

Composition	Tm (°C)	Ton (°C)	Heat of fusion ($J \cdot g^{-1}$)	% of crystallinity
100 wt.% PEEK	349.3	322.3	58.9	45
90 wt.%PEEK-10 wt.%Al_2O_3	343.7	320.1	55.8	50
5P-1A (70 wt.%PEEK-30 wt.%Al_2O_3)	344.3	316.7	40.1	44
4P-2A (40 wt.%PEEK-60 wt.%Al_2O_3)	344.4	317.7	18.4	39
3P-3A (20 wt.%PEEK-80 wt.%Al_2O_3)	344.0	317.5	11.1	37

As expected, the heat of fusion of the composites (see Table 5.15) decreased with decreasing amount of PEEK. Knowing that the enthalpy of melting of a polymer is directly proportional to the % of crystallinity (see section 5.3.1) [274, 275], that the heat of fusion of 100% pure crystalline PEEK is 130 $J \cdot g^{-1}$ [10, 26, 205] and taking into consideration the relative amount of PEEK in the different composites powder, it was possible to estimate the % of crystallinity of all the composites using the following formula [26, 205]:

$$\%\ of\ crystallinity = \frac{heat\ of\ fusion \cdot 100}{130 \cdot wt.\%PEEK} \qquad [5.14]$$

The results are listed in Table 5.15 and it seemed that the composite crystallinity was similar or higher than that of pure PEEK when the nano-Al_2O_3 content was lower than 30 wt.%, probably because of the heterogeneous nucleation effect of the nano-Al_2O_3 that enhanced the PEEK crystallization [3, 26, 205]. Higher amounts of nano-Al_2O_3 decreased the PEEK crystallinity probably because of the reduced mobility of the polymer chains in the composites [26, 205].

The TGA (Figure 5.55) and DTA (Figure 5.56) analyses were carried out to study the thermal stability of the composites in air and to understand how the amount of nano-Al_2O_3 influenced the composite degradation temperature (Td). Td was chosen as the temperature at which the samples lost 10 wt.%, as described by Goyal et al. [3, 27, 28], and the values are reported in Table 5.16. For each experiment ~10-12 mg of powder were employed [27] since it was observed that the amount of powder analysed could strongly influence the final results; in

fact the degradation temperature of pure PEEK varied from 564 to 629°C when the sample size varied from 5.71 to 23.9 mg.

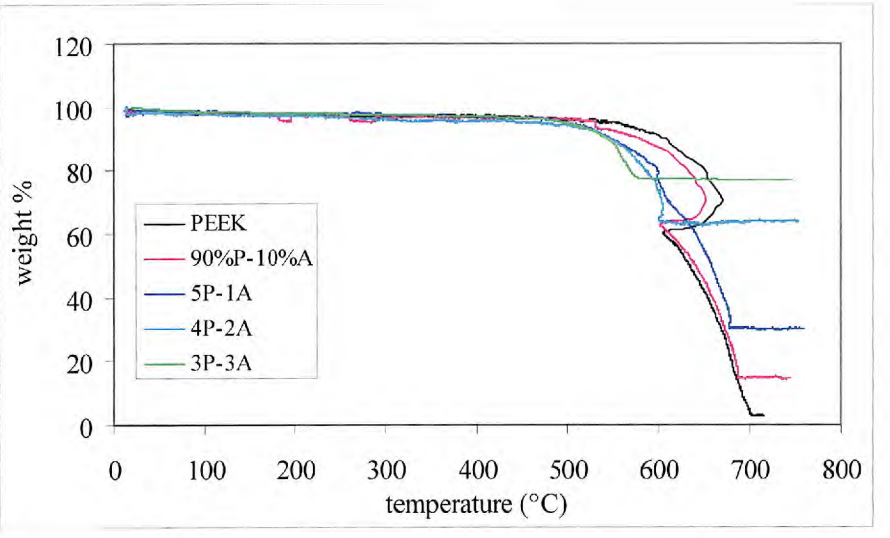


Figure 5.55 Comparison between the weight variations with the temperature of PEEK-nano-Al_2O_3 composite powders with different amounts of PEEK (TGA analysis).

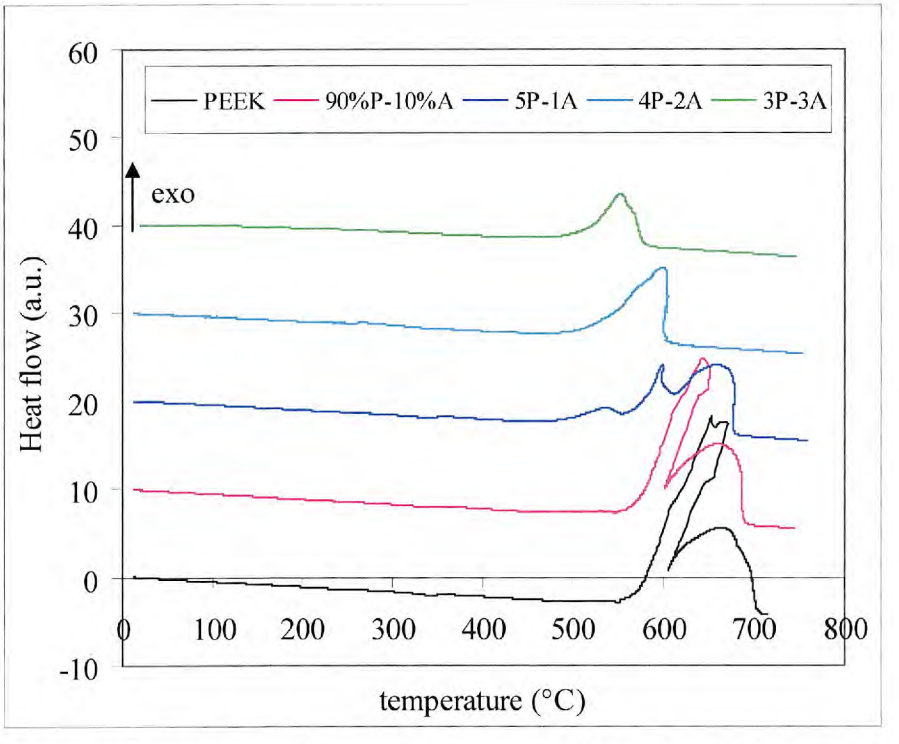


Figure 5.56 Comparison between the heat flow variations with the temperature of PEEK-nano-Al_2O_3 composite powders with different amounts of PEEK (DTA analysis).

From the Td reported in Table 5.16 and the TGA analysis in Figure 5.55 it emerged that pure PEEK was thermally stable at temperatures higher than those of the composites and that Td decreased with increasing amount of nano-Al_2O_3, reaching a constant temperature for nano-

Al_2O_3 content > 30 wt.%. The DTA plots reported in Figure 5.56 show that the PEEK in the PEEK-nano-Al_2O_3 composites started to decompose at slightly lower temperatures compared to pure PEEK with the decomposition exothermic peaks moving to lower temperatures as the amount of nano-Al_2O_3 in the composite increased. The decomposition of pure PEEK and of the mixture containing 90 wt.% PEEK-10 wt.% nano-Al_2O_3 produced two exothermic peaks, whereas the 40 wt.% PEEK-60 wt.% nano-Al_2O_3 and 20 wt.% PEEK-80 wt.% nano-Al_2O_3 mixtures exhibited just one exothermic peak probably for the smaller amount of decomposing material. It is interesting to note that the 70 wt.% PEEK-30 wt.% nano-Al_2O_3 mixture showed three exothermic decomposition peaks: the two at higher temperatures were equivalent to the decomposition peaks observed for the high PEEK containing mixtures and the one at lower temperature was equivalent to the decomposition peak of the 20 wt.% PEEK-80 wt.% nano-Al_2O_3 mixture. The Td found for the 90 wt.% PEEK-10 wt.% nano-Al_2O_3 and for the 70 wt.% PEEK-30 wt.% nano-Al_2O_3 composites (Table 5.16) were significantly similar to the data reported by Kuo et al. [26] and Goyal et al. [3] for composites containing 2.5-10 wt.% and 1.25-30 wt.% of nano-Al_2O_3. The main difference between the results obtained here and those reported in the literature was the Td of pure PEEK being 559 [26] and 556°C [3] significantly lower than the 608°C found from the TGA analysis.

Table 5.16 Degradation temperatures for PEEK-nano-Al_2O_3 composites with different compositions.

Composition	Td (°C)
100 wt.% PEEK	608
90 wt.%PEEK-10 wt.% Al_2O_3	579
5P-1A (70 wt.%PEEK-30 wt.% Al_2O_3)	547
4P-2A (40 wt.%PEEK-60 wt.% Al_2O_3)	546
3P-3A (20 wt.%PEEK-80 wt.% Al_2O_3)	544

5.5.9 Heat-treatment of the composite coatings

The heat-treatment after the deposition is a fundamental step for the production of useful coatings since it increases the substrate/coating adhesion and improves the coating micro-structure eliminating porosity, as observed for the PEEK films in section 5.3.5. According to the thermal analysis reported in section 5.5.8, the nano-Al_2O_3 inclusions were seen to slightly decrease the PEEK melting temperature and therefore the optimum heat-treatment conditions for PEEK coatings (343°C for 30 min with a heating rate of 10°C·min^{-1} (see section 5.3.5)) were employed to heat-treat composite samples deposited applying a difference of potential of 30 V for 3 min. The composite coatings deposited from the three suspensions (3P-3A, 4P-2A and 5P-1A) and heat-treated under these conditions were quite uniform over the whole area coated, as shown in Figure 5.57. These coatings were all considerably similar (Figure 5.57)

except for a slightly different colour; the higher the PEEK concentration in the film the darker the coatings due to the characteristic brown colour of the melted PEEK. In order to test how the heat-treatment conditions influenced the substrate/coating adhesion a qualitative test was carried out by simply scratching manually the coating with a plastic pointy object. From this analysis it resulted that these coatings were scratch resistant, as qualitatively demonstrated by Figure 5.58.

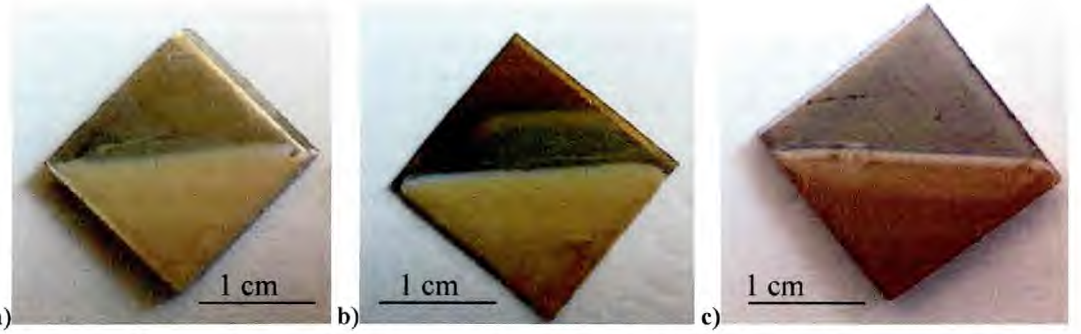


Figure 5.57 Images of a) sample deposited from the 3P-3A, b) the 4P-2A, and c) the 5P-1A suspension and heat-treated at 343°C with a heating rate of 10°C·min^{-1} and 30 min holding time.

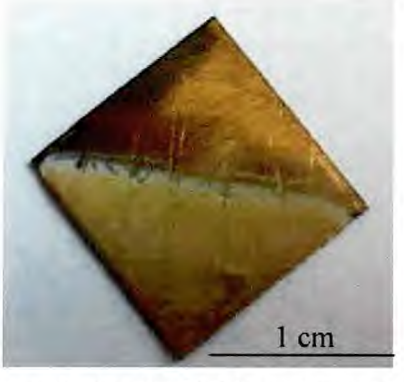


Figure 5.58 Image of a sample coated using the 4P-2A suspension and heat-treated at 343°C with a heating rate of 10°C·min^{-1} and 30 min holding time. After the heat-treatment step the coating was manually scratched with a plastic pointy object to qualitatively test the substrate/coating adhesion.

SEM microstructural analysis of coatings deposited from 3P-3A and 4P-2A suspensions and heat-treated at 343°C for 30 min with a heating rate of 10°C·min^{-1} demonstrated that there were still numerous cracks and that the PEEK particles maintained their original shape, as if they were not molten. The microstructures of 3P-3A and 4P-2A composite films were considerably similar due to the high nano-Al_2O_3 content and therefore, for simplicity, just the analysis of the 4P-2A films is discussed here. The analysis carried out on 4P-2A coatings are shown in Figure 5.59; it is evident that the coatings still presented few cracks (Figure 5.59 a) and b)), that the PEEK particles maintained their original shape after melting (Figure 5.59 c)) and that the threefold heavier nano-Al_2O_3 did not sink in the molten PEEK but was still distributed on the top of the coating (Figure 5.59 d)). The fact that the PEEK particles did not deform was unexpected considering that they were completely molten and deformed in pure

PEEK coatings after heat-treatment under the same conditions, as shown in Figure 5.23 a) and b) and considering that the thermal analysis in Figure 5.54 and in Table 5.15 showed that the melting point of the PEEK-nano-Al_2O_3 mixture was ~5°C lower than that of pure PEEK. Hence, in order to determine if holding the samples at 343°C for longer time would melt and deform the PEEK particles, further experiments were carried out. SEM images showing the surfaces of 4P-2A coatings heat-treated for 2, 5 and 20 h (at 343°C with 10°C·min^{-1} heating rate) are presented in Figures 5.60-5.62. From the visual inspection of these micrographs (Figures 5.60-5.62), it can be seen that there were still numerous cracks and some lumps on the surfaces of all the coatings indicating that the PEEK was still not completely molten/deformed (see Figures 5.60-5.62).

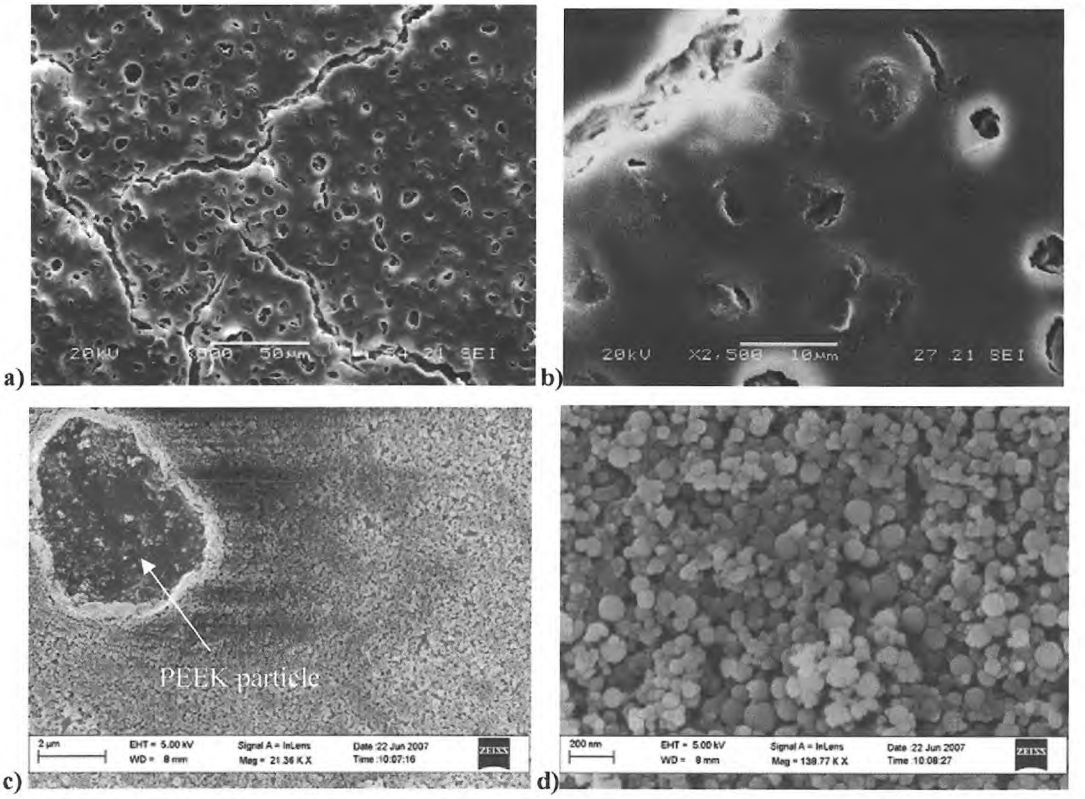


Figure 5.59 SEM images of PEEK-nano-Al_2O_3 films deposited from the 4P-2A suspension and heat-treated at 343°C with a heating rate of 10°C·min^{-1} and 30 min holding. a) at x500, b) at x2500, c) showing a PEEK particle surrounded by nano-Al_2O_3 and d) the microstructure of the nano-Al_2O_3 top layer.

The fact that PEEK particles in 3P-3A and 4P-2A composite films did not deform even though the melting temperature was reached (thermal analysis in Fig. 5.54 and Tab. 5.15 and changed in colour shown in Fig. 5.57) could be probably due to the layer of nano-Al_2O_3 particles surrounding the PEEK particles that could obstruct the flow of the molten polymer. The lack of flow of PEEK in PEEK-nano-Al_2O_3 composites was also observed when pellets containing 70 wt.% PEEK-30 wt.% nano-Al_2O_3, 40 wt.% PEEK-60 wt.% nano-Al_2O_3 and 20 wt.% PEEK-80 wt.% nano-Al_2O_3 were prepared by manually pressing the mixed powder in a

cylindrical die and then heat-treated at 343°C for 30 min with a heating rate of 10°C·min^{-1}. Figure 5.63 shows that the composite pellets containing between 20 and 70 wt.% of PEEK maintained the starting shape during heat-treatment (polymer did not flow), a part from a volume contraction due to the shrinkage of the PEEK during melting as observed in Figure 5.19, whereas the pure PEEK pellet completely melted and deformed.

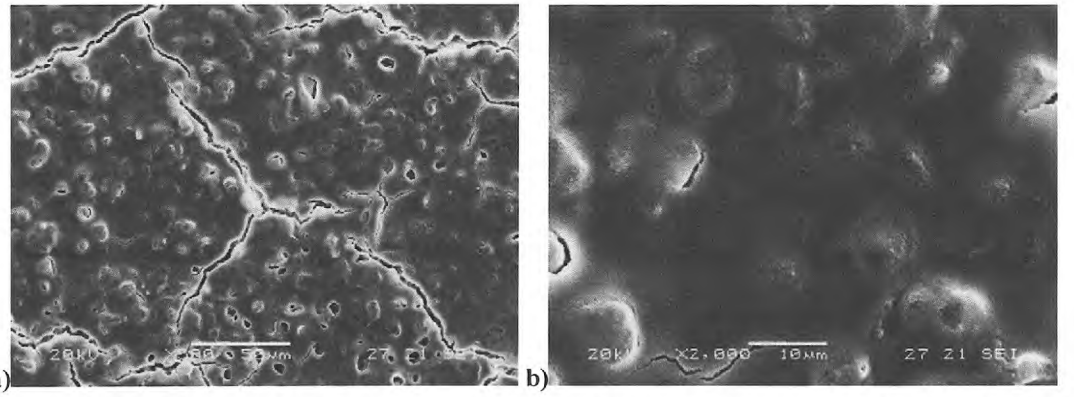


Figure 5.60 SEM images of a film deposited from the 4P-2A suspension and heat-treated at 343°C with a heating rate of 10°C·min^{-1} and 2 h holding time. a) low and b) high magnification.

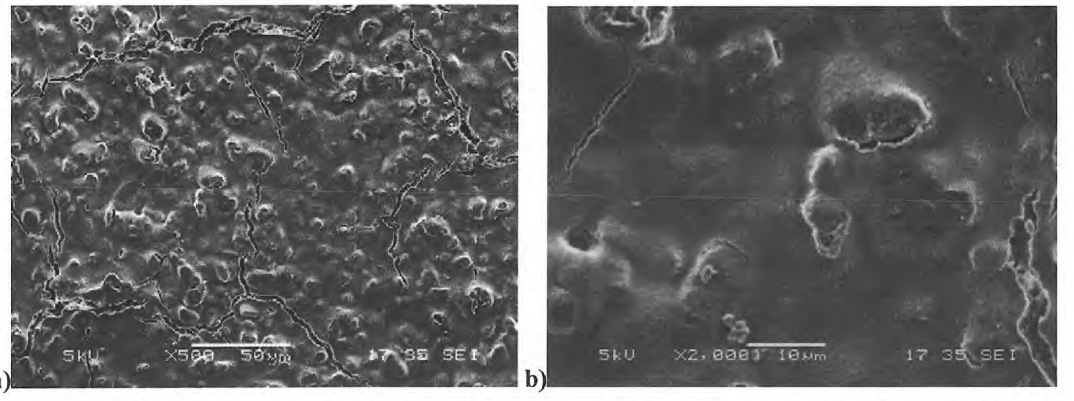


Figure 5.61 SEM images of a film deposited from the 4P-2A suspension and heat-treated at 343°C with a heating rate of 10°C·min^{-1} and 5 h holding time. a) low and b) high magnification.

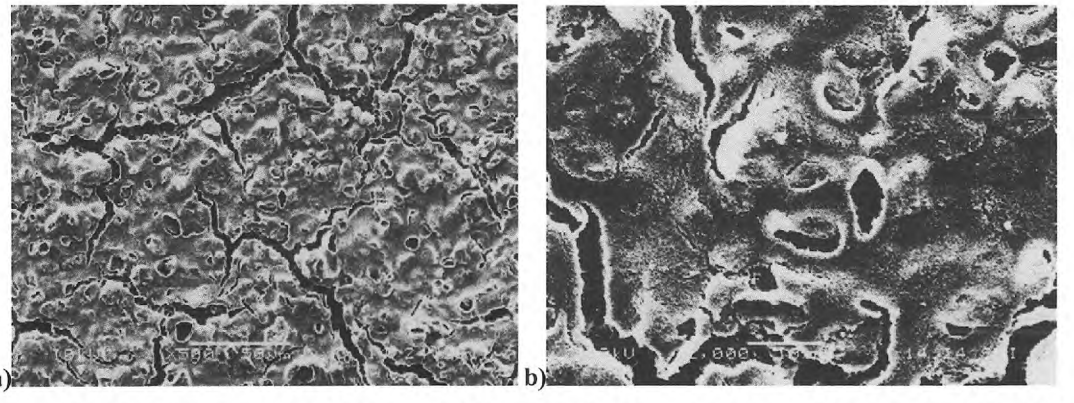


Figure 5.62 SEM images of a film deposited from the 4P-2A suspension and heat-treated at 343°C with a heating rate of 10°C·min^{-1} and 20 h holding time. a) low and b) high magnification.



Figure 5.63 Image of pellets containing from left to right: 20 wt.% PEEK-80 wt.% nano-Al_2O_3, 40 wt.% PEEK-60 wt.% nano-Al_2O_3, 70 wt.% PEEK-30 wt.% nano-Al_2O_3 and pure PEEK prepared by manually pressing the powder in a cylindrical die and heat-treated at 343°C for 30 min with a heating rate of 10°C·min^{-1}.

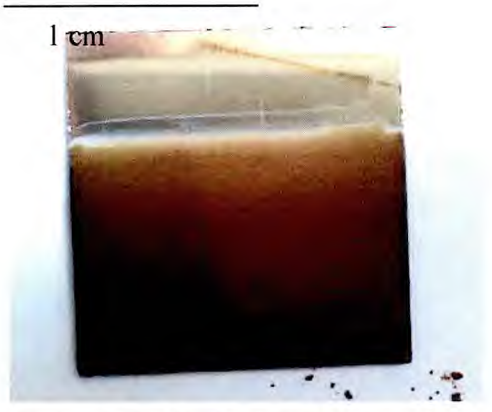


Figure 5.64 PEEK-nano-Al_2O_3 composite film deposited from a 4P-2A suspension and heat-treated at 400°C with a heating rate of 10°C·min^{-1} and 2 hours holding time.

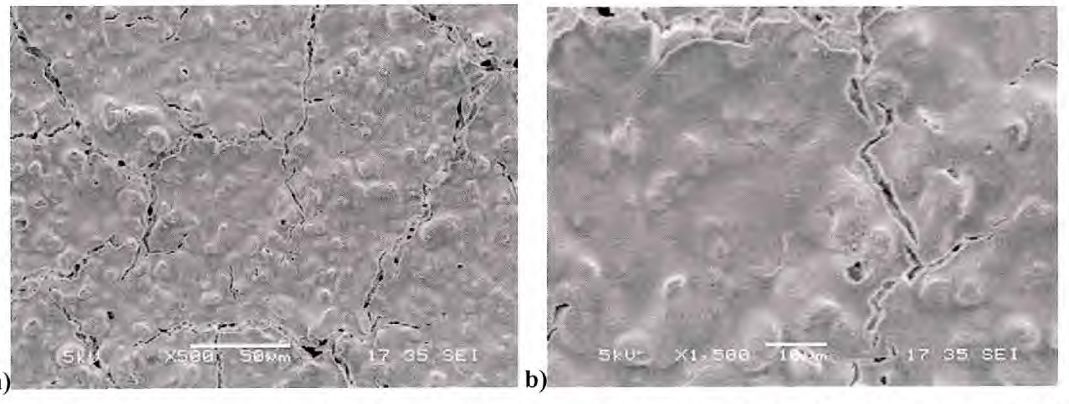


Figure 5.65 SEM images of a film deposited from the 4P-2A suspension and heat-treated at 400°C with a heating rate of 10°C·min^{-1}and 2 h holding time. a) low and b) high magnification.

Considering that the PEEK in the composites did not flow at 343°C, the heat-treatment temperature was increased to 400°C. A sample deposited from the 4P-2A suspension and heat-treated at 400°C for 2 h with a heating rate of 10°C·min^{-1} is shown in Figure 5.64. The SEM microstructure analysis of this coating (shown in Figure 5.65) shows that even after the heat-treatment the film still presented numerous cracks and some PEEK particles maintaining their

original shape. This sample (Figure 5.64) was dark brown as the sample heat-treated at 343°C for 20 h with a heating rate of 10°C·min^{-1} and shown in Figure 5.66 a). It should be noted that the films heat-treated at 343°C for 20 h (Figure 5.66) and those heat-treated at 400°C for 2 h (Figure 5.64) were easier to scratch off using a plastic pointy object compared to the films heat-treated at 343°C for 30 min (Figure 5.58). The poor mechanical integrity observed in the coatings heat-treated at higher temperatures or for longer time was probably due to the partial decomposition of PEEK under these conditions (343°C for 20 h and 400°C for 2 h), as also shown in the SEM images of the cross sections (Figure 5.67). The cross section of a 4P-2A coating heat-treated at 343°C for 5 h (Figure 5.67 a)) showed a uniform, pore-free film and the melted PEEK very well infiltrated into the substrate surface; whereas a 4P-2A coating heat-treated at higher temperatures (400°C for 2 h) (Figure 5.67 b)) presented numerous cavities probably produced during the mechanical polishing of the cross section and due to the weakness of the partially decomposed PEEK. The partial decomposition of PEEK during heat-treatment at 400°C was further confirmed by Figure 5.68, showing a pure PEEK coatings heat-treated at the same temperature for 2 h and partially decomposed.

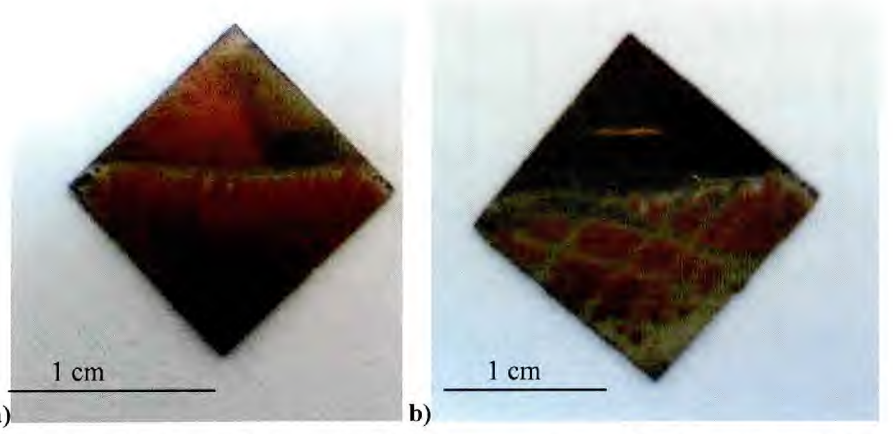
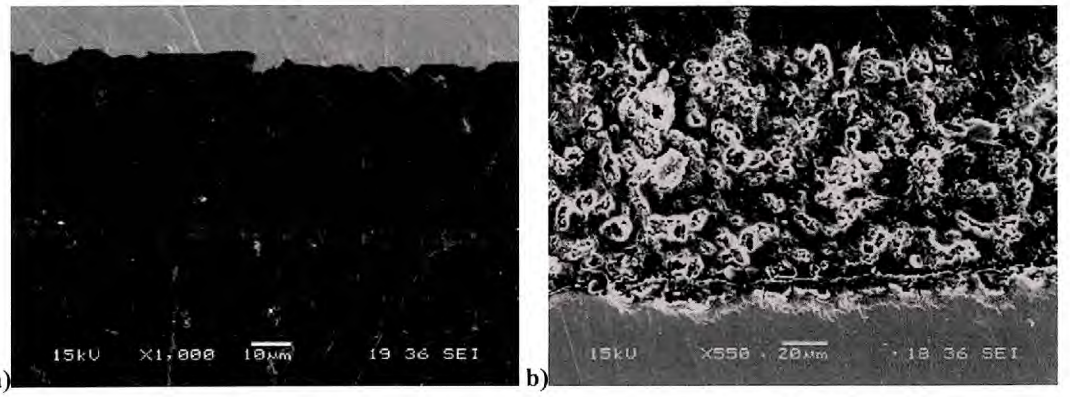


Figure 5.66 a) Sample deposited from the 4P-2A suspension and heat-treated at 343°C with a heating rate of 10°C·min^{-1} and 20 h holding time, b) The same sample after manually scratching the surface with a plastic pointy object to qualitatively test the substrate/coating adhesion.

From this research on PEEK-nano-Al_2O_3 composite coatings deposited from 4P-2A and 3P-3A suspensions it resulted that the best heat-treatment conditions were 343°C for 30 min with a heating rate of 10°C·min^{-1}, as also observed for pure PEEK coatings and described in section 5.3.5, even though the PEEK particles did not flow at the melting temperature because of the high alumina content in these films. The same heating conditions were also applied to heat-treat 5P-1A coatings that differ from those just analysed for the higher PEEK content (70 wt.% instead of 20-40 wt.%). The SEM microstructure analysis in Figure 5.69 a) demonstrates that the PEEK in 5P-1A composites was completely melted after the heat treatment and presented a similar structure to that of pure PEEK films (Figure 5.23), probably because the lower alumina content did not obstruct the flowing of the melted PEEK. Nano-Al_2O_3 particles

are still visible on the coating surface, as shown in Figure 5.69 b). Figure 5.69 demonstrates that it was possible to produce crack-free PEEK-nano-Al_2O_3 composite coatings and that the heat-treatment employed was suitable for the preparation of dense PEEK composite films.



a) b)

Figure 5.67 SEM images of the cross sections of films deposited from the 4P-2A suspension and heat-treated a) at 343°C for 5 h with a heating rate of 10°C·min^{-1} b) at 400°C for 2 h with a heating rate of 10°C·min^{-1}.

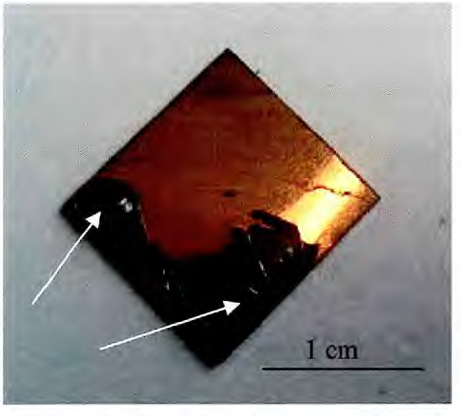
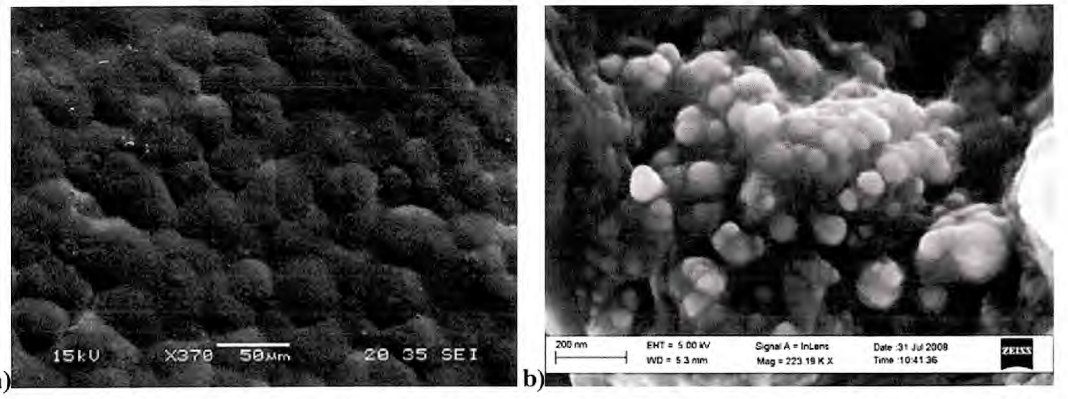


Figure 5.68 Image of a PEEK coating heat-treated at 400°C for 2 h with 10°C·min^{-1} heating rate with arrows showing the partially decomposed PEEK.



a) b)

Figure 5.69 SEM images of a film deposited from a 5P-1A suspension and heat-treated at 343°C with a heating rate of 10°C·min^{-1} and 30 min holding time. a) low and b) high magnification.

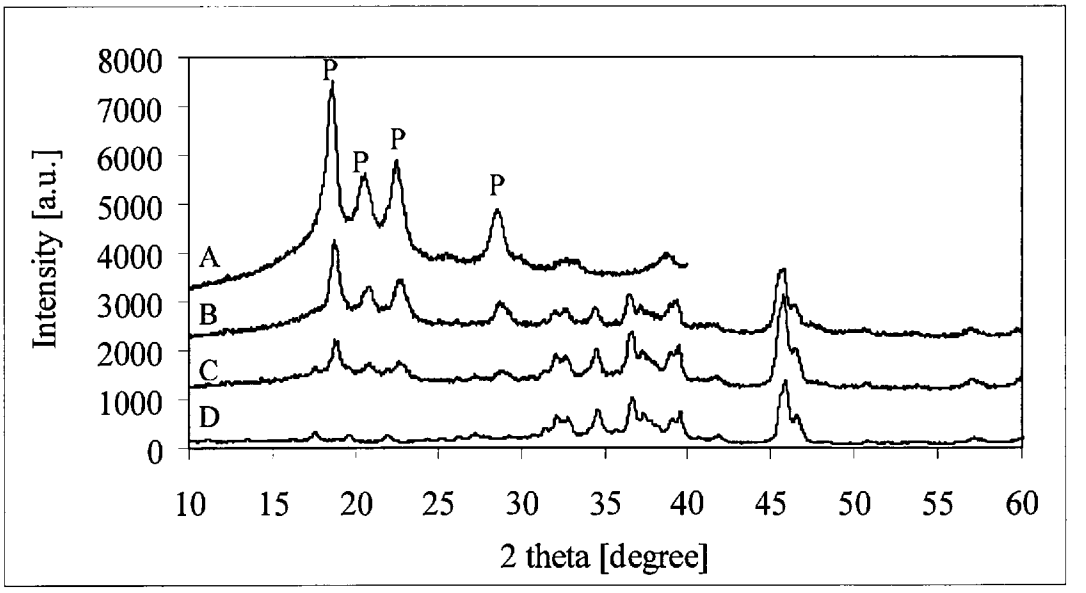


Figure 5.70 XRD spectra of A) pure PEEK powder (P indicates the main PEEK peaks), and pellets containing B) 70 wt.% PEEK-30 wt.% nano-Al_2O_3, C) 40 wt.% PEEK-60 wt.% nano-Al_2O_3 all heat-treated at 343°C with a heating rate of 10°C·min^{-1} and 30 min holding, D) pure nano-Al_2O_3. For clarity, scans A, B and C have been displaced upward by 3000, 2000, 1000 cps, respectively.

From the comparison of the XRD patterns of PEEK before and after heat-treatment an increase of the crystallinity was observed (see Fig. 5.25). In order to identify the influence of different amounts of nano-Al_2O_3 on the variation of the PEEK crystallinity during the heat-treatment the XRD of pure PEEK (spectrum A in Fig 5.70) and pure nano-Al_2O_3 (spectrum D in Fig. 5.70) have been compared with the XRD of pellets containing 70 wt.% PEEK-30 wt.% nao-Al_2O_3 (spectrum B in Fig. 5.70) and 40 wt.% PEEK-60 wt.% nano-Al_2O_3 (spectrum C in Fig. 5.70). The 20 wt.% PEEK-80 wt.% nano-Al_2O_3 spectrum was not reported since the PEEK signals were too low due to the small content of PEEK in the composite. PEEK, 70 wt.% PEEK-30 wt.% nano-Al_2O_3 and 40 wt.% PEEK-60 wt.% nano-Al_2O_3 pellets were heat-treated at 343°C for 30 min with a heating rate of 10°C·min^{-1} before XRD analysis. The major diffraction peaks for PEEK are between 2θ 15° and 30° (indicated by a P in spectrum A in Fig. 5.70) and they are clearly visible in the XRD patterns of 70 wt.% PEEK-30 wt.% nano-Al_2O_3 (spectrum B in Fig. 5.70) and 40 wt.% PEEK-60 wt.% nano-Al_2O_3 (spectrum C in Fig. 5.70) composites. The major diffraction peaks for the nano-Al_2O_3 powder are between 2θ 10° and 70° (Fig. 4.47 in section 4.5.1), but just the diffraction pattern between 2θ 10° and 60° is shown in plot D in Fig. 5.70. From the comparison of the XRD patterns of the composites with the starting powders, it is clear that no diffraction peaks have been created or have disappeared during the heat-treatment and therefore it can be concluded that no interfacial interaction has occurred between the PEEK and the nano-Al_2O_3 particles, at least under detection limit of XRD, as also reported by Lai et al. [26, 201] for PEEK-nano-SiO_2 composites and by Kuo et al. [26] and Goyal et al. [3] for PEEK-nano-Al_2O_3 composites. Conversely, it has been reported in

the literature that other organic-inorganic composites, such as poly(vinylidene fluoride)-organophilic clay nanocomposites prepared by melt intercalation technique [281] and polyamide-6/SiO_2 (PA6/SiO_2) composite prepared by blending method [282], presented a modification of the diffraction pattern compared to the pure constituents.

5.5.10 Mechanical properties

In this research PEEK and PEEK-nano-Al_2O_3 composite coatings with three different compositions have been successfully deposited by EPD. In this section the mechanical properties of the deposited and heat-treated (343°C for 30 min with 10°C·min^{-1} heating rate) coatings have been investigated using scratch test and micro-hardness. Moreover, since not many studies were reported in the literature for PEEK-nano-Al_2O_3 composites and most of them were carried out for low nano-Al_2O_3 concentrations (0-30 wt.%) [3, 24, 26, 29, 205, 206], it was necessary to gain a better understanding of the properties of the composites through the measurement of the hardness and the compression strength of pellets. The pellets had the same compositions of the three PEEK-nano-Al_2O_3 composite coatings described in the previous sections: 20 wt.% PEEK-80 wt.% nano-Al_2O_3 (as in 3P-3A coatings), 40 wt.% PEEK-60 wt.% nano-Al_2O_3 (as in 4P-2A coatings), 70 wt.% PEEK-30 wt.% nano-Al_2O_3 (as in 5P-1A coatings). Furthermore, pellets with a lower amount of nano-Al_2O_3 (as recommended in the literature for PEEK composites [24, 26, 29, 201-205]): 90 wt.% PEEK-10 wt.% nano-Al_2O_3 were also fabricated. The pellets were pressed manually in a cylindrical steel dye to reproduce as closed as possible the conditions of materials produced by EPD. Before testing all pellets were heat-treated in the same conditions employed for the coatings (343°C for 30 min with a heating rate of 10°C·min^{-1}). Macroscopic images of these pellets are shown in Figure 5.63. The 90 wt.% PEEK-10 wt.% nano-Al_2O_3 pellets and the pure PEEK pellets presented in fact a too high PEEK content and deformed during heat-treatment.

The residual depths of three scratches made on each sample (PEEK coating and films deposited from 3P-3A, 4P-2A and 5P-1A suspensions) were similar within the experimental error indicating that the coatings were homogeneous. Figure 5.71 compares the residual depths (depth of the scratch track after the scratch test was carried out) for scratches made on PEEK coatings deposited as described in section 5.3 and on PEEK-nano-Al_2O_3 composite films deposited from 3P-3A, 4P-2A and 5P-1A suspensions. From the comparison of the residual depth (Fig. 5.71) made on the four different coatings it was clear that the coating thickness of pure PEEK, 3P-3A and 4P-2A films were similar (~ 30 μm), whereas the 5P-1A films was thicker (~ 100 μm), e.g. the indenter penetration in 5P-1A coatings was much deeper than in the other coatings due to their higher thickness, while for the other films the indenter penetration was stopped by the substrate. Since it was difficult to compare the results obtained due to different contribution of the substrate in different situations; it was decided to compare just the initial part of the scratch test analysis where the effect of the coating deformation was

predominant. The comparison of the residual depth of the scratches in the first part of the analysis (Fig. 5.71) shows that the scratch track was deeper in composite coatings rich in nano-Al_2O_3 (deposited from 3P-3A and 4P-2A suspensions) than in pure PEEK and 5P-1A coatings. In particular it seemed that the 5P-1A films were more scratch resistant than pure PEEK films and that 3P-3A and 4P-2A films under scratch test conditions were very similar (Fig. 5.71).

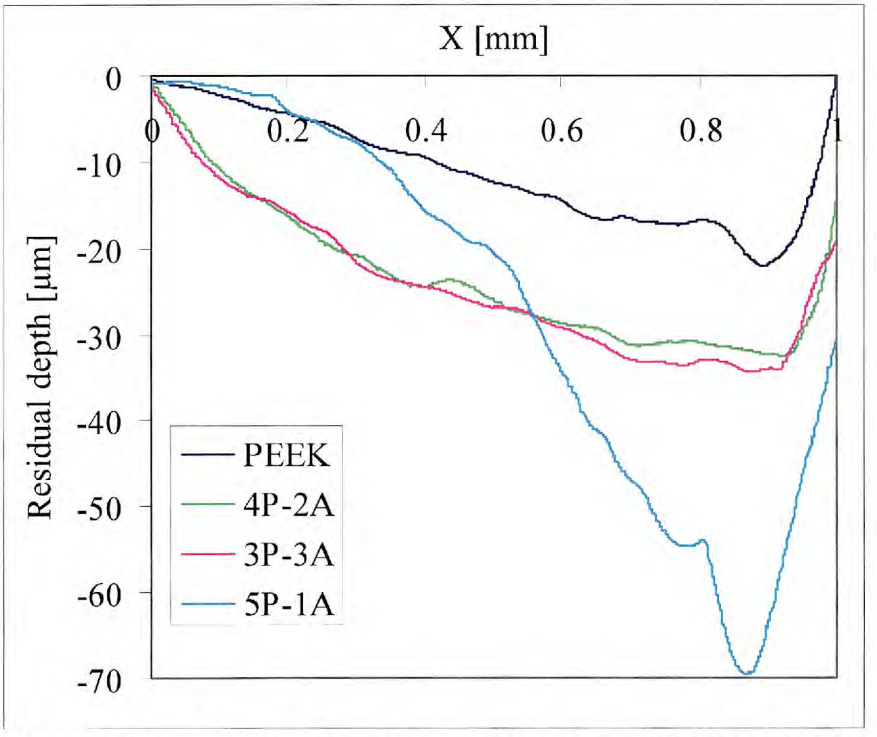


Figure 5.71 Residual depth profiles of the scratches carried out on PEEK and PEEK-nano-Al_2O_3 coatings deposited from 3P-3A, 4P-2A and 5P-1A suspensions applying a progressive load between 0 and 20 N.

From the analysis of the tracks left by the scratches it is possible to evaluate qualitatively the adhesion between substrate and coating. In the pure PEEK coatings and in the 5P-1A coatings the indenter did not produce cracks and the coatings remained fully adherent to the substrate, as shown for PEEK films in Figure 5.72 a). However, conformal cracking (semicircular trajectory parallel to the indenter only within the scratch) was observed, as suggested by Burnett and Rickerby [263]. In the coatings deposited from the 3P-3A and 4P-2A suspensions, spalling failures (due to compressive stresses preceding the moving stylus) were observed as suggested by Burnett and Rickerby [263]. The spallation produced the almost total delamination of the coatings that flaked off the substrates, as shown for 3P-3A films in Figure 5.72 b). The reduced substrate/coating adhesion in composite coatings with high nano-Al_2O_3 content compared to pure PEEK films was probably due to the presence of nano-Al_2O_3 that significantly reduced the PEEK-substrate contact area, which in section 5.3.5 was considered responsible for the adhesion of pure PEEK films through a mechanical interlocking mechanism between the two materials. This result suggests that, in order to obtain good substrate/coating

adhesion, the amount of nano-Al_2O_3 in the composites should be maximum 30 wt.% (achieved from 5P-1A suspensions) to exploit the binding effect of the polymer, e.g. the PEEK acting as a continuous matrix where nano-Al_2O_3 particles are embedded with no or negligible Al_2O_3-Al_2O_3 particle contact.

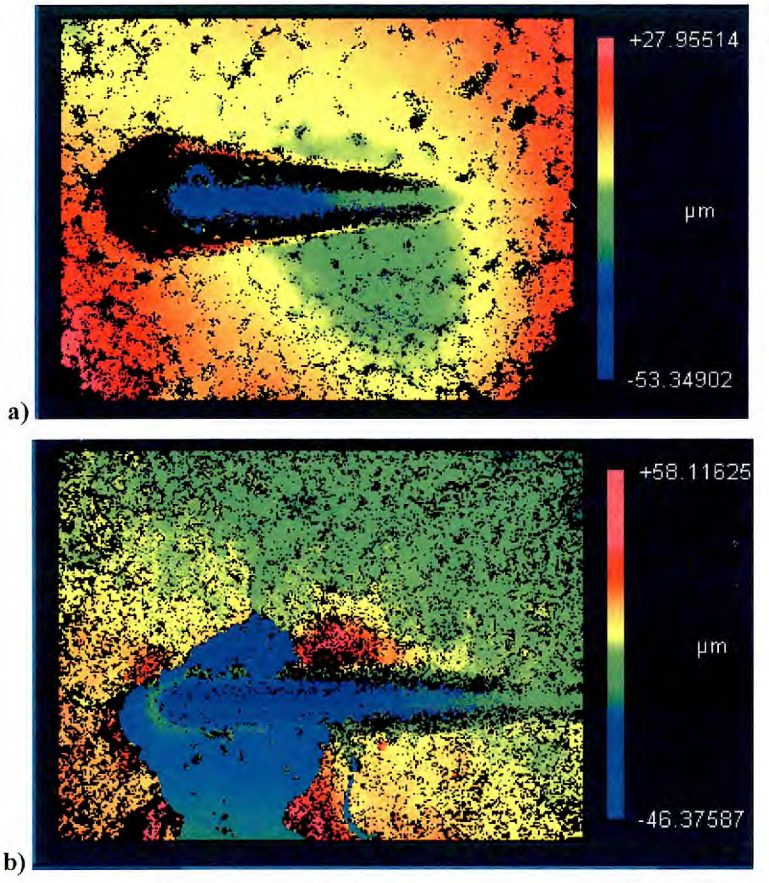


Figure 5.72 Surface maps of the scratch tracks left on a) pure PEEK and b) 3P-3A coatings applying a progressive load between 0 and 20 N. The images were obtained by white light interferometry (Zygo®).

Table 5.17 Micro-hardness results obtained for the PEEK and PEEK-nano-Al_2O_3 (3P-3A, 4P-2A and 5P-1A suspensions) composite coatings.

Samples	Micro-hardness HV		
PEEK	25 ± 2	29 ± 4	25 ± 2
5P-1A	23 ± 8	26 ± 9	24 ± 5
4P-2A	6 ± 2	4.0 ± 0.7	4.8 ± 0.6
3P-3A	6 ± 2	4.4 ± 0.5	6 ± 2

The micro-hardness of PEEK-nano-Al_2O_3 composite coatings deposited from the 3P-3A, 4P-2A and 5P-1A suspensions and of pure PEEK coatings was measured. The lowest possible load available in the instrument (0.245 N) was applied to measure the properties of the coatings but the indentation depth was in all cases more than 1/10 of the coating thickness. It is therefore

possible that the measured hardness values were not accurate and contained contributions from both the substrate (which was measured at 170 ± 17 HV) and the coating [263]; for this reason, the hardness values measured should not be considered as absolute values. However, since all the films, a part from those deposited from 5P-1A suspensions, were of similar thickness, it could be assumed that the substrate contribution to the final value was constant and so the measurements could be used to compare and rank the different films. The PEEK coating hardness values shown in Table 5.17 are in agreement with the results reported in the literature (e.g. 21.7 HV [26], 23.4 HV [201], 22-24 HV [7], 25 HV [191], 24 HV [209] and 24.6 HV [11]). The nano-Al_2O_3 particles employed in this research are a mixture between γ-, δ- and δ*-Al_2O_3 phases and it has been reported in the literature that the hardness of both γ-Al_2O_3 and δ-Al_2O_3 is around 1600 HV [283]. Therefore, it was expected that adding hard nano-Al_2O_3 particles to the PEEK matrix the hardness of the composites would increase compared to the hardness of pure PEEK. However the results obtained and listed in Table 5.17 show that the micro-hardness of the PEEK-nano-Al_2O_3 composites deposited from 3P-3A and 4P-2A suspensions was much lower than that of pure PEEK while the micro-hardness of the 5P-1A films was in the same range of the PEEK hardness.

The deeper penetration of the indenter into the composites highly rich in nano-Al_2O_3 (deposited from 3P-3A and 4P-2A) during scratch test and the decrease of the coating micro-hardness with the addition of high concentration of nano-Al_2O_3 are unexpected results. However, several plausible explanations for these results can be put forward as follows:

- incomplete densification, e.g. the presence of cracks and porosity in the coatings;
- low cohesion between PEEK and nano-Al_2O_3 in the composites, e.g. the presence of weak interfaces which would facilitate penetration of the indenter;
- too high concentration of nano-Al_2O_3 in the films, e.g. the amount of PEEK is not enough to keep the coating together and the behaviour is more similar to a brittle nano-Al_2O_3 film due to the high number of weak Al_2O_3-Al_2O_3 particle contacts.

These explanations are backed up by some observations. For example from the analysis of the SEM images of the 4P-2A coatings from the top (Figure 5.59) some cracks were visible even after the heat-treatment, but the cross section analysis (Figure 5.67 a)) showed that the films were highly dense and therefore porosity could not explain the lowest hardness observed.

Another possible explanation is the low cohesion between PEEK and nano-Al_2O_3 that rendered the films less resistant to deformation compared to pure PEEK films. In order to evaluate the cohesion PEEK and nano-Al_2O_3 two layers sandwich pellet (PEEK powder in the lower part and nano-Al_2O_3 powder on top) was produced and heat-treated at 343°C for 30 min; the PEEK melted during the treatment and the extremely brittle alumina layer on top of it cracked and fell off during handling (Fig. 5.73 a)). The contact area between PEEK and nano-Al_2O_3 was analysed by SEM (Fig. 5.73 b)) after carefully scratching with a spatula and cleaning in acetone to eliminate all the loose nano-Al_2O_3 particles. This surface consisted of a

continuous layer of nano-Al_2O_3 demonstrating a good cohesion between the two materials, as also reported by Nandan et al. [25] that stated that PEEK is a good binder for ceramic materials. A further confirmation of this finding was obtained by the analysis of the PEEK part of the two layers sandwich pellet shown in Figure 5.73 c); the PEEK melted and flowed under the alumina pellet dragging also some nano-Al_2O_3 particles that would not be embedded in the PEEK if the cohesion between the two materials was poor.

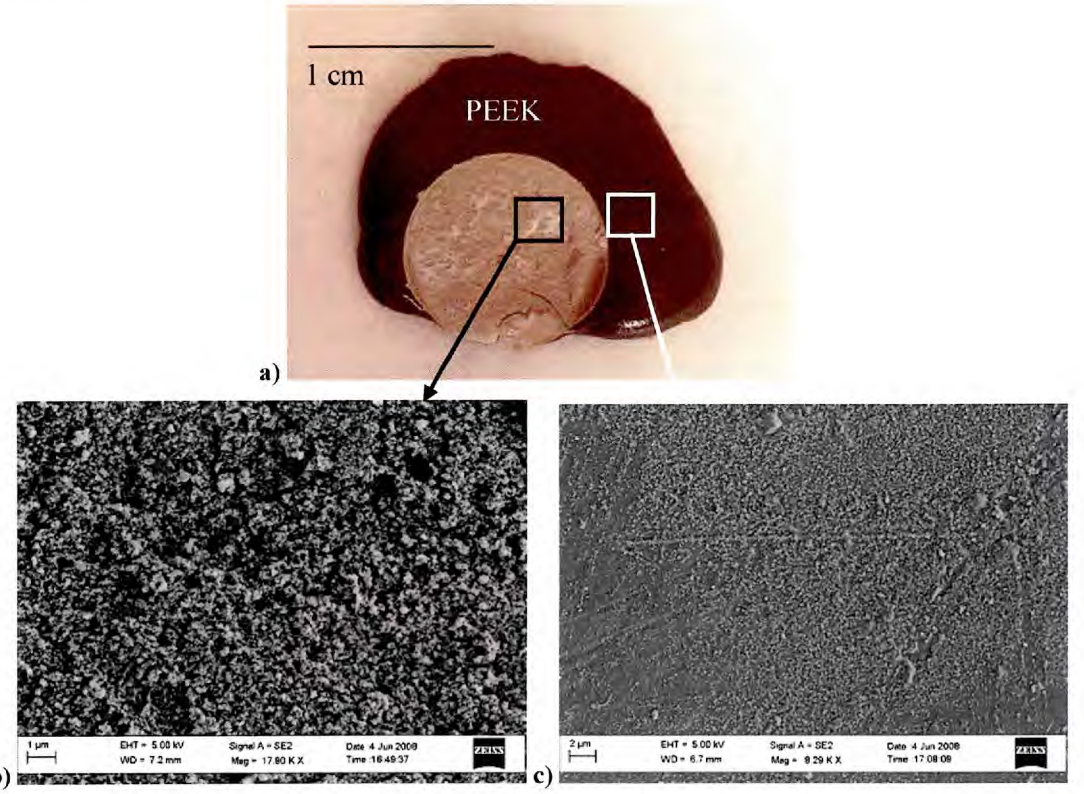


Figure 5.73 a) Image of the two layers PEEK-nano-Al_2O_3 sandwich pellets after heat-treatment. b) SEM images of the contact area between PEEK and nano-Al_2O_3 in the sandwich pellets and b) SEM image of the PEEK side.

Therefore, the more plausible explanation for the poor mechanical properties of the coatings deposited from 3P-3A and 4P-2A suspensions is the high amount of nano-Al_2O_3 particles in these composites (~80 and ~60 wt.%, respectively). The high Al_2O_3 concentration instead of increasing the hardness of the coatings increased their brittleness, as the alumina at the temperature employed (343°C) does not sinter, rendering the coatings similar to pure alumina films, that were observed to be brittle and to easily flake off the substrates (Fig. 5.32 in section 5.4.4). This explanation was further supported by the hardness measurements on the pellets reported in Figure 5.74, that clearly shows that composites with low nano-Al_2O_3 content (< 30 wt.%) exhibit higher hardness than pure PEEK, as also reported in the literature [26]. When the nano-Al_2O_3 content increased over 30 wt.% the hardness dramatically decreased because of too many Al_2O_3-Al_2O_3 contacts and the lack of PEEK matrix to keep together the composite material.

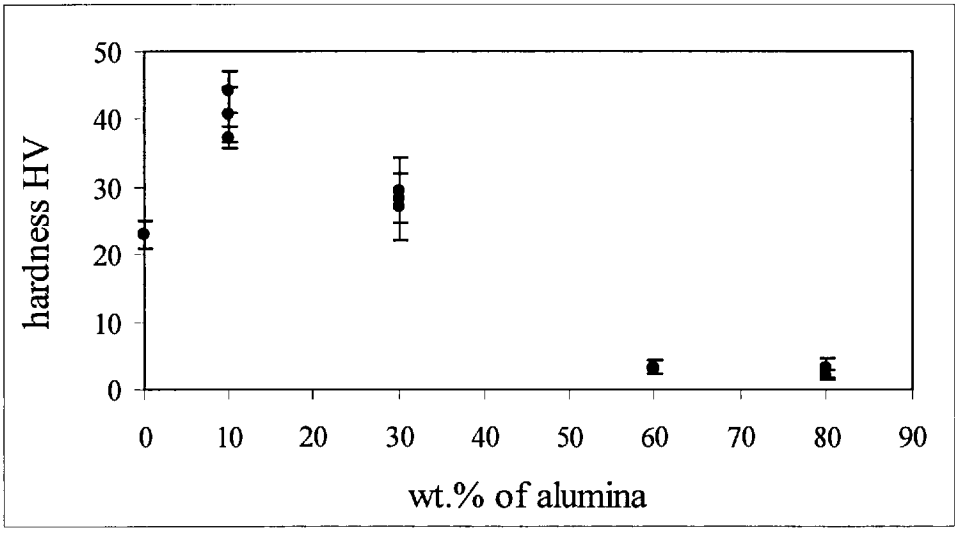


Figure 5.74 Micro-hardness values obtained from pure PEEK and PEEK-nano-Al_2O_3 composite pellets with increasing nano-Al_2O_3 content.

Beyond the decrease in hardness, also the compression strength of composite pellets extremely decreased with increasing nano-Al_2O_3 content. Figure 5.75 shows typical stress-strain curves for cylindrical specimens; the stress was calculated using:

$$\text{Stress} = F/A \qquad [5.15]$$

where F is the compression force applied and A the area of the cross section. The strain was calculated using:

$$\text{Strain} = \Delta H \cdot 100/H \qquad [5.16]$$

where ΔH is the difference in height and H is the starting height of the specimen. For each pellet composition (20 wt.% PEEK-80 wt.% nano-Al_2O_3, 40 wt.% PEEK-60 wt.% nano-Al_2O_3 and 70 wt.% PEEK-30 wt.% nano-Al_2O_3) five experiments were carried out at room temperature and all the results are shown in Figure 5.75. This test showed a compression strength between 50 and 70 MPa for the 70 wt.% PEEK-30 wt.% nano-Al_2O_3 composition and extremely lower compression strengths for the 40 wt.% PEEK-60 wt.% nano-Al_2O_3 composite with 6-8 MPa and for the 20 wt.% PEEK-80 wt.% nano-Al_2O_3 pellet with 1-2 MPa. All these data were much lower compared to the value of compression strength for pure PEEK reported in the literature (130-170 MPa [190]). The compression strength of pure PEEK was not measured in this study because the pellets could not be prepared using the same procedure employed for the preparation of the composite pellets, since the PEEK melted and deformed during the heat-treatment (see Figure 5.63), and therefore the composite data were compared with the data in the literature.

The decrease in compression strength with the increase of alumina is probably due to the too high alumina concentration in the composites, in particular the 20 wt.% PEEK-80 wt.% nano-Al_2O_3 composites completely disintegrated applying a considerably small stress (1-2 MPa) (Fig. 5.76 a)) while the other two compositions containing higher amounts of PEEK (70

wt.% PEEK-30 wt.% nano-Al_2O_3 and 40 wt.% PEEK-60 wt.% nano-Al_2O_3) were more resistant to fracture in compression (Fig. 5.76 b) and c)).

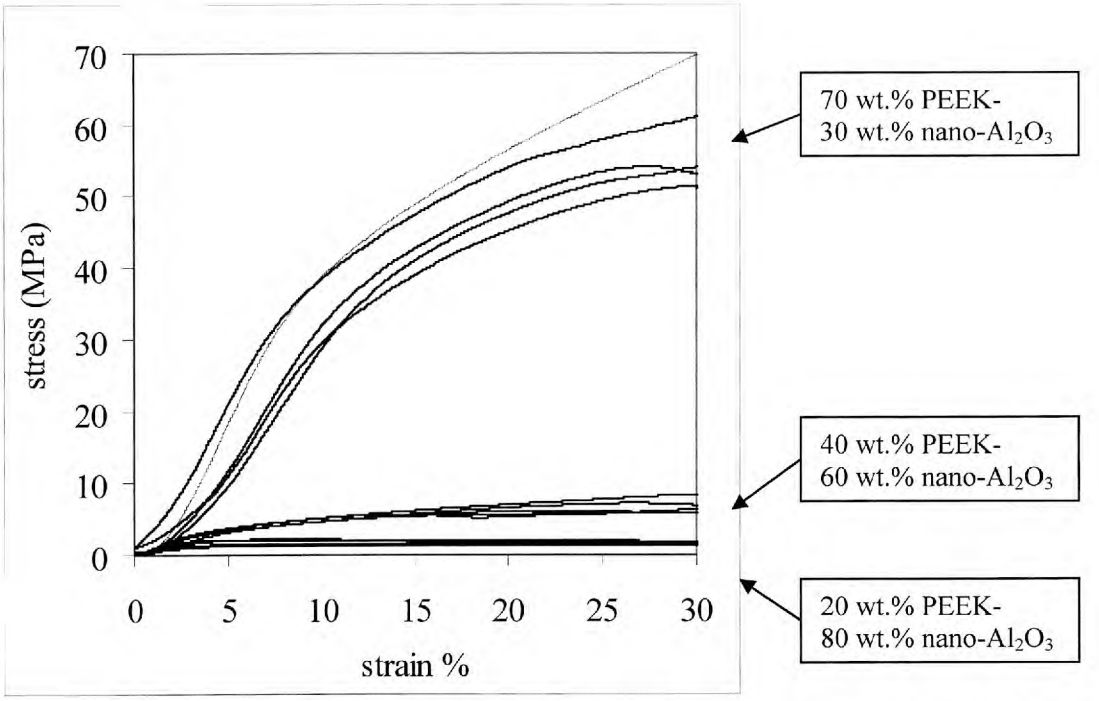


Figure 5.75 Compressive stress-strain curves for PEEK-nano-Al_2O_3 composite pellets (20 wt.% PEEK-80 wt.% nano-Al_2O_3, 40 wt.% PEEK-60 wt.% nano-Al_2O_3 and 70 wt.% PEEK-30 wt.% nnao-Al_2O_3) tested at room temperature. Note that pure PEEK has compression strength of 130-170 MPa [190].



Figure 5.76 Images of the pellets after the compression strength test: a) 20 wt.% PEEK-80 wt.% nano-Al_2O_3, b) 40 wt.% PEEK-60 wt.% nano-Al_2O_3 and c) 70 wt.% PEEK-30 wt.% nano-Al_2O_3.

From the micro-hardness and compression strength results on PEEK-nano-Al_2O_3 bulk materials reported in this section (Fig. 5.74-5.75) it seemed that the best PEEK-nano-Al_2O_3 composite should have the lowest possible Al_2O_3 content compatible with an increase of mechanical properties, in agreement with other literature findings [24-29, 205, 206]. Considering the compositions of the PEEK-nano-Al_2O_3 composite coating deposited by EPD in this investigation the one presenting the lowest amount of nano-Al_2O_3 was deposited from the 5P-1A suspension and contained 70 wt.% PEEK-30 wt.% nano-Al_2O_3. The hardness and resistance to scratch of this kind of film (5P-1A) was similar to that of pure PEEK films.

5.5.11 Corrosion Resistance

Stainless steels are employed in numerous applications in almost every field of human activity for their good corrosion resistance properties due to the presence of a 2-4 nm thin passive film on their surface [238, 239]. However, stainless steels are susceptible to pitting corrosion in a neutral aqueous solution containing as little as 1 mM of chloride Cl^-; this localized dissolution is one of the most frequent and disastrous causes of failure of metallic structures [267, 268]. The presence of pitting corrosion can be detected by measuring the passive current density that can be as high as 1 $A \cdot cm^{-2}$, whereas in normal dissolution conditions it is in the range of $nA \cdot cm^{-2}$ [267]. In this research project the corrosion resistance of PEEK and PEEK-nano-Al_2O_3 coatings deposited on stainless steel was investigated to examine if beyond other properties PEEK-nano-Al_2O_3 coatings can also protect the stainless steel from pitting corrosion.

The localised corrosion behaviour of the stainless steel-composite films deposited from the 3P-3A, 4P-2A and 5P-1A suspensions (applying 30 V for 3 min) and of pure PEEK films deposited as described in section 5.3 were determined by electrochemical measurements and compared with the corrosion resistance of the as received stainless steel AISI 316L. The results are shown by the polarization curves in Figure 5.77. In this experiment the corrosion resistance is related to the sharp increase in current corresponding to pitting corrosion. The potential at which this occurs is termed the 'pitting potential' and its value can be used comparatively. In this study the potential value required to produce a current density of 1 $mA \cdot cm^{-2}$ are compared. It is important to note that the results produced by this kind of experiment are strongly related to the surface properties of the samples analysed and therefore a variation between the data was expected, several tests were therefore performed and average values considered. The average pitting potential of the as-received stainless steel AISI 316L substrates was +405 mV (SCE), whereas the PEEK-nano-Al_2O_3 composite coatings presented better corrosion resistance in chloride environment with a pitting potential of +490 mV (SCE) for 3P-3A coatings, +755 mV (SCE) for 4P-2A coatings and +1255 mV (SCE) for 5P-1A films (although the slow current rise may indicate that crevice corrosion is occurring, the films however did not detach.). Whilst some variation in the pitting potential is expected, the 4P-2A films displayed differences of several hundreds of mV, probably due to the irreproducibility of the surfaces due to cracking in the coatings. The PEEK films repeatedly showed a "noisy" electrochemical response, as shown in Figure 5.77 b), with no defined current increased and the samples showed severe crevice corrosion with, in the worst case, complete delamination and detachment of the coating from the substrate, as shown in Figure 5.78.

From these results, it could be concluded that in chloride environment the PEEK-nano-Al_2O_3 composite films were more corrosion resistant than uncoated stainless steel and stainless steel covered by pure PEEK films.

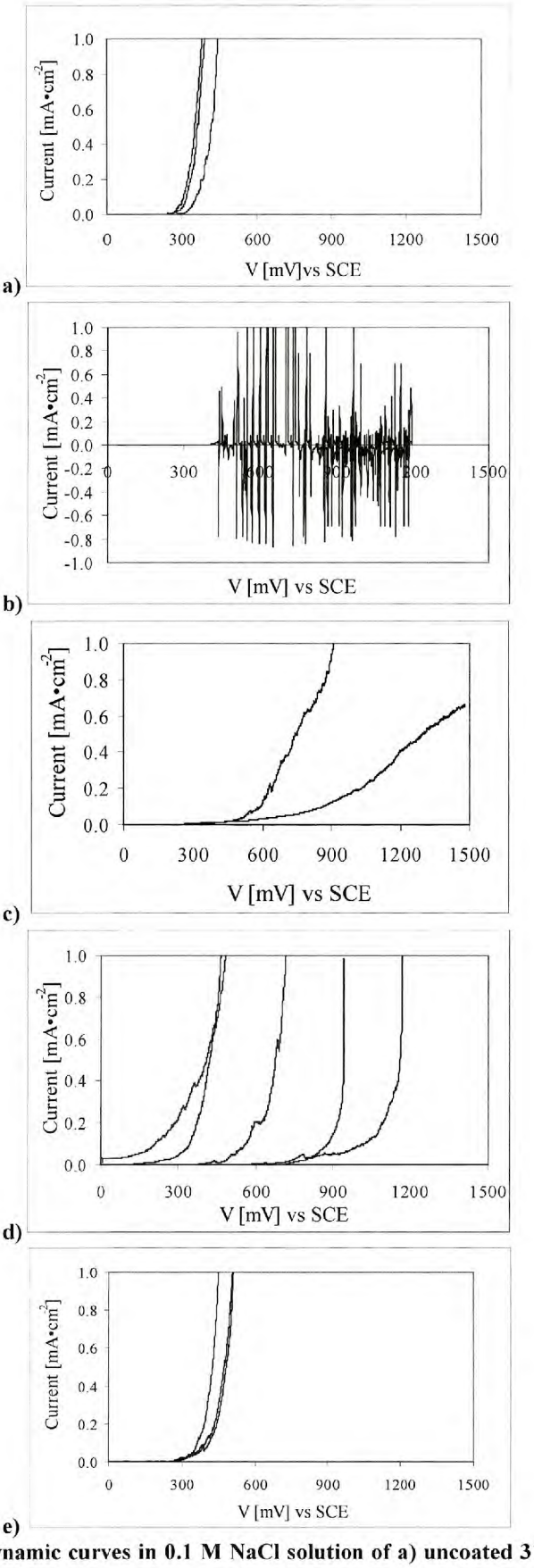


Figure 5.77 Potentiodynamic curves in 0.1 M NaCl solution of a) uncoated 316L stainless steel, b) pure PEEK films and composite coatings deposited from c) 5P-1A, d) 4P-2A and e) 3P-3A suspensions.



Figure 5.78 Image of a PEEK film after electrochemical measurement showing severe crevice corrosion and detachment of the coating from the substrate.

5.5.12 Tape test

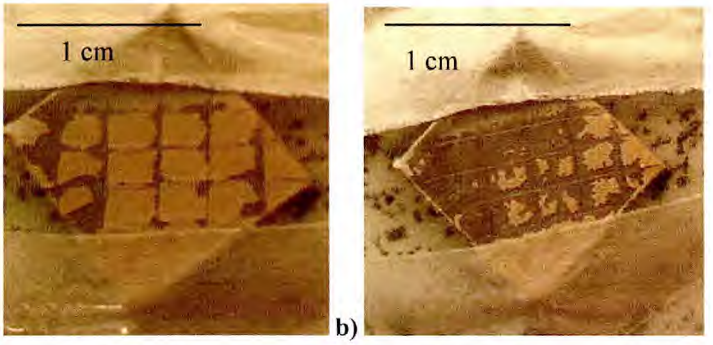


Figure 5.79 Images of a) a 3P-3A film after cutting and b) after tape test.

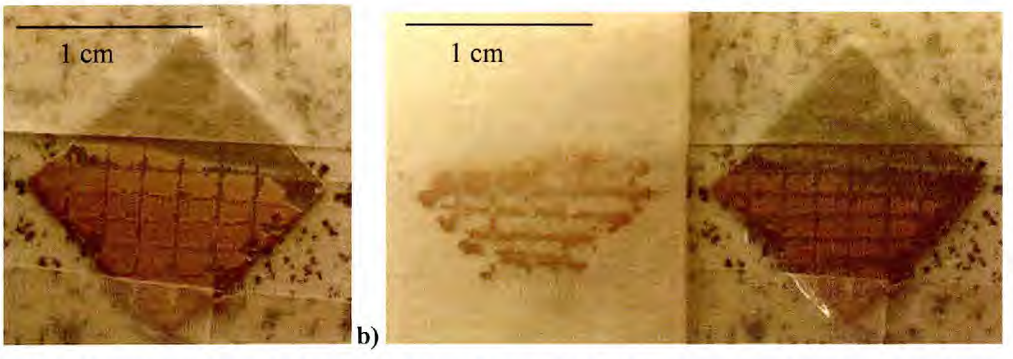


Figure 5.80 Images of a) a 4P-2A film after cutting and b) after tape test, showing both the tape and the film left on the substrate.

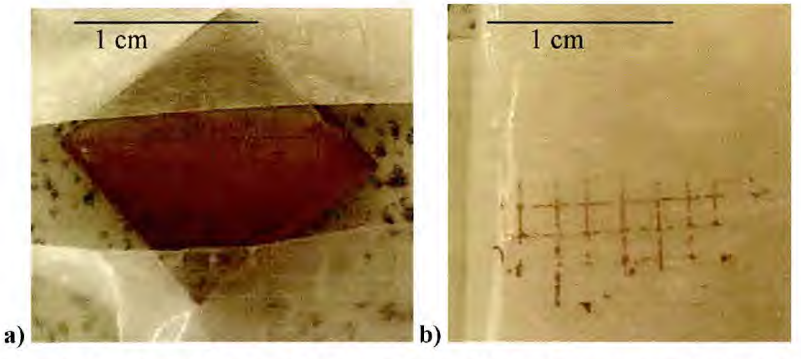


Figure 5.81 Images of a) a 5P-1A film and b) the tape used for the tape test, both pictures were taken after the test.



Figure 5.82 Image of a pure PEEK film and the tape used for the tape test, both pictures were taken after the test.

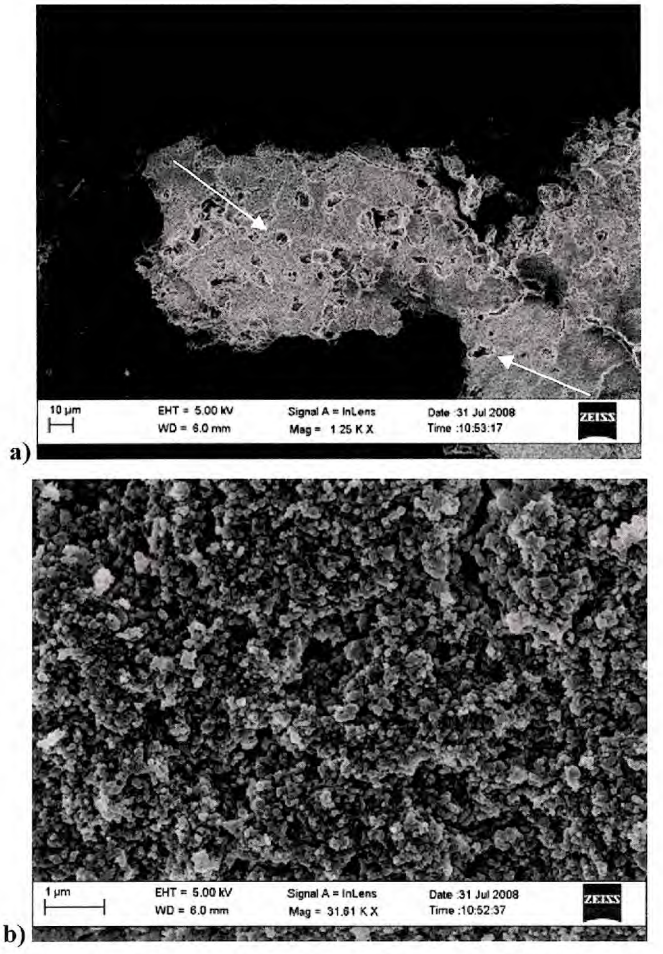


Figure 5.83 SEM images of a part of a 4P-2A film peeled off during the tape test showing a) a low magnification image of the part detached showing holes (arrows) with shape similar to PEEK particles and b) high magnification image showing the high nano-Al_2O_3 content.

The general function of a coating is to protect or decorate the substrate and for this reason a good substrate/coating adhesion is fundamental. In this study the adhesion of the PEEK and PEEK-nano-Al_2O_3 composite coatings, deposited from 3P-3A, 4P-2A and 5P-1A suspensions, on as-received stainless steel substrates was qualitatively assessed using the tape test standard method described in section 3.14. The aim of this study was to underline the differences in adhesion of coatings with different nano-Al_2O_3 content by comparing the experimental results

with the illustrations reported in Table 3.2. Four samples for each composition were tested and a representative result for each composition is reported in Figures 5.79-5.82.

It was found that the adhesion of the films deposited from 3P-3A suspensions was really poor. The coatings started to flake off already during cutting the films in the first step of the test (see Figure 5.79 a)) and after the tape was removed more than 65% of the film was detached (Figure 5.79 b)). The films deposited from the 4P-2A suspensions were more adherent to the substrate; less material flaked off during the cutting (Figure 5.80 a)) compared to the 3P-3A films and between 35 and 65% of the coating was removed by the tape during the test (Figure 5.80 b)). The 5P-1A films were much better adherent than the two previous samples with between 5% and 15% of material removed by the tape (Figure 5.81 a)) and all the removed parts were in correspondence to the cuts made in the film (Figure 5.81 b)). The pure PEEK coatings were fully adherent with no material removed (Figure 5.82). All these results were in agreement with the findings described in section 5.5.10, from which it emerged that the nano-Al_2O_3 content in the composite films should be as low as possible because the high number of weak Al_2O_3-Al_2O_3 particle contacts made the coatings weak and reduce their structural integrity. This explanation is further proved by SEM images of a part of a 4P-2A film peeled off during the tape test (Figure 5.83) which shows the high alumina content in the part of the coating in which failure took place (Figure 5.83 b)) and some voids (Figure 5.83 a)) with shapes similar to that of PEEK particles, as those shown in Figure 5.59, that further underline the low mechanical integrity of the film.

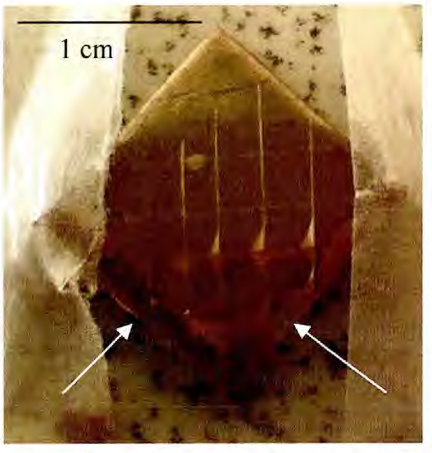


Figure 5.84 Image of a pure PEEK film after immersion in 0.1 M NaCl solution for 1 week and following the tape test.

Since the composite coatings were more resistant to corrosion than the stainless steel and the pure PEEK films in 0.1 M NaCl solution (see section 5.5.11), it was interesting to determine if the substrate/coating adhesion was influenced by the immersion in this solution. The 5P-1A and the pure PEEK films were therefore immersed in 0.1 M NaCl solution for 1 week and then tested. The other two composite films (3P-3A and 4P-2A) were not considered

in this second study since their adhesion was poor. From this analysis it resulted that the adhesion of the 5P-1A films was not modified by the immersion in NaCl solution, whereas the adhesion of the PEEK coatings considerably varied. It was observed that some part of the PEEK coatings changed colour after the immersion in the chloride solution, probably due to partial detachment, and that these parts peeled off during the adhesion test, consequently the adhesion worsen from 100% (without immersion) to 85-95% (after immersion), as shown in Figure 5.84. These results were in agreement with the detachment of the PEEK films observed during the corrosion studies, which were shown in Figure 5.78.

5.6 Summary

EPD was successfully applied to deposit on stainless steel plates pure PEEK and pure nano-Al_2O_3 coatings and, for the first time, PEEK-nano-Al_2O_3 composite films were also deposited. The microstructure, morphology and composition of all the deposited coatings were reproducible and thus EPD can be considered a convenient low cost method to produce PEEK and PEEK-nano-Al_2O_3 films on metallic substrates. The composition of the PEEK-nano-Al_2O_3 composite coatings was varied by changing the ratio between the two materials in the starting suspension. The addition of alumina seemed to decrease the melting temperature and the degradation temperature of pure PEEK. From the mechanical properties of the deposited samples after heat-treatment, it was clear that coatings with high nano-Al_2O_3 content were rather weak due to extensive Al_2O_3-Al_2O_3 particle contacts and that the mechanical properties were increased by lowering the nano-Al_2O_3 concentration. The composite films with lower alumina content, and therefore better properties, were deposited from 5 wt.% PEEK-1 wt.% nano-Al_2O_3 suspensions and contained 70 wt.% PEEK-30 wt.% nano-Al_2O_3. Moreover, these composite films in chloride environment resulted more corrosion resistant than uncoated stainless steel and stainless steel substrates covered by pure PEEK films.

6. Conclusions and further work

The results of this research project have demonstrated that electrochemical techniques, such as electrodeposition, electro co-deposition and electrophoretic deposition, can be successfully employed to deposit single phase (Ni, PEEK, Al_2O_3) and composite (Ni-Al_2O_3, PEEK-Al_2O_3, Ni-Al) coatings on metallic substrates. The main advantages of these low-temperature deposition techniques over other deposition methods are the ability to produce thin films on substrates with large size as well as the low cost of the equipment and of the deposition process itself (low temperature and ambient pressure).

i) Nickel and Ni-Al_2O_3 coatings

1. The surface preparation before deposition was identified as being a fundamental step to achieve good substrate/coating adhesion. The mechanical treatment increased the substrate surface roughness, which was considered to be the reason for an improved substrate/coating adhesion due to an interlocking mechanism between the two materials. Ultrasonically cleaning in acetone effectively removed grease, oil and eventual particles from the surface assuring the production of sharp, uniform and well defined interfaces.
2. Nanocrystalline Ni coatings of 20 μm thickness were successfully deposited galvanostatically from a nickel sulphate plating bath at room temperature (without the need for pulsing or grain refining additives).
3. The optimised conditions employed for nickel deposition were successfully applied to co-deposit both Al (micron size) and Al_2O_3 (both sub-micron and nano size) particles in the Ni films. The distribution and concentration of Al_2O_3 particles in the coatings depended on the solution hydrodynamics and on the conditions employed (particle concentration in the bath, particle size and current density). The amount of Al_2O_3 particles co-deposited in the films increased with the particle concentration in the bath and strongly depended on the metal deposition rate (applied current density), the flux of particles at the cathode, their residence time at the metal/solution interface and their size.
4. The addition of Al_2O_3 particles influenced both the microstructure and the crystallinity of the nickel matrix. Further work is needed to understand the underlying mechanism that controls the texture in Ni-nano-Al_2O_3 composite films, in particular to explain the anomalous behaviour observed when a current density of -10 $mA \cdot cm^{-2}$ was applied (see section 4.5.6).
5. The hardness of the Ni-Al_2O_3 composite films was higher than that of pure Ni.
6. Pure nickel and Ni-Al_2O_3 composite films were less corrosion resistant than stainless steel in both chloride and acid environment. In chloride environment the Ni-sub-micron-Al_2O_3 composite films presented better corrosion resistance than pure Ni and Ni-nano-Al_2O_3 films. From these results it emerged that the Ni and Ni-Al_2O_3 coatings did not

enhance the *general* corrosion resistance of stainless steel. It would be interesting to determine if these coatings would be beneficial for other metallic materials, e.g. mild steel; assuming that the deposition process will not be influenced by the substrate material (if the substrate is a metal).

Further Work

Nanocrystalline Ni

Nanocrystalline nickel coatings with grain size between 29 and 45 nm (measured from the XRD line broadening) were successfully deposited galvanostatically (direct current) from a nickel sulphate plating bath with and without Al_2O_3 particles. The ability to deposit nanocrystalline nickel from a plating bath without the addition of additives and applying direct current was in agreement with the findings reported by other authors [38, 39, 85, 90, 117, 243] but in disagreement with the information published in a patent [284]. The patent stated that in order to produce nanocrystalline nickel with average grain size < 11 nm from a nickel sulphate bath the use of pulsed direct current density and the addition of saccharin are essential. The understanding of the effects of these two parameters was beyond the aims of this project. However, it would be interesting to further analyse how the type of current density (e.g. direct current versus pulse direct current) and the presence of additives (e.g. saccharine and thiourea) influence the grain size of the deposited nickel. It would be also of interest to analyse if by varying the deposition conditions (e.g. bath temperature, solution pH and current density) it could be possible to further reduce the nickel grain size using the same bath employed in this research.

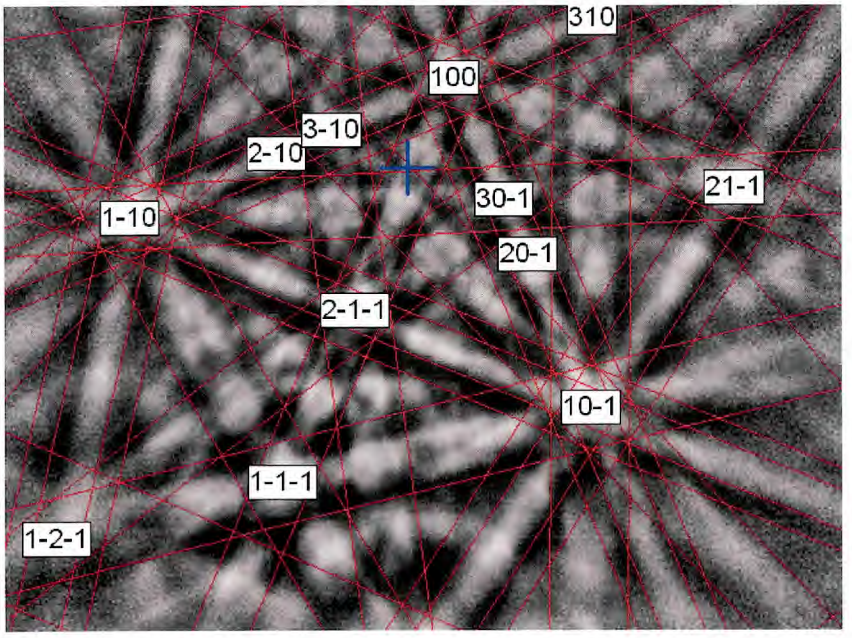


Figure 6.1 Fit to Kikuchi pattern for nickel reflections recorded from a pixel on a FIB milled and polished surface.

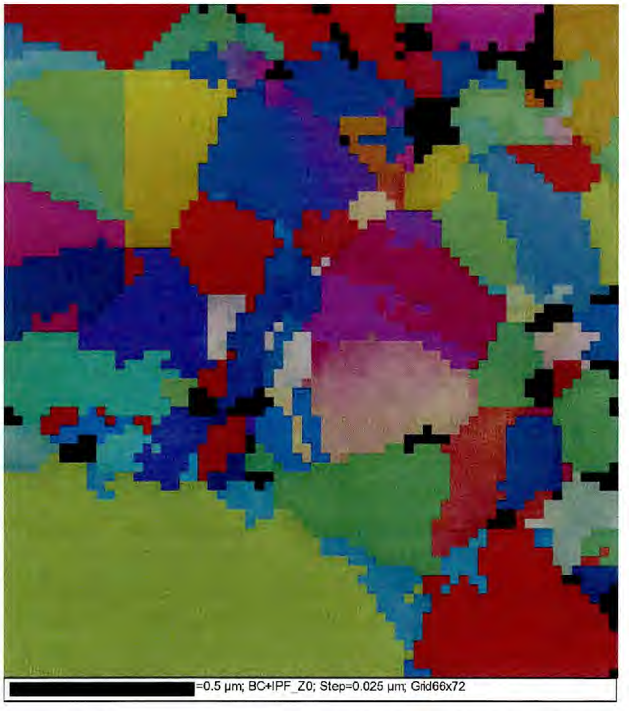


Figure 6.2 Grain lattice orientation maps of a Ni coating, with each colour representing a grain obtained with a FIB instrument equipped with electron backscatter diffraction (EBSD). The picture is pixeleted because of the resolution employed (25 nm).

In order to introduce the suggested further work in the field of Ni coatings, a short preliminary investigation carried out using a FIB instrument equipped with electron backscatter diffraction (EBSD)[1] is briefly described here. The top surface of a pure Ni film deposited applying a current density of -10 $mA \cdot cm^{-2}$ was analysed using EBSD. The analysis of the polished (2 keV and 25 pA) top surface of the Ni film produced the Kikuchi diffraction pattern shown in Figure 6.1 and the Ni grain map shown in Figure 6.2. Figure 6.2 shows in different colours the Ni grains of the area analysed and demonstrates that the grain size varied from 28 to 695 nm with an average of 98 ± 141 nm. This result indicates that further measurements have to be carried out and resolution lower than 25 nm has to be employed (using the FIB instrument) to obtain more reliable and representative grain size values. It is interesting to note that the smaller grain size measured with this method (28 nm) was in agreement with the value calculated from the XRD line broadening (40 ± 1 nm) and discussed in chapter 4.

Deposition of other Composite Materials

From the experiments carried out to deposit Ni-Al_2O_3 composite films it seemed that the amount of co-deposited Al_2O_3 particles increased with particle concentration in the bath and strongly depended on the metal deposition rate, the flux of particles at the cathode and their residence time at the metal/solution interface. If these are the three and only factors influencing the co-deposition of the second phase and the particles are incorporated in the films just

[1] Experiment carried out at Zeiss, Oberkochen, Germany by Richard J. Chater.

because they are at the interface metal-solution when the film is growing it is expected that similar results would be obtained when different particles with the same size are added to the plating bath. Contradictory results on this matter were reported in the literature, e.g. α-Al_2O_3 and γ-Al_2O_3 particles and Al_2O_3 and TiO_2 particles were incorporated at different rates in the same plating conditions (more details on these finding were reported in section 2.2.2). Consequently, in order to achieve a better understanding on the factors influencing the co-deposition mechanism it would be interesting to carry out the same set of experiments described in section 4.5 keeping all the parameters unvaried and using different types of particles (for example SiC, TiO_2). The chosen particles need to have the same size of the sub-micron and nano-Al_2O_3 particles employed in this research since different particle size can influence the co-deposition results. The same kind of experiments could be also carried out using Al particles as a second phase, to complete the research started in the framework of this project and described in section 4.6. It has to be taken into consideration that the major part of the Al particles co-deposited in the Ni film was ground away during sample preparation for cross section analysis. Therefore, in order to determine the amount of Al particles co-deposited using image analysis of the coating cross section, a FIB instrument should be employed using conditions similar to those applied for the analysis of Ni-nano-Al_2O_3 composites, described in section 4.5.3.

Determination of the wear resistance of Ni-Al_2O_3 composite films

Considering that the hardness of the Ni-Al_2O_3 composite coatings was higher than that of pure Ni, it would be interesting to determine if the addition of alumina would also increase the wear resistance properties of these films.

ii) PEEK and PEEK-nano-Al_2O_3 coatings

1. Heat-treatment after EPD (343°C for 30 min) was a fundamental step to produce well-adherent PEEK and PEEK-nano-Al_2O_3 films on stainless steel substrates. During the heat-treatment the PEEK melted and permeated into the substrate surface cavities and solidified during cooling providing a mechanical interlocking effect between substrate and coating, thus resulting in strong interfacial adhesion.
2. The electrophoretic deposition yield of PEEK-nano-Al_2O_3 composites increased logarithmically with deposition time and linearly with the applied potential (electric field).
3. The composition of PEEK-nano-Al_2O_3 composite coatings could be varied and controlled with sufficient precision by changing the ratio between the two materials in the starting suspension.
4. From the mechanical properties (micro-hardness, scratch resistance and compression strength) of the deposited coatings after heat-treatment, it was clear that a too high Al_2O_3

concentration in the films produced rather weak coatings due to extensive Al_2O_3-Al_2O_3 particle contacts and that the mechanical properties could be increased by lowering the nano-Al_2O_3 concentration (< 30 wt.%). In this research, composite films with lower alumina content, and therefore better mechanical properties, were deposited from 5 wt.% PEEK-1 wt.% nano-Al_2O_3 suspensions and contained 70 wt.% PEEK-30 wt.% nano-Al_2O_3.

5. The melting temperature and the degradation temperature of PEEK decreased with the addition of nano-Al_2O_3.
6. PEEK-nano-Al_2O_3 composite films deposited from the 5P-1A suspension were more corrosion resistant than uncoated stainless steel in chloride environment (0.1 M NaCl) and therefore this kind of coating can be applied to protect stainless steel from pitting corrosion. These composite coatings also presented better corrosion properties than pure PEEK films and their adhesion to the stainless steel substrate was not decreased by immersion in 0.1 M NaCl solution for 1 week, while the adhesion of pure PEEK films was considerably reduced by this treatment.

Further work

Decrease of the alumina concentration in the composite films

New studies could be carried out to further decrease the Al_2O_3 concentration in these films starting from different precursor materials. For example, it can be possible that using smaller PEEK particles in a suspension with a 5.5P-0.5A composition, the nano-Al_2O_3 particles would sufficiently coat the PEEK particles to produce a suspension of charged composite particles with enough stability for successful EPD. Another possible way to achieve different PEEK-Al_2O_3 ratios is to employ a different electrode configuration, e.g. the substrate lying horizontally in the EPD cell. In this case, it would be possible to increase the PEEK content in the films due to the higher sedimentation on the substrate of this material compared to the lighter nano-Al_2O_3 particles. This kind of deposition set-up can be employed just if the coating is needed only on one side of the substrate and it has not been explored in this research.

Determination of the wear resistance of PEEK-nano-Al_2O_3 composite films

Since the hardness of PEEK-nano-Al_2O_3 films deposited from the 5P-1A suspension was slightly higher than that of pure PEEK it would be interesting to determine if the addition of alumina would also increase the wear resistance properties of these composite films broadening their possible applications.

Deposition of PEEK-nano-Al_2O_3 composite films on complex shape substrates

Considering that microstructure, morphology and composition of PEEK and PEEK-nano-Al_2O_3 coatings on metallic substrates were reproducible and that in few minutes it was possible

to deposit relatively thick coatings (< 100 μm), EPD can be considered a convenient low cost method to produce films on metallic and complex shape substrates. For example, films with uniform thickness were homogeneously deposited on metallic tubes (see Figure 6.3 a)) and on NiTi wires (see Figure 6.3 b)) from a 4P-2A suspension applying an electric field of 15 $V \cdot cm^{-1}$ for 3 min and using the cylindrical EPD cell configuration (see Figure 5.2).[2]

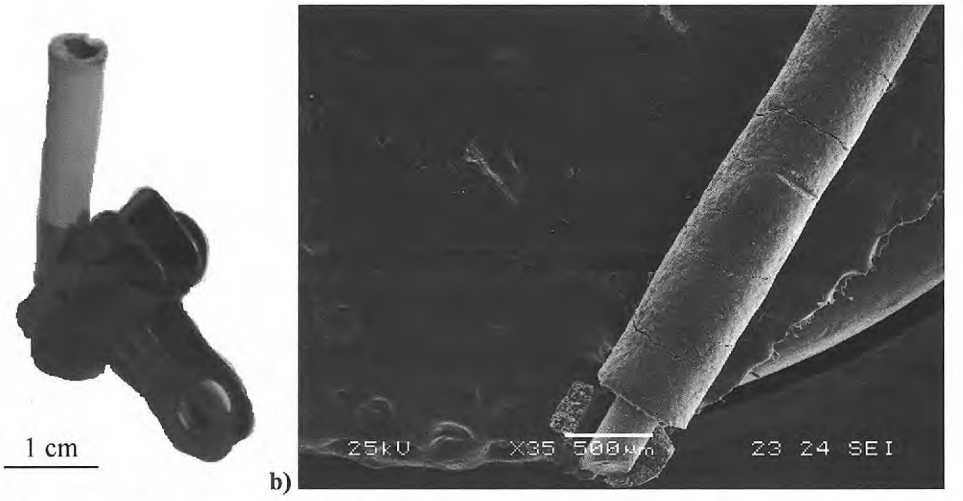


Figure 6.3 a) Image of a PEEK-nano-Al_2O_3 (4P-2A) film deposited on a metallic cylindrical tube and b) SEM image of a NiTi wire coated with PEEK-nano-Al_2O_3 film by EPD using a 4P-2A suspension. Both coatings were sintered at 343°C with a heating rate of 10°C·min^{-1} and 30 min holding time.

Thus, while a number of different experiments remain to be carried out in order to fully characterise the composite coatings and to understand some of the effects that the process parameters have on the coating properties, the present project has demonstrated the convenience of electrochemical techniques for the development of coatings based on tailored combination of metals, ceramics and polymers.

[2] Experiments carried out by John O`neill and described in his final year BEng research project report (Imperial College London, Department of Materials, 2008).

References

1. Vidrine, A. B. and Podlaha, E. J., Composite electrodeposition of ultrafine γ-alumina particles in nickel matrices Part I: Citrate and chloride electrolyte. J. App. Electrochem., 31, 2001, 461-468.
2. Webb, P. R. and Robertson, N. L., Electrolytic Codeposition of Ni-gamma Al_2O_3 Thin Films. J. Electrochem. Soc., 141, 1994, 669-673.
3. Goyal, R. K., Tiwari, A. N., Mulik, U. P. and Negi, Y. S., Novel high performance Al_2O_3/poly (ether ether ketone) nanocomposites for electronics applications. Composites Science and Technology, 67, 2007, 1802-1812.
4. Pedraza, F., Gomez, C., Carpintero, M. C., Hierro, M. P. and Perez, F. J., On the aluminisation of stainless steel by CVD in fluidised beds. Surf. Coat. Tech., 190, 2005, 223-230.
5. Totemeier, T. C., Wright R. N. and Swank, W. D., FeAl and Mo-Si-B intermetallic coatings prepared by thermal spraying. Intermetallics, 12, 2004, 1335-1344.
6. Zhang, G., Liao, H., Cherigui, M., Paulo Davim, J. and Coddet, C., Effect of crystalline structure on the hardness and interfacial adherence of flame sprayed poly(ether-ether-ketone) coatings. European Polymer Journal, 43, 2007, 1077-1082.
7. Palathai, T., Tharajak, J. and Sombatsompop, N., Hardness, adhesion index and microstructure of PEEK coating on Al or Fe substrate by LVOF flame spray. Mat. Sci. Eng. A, 485, 2008, 66-73.
8. Li, J., Liao, H. and Coddet, C., Friction and wear behavior of flame-sprayed PEEK coatings. Wear, 252, 2002, 824-831.
9. Normand, B., Takenouti, H., Keddam, M., Liao, H., Monteil, G. and Coddet, C., Electrochemical impedance spectroscopy and dielectric properties of polymer: application to PEEK thermally sprayed coating. Electrochim. Acta, 49, 2004, 2981-2986.
10. Simonin, L. and Liao, H., Characterization of flame-sprayed PEEK coatings by FTIR-ATR, DSC and acoustic microscopy. Macromolecular Materials and Engineering, 283, 2000, 153-162.
11. Zhang, G., Liao, H., Yu, H., Ji, V., Huang, W., Mhaisalkar, S. G. and Coddet, C., Correlation of crystallization behavior and mechanical properties of thermal sprayed PEEK coating. Surf. Coat. Tech., 200, 2006, 6690-6695.
12. Turunen, E., Varis, T., Gustafsson, T. E., Keskinen, J., Falt, T. and Hannula, S. P., Parameter optimization of HVOF sprayed nanostructured alumina and alumina-nickel composite coatings. Surf. Coat. Tech., 200, 2006, 4987-4994.
13. Huang, Y., Development of electroless NiP-PTFE-SiC composite coating. Surf. Coat. Tech., 167, 2003, 207-211.
14. Gaida. B., Electroplating science, 1st ed., Robert Dreper Ltd, Teddington, 1970.
15. Hovestad, A. and Janssen, L. J. J., Electrochemical codeposition of inert particles in a metallic matrix. Journal of Applied Electrochemistry, 25, 1995, 519-527.
16. Stojak, J. L., Fransaer, J. and Talbot, J. B., Review of electrocodeposition. Advannces in electrochemical science and engineering, 7, 2002, 193-223.
17. Van der Biest, O. O. and Vandeperre, L. J., Electrophoretic deposition of materials. Annual Review of Material Science, 29, 1999, 327-352.
18. Boccaccini, A. R. and Zhitomirsky, I., Application of electrophoretic and electrolytic deposition techniques in ceramics processing. Current Opinion in Solid State and Mat. Sci., 6, 2002, 251-260.
19. Boccaccini, A. R., Roether, J. A., Thomas, B. J. C., Shaffer, M. S. P., Chavez, E., Stoll, E. and Minay, E. J., The electrophoretic deposition of inorganic nanoscaled materials-A review. Journal of the Ceramic Society of Japan, 114, 2006, 1-14.
20. Besra, L. and Liu, M., A review on fundamentals and applications of electrophoretic deposition (EPD). Progress in materials science, 52, 2007, 1-61.
21. Heavens, S. N., Electrophoretic deposition as a processing route for ceramics. Advanced Ceramic Processing and Technology, Noyes Publications, Park Ridge, New Jersey, 1990, 255-283.
22. Sarkar, P. and Nicholson, P. S., Electrophoretic deposition (EPD): Mechanism, Kinetics, and Application to Ceramics. J. Am. Ceram. Soc., 79, 1996, 1987-2002.

23. Corni, I., Ryan, M. P. and Boccaccini, A. R., Electrophoretic deposition: From traditional ceramics to nanotechnology. J. Eur. Cer. Soc., 28, 2008, 1353-1367.

24. Qiao, H. B., Guo, Q., Tian, A. G., Pan, G. L. and Xu, L. B., A study on friction and wear characteristics of nanometer Al_2O_3/PEEK composites under the dry sliding condition. Tribology International, 40, 2007, 105-110.

25. Nandan, B., Lal, B., Pandey, K. N., Alam, S., Kandpal, L. D. and Mathur, G. N., Studies on high performance PEEK based alumina composites. Journal of polymer materials, 18, 2001, 135-140.

26. Kuo, M. C., Tsai, C. M., Huang, J. C. and Chen, M., PEEK composites reinforced by nano-sized SiO_2 and Al_2O_3 particulates. Materials Chemistry and Physics, 90, 2005, 185-195.

27. Goyal, R. K., Negi, Y. S. and Tiwari, A. N., High performance polymer composites on PEEK reinforced with aluminium oxide. Journal of Applied Polymer Science, 100, 2006, 4623-4631.

28. Goyal, R. K., Tiwari, A. N., Mulik. U. P. and Negi, Y. S., Dynamic mechanical properties of Al_2O_3/Poly(etheretherketone) composites. J. of Applied Polymer Sci., 104, 2007, 568-575.

29. Xiong, D. S., Lin, J. M. and Liu, L. L., Tribological properties of nano-Al_2O_3/PEEK composites. Key Eng. Mater., 330-332, 2007, 1239-1242.

30. Atkins, P. W., Physical Chemistry, 6th ed., Oxford University Press, Oxford, 1998.

31. Atkins, P. W., General Chemistry, Scientific American Book, New York, 1989.

32. Brugger, R., Nickel plating, 1st ed., Robert Draper Ltd, Teddington, 1970.

33. Dennis, J. K. and Such, T. E., Nickel and Chromium plating, 2nd ed., Butterworths, London, 1986.

34. Motoyama, M., Fukunaka, Y., Sakka, T., Zhou. Y. and Ogata, Y. H., Effect of surface pH on electrodeposited Ni films. J. Electrochem. Soc., 153, 2006, C502-C508.

35. Zhao, H., Liu, L., Zhu, J., Tang, Y. and Hu, W., Microstructure and corrosion behavior of electrodeposited nickel prepared from a sulphamate bath. Mater. Lett., 61, 2007, 1605-1608.

36. Moti, E., Shariat, M. H. and Bahrololoom, M. E., Influence of cathodic overpotential on grain size in nanocrystalline nickel deposition on rotating cylinder electrodes. Journal of Applied Electrochemistry, 38, 2008, 605-612.

37. Dai, C. Y., Pan, Y., Jiang, S. and Zhou, Y. C., The effect of prepared parameters on the microstructure of electrodeposited nanocrystalline nickel coating. Surface review and letters, 11, 2004, 433-442.

38. Ebrahimi, F. and Ahmed, Z., The effect of current density on properties of electrodeposited nanocrystalline nickel. Journal of Applied Electrochemistry, 33, 2003, 733-739.

39. Cziraki, A., Fogarassy, B., Gerocs, I., Toth-Kadar, E. and Bakonyi, I. Microstructure and growth of electrodeposited nanocrystalline nickel foils. J. Mat. Sci., 29, 1994, 4771-4777.

40. Rashidi, A. M. and Amadeh, A., The effect of current density on the grain size of electrodeposited nanocrystalline nickel coatings. Surf. Coat. Tech., 202, 2008, 3772-3776.

41. Amblard, J., Epelboin, I., Froment, M. and Maurin, G., Inhibition and nickel electrocrystallization. Journal of Applied Electrochemistry, 9, 1979, 233-242.

42. Bozzini, B., Mass-transport effects on texture formation of nickel electrodeposits. Materials Chemistry and Physics, 66, 2000, 278-285.

43. Wakabayashi, H., Sato, N., Sone, M., Takada, Y., Yan, H., Abe, K., Mizumoto, K., Ichihara, S. and Miyata, S., Nano-grain structure of nickel films prepared by emulsion plating using dense carbon dioxide. Surf. Coat. Tech., 190, 2005, 200-205.

44. Wang, L., Gao, Y., Xu, T. and Xue, Q., A comparative study on the tribological behavior of nanocrystalline nickel and cobalt coatings correlated with grain size and phase structure. Materials Chemistry and Physics, 99, 2006, 96-103.

45. Weil, R. and Cook, H. C., Electron-Microscopic Observations of the Structure of Electroplated Nickel. J. Electrochem. Soc., 109, 1962, 295-301.

46. Banovic, S. W., Barmak, K. and Marder, A. R., Microstructural characterization and hardness of electrodeposited nickel coatings from a sulphamate bath. J. Mat. Sci., 33, 1998, 639-645.

47. Liu, H. and Chen, W., Electrodeposited Ni-Al composite coatings with high Al content by sediment co-deposition. Surf. Coat. Tech., 191, 2005, 341-350.

48. Liu, H. and Chen, W., Reactive oxide-dispersed Ni_3Al intermetallic coatings by sediment co-deposition. Intermetallics, 13, 2005, 805-817.

49. Stappers, J. and Fransaer, J., Growth of metal around particles during electrodeposition. J. Electrochem. Soc., 153, 2006, C472-C482.

50. Peng, X., Li, T. and Yang, W. Y., Effect of La_2O_3 particles on the oxidation of electrodeposited Nickel Films. Oxidation of Metals, 51, 1999, 291-315.

51. Viswanathan, M. and Ghouse, M., Occlusion plating of Nickel-graphite composites. Metal finishing, 77, 1979, 67-69.

52. Oberle, R. R., Scanlon, M. R., Cammarata, R. C. and Searson, P. C., Processing and hardness of electrodeposited Ni/Al_2O_3 nanocomposites. Applied Physics Letters, 66, 1995, 19-21.

53. Tu, W. Y., Xu, B. S., Dong, S. Y., Wang, H. D. and Bin, J., Chemical and electrocatalytical interaction: influence of non-electroactive ceramic nanoparticles on nickel electrodeposition and composite coating. J. Mat. Sci., 43, 2008, 1102-1108.

54. Xu, B., Fretting wear-resistance of Ni-base electro-brush plating coating reinforced by nano-alumina grains. Mater. Lett., 60, 2006, 710-713.

55. Tu, W. Y., Xu, B. S., Dong, S. Y., Jiang, B. and Du, L. Z., Effect of n-Al_2O_3 on electrochemical nucleation and chemical binding interaction in nickel electrodeposition. Transactions of nonferrous metals society of China, 15, 2005, 889-896.

56. Hammond, R. A. F., Nickel plating from sulphamate solutions. Met. Fin. Journal, 1970, 169-176.

57. Nwoko, V. O. and Shreir, L. L., Electron micrographic examination of electrodeposited dispersion -hardened nickel. Journal of Applied Electrochemistry, 3, 1973, 137-141.

58. Low, C. T. J., Wills, R. G. A. and Walsh, F. C., Electrodeposition of composite coatings containing nanoparticles in a metal deposit. Surf. Coat. Tech., 201, 2006, 371-383.

59. Naploszek-Bilnik, I., Budniok, A., Losiewicz, B., Pajak, L. and Lagiewka, E., Electrodeposition of composite Ni-based coatings with the addition of Ti or/and Al particles. Thin Solid Films, 474, 2005, 146-153.

60. Guglielmi, N., Kinetics of the deposition of the inert particles from electrolytic baths. J. Electrochem. Soc., 119, 1972, 1009-1012.

61. Qu, N. S., Chan, K. C. and Zhu, D., Pulse co-electrodeposition of nano Al_2O_3 whiskers nickel composite coating. Scripta Materialia, 50, 2004, 1131-1134.

62. Bund, A. and Thiemig, D., Influence of bath composition and pH on the electrocodeposition of alumina nanoparticles and nickel. Surf. Coat. Tech., 201, 2007, 7092-7099.

63. Bund, A. and Thiemig, D., Influence of bath composition and pH on the electrocodeposition of alumina nanoparticles and copper. Journal of Applied Electrochemistry, 37, 2007, 345-351.

64. Susan, D. F., Barmak, K. and Marder, A. R., Electrodeposited Ni-Al particle composite coatings. Thin Solid Films, 307, 1997, 133-140.

65. Bazzard, R. and Boden, P. J., Nickel-Chromium alloys by codeposition: Part I-Codeposition of chromium particles in a nickel matrix. Transactions of the Instit. Met. Finish., 50, 1972, 63-69.

66. Graydon, J. W. and Kirk, D. W., Suspension Electrodeposition of phosphorus and copper. J. Electrochem. Soc., 237, 1990, 2061-2066.

67. Verelst, M., Bonino, J. P. and Rousset, A., Electroforming of metal matrix composite: dispersoid grain size dependence of thermostructural and mechanical properties. Mat. Sci. Eng. A, 135, 1991, 51-57.

68. Suzuki, Y. and Asai, O., Adsorption-codeposition process of Al_2O_3 particles onto Ag-Al_2O_3 dispersion films. J. Electrochem. Soc., 134, 1987, 1905-1910.

69. Brandes, E. A. and Goldthorpe, D., Electrodeposition of cermets. Metallurgia, 1967, 76, 195.

70. Kuo, S. L., Chen, Y. C., Ger, M. D. and Hwu, W. H., Nano-particles dispersion effect on Ni/Al_2O_3 composite coatings. Materials Chemistry and Physics, 86, 2004, 5-10.

71. Williams, R. V. and Martin, P. W., Electrodeposited Composite Coatings. Transactions of the Institute of Metal Finishing, 42, 1964, 182-188.

72. Sautter, F. K., Electrodeposition of dispersion-hardened nickel-Al_2O_3 alloys. J. Electrochem. Soc., 110, 1963, 557-560.

73. Steinbach, J. and Ferkel, H., Nanostructured Ni-Al_2O_3 films prepared by DC and pulsed DC electroplating. Scripta Materialia, 44, 2001, 1813-1816.

74. Xiong-Skiba, P., Engelhaupt, D.; Hulguin, R. and Ramsey, B., Effect of Pulse Plating Parameters on the Composition of Alumina/Nickel Composite. J. Electrochem. Soc., 2005, 152, C571-C576.

75. Chen, L., Wang, L., Zeng, Z. and Xu, T., Influence of pulse frequency on the microstructure and wear resistance of electrodeposited Ni-Al_2O_3 composite coatings. Surf. Coat. Tech., 201, 2006, 599-605.

76. Vereecken, P. M., Shao, I. and Searson, P. C., Particle codeposition in nanocomposite films. J. Electrochem. Soc., 147, 2000, 2572-2575.

77. Shao, I., Vereecken, P. M., Cammarata R. C. and Searson, P. C., Kinetics of particle codeposition of nanocomposites. J. Electrochem. Soc., 149, 2002, C610-C614.

78. Shao, I. and Vereecken, P. M., Synthesis and characterization of particle-reinforced Ni/Al_2O_3 nanocomposites. Journal of Materials Research, 17, 2002, 1412-1418.

79. Muller, B. and Ferkel, H., Al_2O_3-nanoparticle distribution in plated nickel composite films. Nanostructured Materials, 10, 1998, 1285-1288.

80. Celis, J. P., Roos, J. R. and Buelens, C. A, Mathematical model for the electrolytic codeposition of particles with a metallic matrix. J. Electrochem. Soc., 134, 1987, 1402-1408.

81. Chen, L., Wang, L., Zeng, Z. and Zhang, J., Effect of surfactant on the electrodeposition and wear resistance of Ni-Al_2O_3 composite coatings. Mat. Sci. Eng. A, 434, 2006, 319-325.

82. Ferkel, H., Muller, B. and Riehemann, W., Electrodeposition of particle-strengthened nickel films. Mat. Sci. Eng. A, 234-236, 1997, 474-476.

83. Balaraju, J. N., Kalavati and Rajam, K. S., Influence of particle size on the microstructure, hardness and corrosion resistance of electroless Ni-P-Al_2O_3 composite coatings. Surf. Coat. Tech., 200, 2006, 3933-3941.

84. Banovic, S. W., Barmak, K. and Marder, A. R., Characterization of single and discretely-stepped electro-composite coatings of nickel-alumina. J. Mat. Sci., 34, 1999, 3203-3211.

85. Aruna, S. T., Diwakar, S., Jain, A. and Rajam, K. S., Comparative study on the effect of current density on Ni and Ni-Al_2O_3 nanocomposite coatings produced by electrolytic deposition. Surf. Eng., 21, 2005, 209-214.

86. Alirezaei, S., Monirvaghefi, S. M., Salehi, M. and Saatchi, A., Effect of alumina content on surface morphology and hardness of Ni-P-Al_2O_3 (α) electroless composite coatings. Surf. Coat. Tech., 184, 2004, 170-175.

87. Alirezaei, S., Monirvaghefi, S., Salehi, M., Saatchi, A., Kargosha, M., Effect of alumina content on wear behaviour of Ni-P-Al_2O_3(α) electroless composite coatings. Surf. Eng., 21, 2005, 60-66.

88. Neralla, S., Kumar, D., Yarmolenko, S. and Sankar, J., Mechanical properties of nanocomposite metal-ceramic thin films. Composites Part B: Engineering, 35, 2004, 157-162.

89. Ding, X. M., Merk, N. and Ilschner, B., Mechanical behaviour of metal-matrix composite deposits. J. Mat. Sci., 33, 1998, 803-809.

90. Srivastava, M., Grips, V. K. W. and Rajam, K. S., Influence of SiC, Si_3N_4 and Al_2O_3 particles on the structure and properties of electrodeposited Ni. Mater. Lett., 62, 2008, 3487-3489.

91. Wang, S., Characterization of electroplated Ni/SiC and Ni/Al_2O_3 composite coatings bearing nanoparticles. Journal of Materials Research, 18, 2003, 1566-1574.

92. Thiemig, D., Bund, A. and Talbot, J. B., Influence of hydrodynamics and pulse plating parameters on the electrocodeposition of nickel-alumina nanocomposite films. Electrochim. Acta, *In Press*.

93. Feng, Q., Li, T., Zhang, Z., Zhang, J., Liu, M. and Jin, J., Preparation of nanostructured Ni/Al_2O_3 composite coatings in high magnetic field. Surf. Coat. Tech., 201, 2007, 6247-6252.

94. Du, L., Xu, B., Dong, S., Yang, H. and Tu, W., Study of tribological characteristics and wear mechanism of nano-particle strengthened nickel-based composite coatings under abrasive contaminant lubrication. Wear, 257, 2004, 1058-1063.

95. Verelst, M., Bonino, J. P., Brieu, M. and Rousset, A., Thermomechanical properties of Ni-Al_2O_3 metal matrix composites produced by electroforming. Mat. Sci. Eng. A, 191, 1995, 165-169.

96. Shrestha, N. K., Sakurada, K., Masuko, M. and Saji, T., Composite coatings of nickel and ceramic particles prepared in two steps. Surf. Coat. Tech., 140, 2001, 175-181.

97. Szczygiel, B. and Kolodziej, M., Composite Ni/Al_2O_3 coatings and their corrosion resistance. Electrochim. Acta, 50, 2005, 4188-4195.

98. Erler, F., Jakob, C., Romanus, H., Spiess, L., Wielage, B., Lampke, T. and Steinhauser, S., Interface behaviour in nickel composite coatings with nano-particles of oxidic ceramic. Electrochim. Acta, 48, 2003, 3063-3070.

99. Hamdy, A. S., Shoeib, M. A., Hady, H., Abdel Salam, O. F., Corrosion behavior of electroless Ni-P alloy coatings containing tungsten or nano-scattered alumina composite in 3.5% NaCl solution. Surf. Coat. Tech., 202, 2007, 162-171.

100. Ciubotariu, A. C., Benea, L., Lakatos-Varsanyi, M. and Dragan, V., Electrochemical impedance spectroscopy and corrosion behaviour of Al_2O_3-Ni nano composite coatings. Electrochim. Acta, 53, 2008, 4557-4563.

101. Szczygiel, B., and Kolodziej, M., Corrosion resistance of Ni/Al_2O_3 coatings in NaCl solution. Transactions of the Institute of Metal Finishing, 83, 2005, 181-187.

102. Sathiaraj, T. S. and Thangaraj, R., The experimental and calculated optical properties of coatings using effective medium theories. Journal of Physics D: Applied Physics, 30, 1997, 769-775.

103. Marshall, G. W., Lewis, D. B., Clayton, D., Blake, K. and Dodds, B., The electrodeposition of Ni-P-Al_2O_3 deposits. Surf. Coat. Tech., 96, 1997, 353-358.

104. Nagarajan, N. and Nicholson, P. S., Nickel-alumina functionally graded materials by electrophoretic deposition. J. Am. Ceram. Soc., 87, 2004, 2053-2057.

105. Ferrari, B., Sanchez-Herencia, A. J. and Moreno, R., Nickel-alumina graded coatings obtained by dipping and EPD on nickel substrates. J. Eur. Cer. Soc., 26, 2006, 2205-2212.

106. Windes, W. E., Zimmerman, J. and Reimanis, I. E., Electrophoretic deposition applied to thick metal-ceramic coatings. Surf. Coat. Tech., 157, 2002, 267-273.

107. Vidrich, G., Castagnet, J. and Ferkel, H., Dispersion behavior of Al_2O_3 and SiO_2 nanoparticles in nickel sulfamate plating baths of different compositions. J. Electrochem. Soc., 152, 2005, C294-C297.

108. Karayianni, C. H. and Vassiliou, P., A study on the reflectance of composite nickel electrodeposits. J. Mat. Sci. Letters, 17, 1998, 389-390.

109. Peipmann, R., Thomas, J. and Bund, A., Electrocodeposition of nickel-alumina nanocomposite films under the influence of static magnetic fields. Electrochim. Acta, 52, 2007, 5808-5814.

110. Barmak, K., Banovic, S., Petronis, C., Susan, D. and Marder, A. R., Structure of electrodeposited graded composite coatings of Ni–Al–Al_2O_3. Journal of Microsopy, 185, 1997, 265-274.

111. Dong, S., Beake, B. D., Parkinson, R., Xu, B., Hu, Z. and Bell, T., Determination of hardness and Young's modulus of brush plated nano-Al_2O_3/Ni composite coating by nanoindentation testing. Surf. Eng., 19, 2003, 195-199.

112. Dong, Y. S., Lin, P. H. and Wang, H. X., Electroplating preparation of Ni-Al_2O_3 graded composite coatings using a rotating cathode. Surf. Coat. Tech., 200, 2006, 3633-3636.

113. Bapu, G. N. K. R. and Jayakrishnan, S., Oxidation characteristics of electrodeposited nickel-zirconia composites at high temperature. Materials Chemistry and Physics 2006, 96, 321-325.

114. Wang, W., Hou, F. Y., Wang, H. and Guo, H. T., Fabrication and characterization of Ni-ZrO_2 composite nano-coatings by pulse electrodeposition. Scripta Materialia, 53, 2005, 613-618.

115. Möller, A. and Hahn, H., Synthesis and characterization of nanocrystalline Ni/ZrO_2 composite coatings. NanoStructured Materials, 12, 1999, 259-262.

116. Qu, N. S., Zhu, D. and Chan, K. C., Fabrication of Ni-CeO_2 nanocomposite by electrodeposition. Scripta Materialia, 54, 2006, 1421-1425.

117. Li, J., Jiang, J., He, H. and Chen, Y. C., Synthesis, microstructure, and mechanical properties of TiO_2/Ni nanocomposite coatings. J. Mat. Sci. Letters, 21, 2002, 939-941.

118. Benea, L., Bonora, P. L., Borello, A., Martelli, S., Wenger, F., Ponthiaux, P. and Galland, J., Preparation and investigation of nanostructured SiC-nickel layers by electrodeposition. Solid State Ionics, 151, 2002, 89-95.

119. Kaisheva, M. and Fransaer, J., Influence of the surface properties of SiC particles on their codeposition with nickel. J. Electrochem. Soc., 151, 2004, C89-C96.

120. Ger, M. D. Electrochemical deposition of nickel/SiC composites in the presence of surfactants. Materials Chemistry and Physics, 87, 2004, 67-74.

121. Zhou, Y., Peng, X. and Wang, F., Size effect of Al particles on oxidation of electrodeposited Ni-Al composite coatings. Oxidation of Metals, 64, 2005, 169-183.

122. Zhou, Y., Peng, X. and Wang, F., Oxidation of a novel electrodeposited Ni-Al nanocomposite film at 1050C. Scripta Materialia, 50, 2004, 1429-1433.

123. Susan, D. F, and Marder, A. R., Oxidation of Ni-Al base electrodeposited composite coatings. I: Oxidation kinetics and morphology at 800C. Oxidation of Metals, 57, 2002, 131-157.

124. Naploszek-Bilnik, I., Budniok, A. and Lagiewka, E., Electrolytic production and heat-treatment of Ni-based composite layers containing intermetallic phases. J. Alloys Comp., 382, 2004, 54-60.

125. Sarkar, P. Synthesis and microstuctural manipulation of ceramics by electrophoretic deposition. J. Mat. Sci., 39, 2004, 819-823.

126. Fukada, Y., Nagarajan, N, Mekky, W., Bao, Y., Kim, H. S. and Nicholson, P. S., Electrophoretic deposition-mechanisms, myths and materials. J. Mat. Sci., 39, 2004, 787-801.

127. Hayashi, S., Aoki, T. and Nakagawa, Z. E., Preparation of free standing alumina thick film by electrophoretic deposition using formed carbon powder as electrode. J. Ceram. Soc. Japan, 113, 2005, 513-518.

128. Ferrari, B. and Moreno, R., Electrophoretic deposition of aqueous alumina slips. J. Eur. Cer. Soc., 17, 1997, 549-556.

129. Gutierrez, C. P., Mosley, J. R. and Wallace, T. C., Electrophoretic deposition: a versatile coating method. J. Electrochem. Soc., 109, 1962, 923-927.

130. Ferrari, B., Sanchez-Herencia, A. J. and Moreno, R., Aqueous electrophoretic deposition of Al_2O_3/ZrO_2 layered ceramics. Mater. Lett., 35, 1998, 370-374.

131. Fischer, R., Fischer, E., De Portu, D. and Roncari, E., Preparation of ceramic micro-laminate by electrophoresis in aqueous system. J. Mater. Sci. Lett., 14, 1995, 25-27.

132. Sarkar, P., Datta, S. and Nicholson, P. S., Functionally graded ceramic/ceramic and metal/ceramic composites by electrophoretic deposition. Composites Part B, 28, 1997, 49-56.

133. Boccaccini, A. R., Cho, J., Roether, J. A., Thomas, B. J. C., Minay, E. J. and Shaffer, M. S. P., Electrophoretic deposition of carbon nanotubes. Carbon, 44, 2006, 3149-3160.

134. Boccaccini, A. R., Van der Biest, O. O. and Talbot, J. B., Electrophoretic Deposition: Fundamental and Applications. The Electrochemical Society, Pennington, US, 2002.

135. Boccaccini, A. R., Van der Biest, O. O. and Clasen, R., Electrophoretic Deposition: Fundamentals and Applications II. Key Eng. Mater., 2006, 314.

136. De Riccardis, M. F., Carbone, D. and Rizzo, A., A novel method for preparing and characterizing alcoholic EPD suspensions. Journal of Colloid and Interface Science, 307, 2007, 109-115.

137. Wang, G., Sarkar, P. and Nicholson, P. S., Influence of acidity on the electrostatic stability of alumina suspensions in ethanol. J. Am. Ceram. Soc., 80, 1997, 965-972.

138. Powers, R. W., Electrophoretic forming of beta-alumina ceramic. J. Electrochem. Soc, 122, 1975, 490-500.

139. Moreno, R. and Ferrari, B., Effect of the slurry properties on the homogeneity of alumina deposits obtained by aqueous electrophoretic deposition. Materials Research Bulletin, 35, 2000, 887-897.

140. Hamaker, H. C., Formation of a deposit by electrophoresis. Transaction of the Faraday Society, 36, 1940, 279-287.

141. Hamaker, H. C. and Verwey, E. J. W., The role of the forces between the particles in electrodeposition and other phenomena. Transaction of the Faraday Society, 26, 1940, 180-185.

142. Grillon, F., Fayeulle, D. and Jeandin, M., Quantitative image analysis of electrophoretic coatings. J. Mat. Sci. Lett., 11, 1992, 272-275.

143. Brown, D. R. and Salt, F. W., The mechanism of electrophoretic deposition. J. Appl. Chem., 15, 1965, 40-48.

144. Koelmans, H., Suspensions in non aqueous media. Philips Res. Rep., 10, 1955, 161-193.

145. Solomentsev, Y., Guelcher, S. A., Bevan, M. and Anderson, J. L., Aggregation dynamics for two particles during electrophoretic deposition under steady fields. Langmuir, 16, 2000, 9208-9216.

146. Sides, P. J., Electrohydrodynamic particle aggregation on an electrode driven by an alternating electric field normal to it. Langmuir, 17, 2001, 5791-5800.

147. Guelcher, S. A., Solomentsev, Y. and Anderson, J. L. Aggregation of pairs of particles on electrodes during electrophoretic deposition. Powder Technology, 110, 2000, 90-97.

148. Perez, A. T., Saville, D. and Soria, C., Modeling the electrophoretic deposition of colloidal particles. Europhys. Lett., 55, 2001, 425-431.

149. Greil, P., Cordelair, J. and Bezold, A., Discrete element simulation of ceramic powder processing. Z Metallk, 92, 2001, 682-689.

150. Sarkar, P., De, D., Yamashita, K., Nicholson, P. S. and Umegaki, T., Mimicking nanometer atomic processes on a micrometer scale via electrophoretic deposition. J. Am. Ceram. Soc., 83, 2000, 1399-1401.

151. Anne, G., Vanmeensel, K., Vleugels, J. and Van der Biest, O. O., A mathematical description of the kinetics of the electrophoretic deposition process for Al_2O_3-based suspensions. J. Am. Ceram. Soc., 88, 2005, 2036-2039.

152. Anne, G., Neirinck, B., Vanmeensel, K., Van der Biest, O. and Vleugels, J., Influence of electrostatic interactions in the deposit on the electrical field strength during electrophoretic deposition. Key Eng. Mater., 314, 2006, 181-186.

153. Anne, G., Neirinck, B., Vanmeensel, K., Van der Biest, O. and Vleugels, J., Throwing power during electrophoretic deposition. Key Eng. Mater., 314, 2006, 187-191.

154. Anne, G., Neirinck, B., Vanmeensel, K., Van der Biest, O. and Vleugels, J., Origin of the potential drop over the deposit during electrophoretic deposition. J. Am. Ceram. Soc., 89, 2006, 823-828.

155. Van Tassel, J. J. and Randall C. A., Role of ion depletion on the electrophoretic deposition of alumina powder from ethanol with increasing quantities of HCl. J. Mat. Sci., 41, 2006, 8031-8046.

156. Ristenpart, W. D., Aksay, I. and Saville, D., Electrohydrodynamic flow around a colloidal particle near an electrode with an oscillating potential. Journal of Fluid Mechanics, 575, 2007, 83-109.

157. Ristenpart, W. D., Aksay, I. A. and Saville, D. A., Electrically driven flow near a colloidal particle close to an electrode with a faradaic current. Langmuir, 23, 2007, 4071-4080.

158. Mohanty, G., Besra, L., Bhattacharjee, S. and Singh, B. P., Optimization of electrophoretic deposition of alumina onto steel substrates from its suspension in iso-propanol using statistical design of experiments. Materials Research Bulletin, 43, 2008, 1814-1828.

159. Ciou, S. J., Fung, K. Z. and Chiang, K. W., A comparison of the artificial neural network model and the theoretical model used for expressing the kinetics of electrophoretic deposition of YSZ on LSM. Journal of power sources, 175, 2008, 338-344.

160. Wang, Y. H., Chen, Q. Z., Cho, J. and Boccaccini, A. R., Electrophoretic co-deposition of diamond/borosilicate glass composite coatings. Surf. Coat. Tech., 201, 2007, 7645-7651.

161. Boccaccini, A. R., MacLaren, I., Lewis, M. H. and Ponton, C. B., Electrophoretic deposition infiltration of 2-D woven SiC fibre mats with mixed sols of mullite composition. J. Eur. Cer. Soc., 17, 1997, 1545-1550.

162. Yousefpour, M., Afshar, A., Chen, J. and Zhang, X., Electrophoretic deposition of porous hydroxyapatite coatings using polytetrafluoroethylene particles as templates. Mat. Sci. Eng. C, 27, 2007, 1482-1486.

163. Castro, R., Marcos, P., Sakamoto, E. and Gouvea, D., Surface reactivity and electrophoretic deposition of ZrO_2-MgO mechanical mixture. J. Mat. Sci., 42, 2007, 6946-6950.

164. Singh, I., Kaya, C., Shaffer, M., Thomas, B. and Boccaccini, A. Bioactive ceramic coatings containing carbon nanotubes on metallic substrates by electrophoretic deposition. J. Mat. Sci., 41, 2006, 8144-8151.

165. Pang, X. and Zhitomirsky, I., Electrophoretic deposition of composite hydroxyapatite-chitosan coatings. Materials Characterization, 58, 2007, 339-348.

166. Kaya, C. Al_2O_3-Y-TZP/Al_2O_3 functionally graded composites of tubular shape from nano-sols using double-step electrophoretic deposition. J. Eur. Cer. Soc., 23, 2003, 1655-1660.

167. Bartuli, C., Valente, T., Casadei, F. and Tului, M., Advanced thermal spraying coatings for tribological applications. Proceedings of the Institution of mechanical Engineers Part L-Journal of Materials-Design and Applications, 221, 2007, 175-185.

168. Boccaccini, A. R. and Trusty, P. A., Electrophoretic deposition infiltration of metallic fabrics with a boehmite sol for the preparation of ductile-phase-toughened ceramic composites. J. Mat. Sci., 33, 1998, 933-938.

169. Boccaccini, A. R., Schindler, U. and Kruger, H. G., Ceramic coatings on carbon and metallic fibres by electrophoretic deposition. Mater. Lett., 51, 2001, 225-230.

170. Uchikoshi, T., Suzuki, T. S., Okuyama, H., Sakka, Y. and Nicholson, P. S., Electrophoretic deposition of alumina suspension in a strong magnetic field. J. Eur. Cer. Soc., 24, 2004, 225-229.

171. Uchikoshi, T., Suzuki, T. S., Okuyama, H. and Sakka, Y., Control of crystalline texture in polycrystalline alumina ceramics by electrophoretic deposition in a strong magnetic field. Journal of Materials Research, 19, 2004, 1487-1491.

172. Tang, F., Uchikoshi, T., Ozawa, K. and Sakka, Y., Electrophoretic deposition of aqueous nano-gamma-Al_2O_3 suspensions. Materials Research Bulletin, 37, 2002, 653-660.

173. Choudhary, J. Y., Ray, H. S. and Rai, K. N., Electrophoretic deposition of Alumina from aqueous suspensions. Trans. J. Br. Ceram. Soc., 81, 1982, 189-193.

174. Ferrari, B., Farinas, J., Moreno, R., Determination and control of metallic impurities in Alumina deposits obtained by aqueous electrophoretic deposition. J. Am. Ceram. Soc., 84, 2001, 733-739.

175. Braun, A., Falk, G. and Clasen, R., Transparent polycrystalline alumina ceramic with sub-micrometre microstructure by means of electrophoretic deposition. Materialwissenschaft und Werkstofftechnik, 37, 2006, 293-297.

176. Wang, X., Ma, J., Maximenko, A., Olevsky, E. A., Stern, M. B. and Guenin, B. M., Sequential deposition of copper/alumina composites. J. Mat. Sci., 40, 2005, 3293-3295.

177. Stoll, E., Mahr, P., Kruger, H. G., Kern, H., Thomas, B. J. C. and Boccaccini, A. R., Fabrication technologies for oxide-oxide ceramic matrix composites based on electrophoretic deposition. J. Eur. Cer. Soc., 26, 2006, 1567-1576.

178. Chen, C. Y., Chen, S. Y. and Liu, D. M., Electrophoretic deposition forming of porous alumina membranes. Acta Materialia, 47, 1999, 2717-2726.

179. Anne, G., Vanmeensel, K., Vleugels, J. and Van der Biest, O., Influence of the suspension composition on the electric field and deposition rate during electrophoretic deposition. Colloids and Surfaces A: Physicochemical and Engineering Aspects, 245, 2004, 35-39.

180. Sun, H., Quan, X., Chen, S., Zhao, H. M. and Zhao, Y. Z., Preparation of well-adhered gamma-Al_2O_3 washcoat on metallic wire mesh monoliths by electrophoretic deposition. Applied surface science, 253, 2007, 3303-3310.

181. Belaroui K., Rapillard G., Bowen P., Hofmann H. and Shklover V., Nanocrystalline coatings by Electrophoretic deposition (EPD). Key Eng. Mater., 206-213, 2002, 519-522.

182. Sarkar, P. and Nicholson, P. S., Mechanism and Kinetics of Electrophoretic Deposition of Al_2O_3. Ceramic Transactions, 62, 1996, 271-279.

183. Besra, L., Samantaray, P., Bhattacharjee, S. and Singh, B., Electrophoretic deposition of alumina on stainless steel from non-aqueous suspension. J. Mat. Sci., 42, 2007, 5714-5721.

184. Wang, G. and Nicholson, P. S., Influence of acidity on the stability and rheological properties of ionically stabilized alumina suspensions in ethanol. J. Am. Ceram. Soc., 84, 2001, 84, 1977-1980.

185. Kaya, C., Kaya, F., Boccaccini, A. R. and Chawla, K. K., Fabrication and characterisation of Ni-coated carbon fibre-reinforced alumina ceramic matrix composites using electrophoretic deposition. Acta Materialia, 49, 2001, 1189-1197.

186. Boccaccini, A. R. and Kaya, C., Alumina ceramics based on seeded boehmite and electrophoretic deposition. Ceramics International, 28, 2002, 893-897.

187. Wang, C., Ma, J. and Cheng, W., Formation of polyetheretherketone polymer coating by electrophoretic deposition method. Surf. Coat. Tech., 173, 2003, 271-275.

188. Boccaccini, A. R., Peters, C., Roether, J. A., Eifler, D., Misra, S. K. and Minay, E. J., Electrophoretic deposition of polyetheretherketone (PEEK) and PEEK/Bioglass® coatings on NiTi shape memory alloy wires. J. Mater. Sci., 41, 2006, 8152-8159.

189. Ma, J., Wang, C. and Liang, C. H., Colloidal and electrophoretic behavior of polymer particulates in suspension. Mat. Sci. Eng. C, 27, 2007, 886-889.

190. Rae, P. J., Brown, E. N. and Orler, E. B., The mechanical properties of poly(ether-ether-ketone) (PEEK) with emphasis on the large compressive strain response. Polymer, 48, 2007, 598-615.

191. Kurtz, S. M. and Devine, J. N., PEEK biomaterials in trauma, orthopedic, and spinal implants. Biomaterials, 28, 2007, 4845-4869.

192. Zhang, G., Leparoux, S., Liao, H. and Coddet, C., Microwave sintering of poly-ether-ether-ketone (PEEK) based coatings deposited on metallic substrate. Scripta Materialia, 55, 2006, 621-624.

193. Zhang, G., Liao, H., Li, H., Mateus, C., Bordes, J. M. and Coddet, C., On dry sliding friction and wear behaviour of PEEK and PEEK/SiC-composite coatings. Wear, 260, 2006, 594-600.

194. Lu, Z. P. and Friedrich, K., On sliding friction and wear of PEEK and its composites. Wear, 181-183, 1995, 624-631.

195. Hanchi, J. and Eiss, N. S., Dry sliding friction and wear of short carbon-fiber-reinforced polyetheretherketone (PEEK) at elevated temperatures. Wear, 203-204, 1997, 380-386.

196. Flock, J., Friedrich, K. and Yuan, Q., On the friction and wear behaviour of PAN- and pitch-carbon fiber reinforced PEEK composites. Wear, 225-229, 1999, 304-311.

197. Zhang, Z., Breidt, C., Chang, L. and Friedrich, K., Wear of PEEK composites related to their mechanical performances. Tribology International, 37, 2004, 271-277.

198. Cirino, M., Pipes, R. B. and Friedrich, K., The abrasive wear behaviour of continuous fibre polymer composites. J. Mat. Sci., 22, 1987, 2481-2492.

199. Jacobs, O., Jaskulka, R., Yan, C. and Wu, W., On the effect of counterface material and aqueous environment on the sliding wear of carbon fibre reinforced polyetheretherketone (PEEK). Tribology Lett., 19, 2005, 319-329.

200. Jacobs, O., Jaskulka, R., Yan, C. and Wu, W., On the effect of counterface material and aqueous environment on the sliding wear of various PEEK compounds. Tribology Lett., 18, 2005, 359-372.

201. Lai, Y. H., Kuo, M. C., Huang, J. C. and Chen, M., On the PEEK composites reinforced by surface-modified nano-silica. Mat. Sci. Eng. A, 458, 2007, 158-169.

202. Wang, Q., Xu, J., Shen, W. and Liu Weimin, An investigation and wear properties of nanometer Si_3N_4 filled PEEK. Wear, 196, 1996, 82-86.

203. Wang, Q., Xue, Q., Liu, H., Shen, W. and Xu, J., The effect of particle size of nanometer ZrO_2 on the tribological behaviour of PEEK. Wear, 198, 1996, 216-219.

204. Wang, Q. H., Shen, W., Xu, J. and Xue, Q., The effect of nanometer SiC filler on the tribological behavior of PEEK. Wear, 209, 1997, 316-321.

205. Kuo, M. C., Huang, J. C. and Chen, M., Non-isothermal crystallization kinetic behavior of alumina nanoparticle filled poly(ether ether ketone). Mater. Chem. Phys., 99, 2006, 258-268.

206. Sliding member for use with lightweight metal. Patent Number 5,836,589 Nov.17, 1998.

207. Converse, G. L., Yue, W. and Roeder, R. K., Processing and tensile properties of hydroxyapatite-whisker-reinforced polyetheretherketone. Biomaterials, 28, 2007, 927-935.

208. Nisa, V. S., Rajesh, S., Murali, K. P., Priyadarsini, V., Potty, S. N. and Ratheesh, R., Preparation, characterization and dielectric properties of temperature stable $SrTiO_3$/PEEK composites for microwave substrate applications. Composites Science and Technology, 68, 2008, 106-112.

209. Goyal, R. K., Negi, Y. S. and Tiwari, A. N. Preparation of high performance composites based on aluminium nitride/polyetheretherketone and their properties. Eur. Polym. J., 41, 2005, 2034-2044.

210. Goyal, R. K., Tiwari, A. N., Mulik, U. P. and Negi, Y. S., Effect of aluminium nitride on thermomechanical properties of high performance PEEK. Composites Part A: Applied Science and Manufacturing, 38, 2007, 516-524.

211. Dwivedi, M., Alam, S. and Verma, G. L., Effect of nano-barium titanate on the mechanical, electrical and solubility performance of ferrite-filled poly(etheretherketone) composites. Polymer International, 54, 2005, 401-405.

212. Dwivedi, M., Alam, S. and Verma, G., Effect of nano-barium titanate on thermal stability of ferrite filled poly-ether-ether-ketone (PEEK) composites. Journal of Thermal Analysis and Calorimetry, 77, 2004, 947-955.

213. Zhou, B., Ji, X., Sheng, Y., Wang, L. and Jiang, Z., Mechanical and thermal properties of poly-ether ether ketone reinforced with $CaCO_3$. European Polymer Journal, 40, 2004, 2357-2363.

214. Zhuang, G. S., Sui, G. X., Meng, H., Sun, Z. S. and Yang, R., Mechanical properties of potassium titanate whiskers reinforced poly(ether ether ketone) composites using different compounding processes. Composites Science and Technology, 67, 2007, 1172-1181.

215. MetroPro Reference Guide, www.zygo.com, Zygo Corporation, Middlefield, Connecticut, 2004.

216. Miki, N. and Spearing, S. M., Effect of nanoscale surface roughness on the bonding energy of direct-bonded silicon wafers. Journal of Applied Physics, 94, 2003, 6800-6806.

217. Adell, V., Cheeseman, C. R., Ferraris, M., Salvo, M., Smeacetto, F. and Boccaccini, A. R., Characterising the sintering behaviour of pulverised fuel ash using heating stage microscopy. Materials Characterization, 58, 2007, 980-988.

218. ZetaProbe Software Operator's Manual, Version 2.13, Colloidal Dynamics, 2005.

219. ZetaProbe-Zeta Potential Analyser-Technical User Manual, Version 2.1, Colloidal Dynamics, 2002.

220. Wang, G. and Nicholson, P. S., Heterocoagulation in ionically stabilized mixed-oxide colloidal dispersions in ethanol. J. Am. Ceram. Soc., 84, 2001, 1250-1256.

221. Victrex® High performance PEEK™ polymers. Materials Properties Guide. www.victrex.com.

222. Safety Data Sheet of nano size Aluminium oxide (544833) Sigma Aldrich

223. Jain, A. K., Mao, J. and Mohiuddin, K. M., Artificial neural networks: A tutorial. Computer, 29, 1996, 31-44.

224. De Viterbo, V. D. and Belchior, J. C., Artificial neural networks applied for studying metallic complexes. Journal of Computational Chemistry, 22, 2001, 1691-1701.

225. www.statsoft.com/textboob/stneunet.html. (Statsoft electronic textbook ©) accessed on 03.01.08

226. Kasabov, N. N., Foundations of Neural Networks, Fuzzy Systems, and Knowledge Engineering, The MIT Press, 1996, 256-258.

227. Swaraj, P., Surface Coatings: Science and Technology, 2nd ed., John Wiley & Sons, London, 1996, chapter 6.2.

228. http://faculty.vassar.edu/lowry/webtext.html accessed on 09.10.08

229. Staia, M. H., Ramos, E., Carrasquero, A., Roman, A., Lesage, J., Chicot, D. and Mesmacque, G., Effect of substrate roughness induced by grit blasting upon adhesion of WC-17% Co thermal sprayed coatings. Thin Solid Films, 377, 2000, 657-664.

230. Guilemany, J. M., Nutting, J., Sobolev, V. V., Dong, Z., de Paco, J. M., Calero, J. A. and Fernandez, J., Interface structures of high velocity oxy-fuel sprayed WC-Co coating on a copper substrate. Mat. Sci. Eng. A, Structural materials, 232, 1997, 119-128.

231. Wang, Y. Y., Li, C. J. and Ohmori, A., Influence of substrate roughness on the bonding mechanisms of high velocity oxy-fuel sprayed coatings. Thin Solid Films, 485, 2005, 141-147.

232. Arrigoni, M., Barradas, S., Braccini, A., Dupeux, M., Jeandin, M., Boustie, M., Bolis, C. and Berthe, L., A comparative study of three adhesion tests (EN 5829 similar to ASTM C633, LASAT (LASer Adhesion Test), and bulge and blister test) performed on plasma sprayed copper deposited on aluminium 2017 substrates. Journal of Adhesion Science and Technology 20, 2006, 471-487.

233. Liu, Z. and Gao, W., The effect of substrate on the electroless nickel plating of Mg and Mg alloys. Surf. Coat. Tech., 200, 2006, 3553-3560.

234. Ye, M., Delplancke, J., Berton, G., Segers, L., Winand, R., Characterization and adhesion strength study of Zn coatings electrodeposited on steel substrates. Surf. Coat. Tech., 105, 1998, 184-188.

235. Khan, A. N., Lu, J. and Liao, H., Effect of residual stresses on air plasma sprayed thermal barrier coatings. Surf. Coat. Tech., 168, 2003, 291-299.

236. Mu, H., Seok, J. and Lin, R. Y., Nickel thin film coatings on steels with electroless plating and sputter deposition. J. Electrochem. Soc., 150, 2003, C67-C72.

237. Serek, A. and Budniok, A., Electrodeposition and thermal treatment of nickel layers containing titanium. Journal of Alloys and Compounds, 352, 2003, 290-295.

238. Olsson, C. O. A. and Landolt, D., Passive films on stainless steels--chemistry, structure and growth. Electrochim. Acta, 48, 2003, 1093-1104.

239. Wegrelius, L., Falkenberg, F. and Olefjord, I., Passivation of stainless steels in hydrochloric acid. J. Electrochem. Soc., 146, 1999, 1397-1406.

240. Oblonsky, L., Ryan, M. P. and Isaacs, H. S., In situ determination of the composition of surface films formed on Fe-Cr alloys. J. Electrochem. Soc., 145, 1998, 1922-1932.

241. Pourbaix, M., Atlas of electrochemical equilibria for aqueous solutions, 2nd ed., Permagon Press; Oxford, 1974.

242. Trethewey, K. R. and Chamberlain, J., Corrosion for Science and Engineering, 2nd ed., Addison Wesley Longman Limited, Harlow, England, 1995.

243. Srivastava, M., Grips, V. K. W. and Rajam, K. S., Electrochemical deposition and tribological behaviour of Ni and Ni-Co metal matrix composites with SiC nano-particles. Applied surface science, 253, 2007, 3814-3824.

244. Stroumbouli, M., Gyftou, P., Pavlatou, E. A. and Spyrellis, N., Codeposition of ultrafine WC particles in Ni matrix composite electrocoatings. Surf. Coat. Tech., 195, 2005, 325-332.

245. Reddy, B. S. B., Das, K., Datta, A. K. and Das, S., Pulsed co-electrodeposition and characterization of Ni-based nanocomposites reinforced with combustion-synthesized, undoped, tetragonal-ZrO_2 particulates. Nanotechnology, 19, 2008, art. num. 115603.

246. Garcia-Lecina, E., Garcia-Urrutia, I., Diez, J. A., Salvo, M., Smeacetto, F., Gautier, G., Seddon, R. and Martin, R., Electrochemical preparation and characterization of Ni/SiC compositionally graded multilayered coatings. Electrochim. Acta, 2008, *In Press*.

247. Kubisztal, J., Budniok, A. and Lasia, A., Study of the hydrogen evolution reaction on nickel-based composite coatings containing molybdenum powder. International Journal of Hydrogen Energy, 32, 2007, 1211-1218.

248. Lira-Cantu, M., Morales Sabio, A., Brustenga, A. and Gomez-Romero, P. Electrochemical deposition of black nickel solar absorber coatings on stainless steel AISI316L for thermal solar cells. Solar Energy Materials and Solar Cells, 87, 2005, 685-694.

249. Hou, F., Wang, W. and Guo, H., Effect of the dispersibility of ZrO_2 nanoparticles in Ni-ZrO_2 electroplated nanocomposite coatings on the mechanical properties of nanocomposite coatings. Applied surface science, 252, 2006, 3812-3817.

250. Brett, C. M. A. and Brett, A. M. O., Electrochemistry Principles, Methods and Applications, Oxford University Press, Oxford, 1993.

251. Njau, K. N. and Janssen, L. J. J., Electrochemical reduction of nickel ions from dilute solutions. Journal of Applied Electrochemistry, 25, 1995, 982-986.

252. Amblard, J., Froment, M., Maurin, G., Spyrellis, N. and Trevisan-Souteyrand, E. Nickel electrocrystallization-from nucleation to textures. Electrochim. Acta, 28, 1983, 909-915.

253. Panek, J. and Budniok, A., Production and electrochemical characterization of Ni-based composite coatings containing titanium, vanadium or molybdenum powders. Surf. Coat. Tech., 201, 2007, 6478-6483.

254. Cullity, B. D., Elements of X-ray diffractions, 2nd ed., Addison-Wesley Publishing Company Inc., Reading, Massachusetts 1978, 99-106 and 281-295.

255. Park, Y. S., Kim, K. H., Lee, J. J., Kim, H. S.; Kang, T. W., Jiang, H. X. and Lin, J. Y., X-ray diffraction analysis of the defect structure in $Al_xGa_{1-x}N$ films grown by metalorganic chemical vapor deposition. J. Mat. Sci., 39, 2004, 1853-1855.

256. Aruna, S., Bindu, C., Ezhil Selvi, V., Grips, V. K. and Rajam, K. S., Synthesis and properties of electrodeposited Ni/ceria nanocomposite coatings. Surf. Coat. Tech., 200, 2006, 6871-6880.

257. Schmickler, W., Interfacial electrochemistry. Oxford University Press, Oxford, 1996, 129-131.

258. Löffler, L. and Mader, W., Anisotropic X-ray diffraction peak broadening and twinning in diaspore-derived corundum, J. Eur. Cer. Soc., 25, 2005, 639-648.

259. Rawle, A., Basic principles of particle size analysis. Technical paper. Malvern Instruments Ltd.

260. Degarmo, E. P.; Black, J. T. and Kohser, R. A., Materials and Processes in Manufacturing, 9th ed., Wiley, USA, 2003, 794.

261. Lekström, M. and Shollock, B., Method to prepare TEM sections from Ni-base superalloys using the in situ lift-out technique on a single-beam FIB instrument. Poster presentation at NanoFib 2007, Manchester, 29 June 2007.

262. Wilson, J. R., Kobsiriphat, W., Mendoza, R., Chen, H. Y., Hiller, J. M., Miller, D. J., Thornton, K., Voorhees, P. W., Adler, S. B. and Barnett, S. A., Three-dimensional reconstruction of a solid-oxide fuel-cell anode. Nature Materials, 5, 2006, 541-544.

263. Burnett, P. J. and Rickerby, D. S., The relationship between hardness and scratch adhesion. Thin Solid Films, 154, 1987, 403-416.

264. Matsuda, K. Effects of substrate and friction on Vickers indentation of electroplated coatings. Journal of Physics D: Applied Physics, 41, 2008, art. num. 074018.

265. Chandler, H., Hardness Testing, 2nd ed., ASM International, Materials Park OH, 1999.

266. Lampke, T., Leopold, A., Dietrich, D., Alisch, G. and Wielage, B., Correlation between structure and corrosion behaviour of nickel dispersion coatings containing ceramic particles of different sizes. Surf. Coat. Tech., 201, 2006, 3510-3517.

267. Ryan, M., Williams, D. E., Chater, R. J., Hutton, B. M. and McPhail, D. S., Why stainless steel corrodes. Nature, 415, 2002, 770-774.

268. Abd El Meguid, E. A., Mahmoud, N. A. and Gouda, V. K., Pitting corrosion behaviour of AISI 316L steel in chloride containing solution. British Corrosion journal, 33, 1998, 42-48.

269. Hu, F., Chan, K., Song, S., Yang, X. Enhancement of corrosion resistance of electrocodeposited Ni SiC composites by magnetic field. Journal of solid state electrochemistry, 11, 2007, 745-750.

270. Medeliene, V. The influence of B_4C and SiC additions on the morphological, physical, chemical and corrosion properties of Ni coatings. Surf. Coat. Tech., 154, 2002, 104-111.

271. Garcia, I., Conde, A., Langelaan, G., Fransaer, J. and Celis, J. P. Improved corrosion resistance through microstructural modifications induced by codepositing SiC-particles with electrolytic nickel. Corrosion Science, 45, 2003, 1173-1189.

272. Mishra, R. and Balasubramaniam, R., Effect of nanocrystalline grain size on the electrochemical and corrosion behavior of nickel. Corrosion Science, 46, 2004, 3019-3029.

273. Bas, C., Grillet, A. C., Thimon, F. and Alberola, N. D., Crystallization kinetics of poly(aryl ether ether ketone): Time-temperature-transformation and continuous-cooling-transformation diagrams. European Polymer Journal, 31, 1995, 911-921.

274. www.tainstrumrnts.co.jp/application/pdf/Thermal_Library/ApplicationsBriefs/TA123.pdf Blaine, R. L., Determination of Polymer Crystallinity by DSC, TA Instruments, New Castle DE 19720, USA, accessed on 21.05.08.

275. Hatakeyama, T. and Quinn, F. X., Thermal Analysis. Fundamentals and Applications to Polymer Science, 2nd ed., John Wiley and Sons, Chichester, England, 1999, 105-106.

276. Kurnosov, D. A. Influence of the interelectrode distance in electrophoretic cold cathode fabrication on the emission uniformity. Applied surface science, 215, 2003, 232-236.

277. Arous, M., Amor, I. B., Kallel, A., Fakhfakh, Z. and Perrier, G., Crystallinity and dielectric relaxations in semi-crystalline polyetheretherketone. Journal of Physics and Chemistry of Solids, 68, 2007, 1405-1414.

278. Hay, J. N., Langford, J. I. and Lloyd, J. R., Variation in unit cell parameters of aromatic polymers with crystallization temperature. Polymer, 30, 1989, 489-493.

279. Taylor, J. R., An Introduction to Error Analysis: The Study of Uncertainties in Physical Measurements, 2nd ed., University Science Books, 1982, 290-291.

280. Pang, X. and Zhitomirsky, I., Electrodeposition of nanocomposite organic-inorganic coatings for biomedical applications. International Journal of Nanoscience, 4, 2005, 1-10.

281. Priya, L. and Lloyd, J. R., Poly(vinylidene fluoride)/clay nanocomposites prepared by melt intercalation: Crystallization and dynamic mechanical behavior studies. Journal of Polymer Science Part B: Polymer Physics, 40, 2002, 1682-1689.

282. Wang, H. L., Shi, T. J., Yang, S. Z. and Hang, G. P., Crystallization behavior of PA6/SiO_2 organic-inorganic hybrid material. Materials Research Bulletin, 41, 2006, 298-306.

283. Habib, K. A., Saura, J. J., Ferrer, C., Damra, M. S., Gimenez, E. and Cabedo, L., Comparison of flame sprayed Al_2O_3/TiO_2 coatings: Their microstructure, mechanical properties and tribology behavior. Surf. Coat. Tech., 201, 2006, 1436-1443.

284. Erb, U., El-sherik, A. M., Cheung, C. K. S. and Aus, M. J., Nanocrystalline metals. Int. Pub. Num. WO/94/12695.

Appendix 1. Mechanical treatments on stainless steel substrates employed for nickel deposition.

i) Surface in as-received condition

The as-received surface was not smooth as shown in the optical microscope picture reported in Figure A.1. The surface roughness was measured by means of Zygo® in 9 points obtaining the rms and Ra values listed in Table A.1 and the bearing ratio plots shown in Figure A.2. From these data it seemed that the surface was uniform all over the sample and that it can be represented by the 3D plot in Figure A.3.

Table A.1 Roughness values for the 2 mm thick stainless steel AISI 316L in as-received condition.

Point	1	2	3	4	5	6	7	8	9	Average
rms (μm)	0.348	0.317	0.319	0.310	0.316	0.312	0.325	0.314	0.309	0.32 ± 0.01
Ra (μm)	0.203	0.176	0.177	0.173	0.171	0.175	0.188	0.177	0.168	0.18 ± 0.01

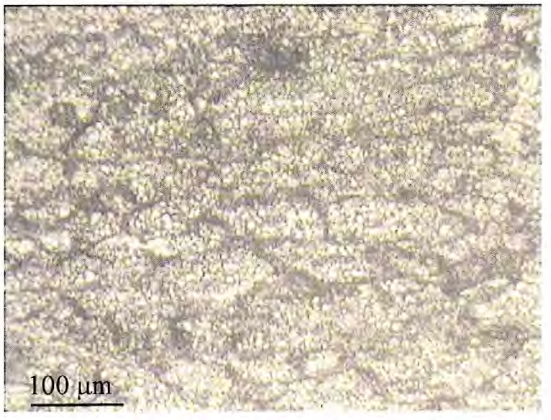


Figure A.1 Optical microscopy picture of the as-received 2 mm thick stainless steel substrate.

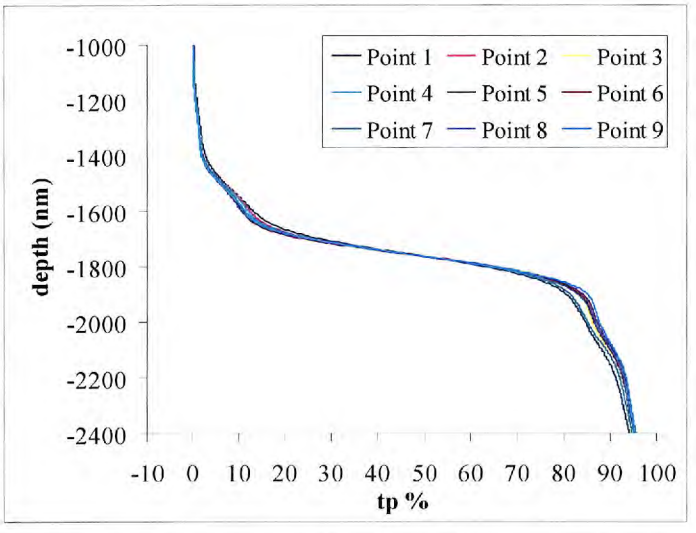


Figure A.2 Bearing ratio plots of the as-received surface of the 2 mm thick stainless steel substrate.

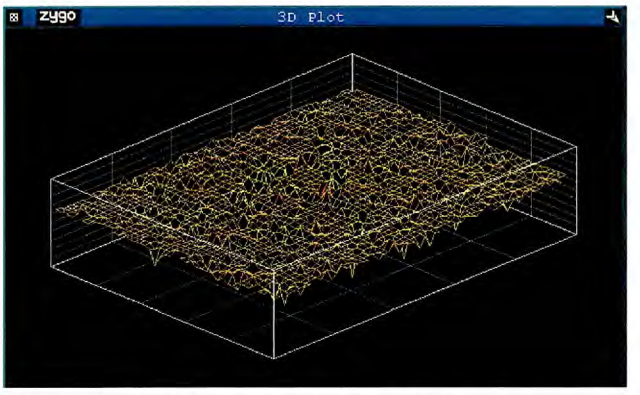


Figure A.3 3D plot of the surface of the as-received 2 mm thick stainless steel AISI 316L substrate. This area is 1.46 mm x 1.10 mm and the height of the block is 80 µm.

ii) Surface polished with 1 µm diamond paste

Table A.2 Roughness values for the 2 mm thick stainless steel substrate polished with 1 µm diamond paste.

Point	1	2	3	4	5	6	Average
rms (µm)	0.076	0.080	0.068	0.078	0.037	0.056	0.07 ± 0.02
Ra (µm)	0.055	0.063	0.051	0.062	0.028	0.038	0.05 ± 0.01

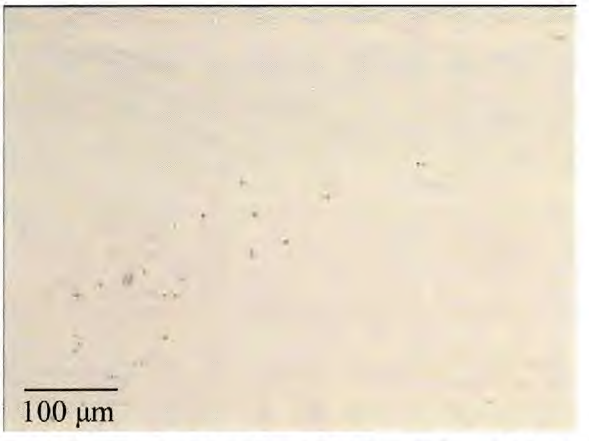


Figure A.4 Optical microscopy picture of the 2 mm thick stainless steel substrate surface polished with 1 µm diamond paste.

The surface of the stainless steel substrate mechanically polished with 1 µm diamond paste was smooth as shown in Figure A.4. This surface was analyzed in 6 points obtaining the values listed in Table A.2 and the bearing ratio plots shown in Figure A.5. Analysing the rms and Ra values (Table A.2), it seemed that the surface roughness was quite uniform on the whole sample and it was possible to represent it by the 3D plot shown in Figure A.6. While comparing the bearing ratio plots (Figure A.5) it can be seen that each point presented slightly different characteristics. This can be explained considering a possible microscopic tilting of the surface in the different points and therefore it can be conclude that the surface is smooth and uniform all over the sample area.

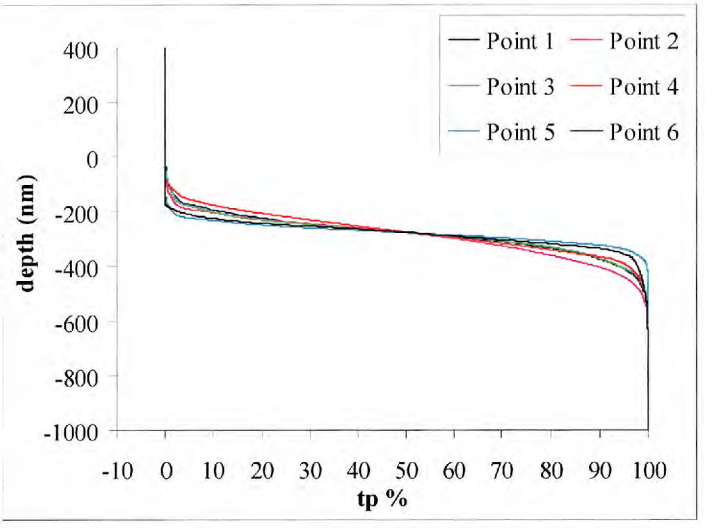


Figure A.5 Bearing ratio plots of the 2 mm thick stainless steel substrate polished with 1 µm diamond paste.

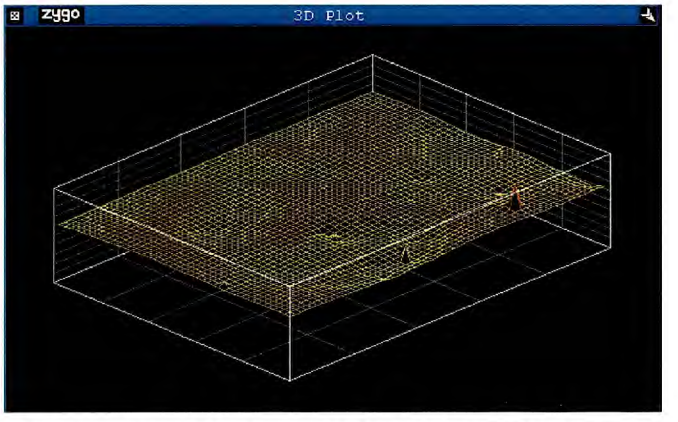


Figure A.6 3D plot of the surface of the 2 mm thick stainless steel substrate polished with 1 µm diamond paste. This area is 1.46 mm x 1.10 mm and the height of the block is 80 µm.

iii) Surface polished with 3 µm diamond paste

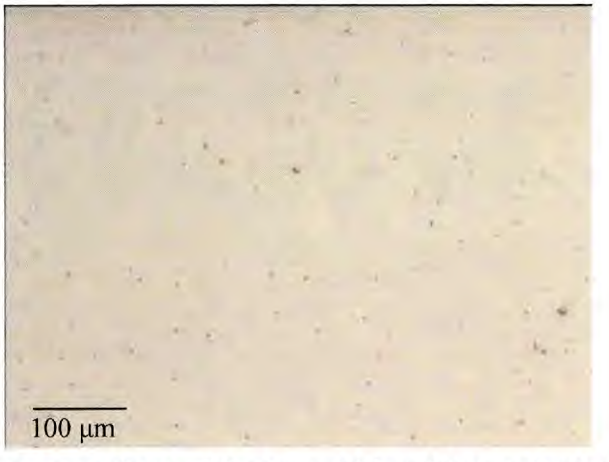


Figure A.7 Optical microscopy picture of the 2 mm thick stainless steel substrate surface polished with 3 µm diamond paste.

Table A.3 Values for the 2 mm thick stainless steel substrate polished with 3 µm diamond paste.

Point	1	2	3	4	5	6	Average
Rms (µm)	0.152	0.058	0.053	0.061	0.049	0.071	0.07 ± 0.02
Ra (µm)	0.099	0.030	0.032	0.044	0.027	0.053	0.04 ± 0.02

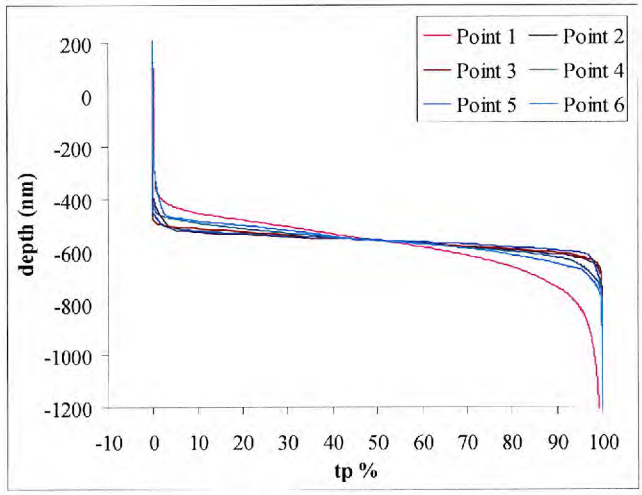


Figure A.8 Bearing ratio plots of the 2 mm thick stainless steel substrate polished with 3 µm diamond paste.

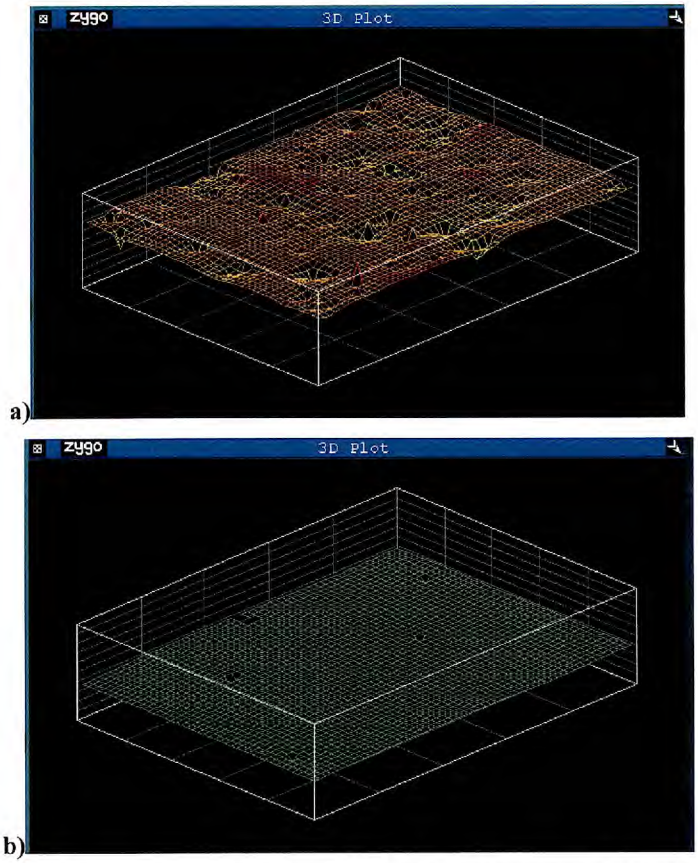


Figure A.9 3D plots of the surface a) in point 1, b) in the major area of the 2 mm thick stainless steel AISI 316L substrate polished with 3µm diamond paste. Each point has an area of 1.46 mm x 1.10 mm and the height of the block is 80 µm.

The stainless steel surface mechanically polished with 3 μm diamond paste was quite smooth, as shown in Figure A.7. Six points of this surface were analyzed obtaining the bearing ratio plots shown in Figure A.8 and the values in Table A.3. From these data two different areas can be distinguished: point 1 in which the surface appeared to be quite rough (see 3D plot in Figure A.9 a)) and the rest of the surface that seems to be flat and smooth (see 3D plot in Figure A.9 b)). The small differences that can be observed in the bearing ratio plots for points 2 to 6 (Figure A.8) can be explained considering the microscopic tilting of the surface.

iv) Surface ground with 800 grit SiC paper

Table A.4 Roughness values for the 2 mm thick stainless steel ground with 800 grit SiC paper.

Point	1	2	3	4	5	6	7	8	9	Average
rms (μm)	0.261	0.250	0.253	0.241	0.240	0.260	0.253	0.233	0.230	0.25 ± 0.01
Ra (μm)	0.182	0.171	0.172	0.162	0.162	0.181	0.174	0.153	0.148	0.17 ± 0.01

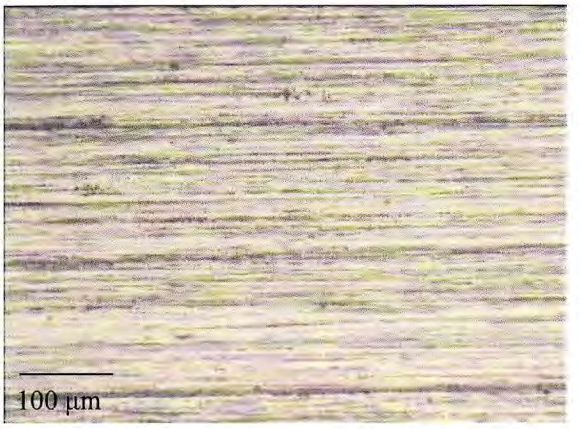


Figure A.10 Optical microscopy picture of the 2 mm thick stainless steel substrate surface ground with 800 grit SiC paper.

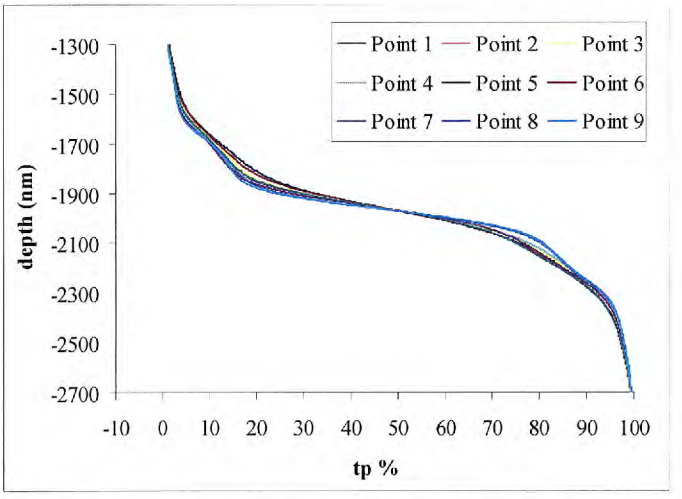


Figure A.11 Bearing ratio plots of the surface of the 2 mm thick stainless steel substrate ground with 800 grit SiC paper.

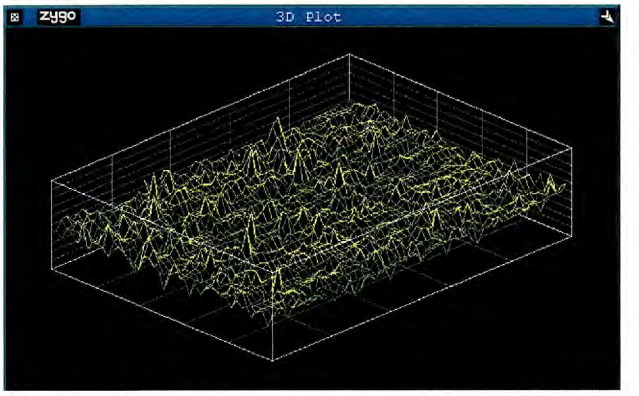


Figure A.12 3D plot of the surface of the 2 mm thick stainless steel AISI 316L substrate ground with 800 grit SiC paper. This area is 1.46 mm x 1.10 mm and the height of the block is 80 µm.

The surface ground with 800 grit SiC paper presented aligned scratches, as shown in Figure A.10. The surface was analyzed in 9 points obtaining the bearing ratio plots shown in Figure A.11 and the data listed in Table A.4. Analysing these data it resulted that the surface was uniform over the sample and it can be represented by the 3D plot shown in Figure A.12.

Appendix 2. Chemical treatments on stainless steel substrates employed for nickel deposition.

A) Chemical etching with 10% H_2SO_4

i) Surface as-received

From the analysis of the rms and Ra values reported in Table B.1 and of the bearing ratio plots, it seemed that the surface roughness of the as-received sample before and after chemical etching with a 10% H_2SO_4 solution for 30 s was quite uniform in the whole sample (bearing ratio plots completely overlapped).

Table B.1 Roughness values of as-received stainless steel samples before and after chemical etching with 10% H_2SO_4 for 30 s.

	Before etching		*After etching with a solution 10% of H_2SO_4 for 30 s*	
Point	rms (μm)	Ra (μm)	rms (μm)	Ra (μm)
1	0.322	0.198	0.297	0.168
2	0.312	0.172	0.311	0.177
3	0.306	0.176	0.294	0.167
4	0.313	0.173	0.288	0.161
5	0.324	0.181	0.316	0.179
6	0.299	0.166	0.297	0.161
7	0.297	0.168	0.336	0.187
8	0.296	0.166	0.303	0.172
9	0.293	0.173	0.305	0.167
Average	0.31 ± 0.01	0.17 ± 0.01	0.31 ± 0.01	0.171± 0.009

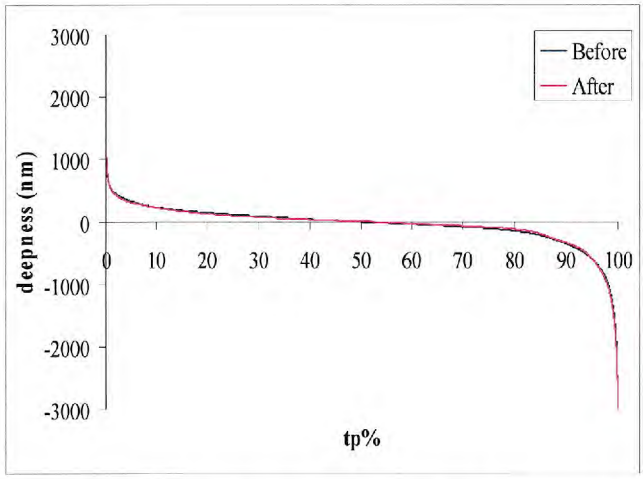


Figure B.1 Bearing ratio plots of the as-received stainless steel substrate surface before and after chemical etching with 10% H_2SO_4 for 30 s.

In order to evaluate the effect of chemical etching on the surface roughness, the roughness values (rms and Ra) obtained before and after chemical etching (Table B.1) and a

bearing ratio plot obtained before etching and one after etching, chosen as representative of the whole surface, were compared (Figure B.1). The rms and Ra values did not changed with the chemical treatment (data significantly similar using t-test) and the bearing ratio plots were completely overlapped, therefore it is possible to assert that the treatment with a solution of 10% of H_2SO_4 for 30 s did not influence the roughness of the as-received surface.

ii) Surface ground with 800 grit SiC

Table B.2 Roughness values of stainless steel AISI 316L samples ground with 800 grit SiC paper before and after chemical etching with 10% H_2SO_4 for 30 s.

	Before etching		*After etching with a solution 10% of H_2SO_4 for 30 s*	
Point	rms (μm)	Ra (μm)	rms (μm)	Ra (μm)
1	0.370	0.267	0.366	0.266
2	0.323	0.238	0.322	0.241
3	0.301	0.225	0.313	0.229
4	0.291	0.215	0.289	0.217
5	0.306	0.225	0.306	0.227
6	0.331	0.240	0.322	0.238
7	0.310	0.225	0.306	0.223
8	0.303	0.224	0.299	0.221
9	0.298	0.222	0.302	0.228
Average	0.31 ± 0.02	0.23 ± 0.02	0.31 ± 0.02	0.23 ± 0.01

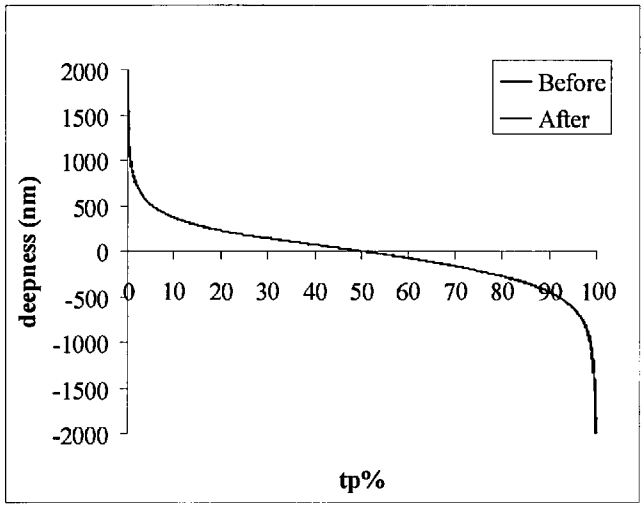


Figure B.2 Bearing ratio plots of the stainless steel AISI 316L substrate surface ground with 800 grit SiC paper before and after chemical etching with 10% H_2SO_4 for 30 s.

From the comparison of the rms and Ra values (Table B.2) and the analysis of the bearing ratio plots it seemed that the surface roughness of the sample ground with 800 grit SiC paper before and after chemical etching with a solution 10% of H_2SO_4 for 30 s was quite uniform in the whole sample. In order to evaluate the effect of chemical etching on the surface roughness, the bearing ratio plot in one point of the sample before etching was compared with one obtained after etching, considering the two plots as representative of the whole surface in

the two conditions. The two plots, shown in Figure B.2, were completely overlapped and therefore it was possible to affirm that the treatment with a solution of 10% H_2SO_4 for 30 s did not influence the roughness of the surface ground with 800 grit SiC paper. The same conclusion was also reached comparing the rms and Ra values before and after the chemical etching treatment (data significantly similar using t-test), listed in Table B.2.

B) Chemical etching with 18% HCl

i) Surface as-received

Considering the rms and Ra values listed in Table B.3 and the bearing ratio plots, it resulted that the surface roughness of the sample as-received before and after chemical etching with a 18% solution of HCl for 5 min was uniform in the whole sample.

Table B.3 Roughness values of the as-received stainless steel AISI 316L samples before and after chemical etching with 18% HCl for 5 min.

	Before etching		*After etching with a solution 18% of HCl for 5 min*	
Point	rms (μm)	Ra (μm)	rms (μm)	Ra (μm)
1	0.337	0.198	0.330	0.197
2	0.317	0.205	0.335	0.191
3	0.313	0.179	0.328	0.190
4	0.351	0.201	0.350	0.197
5	0.325	0.192	0.326	0.187
6	0.338	0.189	0.357	0.201
7	0.318	0.185	0.314	0.211
8	0.326	0.179	0.334	0.194
9	0.327	0.183	0.340	0.185
Average	0.33 ± 0.01	0.19 ± 0.01	0.33 ± 0.01	0.195 ± 0.008

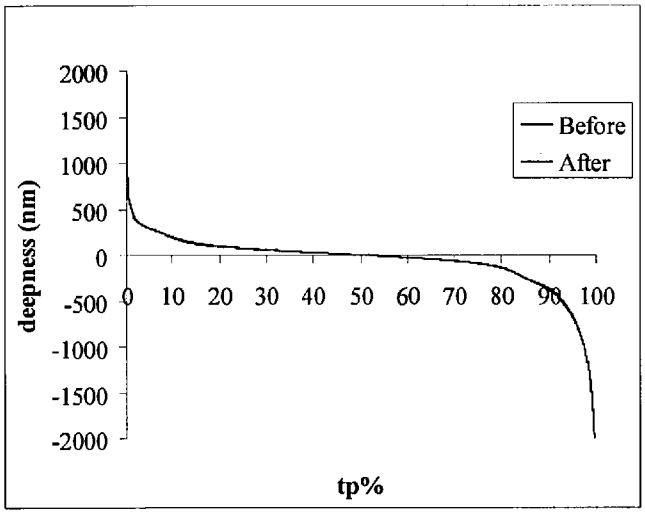


Figure B.3 Bearing ratio plots of the as-received stainless steel substrate surface before and after chemical etching with 18% HCl for 5 min.

Comparing two bearing ratio plots representative of the whole surface (Figure B.3), and the rms and Ra values (Table B.3) obtained before and after chemical etching with hydrochloric acid, it seemed that this treatment did not modify the surface roughness (bearing ration plots completely overlapped and rms and Ra data significantly similar using t-test).

ii) Surface ground with 800 grit SiC paper

Table B.4 Roughness values of the stainless steel sample ground with 800 grit SiC paper before and after chemical etching with 18% HCl for 5 min.

	Before etching		*After etching with a solution 18% of HCl for 5 min*	
Point	rms (μm)	Ra (μm)	rms (μm)	Ra (μm)
1	0.310	0.256	0.292	0.217
2	0.283	0.210	0.274	0.202
3	0.292	0.214	0.288	0.212
4	0.292	0.216	0.288	0.214
5	0.283	0.210	0.280	0.208
6	0.300	0.222	0.300	0.222
7	0.295	0.220	0.299	0.223
8	0.285	0.213	0.290	0.216
9	0.287	0.213	0.283	0.209
Average	0.292 ± 0.009	0.22 ± 0.01	0.288± 0.008	0.214± 0.007

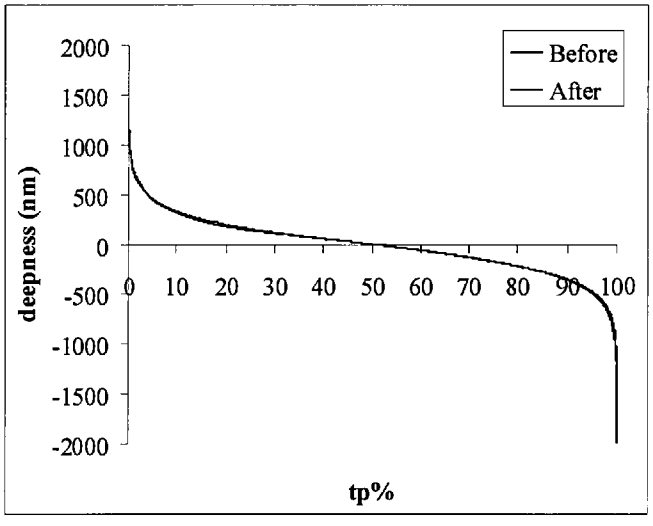


Figure B.4 Bearing ratio plots of the surface of the stainless steel substrate ground with 800 grit SiC paper before and after chemical etching with 18% HCl for 5 min.

From the analysis of the rms and Ra data reported in Table B.4 and of the bearing ratio plots the surface roughness of the sample ground with 800 grit SiC paper before and after chemical treatment with HCl resulted uniform. Therefore it was possible to compare a bearing ratio plot in one point of the sample before etching with one obtained after etching, considering these two plots representative of the whole surface in the two conditions. The two bearing ratio curves shown in Figure B.4 were completely overlapped and the rms and Ra values (Table B.4)

before and after chemical etching were significantly similar using t-test; therefore it could be concluded that the chemical etching did not modify the surface roughness.

C) Chemical etching with 25% HNO_3

i) Surface as-received

Table B.5 Roughness values of the as-received stainless steel AISI 316L samples before and after chemical etching with 25% HNO_3 for 10 s.

	Before etching		*After etching with a solution 25% of HNO_3 for 10 s*	
Point	rms (μm)	Ra (μm)	rms (μm)	Ra (μm)
1	0.371	0.198	0.405	0.219
2	0.399	0.205	0.377	0.198
3	0.354	0.188	0.380	0.210
4	0.399	0.208	0.370	0.211
5	0.385	0.200	0.389	0.209
6	0.372	0.192	0.396	0.205
7	0.365	0.196	0.386	0.204
8	0.404	0.208	0.393	0.109
9	0.384	0.200	0.408	0.218
Average	0.38 ± 0.02	0.199 ± 0.007	0.39 ± 0.01	0.207 ± 0.009

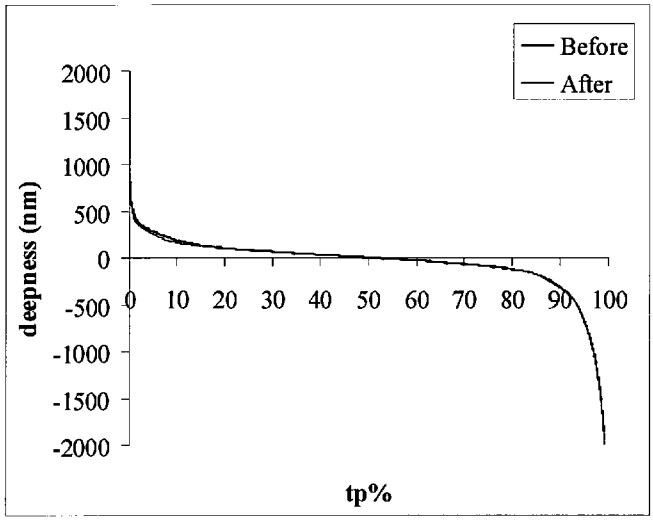


Figure B.5 Bearing ratio plots of the as-received stainless steel AISI 316L substrate surface before and after chemical etching with 25% HNO_3 for 10 s.

From the analysis of the rms and Ra data (see Table B.5) and of the bearing ratio plots, it seemed that the surface roughness of the as-received sample before and after chemical treatment with nitric acid were uniform. A bearing ratio plot of the sample before etching, representative of the whole surface, was compared with one after etching and the two curves (Figure B.5) were completely overlapped. The rms and Ra values (Table B.5) before and after chemical etching were significantly similar using t-test; therefore it could be concluded that the chemical etching did not modify the surface roughness of the as-received sample.

ii) Surface ground with 800 grit SiC paper

Table B.6 Roughness values of the stainless steel sample ground with 800 grit SiC paper before and after chemical etching with 25% HNO_3 for 10 s.

	Before etching		*After etching with a solution 25% of HNO_3 for 10 s*	
Point	rms (μm)	Ra (μm)	rms (μm)	Ra (μm)
1	0.330	0.250	0.312	0.245
2	0.326	0.244	0.295	0.223
3	0.315	0.235	0.313	0.238
4	0.308	0.233	0.307	0.231
5	0.311	0.234	0.294	0.221
6	0.341	0.257	0.342	0.223
7	0.312	0.243	0.323	0.246
8	0.327	0.246	0.312	0.236
9	0.331	0.248	0.340	0.254
Average	0.32 ± 0.01	0.243 ± 0.008	0.32 ± 0.02	0.24 ± 0.01

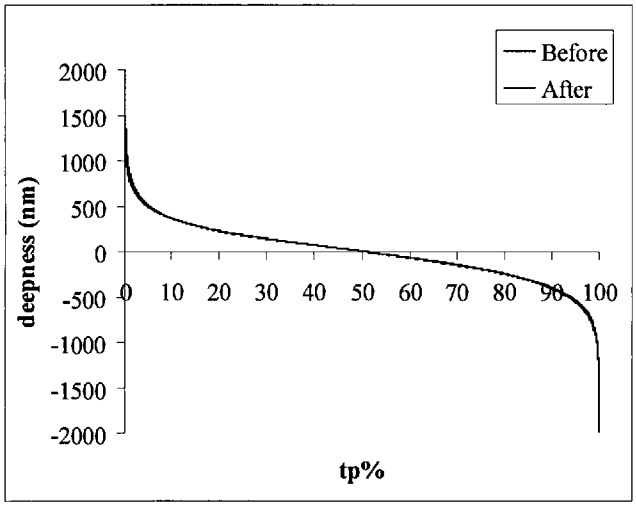
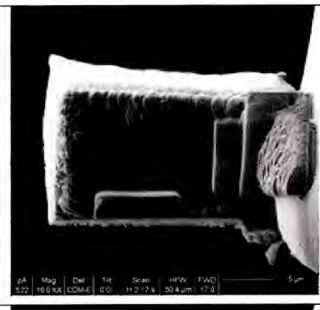
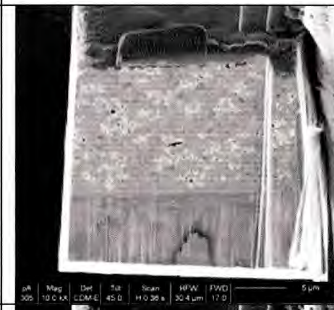
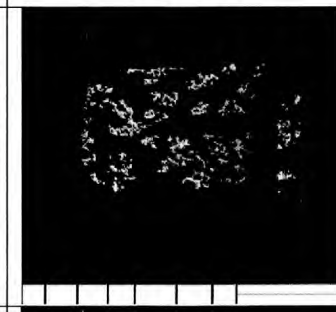
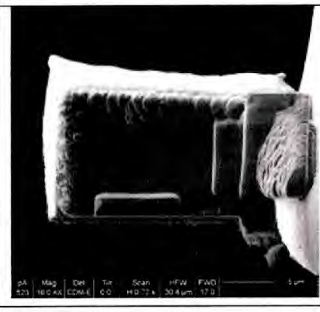
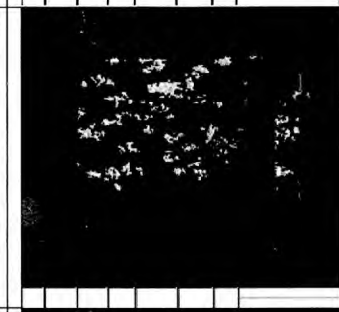
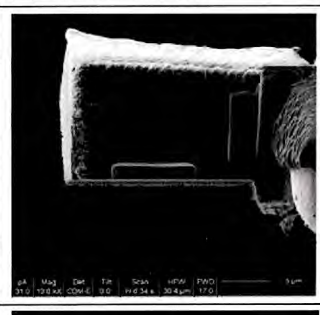
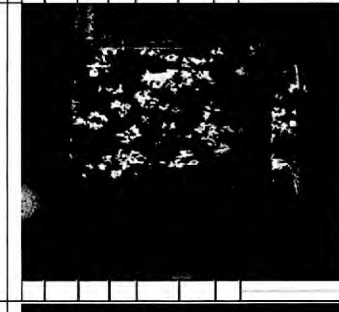
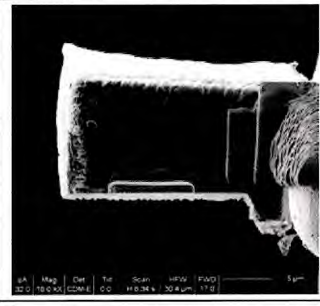
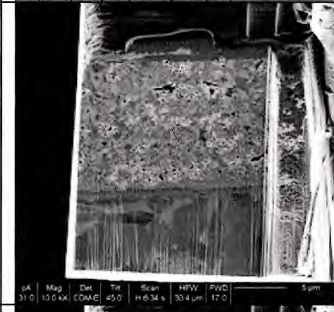
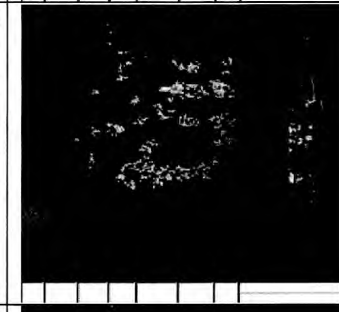
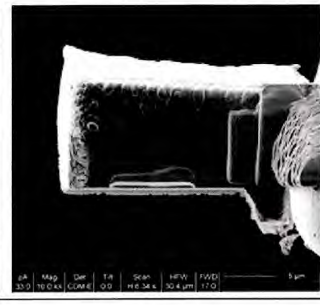
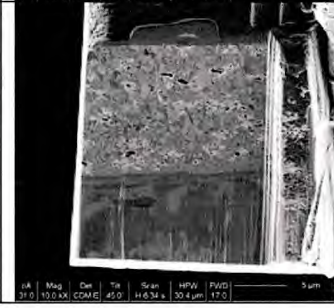
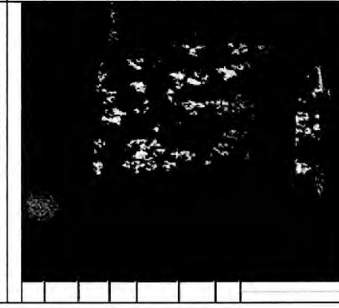


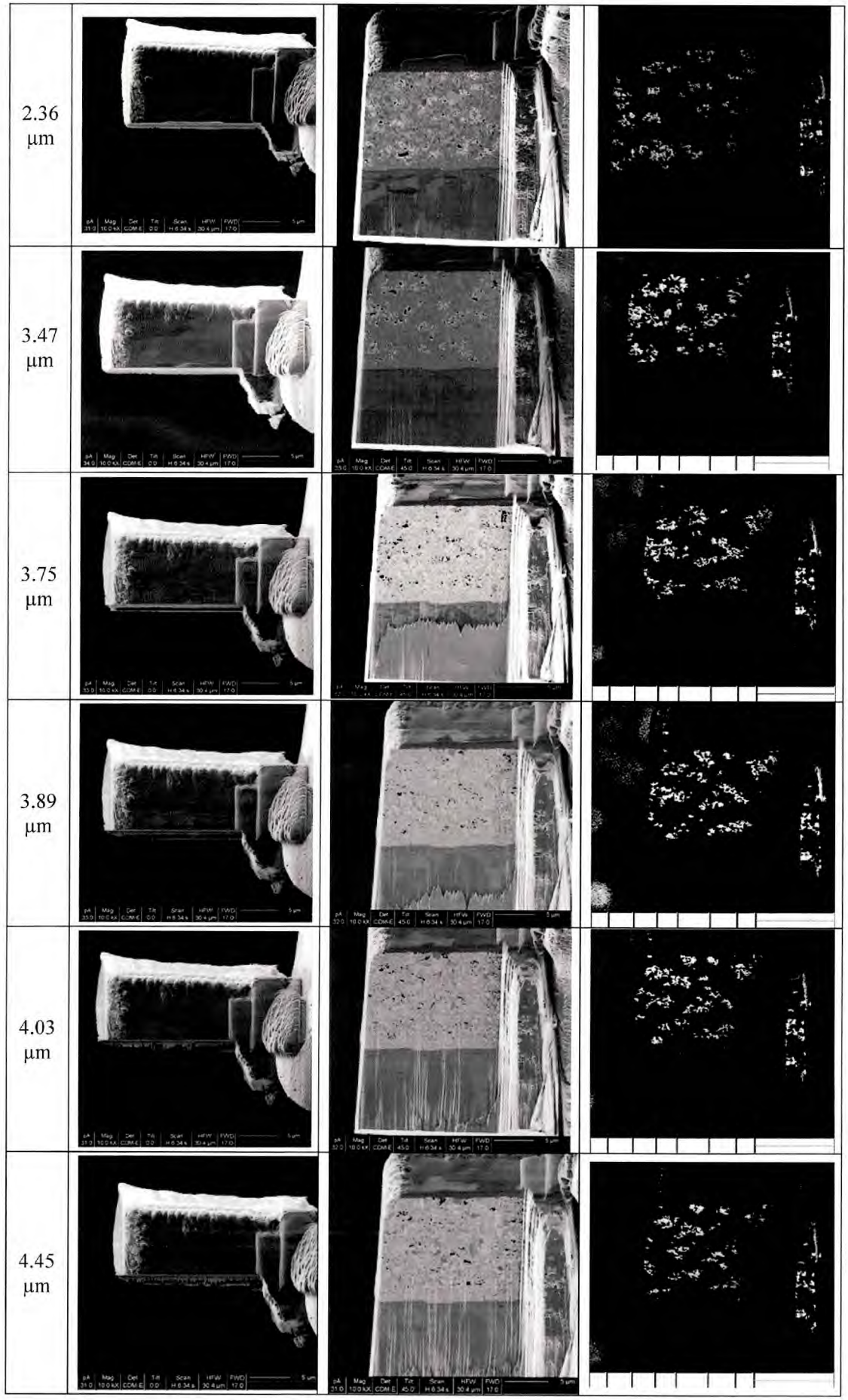
Figure B.6 Bearing ratio plots of the stainless steel substrate surface ground with 800 grit SiC paper before and after chemical etching with 25% HNO_3 for 10 s.

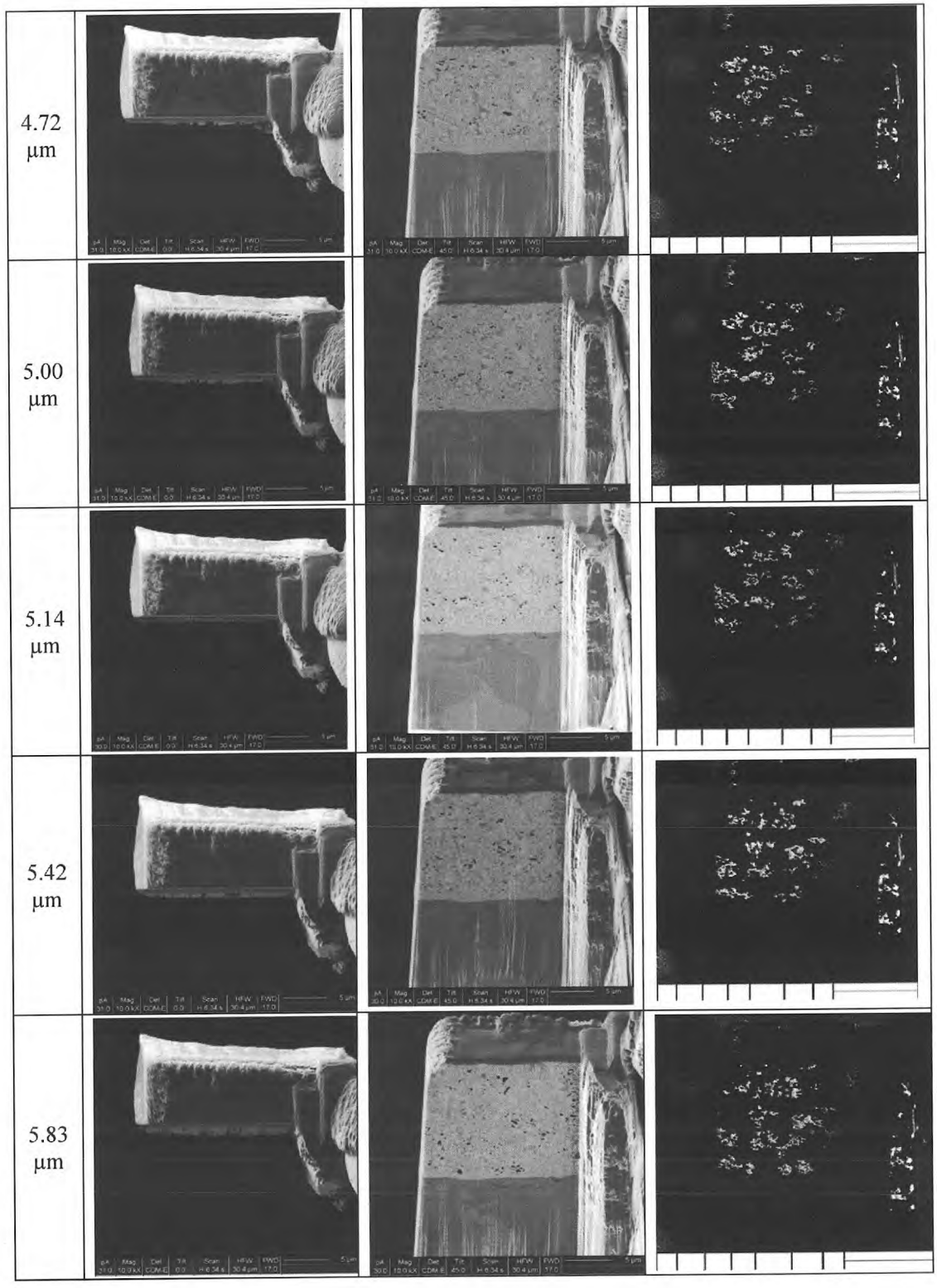
Analysing the rms and Ra values (Table B.6) and the bearing ratio plots it seemed that the roughness of the sample ground with 800grit SiC paper before and after the chemical treatment were uniform. The rms and Ra data obtained before and after chemical etching with a 25% solution of HNO_3 for 10 s were significantly similar using t-test and the two bearing ratio plots acquired before and after the treatment, chosen as representative of the whole surface, were completely overlapped as shown in Figure B.6. Therefore it was concluded that the roughness of the surface ground with 800 grit SiC did not change due to the chemical treatment with nitric acid.

Appendix 3. 3D reconstruction of a Ni-Al_2O_3 composite coating

Table C.1 List of all the FIB-SIMS images used for the 3D reconstruction of a Ni-sub-micron-Al_2O_3 composite coatings

Cut out	Top	Surface	SIMS Al mapping
0			
0.42 µm			
0.97 µm			
1.53 µm			
2.08 µm			


2.36 µm
3.47 µm
3.75 µm
3.89 µm
4.03 µm
4.45 µm


4.72 µm
5.00 µm
5.14 µm
5.42 µm
5.83 µm

Appendix 4. List of conference presentations and publications originated from this work

Poster presentations:

- Euromat 2007, Nuremberg (Germany), 10th-13th September 2007. Poster title: "Deposition of Composite Coatings on Metals using Electrochemical Processes".
- Annual meeting of the Composite Centre, Imperial College London, London (UK), 25th September 2007. Poster title: "Deposition of Composite Coatings on Metals using Electrochemical Processes".
- 3rd International Conference on Electrophoretic Deposition: Fundamentals and Applications, Awaji Yumebutai International Conference Center, Hyogo, (Japan), 5th-9th October 2008. Poster title: "Electrophoretic deposition of PEEK and PEEK-Alumina composite coatings on stainless steel".

Published papers:

- Ilaria Corni, Mary P. Ryan and Aldo R. Boccaccini, "Electrophoretic deposition: from traditional ceramics to nanotechnology." Journal of the European Ceramic Society, 28, 2008, 1353-1367.
- Ilaria Corni, Nico Neumann, Dietmar Eifler and Aldo R. Boccaccini, "Polyetheretherketone (PEEK) coatings on stainless steel by electrophoretic deposition." Advanced Engineering Materials, 6, 2008, 559-564.
- Ilaria Corni, Nico Neumann, Saša Novak, Katja König, Paolo Veronesi, Qizhi Chen, Mary P. Ryan, Aldo R. Boccaccini, "Electrophoretic deposition of PEEK-nano alumina composite coatings on stainless steel." Surface and Coating Technology, 203, 2009, 1349-1359.
- Ilaria Corni, Maria Cannio, Marcello Romagnoli, Aldo R Boccaccini, "Application of a Neural Network approach to the Electrophoretic Deposition of PEEK-alumina composite coatings." Materials Research and Bulletin, in press.